Imperial College London

Department of Earth Science and Engineering
Department of Chemistry

Electrode, Electrocatalyst and Electrolyte Development for Hybrid Redox Flow Batteries

Benedict Arthur Simon

March 2022

Submitted in part fulfilment of the requirements for the degree of
Doctor of Philosophy at Imperial College London

I hereby declare that this thesis and the work reported herein was composed by and originated entirely from me. Information derived from the published and unpublished work of others has been acknowledged in the text and references are given in the lists of references.

Benedict Arthur Simon
March 2022

The copyright of this thesis rests with the author and is made available under a Creative Commons Attribution Non-Commercial No Derivatives licence. Researchers are free to copy, distribute or transmit the thesis on the condition that they attribute it, that they do not use it for commercial purposes and that they do not alter, transform or build upon it. For any reuse or redistribution, researchers must make clear to others the licence terms of this work.

Abstract

The development of new electrochemical devices and their subsequent widespread adoption alongside our energy grids is critical to support the incoming wave of renewable energy generation and the transition to net zero. Hybrid redox flow batteries are a promising alternative energy storage technology that could ultimately provide inexpensive and sustainable large scale energy storage solutions compared to their lithium-based counterparts. Technological improvements rely on improved understanding of the processes occurring in these devices. This thesis focuses on three aspects essential to all electrochemical devices – the electrode, electrocatalyst and electrolyte. First, electrochemical and tomographic imaging analyses are combined to understand the effect of electrode microstructure properties on the performance of a non-aqueous redox flow battery. With the help of a one dimensional model, mass-transfer coefficients are gathered from the experimentally determined polarisation curves and affirm the results positively linking electrode permeability to overall cell performance. Second, the synthesis and optimisation of a multifunctional, nitrogen-doped carbon based electrocatalyst is outlined. The active site of the electrocatalyst is examined using a suite of physical characterisation techniques and is shown to have intriguing versatility across the pH spectrum towards catalysing both oxygen and hydrogen fundamental reactions. This catalyst is then tested, with a variety of success, in two fuel cell devices and, alongside the electrodes tested in the first section, in a hydrogen-manganese hybrid redox flow battery. Finally, the aqueous liquid electrolyte involved in this hybrid redox flow battery is scrutinised. Two in-operando analytical techniques are developed, providing improved handles on real-time solution-phase manganese species concentration in the electrolyte. The production of solid manganese oxides significantly alters solution equilibria making the deconvolution of electrochemical and adjacent, simultaneous chemical processes complex.

Acknowledgments

I would sincerely like to thank my supervisors – Profs. Anthony Kucernak and Nigel Brandon – for giving me the opportunity and freedom to develop as a researcher and learn so much electrochemistry. Anthony, thank you for welcoming me into your group and for humouring me as I went down countless rabbit-holes. I really appreciate the patience, time and effort you have spent on coaxing me out of them, teaching me and suggesting new avenues to explore. Nigel, thank you for being so supportive, positive and open throughout my PhD and frank when needed. Thanks must also go to Dr. Peter Klusener for checking in and asking the tough questions throughout the PhD and to Shell International BV. for providing financial support.

I owe a huge amount to all the members of the Kucernak group, past and present. You always made 'the day-to-day' worth it. Special thanks must go to (in alphabetic order) Andres, Asad, Colleen and Jack – primarily for your friendship – I am in huge debt to you all and I hope to repay you over the coming years. Academically, Andres and Asad, thank you so much for (essentially) supervising me at times – I really appreciated your positivity, and the feeling of working in a team with you both made for some of my most enjoyable (nerdy) research moments. Colleen, thank you for permanently having snacks available and really for being an emotional support when things (big and small) were difficult. It was great spending early mornings in the lab with you – I don't know if I could have done it without you. Jack, thank you for just being an all-round hero – the Kucernak group and its machines are very lucky to have you.

Andrea and Cata – I am so grateful to you both for keeping 'the MIT project' alive, for helping me get it over the line and for tolerating me over the years. It has been a privilege to work with you both – I've loved it – and I am lucky to have you as friends. Harry and Charlotte – there is too much to thank you two for, but coffee mornings, lunches and general 'chat' with you two softies has certainly been morale-boosting. No, really – you two are great and have been huge supports to me over the years – I look forward to many more pints with you both in the years to come. Thanks to Harvey, Rid, Kevin, Katherine and Ashkan for their friendly faces and practical help along the way too.

I am extremely lucky to have so many good friends. For the sake of my word-count, I can't include anecdotes about each of you, but the following certainly deserve a mention: Imo,

Marina, Harry, Ed, Marcus, Ali, Jez, Beatrix, Tom, Jacob, Kench, Dani, Rachel, Amy, Liana, Jenny, Cory, Thomas, Myles, Evett, Harvey, Ben, Amelia, Max, Murdoch, Jack, Hole, Ali, Eliza, Grace, Katy, Jack and the rest of the Balliol lot and Shlondon members. Thank you all for your friendship, support and love.

Of course, some people have to put up with me more than others so, firstly to James who I've been lucky to call my landlord and housemate for the duration of this PhD. Thank you for your tolerance and calm with me over the course of these four years – I know it can't have been easy. I look forward to hosting many more over-the-top parties with you in the coming years. Josh, Will and Ross, thank you for being the excellent people you are and for being so thoughtful, frank and generous over the years – it is a privilege to have you all as some of my nearest and dearest. Erin thank you for being such a great companion from across the pond – I have loved the long phone calls over the years and look forward to many in-person dinners, drinks and 'occasions' in future. Hector, as 'quite a big name *in the London art scene,' thank you for making time to see and entertain me – I am looking forward to benefitting from your newfound penchant for cooking. Iona – thank you for all the dinners, walks and for always being there for me. Ed, thank you for tolerating my complete uselessness over the years, for always being good for a pint and being an all-round excellent guy – I hope we can 'not contribute' to many more pub quizzes in future. Richard and Archie thank you for being such high quality, reliable and grounded mates over the years – I look forward to many more to come. Soph, thank you for your advice, generosity and for always making time for me. Matt, thank you for all the holidays, sport, dinners and drinks over the years and for always, always bringing out my competitive side. Evie – thank you for making the last year so exciting, for putting up with and supporting me lovingly, through the highs and lows and for having (often completely unfounded) confidence in me.

You are all very important to me and I love you all very much.

To Granny, Norma and all the dogs – while sadly none of you can read this for a variety of reasons, it would feel wrong for you not to be mentioned – you have all been such important parts of my life – I am so grateful to you all. Grandpa – I want to thank you for being such a brilliant role model and for making me laugh with your funny emails – I love you and think of you a lot. Finally, my family: Gog and Bean thank you for being perfectly excellent little sisters and for being a permanent source of support (and entertainment) – always able to put a smile

on my face. Mum and Dad, I have you to thank for everything. You have showered me with every form of support there is, and I am so grateful. I love you both with all your imperfection. I wouldn't be me without you four, so thank you.

There is only so much one can say in Acknowledgements – I could (and would like to) write a whole individual 'acknowledgements' for most of the people mentioned here. In the interest of time we had better get on with it now, though.

| For Mum, Dad, Lucy and Emma |

“It always seems impossible until it’s done” – Nelson Mandela

“If you can meet with Triumph and Disaster
And treat those two impostors just the same;
...
—you’ll be a Man, my son” – Rudyard Kipling

"It's more fun to talk with someone who doesn't use long complicated words but rather short, easy words like 'What about lunch?' – A. A. Milne.

Contents

Abstract **3**

Acknowledgments **4**

Contents **10**

List of figures **16**

List of tables **28**

Abbreviations **30**

Chapter 1: Introduction **35**

Part I: Overview **35**

1.1 Context and Motivation 35

Part II: Literature review **37**

1.2 Redox flow battery chemistry and configuration 37
1.2.1 Solvents 39
1.2.2 Phase configuration 40
1.2.2.1 Liquid-liquid 41
1.2.2.2 Liquid-solid 41
1.2.2.3 Gas-gas 42
1.2.2.4 Liquid-gas 43
1.2.3 Redox species 44
1.2.3.1 Inorganic 44
1.2.3.2 Organic 45
1.2.3.3 Gaseous 48
1.2.4 Redox flow battery-type systems 54

1.3 Materials 57
1.3.1 Electrodes 57
1.3.1.1 Porous electrode types, flow fields and RFB cell preparation 58
1.3.1.2 Characterisation 61
1.3.1.3 State of the art 64
1.3.2 Electrocatalysts 66
1.3.2.1 Types 67
1.3.2.2 Probing the active site 74
1.3.3 Separators 77
1.3.3.1 Types 77
1.3.3.2 State of the art 78

1.4 Conclusions 79

Part III: Thesis outline 81

1.5 Aims 81
1.5.1 Questions and objectives 81

1.6 Thesis structure 83

1.7 References 84

Chapter 2: Experimental methods and characterisation 94

2.1 Physical methods 94
2.1.1 Scanning electron microscopy (SEM) 94
2.1.2 Transmission electron microscopy (TEM) 95
2.1.3 Energy dispersive X-ray spectroscopy (EDX) 97
2.1.4 X-ray diffraction (XRD) 98
2.1.5 X-ray photoelectron spectroscopy (XPS) 99
2.1.6 X-ray absorption spectroscopy (XAS) 99
2.1.6.1 XAS data processing 101
2.1.7 X-ray computed tomography (XCT) 103
2.1.8 Ultraviolet-visible spectroscopy (UV-vis) 104
2.1.9 Electron paramagnetic resonance (EPR) 105
2.1.10 Inductively coupled plasma mass spectrometry (ICP-MS) 107
2.1.11 Nitrogen physisorption – Brunauer–Emmett–Teller (BET) 107
2.1.12 Thermal treatments and activation methods 108

2.2 Electrochemical methods 109
2.2.1 Theory – kinetics and electrokinetics 109
2.2.2 Voltammetry – cyclic / linear sweep (CV / LSV) 114
2.2.3 Electrochemical impedance spectroscopy (EIS) 115
2.2.4 Assembly of electrochemical devices 117
2.2.4.1 Three electrode cell 117
2.2.4.2 Redox flow batteries 117
2.2.5 Rotating (ring) disk electrode (RDE and RRDE) 119
2.2.5.1 Theory 119
2.2.5.2 Application (performance parameters) 121
2.2.6 Chrono- and polarisation methods 122
2.2.6.1 Theory 122
2.2.6.2 Application (performance parameters) 124

2.3 References 124

Chapter 3: Investigating the effect of solvent properties and electrode microstructure on the performance of a symmetric organic redox flow battery 126

3.1 Introduction 126

3.2 Methodology 129
3.2.1 Electrolyte preparation 129

3.2.2 Electrolyte characterisation 130
3.2.3 Electrode and separator preparation 131
3.2.4 Flow cell preparation 132
3.2.5 Flow cell experiments 133
3.2.6 X-ray computed tomography measurements 134
3.2.7 Segmentation technique 135
3.2.8 Pore network model 138
3.2.9 One-dimensional continuum model 139
3.3 Results and discussion 141
3.3.1 Microstructural analysis 142
3.3.2 Pressure drop and permeability 146
3.3.3 Zero-gap RFB performance as a function of electrode and solvent 147
3.3.4 Mass-transfer coefficients 156
3.4 Conclusions 161
3.5 Appendix 163
3.5.1 Species diffusivity calculation 163
3.5.2 SEM-EDX fluorine absence confirmation 164
3.5.3 Resistance contributions to polarisation measurements 164
3.5.4 Complete EIS data and ECM fitting 165
3.5.5 ECM fittings and EIS results 167
3.5.6 1D model parameters 168
3.5.7 Polarisation results – experimental and model fit 168
3.5.8 Polarisation results and 1D model fitting 170
3.5.9 Correlating microstructural properties with performance metrics 171
3.5.10 Electrical and pumping power assessment 171
3.5.11 Distribution of concentration, overpotential, and ionic current density 173
3.6 References 174
Chapter 4: Synthesis and characterisation of a low iridium, ZIF-67-based multifunctional electrocatalyst 178
4.1 Introduction 178
4.2 Methodology 182
4.2.1 Catalyst preparation 182
4.2.1.1 Carbon catalysts 182
4.2.1.2 Commercial iridium-based catalysts 183
4.2.2 Ink preparation 183
4.2.3 Physical characterisation 183
4.2.3.1 Nitrogen physisorption (Brunauer–Emmett–Teller – BET) 183
4.2.3.2 Electron microscopy 184
4.2.3.3 X-ray diffraction (XRD) 184
4.2.3.4 X-ray photoelectron spectroscopy (XPS) 184
4.2.3.5 X-ray absorption spectroscopy (XAS) 184

4.2.3.6 Inductively coupled plasma – mass spectrometry (ICP-MS) 185
4.2.4 Electrochemical characterisation 185
4.3 Results and discussion 187
4.3.1 Synthesis and initial characterisation 187
4.3.2 Physical characterisation 192
4.3.3 Catalyst performance 202
4.4 Conclusions 209
4.4.1 Future work 210
4.4.1.1 Synthesis improvements using sustainable materials 210
4.4.1.2 Active site understanding 210
4.4.1.3 Catalyst capability 211
4.5 Appendix 211
4.5.1 Supplementary information for synthesis optimisation 211
4.5.2 Supplementary physical characterisation 214
4.5.3 Supplementary electrochemical measurements 215
4.6 References 217
Chapter 5: Application of ZIF-based electrocatalysts and various electrodes in multiple electrochemical devices 220
5.1 Introduction 220
5.2 Methodology 222
5.2.1 Alkaline anion exchange membrane fuel cell 222
5.2.1.1 Electrode preparation 222
5.2.1.2 Fuel cell assembly 224
5.2.1.3 Fuel cell experiments 224
5.2.2 Proton exchange membrane fuel cell 226
5.2.2.1 Electrode preparation 226
5.2.2.2 Fuel cell assembly 227
5.2.2.3 Fuel cell experiments 227
5.2.3 Manganese / hydrogen hybrid redox flow battery 229
5.2.3.1 Electrode preparation 229
5.2.3.2 Electrolyte preparation 229
5.2.3.3 Hybrid redox flow battery assembly 230
5.2.3.4 Hybrid redox flow battery experiments 230
5.3 Results and discussion 233
5.3.1 Alkaline anion exchange membrane fuel cell 233
5.3.2 Proton exchange membrane fuel cell 235
5.3.3 Manganese – hydrogen hybrid redox flow battery 237
5.4 Conclusions 240
5.4.1 Future work 242
5.4.1.1 AEMFC 242

5.4.1.2 PEMFC 242
5.4.1.3 Mn/H_2 243
5.5 Appendix 243
5.5.1 Supplementary catalyst layer preparation 243
5.5.2 Manganese hydrogen hybrid redox flow battery setup 244
5.6 References 246
Chapter 6: In-operando techniques examining manganese speciation during manganese / hydrogen hybrid redox flow battery operation 248
6.1 Introduction 248
6.1.1 Manganese chemistry review 251
6.1.1.1 Chemical speciation and transformations of manganese species 252
6.1.1.2 Electrochemical transformations of manganese species 257
6.1.2 Titanium chemistry review 260
6.1.3 Manganese-titanium electrolyte 263
6.1.4 In-operando techniques for electrochemical systems 265
6.2 Methodology 267
6.2.1 Electrolyte preparation 267
6.2.1.1 Speciation in a titanium / sulfate system 268
6.2.2 Hybrid-redox flow battery setup 269
6.2.3 Hybrid redox flow battery experiments 270
6.2.4 Electrolyte characterisation 271
6.2.5 In-operando techniques 272
6.2.5.1 In-operando UV-vis spectroscopy 273
6.2.5.2 In-operando electron paramagnetic resonance spectroscopy 274
6.2.6 Thermodynamic analysis of manganese speciation as a function of state of charge 275
6.3 Results 276
6.3.1 Standard charging, discharging and conductivity analysis 276
6.3.2 Voltage efficiency as a function of state of charge 280
6.3.3 Overcharge of the hybrid redox flow battery 283
6.3.4 Deconvolution of speciation chemistry as a function of state of charge 290
6.3.4.1 In-operando EPR measurements 290
6.3.4.2 In-operando UV-vis measurements 296
6.3.4.3 Combining in-operando techniques 301
6.3.4.4 Transient analysis using UV-vis and EPR 302
6.4 Discussion 307
6.4.1 Systematic thermodynamic modelling of speciation 307
6.4.2 Interpretation of results 315
6.5 Conclusions 321
6.5.1 Future work 322

6.6 Appendix 323
6.6.1 Manganese (III) stabilisation techniques 323
6.6.2 UV-vis peak comparison 324
6.6.3 EPR based manganese concentration calculations for a slow cycle 324
6.6.4 Extra EPR transients 325
6.7 References 325
Chapter 7: Conclusions 329
7.1 Final conclusions 329
7.1.1 Chapter 3 330
7.1.2 Chapter 4 331
7.1.3 Chapter 5 332
7.1.4 Chapter 6 333
7.2 Future work 334
7.2.1 Electrode development 335
7.2.2 Electrocatalyst development 335
7.2.3 Electrolyte development 336

List of figures

Figure 1.1: Illustration of a redox flow battery with schematic arrows in the membrane / separator indicating the movement of ions in either direction depending on the system and if it is charging or discharging. 38
Figure 1.2: Two examples of hybrid RFB configurations (a) membrane-free liquid-solid and (b) liquid-gas utilising a cylinder. 41
Figure 1.3: Principles of operating polymer electrolyte fuel cells (PEFCs). (a) A proton exchange membrane fuel cell (PEMFC). (b) An alkaline anion exchange membrane fuel cell (AEMFC). 43
Figure 1.4: Modified from Yang et al. with additional standard potentials of redox couples added.[73] The pink shaded region indicates the thermodynamic region in which users can operate without water splitting. From a kinetic perspective, HER and OER occur at more negative and more positive potential, respectively. 47
Figure 1.5: Visual schematic representations of the oxygen reduction reaction in alkaline via: (a) a four-electron mechanism; or, (b) a two-electron mechanism.[76,77] 50
Figure 1.6: OER mechanisms via (a) an adsorbate evolving mechanism or (b) a proposed lattice oxygen mechanism using a perovskite (ABO_3) catalyst structure in alkaline conditions.[82,84,86] Green, orange, red and grey spots represent $metal_A$, $metal_B$, oxygen and vacancies in a perovskite framework, respectively. 51
Figure 1.7: (a) Proposed iagrammatic representations of HOR mechanisms in dilute alkaline electrolyte for mono- and bi-metallic catalysts where M1 represents a metal capable of dissociative adsorption of molecular hydrogen, Mp represents a precious metal capable of forming H_{upd} in alkaline electrolyte and Mb represents a base metal site with adsorbed hydroxide species. IHP and OHP stand for the inner and outer Helmholtz plane, respectively. (b) 3D schematic using volcano plots (generated using measurements based entirely on voltammetry) to display the exchange current density as a function of the apparent hydrogen binding energy on a pH scale.[95] 53
Figure 1.8: Flow chart displaying some examples of routes to established technologies. After choosing the solvent and phase configuration, two redox species can be chosen. 54
Figure 1.9: (a) Scanning electron microscopy micrographs with a 1 mm scale bar inserted (a.i) Carbon graphite felt (GFA5, SGL),[138] (a.ii) Freudenberg carbon paper and (a.iii) AvCarb 7497 carbon cloth. (b) two 'flow-by' (b.i-ii) and two 'flow-through' (b.iii-iv) flow field types (b.i) serpentine, (b.ii) parallel, (b.iii) interdigitated and (b.iv) parallel and (c) a generalised exploded diagram modified from reference.[138] 60
Figure 1.10: (a) A standard RFB setup with different redox couples either side of a selective membrane. (b) The electrolyte flow cell is used with a stable, well-defined redox couple ensuring a single and controlled state of charge assuming rapid reversible reactions (c) The symmetric flow cell uses the same redox couple in each of the two reservoirs separated by a membrane. (d-f) are visual examples of physical characterisation and modelling tools – (d) is a 2D SEM micrograph, (e) represents modelling tools and 3D reconstruction software (TauFactor 'plug-in' yielding tortuosity factor, τ, porosity, ε, and volumetric specific surface area, VSSA, and; Avizo, respectively) and (f) is an

extension of the 3D reconstruction using the maximal-ball algorithm to estimate pore size for a pore network model (PNM). 62
Figure 1.11: (a) One application of SliceGAN in the generation of a new SOFC electrode.[163] (b) Comparison between traditional fibre electrodes and real (top right) and hypotetical new designer electrodes (bottom row).[167] (c) A diagram outlining the properties focussed on in the production of new electrospun electrode materials.[168] 65
Figure 1.12: (a) Schematic for using functionalised carbon-based ZIF starting materials for SAC synthesis.[181] (b) Crystal structures for common metal- / mixed-metal oxide electrocatalysts: from left to right, rutile (RuO_2), perovskite (ABO_3) and spinel (AB_2O_4).[207] T_d and O_h stand for tetrahedral and octahetral sites, respectively. (c) Schematic of graphitic sheet development from Ni-coated KCl moieties.[210] (d) Examples of platinum architectures used in cathode catalysts, alongside qualitative 'technology readiness level'.[185] 71
Figure 1.13: Venn diagram representing multifunctionality of catalyst types. 73
Figure 1.14: Diagrammatic representations of active site characterisation methods. (a) LHS: Progressive images of FIB-SEM milling a metal surface into a needle shaped sample for atom probe tomography;[227] and, RHS: a simplified diagram of how APT is carried out;[232] (b) In-situ spatially coherent configuration for the combination of transmission-mode synchrotron XRD and fluorescence-detected XAS;[231] (c) IL-TEM showing catalyst material 'before' and 'after' a short corrosion step;[223] and, (d) Two high mass transport systems used to assess realistic electrocatalyst capability – Top: Floating electrode schematic;[183] and, Bottom: gas accessible membrane electrode.[233] 75
Figure 1.15: Examples of monomer units for (a) proton exchange membranes (Nafion®) and (b) anion exchange membranes (Aemion™, IONOMR). 79
Figure 2.1: Schematic illustration of a scanning electron microscope.[1] 94
Figure 2.2: Schematic illustration of a transmission electron microscope.[1] 96
Figure 2.3: Simplified graphical representation of X-ray constructive and destructive interference alongside parameters required for Bragg's Law calculations. The present example illustrated here displays destructive interference. 98
Figure 2.4: Diagram illustrating basic XAS theory. (a) Simplified orbitals with excitations to (bound) unfilled orbitals or (unbound) ionisation (XANES);[5] and, (b) Normalised X-ray absorption spectrum indicating the X-ray absorption near edge structure and the extended X-ray absorption fine structure on a iridium nanoparticle-containing electrocatalyst sample; and, (c) a simplified oscillation interaction during EXAFS signal production.[6] 100
Figure 2.5: Normalised XAS spectrum showing correction for the rest of the dataset. 102
Figure 2.6: XAS background removal and normalisation of a iridium foil sample measured in transmission mode. (a) Pre-processed spectrum showing the pre- and post-edge fittings alongside the background fitting; and, (b) the resulting normalised XAS spectrum. EXAFS region processing using iridium containing sample (Ir_NC_900_900, vide infra) (c) 'k space' plots converting the EXAFS region to wavelength energy scale using a k weighting of 2; and, (d) conversion of 'k space' into 'R space' using a Fourier transform. All processing was carried out in Athena. 103
Figure 2.7: Image illustrating XCT setup. 104

Figure 2.8: (a) Magnetic field dependant Zeeman splitting of energy levels for single unpaired electron represented in absorption (solid) or first derivative (dotted) mode; and, (b) LHS: classic dipolar interaction between electron and nuclear magnetic moments, and RHS: high-field approximation (i.e. Zeeman splitting much larger than degeneracy) for observed transitions in an Mn^{2+} species (assumes positive hyperfine constant and hyperfine term is larger than Zeeman splitting).[11,12] 105
Figure 2.9: Photograph of a TriStar II Plus nitrogen physisorption analyser, Micromimeritics. 108
Figure 2.10: Photograph of the tube furnace and plasma chamber used. 109
Figure 2.11: Generalised polarisation curve overlayed with sources of overpotential.[17] 113
Figure 2.12: (a) Cyclic potential sweep and (b) resulting cycling votammogram. 114
Figure 2.13: (a) Incident AC voltage and current response; and, (b) a simple Nyquist plot.[21] 115
Figure 2.14: Representative Nyquist plot with regions of interest qualitatively highlighted and an inserted equivalent circuit model. This Nyquist plot was collected with a zero-gap symmetric RFB cell utilising a porous carbon cloth electrode with a quasi-reversible active species ($TEMPO^{\bullet}/TEMPO^{+}$) dissolved in a MeCN-based electrolyte. 116
Figure 2.15: Idealised direction of flow of electrolyte when using a rotating (ring) disk electrode. 120
Figure 2.16: Summary of ORR / OER metrics. (a) Representative RDE polarisation curves for the ORR (blue) and OER (red); and, (b) a Tafel plot with Equation (2.21) inserted.[19,25] 122
Figure 3.1: A cartoon representation of the terms intra-pore and inter-pore mass transport processes. The left hand cartoon represents a 2D cross section of a porous electrode material. The large arrows indicate inter-pore bulk flow of electrolyte through the porous matrix. The magnified region shows intra-pore transport from the bulk (with active species i, concentration, c_i) to the active electrode surface (where the concentration of the species i is, c_i^s).[1] 127
Figure 3.2: Images of (a) electrode materials; (b) symmetric cell casing showing flow-through flow plate, an end plate with overlayed flow direction inserted and some electrodes in-situ during disassembly. (c) Schematic showing the chemical composition of the symmetric cell setup during operation.[1] 133
Figure 3.3: Compression rig and radiographs showing an example of a carbon electrode being iteratively compressed in a compression rig, to mimic experimental conditions, ahead of 360° XCT scanning.[1] 135
Figure 3.4: A step-by-step graphic representation of the image processing technique carried out for all carbon electrodes in. 136
Figure 3.5: Schematic of the 1D model considering half of the separator-electrode-assembly with key dimensions and pertinent boundary conditions. 140
Figure 3.6: Images showing microstructural properties and morphological information over the carbon electrodes. Scanning electron microscopy images (top two rows) and representative 3D renderings (with a through plane area of 1.96 mm^2) of the electrodes used in this chapter.[1] 142

Figure 3.7: Pore size distribution alongside extracted of pore network for each of the tested electrodes. The colour bar on the right hand side pertains to the extracted spherical pores in the pore network insert. 143
Figure 3.8: Calculated pressure drops as a function of characteristic velocity using (a) PC and (b) MeCN as solvents. The values for each electrolyte are averaged for the two directions of in-plane flow (i.e. y and z). 146
Figure 3.9: Current-potential curves as a function of flow rate. Measured potentials are displayed alongside their respective iR (ohmic / HFR) corrections and resulting 'iR-corrected' polarisation curves. These measurements were gathered using an AvCarb 1071 electrode with MeCN-type electrolyte (Figure A3.16).[1] 148
Figure 3.10: (a) - (b) Nyquist and (c) - (d) polarisation curves for electrochemical tests using AvCarb 7497 electrodes in PC-based ((a) & (c)) and MeCN-based ((b) & (d)) electrolytes. The colour shading represents chosen characteristic flow velocities. 150
Figure 3.11: Comparison of mass-transport resistances recorded during electrochemical impedance spectroscopy experiments, calculated using an equivalent circuit model. Experiments were carried out using either PC (top) or MeCN (bottom) as the solvent during electrolyte preparation. 151
Figure 3.12: Graph showing correlation between the ability for the electrode to reach high current density and with low overpotential (ASR_{25}) as a function of the calculated permeability at the highest and lowest flow rates in: (a) PC- of (b) MeCN-based electrolyte. ASR_{25} indicated the area specific resistance calculated at a current density of 25 mA cm^{-2} using the 1D fitted model simulations. At low flow rate, Freudenberg H23 did not reach 25 mA cm^{-2} in either solvent because the cell cut-off voltage was reached first, these points are therefore omitted. 156
Figure 3.13: Correlation between electrode performance factor and mean linear velocity for electrodes using (a) PC-; or (b) MeCN-based electrolytes. (c) Dimensionless parameter correlations for each electrode in each electrolyte on a logarithmic graph with the Sherwood number plotted as a function of the Reynolds number. Gradients are displayed along their line respective best fit lines. 160
Figure A3.14: The UME CVs for trials 1-3 for the (a-c) PC- and (d-f) MeCN-based electrolytes. For all CVs, a 10 mV s^{-1} was used under quiescent conditions with a 10 μm diameter Pt UME, a Pt mesh counter electrode, and a Ag/AgCl reference electrode. ..163
Figure A3.15: Scanning electron microscopy coupled with energy dispersive X-Ray spectroscopy, showing no fluorinated croups in AvCarb MGL370 matrix. 164
Figure A3.16: Separation of ohmic potential contribution from the cell potential leaving the iR-corrected potential illustrating the effect of flow rate on relative ohmic / HFR vs. charge / mass-transfer resistances in MeCN for each electrode (a-d). 165
Figure A3.17: iR corrected Nyquist plots showing experimental and modified Randles circuit fits for all electrodes (a-d) tested at each velocity in (i) PC- or (ii) MeCN-based electrolyte. 166
Figure A3.18: Complete set of polarisation curves with accompanying model fits. 169
Figure A3.19: Plots showing a lack of correlation between several commonly used microstructural properties: (a) volume-specific surface area, (b) porosity and, (c) tortuosity. (d) shows the positive correlation between permeability and ASR_{25} relealing

its importance relative to the other microstructural properties. The performance metric used here was recorded in a high-flow (5.0 cm s^{-1}) zero-gap flow-through RFB using MeCN as the supportiong solvent. 171
Figure A3.20: The ratio of input pumping power to output electrical power at a calculated 0.025 V iR-corrected potential (during polarisation), as a function of characteristic flow rate in (a) PC and (b) MeCN (assumes a pump efficiency of 75%). The parity (dotted) line indicates the ratio below which there is no net generated power.[1] 172
Figure A3.21: Distribution of concentration of (a) $TEMPO^{\bullet}$, and (b) $TEMPO^{+}$, (c) overpotential, and (d) ionic current density, along the cathode thickness when a discharge current density of 25 mA m^{-2} is applied to AvCarb 7497 carbon cloth in PC- (dashed line) and MeCN-based (solid line) electrolytes and under the four flow velocities tested. 174
Figure 4.1: Scanning electron microscopy images of ZIF-67 with varied morphology demonstrating controlled MOF synthesis. 187
Figure 4.2: Progressive ORR and OER perforamcne improvement of catalyst synthesis on a RRDE in 0.1M KOH at a rotation speed of 1600 rpm, scan rate of 5 mV s^{-1} and a catalyst loading of 0.4 mg_{cat} cm^{-2} 189
Figure 4.3: Heat map representing overall performance of catalyst according to the 'Bifunctionality' score towards fundamental oxygen reactivity, as a function of T_1 and T_2. 191
Figure 4.4: (a) Transmission electron microscope images showing agglomerated cobalt particles and (circled in red) iridium nanoparticles and, (b) line-scan energy dispersive X-ray spectroscopy images over a catalyst with and without iridium included in the reflux step 192
Figure 4.5: For each of the catalysts: (a) N_2 absorption–desorption isotherms; and, (b) pore size distribution measurements. 195
Figure 4.6: Comparison of an XPS response for an Ir_NC_900_900 electrocatalyst sample with simulated signal components and resulting fitting envelope for the (a) Ir 4f; (b) N 1s; and, (c) Co 2p characteristic binding energies. 196
Figure 4.7: Calculated relative concentrations of N-sites in catalyst samples varying (a) T_1; and, (b) T_2. 198
Figure 4.8: XAS measurements for the catalyst samples and standards. (a) Normalised responses following X-ray absorption near edge spectroscopy at the Ir L_{III} edge; and, (b) extended X-ray absorption fine spectra. Pink dashed lines indicate the inter-atomic distance between Ir-atoms in the provided standards and FMo and TMo indicate measurements recorded in fluorescence or transmission mode, respectively. 199
Figure 4.9: XAS analysis outlining in (a) the similarity in Premetek character with Ir_NC_1000_900 as well as the differences in Premetek sample measurements as a function of analysis mode; and, (b) a linear combination (LC) fitting Ir_NC_900_900 with IrO_2 and Premetek character – purple and green lines show their relative contributions to the overall fit (86.5 and 13.5 %, respectively). 200
Figure 4.10: Weight percentages of (a) iridium and (b) cobalt in Ir_NC_T1_T2 catalysts and standards. Each weight percentage measurement was gathered from individual samples of catalyst and underwent just one of the three heating regimes set out in Table 4.1. ..202

Figure 4.11: (a) ORR and (b) OER responses from Ir_NC_900_900 in a variety of pHs. (c) Tafel slopes pertaining to kinetic region in ORR curves indicated by arrows in each specific pH. The kinetic current is plotted due to the availability of a limiting current in ORR on RDE (d) Tafel slopes pertaining to kinetic region in OER curves indicated by arrows in each specific pH. The log of the observed current density is plotted as there is no limiting current. (e) Progressive overpotentials (as a function of cycle number) accocaited with $E_{1/2}$ in ORR region and E_{10} in the OER region. RDE conditions: catalyst loading: 0.4 mg_{cat} cm^{-2}; rotation rate: 1600 rpm; scan rate: 5 mV s^{-1}.....203
Figure 4.12: RDE experiments showing Ir_NC_900_900 catalysing fundamental hydrogen reactions in (a) basic (0.1 M KOH) or (b) acidic (0.5 M H_2SO_4) conditions. These experiments were carried out using an RDE at a scan rate of 2 mV s^{-1}, with a rotation rate of 1600rpm and a catalyst loading of 0.2 mg_{cat} cm^{-2}. 206
Figure 4.13: Rotating disk electrode measurements displaying the potential (vs. RHE) and mass activities as a function of iridium concentration in base ((a) and (c)) and acid ((b) and (d)). The iridium concentration assumed for this dataset is 2.49 wt% (i.e. the measurement after one week of catalyst leaching). The catalyst loading for these experiments was 0.2 mg_{cat} cm^{-2} and the rotation rate was 1600 rpm.....207
Figure 4.14: Summary of chronoamperometric holds on RDE using the Ir_NC_900_900 electrocatalyst. Basic experiments ((a) and (c)) were carried out using 0.1 M KOH; acid experiments ((b) and (d)) were carried out using 0.5 M H_2SO_4. Rotation rate: 1600 rpm; catalyst loading of 0.2 mg_{cat} cm^{-2}.....208
Figure A4.15: Linear sweep voltammograms of backgrounds highlighting the presence of oxygen dissolved in solution after purging nitogen gas for 30 minutes using the in-house desinged sparger versus the background when purging with argon. 212
Figure A4.16: Rotating disk electrode ORR (a) and (b) and OER (c) and (d) measurements for Ir_NC_T_1_T_2 catalysts. Variation in T_1 pyrolysis temperature for the ORR and OER reactions are shown on the left hand side – (a) and (c); and T_2 pyrolysis temperature variation is on the right hand side – (b) and (d). Catalyst loading of 0.4 mg_{cat} cm^{-2}, scan rate of 5 mV s^{-1} and a rotation rate of 1600 rpm.....213
Figure A4.17: X-ray diffraction patterns of the catalysts with (blue) and without (red) iridium included in the reflux step compared with database XRD patterns of graphite, iridium and cobalt for comparison.....214
Figure A4.18: Histograms outlining the cumulative pore volume for each of the catalysts. 215
Figure A4.19: (a) full energy range 'peak search' over a sample of Ir_NC_900_900 highlighting characteristic elemental orbital signals. (b) Measurement of the Ir 4f region in Blank_NC_900_900 to find 'background' Co 3p signal ratios underneath other samples' Ir 4f signals. 215
Figure A4.20: RDE durability tests in 0.1 M KOH using Ir_NC_900_900 with a catalyst loading of 0.4 mg_{cat} cm^{-2}, scan rate of 50 mV s^{-1} and a rotation speed of 1600 rpm.....216
Figure A4.21: Iridium weight percentages measured by ICP-MS following different heating regimes with accompanying mass activities at E_{10} for the oxygen evolution reaction with a catalyst loading of 0.4 mg_{cat} cm^{-2}. It should be noted that the iridium content in Ir_Premetek was stated to be 20 wt %, amounting to 100 A g_{Ir}^{-1}.....216

Figure 5.1: Alkaline anion exchange membrane fuel cell schematic. The 850 Fuel Cell Test Station controls the flow, humidity and temperature of the gas into the cell. Heating rods are inserted into the end plates controlling the cell temperature. 225
Figure 5.2: Proton exchange membrane fuel cell schematic. The 850 Fuel Cell Test Station controls the flow, humidity and temperature of the gas into the cell. Heating rods are inserted into the end plates controlling the cell temperature. 228
Figure 5.3: Mn/H_2 hydrogen redox flow battery experimental schematic. The system as a whole is controlled by an exterally connected potentiostat. Electrolyte flow on the liquid side is controlled by a peristaltic pump. Hydrogen flow on the gas side is controlled by a mass-flow controller positioned between an electrolyser and the cell. 231
Figure 5.4: Alkaline anion exchange membrane fuel cell polarisation data using in-house synthesised electrodes flowing oxygen and hydrogen over the cathode and anode, respectively. (a) and (b) show the voltage and power density curves without and with an iR-correction, respectively. (c) shows the area specific resistances encountered during each of these polarisation experiments. 235
Figure 5.5: Proton exchange membrane fuel cell tests using Ir_NC_900_900 as the catalyst at the anode and a commercial platinum electrode (JM, 0.4 mg_{Pt} cm^{-2}) at the cathode with an active are of 5 cm^2. (a) and (c) show the polarisation curves free of iR correction with oxygen and air flowing over the anode resectively; (b) and (d) show their iR-corrected counterparts. The HFR during these potential holds is displayed in (e). Oxygen tests are carried out with a flow rate of 200 sccm on both sides of the cell. Air tests are carried out with flow rates of: hydrogen at 300 sccm and air at 1000 sccm. The cell temperature was 80 °C and gases have an RH of 100 %. 236
Figure 5.6: (a) and (b) utilise a manganese hydrogen hRFB system employing two layers of AvCarb 1071, Nafion 212 and a commercial platinum electrode where; (a) potential is plotted as a function of the specific capacity for a series of charge (solid line) and discharge (dashed line) cycles at different current densities. The dotted line at 26.8 Ah L^{-1} which corresponds to the theoretical maximum specific capacity for 20 mL of this electrolyte; (b) summarises the voltage (left half filled square), coulombic (right half filled square) and their product, the energy efficiency (full square) of a number of cycles with this specific assembly. (c) A summary of the average voltage efficiencies and achieved specific capacities of the cycles measured at a specific current density. Different colours represent different configurations. Nafion 212 was used in each of these configurations. 237
Figure 5.7: Polarisation curves examining the capability of electrode materials in a manganese hydrogen redox flow battery. (a) and (b) display polarisation (left hand axes) and power curves (right hand axes) without and with iR-corrections (respectively) for each of variations in liquid side electrode configuration and the gas side variation using Ir_NC_900_900 alongside 3 layers of AvCarb 1071 (magenta). (c) HFR responses during polarisation experiments. (d) Alternative representation of (b) using compressed thickness of electrodes in liquid side to display volumetric power densities. 239
Figure A5.8: Images of electrodes (5 cm^2) with (a) the words and (b) the best catalyst layers achieved using a drop casting method with inks containing anion exchange polymer. Catalyst layers deposited by (c) spray coating and (d) drop casting (this electrode not

used in this work) nafion-containing inks for using in PEMFC and Mn/H_2 electrochemical devices. 244
Figure A5.9: Image displaying how electrodes were spray-coated with electrocatalyst while fixed to a hotplate....244
Figure A5.10: Screengrab of spreadsheet used to calculate number of gaskets needed. 245
Figure A5.11: Photographs of manganese-hydrogen hRFBs operated by different potentiostats and testing systems: top left – Gamry 600; top right – 857 Redox Flow Cell Test System; and, bottom – 850 Fuel Cell Test System. 245
Figure 6.1: Pourbaix diagram for manganese. This diagram includes the region corresponding to the redox stability of water (dashed lines with gradient -0.059 V pH^{-1}). 251
Figure 6.2: Manganese oxide crystal structures.[28] 255
Figure 6.3: Above: (c) Pourbaix free-energy planes of metastable β-MnOOH, γ-MnOOH, R-MnO2, and full aqueous stability region of Mn3O4. (d) Projection of aqueous metastability regions onto E-pH axis.[31] Below: Schematic representation of remnant metastability in a crystallization pathway (a) Free-energy of three phases (supersaturated solution (gray), M (green), S (blue)) as a function of the surface-area-to-volume ratio, 1/R (R is a particle radius). The gray line corresponds to the free-energy of a supersaturated solution, green is a metastable phase M that is size-stabilized by a low surface energy (given by the slope), and blue is the bulk equilibrium phase S, with high surface energy. (b) Phase diagram in the 1/R axis created from the projection of lowest free-energy phases. (c) A multistage crystallization pathway (red arrow in a) proceeds downhill in energy, but phase transformations are limited by nucleation. Crystal growth of M prior to the induction of S means M can grow into a size-regime where phase M is metastable. S will then nucleate, and quickly grow by consuming M via dissolution-reprecipitation. The characteristic length scale of size-driven phase transitions lies in the 2 nm–50 nm range.[32] 256
Figure 6.4: Manganese speciation map in an acid environment. 260
Figure 6.5: Pourbaix diagram for Titanium using hydrated titanium species.[43] 261
Figure 6.6: Photographs of partially oxidised Mn^{2+} solution with and without a Ti^{4+} additive. 264
Figure 6.7: Average sulfate anion charge. 268
Figure 6.8: Schematic outlining the in-operando experimental techniques used alongside the hRFB setup....272
Figure 6.9: Images displaying a full UV-vis hRFB cell operando setup and with specific component features. The images in the lower right part of the figure display the flow cell used with a small path length. 273
Figure 6.10: (a) Image showing in-operando EPR arrangement. (b) Diagram of flow cell in within the resonator with relevant safeguards. 275
Figure 6.11: (a) General form of potential-time profiles for a Mn/H_2 hRFB during charging and discharging cycles at current densites of 50, 75 and 100 mA cm^{-2}. (b) Equivalent potential profiles using specific capacity and SOC as x-axes – this plot includes the theoretical specific capacity of the electrolyte. (c) and (d) show the HFR responses during these charges and discharges using respective x-axes. These experiments were

carried out using an electrolyte volume of 400 mL (leading to the theoretical specific capacity of 26.9 Ah L^{-1} assuming a straight-forward single electron process).....277
Figure 6.12: (a) Conductivity readings and corresponding solution resistances. Conductivity measurements were taken in triplicate during a 75 mA cm^{-2} simple charge / discharge cycle of 100 mL electrolyte. (b) The top set of curves display the HFR measurement during this standard cycle and below is the calculated membrane resistance. 279
Figure 6.13: (a) Potential responses as a function of SOC alongside voltage efficiency. (b) Voltage efficiencies as a function of SOC for each current denisity without (solid lines) or with (dashed lines) three hour transient between charge and discharge arms. (c) Potential transients after charges to cut off at different current denisties. (d) Nyquist plots measured during potential transient after each charge at different current densities. Colours of Nyquist plots are associated with corresponding coloured asterisks in (c). 282
Figure 6.14: (a) Potential profiles as a function of state of charge illustrating iterative charging to 20, 40, 60 and 80 % state of charge. (b) summary of the voltage efficiencies (as a function of state of charge) for each of the iterative cycles outlined in (a). These cycles were carried out at 75 mA cm^{-2} using a Mn/H_2 hRFB using 200 mL of room temperature electrolyte at a rate of 50 mL min^{-1}.....283
Figure 6.15: Data showing equivalent plots to those previously displayed but cycling the battery at 25 mA cm^{-2} – plots showing equivalent profiles using a current density of 100 mA cm^{-2} are shown for comparison. (a) Potential profiles using specific capacity and SOC as x-axes – including the theoretical specific capacity of the electrolyte. (b) shows the HFR responses during these charges and discharges using the same x-axes. (c) The voltage efficiencies for these cycles with (dashed line) and without (solid line) a resting period at the maximum SOC. (d) The potential transients for the cycles that incorporated a resting period at maximum SOC. These experiments were carried out using an electrolyte volume of 400 mL. 286
Figure 6.16: (a) V/t profile displaying iterative charging of a Mn/H_2 hRFB in approximately 5 % SOC steps. In between each step, OCP mini-transients are recorded in which the OCP is tracked over 120 seconds and an impedance is run over c.a. three minutes between each 'mini-transient'. Some selected transients are inset in the spare regions in the graph visually outlining how information is gathered from these transients for (b); (b) Final potentials after the mini transients (charging arm – red, discharging arm – blue) are recorded on the left hand axis (squares) while the change in potential in the latter part of the mini-transient is recorded on the right hand axis (triangles).....288
Figure 6.17: Impedance measurements in Nyquist plot form during (a) charge and (b) discharge of a cell at 25 mA cm^{-2}. Colour bar roughly indicates the SOCs. 289
Figure 6.18: (a) An example of a first derivative EPR response to a sample containing Mn^{2+} with a concentration of c.a. 0.25 mol dm^{-3} measured in a capilliary tube. (b) A 3D stack of first derivative responses from the EPR resonator displaying how the signal changes as an hRFB cell is charged and discharged. (c) Calibration curve showing [Mn^{2+}] measured individually and in the in-operando fashion – this was carried out to ensure [Mn^{2+}] can be deduced in further in-operando experiments.....291
Figure 6.19: (a) A simple charge discharge curve with accompanying Mn^{2+} concentration measurements from EPR (black dashed line) with SOC values calculated using coulomb

counting (red solid line). The green bar indicates a short OCP tracking pause at max SOC. The solid fluorescent green line overlay is an extrapolation of the Mn^{2+} concentration from the beginning of the cycle. (b) The measured Mn^{2+} concentration and the resulting calculated concentrations of Mn^{3+} and Mn^{4+} species using the methods outlined in the main text. These measurements were taken using a hRFB Mn/H_2 cell cycled at 75 mA cm^{-2} with 180 mL electrolyte.....293
Figure 6.20: (a) Mn^{2+} (measured)-, (b) Mn^{3+}- and, (c) Mn^{4+}-concentration profiles as a function of state of charge while cycling at different current densities. The volume of the electrolyte used in these systems was 180 mL and the state of charge was calculated according to the number of coulombs passed into solution.....295
Figure 6.21: UV-vis baseline testing. H2SO4, stock acidified titanium oxysulfate solution and discharged electrolyte (containing Mn species).....298
Figure 6.22: (a) Simple potential profile during charging step with OCP transient. (b) UV-vis absorption spectra during charging regime and OCP transient. 299
Figure 6.23: (a) UV-vis spectra with overlayed peak tracking (solid lines) compared with single wavelengths (dotted lines) and (b) back-calculated calibration curves for Mn^{3+} concentration as a function of state of charge. A calibration point was used as this is the highest state of charge where neither signal is significantly affected by the low wavelength band. 300
Figure 6.24: Combined UV-vis and EPR analysis. Concentrations from UV-vis measurements are calculated using the higher wavelength peak (at 840 nm). Mn^{2+} concentrations are measured by EPR and the inferred concentrations of the oxidised states from these measurements is shown here.....301
Figure 6.25: UV-vis transient information (a) Simple potential profile during stepwise charging with intermittent resting times. (b) The additional spectra now included show a slow charge to SOC 92 (blue lines) followed by a chemical process (orange lines) leading to the formation of solids that scatter the incident light (likely due to disproportionation). (c) In-operando UV-vis spectra of the electrolyte during the electrochemical discharge. It is important to point out that the very defined shape are not recovered at equivalent states of charge during the discharge arm. The grey arrow in this figure represents time. In both (b) and (c) the grey arrow represents time. *Unfortunately, the UV-vis spectrophotometer malfunctioned c.a. 5 % before the end of the discharge – meaning there was still some un-reduced Mn^{3+} still present in solution – hence the signal at c.a. 522 nm in (c).....303
Figure 6.26: EPR transient information (a) a schematic of liquid-side of hRFB with exaggerated species concentration gradient across the Tank, Cell and EPR during operation and (b) after the system has reached a uniform state. (c) Mn^{2+} concentrations separated into 'reaction' (blue) and 'instrumental' (grey) components with their respective model fits. (d) Original Mn^{2+} concentration measurements with the model fit. 305
Figure 6.27: Thermodynamic calculations of species' concentration accounting for speciation assuming all activity coefficients are unity. Case 1 represents the ideal case where Mn^{2+} and Mn^{3+} exist as isolated, well-behaved ions. Case 2 introduces a single hydrolysis of the Mn^{3+} ion forming $Mn(OH)^{2+}$. Case 3 introduces titanium species. 309

Figure 6.28: Thermodynamic calculations of species' concentration accounting for speciation assuming all activity coefficients are unity. Case 4 introduces the effect of γ-MnOOH precipitation. Case 5 shows a more simplified case where Mn^{3+} hydrolysis and titanium species are not considered. In addition, an equilibrium constant of 50 ($K_{Mn(2+)/MnO2} = 50$) is used here – note: this is far too low and is 'unphysical' but is used to illustrate the effect (thermodynamically) of including MnO_2 in the speciation of the system. Reasonable values of the equilibrium constant for the formation of MnO_2 is shown in the appendix and presents a number of additional problems to the other manganese species' concentrations. 310
Figure 6.29: Notional values of K illustrating the thermodynamic boundary at which it is expected for solids to be precipitated. Vertical lines indicate the calculated formation constants associated with different solid polymorphs. (a) shows the notional values of K at which solids (a) MnOOH and (b) MnO_2 will start precipitating. 312
Figure 6.30: Thermodynamic calculation of species' concentration accounting for speciation assuming all activity coefficients are unity and with a reasonable formation constant for γ-MnO_2. Solid formation starts immediately as Mn^{3+} formation energy is much more positive than MnO_2. 313
Figure 6.31: (a) and (b) Variation of notional values of K at which point solids (a) MnOOH and (b) MnO_2 are expected to start to precipitating, as a funtion of sulfur concentration. (c) and (d) show the proton concentrations for the point at which precipitiation is expected to occur for a given K. 314
Figure 6.32: EPR measurements (Mn^{2+}) and calculations (Mn^{3+} and Mn^{4+}) compared with thermodynamic calculations outlined in Case 4 and Case 5 in which solids (γ-MnOOH and hypothetical *-MnO_2) are formed. The hRFB cell used was charged at 150 mA cm^{-2} using the in-operando EPR setup and the measured Mn^{2+} concentration is shown in (a), alongside the thermodynamically calculated Mn^{2+} concentrations in Case 4 and Case 5. (b) The caluclated Mn^{3+} concentration from EPR measurements alongside the solution-phase Mn^{3+} species accounted for alongside the formation of solids. (c) The calculated Mn^{4+} species (from Mn^{2+} EPR measurements) and thermodynamically calculated concentrations of solid species....318
Figure 6.33: Schematic illustration of the processes occuring in the electrolyte and at the fibres in a standard cycle (> 25 mA cm^{-2}) with no relaxation period at maximum SOC. Solid species from c.a. SOC 40 are shown with a white outline here – this is just to show their existance and suggested growth trajectory (not because the acutal particles are in any way white). 319
Figure A6.34: Schematic demonstrating techniques potentially used to stabilise Mn^{3+} in solution. Energy axis is not to scale. 323
Figure A6.35: Ratio in absorbances for UV-vis signals at high (840 nm) vs low (522 nm) wavelenths....324
Figure A6.36: Measured concentration of Mn^{2+} alongside theoretical calculations for a slow cycle using a current density of 25 mA cm^{-2} with an electrolyte volume of 180 mL....324
Figure A6.37: Repeated concentration transient fittings after charging 180 mL electrolyte at 75 mA cm^{-2} to the maximum SOC (until cut-off)....325

Figure A6.38: All (a) Mn^{2+} concentration and (b) cell potential transients at different SOCs. 325

List of tables

Table 1.1: Progression of quinone-derived redox couples in alkaline conditions. Capacity fade rate progressively becomes smaller with each developing structure. The 'Electron conc.' represents the number of moles of electrons each redox couple is able to utilise per litre of electrolyte. The redox potential for each couple is shown and the value in parenthesis is the OCP of the respective couple with $K_4Fe(CN)_6$ (which has a redox potential of 0.50 V vs. SHE). The acronyms are as follows: DMBQ = 2,5-dimethyl-3,6-dihydroxyl-1,4-benzoquinone,[66] DHBQ = dihydroxybenzoquinone,[67] DHAQ = 2,6-dihydroxyanthraquinone,[68] 2,6-DBEAQ = 4,4'-((9,10-anthraquinone-2,6-diyl)dioxy)dibutyrate,[69] 2,6-DPPEAQ = (((9,10-dioxo-9,10-dihydroanthracene-2,6-diyl) bis(oxy))bis(propane-3,1-diyl))bis(phosphonic acid).[64,70] 46
Table 1.2: Comparison of chosen systems using system-level figures of merit. 57
Table 3.1: Relevant electrolyte properties measured (N=3): ionic conductivity, σ_e; density, ρ_e; viscosity, μ_e; and species diffusivity, D (3dp). 131
Table 3.2: Carbon electrode and separator specifications.[28–31] 132
Table 3.3: Microstructural parameters from SEM, XCT and TauFactor. 144
Table 3.4: Calculated permeabilities using pressure drop calculations from PNM simulation. 147
Table 3.5: The area specific resistance calculated using the iR-corrected 1D model values at 25 mA cm^{-2} (3sf). The area specific resistance has been calculated for each electrode, in each supporting solvent at the highest (5.0 cm s^{-1}) and lowest (0.5 cm s^{-1}) characteristic flow velocities. (Parentheses indicate that 250 A m^{-2} was not reached before the cell cut-off potential was reached, the highest current density modelled is indicated next to the associated ASR.) 153
Table 3.6: Ranges of characteristic dimensionless numbers for electrodes and performance values (3sf). 160
Table A3.7: Experimental high frequency resistances and all electrochemical impedance spectroscopy equivalent circuit model parameters for four electrodes, at four flow rates in two different electrolytes (* = dimensionless). 167
Table A3.8: 1D continuum model parameters. 168
Table A3.9: Summary of results of 1D continuum model after fitting to galvanostatic polarisation data (3sf). 170
Table 4.1: ICP-MS sample preparation heating regimes. 185
Table 4.2: Collection of nitrogen physisorption surface area and BJH desorption cumulative volume measurements. 194
Table 4.3: Overview of XPS measurements across each of the elements of interest and a breakdown of how the nitrogen components are split into their respective environments. Surf. comp. denotes 'Surface composition' and 'Quat.' denotes 'Quaternary'. 197
Table A4.4: Bifunctionality calculations varying T_1 and T_2. The average bifunctionality score is taken across the dataset and then subtracted from the individual scores in order to normalise around a zero value. Bifunctionality scores were then multiplied by 100 to return 'sensible' values. This metric places more value on ORR (highighted by the weighing of the ORR_{coeff}. 212

Table 5.1: AEMFC membrane electrode assemblies. ‘AEI’ denotes ‘anion exchange ionomer’. The number in parentheses indicates the catalyst loading in mg_{PGM} cm^{-2}. ...225
Table 5.2: Flow-through configuration of electrode and membrane materials for testing in a manganese-hydrogen hybrid redox flow battery. MEA = Membrane electrode assembly. (Parentheses alongside liquid and gas side electrodes indicates number of electrode layers used and the catalyst loading in mg_{PGM} cm^{-2}, respectively.) 232
Table 6.1: A summary of Gibbs free energies of formation for relevant sulfur species.....250
Table 6.2: A summary of Gibbs free energies of formation for relevant manganese species. “★" indicates that this free energy was collected from computationally calculated values. 260
Table 6.3: A summary of Gibbs free energies of formation for relevant titanium species....263
Table 6.4: Aqueous electrolyte composition used in this work. 268
Table 6.5: Parameters extracted from Mn^{2+} concentration transient tracking. mM = milli-molar = mmol dm^{-3}. “Exp. dur.” denotes “Experiment duration”. “inst.”denotes “instrumental”. “reac.” denotes “reaction”. 306
Table 6.6: Modelled scenarios with incremental changes. Atomic concentrations are stated here to avoid confusion as a result of speciation. ‘Form. const.’ denotes ‘Formation constant’. 308

Abbreviations

Acronyms

2D	two dimensional/dimensions
3D	three dimensional/dimensions
a	anodic
a.u.	arbitrary units
AEMFC	(alkaline) anion exchange membrane fuel cell
AEM	anion exchange membrane
APT	atom probe tomography
ASR	area-specific resistance
BET	Brunauer–Emmett–Teller
BL	boundary layer
BOP	balance of plant
BV	Butler-Volmer
c	cathodic
CAG	carbon aerogel
CE	coulombic efficiency
CT	charge transfer
CV	cyclic voltammetry / voltammogram
DFT	density functional theory
dl	diffusion limited
DI	de-ionised
DoE	Department of Energy
EC	electrochemical conversion
EDX	energy dispersive X-ray spectroscopy
EE	energy efficiency
EELS	electron energy loss spectroscopy
EES	electrochemical energy storage
EIS	electrochemical impedance spectroscopy
EPR	electron paramagnetic resonance
EV	electric vehicle
EXAFS	extended X-ray absorption edge fine structure
GAME	gas accessible membrane electrode

GAN	generative adversarial networks
GDE	gas diffusion electrode
GDL	gas diffusion layer
FBFF	flow-by flow field
FC	fuel cell
FE	floating electrode
FIB	fast ion beam
FMo	fluorescence mode
FTFF	flow-through flow field
FWHM	full width at half maximum
HAADF	high-angle-annular dark-field
HBE	hydrogen binding energy
HER	hydrogen evolution reaction
HFR	high frequency (ohmic) resistance
HOR	hydrogen oxidation reaction
hRFB	hybrid redox flow battery
HRTEM	high resolution transmission electron microscopy
Hz	hertz
ICP-MS	inductively coupled plasma – mass-spectrometry
Im	imaginary
LFP	lithium iron phosphate
LHS	left-hand side
lim	limiting
LP	large particle
LSV	linear sweep voltammetry
MEA	membrane electrode assembly
MeCN	acetonitrile
MIP	mercury intrusion porosimetry
ML	machine learning
MOF	molecular organic framework
MPL	microporous layer
MT	mass-transport
NASICON	Na super ion conductor

NC	nitrogen doped carbon
NMC	nickel manganese cobalt
OCP	open-circuit potential
ODAN	oligomerised diaminonaphthalene
OER	oxygen evolution reaction
ORR	oxygen reduction reaction
PAN	Polyacrylonitrile
PC	propylene carbonate
PEFC	polymer electrolyte fuel cell
PEM	proton exchange membrane
PEMFC	proton exchange membrane fuel cell
PGM	platinum group metal
PHS	pumped hydro storage
PNM	pore network model
POCO	Petrolium Oil Company (specific graphite brand)
ppb	parts per billion
ppm	parts per million
PSD	pore size distribution
PTFE	polytetrafluoroethylene
RDE	rotating disk electrode
RDS	rate determining step
Re	real / Reynolds
REV	representative elementary volume
RFB	redox flow battery
RH	relative humidity
RHE	reversible hydrogen electrode
RHS	right-hand side
RRDE	rotating ring disk electrode
SAC	single atom catalysts
sccm	standard cubic centimetres per second
SEM	scanning electron microscopy
SHE	standard hydrogen electrode
SOC	state of charge

SOFC	solid oxide fuel cell
SP	small particle
SSA	specific surface area
STEM	scanning transmission electron microscopy
$TEABF_4$	tetraethyl-ammonium tetrafluoroborate
TEM	transmission electron microscopy
TEMPO	2,2,6,6-tetramethyl-1-piperidinyloxy
TGA	thermogravimetric analysis
TM	transition metal
TMo	transmission mode
TOF	time of flight
UME	ultramicroelectrode
UV-vis	ultraviolet-visible (spectroscopy)
VE	voltage efficiency
VRFB	all-vanadium redox flow battery
VSSA	volume-specific surface area, $m^2\ m^{-3}$
WE	working electrode
XANES	X-ray near-edge structure
XAS	X-ray absorption spectroscopy
XCT	X-ray computed tomography
XPS	X-ray photoelectron spectroscopy
XRD	X-ray diffraction
ZIF	zeolitic imidazolate framework

Latin symbols

a	cross-sectional area, m^2 | empirical parameter in power law, -
A	absorbance, -
c	concentration, mol dm^{-3}
d	diameter, m
D	diffusivity, $m^2\ s^{-1}$
E	potential, V | energy, kg $m^2\ s^{-2}$
G	Gibbs energy, J
i	current, A
I	intensity, J | current, A

j	current density, mA cm^{-2}
k	reaction rate constant
k_m	mass-transfer coefficient, m s^{-1}
K	permeability, m^2 | equilibrium constant
M	molar, mol dm^{-3}
n	number (e.g. of electrons), -
Ox	oxidation state, -
P	pressure, Pa
Q	charge, C
R	resistor elements | resistance, Ω
t	time, s
T	temperature, K
v	velocity, m s^{-1}
x, y, z	cartesian co-ordinates, m
Z	impedance (Im, imaginary | Re, real)

Greek symbols

α	absorption coefficient, m^2 mol^{-1} (UV-vis) | transfer coefficients
ρ	density, kg dm^{-3}
Δ	difference
ε	porosity; volume fraction
η	overpotential, V
κ	transmission coefficient, -
λ	wavelength, m
μ	viscosity, Pa s | absorption coefficient, m^{-1} (XAS)
ν	frequency, s^{-1} | scan rate, V s^{-1}
σ	conductivity, mS cm^{-1}
τ	tortuosity | characteristic time, s | time scale, s

Physical constants

Avogadro's constant	N_A	6.022×10^{23}	mol^{-1}
Bohr magneton	μ_B	9.274×10^{-21}	J T^{-1}
Boltzmann constant	k_B	1.381×10^{23}	m^2 kg s^{-2} K^{-1}
Faraday's constant	F	96485	C mol^{-1}
Ideal gas constant	R	8.314	J mol^{-1} K^{-1}
Planck's constant	h	6.626×10^{-34}	m^2 kg s^{-1}

Chapter 1

Introduction

"If you don't start somewhere, you're gonna go nowhere." – Bob Marley

Part I: Overview

1.1 Context and Motivation

The explosive growth in energy demand in recent years alongside an urgent need to reduce greenhouse gas emissions has led to the installation of large scale renewable energy generation. In 2020 the UK generated 134 TWh of renewable energy – an increase of 61% since 2015 and an increase of 406 % since 2010.[1] While this influx of renewable capacity is generally positive as, by definition, renewable electricity generation produces no greenhouse gases, it can have some negative side-effects. For instance, electricity grids may be destabilised as a result of the unreliable power output profiles of these renewable energy sources – The Intermittency Problem. Energy generation from wind turbines is particularly difficult to predict as a result of changeable 'weather' (especially in the UK) and, while 'daylight' hours are predictable, solar panel arrays are significantly affected by both intermittent or permanent cloud cover.[2]

One solution to this problem is to position large-scale energy storage systems (~10s of mega-watts in size) between these intermittent generators and the electricity grid. Historically, flexible baseload energy delivery for the UK was provided by coal, oil and now natural gas – intermittent renewables plus storage can now provide a significant part of baseload, replacing these fossil-fuel-based, highly polluting sources. Pumped hydro-storage (PHS) dominates the installed capacity of large-scale energy storage (globally, and) in the UK.[3] These systems have several drawbacks including uneconomic transmission costs – PHS sites tend to exist far from energy demanding centres like cities – and relatively slow response times (to commands from the grid operator). Both in the UK and globally, a more distributed large scale energy storage

ecosystem is required to reflect the dispersed nature of renewable generation sites. To reflect this, a more modular geographically versatile type of energy storage is required.

Electrochemical energy storage (EES) devices, in the form of batteries utilising lithium-ion (Li-ion) chemistries, have already demonstrated broad and pervasive use in industry and, indeed, our daily lives. Lithium iron-phosphate (LFP) and lithium nickel manganese cobalt (NMC) technologies are widely used in everything from television remotes to smartphone batteries to electric vehicles (EVs).[4,5] Increasingly though, domestic and commercial deployments of stationary EES devices are rolling out.[6–10] A comprehensive case outlining the benefits of implementing storage at scale has been made,[11] and the total global stationary battery capacity is expected to increase (from 11 GWh in 2017 to) as much as 181 – 421 GWh by 2030.[2]

However, while Li-ion chemistries are technologically sound and scalable (to an extent), they should not be burdened with the entire EES requirement. Continuing to mine lithium in the way we do today is non-sustainable and significant improvements in lithium recovery and recycling methods is needed. Additionally, the accompanying metals in current battery technologies, such as nickel and cobalt, can be dangerous if handled incorrectly and their origin countries can have irresponsible child-labour attitudes. Alternative chemistries and technologies will be needed to cater for the broad requirements globally, some applications of which are, undoubtedly, unknown. For instance, electrochemical conversion (EC) devices such as electrolysers and fuel cells (FCs) can be co-located with one another to produce hydrogen and use it to continuously power energy-demanding sites such as data centres. In this instance, FCs are a more appropriate technology for the application required, demonstrating the solution to sustainable energy generation will come in ‘patchwork’ form.

Redox flow batteries (RFBs) are a relatively nascent EES technology. In its classical form, energy, stored in a liquid electrolyte, is housed in external tanks and continuously flowed through a central cell undergoing a electrochemical reaction in the process. This decoupling of a battery’s power output and capacity makes RFBs uniquely flexible compared to their Li-ion cousin from both an application and chemical point of view. While this technology is still (relatively) in its infancy, its modular design provides a promising alternative for large-scale EES deployments from both a power (n × 0.3 – 10 MW) and energy (1 – 40 MWh) perspective.[12] This is discussed in further detail in subsequent parts.

The central motivation of this work is to contribute to the development of RFBs. While one should remain cognisant of the economic barriers that stand between RFBs and broad acceptance for commercial roll-out, this work will argue that, in many ways, RFBs provide a superior and more sustainable EES offering compared to Li-ion. As will be discussed in later sections, one of the drawbacks of pure liquid-liquid RFBs is 'crossover' resulting in potential electrolyte contamination and capacity loss. Drawing on inspiration from FCs, hybrid RFB (hRFB) technologies have been developed to overcome this problem where, following crossover, liquid-gas phase separation can be easily handled. Ultimately, this work will come to demonstrate this via examination of a liquid-gas hRFB system in the final results chapter.

This chapter is split into two further parts. The following part (Part II) provides the background required to contextualise the subsequent chapters. Recent literature is reviewed, interrogating critical aspects of RFBs, such as electrode microstructure, electrocatalyst development, electrolyte composition, system performance, chemical / mechanical properties and operational geometries. In the final part (Part III), this chapter culminates in a series of research questions this work intends to address and the overall thesis structure.

Part II: Literature review

1.2 Redox flow battery chemistry and configuration

EES devices will, and indeed are, playing a central role in the transition towards a greener energy grid. Lithium-based chemistries have been at the centre of the broad commercial development of light-weight, portable devices for decades and, in the 2000s, the domestic electric vehicle market began to widely adopt lithium-based technologies for automotive purposes.[4,13] Since 2014, large-scale lithium-based energy storage systems have started to be commissioned onto the grid,[14] with plans to significantly increase the capacity over the coming years. While these developments are very positive and will certainly help support the transition to net-zero, as discussed earlier, lithium is a finite resource and alternative chemistries need to be explored to continue this expansion. RFBs have several characteristics that make it them potentially more compelling and more sustainable alternative.

Several excellent reviews focussing on different aspects of RFBs have been produced.[15–24] Each of them describe several advantages of RFBs compared to other forms of energy storage. Among them are scalability, stability, moderate maintenance costs, high roundtrip efficiency and therefore long service life.[17] The greatest advantage, however, is the ability to decouple energy capacity and power output allowing for flexible modular battery design according to application. The power output is varied either by changing the active area of the cell or by altering the number of cells in the stack. The capacity is modified by adjusting the volume / capacity of the 'tank' or by changing the composition of the electrolyte. In short, unlike conventional batteries, the energy is stored in 'tanks' external to the central cell rather than in the electrodes (in the cells) themselves. This layout and flow of liquid through this system also ensures effective temperature management of the cell, mitigating risks such as thermal runaway usually associated with high energy density storage systems. As with all devices though, there are drawbacks – the energy density of RFB electrolytes is lower than solid state batteries, it is currently expensive to manufacture the system components (membrane prices remain disproportionally high)[25] and electrolyte crossover is a common problem which, unchecked, causes permanent capacity degradation. One of the greatest milestones researchers and industrial developers are attempting to achieve is a cost target of \$150 kWh^{-1} for utility scale energy storage systems.[26] The figure below shows an illustration of a classical RFB – one in which the reversible electrode processes involve soluble, solution-based species (Figure 1.1).

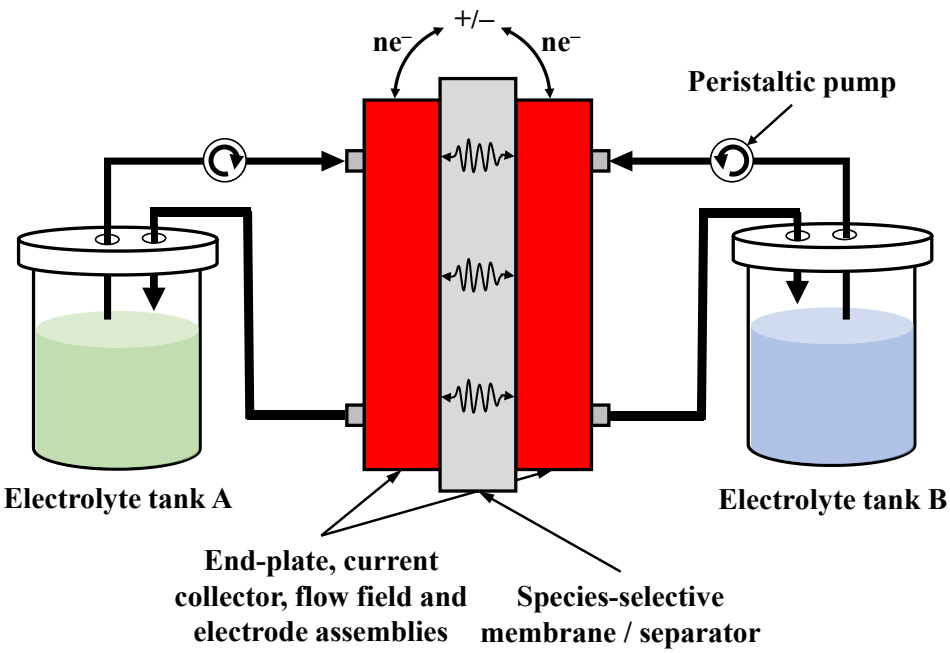


Figure 1.1: Illustration of a redox flow battery with schematic arrows in the membrane / separator indicating the movement of ions in either direction depending on the system and if it is charging or discharging.

Operationally, a RFB exploits redox active species to provide a source or sink of electrons via an external circuit. During the charge or discharge step, using pumps, the soluble redox active material passes through the electrodes and are oxidised or reduced as a result of the potential difference between the electrodes and their respective redox couples. This potential difference (polarisation) induces the transfer of electrons between redox active species and electrodes – an electrochemical reaction – thereby satisfying the demand / supply of the external circuit. There are several ways RFBs can be controlled including by changing the flow rate, temperature of the electrolyte / cell components or by adjusting the charging / discharging rates.

RFBs, and hybrids thereof, are defined by the solvent, phase configuration and redox active species used on each side of the separator. The following section focusses on the pros and cons associated with the solvent that makes up the essential liquid electrolyte. It is essential that researchers carefully consider the solvent in which the active species is dissolved. The solubility, stability and safety of the active species and system as a whole relies heavily on the solvent.

1.2.1 Solvents

In RFB research, the electrolyte refers to the solution that holds the charge carrier. This is made up of the redox active species (see Section 1.2.3), the solvent in which it is dissolved and any supporting salts (if needed to support the active species or make it more soluble). RFBs can be broadly split into two types based on the solvent used – non-aqueous and aqueous. Aqueous RFBs are those that have water-soluble redox species and, predictably, non-aqueous RFBs utilise organic solvents to support its redox species. These chemistries both have significant benefits and drawbacks.

Electrolytes that use water as the solvent (aqueous electrolytes) tend to be inexpensive, safer (intrinsically non-flammable) and, depending on the active species and supporting salt used, have higher conductivities. The main drawback, compared to non-aqueous electrolytes, is that the potential window in which the user can operate is smaller as, at too high a potential difference, the evolution of hydrogen and oxygen (water splitting) occurs. Electrolytes that use organic solvents are more expensive, not only because of solvent expense, but also because of the salts necessary to stabilise and raise the electrolyte conductivity.[16] They are also more difficult to handle (glovebox often required) and their physical properties such as moisture and air sensitivity, flammability (due to high vapour pressure) and toxicity make them less safe.[27]

However, high energy densities due to the lack of water splitting constraints and enormous flexibility in chemistry is attributed to non-aqueous electrolytes. The tuneable nature of the supporting solvent-salt matrices allow these electrolytes to harbour more exotic multi-electron transfer redox species, such as the phenazine molecule, and pair them with other redox couples resulting in reduction potential differences of over 1.5 V.[28] Acetonitrile is a commonly used solvent for non-aqueous RFBs – a particularly attractive feature of this solvent is its low surface tension which makes it good at permeating through porous electrode structures. Common supporting salts include tetraethyl-ammonium tetrafluoroborate ($TEABF_4$).

While there is less flexibility in raising the energy density in aqueous electrolytes, varying the pH affords some level of control over species solubility and stability. Some redox species are severely affected by the pH of the solution. hRFB systems are especially prone to changes in pH as a result of, for instance, protons travelling across the membrane to the liquid side (lowering the pH) or away from the liquid side (raising the pH), especially in liquid-gas hRFB systems. Another example where pH regulation is essential is in all-iron hRFBs (liquid-solid) where, given the high cell potential of the aqueous system (1.2 V), hydrogen evolution occurs as a result of water splitting. This causes an increase in pH and the precipitation of $Fe(OH)_2$ which is insoluble in water.[29]

1.2.2 Phase configuration

Given RFBs of all phase configurations must have some liquid flow component, there are a few major advantages over Li-ion batteries that these systems possess. The first is the improved level of control over thermal management in the system and therefore augmented safety; and the second, as alluded to earlier, is the ability to store electrolyte externally and therefore independently control the capacity of the battery. In addition to Figure 1.1, the following figure outlines the additional two hRFB phase configurations (Figure 1.2). The three main RFB and hRFB phase configurations are discussed in the following sections alongside a brief mention of gas-gas (fuel cell) systems. This work focusses on separate liquid-liquid and liquid-gas systems.

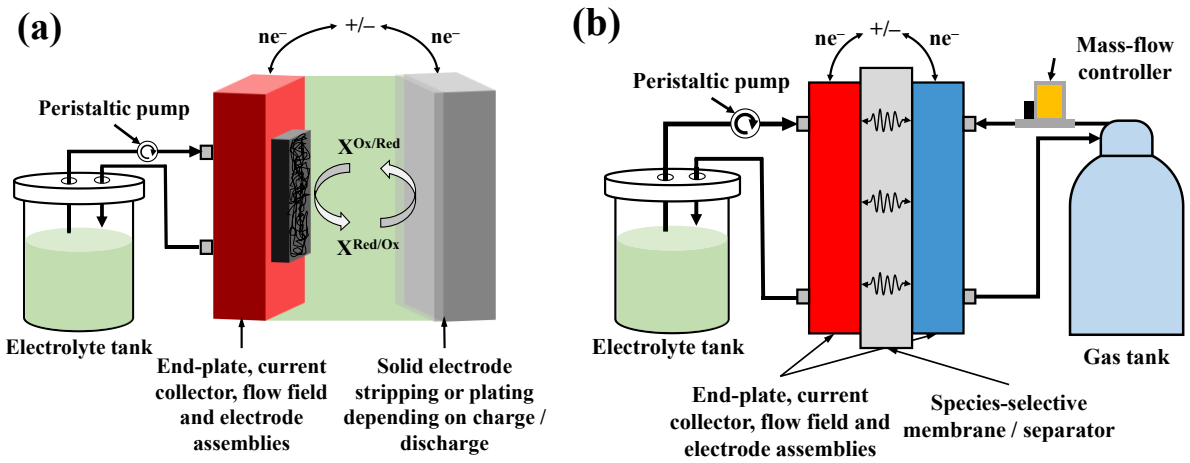


Figure 1.2: Two examples of hybrid RFB configurations (a) membrane-free liquid-solid and (b) liquid-gas utilising a cylinder.

1.2.2.1 Liquid-liquid

Before tackling hybrid systems, pure RFBs must again be considered. In their classical form, as depicted in Figure 1.1, RFBs have two external tanks containing active species in a liquid electrolyte which remains in the liquid phase before and after any redox process. One of the main benefits of this liquid-liquid configuration is the simplified system engineering – once leakage issues are overcome, handling and controlling the liquid electrolyte is manageable and straightforward with tuneable and facile cleaning procedures. Another benefit associated with this phase arrangement is the state of the membrane – unlike in liquid-gas configurations – the membrane is always hydrated uniformly.

However, there are considerable issues with this phase configuration. Crossover poses the largest drawback, if active species cross the separator material, this leads to a decrease in device capacity and potentially problematic mixing, producing unwanted side products. A higher probability of leakage due to liquid flowing in both sides of the membrane is present – leakage, clearly leads to a decrease in battery capacity and potentially dangerous consequences. From an energy density perspective liquid-liquid systems have the lowest power density because of the limited solubility of active species.

1.2.2.2 Liquid-solid

Liquid-solid configurations are hRFBs and draw half their influence from RFBs and half from solid state batteries. They come in two forms. The first is with a membrane, where the solid (usually metal) is pressed against a membrane material and a liquid is flowed over / through an electrode pressed against the other side of the membrane. The second is a membrane-less configuration, as shown in Figure 1.2 (a). In both configurations, the solid electrode undergoes

plating (solution based species become solid) and etching / dissolution during the redox processes depending if the cell is charging or discharging. The benefit of this type is the considerably low maintenance the solid electrode requires and the avoidance of crossover issues

The drawbacks associated with this configuration are significant. The system capacity is limited by the amount of solid that can 'fit' in the system. In systems containing a membrane, upon repeated cycling, dendrites form that can potentially penetrate the membrane and short-circuit the system.[30] This is not a problem with membrane-less configurations, however these systems can be adversely affected by the convectional flow over the solid causing additional pressure drop over the solid electrode. These devices are not considered in this work but are an interesting technology that has found commercial interest.[31]

1.2.2.3 Gas-gas

While, technically, gas-gas systems are not RFBs, from a phase configuration perspective they have pertinent qualities that potentially lend themselves to next-generation RFBs. Section 1.2.3 discusses the gaseous redox species that can potentially be used in hRFBs. This sub-section focusses more generally on the gas-gas phase configuration employed largely by FCs.

The first alkaline fuel cell was invented by Francis Bacon the 1930s,[32] and since the National Aeronautics and Space Administration (NASA) started using this technology in the 1960s, several other types of fuel cell have been developed.[33] Today, a number of established fuel cell technologies and companies exist and are the subject of intense research including solid oxide fuel cells (SOFCs),[34,35] molten carbonate fuel cells (MCFCs),[36] direct methanol fuel cells (DMFCs)[37,38] and polymer electrolyte fuel cells (PEFCs).[39–44] Each of these technologies have different operational requirements but the common principle is the same: they are EC devices that convert chemical energy (fuel, often in the form of hydrogen) into electrical energy via oxidation (often using oxygen from the air).

Polymer electrolyte fuel cells (PEFCs) utilise a polymer electrolyte / membrane that selectively allows ions to pass from one side of the cell to the other (Figure 1.3). Their compact design and relatively low (compared to SOFCs) operating temperature (60 – 120 °C) make them scalable, power dense and suitable for use in both stationary and transport applications. Compared to combustion engines or gas peakers, PEFCs do not emit hazardous by-products

and find ideal application in, particularly long-haul, automotive transport, potentially air travel[45] and, as previously mentioned, energy provision for data centres.

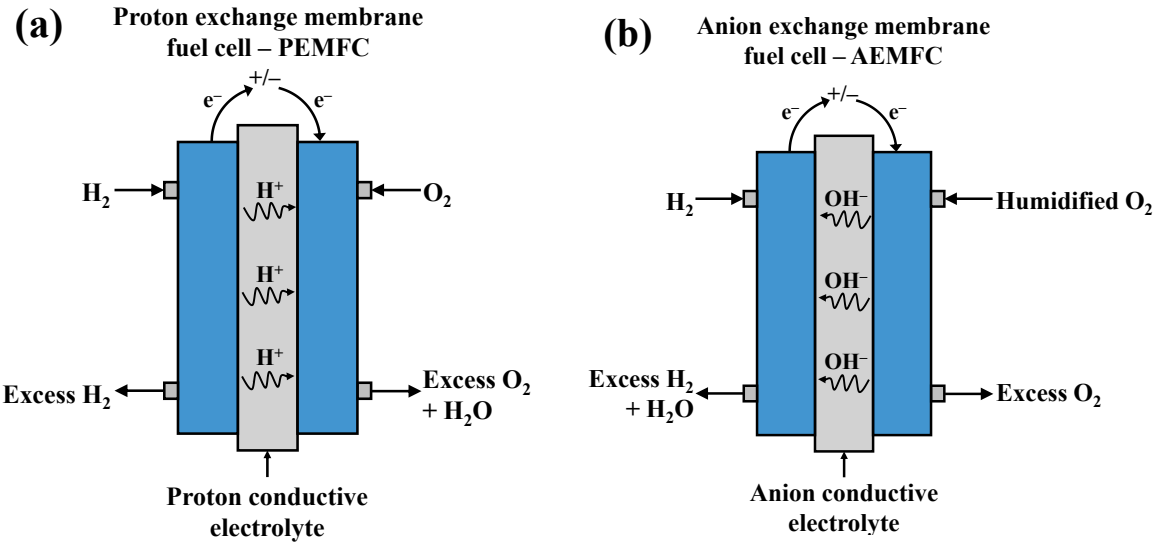


Figure 1.3: Principles of operating polymer electrolyte fuel cells (PEFCs). (a) A proton exchange membrane fuel cell (PEMFC). (b) An alkaline anion exchange membrane fuel cell (AEMFC).

Figure 1.3 shows the processes occurring in two main types of PEFC: (a) a proton exchange membrane fuel cell (PEMFC); and, (b) an alkaline anion exchange membrane fuel cell (AEMFC). The devices are defined by the type of ion that can pass through the membrane. For a PEMFC, hydrogen ions (protons) pass through the membrane and hydroxide ions (anions) travel across the membrane in an AEMFC. The processes occurring at each electrode are different across devices because of the different pH environment. The redox species involved and processes these devices carry out are discussed in more detail in Section 1.2.3.3.

1.2.2.4 Liquid-gas

Liquid-gas configurations (like liquid-solid) are another form of hRFB. This arrangement draws on two different electrochemical devices – the RFB and the FC – these hRFB systems are sometimes referred to as 'Regenerative Fuel Cells'. One of the main benefits of tying these technologies together is the facile phase separation following unwanted crossover reaction – the only minor exception to this benefit is when the species that has crossed over is damaging or poisoning the electrocatalysts aiding the gaseous electrochemical process. However, usually the main crossover species does not poison catalysts – separators and electrocatalysts are discussed later, in Section 1.3.3. The gaseous energy carrier can be either safely compressed in cylinders (as shown in Figure 1.2 (b)), produced in electrolysers, or, in the case of when an

oxygen redox couple is required, not stored at all ('air-breathing'). These gas storage methods significantly influence the energy density associated with the system.

FC research helpfully informs the engineering aspects of this phase configuration. Significant scrutiny of water / liquid management within FC electrodes and gas diffusion layers (GDLs) has been carried out. As well as the deep understanding and reliability of hydrogen (especially) and oxygen redox processes. The liquid-gas configuration is examined later in this thesis as it is considered to be the most technologically interesting.

1.2.3 Redox species

There are a wide range of redox species available. In RFBs, it is advantageous for redox processes to be efficient, with highly reversibility and fast kinetics. Redox species consist of metals, molecules or compounds that exist in a well-defined reduced or oxidised (redox) state. These 'redox couples' require an electron to convert from the oxidised to the reduced species. The potential at which this occurs is called the standard reduction potential and is relative to the reversible hydrogen electrode (RHE). There are several types of redox chemistry and they fall into three main categories: inorganic ions and metal complexes, metal-free organic molecules and gas-phase processes.[46]

1.2.3.1 Inorganic

Initially, researchers focussed on metal and halogen ions as they are easily soluble in water. The halogens, especially bromine and iodine were the most intensely studied as their redox potentials fall within the bounds of water electrolysis (*vide infra*).[46] The iron-chromium RFB system was the first to be explored taking advantage of Fe^{3+}/Fe^{2+} (0.77 vs. standard hydrogen electrode (SHE)) and Cr^{3+}/Cr^{2+} (-0.41 V vs. SHE) redox couples resulting in a cell voltage of 1.18 V.[47,48] Later, Skyllas-Kazacos et al. took advantage of the rich redox chemistries of vanadium, pairing the V^{2+}/V^{3+} and VO_2^{+}/VO^{2+} redox couples resulting in a cell voltage of 1.26 V.[49,50] Unlike the iron-chromium system, vanadium chemistry is robust and capable of achieving high concentrations, and therefore energy densities, at sufficient acidity. All vanadium RFBs (VRFBs) are the most extensively studied redox chemistry. They have demonstrated high power densities,[51–53] and have given extensive insights in to how RFBs generally operate. However, price fluctuations of vanadium ores and volatility associated with global stainless steel demand hinder its broad commercial rollout.[54] Several other inorganic

redox chemistries have been trialled such as zinc (Zn/Zn^{2+} -0.76 V vs. SHE) , bromine (Br_2/Br^- 1.09 V vs. SHE) and manganese (Mn^{2+}/Mn^{3+} 1.51 V vs. SHE).

Transition metal (TM) complexes use peripheral (often) organic ligands to enhance solubility and stability. During a redox process, these complexes undergo electron transfers that, depending on the tuneable ligand type, are either carried out via an inner- or outer-sphere electron transfer. There are several mono- / multi-dentate ligands that coordinate to central metal ions in specific ways, the nature of this binding affects the kinetics of the system and has been explored previously.[55] Matsuda et al. were the first to employ organic ligands in a ruthenium bipyridine (bpy, a bidentate, pyridinyl-derived, chelating ligand) based RFB system – $[Ru(bpy)_3]^{z+/(z+1)}$ (where z is 1 or 2 for the redox couples either side of the separator).[56] At 2.6 V the open circuit potential (OCP) and energy density for this system is high, however the energy efficiencies are low (40 %) as a result of the charge transfer resistances.[56] High energy efficiencies of nearly 100 % have been reached using actinide-based chemistries with ketonate-derived ligands.[57,58] These energy efficiencies are very high (much higher than analogous vanadium systems) as a result of very small changes in cation size during charge transfer,[59] however are impractical given their radioactivity and high cost.[16] The open format associated with organometallic metallocene (metal centre sandwiched between two cyclopentene rings) redox couples make their charge transfer kinetics fast. Hwang et al. reported a discharge voltage of 2.2 V between a bromoferrocene redox couple (BrFc, 0.219 V vs. Ag/Ag^+) and bis(cyclo-pentadienyl) $cobalt^{3+}$ ($CcPF_6$, -1.830 V vs. Ag/Ag^+).[60] While the types of available TM complex are diverse and extensive, the solubility of these compounds are often low and require specific, expensive salts to dissolve into solution.

1.2.3.2 Organic

Without being constrained by the limits and shortage of reasonably priced metals on the periodic table, metal-free organic molecules offer extensive, nearly unlimited, variation and structural diversity in chemistry. Quinones,[61] viologens, aza-aromatics, nitroxide radicals, quionoxalines[62] and thiophenes[63] all have shown promising capability in RFB systems.[64] However, organics, generally, do not show very high stability in solution – at least, not on the timescale required for long term energy storage solutions (years). Until recently quinones, arguably the most promising or these organic molecules, had capacity fade rates commonly exceeding 0.1 % per day.[65,66] This rate needs to be reduced significantly in order to reach the

levelised cost of storage goals for an RFB and therefore understanding and improving the chemical stability of these organic active species in aqueous conditions is critical.[64]

Table 1.1: Progression of quinone-derived redox couples in alkaline conditions. Capacity fade rate progressively becomes smaller with each developing structure. The 'Electron conc.' represents the number of moles of electrons each redox couple is able to utilise per litre of electrolyte. The redox potential for each couple is shown and the value in parenthesis is the OCP of the respective couple with $K_4Fe(CN)_6$ (which has a redox potential of 0.50 V vs. SHE). The acronyms are as follows: DMBQ = 2,5-dimethyl-3,6-dihydroxyl-1,4-benzoquinone,[66] DHBQ = dihydroxybenzoquinone,[67] DHAQ = 2,6-dihydroxyanthraquinone,[68] 2,6-DBEAQ = 4,4'-((9,10-anthraquinone-2,6-diyl)dioxy)dibutyrate,[69] 2,6-DPPEAQ = (((9,10-dioxo-9,10-dihydroanthracene-2,6-diyl) bis(oxy))bis(propane-3,1-diyl))bis(phosphonic acid).[64,70]

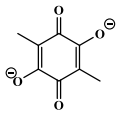
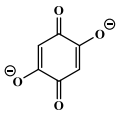
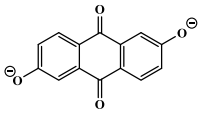
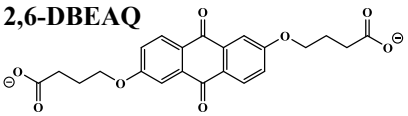
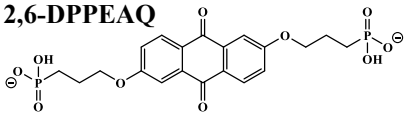
Acronym & deprotonated oxidised species	Capacity fade rate % / cycle	% / day	Electron conc. / M	Redox potential / V *vs.* SHE	pH
DMBQ 	**0.11**	**22**	**0.2**	**–0.75 (➞ 1.25)**	**14**
DHBQ 	**0.24**	**9**	**1**	**–0.72 (➞ 1.22)**	**14**
DHAQ 	**0.1**	**8**	**1**	**–0.68 (➞ 1.18)**	**14**
2,6-DBEAQ 	**0.001**	**0.04**	**2**	**–0.54 (➞ 1.04)**	**14**
2,6-DPPEAQ 	**0.0004**	**0.014**	**2**	**–0.47 (➞ 0.97)**	**9 – 13**

Table 1.1 demonstrates how development of new quinone-derived organic redox couples can significantly improve fade rates. As these redox couples have been developed, various chemical decomposition pathways have been established. During polarisation, benzoquinone moieties (molecules with just one ring, i.e. DMBQ and DHBQ) can suffer from gem-diol formation followed by Michael addition or tautomerisation.[64,71] The anthraquinone moieties avoid this chemical degradation pathway by taking advantage of fusing rings (and removing the reactive ortho-/meta- sites on the single benzene ring) and are more stable because of their ability to distribute the negative charge around the molecule (via its resonance structures). DHAQ has been shown to decompose via disproportionation and dimerization.[65] This dimerization is avoided by the addition of alkyl-carboxylate (2,6-DBEAQ) and alkyl-phosphonic acid (2,6-DPPEAQ) groups, sterically hindering this decomposition pathways. Finally, given these systems operate in strongly basic conditions, nucleophilic substitution can

occur (as OH^- ions are aggressive nucleophiles). Phosphonic acid groups have a slightly lower pK_a compared with carboxylic acid groups meaning their stability is higher at lower pHs. A side effect of these successive improvements is that the reduction potential of each of these couples is made more positive thereby narrowing the charge / discharge potentials in the full system.[64] However, while this is unfavourable, increasing the reduction potentials of these couples makes the reduced form more thermodynamically stable.[69] This progression of quinone-based aqueous organic electrolytes is a good example of methodical improvement, demonstrating holistic assessment of redox couples at every stage.

Another organic redox couple family to note are nitroxide radicals. The first non-aqueous all organic RFBs was demonstrated using 2,2,6,6-Tetramethyl-1-Piperidinyloxy (TEMPO) and N-Methylphthalimide redox couples in 2011 (with a cell potential of 1.60 V).[72] TEMPO radicals possess a quasi-reversible redox couple between the radical and its oxoammonium cation and the kinetics are faster than most metal-based redox couples.

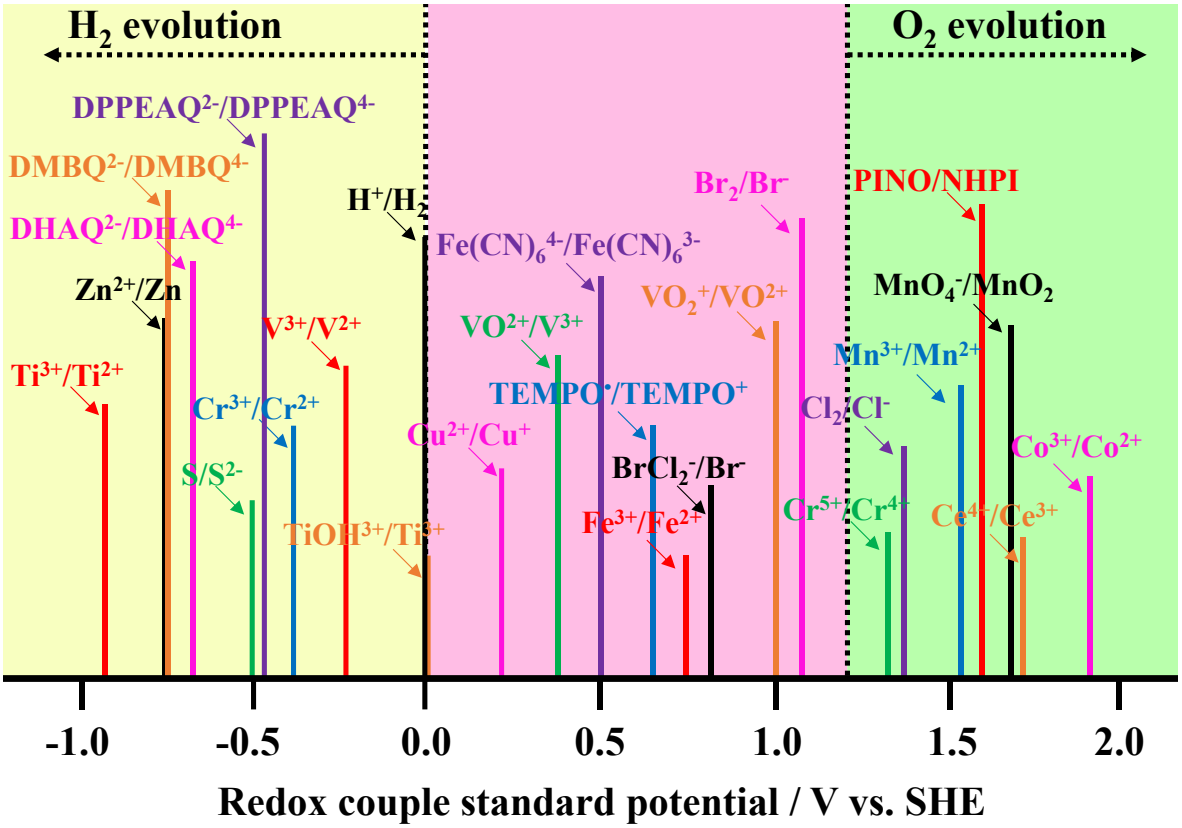


Figure 1.4: Modified from Yang et al. with additional standard potentials of redox couples added.[73] The pink shaded region indicates the thermodynamic region in which users can operate without water splitting. From a kinetic perspective, HER and OER occur at more negative and more positive potential, respectively.

Figure 1.4 shows a series of well known redox couples, note the inclusion of the hydrogen redox couple (at 0.0 V vs. SHE) – this redox couple is important for researchers attempting to

construct a liquid-gas hRFB system (introduced in Section 1.2.2.4). These additional gaseous couples are discussed in the following section.

1.2.3.3 Gaseous

While this section largely focusses on species appropriate for use within a RFB, gaseous couples involving hydrogen and oxygen can be used as the active species in hRFBs, as alluded to in Sections 1.2.2.3 and 1.2.2.4. Water electrolysis has demonstrated how oxygen can be used as an instrumental redox species while FC research and development has played a crucial role in how the research community and industry have harnessed hydrogen as an energy vector. These technologies can inform hRFB research and therefore a short background of FCs will be presented here followed by a discussion of the mechanisms and limitations of the equations associated with the fundamental reactions of oxygen and hydrogen.

In a PEMFC, hydrogen passes over the anode and is converted to protons releasing two electrons to the external circuit in the process. Meanwhile, at the cathode, oxygen (the oxidant) is reduced with the electrons from the external circuit and the protons arriving from the proton exchange membrane, and water is formed as a by-product – later expelled via the cathode exhaust. The equations for these electrochemical reactions are outlined here (Equations (1.1) and (1.2)):

$$\text{Anode reaction:} \quad H_2 \longrightarrow 2H^+ + 2e^- \quad E^0 = 0.000\ \text{V}\ vs.\ \text{SHE} \tag{1.1}$$

$$\text{Cathode reaction:} \quad \tfrac{1}{2}O_2 + 2H^+ + 2e^- \longrightarrow H_2O \quad E^0 = 1.229\ \text{V}\ vs.\ \text{SHE} \tag{1.2}$$

In an AEMFC, hydrogen again passes over the anode and is converted to protons via an electrochemical oxidation reaction releasing two electrons to the external circuit. But then, instead of passing through the membrane (as in a PEMFC), the protons combine with incoming hydroxide ions formed at the cathode that have passed through the anion exchange membrane to form water. The equations for these electrochemical reactions are outlined here (Equations (1.3) and (1.4)) and the overall cell potential for both systems comes to 1.229 V:

$$\text{Anode reaction:} \quad H_2 + 2OH^- \longrightarrow 2H_2O + 2e^- \quad E^0 = -0.828\ \text{V}\ vs.\ \text{SHE} \tag{1.3}$$

$$\text{Cathode reaction:} \quad \tfrac{1}{2}O_2 + H_2O + 2e^- \longrightarrow 2OH^- \quad E^0 = 0.401\ \text{V}\ vs.\ \text{SHE} \tag{1.4}$$

The central difference between these systems is the ion that travels across their membranes and the pH at which these electrochemical reactions take place. In a PEMFC, the low pH enables the hydrogen oxidation reaction (HOR) to occur at the anode with fast kinetics however, when operating the AEMFC, the HOR becomes significantly slower. A similar pH-dependant give-and-take occurs at the cathode, when operating a PEMFC (low pH), the ORR reaction limits the system whereas, in an AEMFC (high pH), the ORR reaction is more facile. The membrane capability (*vide infra*) lies at the heart of the relative dominance of PEMFCs compared to AEMFCs and is discussed in Section 1.3.3.

Oxygen reduction reaction (ORR)

Oxygen is reduced from its diatomic form via the oxygen reduction reaction (ORR). The ORR is one of the two electrochemical processes that occur in two types of next generation energy devices – FCs and metal air batteries. It has been the task of researchers to harness this reaction and efficiently overcome oxygen's strong bond energy (498 kJ mol^{-1}). Platinum group metal (PGM) (and, more recently, sophisticated carbon-based) electrocatalysts are typically used to activate the double bond and lower the energy barrier to enable the reduction to occur. The widely observed sluggish kinetics observed for ORR is attributed to the oxygen molecule undergoing complex, energy intensive multistep mechanisms depending on the environment in which the conversion is occurring and the electrocatalyst being used. Generally there are four dominant steps in solution-based ORR: (a) O_2 molecules diffuse from the bulk solution and adsorb at the surface of the electrocatalyst; (b) electron transport from the external circuit to the adsorbed O_2 molecules; (c) weakening and splitting of the double bond; and, (d) removal of the produced OH^- ions into solution.[74] While the mechanism is not fully understood and debate as to the experimental elucidation of the reaction mechanism is ongoing,[75] there are two dominant mechanistic pathways – a four electron pathway (does not involve a peroxide forming intermediate step) or a 2+2 electron pathway (involves the formation of a peroxide intermediate) – these contrasting mechanisms are shown in Figure 1.5:

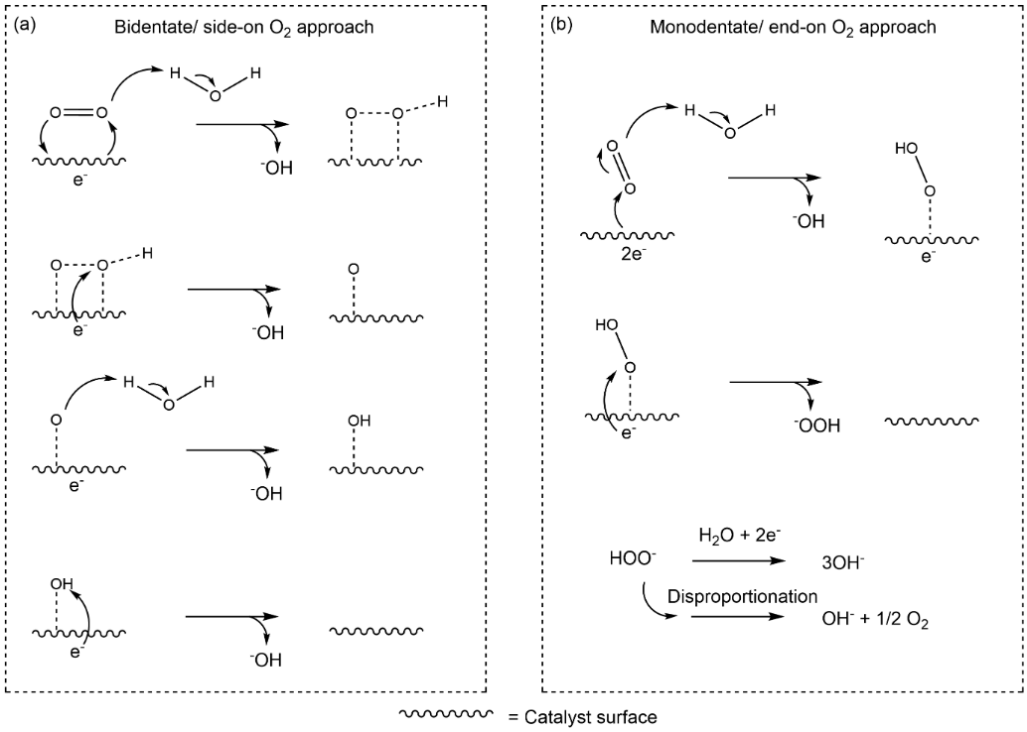


Figure 1.5: Visual schematic representations of the oxygen reduction reaction in alkaline via: (a) a four-electron mechanism; or, (b) a two-electron mechanism.[76,77]

These two pathways both occur to varying degrees in any electrochemical device. Platinum based electrocatalysts largely induce ORR via the four electron pathway as interaction between Pt and the oxygen is strong, meaning the O–O bond is broken before the second electron transfer.[78] For carbon-based electrodes, it is common for a combination of 2+2 and four electron pathways to take place simultaneously. The peroxide formation associated with the 2+2 pathway can be problematic as a result of oxidation / degradation of the carbon support / catalyst material and the FC's flow field.[79] The ORR reaction is highly pH dependent too – it is found to proceed much faster in alkaline conditions (compared to acidic conditions) either due to the presence of superoxo / peroxo ions, where the first electron transfer produces O_2^- as the rate determining step (RDS), or as a result of deprotonation at the active site.[80] Electrocatalysts that aid this reaction and the metrics by which they are judged are discussed in the following sections and chapters.

Oxygen evolution reaction (OER)

The oxygen evolution reaction (OER) proceeds via a four electron process. The OER plays a central role in water splitting and, given its relatively sluggish kinetics, is the focus of the significant research. To date, PGM catalysts (e.g. IrO_2 and RuO_2) have been shown to be the best OER catalysts, however their expense and scarcity makes it financially and

environmentally imperative to seek low-cost alternatives.[81] Carbon-based catalysts are usually where researchers 'start' when looking for alternative low-cost catalysts – the OER proceeds at high potential and carbon materials undergo oxidative degradation at these high potentials meaning that careful design of low-cost OER catalysts is needed.

The Sabatier principle was, for a long time, thought to best describe the overpotential associated with the OER mechanism – it states that the best catalyst in terms of displaying the minimum overpotential binds oxygen (or oxygenated species / intermediates) on its surface neither too strongly or too weakly.[82] This school of thought – the adsorbate evolving mechanism – has been progressively challenged following both experimental and theoretical observation that lattice oxygen may be involved in the mechanism.[83,84] That is, the O^{2-} lattice oxygen in a metal oxide catalyst is involved in the evolution of oxygen. However, following recent quantitative studies evidencing negligible lattice oxygen evolution, it is suggested that this is not a catalytic mechanism, but rather an unwanted side reaction associated with catalyst degradation.[85]

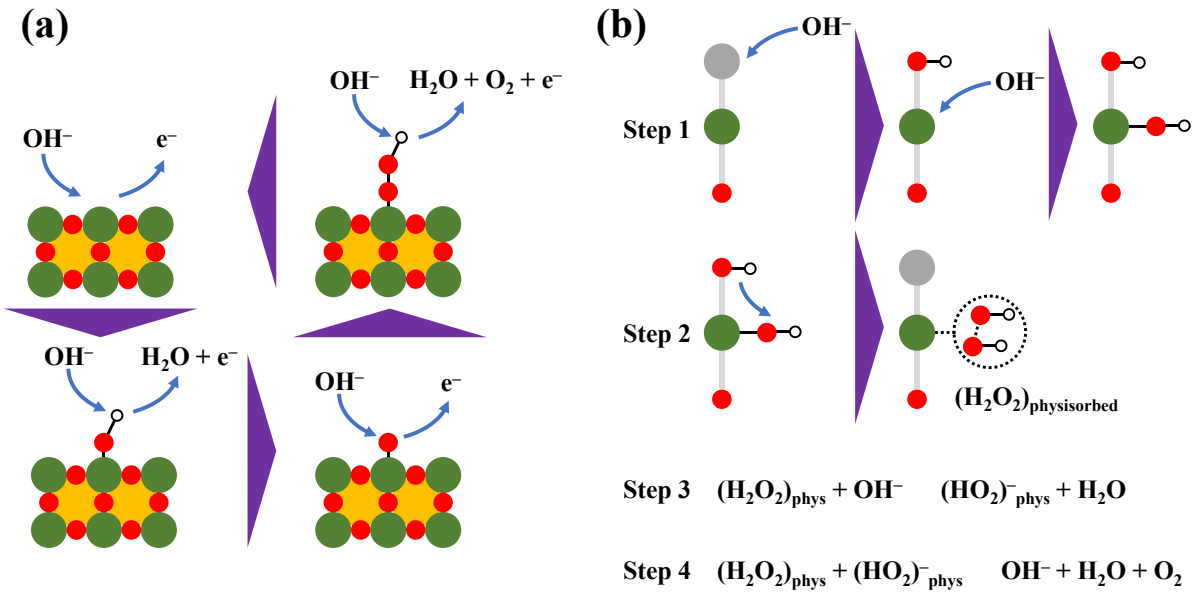


Figure 1.6: OER mechanisms via (a) an adsorbate evolving mechanism or (b) a proposed lattice oxygen mechanism using a perovskite (ABO_3) catalyst structure in alkaline conditions.[82,84,86] Green, orange, red and grey spots represent $metal_A$, $metal_B$, oxygen and vacancies in a perovskite framework, respectively.

Figure 1.6 depicts proposed mechanisms via the (a) traditional adsorbate evolving mechanism and (b) the proposed lattice oxygen mechanism on a perovskite (ABO_3) structure in alkaline conditions. In this example, hydroxide ions are used to fill an oxygen vacancy but it should be noted that the oxygen could originate from an O^{2-} moiety already in the oxide-containing

catalyst. Electrocatalyst exploration is discussed in further detail in later sections, however, the main issue with the OER is the prohibitively high oxidising potentials.

Hydrogen oxidation and hydrogen evolution reaction (HOR / HER)

Hydrogen is increasingly being used as an energy vector in hRFBs.[87] The hydrogen oxidation reaction (HOR) and hydrogen evolution reaction (HER) are the electrochemical processes occurring at the anode and cathode in FCs and electrolysers, respectively. These processes rarely limit devices' operating capability. Similar to the ORR and OER processes, HOR and HER are highly pH dependant, with higher overpotentials needed in base to achieve similar currents in acid.[88] This fact, along with the availability of efficient proton exchange membranes, has made PEMFCs and PEM water electrolysers the more developed and advanced technologies.

The HER is more facile than the HOR due to the more complex nature of the HOR mechanism.[89] In acid, the mechanism for the HER reaction is well established. However, there is not widespread agreement on the mechanism of the HOR reaction in alkaline conditions – different interpretations have been proposed.[90,91] There are broadly two schools of thought that influence the HOR mechanism: (1) pH dependant hydrogen binding energy (HBE), and (2) bifunctional theory based on contributions from both hydrogen and hydroxide adsorption. The first suggests that the HBE is the sole descriptor of HOR activity and accounts for the sluggish performance in alkaline as a result of the greater hydrogen binding in base compared to acid.[92,93] The second theory, based on voltammetry, considers a bifunctional mechanism where both catalyst oxophilicity and optimised HBE benefit the HOR performance – this theory accounts for the higher HOR activity on oxophilic Ru and PtRu catalysts compared to 'plain' Pt catalysts in alkaline solution.[90,94] Figure 1.7 (a) shows simplified representations of the HOR mechanism involving mono- and bi-metallic species. An alternative metric used to evaluate HOR performance is the apparent HBE (HBE_{app}). This involves both the HBE and the water absorption energy, thereby asserting that intrinsic HBE is pH independent while accepting that water adsorption strength is lowered with more alkaline conditions.[90] Volcano plots outlining catalysts exchange currents as a function of HBE_{app} and pH are displayed in Figure 1.7 (b).[95]

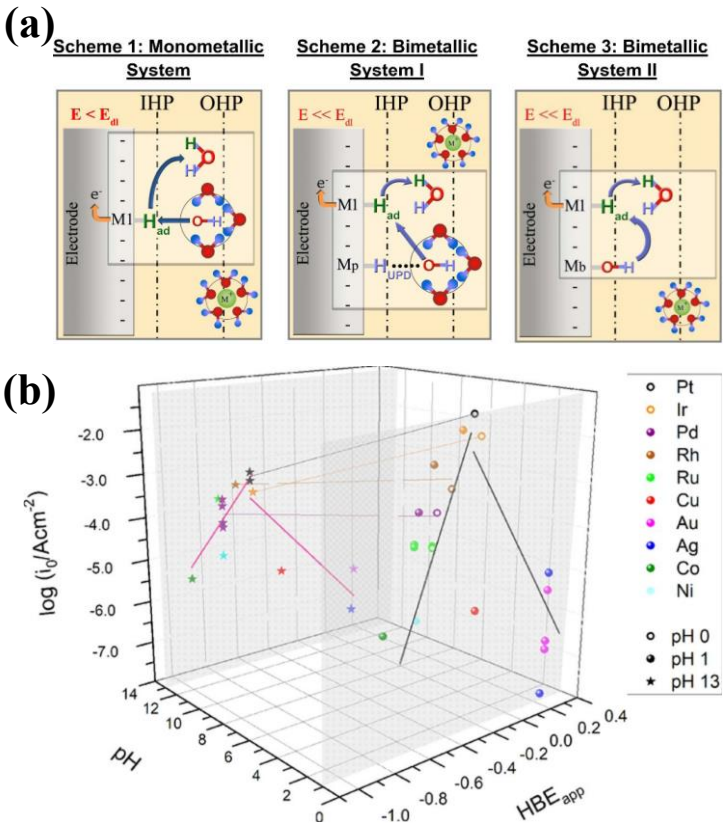


Figure 1.7: (a) Proposed iagrammatic representations of HOR mechanisms in dilute alkaline electrolyte for mono- and bi-metallic catalysts where M1 represents a metal capable of dissociative adsorption of molecular hydrogen, Mp represents a precious metal capable of forming H_{upd} in alkaline electrolyte and Mb represents a base metal site with adsorbed hydroxide species. IHP and OHP stand for the inner and outer Helmholtz plane, respectively. (b) 3D schematic using volcano plots (generated using measurements based entirely on voltammetry) to display the exchange current density as a function of the apparent hydrogen binding energy on a pH scale.[95]

It should be noted that, given this evidence for pH dependence on the HBE is based on voltammetry it can not be considered a realistic representation of real systems. Chen et al. carry out a more detailed analysis demonstrating that pH peaks on, in this case, a Pd monolayer are due dependant on anion adsorption (not hydrogen adsorption).[96] They conclude that during the HOR mechanism, rather than it just involving the adsorption and desorption of hydrogen, other anions, such as hydroxyl (or perchlorate if $HClO_4$ is used) are adsorbed at the active site.[96]

Given the high efficiency of PGM electrocatalysts the main challenge for the scientific community has been to find alternative, more sustainably sourced, inexpensive catalysts that are durable and perform sufficiently well to replace PGM-based electrocatalysts. An alternative way of approaching this problem is to reduce the amount of PGM-based electrocatalysts used in these electrodes. Solutions to this issue, the mechanistic processes, and the intricacies of the electrocatalyst active site, are discussed in later sections.

1.2.4 Redox flow battery-type systems

It is the job of researchers to find appropriate combinations of solvent, phase configuration and active species to develop RFB systems for specific application. The following flow chart (Figure 1.8) shows how RFB or hRFB devices might be chosen and devised. The only type of system not included in this discussion is the 'Liquid-solid' phase configuration as it is not studied in this work. Some existing technologies outlined in previous sections are discussed and evaluated according to various figures of merit in the following section.

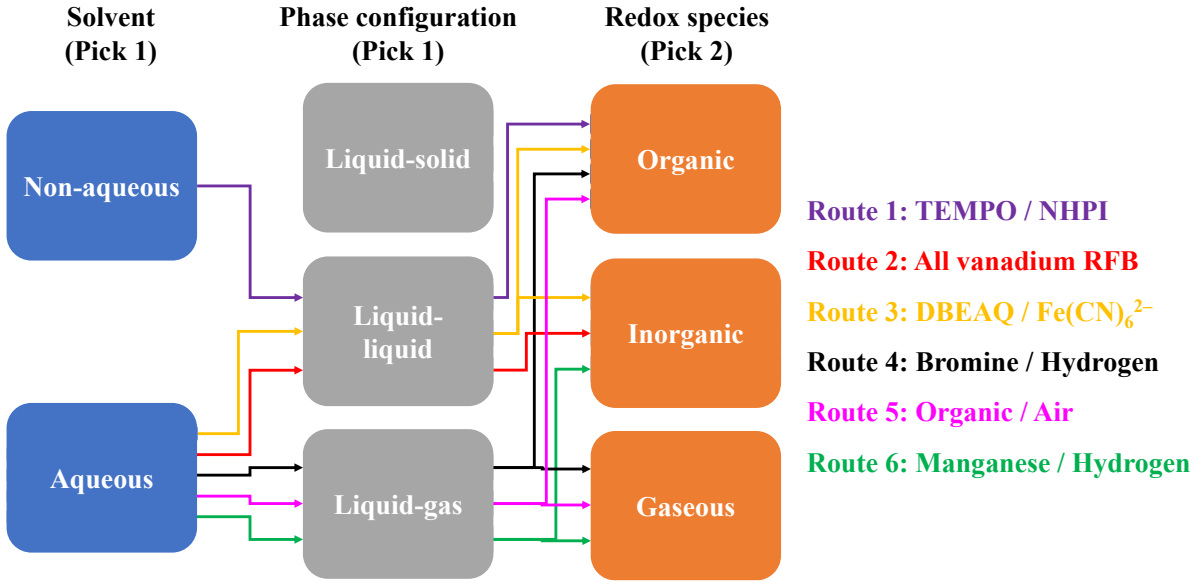


Figure 1.8: Flow chart displaying some examples of routes to established technologies. After choosing the solvent and phase configuration, two redox species can be chosen.

Of the systems displayed in Figure 1.8, the non-aqueous TEMPO / NHPI RFB system is the least explored (represented via Route 1, purple line).[97] Together, TEMPO and this alternative nitroxide-radical redox couple: N-hydroxyphthalimide (NHPI) and phthalimide N-oxyl (PINO), have a reduction potential of 1.30 V vs. the normal hydrogen electrode (NHE), making it the most positive reversible radical redox potential known.[98] Having been paired with an anthraquinone, this couple has also recently found use in a semi-aqueous RFB with an overall cell voltage of 1.15 V.[97] The VRFB and DBEAQ system (red and dark yellow, Route 2 and 3, respectively) have already been discussed but neatly highlight how researchers can easily couple any combination of inorganic and organic couple in aqueous systems.

The zinc redox couple has received considerable attention in recent years as a result of is abundance, low cost and recyclability.[99] The first zinc-air battery involving flow was reported in 1966 and, since then, the technology (involving flow or otherwise) is broadly

commercialised and finds application in devices ranging from hearing aids to utility scale storage.[100,101] Lin et al. recently tested their carbon metal fabrics in a small scale stationary system. While the current densities used were low (0.5 mA cm^{-2}), over 800 cycles were successfully carried out with an open-backed setup with an air-permeable Ni-foam current collector.[102] Coupling established redox couples with the oxygen redox couple provides the ability to significantly increase the energy density of an electrochemical device as either the oxygen can be compressed (leading to lower volume requirement) or, one side of the battery could be 'air-breathing'.

The fuchsia path (Route 5) represents a series of ambitious proof of concept organic-air systems have demonstrated the challenges that remain for hRFB systems involving the air electrode, but primarily the shortfalls of electrocatalysts.[103] Manthiram et al. have circumvented the need for a bifunctional catalyst by utilising a decoupled positive electrode configuration whereby two separate catalysts are used on the same side of an electrode.[104] While this configuration cleverly avoids the need for a single electrode material and successfully proves the organic-air concept – in order for hybrid-air RFB systems to progress, air-breathing electrodes require effective bifunctional electrocatalysts that can reversibly perform the ORR and OER – there are still significant shortcomings in these materials from a performance, expense and durability perspective (discussed in later sections and chapters).

As previously discussed, much lower overpotentials are required to perform the HOR and HER and so using this reliable redox couple is an effective way of ensuring stability on one side of a RFB. First reported in 2013,[105] a vanadium (+4/+5) redox couple has been used as a counter couple to hydrogen in a 'Regenerative Hydrogen-Vanadium Fuel Cell' and shows promising performance with high durability.[87] But, as previously mentioned, vanadium ore price is volatile and too high for broad commercial rollout. As a low cost alternative, manganese has received increased attention recently as a result of its broad redox chemistry both from industry and academia.[106,107] As the Earth's 12th most abundant element, it is of significant interest to researchers and those in industry with the need to reduce the cost of their active materials. The manganese-hydrogen hRFB was first reported in 2018 and exemplifies Route 6 in Figure 1.8 (green line). This system utilises a titanium additive that enables the stabilisation of MnO_2 in the charged state such that recovery of the full system capacity is possible on discharge. While promising, there are still unknowns about the nature of this electrolyte at high SOC. This is system is further introduced and scrutinised in Chapters 5 and 6.

The halogen-hydrogen hRFB has recently gained interest because of its fast, reversible kinetics, long durability and low cost reactant materials.[108] Of the hydrogen-halogen systems, the H_2-Br_2 cell has attracted the most industry attention as a result of the very high power densities, high round-trip efficiencies, high solubility or active species and low vapour pressure.[108] This system is represented via Route 4 (Figure 1.8, black line). Durability tests at 400 mA cm^{-2} lasting over 130 days with this system were recently reported with only a 7 % decrease in energy efficiency.[109] Technoeconomic analysis carried out by Elestor (a Dutch H_2-Br_2 battery manufacturer) has established that, from a cost perspective, capital investments into an H_2-Br_2 system are equivalent to Li-ion.[110] While this is a very promising technology, toxicity of the active species is unavoidable and will require further public reassurance for broad roll-out. Finally, an organic hydrogen system has recently been reported using an off-the-shelf functionalised benzoquinone,[111] and work is ongoing to develop further interesting and alternative systems with higher equilibrium potentials (compared to 0.85 V). As discussed in previous sections there is limitless opportunity in the tuning of organic molecules, however, concerns over active species stability and crossover must be taken into account when assembling these factors can have irreversible capacity and poisoning consequences, respectively.[112]

Table 1.2 compares easily comparable RFB device characteristics. Energy and power densities compared here reflect the solubility of active species encompass their electrokinetics. ('Durability', for instance, is not compared because of the vastly different techniques researchers use to test this particular aspect).

Table 1.2: Comparison of chosen systems using system-level figures of merit.

System	Phase Config.	Crossover?	Energy density / Wh L^{-1}	Power density / W cm^{-2}	Reference
All-Vanadium	LL	Yes	20-30	0.56	[113]
Zinc-Air	LG	No	256	0.195	[114]
TMAP-TEMPO	LL	Yes	100.3	0.099	[115]
DBEAQ-$K_4Fe(CN)_6$	LL	Yes	1.1	0.24	[69]
Bromine-Hydrogen	LG	No	195.8	1.4	[116,117]
Organic-Air	LG	No	20.6	0.050?	[118]
Manganese-Hydrogen	LG	No	33.0	1.41	[106]

1.3 Materials

1.3.1 Electrodes

Typically, RFB systems use electrodes that comprise fibres (c.a. 7 – 10 μm diameter) synthesised from polymer precursors such as polyacrylonitrile (PAN) via carbonisation.[119] These porous electrodes are central to the effective operation of RFBs and affect resistive 'losses' (ohmic – sometimes referred to as high frequency resistance – HFR), charge transfer and mass transport) associated with the system. Advantageous attributes usually include high surface area (providing more active sites for redox reactions to occur at), high permeability and low contact resistance summing to the overall ability to uniformly distribute electrolyte over the whole electrode.[120] While each of these qualities have an appreciable effect on the resistive losses (overpotential) associated with the cell, the dependency varies, in large part, as a function of the environment in which the electrode is placed (i.e. the redox couple used and the solvent in which it is dissolved – the electrolyte).

The main limiting factor to the broad commercialisation of RFBs is high capital costs.[15] The majority of these costs come with the materials within the stack (e.g. high membrane and machined flow field costs), however it is also critical to understand the transport phenomena occurring inside the electrodes.[121] Battery performance, especially power density, relies heavily on making the most of the entire electrode volume. The electrode porous structure including porosity pore size and pore shape defines the hydraulic permeability and therefore

the mass transport of the active species significantly.[121,122] Careful control of pore character is necessary to optimise for maximum permeability and surface area. Zhou et al. developed a dual scale porous carbon electrode that exhibits pores of (broadly) two different sizes and shows enhanced performance in a VRFB.[123] Adjacent methods used to force the best performance out of electrodes include varying the operating conditions (e.g. cell temperature and flow velocity) and the use of different flow through flow fields (FTFFs) and electrodes with interesting, circular, geometries.[124]

It is worth mentioning that carbon is not the only material used when preparing electrodes for RFBs. Nickel,[125] copper[126] and titanium[127] based electrodes are used in RFB setups too, though their relative expense makes them a poor candidates for widespread adoption. Carbon-based porous electrodes influence the efficiency, cost and durability of RFB systems and, in order to make them competitive with more established technologies, it is essential to improve design and reduce costs of these porous carbon electrodes.

1.3.1.1 Porous electrode types, flow fields and RFB cell preparation

There are three main types of porous carbon electrode – felts, papers and cloths – SEM micrographs are shown in Figure 1.9 outlining their surface morphology. Graphite felts (Figure 1.9 (a.i)) have been the electrode type of choice for VRFBs at both commercial and research levels for many years.[23,128,129] Felts have a relatively open format with high permeability allowing for electrolyte to easily pass around the porous matrix volume. Graphite felt's versatility and flexibility enables them to compress allowing for a well-sealed system with low contact-resistance. The main drawback associated with graphite felts is that they require high pumping power to achieve fast enough flow through the electrodes and the need for thicker felts for high surface areas.

Recently though, the dominance of graphite felt has waned following reports of impressive power densities of 557 mW cm^{-2} (at 60 % SOC) being reached using carbon papers (Figure 1.9 (a.ii)) with thicknesses an order of magnitude lower than that of felts.[113] Amongst manufacturers there is increasingly a trend towards using carbon papers (and cloths) as they are thinner, reduce the repeat unit length and allow higher volumetric performance which leads to reduced stack costs. Elestor have opted for an off the shelf carbon paper (thickness 0.2 – 0.4 mm) to act as the liquid diffusion electrode in their hydrogen-bromine hRFB.[110] These thinner carbon papers are extensively examined in studies involving PEMFCs and often in conjunction

with a GDL supporting electrocatalysts.[130] Equivalent performance enhancing techniques suitable for RFB technologies are being carried out, for instance, via electrophoretic deposition on carbon papers[87] and controlled thermal treatments.[131] Zhang et al. and others have examined the flow properties through porous media in detail using model-based frameworks providing valuable insight for manufacturers and experimentalists synthesising these electrodes.[132] Tomographic imaging coupled with a pore network model (PNM) has demonstrated the potential existence of dominant electrolyte flow paths through carbon paper electrodes.[133]

Carbon cloths are a relatively nascent carbon electrode type. These ordered and periodic electrode structures consist of fibres grouped into tows / bundles that are threaded together in a variety of ways appearing with a unique weave pattern when observed in the through-plane dimension (Figure 1.9 (a.iii)).[134] Several articles have demonstrated the electrochemical superiority of woven vs. non-woven materials citing their enhanced ability to distribute electrolyte over the whole electrode surface,[122,135,136] Only recently, however, has any attempt to directly ascertain a relationship between weave pattern and electrochemical and hydrodynamic performance.[134] RFB cells utilising carbon cloths with simple weave patterns (one-over, one-under) have, so far, been shown to demonstrate the best performance.[134] Functionalisation of carbon cloths using nanotubes (enhancing surface area) and inserting heteroatoms into the graphitic fibres (inducing more electropositive neighbouring carbon atoms that serve as active sites)[137] is demonstrating the flexibility porous, fibrous carbon electrodes have while retaining the benefits of long range order / directionality.

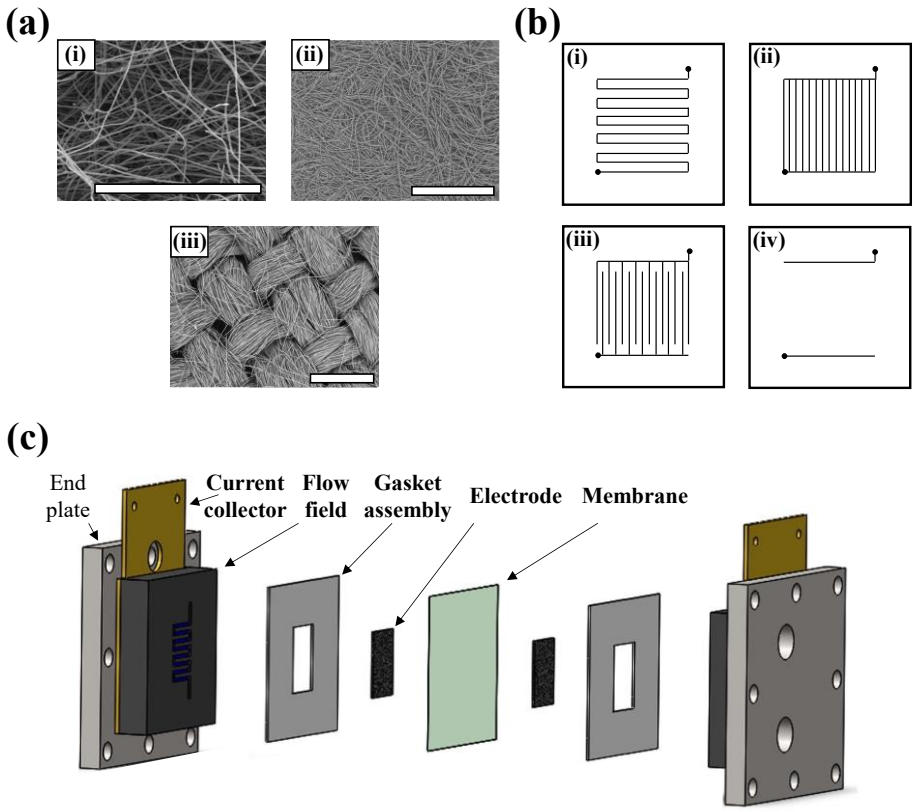


Figure 1.9: (a) Scanning electron microscopy micrographs with a 1 mm scale bar inserted (a.i) Carbon graphite felt (GFA5, SGL),[138] (a.ii) Freudenberg carbon paper and (a.iii) AvCarb 7497 carbon cloth. (b) two 'flow-by' (b.i-ii) and two 'flow-through' (b.iii-iv) flow field types (b.i) serpentine, (b.ii) parallel, (b.iii) interdigitated and (b.iv) parallel and (c) a generalised exploded diagram modified from reference.[138]

Flow fields play a key role in ensuring effective electrolyte transport through electrodes. Figure 1.9 (b) illustrates examples of flow fields – those that have a clear, machined path through the POCO graphite flow field are generally known as 'flow-by' flow fields, such as serpentine and parallel (Figure 1.9 (b.i) and (b.ii)). 'Flow-through' flow fields are those that force electrolyte through the electrode to some degree, such as interdigitated and 'flow-through,' respectively shown in Figure 1.9 (b.iii) and (b.iv). Flow-fields have a significant effect on the performance of the system.[139,140] Serpentine flow fields are the most commonly used, however, depending on the type of system / electrolyte the flow-through flow field might be advantageous. Before cell assembly, the user needs to decide how compressed the electrodes need to be after tightening – the 'pinch'. Typically electrodes are compressed between to about 70 – 80% of their original thickness (i.e. by 20 – 30%). The way this is controlled in the cell is by cutting gasket material and layering them until the requisite thickness is reached. Cell compression is important to ensure good contact between the electrode and both the membrane and conductive flow field –studies have been carried out investigating this dependency.[141,142]

After these preparatory steps are taken, the final step before cell assembly is to complete electrode pre-treatment. Pre-treatment is essential to exploit the full potential of the electrodes used in RFBs. Carbon electrode materials have, to date, largely been designed to accommodate the needs / design requirements of FCs, providing functionalities such as water expulsion, gas distribution and conduction of heat.[143] While these functionalities are significant, they are not centrally important for RFB electrodes – heat is thermally managed, easily controlled and dissipated by electrolyte stored in external tanks. Uniform distribution of liquid electrolyte providing access to high-surface area electrodes is a central functionality that needs to be optimised for electrode use in RFBs (*vide infra*).[119] Electrodes are therefore modified/ treated before use in an RFB system. Skyllas-Kazacos et al. were among the first to demonstrate the performance benefits associated with oxidative heat treatments,[144] and many have since attributed augmented performance to this surface functionality.[23,145] Recently, an instructive, methodical survey of heat treatments carried out by Greco et al. revealed that, for VRFBs using SGL 29AA carbon paper electrodes, the optimal conditions for thermal pre-treatment was 475 °C under air for 30 h.[131] An excellent timeline summarising progress in electrode treatments can be found at the following reference.[23] There are many other kinds of pre-treatment for electrodes such as immersing the electrode in acid or alkali[122] solutions for a period before use, hydrothermal ammoniated treatment to introduce N-atoms creating more electropositive neighbouring carbon atoms[146] and plasma treatment.[147] Each of these treatments induces augmented performance and, again, attributes this to different characteristics such as surface functionalisation, greater graphitic edge site population, higher electrode surface area and improved wettability.[131] Once this final electrode preparation is complete, the cell can be assembled using guiding pins and is then tightened using a torque wrench.

1.3.1.2 Characterisation

Several types of characterisation and diagnostic techniques are used in RFB system / component inspection – they are summarised comprehensively in a review published by Gandomi et al.[148] Electrochemical techniques such as (galvanostatic or potentiostatic) polarisation, cycling and electrochemical impedance spectroscopy (EIS) are usually used to ascertain the overall cell performance in standard cells (Figure 1.10 (a), via power curves, E/t plots and Nyquist plots, respectively, see Chapter 2 for more detail). It is challenging to discern between specific components of a RFB cell (i.e. electrolyte, electrode or membrane) during cell operation, however, some specific in-situ cell setups allow operators to focus solely on the electrode. The Brushett group have developed reliable zero-gap flow cell setups that allows

users to deconvolute resistive losses in the contributing to the overall cell resistance at specific states of charge (Figure 1.10 (b)) and isolate specific transport issues within electrodes (Figure 1.10 (c)).[120]

The configurations outlined in Figure 1.10 (b) and (c) have been used to uncover interesting findings about the relationship between electrode type / microstructure and overall cell performance via electrolyte viscosity,[149] porosity,[150] permeability[151] and mass-transfer[152] parameters.

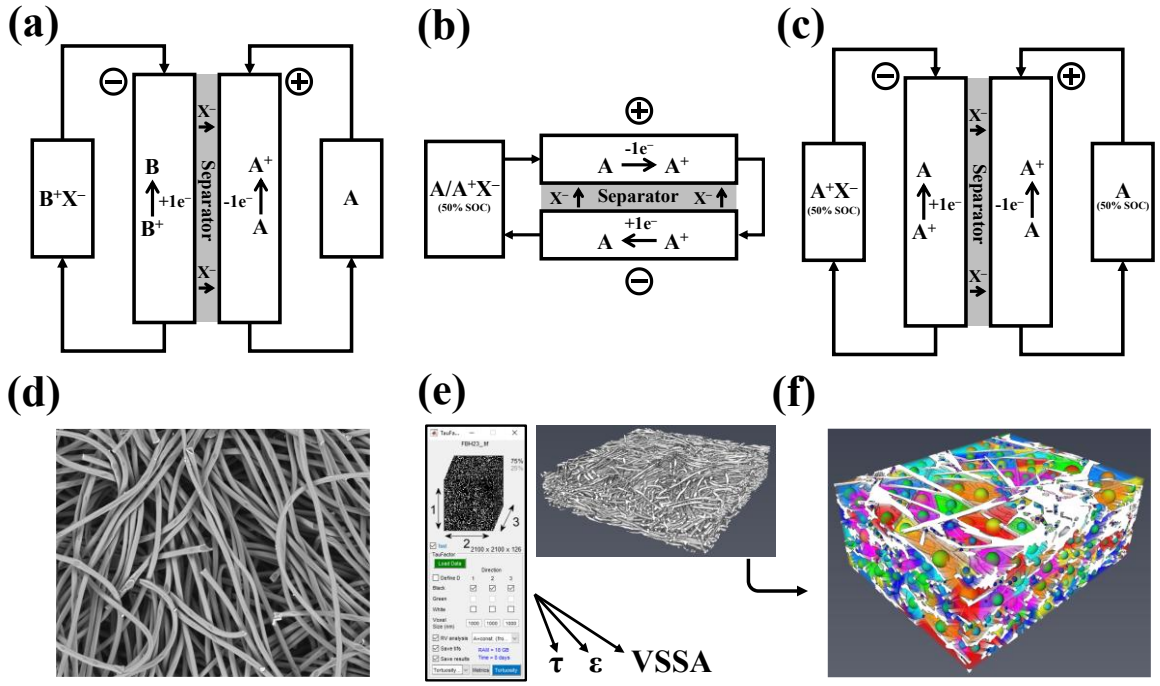


Figure 1.10: (a) A standard RFB setup with different redox couples either side of a selective membrane. (b) The electrolyte flow cell is used with a stable, well-defined redox couple ensuring a single and controlled state of charge assuming rapid reversible reactions (c) The symmetric flow cell uses the same redox couple in each of the two reservoirs separated by a membrane. (d-f) are visual examples of physical characterisation and modelling tools – (d) is a 2D SEM micrograph, (e) represents modelling tools and 3D reconstruction software (TauFactor 'plug-in' yielding tortuosity factor, τ, porosity, ε, and volumetric specific surface area, VSSA, and; Avizo, respectively) and (f) is an extension of the 3D reconstruction using the maximal-ball algorithm to estimate pore size for a pore network model (PNM).

While in-situ electrochemical techniques for understanding the processes that occur in electrodes are available, they are time-consuming for experimentalists. Ex-situ techniques such as scanning electron microscopy (SEM), Brunauer–Emmett–Teller (BET) theory and X-ray computed tomography (XCT) measure electrodes' physical characteristics. SEM informs users about the topographical surface features of the electrode, BET is a non-destructive method for measuring surface area of the electrode and XCT enables operators to extract three-dimensional (3D) information about these carbon based porous structures such as porosity, volume-specific surface areas and tortuosity factors. These are all examples of non-destructive and non-invasive

methods for measuring electrode characteristics. Mercury Intrusion Porosimetry (MIP) and Fast Ion Beam-SEM (FIB-SEM) are invasive / destructive equivalents of BET and SEM, respectively, and are used extensively in the carbonaceous porous electrode community.[134] These characterisation techniques are discussed in greater detail in Chapter 2.

XCT has gathered considerable interest in recent years with a 10-fold increase in the number of research articles with a title including the term "X-ray computed tomography" between 1999 and 2019 (34 vs. 363). Originally used for medical imaging purposes,[153] XCT has also found application in Earth Science and Minerals Processing where metal density can be used to track dissolution of copper metal within rock columns.[154] More recently, XCT has found use at a micro-level in imaging fibrous carbon materials. Post-processing, using imaging programmes such as Fiji and Avizo yields 3D reconstructions and of these porous structures and further computational effort can uncover interesting fluid flow findings.[155] Alongside these informative 3D images (Figure 1.10 (e) and (f)), open-source software such as TauFactor, a MATLAB 'plug-in', have been developed to extract useful information, such as volumetric specific surface area, porosity and tortuosity, from 3D segmented images.[156] TauFactor uses an informed machine learning (ML) approach to segment a stack of 2D images based on a users input.

Model-based approaches are also intensely studied.[157] Multi-dimensional models use various approaches to species and kinetic transport processes, the most relevant to this work is the conventional Butler Volmer (BV) approach which is commonly used to describe the net rate of charge transfer in an electrochemical device.[151,158–161] XCT images have been used as the framework around which pore network models (PNMs) and lattice Boltzmann simulations are developed.[132] Each of these modelling techniques have their advantages and disadvantages. PNM models require considerably less computing power than continuum models however their shortcomings are associated with very simplified approximation of the pore phase resulting in potential under- / over-estimates of real surface areas.[133] Mistry et al. discuss in a recent review the importance of ML in electrochemical scientific research and how it can contribute to researchers being more selective with where they focus efforts by leveraging model predictions.[162]

1.3.1.3 State of the art

Recently, Gayon-Lombardo et al. and Kench et al. implemented statistics and parameter based, deep convolutional generative adversarial networks (GANs) to generate 2D and 3D n-phase microstructural data for the improved design and screening of SOFC and battery solid electrodes (Figure 1.11 (a)).[163,164] While interesting and exciting these ML techniques are currently non-transferrable to fibrous carbon electrodes. This is due to the question of the representative elementary volume (REV). The REV not only defines the statistically representative sample to determine properties, but also the minimum size required that, within error, results in the same response everywhere else across the volume.[165] It must be large enough to be a meaningful volumetric average of the discrete microstructure; and small enough to not be affected by any large-scale heterogeneity of the porous medium.[166] The problem is also encountered by those examining fibrous electrode images in XCT post-processing and subsequently running models over them as assumptions about representativity of the sample need to be made. Modellers test representativity using a three point correlation function which, so far, has not reliably been passed by fibrous electrodes.

Similarly to the sequential development of electrolytes (Table 1.1), the aim of several experimental publications has been to inform researchers and manufacturers about the important aspects of microstructural design in electrodes. Following their initial finding that bimodal pore size distributions were advantageous for electrolyte distribution around a porous carbon electrode,[150] Forner-Cuenca and Wan et al. developed a new method for fabricating ‘designer electrodes’ with either polyporous (with macrovoids, electrolyte highways), isoporous or porosity gradient electrodes suitable for a variety of RFB applications (Figure 1.11 (b)).[167] Scalability is critical in the roll-out of any new technology – in this case, it is important to holistically consider fabrication and manufacturing limits as well as the associated costs.[120]

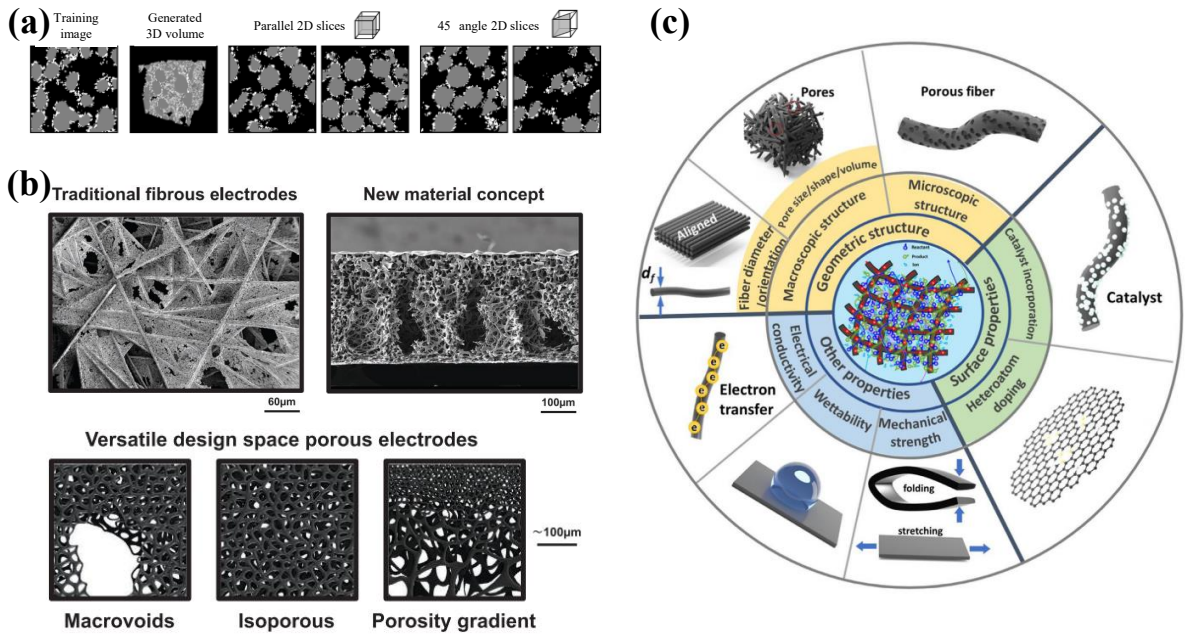


Figure 1.11: (a) One application of SliceGAN in the generation of a new SOFC electrode.[163] *(b) Comparison between traditional fibre electrodes and real (top right) and hypotetical new designer electrodes (bottom row).*[167] *(c) A diagram outlining the properties focussed on in the production of new electrospun electrode materials.*[168]

A recent review outlines the substantial progress in controlled functionalisation of electrospun materials (Figure 1.11 (c)).[168] Similar to the designer electrodes mentioned above, this review highlights the current focuses of electrospun materials as, (1) enhancing mass transport by tailoring fibre diameter / orientation or by creating secondary pores and, (2) improving surface properties via heteroatom doping and electrocatalyst decoration. The electrospinning technique has recently merged fabrication of functionalised carbon-metal fabrics with carbon nanotubes – another popular feature used to decorate carbon fibres significantly increasing surface areas – finding interesting application in zinc-air batteries.[102] Carbon aerogels (CAGs) are another exciting development in the diversification of methods by which electrodes are fabricated. In a forthcoming paper from our research group, it is shown that CAGs are highly tuneable (in terms of N-doping) and shown to effectively increase the electrode surface area.[169] These findings contribute to promising pathways towards RFB power density increases – making them more competitive with their lithium-based counterparts.[170] Again, similar to the electrospun materials, one potential future use case for CAGs is to decorate / dope their monoliths with electrocatalysts specific for the redox process occurring on that side of the battery. This would involve careful electrocatalyst selection for co-synthesis with the aerogel monolith.

Electrode materials, electrode geometries and electrode fabrication methods continue to develop with the aim of developing electrodes that are able to enable high power density, long duration and inexpensive RFB systems. Meanwhile, adjacently, electrocatalysts are being developed to reduce overpotentials and enable kinetically sluggish reactions to proceed – this development is discussed in the following section.

1.3.2 Electrocatalysts

Electrocatalysts are an essential component in many electrochemical devices and, as such, significant effort is directed at their development. Electrocatalysts are needed, primarily, to reduce the activation energy and overpotential required for electrochemical reactions. As briefly mentioned in Section 1.2.3.3, the hydrogen and oxygen fundamental electrochemical reactions that occur in PEMFCs require electrocatalysts for efficient operation. With a view to expanding the breadth of RFB hybrid technologies it is prudent to explore these intensely studied electrocatalysts for use in the gas side of an hRFB system (introduced in Section 1.2.2.4).

In FC research, in both acid and alkali conditions, the centrally difficult problem to resolve is the large 0.3 – 0.4 V loss in potential mostly at the cathode – i.e. during the ORR.[171] To date, platinum continues to be the catalyst with the highest electrocatalytic activity for both the HOR and ORR. In order to make these devices competitive with, internal combustion engines in the case of FCs, or gas peakers in the case of RFBs, the capital costs of these electrochemical systems needs to decrease.[26] This depends, in part, on PGM prices and either a decrease in catalyst loading on the electrode,[172] or the development of new, inexpensive electrocatalysts to replace these precious metal catalysts. Some recent cost analysis calculated the catalyst and its application to account for 41 % of the total capital cost of the FC stack in a light-duty vehicle (membrane accounted for 8 %).[74,173] Briefly, up-to-date cost analyses for membrane-electrode assemblies (MEAs) in FCs are difficult to find given commercial competitiveness and balance of plant considerations however, membrane materials are considered to significantly contribute to device capital costs. In the case of FCs, it is challenging to use non-PGM catalysts due to the harshly acidic or basic conditions and the need to reach high power densities at demanding overpotentials for transport and stationary purposes.[174] In the RFB case, as discussed in Section 1.2.2.4, introducing gaseous redox couples can improve system power densities and so it is important to have sufficiently inexpensive catalysts to support this growth in hybrid systems.

The pH dependence of catalysts should not go unmentioned. As discussed in Section 1.2.3.3, electrochemical devices are operated in pH-specific environments. PEMFCs are operated in acidic environments and AEMFCs, as the name suggests, are operated in alkaline conditions. RFBs can be operated in conditions across the pH scale – it is up to researchers to pair redox couples with suitable counter couples and membranes / separators with appropriate selectivity. The catalysts used in these devices therefore need to be able to resist harsh acidic or alkaline conditions. There are some overarching realities about the reactions themselves that must be accepted with testing these catalysts, for instance, the hydrogen reactions are slower in base than they are in acid while the oxygen reactions are faster in alkaline conditions than they are in acid. The kinetics of the HOR reaction in Pt/C is two to three orders of magnitude slower on moving from acid to alkaline solution meaning that more Pt is required.[88,175]

One of the main issues facing electrocatalyst development is the lack of standardised electrochemical protocols which prevents facile comparison of electrocatalyst performance.[176] In 2019, Wei et al. set out robust benchmarking techniques for the design of experimental setup, data post-processing methodology and performance parameters selection for each of the fundamental hydrogen and oxygen reactions in FCs and water electrolysers.[176] This work is relatively new but will, hopefully, make comparing catalysts significantly simpler. Publications on electrocatalysts usually focus on just one or two of the four central processes: HOR, HER, ORR and OER, and usually in just one pH at a time. This is reasonable, as each of them have specific requirements for their development. The following section provides a general survey of electrocatalyst type sorted by electrochemical process.

1.3.2.1 Types

Zeolitic imidazolate frameworks

Zeolitic imidazolate frameworks (ZIFs) are a subclass of a broader family of hybrid materials named metal organic frameworks (MOFs). MOFs are a crystalline class of materials that are characterised by the coordination of (usually) a central metal ion surrounded by an array of organic ligands – they known for their very high surface areas, crystallinity and visually pleasing structures.[177] Specifically, ZIFs are characterised by a tetrahedrally co-ordinated central transition metal ion such as iron, cobalt or zinc. The surrounding ligands are imidazolate linkers (that is, a reduced form of imidazole-type molecule, sometimes referred to as "Im^{-}").[178] Any 'ZIF' material is followed by a number, determined by the metal ion and the exact imidazolate linker used. For example, ZIF-8 and ZIF-67 are some of the more common ZIF

materials that are made up of, the simplest imidazolate coordinating ligand (with no substituents) and a central zinc or cobalt ion, respectively.[179] ZIF materials have found application in a range of sectors including carbon capture, molecular sieves and drug discovery.[179,180] Electrocatalysts are a focus in this work and ZIF-67 was chosen as a substrate material because of its structure and its cobalt and high nitrogen containing character. Other ZIF materials, such as ZIF-8, have been used as catalysts in their own right, or as substrates onto which single atoms are dispersed.[181,182] These materials have been shown to have extremely high activities towards especially ORR.[182] It is important to explore alternative catalyst materials such as these in order to bring down the costs of catalysts in, for instance, PEMFCs (PGM catalysts account for up to 60% of the overall cost of a FC stack).

Catalysts for the oxygen reduction reaction

Platinum catalysts have always been the dominant catalyst material used for the ORR in FCs.[174] Given its expense, as discussed above, researchers have endeavoured to use increasingly low amounts in both analytical tools (0.16 μg_{Pt} cm^{-2}),[183,184] and at device-level (< 125 mg_{Pt} cm^{-2}).[185] Another method for reducing platinum loading is by alloying platinum with other, inexpensive metals anticipating that combinations of Pt-M might both reduce expense and increase onset and halfwave potentials (due to favourable interactions between their molecular orbitals).[75] One successful instance of this, and again demonstrating effective communication between modellers and experimentalists, was the identification, via DFT, of platinum alloyed with early transition metals such as scandium and yttrium. Experimental testing of these catalysts on an RDE demonstrates significantly augmented catalyst activities due to weaker active site-intermediate binding(Pt_3Y > Pt_3Sc > Pt).[186] It should be noted, however, that these catalysts do not show promising activity in real systems, and, while achieving higher currents at 0.9 V is impressive on RDE, rarely is this an indicator of high power and durability in real systems such as PEMFCs. In fact, it is worth stating that predicating expected performance in fuel cells on measurements made at 0.9 V is a poor approach – not least because this is not a relevant potential for regular FCs operation. Zalitis et al. showed, for PtCo catalysts, the higher performance at 0.9 V is short-lived and, at lower potentials (more relevant to FC operation), Pt exceeds the performance of PtCo.[187]

Besides platinum, carbon supported catalysts are a popular area for ORR research – this is mainly because carbon in its basic powder form is inexpensive and it does not deteriorate at ORR potentials (0.5 – 0.9 V). Phosphides,[188] sulfides[189] and nitrides[190] have been appended in

various different ways to graphitised carbon supports. As a result of the differing electronegativities of these heteroatoms compared to carbon (C = 2.55, S = 2.58, N = 3.04 and P = 2.19 – Pauling scale), carbon–heteroatom bonds have diverse polarity making either carbon or phosphorous attractive sites for reactants. Transition metal and mixed-metal oxides have also been used extensively as ORR catalysts with interesting and promising results. Exploring the effect of co-locating metals, alongside the introduction of dopants or vacancies in various types of crystal structure gives rise to a rich research field, however, issues surrounding poor conductivity and dispersibility make progress slow.[191]

Further to the functionalisation of carbon materials using carbon nanotubes or metal oxide nanorods, using intrinsically functionalised carbon materials, such as egg-shells,[192] has become particularly popular. Oligomerised diaminonaphthalene (ODAN) is an example of an intrinsically functionalised (nitrogen-doped) carbon material that has been shown to have high ORR performance as a result of its nitrogen and iron content, high surface area and augmented poison tolerance.[112] Molecular organic frameworks (MOFs) are another example of (more commonly used) intrinsically functionalised material. These have been used successfully as support materials.[193,194] ZIFs, introduced earlier, are a particularly effective, carbon-based functionalised material for electrocatalyst development due to their high nitrogen content. The central metal ion in ZIFs vary – ZIF-8 and ZIF-67 are common zinc and cobalt-based ZIFs, respectively. A particularly interesting and relatively nascent type of ORR catalyst family has been progressing rapidly using these intrinsically functionalised carbon catalysts: single atom catalysts (SACs). SACs, as the name suggests, are catalysts that have dispersed single atom catalysts sites. Usually carbon based, SACs are attractive due to their tuneable and flexible design, maximum utilisation of catalytic sites (and thus high mass activities) and high electrocatalytic performances.[195] Simple synthetic methods have been developed to easily produce these catalysts (e.g. Figure 1.12 (a)).[196] Zhang et al. and Mehmood et al. have systematically developed a number of tuneable ZIF-8-derived ORR catalysts demonstrating impressive activities with halfwave potentials ($E_{1/2}$) of 0.85 V in acid[181] and 0.905 V in alkaline[197] media, respectively.

Controlled tuning and deeper understanding of these materials is key to unlocking further performance.[198] Control over even dispersity of single atomic metal sites is improving and this is linked to nitrogen content,[199] and site nature.[200]

Catalysts for the oxygen evolution reaction

Catalysts for the OER are more elusive. Compared to the ORR, two central problems make OER catalyst development slower. Firstly, our understanding of the OER mechanism is less comprehensive; and secondly, the OER is carried out at much higher potentials (typically ~1.5 – 1.8 V) therefore the catalyst requirements are significantly different. As a result of the need for much higher potentials, both the catalytic material and its support (if it needs one) need to be corrosion resistant. This fact rules out certain forms of carbon material such as carbon black as, even though features such as high conductivity, low costs and acid / alkaline resistance are attractive, above 0.9 V carbon oxidation occurs diminishing the effectiveness of the catalysts.[201] Graphitisation of carbon produces a more electrochemically stable support,[202] however, while more layers of graphitic carbon make the catalyst more durable this comes with a reduction in performance.[203] That said, an unpyrolysed ZIF based structure has been shown to have higher OER performance in alkaline media compared to IrO_2 in not only beginning-of-life RDE measurements, but also a water electrolyser.[204] It is understood, however that iridium oxides are only state of the art OER catalysts in acidic media – not alkaline (alkaline OER catalysts are discussed below).

Precious metals such as iridium and ruthenium are the highest performing and most broadly explored OER catalysts. Both RuO_2 and IrO_2 adopt a TiO_2 rutile structure and display strong performance in both acid and alkali conditions, however at high oxidative potentials over long durations, RuO_2 oxidises to RuO_4 and IrO_2 to IrO_3 resulting in the dissolution of these metals into solution.[205,206]

A series of non-precious metal oxides (and layered double hydroxides, LDH) with perovskite (ABO_3, where A = alkaline/rare earth metal, e.g. Ba or La; and B is a transition metal, e.g. Ni, Co or Fe) and spinel (AB_2O_4, where A and B are usually made up of group 2, group 13 and first row transition metals) structures have been thoroughly investigated (Figure 1.12 (b)).[207] Variations and systematic doping of both of these oxide OER catalyst crystal structures have been carried out revealing interesting patterns and trends about metal-oxide band gap that helps researchers identify causal structure / performance relationships.[207,208] The performance of these structures is heavily dependant on the coordination environments of the active metals in the structure but, generally, these cobalt and nickel oxides are considered to be the state of the art OER catalysts in alkaline conditions. Wang et al. uses this feature effectively, demonstrating

the coordination site dependency of cobalt in either a tetrahedral or octahedral site by replacing Co with inactive metal centres such as Zn and Al.[209]

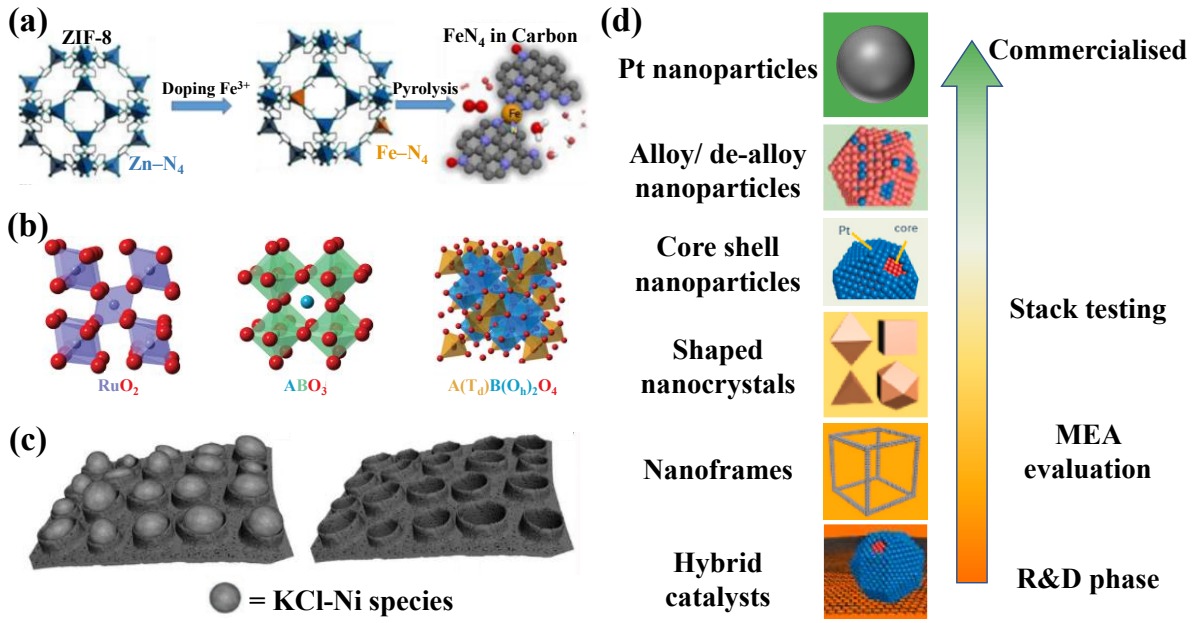


Figure 1.12: (a) Schematic for using functionalised carbon-based ZIF starting materials for SAC synthesis.[181] (b) Crystal structures for common metal- / mixed-metal oxide electrocatalysts: from left to right, rutile (RuO_2), perovskite (ABO_3) and spinel (AB_2O_4).[207] T_d and O_h stand for tetrahedral and octahetral sites, respectively. (c) Schematic of graphitic sheet development from Ni-coated KCl moieties.[210] (d) Examples of platinum architectures used in cathode catalysts, alongside qualitative 'technology readiness level'.[185]

Catalysts for the hydrogen oxidation reaction and hydrogen evolution reaction

As mentioned previously, platinum and its alloys are the most active catalysts for the fundamental hydrogen reactions in acid. In contrast to OER and ORR, the fundamental hydrogen reactions require very little catalyst and overpotential to reliably support high current densities.[176,183] Generally, HER can be performed on a wide variety of catalysts – catalysts suitable for HOR are a subset of these (Figure 1.13).

To date, PGM catalysts are the dominant electrocatalyst type in acid. While platinum itself is the most explored, ruthenium sulfides have recently been shown to perform very well across a series of pHs.[211]

Relative to ORR and HER, development of non-PGM HOR electrocatalysts is still in its infancy. Understanding why metallic surfaces are so strongly favoured as active sites for the HOR is still an open question and so protecting metallic surfaces from severe corrosion in acid media and oxidation under alkaline conditions remains a challenge.[212] One method for

protecting these metallic surfaces has been to cover nickel particles with a thin protective layer thereby protecting them from passivating layers while preserving activity.[213]

One of the central challenges that remain for hydrogen catalysts is to minimise the use of these PGMs in their electrodes. While our understanding of the mechanisms is developing and stimulating exploration into new materials, renewing design principles for catalyst layers and membrane electrode assemblies is allowing for the utilisation of ever smaller amounts of electrocatalyst.[143,185]

Bi- / multi-functional catalysts for fundamental reaction

While there is obvious use for single function catalysts in primary energy conversion devices such as FCs and some primary batteries, bi- / multi-functional catalysts may help to perform reversible electrochemical processes in, for instance, secondary batteries and potentially for using a single catalyst on both sides of PEFC.

Several useful reviews focussing on bifunctional electrocatalysts are available,[214–218] especially that of Hu et al.[219] Ultimately, these reviews focus on the development of metal air batteries, AEMFCs or hRFBs. Wu et al. catalogue c.a. 200 bifunctional oxygen catalysts, helpfully separating them into different catalyst types.[214] Researchers must consider multiple delicate parameters in the development of bifunctional oxygen electrocatalyst catalysts while also endeavouring to keep costs down and scalability possible. Alloyed platinum-iridium catalysts continue to have the highest electrocatalytic performance for the ORR and OER.[220] That said, recently it has been shown by da Silva et al. that significant and rapid degradation occurs following multiple cycles of alloyed Pt/Ir catalysts.[220] This work demonstrates (using IL-TEM) that particle coalescence, growth and detachment are among the biggest contributors to platinum-iridium alloy stability – however particle dissolution dominates this detraction from catalyst longevity.[220] Non-precious metal oxides (TMOs), sulfides (TMSs) and nitrides (TMNs) are relatively inexpensive to synthesise, they have more structural diversity (allowing for catalyst tuning) and have high electrocatalytic performances (for device level consideration). However, the stability of these transition metal catalysts falls short of what would be required at device level and the lower conductivity translates to poorer onset potentials and limiting current densities.[218] Heteroatom- or single metal atom-doped carbon-based catalysts present, arguably, the most promising hybrid electrocatalysts. Carbon materials are tuneable, highly conductive and can act either as a support (typically for the OER reaction)

or an active catalyst with high surface area.[218] As research progresses, carbon supports or carbon-composite supports will be synthesised to be resistant to corrosion at high oxidative potentials, unleashing broad adoption of inexpensive, corrosion-resistant, sustainable electrocatalysts for use in air-breathing electrochemical devices.

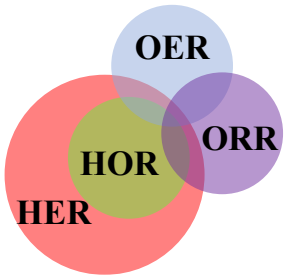


Figure 1.13: Venn diagram representing multifunctionality of catalyst types.

As discussed earlier, all HOR catalysts are at least bifunctional (Figure 1.13) (as it is possible to perform HER using these same catalysts). While performances are often greater for the fundamental hydrogen reactions (much lower overpotentials with high current densities) compared to the ORR and OER, the type of catalysts used are similar. Some researchers have been more ambitious with their endeavour to synthesise multifunctional electrocatalysts. Parra-Puerto et al. surveyed the ORR, OER and HER activity of a series of metal phosphides (M_x-P_y where M = Cr, Co, Ni, Mo and W) in both acid and alkaline conditions.[221] The synthesis method was found to be scalable and the Co_2P was shown to be the best performing of the non-PGMs phosphides tested. A metal free catalyst with a hierarchical structure including stereoscopic holes over its graphite surface was developed by Hu et al. and displays intriguingly high performance in alkaline conditions for the ORR, OER and HER (Figure 1.12 (c)).

While there is no real technological advantage to developing tetra-functional electrocatalysts, very few catalysts can perform all four of the hydrogen and oxygen reactions efficiently. For a given redox couple, achieving high bifunctional capability, clearly, comes with the advantage of not having to introduce decoupled electrode configurations, as demonstrated by Yu et al.[104] One recently reported exception is a partially hydrous RuO_2 nanocluster embedded in a carbon matrix that has been shown to have tetra-functionality.[222] A symmetric water electrolyser utilising this nanocluster catalyst was shown to have a lower potential gap in the HER and OER across the pH spectrum than that of conventional asymmetric electrolysers, and the HOR activity was shown to be level with platinum catalysts, however in addition to acknowledging that carbon materials are unlikely to be stable under high oxidative potentials, the ORR capability falls short of where it would need to be for device application.[222] Methodical research

and further understanding of mechanism and metal-support interactions between single heteroatoms and their (likely carbon-based) supports will give rise to guiding principles on how we can develop catalysts for more than just one function.[198] The following section walks through some examples of how both physical and electrochemical characterisation techniques can tell us more about catalysts active sites, how they interact with reactants and how, therefore, they can be improved.

1.3.2.2 Probing the active site

A particularly challenging and interesting aspect of electrochemistry for researchers is deciphering the form of the active site. In this work, several physical and electrochemical characterisation techniques are used and these are discussed in more detail in Chapter 2. While none of the techniques mentioned in here are used in the remainder of this work, the following paragraphs showcase examples of some techniques cutting-edge technologies used to establish the form of the active site.

Imaging techniques such as transmission electron microscopy (TEM) and focussed ion beam scanning electron microscopy (FIB-SEM). One recent, particularly impressive, use of TEM has been identical location TEM (IL-TEM). Using TEM microgrids as modified floating electrode substrates, Hrnjić et al. showed before and after TEM images of how alloyed Pt-Co particles supported on carbon change following short term polarisation (Figure 1.14).[223,224] FIB-SEM allows the user to view a catalyst or support surface and mill it so as to explore subsurface morphology,[225] using the finely focussed beam of (usually gallium) ions, or to prepare samples for atom probe tomography (APT).[226] APT is one of the newest characterisation techniques in the electrochemists armoury for understanding the active site (Figure 1.14 (a)). This technique provides both 3D images and composition measurements at an atomic level. Samples are fixed by a matrix and then cut to the shape of a thin needle, using FIB-SEM in-situ,[227] and a large electrostatic field is placed at its tip. Following this, atoms are consecutively removed via field evaporation using a laser pulse and projected onto a time-of-flight (TOF) detector.[228] This has recently been carried out with freestanding Pd and carbon-supported platinum nanoparticles providing a proof of concept to systematically visualise catalytic active sites.[229]

One longstanding and important crystallographic characterisation technique is X-ray diffraction (XRD). This technique utilises surface features of structured electrocatalysts. Zhu

et al. review in-situ XRD techniques that have helped to inform scientists about the dynamic structure of electrocatalysts.[230] In-situ techniques provide additional dimensions to already useful characterisation – fluorescence and transmission-mode XRD have been used in tandem to illuminate how cobalt phosphide-based catalysts modify their structure during battery operation (Figure 1.14 (b)).[231] One step on from the type of elastic scattering technique utilised in XRD is X-ray absorption scattering (XAS) – an advanced characterisation technique that utilises inelastic scattering in order to inform the user about the coordination environment and electronic state of the element in question. There are several other intensely useful characterisation techniques such as Raman and Mössbauer spectroscopy, X-ray photoelectron and electron energy loss spectroscopy (XAS and EELS) and thermogravimetric analysis (TGA) that are commonly used but is beyond the scope of this section.

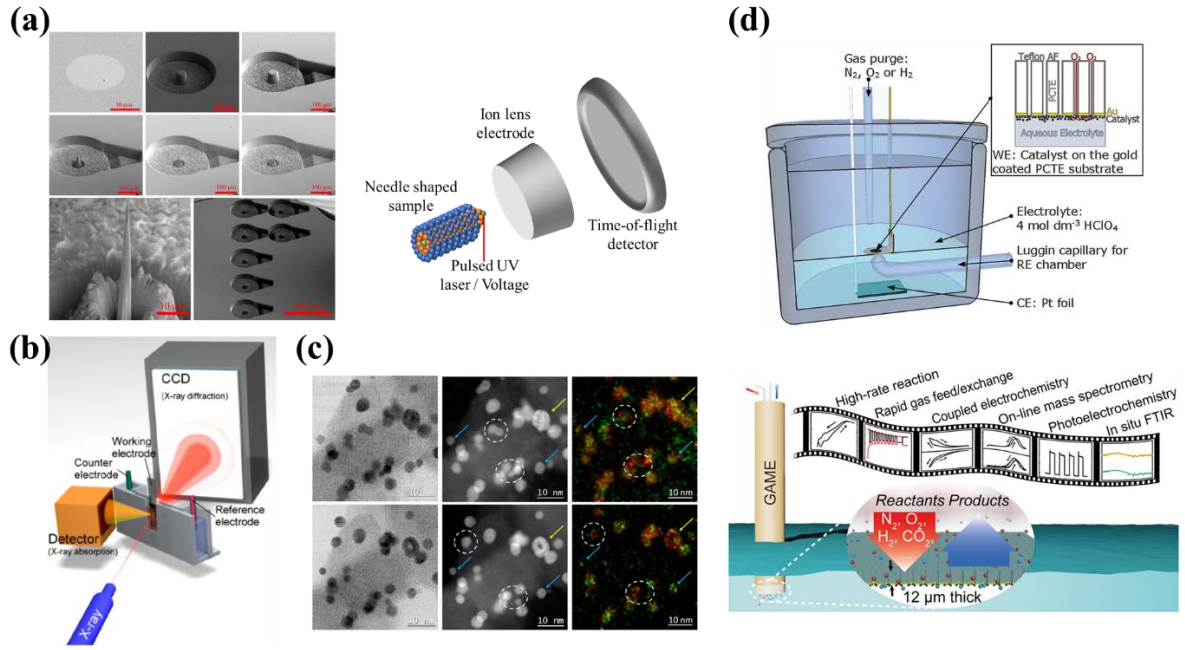


Figure 1.14: Diagrammatic representations of active site characterisation methods. (a) LHS: Progressive images of FIB-SEM milling a metal surface into a needle shaped sample for atom probe tomography;[227] and, RHS: a simplified diagram of how APT is carried out;[232] (b) In-situ spatially coherent configuration for the combination of transmission-mode synchrotron XRD and fluorescence-detected XAS;[231] (c) IL-TEM showing catalyst material 'before' and 'after' a short corrosion step;[223] and, (d) Two high mass transport systems used to assess realistic electrocatalyst capability – Top: Floating electrode schematic;[183] and, Bottom: gas accessible membrane electrode.[233]

While it is useful to probe the electrocatalyst active sites via these physical characterisation methods, especially in-situ, examining the active site electrochemically provides an alternative, arguably more helpful, way of understanding how an electrocatalyst works in a real device. Recently, Jackson et al. demonstrated a controlled poison mitigation strategy for the use of impure hydrogen in hydrogen pumps and PEMFCs.[234] Using well known electrocatalyst poisons (CO and H_2S) the authors establish reliable ways of cleaning electrocatalyst surfaces

with ozone whereby the number of active sites on an electrode needs to be identified. Two important high mass-transport techniques have been developed in the Kucernak research group (Figure 1.14 (d)) – the Floating Electrode (FE) and the Gas Accessible Membrane Electrode (GAME).[183,233] The FE was developed to test the full extent of a catalyst potential by reducing the mass-transport limitations that are present when using a rotating disk electrode (RDE). Using this setup and accompanying computational modelling, researchers have been able to make predictions about 'ideal' platinum particles made of only edges / vertices (the sites that are most active to the hydrogen reaction), make mechanistic inferences about potential site-blocking and suggest upper limits to PEMFC performance (i.e. HOR at 1 A cm^{-2}, at 0.01 V overpotential using 4 μg cm^{-2} of idealised catalyst at 298 K).[235] More recently, the GAME has been developed allowing for rapid switching between gas supplies and transient monitoring. This electrochemical configuration can be coupled with a range of in-situ measurements such as mass spectrometry and Fourier Transform infrared spectroscopy, gleaning insight into how electrocatalyst behave and intricate conversion processes (such as CO_2 reduction and methanol oxidation, respectively).[233] While these high mass-transport techniques go further to demonstrate electrocatalysts' capabilities in a full system, the RDE is still the standard practice used to test catalysts in the literature as kinetic currents are calculable.[176]

As characterisation techniques improve, researchers are better able to understand the intricacies of the catalyst site. This enables them to generate causal relationships and better understand how to maximise catalyst performance. Figure 1.12 (d) summarises quite nicely how, for instance, the pipeline for platinum catalysts is developing.[185] Increasingly elaborate starting materials are being used as intrinsically functionalised carbon based starting materials and display promising results with, for instance, a seaweed biomass precursor being used to derive hierarchical nanoaerogels for ultimate use as a bifunctional electrocatalyst in a zinc air battery.[236] This continued, and often serendipitous, investigation of nature-inspired chemical engineering techniques may yield fruitful, game-changing results.[237]

While the understanding and testing of electrocatalysts is important, ultimately these catalysts are to be used in electrochemical devices for transport and stationary applications.[238] In recent years, we have seen not only improvements in catalyst ability but also improved translation of catalyst materials to devices – this will be critical to the continued development and commercial rollout of these electrochemical technologies. Relevant state of the art catalysts

will be discussed and summarised in the relevant chapter. The following section summarises another essential component of the RFB – the separator.

1.3.3 Separators

Separators play an essential roll in almost all electrochemical devices. The use of a suitable separator is crucial for the proper operation of RFBs. The selectivity as well as thickness of the separator must be considered to control crossover and electrolyte imbalance. Many barriers remain in separator research including the development of an effective AEM and minimising crossover while simultaneously maximising selectivity. These issues will be discussed in the following sections.

1.3.3.1 Types

Within the term 'Separator' there exists a number of more specific ways to refer to the material positioned between the anode and the cathode in an electrochemical device. In FC and RFB research, and indeed in this work, separators are usually referred to as membranes. However there are some notable alternatives before we focus on membranes.

Solid state electrolytes are the most widely used separator as they are commonly used in Li-ion based technologies. Semi- / micro-porous separators are occasionally used in non-aqueous organic RFBs where the way selectivity is achieved is associated with size and steric requirements. The charge carrier, for instance, BF_4^-, is 'small' compared to the counter ions in the electrolyte solution (e.g. tetra-ethyl ammonium, TEA^+) and is able to travel though the semi porous separator. These materials can be derived from a variety of polypropylene, polyethylene and phenolic resin based materials and can be obtained from vendors such as Daramic and Celgard.[239]

In FCs and aqueous RFBs, however, membranes are used to selectively allow the transport of small ions, such as protons and hydroxide, from one side of the device to the other. In a FC or electrolyser, ions travel in one direction. For instance, in an AEMFC, following the reduction of O_2, OH^- ions are delivered from the cathode to the anode via the AEM, where it then assists the oxidation of hydrogen (to form water, Equation (1.3)). Different membranes are used depending on the ion that needs to be transported. In the absence of tailored Poly-flouropolymers are widely used in devices where proton exchange is required, while poly-benzimidazoles (PBI) are among the leaders in the less advanced race to develop effective

anion exchange membranes. It must be noted, however, that the requirements for liquid-liquid systems are likely to be different to electrochemical devices with gas phase processes occurring each side of the membrane (FCs), or indeed liquid-gas hybrid systems (hRFBs). In the absence of tailored membranes for specific phase configurations, these types of membrane are commonly used in RFB systems. The following section focuses on state of the art polymer membranes.

1.3.3.2 State of the art

Before discussing the, more relevant, polymer exchange membranes used in this work, a type of solid state membrane – NASICON (stands for a sodium (Na) Super Ionic Conductor) – is mentioned because of its use in liquid-liquid systems to separate aqueous solutions with different pHs in addition to its application enabling fast charging in sodium batteries.[104,240] Significant efforts have been directed at developing solid state NASICON separators because they hold great promise as energetically dense and safe alternatives to conventional Li-ion batteries.[241]

Different membranes are used depending on the ion that needs to be transported. Nafion® poly-fluoropolymer, with its perfluorinated backbone and sulfonated headgroups provide channels for protons to selectively move through easily (Figure 1.15 (a)). Nafion® was developed first by DuPont in the 1960s and is still the leading PEM material in the industry – this is reflected in the price and is one of the main bottlenecks in the attempt to commercialise these ECs more widely.[32]

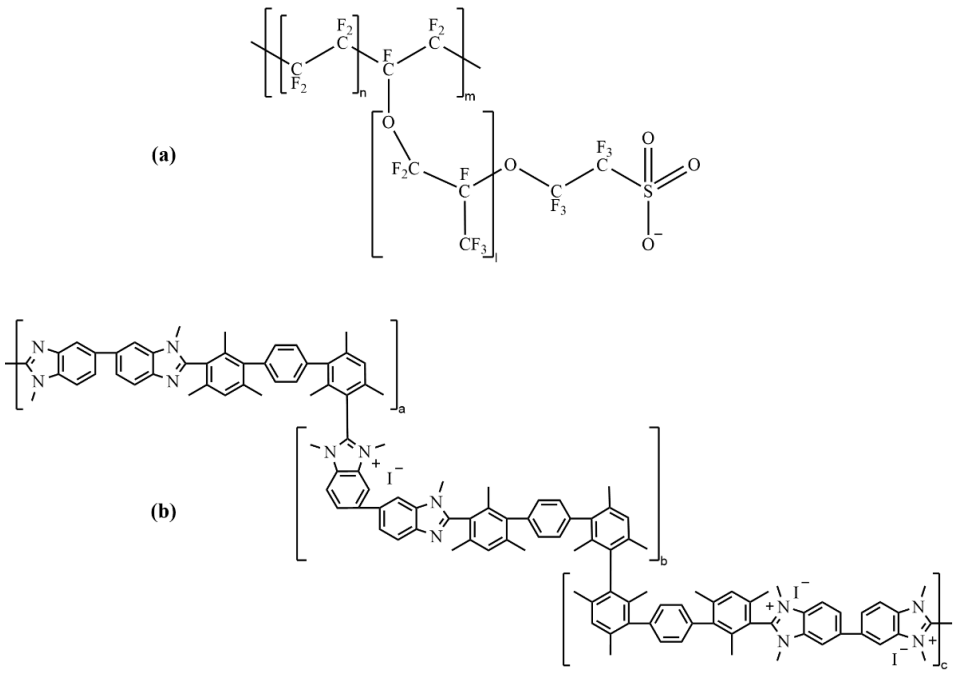


Figure 1.15: Examples of monomer units for (a) proton exchange membranes (Nafion®) and (b) anion exchange membranes (Aemion™, IONOMR).

Figure 1.15 (b) shows the monomer units for an anion exchange membrane. The development of organic cationic polymers has been stunted by the mechanical and chemical degradation caused by aggressive hydroxide ions.[242] Several types of anion transfer head group have been tested,[242] however the high pHs and temperatures consistently induce degradation. One method researchers in this area have begun to employ, following the increased research and industrial interest, is to incorporate stable cationic moieties into the polymer backbone that have few degradation pathways – reducing the number of ways nucleophilic hydroxide groups can degrade the ionomer. Figure 1.15 (b) shows the incorporation of alkylated poly(benzimidazole) alongside bulky, hindering and chemically inactive groups. These AEMs are available from vendors such as Sustanion, IONOMR and Dioxide Materials.

1.4 Conclusions

The first half of this literature review summarised the chemical configuration and the foundational components needed to decide the design of a RFB. The pros and cons associated with aqueous and non-aqueous solvents are discussed first. While non-aqueous solvents have the enticing ability to accommodate higher potentials, aqueous solvents are a more suitable environment from which devices, and technologies as a whole, are likely to emerge due to their greater conductivity, lower cost and generally greater versatility relative to the current non-aqueous offerings. Following this, phase configurations were discussed. Opening with the

classical liquid-liquid RFB system describing, operationally, how RFBs work and the advantages of (specifically) liquid-based systems which are primarily associated with ease of operation and system longevity. Gas-gas systems are briefly mentioned clearly highlighting the advantages of FCs and demonstrating how, joint with a liquid-side couple, technological developments of the RFB could be achieved. The solid and gaseous analogues are then discussed settling on the likelihood that, operationally, the liquid-gas configuration is the most technologically interesting given the known and available soluble active species alongside the extensive (and reliable) FC couples. Some available redox species are then surveyed demonstrating the extensive diversity of systems available to the user. Towards the end of this section, fundamental oxygen and hydrogen reactions are briefly discussed and it is concluded that while harnessing oxygen as an energy carrier is one of the most important objectives for researchers, the overpotentials required to carry out the ORR and OER are too high with current catalysts. Additionally, the use of the hydrogen redox couple in electrochemical devices provides an interesting (reducing) couple that can be easily paired with other redox couples. Ultimately, these foundational chemical components are discussed in a few specific examples and some figures of merit are exemplified and compared in Figure 1.8 and Table 1.2.

Having established the framework around which the RFB or hRFB was to be developed (Figure 1.8), the second half of this literature review focussed on the materials needed for proper operation of the device. Electrodes are broached first – the types, their adjacent flow fields and cell preparation methods are discussed, acknowledging that some electrodes are more suitable than others depending on the solvents or cell configuration involved. In- and ex-situ characterisation methods are summarised and, finally, some relevant state of the art electrode and electrode functionalities are displayed. For the liquid-gas hRFB phase configuration introduced in the first half, hydrogen and oxygen redox couples demanded an outline of FC and electrocatalyst research. Again, methods for characterising these electrocatalysts and their active site are discussed. Finally, separators are discussed, and it was established that polymer membranes are the only relevant technology for this work.

This chapter sets out the high-level context needed to move forward with this work. This chapter began, in Part I, briefly outlining the context and motivation of this work. Part II went on to highlight relevant literature in the fields to which this work looks to contribute. As stated in Part I, each of the subsequent chapters will have shorter, more directly relevant Introduction section in which a more targeted context will be provided. The final part in this chapter, Part

III, outlines this overall aims and research questions that emerge from this literature review – informing the focus of this thesis.

Part III: Thesis outline

1.5 Aims

The ultimate aim for all researchers working to develop EES devices should be to decrease the cost per cycle so that these technologies can become widely available. Similarly, for those working in FC research, the goal is to simultaneously reduce capital cost and increase the power densities that systems are able to achieve for broad technological utility. The literature review in Part II of this chapter provides context and demonstrates that there are several ways these goals can be approached by either improving existing technologies or developing new ones. Improving system efficiency and durability, reducing material costs associated with the electrode, electrocatalyst or electrolyte, as well as enhancing engineering aspects, all contribute to this push towards lowering system cost. With this context in mind, this work methodically evaluates different components of an RFB using conventional and (unconventional) specific performance parameters. The central aim is to improve our understanding of these components so that, moving forward, researchers can make more informed research decisions towards producing low cost EES devices.

1.5.1 Questions and objectives

As all researchers are familiar, questions and objectives morph and multiply over time as more research is carried out. It is important, however, at the outset to state the questions this work seeks to answer and the objectives it looks to achieve. A brief contextual narrative leading to the overall research questions are provided below and these will be revisited in the final chapter of this work:

As outlined in Part II, researchers have designed several types of electrode, methodically varying particular microstructural parameters such as surface area, porosity, geometry, weave pattern and surface functionalisation. In each case, these changes have either positive or negative performance effects when transferred into a device. Even for a given system, however,

there is little experimental literature outlining absolute electrode parameters that lead to greater electrode performance. With this in mind, this work seeks to answer the following question.

- How is the microstructure of porous carbon paper and cloth electrodes related to the performance of the RFB system in which they operate?

The above question focusses on the liquid side (or sides) of a RFB. Following the assertion that new devices need to be developed, liquid-gas hRFBs provide an interesting technological framework on which to build and progress from an energy density perspective. As discussed, using oxygen as a redox couple, has the potential to greatly reduce the cost of electrolyte and increase the energy density of a given device (as the oxygen in air, of course, does not need to be bought or stored). Electrocatalysts are needed to overcome the ORR and OER energy barriers (in turn lowering overpotentials). New types of, for instance, single atom catalysts have been shown to return high (ORR) performance with low metal loadings. From an expense perspective, it would not be effective to use high-cost starting materials – demanding the following question.

- Is it possible to develop an inexpensive, carbon-based, high-performing bifunctional oxygen electrocatalyst?

The ultimate aim of most researchers looking to develop electrocatalysts in this field is to use them in electrochemical devices such as FCs or hRFBs. This work is no different and, with the context of the previous question, this work looks for suitable devices in which to use the developed catalyst in the hope that the catalyst exceeds current state of the art technologies. Additionally, given the nature of this work, extending the learnings of the electrode microstructure to other electrochemical devices would further bolster them. This leads to the 'two-pronged' question that will ultimately be addressed simultaneously, as follows.

- Can this catalyst be used in devices at different pHs and can we validate the 'microstructure / performance' findings?

Continuing the theme of device-level testing and with the overarching goal of reducing capital costs associated with RFBs and their analogues, the following question looks to address the

high cost of soluble aqueous electrolytes and further understand a chemical system with a view to developing an improved understanding of a low-cost, sustainable electrolyte. As mentioned in Part II, manganese has recently been identified as an interesting, low-cost alternative to vanadium which, historically, has suffered high price volatility. The low-cost of manganese (ore) is attributed to its abundance and this has begun to pique commercial interest when applied to a hydrogen-manganese hRFB system. While manganese chemistry is rich and diverse, indeed this is a large part of its attractiveness, the Mn^{4+} oxidation state is often deemed a perilous one due to its fully oxidised, MnO_2, form – the production of which commonly is considered to be irreversible. With titanium additives this manganese-based electrolyte appears to be stabilised and the production of MnO_2 (or, at least one of its polymorphs) is reversible. This chemical system is not fully understood and the following questions seeks to address this.

- Is there a way of developing an enhanced understanding of manganese speciation occurring within a manganese electrolyte during cell cycling?

The following section outlines how the chapters presented in this work are structured to answer these questions.

1.6 Thesis structure

This work focusses on several aspects common to all RFBs. Each chapter is self-contained and is structured in such a way that a short, directly relevant, introduction is provided in order to focus the reader on the subject matter and the chapters' objectives. Following this, a local methodology is provided outlining specific methods contained within the ensuing chapter. The results are then presented alongside the discussion with the aim to have comprehensively answered the research objectives set out in the respective introduction. With the exception of Chapter 5 which aims to tie together the preceding two, the chapters are not directly related to one another, they should be thought of as adjacent pieces of a puzzle relating to the development of improved hybrid flow batteries.

Chapter 2 outlines the foundational theory behind the characterisation and analytical processes used to gather the results presented in the following chapters. The chapter begins with physical characterisation processes that reveal structural information about, mostly, the electrocatalyst developed in this work. The electrochemical characterisation methods that uncover information about the electrochemical processes are ubiquitous and are used throughout this work.

Chapter 3 aims to reveal definitive electrolyte- and microstructure-performance relationships so that electrodes can be used to their full potential. This chapter presents the characterisation of four carbon electrodes using multiple types of analysis. Sophisticated imaging analysis is used to characterise the electrodes and each one is tested in zero-gap symmetric RFB using an organic electrolyte with different supporting solvents.

Chapter 4 presents the synthetic development of a multifunctional electrocatalyst using ZIF-67 as a starting material. Physical and electrochemical characterisation techniques are used to understand the structure of the catalyst. Three-electrode cells are used to test the catalyst in different pH environments for fundamental oxygen and hydrogen reactions. Its intriguing activity and stability aims to provide a new material for the 'air-breathing' catalyst armoury.

Chapter 5 attempts to tie the previous two together by taking the outputs from each and implementing in various devices. Proof of concept tests are carried out using the multifunctional electrocatalyst developed in Chapter 4 in both an AEMFC (alkaline environment) and a PEMFC (acid environment). This chapter goes on to tie Chapters 3 and 4 together by, again, utilising the electrocatalyst and some of the electrodes tested in Chapter 3 in a Mn/H_2 hRFB.

Chapter 6 contains a targeted review of manganese and titanium chemistry followed by an investigation into the solution-phase processes occurring during the charging and discharging in a Mn/H_2 hRFB cell. Two in-operando spectroscopic techniques (UV-visible and electron paramagnetic resonance) are used in order to gain a better handle on the elusive manganese species produced during cell cycling.

Chapter 7 summarises the broad-stroke and chapter-specific conclusions set out in this thesis. Additionally, further to the chapter-specific future work suggestions, starting points for potential future projects are proposed.

1.7 References

1 Our World in Data, https://ourworldindata.org/.
2 IRENA, *Electricity storage and renewables: Costs and markets to 2030*, 2017.
3 IRENA, *Renewable Energy Statistics 2018*, 2018.
4 Nissan Leaf | Electric Cars | Nissan UK, https://www.nissan.co.uk/vehicles/new-

vehicles/leaf.html, (accessed 28 October 2021).
5 Batteries - Why Lithium-ion? - Apple, https://www.apple.com/batteries/why-lithium-ion/, (accessed 25 November 2021).
6 BYD - Build Your Dreams, https://en.byd.com/energy/utility-ess/.
7 Samsung SDI, https://www.samsungsdi.com/ess/energy-storage-system-application.html.
8 Eelpower, https://eelpower.co.uk/.
9 Powervault: home electricity storage, https://www.powervault.co.uk/, (accessed 25 November 2021).
10 Powerwall | Tesla United Kingdom, https://www.tesla.com/en_gb/powerwall, (accessed 25 November 2021).
11 *Roadmap for flexibility services to 2030 (Poyry and Imperial College London) - Committee on Climate Change*, 2017.
12 Vanadium Flow Batteries | Invinity Energy Systems, www.invinity.com, (accessed 8 July 2020).
13 Electric Cars, Solar & Clean Energy | Tesla, https://www.tesla.com/, (accessed 28 October 2021).
14 Power Technology, Three firms team up to commission commercial-scale solar battery project in UK, https://www.power-technology.com/news/newsthree-firms-team-up-to-commission-commercial-scale-solar-battery-project-in-uk-4401214/, (accessed 31 August 2021).
15 A. Z. Weber, M. M. Mench, J. P. Meyers, P. N. Ross, J. T. Gostick and Q. Liu, *J. Appl. Electrochem.*, 2011, **41**, 1137–1164.
16 G. L. Soloveichik, *Chem. Rev.*, 2015, **115**, 11533–11558.
17 E. Sánchez-Díez, E. Ventosa, M. Guarnieri, A. Trovò, C. Flox, R. Marcilla, F. Soavi, P. Mazur, E. Aranzabe and R. Ferret, *J. Power Sources*, 2021, **481**, 228804.
18 P. Alotto, M. Guarnieri and F. Moro, *Renew. Sustain. Energ. Rev.*, 2014, **29**, 325–335.
19 T. Nguyen and R. F. Savinell, *Electrochem. Soc. Interface*, 2010, **19**, 54–56.
20 P. Leung, X. Li, C. Ponce de León, L. Berlouis, C. T. J. Low and F. C. Walsh, *RSC Adv.*, 2012, **2**, 10125–10156.
21 J. H. Vinco, A. E. E. da C. Domingos, D. C. R. Espinosa, J. A. S. Tenório and M. dos P. G. Baltazar, *J. Energy Storage*, 2021, **43**, 103180.
22 I. Iwakiri, T. Antunes, H. Almeida, J. P. Sousa, R. B. Figueira and A. Mendes, *Energies 2021, Vol. 14, Page 5643*, 2021, **14**, 5643.
23 K. J. Kim, M.-S. Park, Y.-J. Kim, J. H. Kim, S. X. Dou and M. Skyllas-Kazacos, *J. Mater. Chem. A*, 2015, **3**, 16913–16933.
24 M. M. Petrov, A. D. Modestov, D. V. Konev, A. E. Antipov, P. A. Loktionov, R. D. Pichugov, N. V. Kartashova, A. T. Glazkov, L. Z. Abunaeva, V. N. Andreev and M. A. Vorotyntsev, *Russ. Chem. Rev.*, 2021, **90**, 677.
25 C. H. L. Tempelman, J. F. Jacobs, R. M. Balzer and V. Degirmenci, *J. Energy Storage*, 2020, **32**, 101754.
26 M. S. Ziegler, J. M. Mueller, G. D. Pereira, J. Song, M. Ferrara, Y. M. Chiang and J. E. Trancik, *Joule*, 2019, **3**, 2134–2153.
27 K. Gong, Q. Fang, S. Gu, S. Fong, Y. Li and Y. Yan, *Energy Environ. Sci*, 2015, **8**, 3515.
28 G. Kwon, S. Lee, J. Hwang, H. S. Shim, B. Lee, M. H. Lee, Y. Ko, S. K. Jung, K. Ku, J. Hong and K. Kang, *Joule*, 2018, **2**, 1771–1782.
29 L. W. Hruska and R. F. Savinell, *J. Electrochem. Soc.*, 1981, **128**, 18.
30 V. Yufit, F. Tariq, D. S. Eastwood, M. Biton, B. Wu, P. D. Lee and N. P. Brandon, *Joule*, 2019, **3**, 485–502.

31 RedFlow, www.redflow.com, (accessed 11 December 2019).
32 M. L. Perry and T. F. Fuller, *J. Electrochem. Soc.*, 2002, **149**, S59.
33 F. Bidault, D. J. L. Brett, P. H. Middleton and N. P. Brandon, *J. Power Sources*, 2009, **187**, 39–48.
34 P. Boldrin and N. P. Brandon, *Nat. Catal.*, 2019, **2**, 571–577.
35 Welcome to Ceres - Pioneers of unique technology, https://www.ceres.tech/, (accessed 28 October 2021).
36 C. Cui, S. Li, J. Gong, K. Wei, X. Hou, C. Jiang, Y. Yao and J. Ma, *Mater. Renew. Sustain. Energy 2021 102*, 2021, **10**, 1–24.
37 X. Li and A. Faghri, *J. Power Sources*, 2013, **226**, 223–240.
38 Blue World Technologies - Developer and manufacturer of methanol fuel cells, https://www.blue.world/, (accessed 28 October 2021).
39 Y. Wang, K. S. Chen, J. Mishler, S. C. Cho and X. C. Adroher, *Appl. Energy*, 2011, **88**, 981–1007.
40 Leading Fuel Cell & Microgrid Solutions Provider | Bloom Energy, https://www.bloomenergy.com/, (accessed 28 October 2021).
41 Zero-Emission Hydrogen Fuel Cell Products - Plug Power, https://www.plugpower.com/fuel-cell-power/, (accessed 28 October 2021).
42 Homepage - AFC Energy, https://www.afcenergy.com/, (accessed 28 October 2021).
43 Home | Intelligent Energy, https://www.intelligent-energy.com/, (accessed 28 October 2021).
44 Bramble Energy, https://www.brambleenergy.com/.
45 Smart Megawatt Stack Fuel Cell Systems Ltd, https://smsfc.com/, (accessed 28 January 2022).
46 F. Pan and Q. Wang, *Molecules*, 2015, **20**, 20499–20517.
47 R. F. Gahn, N. H. Hagedorn, J. S. Ling, R. F. Gahn, N. H. Hagedorn and J. S. Ling, *Natl. Aeronaut. Sp. Adm. Lewis Res. Cent. Brook Park. OH, USA*, 1983, **83**, 25042.
48 L. H. Thaller, *Lewis Res. Centre, NASA*.
49 E. Sum and M. Skyllas-Kazacos, *J. Power Sources*, 1985, **15**, 179–190.
50 M. Skyllas-Kazacos, *J. Electrochem. Soc.*, 1987, **134**, 2950.
51 W. Lu, X. Li and H. Zhang, *Phys. Chem. Chem. Phys.*, 2017, **20**, 23–35.
52 M. L. Perry, R. M. Darling and R. Zaffou, *ECS Trans.*, 2013, **53**, 7–16.
53 H. R. Jiang, J. Sun, L. Wei, M. C. Wu, W. Shyy and T. S. Zhao, *Energy Storage Mater.*, 2020, **24**, 529–540.
54 S. Renner and F. W. Wellmer, *Miner. Econ.*, 2019, **33**, 311–340.
55 G. Davies, *Coord. Chem. Rev.*, 1969, **4**, 199–224.
56 Y. Matsuda, K. Tanaka, M. Okada, Y. Takasu, M. Morita and T. Matsumura-Inoue, *J. Appl. Electrochem.*, 1988, **18**, 909–914.
57 T. Yamamura, N. Watanabe and Y. Shiokawa, *J. Alloys Compd.*, 2006, **408**–**412**, 1260–1266.
58 S. Yoshinobu, Y. Tomoo and S. Kenji, *J. Phys. Soc. Jpn.*, 2006, **75**, 137–142.
59 T. Yamamura, Y. Shiokawa, H. Yamana and H. Moriyama, *Electrochim. Acta*, 2002, **48**, 43–50.
60 B. Hwang, M.-S. Park and K. Kim, *ChemSusChem*, 2015, **8**, 310–314.
61 B. Huskinson, M. P. Marshak, C. Suh, S. Er, M. R. Gerhardt, C. J. Galvin, X. Chen, A. Aspuru-Guzik, R. G. Gordon and M. J. Aziz, *Nature*, 2014, **505**, 195–198.
62 F. R. Brushett, J. T. Vaughey and A. N. Jansen, *Adv. Energy Mater.*, 2012, **2**, 1390–1396.
63 S. H. Oh, C.-W. Lee, D. H. Chun, J.-D. Jeon, J. Shim, K. H. Shin and J. H. Yang, *J. Mater. Chem. A*, 2014, **2**, 19994–19998.

64 D. G. Kwabi, Y. Ji and M. J. Aziz, *Chem. Rev.*, 2020, **120**, 6467–6489.
65 M.-A. Goulet, L. Tong, D. A. Pollack, D. P. Tabor, S. A. Odom, A. Aspuru-Guzik, E. E. Kwan, R. G. Gordon and M. J. Aziz, *J. Am. Chem. Soc.*, 2019, **141**, 8014–8019.
66 P. Sun, Y. Liu, Y. Li, M. A. Shehzad, Y. Liu, P. Zuo, Q. Chen, Z. Yang and T. Xu, *Ind. Eng. Chem. Res.*, 2019, **58**, 3994–3999.
67 Z. Yang, L. Tong, D. P. Tabor, E. S. Beh, M.-A. Goulet, D. De Porcellinis, A. Aspuru-Guzik, R. G. Gordon and M. J. Aziz, *Adv. Energy Mater.*, 2017, **1702056**, 1–9.
68 K. Lin, Q. Chen, M. R. Gerhardt, L. Tong, S. B. Kim, L. Eisenach, A. W. Valle, D. Hardee, R. G. Gordon, M. J. Aziz and M. P. Marshak, *Science*, 2015, **349**, 1529–32.
69 D. G. Kwabi, K. Lin, Y. Ji, A. Aspuru-Guzik, R. G. Gordon, M. J. Aziz, E. F. Kerr, M.-A. Goulet, D. De Porcellinis, D. P. Tabor and D. A. Pollack, *Joule*, 2018, **2**, 1–13.
70 Y. Ji, M.-A. Goulet, D. A. Pollack, D. G. Kwabi, S. Jin, D. De Porcellinis, E. F. Kerr, R. G. Gordon and M. J. Aziz, *Adv. Energy Mater.*, 2019, **9**, 1900039.
71 D. P. Tabor, R. Gómez-Bombarelli, L. Tong, R. G. Gordon, M. J. Aziz and A. Aspuru-Guzik, *J. Mater. Chem. A*, 2019, **7**, 12833–12841.
72 Z. Li, S. Li, S. Liu, K. Huang, D. Fang, F. Wang and S. Peng, *Electrochem. Solid-State Lett.*, 2011, **14**, A171.
73 Z. Yang, J. Zhang, M. C. W. Kintner-Meyer, X. Lu, D. Choi, J. P. Lemmon and J. Liu, *Chem. Rev.*, 2011, **111**, 3577–3613.
74 R. Ma, G. Lin, Y. Zhou, Q. Liu, T. Zhang, G. Shan, M. Yang and J. Wang, *npj Comput. Mater.*, 2019, **5**, 1–15.
75 I. E. L. Stephens, A. S. Bondarenko, U. Grønbjerg, J. Rossmeisl and I. Chorkendorff, *Energy Environ. Sci.*, 2012, **5**, 6744–6762.
76 Z.-F. Huang, J. Wang, Y. Peng, C.-Y. Jung, A. Fisher and X. Wang, *Adv. Energy Mater.*, 2017, **7**, 1700544.
77 X. Ge, A. Sumboja, D. Wuu, T. An, B. Li, F. W. T. Goh, T. S. A. Hor, Y. Zong and Z. Liu, *ACS Catal.*, 2015, **5**, 4643–4667.
78 J. Zhang, *PEM Fuel Cell Electrocatalysts and Catalyst Layers: Fundamentals and Applications*, Springer Science & Business Media, 2008.
79 V. Goellner, V. Armel, A. Zitolo, E. Fonda and F. Jaouen, *J. Electrochem. Soc.*, 2015, **162**, H403.
80 B. B. Blizanac, P. N. Ross and N. M. Markovic, *Electrochim. Acta*, 2007, **52**, 2264–2271.
81 J. Song, C. Wei, Z.-F. Huang, C. Liu, L. Zeng, X. Wang and Z. J. Xu, *Chem. Soc. Rev.*, 2020, **49**, 2196–2214.
82 E. Fabbri and T. J. Schmidt, *ACS Catal.*, 2018, **8**, 9765–9774.
83 J. S. Yoo, X. Rong, Y. Liu and A. M. Kolpak, *ACS Catal.*, 2018, **8**, 4628–4636.
84 A. Grimaud, O. Diaz-Morales, B. Han, W. T. Hong, Y.-L. Lee, L. Giordano, K. A. Stoerzinger, M. T. M. Koper and Y. Shao-Horn, *Nat. Chem.*, 2017, **9**, 457–465.
85 S. B. Scott, J. E. Sørensen, R. R. Rao, Choongman Moon, Jakob Kibsgaard, Yang Shao-Horn and Ib Chorkendorff, *Energy Environ. Sci.*, , DOI:10.1039/D1EE03915F.
86 J. O. Bockris and T. Otagawa, *J. Phys. Chem.*, 2002, **87**, 2960–2971.
87 B. K. Chakrabarti, J. Feng, E. Kalamaras, J. Rubio-Garcia, C. George, H. Luo, Y. Xia, V. Yufit, M. M. Titirici, C. T. J. Low, A. Kucernak and N. P. Brandon, *ACS Appl. Mater. Interfaces*, 2020, **12**, 53869–53878.
88 W. Sheng, Z. Zhuang, M. Gao, J. Zheng, J. G. Chen and Y. Yan, *Nat. Commun.*, 2015, **6**, 1–6.
89 J. Durst, A. Siebel, C. Simon, F. Hasché, J. Herranz and H. A. Gasteiger, *Energy Environ. Sci.*, 2014, **7**, 2255–2260.
90 Y. Qiu, X. Xie, W. Li and Y. Shao, *Chinese J. Catal.*, 2021, **42**, 2094–2104.

91 Y. Cong, B. Yi and Y. Song, *Nano Energy*, 2018, **44**, 288–303.
92 J. K. Nørskov, T. Bligaard, A. Logadottir, J. R. Kitchin, J. G. Chen, S. Pandelov and U. Stimming, *J. Electrochem. Soc.*, 2005, **152**, J23.
93 E. Skúlason, V. Tripkovic, M. E. Björketun, S. Gudmundsdóttir, G. Karlberg, J. Rossmeisl, T. Bligaard, H. Jónsson and J. K. Nørskov, *J. Phys. Chem. C*, 2010, **114**, 18182–18197.
94 J. Li, S. Ghoshal, M. K. Bates, T. E. Miller, V. Davies, E. Stavitski, K. Attenkofer, S. Mukerjee, Z.-F. Ma and Q. Jia, *Angew. Chem. Int. Ed.*, 2017, **56**, 15594–15598.
95 J. Zheng, J. Nash, B. Xu and Y. Yan, *J. Electrochem. Soc.*, 2018, **165**, H27.
96 X. Chen, L. P. Granda-Marulanda, I. T. McCrum and M. T. M. Koper, *Chem. Sci.*, 2020, **11**, 1703–1713.
97 Y. Tian, K.-H. Wu, L. Cao, W. H. Saputera, R. Amal and D.-W. Wang, *Chem. Commun.*, 2019, **55**, 2154–2157.
98 J. E. Nutting, M. Rafiee and S. S. Stahl, *Chem. Rev.*, 2018, **118**, 4834–4885.
99 L. F. Arenas, A. Loh, D. P. Trudgeon, X. Li, C. Ponce de León and F. C. Walsh, *Renew. Sustain. Energ. Rev.*, 2018, 90, 992–1016.
100 M. A. Vertes, E. G. Katsoulis, J. E. Oxley and K. Alfredson, *Leesona Moos Labs Div Leesona Copr Gt. Neck NY*, 1966.
101 Product - Eos Energy Enterprises, https://eosenergystorage.com/products-technology/, (accessed 21 October 2021).
102 X. Liu, M. Ouyang, M. W. Orzech, Y. Niu, W. Tang, J. Chen, M. N. Marlow, D. Puhan, Y. Zhao, R. Tan, B. Colin, N. Haworth, S. Zhao, H. Wang, P. Childs, S. Margadonna, M. Wagemaker, F. Pan, N. Brandon, C. George and B. Wu, *Energy Storage Mater.*, 2020, **30**, 329–336.
103 P. Leung, D. Aili, Q. Xu, A. Rodchanarowan and A. A. Shah, *Sustain. Energy Fuels*, 2018, **2**, 2252–2259.
104 X. Yu and A. Manthiram, *Appl. Energy Mater*, 2018, **1**, 2424–2428.
105 V. Yufit, B. Hale, M. Matian, P. Mazur and N. P. Brandon, *J. Electrochem. Soc.*, 2013, **160**, A856–A861.
106 J. Rubio-Garcia, A. Kucernak, D. Zhao, D. Li, K. Fahy, V. Yufit, N. Brandon and M. Gomez-Gonzalez, *J. Phys. Energy*, 2018, **1**, 015006.
107 RFC Power | The future of energy storage, https://www.rfcpower.com/, (accessed 21 October 2021).
108 K. T. Cho, M. C. Tucker and A. Z. Weber, *Energy Technol.*, 2016, **4**, 655–678.
109 M. C. Tucker, K. T. Cho, F. B. Spingler, A. Z. Weber and G. Lin, *J. Power Sources*, 2015, **284**, 212–221.
110 Y. A. Hugo, W. Kout, G. Dalessi, A. Forner-Cuenca, Z. Borneman and K. Nijmeijer, *Processes*, 2020, **8**, 1492.
111 J. Rubio-Garcia, A. Kucernak, A. Parra-Puerto, R. Liu and B. Chakrabarti, *J. Mater. Chem. A*, 2020, **8**, 3933–3941.
112 D. Malko, T. Lopes, E. Symianakis and A. R. Kucernak, *J. Mater. Chem. A*, 2016, **4**, 142–152.
113 D. S. Aaron, Q. Liu, Z. Tang, G. M. Grim, A. B. Papandrew, A. Turhan, T. A. Zawodzinski and M. M. Mench, *J. Power Sources*, 2012, **206**, 450–453.
114 S. S. Shinde, C. H. Lee, J. Y. Jung, N. K. Wagh, S. H. Kim, D. H. Kim, C. Lin, S. U. Lee and J. H. Lee, *Energy Environ. Sci.*, 2019, **12**, 727–738.
115 Y. Liu, M. A. Goulet, L. Tong, Y. Liu, Y. Ji, L. Wu, R. G. Gordon, M. J. Aziz, Z. Yang and T. Xu, *Chem*, 2019, **5**, 1861–1870.
116 M. Küttinger, R. Brunetaud, J. K. Włodarczyk, P. Fischer and J. Tübke, *J. Power Sources*, 2021, **495**, 229820.

117 M. C. Tucker, K. T. Cho, A. Z. Weber, G. Lin and T. Van Nguyen, *J. Appl. Electrochem.*, 2015, **45**, 11–19.
118 J. Charvát, P. Mazúr, J. Pocedič, P. Richtr, J. Mrlík, J. Kosek, J. Akrman and L. Kubáč, *J. Power Sources*, 2022, **520**, 230811.
119 R. Schweiss, C. Meiser, T. Damjanovic, I. Galbati and N. Haak, *SIGRACET® Gas Diffusion Layers for PEM Fuel Cells, Electrolyzers and Batteries (White Paper); SGL Carbon GmbH*, Bonn, Germany, 2016.
120 A. Forner-Cuenca and F. R. Brushett, *Curr. Opin. Electrochem.*, 2019, **18**, 113–122.
121 X. L. Zhou, T. S. Zhao, L. An, Y. K. Zeng and L. Wei, *J. Power Sources*, 2017, **339**, 1–12.
122 X. L. Zhou, T. S. Zhao, Y. K. Zeng, L. An and L. Wei, *J. Power Sources*, 2016, **329**, 247–254.
123 X. L. Zhou, Y. K. Zeng, X. B. Zhu, L. Wei and T. S. Zhao, *J. Power Sources*, 2016, **325**, 329–336.
124 Q. Zheng, F. Xing, X. Li, T. Liu, Q. Lai, G. Ning and H. Zhang, *J. Power Sources*, 2015, **277**, 104–109.
125 P. Zhao, H. Zhang, H. Zhou and B. Yi, *Electrochim. Acta*, 2005, **51**, 1091–1098.
126 X. Dong, Y. Wang and Y. Xia, *Sci. Rep.*, 2014, **4**, 1–6.
127 X. Lu, F. Li, M. Steimecke, M. Tariq, M. Hartmann and M. Bron, *ChemElectroChem*, 2020, **7**, 737–744.
128 L. F. Castañeda, F. C. Walsh, J. L. Nava and C. Ponce de León, *Electrochim. Acta*, 2017, **258**, 1115–1139.
129 A. Parasuraman, T. M. Lim, C. Menictas and M. Skyllas-Kazacos, *Electrochim. Acta*, 2013, **101**, 27–40.
130 R. W. Atkinson, Y. Garsany, B. D. Gould, K. E. Swider-Lyons and I. V. Zenyuk, *ACS Appl. Energy Mater.*, 2018, **1**, 191–201.
131 K. V Greco, A. Forner-Cuenca, A. Mularczyk, J. Eller and F. R. Brushett, *ACS Appl. Mater. Interfaces*, 2018, **10**, 44430–44442.
132 D. Zhang, A. Forner-Cuenca, O. O. Taiwo, V. Yufit, F. R. Brushett, N. P. Brandon, S. Gu and Q. Cai, *J. Power Sources*, 2020, **447**, 227249.
133 A. Gayon Lombardo, B. A. Simon, O. O. Taiwo, S. J. Neethling and N. P. Brandon, *J. Energy Storage*, 2019, **24**, 100736.
134 K. M. Tenny, A. Forner-Cuenca, Y.-M. Chiang and F. R. Brushett, *J. Electrochem. En. Conv. Stor.*, 2020, **17**, 041108-1–13.
135 Z. He, Z. Chen, W. Meng, Y. Jiang, G. Cheng, L. Dai and L. Wang, *J. Energy Chem.*, 2016, **25**, 720–725.
136 K. M. Tenny, V. S. Lakhanpal, R. P. Dowd, V. Yarlagadda and T. Van Nguyen, *J. Electrochem. Soc.*, 2017, **164**, A2534.
137 M. Hua, T. Chen and H. Ma, *ACS Appl. Energy Mater.*, 2019, **2**, 4316–4324.
138 L. Wei, T. S. Zhao, G. Zhao, L. An and L. Zeng, *Appl. Energy*, 2016, **176**, 74–79.
139 R. M. Darling and M. L. Perry, *J. Electrochem. Soc.*, 2014, **161**, A1381–A1387.
140 H. Sharma and M. Kumar, *J. Power Sources*, 2021, **494**, 229753.
141 J. Millichamp, T. J. Mason, T. P. Neville, N. Rajalakshmi, R. Jervis, P. R. Shearing and D. J. L. Brett, *J. Power Sources*, 2015, **284**, 305–320.
142 L. D. Brown, T. P. Neville, R. Jervis, T. J. Mason, P. R. Shearing and D. J. L. Brett, *J. Energy Storage*, 2016, **8**, 91–98.
143 T. A. M. Suter, K. Smith, J. Hack, L. Rasha, Z. Rana, G. M. A. Angel, P. R. Shearing, T. S. Miller and D. J. L. Brett, *Adv. Energy Mater.*, 2021, **11**, 2101025.
144 B. Sun and M. Skyllas-Kazacos, *Electrochim. Acta*, 1992, **37**, 1253–1260.
145 T. J. Rabbow, M. Trampert, P. Pokorny, P. Binder and A. H. Whitehead, *Electrochim.*

Acta, 2015, **173**, 17–23.
146 T. Wu, K. Huang, S. Liu, S. Zhuang, D. Fang, S. Li, D. Lu and A. Su, *J. Solid State Electrochem. 2011 162*, 2011, **16**, 579–585.
147 E.-M. Hammer, B. Berger and L. Komsiyska, *Int. J. Renew. Energy Dev.*, 2014, **3**, 7–12.
148 Y. A. Gandomi, D. S. Aaron, J. R. Houser, M. C. Daugherty, J. T. Clement, A. M. Pezeshki, T. Y. Ertugrul, D. P. Moseley and M. M. Mench, *J. Electrochem. Soc.*, 2018, **165**, A970–A1010.
149 J. L. Barton, J. D. Milshtein, J. J. Hinricher and F. R. Brushett, *J. Power Sources*, 2018, **399**, 133–143.
150 A. Forner-Cuenca, E. E. Penn, A. M. Oliveira and F. R. Brushett, *J. Electrochem. Soc.*, 2019, **166**, 2230–2241.
151 B. A. Simon, A. Gayon-Lombardo, C. A. Pino-Muñoz, C. E. Wood, K. M. Tenny, K. V. Greco, S. J. Cooper, A. Forner-Cuenca, F. R. Brushett, A. R. Kucernak and N. P. Brandon, *Appl. Energy*, 2022, **306**, 117678.
152 J. D. Milshtein, K. M. Tenny, J. L. Barton, J. Drake, R. M. Darling and F. R. Brushett, *J. Electrochem. Soc.*, 2017, **164**, E3265–E3275.
153 C. Richmond, *BMJ*, 2004, **329**, 687.
154 Q. Lin, S. J. Neethling, L. Courtois, K. J. Dobson and P. D. Lee, *Hydrometallurgy*, 2016, **164**, 265–277.
155 M. D. R. Kok, R. Jervis, P. R. Shearing and J. T. Gostick, *ECS Trans.*, 2017, **77**, 129.
156 S. J. Cooper, A. Bertei, P. R. Shearing, J. A. Kilner and N. P. Brandon, *SoftwareX*, 2016, **5**, 203–210.
157 Q. Xu and T. S. Zhao, *Prog. Energy Combust. Sci.*, 2015, **49**, 40–58.
158 A. J. Bard and L. R. Faulkner, *ELECTROCHEMICAL METHODS: Fundamentals and applications*, 2001.
159 C. A. P. Muñoz, H. H. Dewage, V. Yufit and N. P. Brandon, *J. Electrochem. Soc.*, 2017, **164**, F1717–F1732.
160 J. S. Newman and K. E. Thomas-Alyea, *Electrochemical Systems*, John Wiley & Sons, Inc., New York, 3rd edn., 2004.
161 M. Z. Bazant, *Acc. Chem. Res.*, 2013, **46**, 1144–1160.
162 A. Mistry, A. A. Franco, S. J. Cooper, S. A. Roberts and V. Viswanathan, *ACS Energy Lett.*, 2021, **6**, 1422–1431.
163 S. Kench and S. J. Cooper, *Nat. Mach. Intell. 2021 34*, 2021, **3**, 299–305.
164 A. Gayon-Lombardo, L. Mosser, N. P. Brandon and S. J. Cooper, *npj Comput. Mater.*, 2020, **6**, 1–11.
165 I. V. Zenyuk, D. Y. Parkinson, L. G. Connolly and A. Z. Weber, *J. Power Sources*, 2016, **328**, 364–376.
166 P. A. García-Salaberri, I. V. Zenyuk, A. D. Shum, G. Hwang, M. Vera, A. Z. Weber and J. T. Gostick, *Int. J. Heat Mass Tran.*, 2018, **127**, 687–703.
167 C. T.-C. Wan, R. R. Jacquemond, Y.-M. Chiang, K. Nijmeijer, F. R. Brushett and A. Forner-Cuenca, *Adv. Mater.*, 2021, **33**, 2006716.
168 J. Sun, M. Wu, H. Jiang, X. Fan and T. Zhao, *Adv. Appl. Energy*, 2021, **2**, 100016.
169 A. Parra-Puerto, J. Rubio-Garcia, M. Markiewicz, Z. Zheng and A. Kucernak, *ChemElectroChem*, 2022, **9**, e202101617.
170 H. Qian, A. R. Kucernak, E. S. Greenhalgh, A. Bismarck and M. S. P. Shaffer, *ACS Appl. Mater. Interfaces*, 2013, **5**, 6113–6122.
171 F. H. B. Lima and R. R. Adzic, *Handook of Fuel Cells; Fundamentals Technology and Applications; Volume 5 Advances in Electrocatalysis, Materials, Diagnostics and Durability: Part 1*, Wiley, 2009.

172 A. Kongkanand and M. F. Mathias, *J. Phys. Chem. Lett.*, 2016, **7**, 1127–1137.
173 S. T. Thompson, B. D. James, J. M. Huya-Kouadio, C. Houchins, D. A. DeSantis, R. Ahluwalia, A. R. Wilson, G. Kleen and D. Papageorgopoulos, *J. Power Sources*, 2018, **399**, 304–313.
174 H. A. Gasteiger, S. S. Kocha, B. Sompalli and F. T. Wagner, *Appl. Catal. B Environ.*, 2005, **56**, 9–35.
175 R. Zhao, X. Yue, Q. Li, G. Fu, J.-M. Lee and S. Huang, *Small*, 2021, 2100391.
176 C. Wei, R. R. Rao, J. Peng, B. Huang, I. E. L. Stephens, M. Risch, Z. J. Xu and Y. Shao-Horn, *Adv. Mater.*, 2019, **31**, 1806296.
177 H. C. Zhou, J. R. Long and O. M. Yaghi, *Chem. Rev.*, 2012, **112**, 673–674.
178 K. S. Park, Z. Ni, A. P. Côté, J. Y. Choi, R. Huang, F. J. Uribe-Romo, H. K. Chae, M. O'Keeffe and O. M. Yaghi, *Proc. Natl. Acad. Sci. U. S. A.*, 2006, **103**, 10186–10191.
179 R. Banerjee, A. Phan, B. Wang, C. Knobler, H. Furukawa, M. O'Keeffe and O. M. Yaghi, *Science (80-.).*, 2008, **319**, 939–943.
180 A. Corma, M. J. Díaz-Cabãas, J. L. Jordá, C. Martínez and M. Moliner, *Nature*, 2006, **443**, 842–845.
181 H. Zhang, S. Hwang, M. Wang, Z. Feng, S. Karakalos, L. Luo, Z. Qiao, X. Xie, C. Wang, D. Su, Y. Shao and G. Wu, *J. Am. Chem. Soc.*, 2017, **139**, 14143–14149.
182 A. Mehmood, M. Gong, F. Jaouen, A. Roy, A. Zitolo, A. Khan, M.-T. Sougrati, M. Primbs, A. M. Bonastre, D. Fongalland, G. Drazic, P. Strasser and A. Kucernak, *Nat. Catal.*, 2022, **5**, 311–323.
183 C. M. Zalitis, D. Kramer and A. R. Kucernak, *Phys. Chem. Chem. Phys.*, 2013, **15**, 4329–4340.
184 C. Jackson, L. F. J. M. Raymakers, M. J. J. Mulder and A. R. J. Kucernak, *Appl. Catal. B Environ.*, 2020, **268**, 118734.
185 D. Banham, J. Zou, S. Mukerjee, Z. Liu, D. Yang, Y. Zhang, Y. Peng and A. Dong, *J. Power Sources*, 2021, **490**, 229515.
186 J. Greeley, I. E. L. Stephens, A. S. Bondarenko, T. P. Johansson, H. A. Hansen, T. F. Jaramillo, J. Rossmeisl, I. Chorkendorff and J. K. Nørskov, *Nat. Chem.*, 2009, **1**, 552–556.
187 C. Zalitis, A. Kucernak, X. Lin and J. Sharman, *ACS Catal.*, 2020, **10**, 4361–4376.
188 Y. Lv and X. Wang, *Catal. Sci. Technol.*, 2017, **7**, 3676–3691.
189 C. H. Lee, B. Jun and S. U. Lee, *ACS Sustain. Chem. Eng.*, 2018, **6**, 4973–4980.
190 M. Tahir, N. Mahmood, J. Zhu, A. Mahmood, F. K. Butt, S. Rizwan, I. Aslam, M. Tanveer, F. Idrees, I. Shakir, C. Cao and Y. Hou, *Sci. Rep.*, 2015, **5**, 1–10.
191 Y. Xue, S. Sun, Q. Wang, Z. Dong and Z. Liu, *J. Mater. Chem. A*, 2018, **6**, 10595–10626.
192 H. Wu, J. Geng, H. Ge, Z. Guo, Y. Wang and G. Zheng, *Adv. Energy Mater.*, 2016, **6**, 1600794.
193 H. Huang, K. Shen, F. Chen and Y. Li, *ACS Catal.*, 2020, **10**, 6579–6586.
194 E. Zhang, Y. Xie, S. Ci, J. Jia, P. Cai, L. Yi and Z. Wen, *J. Mater. Chem. A*, 2016, **4**, 17288–17298.
195 J. Zhang, H. Yang and B. Liu, *Adv. Energy Mater.*, 2021, **11**, 2002473.
196 Y. Chen, S. Ji, C. Chen, Q. Peng, D. Wang and Y. Li, *Joule*, 2018, **2**, 1242–1264.
197 A. Mehmood, B. Ali, M. Gong, M. Gyu Kim, J. Y. Kim, J. H. Bae, A. Kucernak, Y. M. Kang and K. W. Nam, *J. Colloid Interface Sci.*, 2021, **596**, 148–157.
198 Y. Mu, T. Wang, J. Zhang, C. Meng, Y. Zhang and Z. Kou, *Electrochem. Energy Rev.*, 2021, **1**, 1–42.
199 J. A. Behan, E. Mates-Torres, S. N. Stamatin, C. Domínguez, A. Iannaci, K. Fleischer, M. K. Hoque, T. S. Perova, M. García-Melchor and P. E. Colavita, *Small*, 2019, **15**,

1902081.
200 Y. Jia, L. Zhang, L. Zhuang, H. Liu, X. Yan, X. Wang, J. Liu, J. Wang, Y. Zheng, Z. Xiao, E. Taran, J. Chen, D. Yang, Z. Zhu, S. Wang, L. Dai and X. Yao, *Nat. Catal.*, 2019, **2**, 688–695.
201 R. Borup, J. Meyers, B. Pivovar, Y. S. Kim, R. Mukundan, N. Garland, D. Myers, M. Wilson, F. Garzon, D. Wood, P. Zelenay, K. More, K. Stroh, T. Zawodzinski, J. Boncella, J. E. McGrath, M. Inaba, K. Miyatake, M. Hori, K. Ota, Z. Ogumi, S. Miyata, A. Nishikata, Z. Siroma, Y. Uchimoto, K. Yasuda, K. Kimijima and N. Iwashita, *Chem. Rev.*, 2007, **107**, 3904–3951.
202 F. Coloma, A. Sepulveda-Escribano, J. L. G. Fierro and F. Rodriguez-Reinoso, *Langmuir*, 2002, **10**, 750–755.
203 Y. Cheng, C. Xu, L. Jia, J. D. Gale, L. Zhang, C. Liu, P. K. Shen and S. P. Jiang, *Appl. Catal. B Environ.*, 2015, **163**, 96–104.
204 S. Ghoshal, S. Zaccarine, G. C. Anderson, M. B. Martinez, K. E. Hurst, S. Pylypenko, B. S. Pivovar and S. M. Alia, *ACS Appl. Energy Mater.*, 2019, **2**, 5568–5576.
205 R. Kötz, H. J. Lewerenz and S. Stucki, *J. Electrochem. Soc.*, 1983, **130**, 825.
206 E. Antolini, *ACS Catal.*, 2014, **4**, 1426–1440.
207 N.-T. Suen, S.-F. Hung, Q. Quan, N. Zhang, Y.-J. Xu and H. M. Chen, *Chem. Soc. Rev.*, 2017, **46**, 337–365.
208 J. O. Bockris and T. Otagawa, *J. Electrochem. Soc.*, 1984, **131**, 290.
209 H.-Y. Wang, S.-F. Hung, H.-Y. Chen, T.-S. Chan, H. M. Chen and B. Liu, *J. Am. Chem. Soc.*, 2015, **138**, 36–39.
210 C. Hu and L. Dai, *Adv. Mater.*, 2017, **29**, 1604942.
211 P. Li, X. Duan, S. Wang, L. Zheng, Y. Li, H. Duan, Y. Kuang and X. Sun, *Small*, 2019, **15**, 1904043.
212 G. Zhao, J. Chen, W. Sun and H. Pan, *Adv. Funct. Mater.*, 2021, **31**, 2010633.
213 G. E. Haslam, X.-Y. Chin and G. T. Burstein, *Phys. Chem. Chem. Phys.*, 2011, **13**, 12968–12974.
214 X. Wu, C. Tang, Y. Cheng, X. Min, S. P. Jiang and S. Wang, *Chem. – A Eur. J.*, 2020, **26**, 3906–3929.
215 H.-F. Wang, C. Tang and Q. Zhang, *Adv. Funct. Mater.*, 2018, **28**, 1803329.
216 S. Zhao, L. Yan, H. Luo, W. Mustain and H. Xu, *Nano Energy*, 2018, **47**, 172–198.
217 W. T. Hong, M. Risch, K. A. Stoerzinger, A. Grimaud, J. Suntivich and Y. Shao-Horn, *Energy Environ. Sci.*, 2015, **8**, 1404–1427.
218 S. Ghosh and R. N. Basu, *Nanoscale*, 2018, **10**, 11241–11280.
219 C. Hu, Q. Dai and L. Dai, *Cell Reports Phys. Sci.*, 2021, **2**, 100328.
220 G. C. Da Silva, M. R. Fernandes and E. A. Ticianelli, *ACS Catal.*, 2018, **8**, 2081–2092.
221 A. Parra-Puerto, K. L. Ng, K. Fahy, A. E. Goode, M. P. Ryan and A. Kucernak, *ACS Catal.*, 2019, **9**, 11515–11529.
222 H. S. Park, J. Yang, M. K. Cho, Y. Lee, S. Cho, S. D. Yim, B. S. Kim, J. H. Jang and H. K. Song, *Nano Energy*, 2019, **55**, 49–58.
223 A. Hrnjić, F. Ruiz-Zepeda, M. Gaberšček, M. Bele, L. Suhadolnik, N. Hodnik and P. Jovanovič, *J. Electrochem. Soc.*, 2020, **167**, 166501.
224 A. Hrnjic, A. R. Kamšek, A. Pavlišič, M. Šala, M. Bele, L. Moriau, M. Gatalo, F. Ruiz-Zepeda, P. Jovanovič and N. Hodnik, *Electrochim. Acta*, 2021, **388**, 138513.
225 R. Chowdhury, Y. Zhao, Y. Xia, M. Ouyang, N. Brandon and A. Banerjee, *Sustain. Energy Fuels*, 2021, **5**, 5193–5204.
226 Kevin Schweinar, R. L. Nicholls, C. R. Rajamathi, Patrick Zeller, Matteo Amati, Luca Gregoratti, Dierk Raabe, Mark Greiner, Baptiste Gault and Olga Kasian, *J. Mater. Chem. A*, 2019, **8**, 388–400.

227 J. E. Halpin, R. W. H. Webster, H. Gardner, M. P. Moody, P. A. J. Bagot and D. A. MacLaren, *Ultramicroscopy*, 2019, **202**, 121–127.
228 Atom Probe Tomography - Introduction to the technique, https://www.cameca.com/products/apt/technique, (accessed 18 October 2021).
229 K. SH, K. PW, P. OO, S. JB, A. JP, L. JY and C. PP, *Ultramicroscopy*, 2018, **190**, 30–38.
230 Y. Zhu, T.-R. Kuo, Y.-H. Li, M.-Y. Qi, G. Chen, J. Wang, Y.-J. Xu and H. M. Chen, *Energy Environ. Sci.*, 2021, **14**, 1928–1958.
231 S.-F. Hung, Y. Zhu, G.-Q. Tzeng, H.-C. Chen, C.-S. Hsu, Y.-F. Liao, H. Ishii, N. Hiraoka and H. M. Chen, *ACS Energy Lett.*, 2019, **18**, 2813–2820.
232 Atom Probe Tomography Animation - video Dailymotion, https://www.dailymotion.com/video/x35mjv7, (accessed 19 October 2021).
233 G. Zhang and A. Kucernak, *ACS Catal.*, 2020, **10**, 9684–9693.
234 C. Jackson, L. F. J. M. Raymakers, M. J. J. Mulder and A. R. J. Kucernak, *J. Power Sources*, 2020, **472**, 228476.
235 C. M. Zalitis, A. R. Kucernak, J. Sharman and E. Wright, *J. Mater. Chem. A*, 2017, **5**, 23328–23338.
236 N. Ma, Y. (Alec) Jia, X. Yang, X. She, L. Zhang, Z. Peng, X. Yao and D. Yang, *J. Mater. Chem. A*, 2016, **4**, 6376–6384.
237 P. Trogadas and M.-O. Coppens, *Chem. Soc. Rev.*, 2020, **49**, 3107–3141.
238 H. A. Gasteiger and N. M. Marković, *Science (80-.).*, 2009, **324**, 48–49.
239 J. Yuan, Z. Z. Pan, Y. Jin, Q. Qiu, C. Zhang, Y. Zhao and Y. Li, *J. Power Sources*, 2021, **500**, 229983.
240 M.-C. Bay, M. Wang, R. Grissa, M. V F Heinz, J. Sakamoto, C. Battaglia, M. Bay, R. Grissa, M. V F Heinz, C. Battaglia Empa, M. Wang and J. Sakamoto, *Adv. Energy Mater.*, 2020, **10**, 1902899.
241 E. Quérel, I. D. Seymour, A. Cavallaro, Q. Ma, F. Tietz and A. Aguadero, *J. Phys. Energy*, 2021, **3**, 044007.
242 A. G. Wright, J. Fan, B. Britton, T. Weissbach, H.-F. Lee, E. A. Kitching, T. J. Peckham and S. Holdcroft, *Energy Environ. Sci.*, 2016, **9**, 2130–2142.

Chapter 2

Experimental methods and characterisation

This chapter provides some background and a general description of the techniques used in this thesis. Specific information, such as sample preparation and experimental detail, are outlined in local methodologies in each respective chapter.

"If I have seen further, it is by standing on the shoulders of giants." – Isaac Newton

2.1 Physical methods

2.1.1 Scanning electron microscopy (SEM)

Scanning electron microscopy (SEM) is an imaging technique commonly used to identify micro- (and in some cases, nano-) level surface topological features on organic and inorganic materials. A focussed beam of electrons is directed through a series of adjustable lenses, apertures and coils to create a magnified image of a sample (Figure 2.1).[1,2] Images / micrographs are produced from the conversion of secondary electrons striking the secondary electron detector.

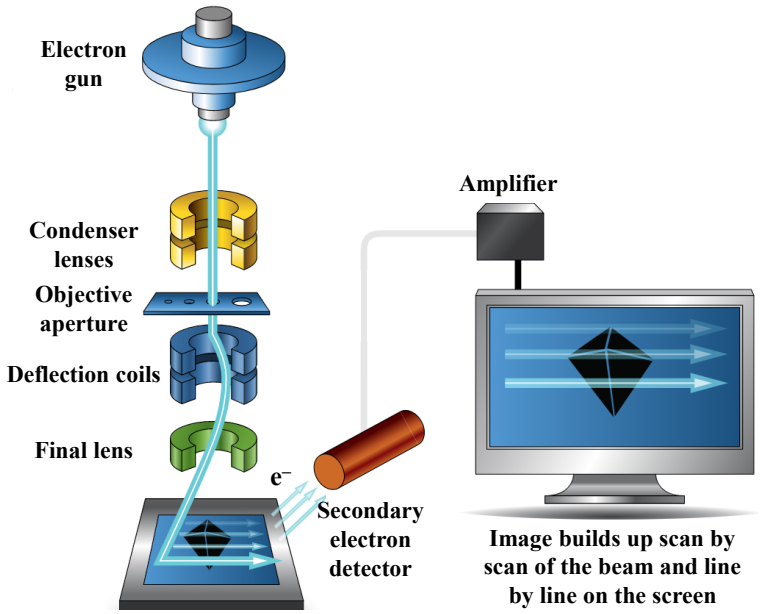


Figure 2.1: Schematic illustration of a scanning electron microscope.[1]

Samples are placed onto the ‘stub’ atop some adhesive carbon tape and, depending on its conductivity, a thin layer of conductive material (e.g. 10 nm chromium) is sputtered to cover the sample. Samples need to be conductive to ensure image quality. Electrons continuously striking the surface of a non-conductive material promotes ‘charging’ and presents as stripes on the resulting micrograph. Samples are then placed in the sample holder transferred into the vacuum chamber. Once the pressure is sufficiently low the electron gun can be turned on and image collection can begin. Brightness, contrast and positional adjustments can be made remotely once the sample has been loaded into scanning electron microscope chamber.

In this work, SEM images were collected using either a Hitachi High-Tech Tabletop TM3030 or a Zeiss Gemini 1525 Field Emission Scanning Electron Microscope situated at the Harvey Flowers Electron Microscopy Suite, Materials department, Imperial College London.

2.1.2 Transmission electron microscopy (TEM)

Transmission electron microscopy (TEM) is another imaging technique used to characterise materials. Compared to a SEM, the main advantage is that higher levels of magnification can be reached. Again, an electron beam is focussed and, in this case, transmitted through a sample. Like a torch directed at an object, a shadow is cast where the light cannot get through – in a TEM, the resulting image is bright where electron beam passes easily through the locations on the sample holder where there is no sample, and the regions where electrons do not pass so easily cast a dark shadow. The range of greys that present over thin particles or at the edge of sample particles reveal interesting structural and crystallographic information about the sample. Figure 2.2 (a) shows schematic representations of the cascade of lenses in the tower and Figure 2.2 (b) shows the types of resulting electrodes that may be produced on interaction with the sample.

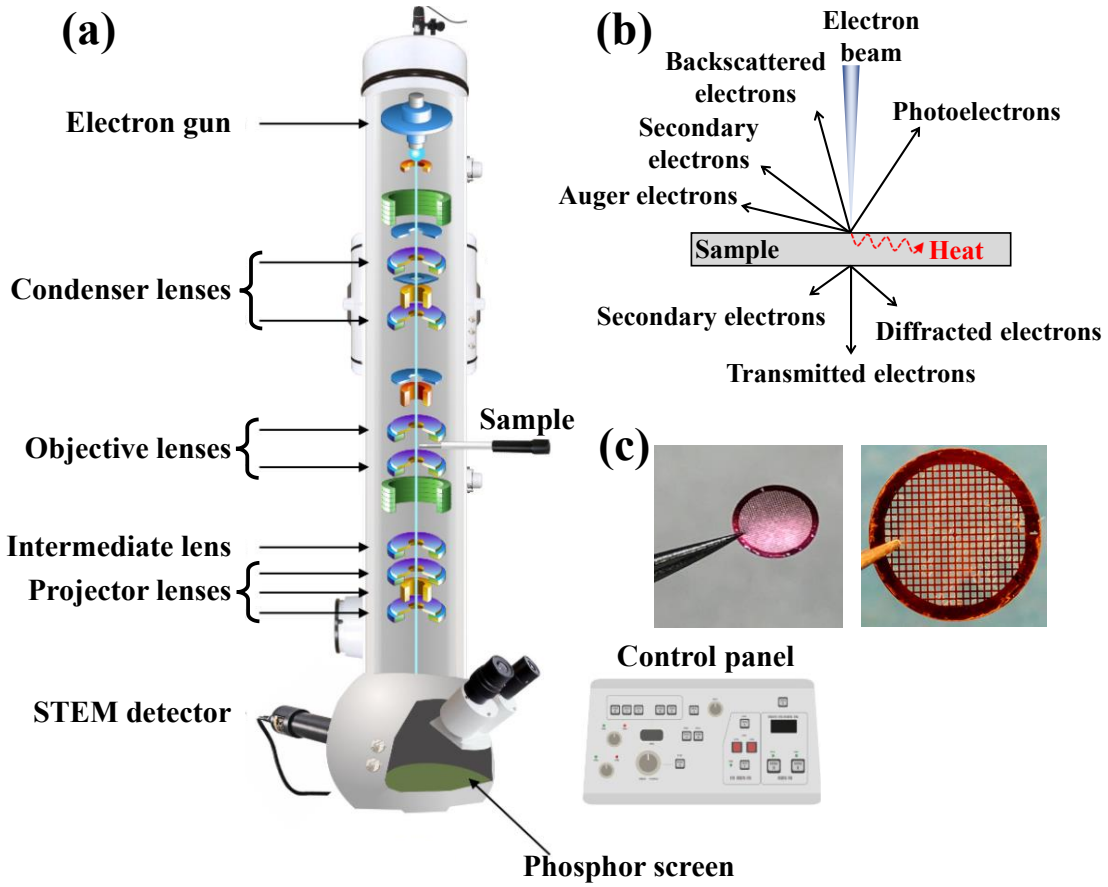


Figure 2.2: Schematic illustration of a transmission electron microscope.[1]

Sample preparation is important in TEM for proper image collection. Small particles or thin films (< 100 nm thick, ideally) of sample return the most insightful images as electrons can most easily pass through them and interact with its atoms. Samples are prepared using thin TEM microgrids ('Holey Carbon Film', 17–20 nm thick, TAAB) Figure 2.2 (c)), generally, in one of two ways. Either a very dilute sample suspension is prepared and the TEM microgrid is dipped into it, or this sample matrix is dropped onto the TEM grid. It should be noted that microgrids are usually made using either carbon, copper or gold substrates – this should be considered before preparing the sample, especially when in scanning TEM (STEM) mode (see next Section on energy dispersive X-ray spectroscopy). There are some additional advanced modes in which TEM can be used such as 'high-resolution TEM' (HRTEM) which uses multiple beams often for phase-contrast imaging and 'high-angle-annular dark-field' STEM (HAADF-STEM) which collects electrons scattered through very high angles (i.e. elements with high atomic masses).

In this work, TEM micrographs were gathered with the help of Dr. Mahmoud Ardakani using a JEOL 2100Plus Electron Microscope situated in the Harvey Flowers Electron Microscopy Suite, Materials department, Imperial College London.

2.1.3 Energy dispersive X-ray spectroscopy (EDX)

Energy dispersive X-ray spectroscopy (EDX) is a form of X-ray microanalytical technique that is used in tandem with a SEM and scanning TEM (STEM) (a specific mode used for TEM elemental analysis). There are crucial differences about how they are used alongside these techniques due to the geometry and layout of the microscopes and the electron beam accelerating voltages. For instance, samples need to be angled in-situ (c.a. 15°) to allow for the use of a different detector.

Together with inducing secondary electron generation (SEM) or transmitting through the sample (TEM), the beam of electrons penetrates the sample and interact with its atoms – this interaction generates two types of X-ray: Continuum / background X-rays and characteristic X-rays. Characteristic X-rays are generated by electrons from higher orbital filling an inner orbital vacancies (vacancies are generated by ionisation from electron-beam electrons) and give characteristic elemental information.

Typically, there are three types of output possibilities based on these X-rays – two qualitative and one quantitative.[1] Firstly, 'Spectrum' where an area is chosen and intensity of X-rays are plotted against their energy – from a spectrum, the user can observe which elements are present in the area selected. Secondly, 'Map' where a micrograph (image) is overlayed with colour representations of elements, the intensity of which is qualitatively reflective of concentration. Thirdly, 'Quantitative' where, based on the number and energy of the X-rays that hit the detector, the sample. Definitive quantitative outputs must treated with caution as sample preparation will affect the readings intensely.

The same instruments as for the SEM and TEM measurements were used for collecting SEM-EDX or STEM. Sample preparation is also identical, however, it should be noted that the conductive material used to coat an SEM sample will have high intensity during SEM-EDX.

2.1.4 X-ray diffraction (XRD)

X-ray diffraction is a non-destructive characterisation technique that uses X-rays to determine and quantify the crystallographic nature of material. This technique is sensitive to both the type and relative positioning of atoms and so can be used for many things including measuring the extent of crystalline content and the spacing between lattice planes.

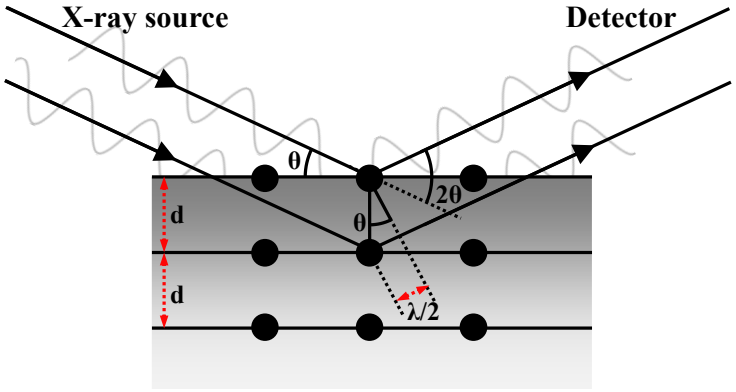


Figure 2.3: Simplified graphical representation of X-ray constructive and destructive interference alongside parameters required for Bragg's Law calculations. The present example illustrated here displays destructive interference.

When the X-rays strike the material in question, the surface atoms' electron cloud are scattered. Figure 2.3 shows how the X-rays that are scattered off consecutive lattice planes interfere with one another constructively or destructively. This X-ray interaction is characterised by the distances between the crystal structures' lattice (which are specific to the material) and the angle with which the X-rays are directed at the material. Bragg's Law is derived by simple geometry and allows the user to calculate the spacing between planes in the atomic lattice – Equation (2.1), where n is an integer, λ is the wavelength of the X-rays (m), d is the distance between crystal planes (m) and θ is the angle of the incident X-rays.

$$n\lambda = 2d\sin\theta \qquad (2.1)$$

One important aspect of XRD sample preparation is that a sufficient amount of sample must be used (enough to cover the circular sample area – usually 1 – 2 cm in diameter). Since only crystal planes parallel to the diffracting plane will be detected, a large number of sample (and therefore crystal) sites in all orientations need to be present during the measurement. XRD can be performed on a number of different types of sample including solid crystalline surfaces. In this work, powder XRD was used and the sample was ground in a pestle and mortar before loading onto the sample holder after which the sample was flattened by a glass slide (to ensure proper XRD measurement). In order to collect the XRD spectra, a Bruker D2 desktop

instrument (Materials department, Imperial College London) was operated at 30 kV, 10 mA and used a Cu Kα radiation source (anode).

2.1.5 X-ray photoelectron spectroscopy (XPS)

X-ray photoelectron spectroscopy (XPS) is a non-destructive surface sensitive spectroscopic technique used to investigate the chemical composition of a material surface. The sample is irradiated with X-rays of known energy, *hv*, and measuring the number and kinetic energy of the ejected photoelectrons yields a spectrum that gives the user information about the species on the surface of the material. Electronic structures of materials can clearly be seen from XPS spectra however, on closer inspection of peaks, additional bonding character / information can be extracted.

One of the main limitations of this system is the depth the X-rays can penetrate. While this should not be a problem for solid, ordered and continuous samples, for porous materials (such as the functionalised carbon powders discussed in this work), this must be kept in mind when evaluating spectra signals – there could be embedded species that have not been reached by the X-rays but that might be available to active species during catalyst utilisation. Additionally, there may be segregation at the surface inferring that, during the XPS measurement, the bulk and the surface composition are not the same,[3] though this is not commonly observed in for carbon based species. In this work, the presumed escape depth of the elastically scattered electrons is 0.5 – 2.0 nm.[4]

XPS measurements were carried out with the help of Dr. Gwilherm Kerherve using a K-Alpha X-ray Photoelectron Spectrometer System (ThermoFisher Scientific), Materials department, Imperial College London.

2.1.6 X-ray absorption spectroscopy (XAS)

Where the function of XRD is to reveal the crystal structures of / within materials, X-ray absorption spectroscopy (XAS) sheds light on the electronic state and coordination environment of a particular atom / element. XAS is an element-selective technique meaning that every element can be individually examined without interference from other species. High energy X-rays are directed at sample materials and they are absorbed by certain atoms in the sample. Core electrons are excited by this absorption. A limited amount of this electromagnetic radiation is transmitted through the sample according to the following equation, where I_t is the

intensity of the transmitted X-rays, I_0 is the energy of the incident X-rays and μ and x are the absorption coefficient (m^{-1}) and sample thickness (m), respectively, Equation (2.2).

$$I_t = I_0 e^{-\mu x} \tag{2.2}$$

Once excited, the core electrons either move to higher unoccupied orbitals, or are ionised (i.e. move to an unbound region) (Figure 2.4 (a)) resulting in a range of potential measurements. Atoms may fluoresce following electrons from higher occupied orbitals filling the 'hole' left by the excited core electron – this florescence can be measured. X-ray absorption spectra are quantified, usually, by comparing the intensity of the incident beam with that of the transmitted however, in some applications / modes, the incident radiation energy is compared to the fluorescence.

As the incident X-ray energy increases, the absorption decreases until the binding energy of a core electron is reached. Once the core electron is excited, there is a sharp increase in absorption. This is known as the absorption 'edge', and it characterises the first of the two main XAS regions: X-ray absorption near-edge structure (XANES) (Figure 2.4 (b)).

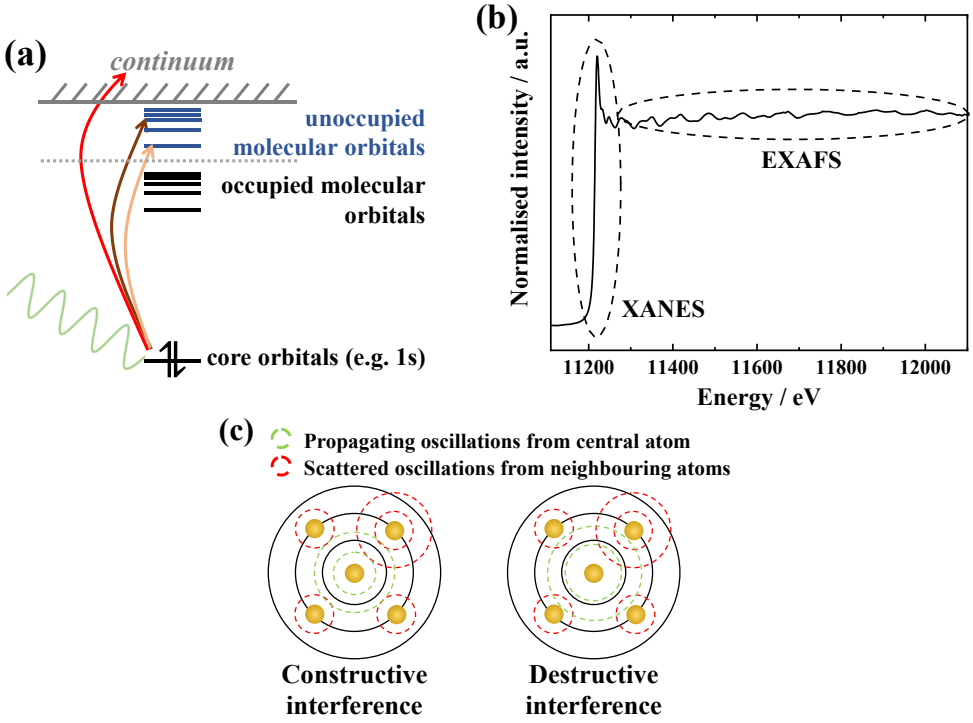


Figure 2.4: Diagram illustrating basic XAS theory. (a) Simplified orbitals with excitations to (bound) unfilled orbitals or (unbound) ionisation (XANES);[5] and, (b) Normalised X-ray absorption spectrum indicating the X-ray absorption near edge structure and the extended X-ray absorption fine structure on a iridium nanoparticle-containing electrocatalyst sample; and, (c) a simplified oscillation interaction during EXAFS signal production.[6]

The resulting energy of the excited photoelectron following excitation is shown by Equation (2.3):

$$E_K = h\nu - E_{\text{binding}} \qquad (2.3)$$

Where E_K is the energy of the excited (K-shell) core electron (kg m^2 s^{-2}), h is Planck's constant (m^2 kg s^{-1}), ν is the photoelectron frequency (s^{-1}) and E_{binding} is the binding energy of the atom. The labelling of the absorption edge depends on the origin of the photoelectron. Electrons excited from a 1s orbital (n = 1) correspond to a K-edges, 2s / $2p_{1/2}$ / $2p_{3/2}$ orbitals (n = 2) correspond to L_I, L_{II} and L_{III} edges. As stated before, following the first 'edge' (ionisation) signal on an XAS spectrum, the absorption decreases – the absorption decrease is accompanied by oscillations in the signal – these oscillations make up the second of the two main XAS regions: extended X-ray absorption edge fine structure (EXAFS). The oscillations in the EXAFS region are characterised by the absorption coefficient (μ) and the nature by which neighbouring atoms scatter and interact (constructively or destructively) with waves propagating out from the original atom centre (Figure 2.4 (b)).

Samples are prepared by thoroughly grinding the solid into a fine powder and producing a thin, smooth, window-like film (roughly 15 × 20 mm) – only a few milligrams are required for this. The nature of the sample enables the experiment to be carried out in either transmission mode (where the X-ray beam penetrates the full sample) or fluorescence mode (for thicker samples where there is weak transmission). In this work, XAS samples were prepared and experiments were carried out in transmission mode by Mr Basit Ali and collated by Dr. Ghulam Ali. Measurements at the Ir L_{III}–edge (11215 eV) were carried out on the 1D KIST-PAL and BL7D beamlines at the Pohang Light Source II (PLS II) in South Korea.

2.1.6.1 XAS data processing

Data processing in this work was carried out with the extremely helpful workshop series by Bruce Ravel in 2011.[7,8] The spectra recorded were processed using the program 'Athena' in the 'Demeter' software package (version 0.9.26).[8] In this work, spectra were normalised for pre- and post- edge, corrected and subsequently plotted in the 'R-space' for EXAFS. Linear combinations of 'standard samples' are also explored. These steps are outlined in the following paragraphs.

Measurements of a reference iridium foil were taken and a correction was made according literature values (Hephaestus) of the Ir L_{III} edge – 11215 eV (dashed line, Figure 2.5).[8]

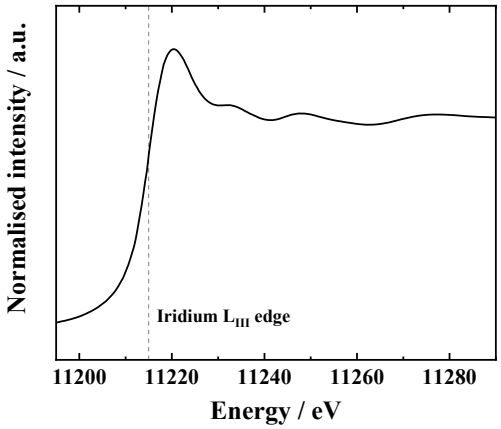


Figure 2.5: Normalised XAS spectrum showing correction for the rest of the dataset.

Once all the data are corrected, the backgrounds can be removed via pre- and post-edge normalisation. The background is due to the interaction between photons and matter, as energy is increased the probability of absorption of photons decreased. The background is corrected by extrapolating a line in the pre-edge region and the post-edge region as shown in Figure 2.6 (a) with the normalised spectrum shown in Figure 2.6 (b). For the iridium L_{III} edge in this work, the pre-edge fitting is linear and modelled to the data between 195 – 50 eV before the Ir edge (E_0) and the post edge is a quadratic function fitted to pass through the middle of the EXAFS oscillations using data from 150 eV after E_0 to 5 eV from the end of the spectrum. The background is generated using a combination of the pre-edge, the post-edge and a polynomial spline function.

EXAFS data are represented in 'k space', referring to the conversion of energy scale to wavelength ($Å^{-1}$) by Equation (2.4). Depending on the element, $\chi(k)$ is plotted as a function of k, k^2 or k^3. Light elements are plotted in lower 'k space' since this is where their impact is appreciated, while heavy elements are more impactful at higher 'k'. In this work, k weightings of 2 were used as this is an appropriate value for the size of iridium.

$$k = \sqrt{\frac{2m_e E}{\hbar^2}} \qquad (2.4)$$

Where m_e is the mass of an electron, $\hbar = h/2\pi$ and h is Planck's constant. EXAFS data is ordinarily represented in 'R space' and this process is, again, performed in Artemis software. A Fourier transform is performed on the EXAFS region to convert 'k space' into 'R space'.

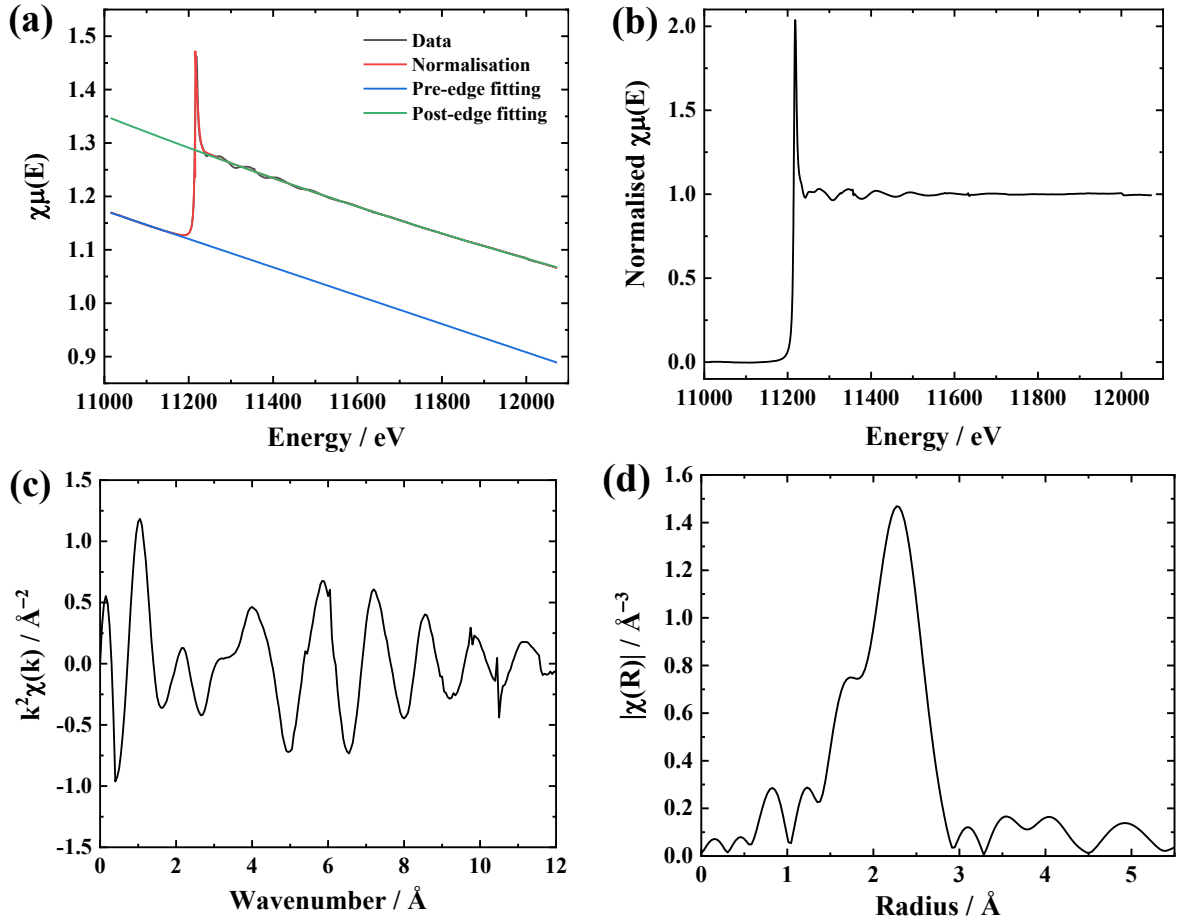


Figure 2.6: XAS background removal and normalisation of a iridium foil sample measured in transmission mode. (a) Pre-processed spectrum showing the pre- and post-edge fittings alongside the background fitting; and, (b) the resulting normalised XAS spectrum. EXAFS region processing using iridium containing sample (Ir_NC_900_900, vide infra) (c) 'k space' plots converting the EXAFS region to wavelength energy scale using a k weighting of 2; and, (d) conversion of 'k space' into 'R space' using a Fourier transform. All processing was carried out in Athena.

2.1.7 X-ray computed tomography (XCT)

X-ray computed tomography (XCT) is a non-destructive imaging technique that uses the attenuation (loss of flux density) of X-rays through a sample to determine positional densities within that sample. There are three essential components (as shown in Figure 2.7): the X-ray source, the sample / sample holder and the detector. The X-ray source (spot size, tube voltage and filament current) is carefully and adjusted according to the sample material. This is because very dense materials will attenuate the X-rays too much and will fail to reveal insightful 3D information. A sample is very slowly rotated while X-ray projections are gathered (c.a. 500 – 3000 projections). Following volume reconstruction, voxels (3D pixels) of 1.5^3 μm^3 were

produced. Volume reconstruction of tomographic data is performed using datos|x,[9] which uses an optimised version of the Feldkamp-Davis-Kress (FDK) cone-beam algorithm.[10] This reconstruction results in a series of 2D greyscale slices that can be segmented and further processed (discussed in further detail in Chapter 3).

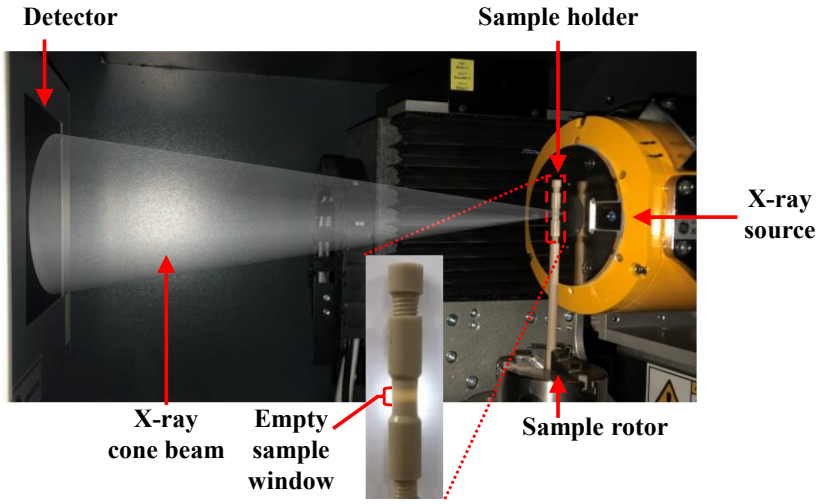


Figure 2.7: Image illustrating XCT setup.

XCT measurements were carried out using a laboratory XCT system (GE Phoenix Nanotom S, Figure 2.7) fitted with a molybdenum target based in the Earth Science and Engineering department, Imperial College London.

2.1.8 Ultraviolet-visible spectroscopy (UV-vis)

Ultraviolet-visible spectroscopy (UV-vis) is an analytical technique that uses light across the UV and visible regions (c.a. 200 – 900 nm). This light is directed at the sample in question and the species in the sample absorb the light at specific wavelengths. A detector is used to measure the level of absorbance of the light at particular wavelengths that have been able to be transmitted through the sample.

The level of absorbance at a given wavelength is proportional to the concentration of the absorbing species in question and is described by the Beer-Lambert law, shown below, where A is the absorbance (dimensionless), α is the absorption coefficient ($m^2\ mol^{-1}$) (or molar attenuation coefficient), c is concentration ($mol\ dm^{-3}$) and l is the length (m).

$$A = \alpha c l \qquad (2.5)$$

Usually, samples are simply placed into standalone (quartz or plastic disposable) cuvettes and then positioned in the line between the source / monochromator-detector path. In this work, an unconventional operando setup was developed using a thin cell (48/Q/0.1 and a CH/2049 holder, Starna) that permits a continuous flow of absorbing species. This operando setup is described in detail in the relevant chapter (*vide infra*). A lab-scale Evolution™ 220 UV-visible Spectrophotometer (ThermoFisher Scientific) was used for the UV-vis experiments carried out in this work.

2.1.9 Electron paramagnetic resonance (EPR)

Electron paramagnetic resonance (EPR) provides information about unpaired electrons in a molecule or material. With a spin quantum number (or state) of S = ½ and a resulting magnetic moment (μ), the electron interacts with a magnetic field, B_0, created by a magnet in the laboratory – this is called the Zeeman effect. The projection of the electron spin can interact with the magnetic field in a parallel (m_s = +½) or anti-parallel state (m_s = -½) (Figure 2.8 (a)) the energy difference, ΔE, between these two states is calculated by the following equation.[11]

$$\Delta E = g\mu_B B_0 \qquad (2.6)$$

Where g is the g-factor (2.0023 for a free electron), μ_B is the Bohr magneton (natural unit of the electron's magnetic moment) and B_0 is the strength of the magnetic field (in Tesla, T).

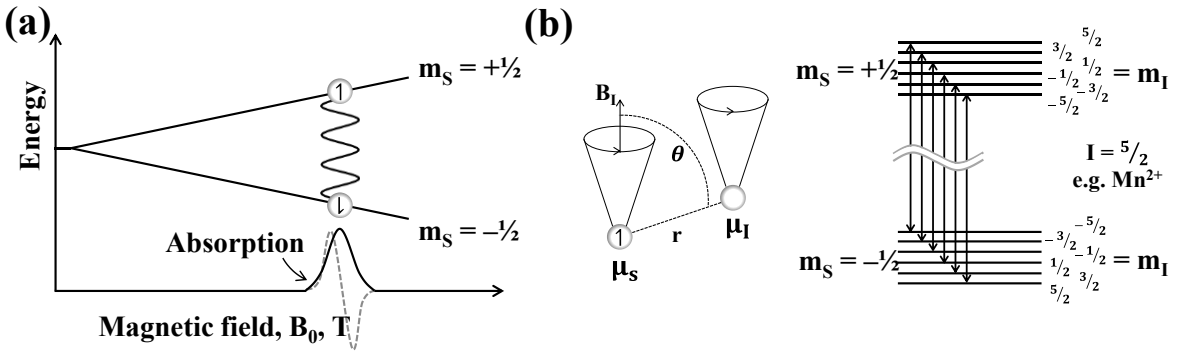


Figure 2.8: (a) Magnetic field dependant Zeeman splitting of energy levels for single unpaired electron represented in absorption (solid) or first derivative (dotted) mode; and, (b) LHS: classic dipolar interaction between electron and nuclear magnetic moments, and RHS: high-field approximation (i.e. Zeeman splitting much larger than degeneracy) for observed transitions in an Mn^{2+} species (assumes positive hyperfine constant and hyperfine term is larger than Zeeman splitting).[11,12]

The interaction between the local magnetic moment created by the electron and the nuclei gives rise to hyperfine splitting and provides a wealth of information about the identity and number of atoms that make up a molecule or complex.[11] The nucleus creates a magnetic field at the electron, B_I, and this field either opposes or augments the laboratory magnetic field. This means

that, for an electron interacting with a hydrogen atom (spin nucleus, I = ½), two signals that are each B_I away from the original signal will be observable. If there are other nuclei nearby, these nuclear spins also contribute to this hyperfine splitting, resulting in the general rule that the number of hyperfine lines is equal to 2nI + 1 where n is the number of symmetry equivalent nuclei and I is the nuclear spin. Nuclei with high nuclear spins, such as transition metal centres, therefore reveal hyperfine interactions.

Most transition metal ions have S > ½ – these are called high-spin systems (not to be confused with high- / low-spin systems in coordination chemistry). In addition to the Zeeman splitting, zero field splitting – degeneracy – must be considered.[13] The nuclear spin in TM nuclei is greater than ½ (e.g. I = 1, 3/2, or 5/2). In commonly used microwave frequencies, the energy of the hyperfine interaction is much smaller than the energy of the electron Zeeman interaction – this is known as the high field approximation.[12] The EPR transitions are therefore characterised by similar energy gaps and the probabilities are similar, leading to equal intensity hyperfine lines (Figure 2.8 (b)). Integer spin species, such as Ni^{2+} (d^8, S = 4), are difficult to detect and require dual mode resonators where magnetic fields can be orientated in orthogonal directions.

EPR is generally carried out two modes: (1) Continuous wave (CW) or (2) Pulse. CW EPR is usually the entry point in any EPR study.[14] The experiments carried out in this work were performed using CW EPR measurements whereby a sample (in a synthetically synthesised quartz tube) is continuously irradiated with low-intensity, monochromatic, standing, microwave radiation inside the microwave cavity while a varied strength magnetic field is scanned. Additionally, the samples were all in solution phase – as with other techniques ensuring that magnetic interactions are averaged and that only isotropic components are measured.[14] A comprehensive, and extremely helpful, tutorial review on the principles and applications of EPR spectroscopy can be found at the following reference.[14]

As described, usually a sample is fixed in the microwave cavity in the resonator however in this work, an unconventional operando setup was developed using a capillary tube that permits a continuous flow of paramagnetic sample species (described in further detail in Chapter 6). A Bruker EMX equipped with an ER4122SHQE resonator was used and operated by Dr. Alberto Collauto in the Chemistry department at Imperial College London. Raw data post-processing was also carried out by Dr. Collauto.

2.1.10 Inductively coupled plasma mass spectrometry (ICP-MS)

Inductively coupled mass spectrometry (ICP-MS) is an elemental analysis technique used to quantify the concentration of solution phase metal ions – this sensitive technique is able to measure not only low concentrations on the parts per million (ppm) scale, but also ultra-low concentrations on the parts per billion (ppb) scale. Samples are transferred to the (nebuliser within the) ICP-MS device where it is mixed with argon to make an aerosol. From there, the sample containing aerosol comes into contact with the high temperature inductively coupled plasma where it is dried, atomised and ionised. Essentially, the solvent and unwanted ions are then filtered using a sophisticated combination of helium gas, an octupole and a hyperbolic quadrupole where they are separated by their mass to charge ratio resulting in a mass spectrum.

Results are collected in two steps: first, a calibration curve is produced by carrying out careful volumetric measurements and creating a variety of 'standards' (200 ppb to using commercially purchased ICP standards (c.a. 1 ppm in concentration). Second, samples are prepared. Proper sample preparation is essential as, especially when ultra-low concentrations are being measured, drastically misleading results can be produced. For instance, when measuring the concentration of iridium-based samples, oxidised Ir^{4+} – IrO_2 – is often present (as a side-product) which is very insoluble. Samples measured in this work were powder based and prepared by leaching all the metal content using aqua regia. Aqua regia provides a harshly acidic and oxidising environment to dissolve all the metal. This is followed by filtration (to remove any solids) and dilution steps typically ending with c.a. 7 – 10 mL of a dilute single or multi-metal matrix.

As an analytical tool, ICP-MS has many advantages compared to related techniques (such as ICP-OES or AAS), including its ability to measure isotope compositions of elements however in this work it was only used to measure concentrations of metals in powder materials. ICP-MS measurements were carried out using an Agilent ICP-MS 7900 spectrometer based in the Chemical Engineering department at Imperial College London.

2.1.11 Nitrogen physisorption – Brunauer–Emmett–Teller (BET)

Nitrogen physisorption using the Brunauer–Emmett–Teller (BET) model is a non-destructive method carried out by measuring the amount of nitrogen absorbed onto the material surface as a function of the imposed pressure, under isothermal conditions. Nitrogen physisorption is used to determine the specific surface area (SSA) and porosity of the catalyst materials. This is often

in order to calculate the surface specific activity of a catalyst. This analyser can measure a wide range of specific surface areas (e.g. 0.01 to greater than 1000 m^2 g^{-1}) higher surface areas can be measured by controlling the amount of sample material. The porous carbon materials measured in this work had surface areas of below 1000 m^2 g^{-1}.[15,16]

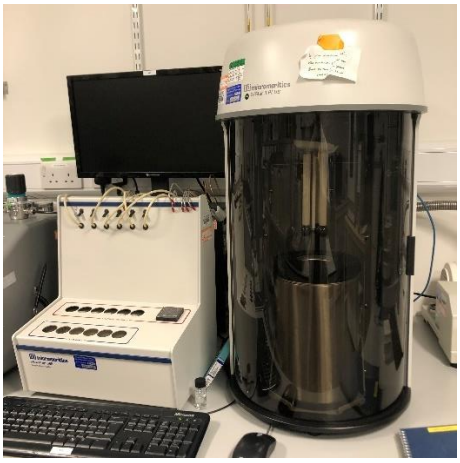


Figure 2.9: Photograph of a TriStar II Plus nitrogen physisorption analyser, Micromimeritics.

Samples can come in different forms, catalyst powders are were the only sample types tested in this work. Catalysts were transferred to BET tubes and dried under a stream of nitrogen at 130 °C overnight before nitrogen physisorption analysis. BET analysis was carried out using a TriStar II Plus Analyser (Micromeritics) (Figure 2.9).

2.1.12 Thermal treatments and activation methods

Carbon-based materials were activated by either thermal or plasma treatment using a furnace or plasma chamber, respectively (Figure 2.10). Thermal treatments are typically carried out under controlled atmospheres – for inert conditions nitrogen and argon are typically used, and for activating conditions, oxygen, ammonia (NH_3) or 5 % H_2 in N_2 are commonly used. Thermal treatments are either used in synthesis steps or in order to activate carbon-based electrodes. Both box and tube furnaces are commonly used and high temperatures of up to 1300 °C are possible (depending on the furnace type) with varied ramp rates (1 – 10 °C min^{-1}). Samples subjected to thermal treatments are typically placed in an alumina holder (e.g. boat) inside a quartz tube. Plasma chambers are typically used to 'clean' non-conductive impurities from the surface of carbon electrodes and, depending on the programme used, functionalise the surface increasing the concentration of surface active sites. Samples subjected to plasma treatment are placed directly adjacent to the plasma-producing source, atop a glass slide.



Figure 2.10: Photograph of the tube furnace and plasma chamber used.

In this work, thermal treatments were largely used during synthesis steps and were carried out using a Carbolite tube furnace (MTF 12/38/400). Plasma treatments were carried out on carbon electrodes (immediately prior to assembling a RFB cell) using a plasma chamber (NANO plasma polymerisation system, Diener Electronic GmbH).

2.2 Electrochemical methods

All electrochemical techniques were carried out on either, an AUTOLAB Potentiostat controlled using 'Nova' software, Potentiostats from Gamry Instruments (600 or 3000) or a Scribner Associates 857 Redox Flow Cell Test System. A good summary of methods by which to test and diagnose electrochemical devices is provided by Gandomi et al.[17]

2.2.1 Theory – kinetics and electrokinetics

For an elementary chemical reaction to occur, an activation barrier needs to be overcome.

$$\mathrm{A} \underset{k_\mathrm{b}}{\overset{k_\mathrm{f}}{\rightleftharpoons}} \mathrm{B} \qquad (2.7)$$

Where A and B are the reactants and products, respectively. The rates, k_f and k_b are the rates for the forward and backward reactions. These rates are correlated with that activation barrier and can be described by the Arrhenius equation:

$$k = A\exp^{-\Delta G^{\ddagger}/RT} \tag{2.8}$$

Where A is a pre-exponential factor that accounts for the statistical probability of collisions leading to reactions, $\Delta G^{\ddagger}$ is the Gibbs free energy of activation needed to reach the transition state (kg m^2 s^{-2} mol^{-1}), R is the ideal gas constant (kg m^2 s^{-2} K^{-1} mol^{-1}), T is the temperature (K). When k_f and k_b are equal, the reaction is said to be in equilibrium and $k = k_0$.

Similarly, an electrochemical reaction can be defined generally as:

$$\mathrm{O} + n\mathrm{e}^- \underset{k_b}{\overset{k_f}{\rightleftharpoons}} \mathrm{R} \tag{2.9}$$

Were O and R are the oxidised and reduced species and n is the number of electrons needed for the reduction. At equilibrium, the reaction will have a reversible potential, E (V), according to the Nernst equation:

$$E = E^0 + \frac{RT}{nF}\ln\left(\frac{c_{\mathrm{Ox}}}{c_{\mathrm{Red}}}\right) \tag{2.10}$$

Where E^0 and F represent the standard reduction potential (V) and Faraday's constant (A s mol^{-1}), respectively. c_{Ox} and c_{Red} are the concentrations of the oxidised and reduced species (mol m^{-3}) (both assumed to have an activity of one).

The rates, k, of the electrochemical processes occurring in this work are of significant interest. Considering the heterogeneous electron transfers – i.e. electron transfers between a solid state electrode and another chemical species – many other processes such as solvent rearrangement and diffusion away from the electrode must occur. While the Gibbs energy ($\Delta_r G$) between the reduced and oxidised species (Equation (2.9)) is related to the electrochemical potential $\Delta G = -nFE$, there is an initial increase in energy, $\Delta G^{\ddagger}$, to reach a transition state. The reaction

rate constant can be defined by the Eyring-Polanyi equation (Equation (2.11)) (the derivation of which can be found in the following references) where k_B is the Boltzmann constant, κ refers to the transmission coefficient (i.e. the rate at which the transition state converts to the reduced species), h is Planck's constant (and B_c has units of s^{-1}):[18]

$$k = B_c e^{(-\Delta G^{\ddagger}/k_B T)} \text{ where, } B_c = \left(\kappa k_B T / h\right) \quad (2.11)$$

Since this electrode reaction is microscopically reversible in the forward ($k_f = k_c$ where 'c' indicates 'cathodic') and backward ($k_b = k_a$ where 'a' indicates 'anodic') direction with activation barriers of, $\Delta_{Red}G^{\ddagger}$ and $\Delta_{Ox}G^{\ddagger}$, respectively the following anodic and cathodic reaction rates are true.

$$k_c = B_c e^{(-\Delta_{Red} G^{\ddagger}/RT)} \quad (2.12)$$

$$k_a = B_a e^{(-\Delta_{Ox} G^{\ddagger}/RT)} \quad (2.13)$$

When a system is perturbed from its reversible potential (E^{rev}) by a potential, the deviation in system potential (E) can be described as the overpotential ($\eta = E - E^{rev}$). This change in overpotential affects the activation energies ($\Delta_{Red}G^{\ddagger}$ and $\Delta_{Ox}G^{\ddagger}$) which are increased and decreased in magnitude with respect to the overall energy of activation $\Delta^{\ddagger}G°$ by a fraction (α) of the change in driving force for the reaction (Equations (2.14) and (2.15)):

$$\Delta_{Red} G^{\ddagger} = \Delta^{\ddagger} G_c^{\circ} + \alpha n F \eta \quad (2.14)$$

$$\Delta_{Ox} G^{\ddagger} = \Delta^{\ddagger} G_a^{\circ} - (1 - \alpha) n F \eta \quad (2.15)$$

The transfer coefficient, sometimes referred to as the symmetry factor (for single elementary step reaction), relates either to the symmetry of the shape of the potential wells that describe the oxidised and reduced form or to how far a species has to cross the double layer to reach the transition state energy.[18] Combining Equations (2.12) – (2.15) reveals:

$$k_c = B_c \exp\left[-\frac{\Delta^{\ddagger} G_c^{\circ} + \alpha n F \eta}{RT}\right] \quad (2.16)$$

$$k_a = B_a \exp\left[-\frac{\Delta^{\ddagger} G_a^{\circ} - (1 - \alpha) n F \eta}{RT}\right] \quad (2.17)$$

These standard cathodic and anodic rate constants are now shown to be exponentially dependant on the change in electrode potential and therefore the net observed current density (j) is also dependant on the applied overpotential.[18] Combining the current densities in each direction (to and from the electrode) and replacing k_a and k_c yields the Butler-Volmer formulation (Equation (2.19)).[18]

$$j = j_a - j_c = nFk_a[\mathrm{R}] - nFk_c[\mathrm{O}] \quad (2.18)$$

$$j = nF[\mathrm{R}]B_a e^{(-\Delta_{Ox}G^{\ddagger}/RT)} - nF[\mathrm{O}]B_c e^{(-\Delta_{Red}G^{\ddagger}/RT)} \quad (2.19)$$

$$j = j_0\left(\exp\left[\frac{(1-\alpha)nF\eta}{RT}\right] - \exp\left[-\frac{\alpha nF\eta}{RT}\right]\right) \quad (2.20)$$

Various steps substituting Equations (2.16) and (2.17) and a taking the overpotential to equal zero in a limiting case reveals the Butler-Volmer equation (Equation (2.20)). Plotting of the natural logarithm of the absolute magnitude of the current density $|j|$ (on the y-axis), against the overpotential, η, (on the x-axis) is called a Tafel plot.

$$\eta = a + bln(j_0) \quad (2.21)$$

The Tafel approximation is assumed in the case where $|\eta| >> RT/F$ (26 mV at 298 K). In this region, the natural log of the current density has a linear relationship with the overpotential (Equation (2.21)). The gradients, b, of the linear regions either side of E^{rev} (the cathodic or anodic processes) relate to the symmetry of the process or, in other words, the degree to which the transition state is similar to the reactant or product. The intersection of extrapolations from these linear regions with the y axis (where $\eta = 0$) are the exchange current densities for that process.

In an full electrochemical device the overpotential, η, is made up of three components that contribute to different degrees, as a function of the applied current. These are outlined below – Equation (2.22):

$$\eta = \eta_{\mathrm{ohmic}} + \eta_{\mathrm{kinetic}} + \eta_{\mathrm{mass-transport}} \quad (2.22)$$

The overpotential is the sum of all the contributions from the sources of resistance losses (Equation (2.22)). The resistive ohmic contribution to the overpotential, sometimes referred to as the iR drop, is (usually) attributed in large part to the membrane, but bulk electrolyte and

electrode resistances also contribute. Minimising η_{ohmic} can be achieved by improving design or material aspects of the cell. The mass-transport resistance is the resistance associated with the active species concentration difference between the bulk and the surface as a result of the transport phenomena in the system. These phenomena include both diffusive and convective types of transport. Convective transport includes transport of active species through the electrode as whole – i.e. pore to pore (inter-pore). Diffusive transport includes transport of active species from the bulk electrolyte to the surface of the electrode / active site – i.e. from bulk electrolyte within pore to pore surface (intra-pore). Mass transport resistance is defined as follows where j_{lim} is the limiting current density:

$$\eta_{mass-transport} = \frac{RT}{nF} \ln\left(\frac{j_{lim} - j}{j_{lim}}\right) \qquad (2.23)$$

Finally, the kinetic resistance (sometimes referred to charge-transfer, CT, or activation loss) represents the energy required to overcome the activation barrier for electron transfer in an electrochemical reaction. This overpotential, again is a function of the current and is described by the Butler – Volmer equation that was discussed previously (Equation (2.20)). Where j is the current density, j_0 is the exchange current density (A m^{-2}), η_{CT} is the charge transfer overpotential and α_c and α_a are the transfer coefficients for the anodic and cathodic processes.

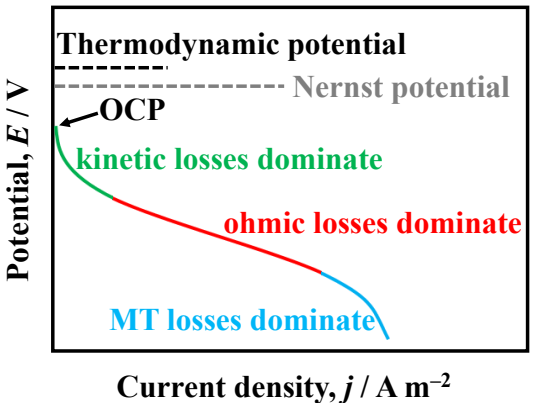


Figure 2.11: Generalised polarisation curve overlayed with sources of overpotential.[17]

Each of the resistive overpotentials mentioned here contribute to the system potential at various current densities. Figure 2.11 shows a generalised galvanostatic (fixed current) polarisation curve. Each part of the curve represents a current density at which that overpotential dominates.

2.2.2 Voltammetry – cyclic / linear sweep (CV / LSV)

Cyclic voltammetry (CV) is used to evaluate the current (A) response to a linear voltage sweep (V) at a certain scan rate, ν (V/s) (Figure 2.12). In a three electrode cell, the current is recorded at the working electrode with respect to a reference, and in a full system the current is measured with respect to the other electrode. In a three electrode cell, a counter electrode is also used to provide an equal and opposite current to the working electrode, maintaining system balance.

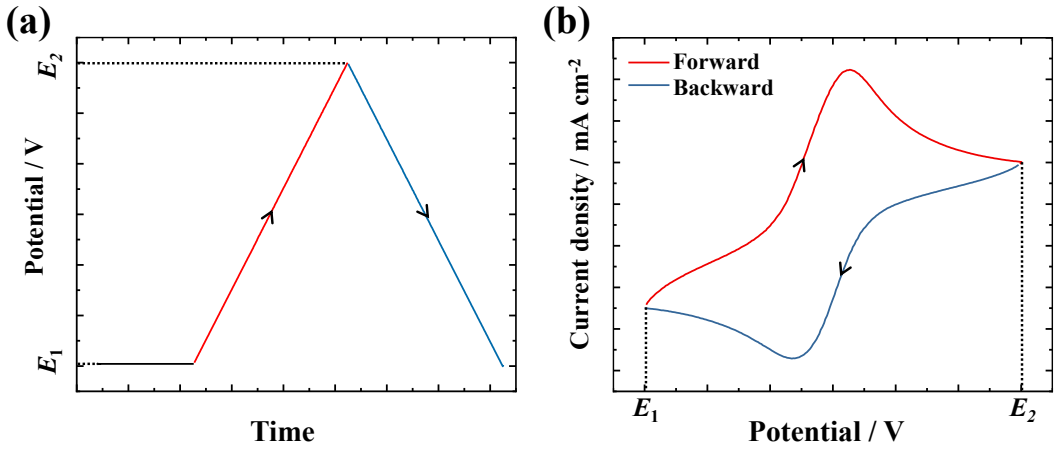


Figure 2.12: (a) Cyclic potential sweep and (b) resulting cycling votammogram.

Cyclic voltammetry is a popular, typically ex-situ electrochemical technique used for initial studies of new systems and redox couples. Researchers use CVs to establish the potential limits for the experiments they want to carry out. The shape of the forward scan of the CV can be explained as follows: as the potential increases, the surface concentration of the oxidised species is depleted, inducing an increased flux of oxidant to the surface of the electrode, this increased flux increases the current. As the potential continues to increase the amount of oxidant will deplete resulting in the reduction of current at the working electrode.[19] This is then mirrored for the backward scan. Linear sweep voltammetry (LSV) is the same as half a CV – i.e. just one of the red / blue (forward / backward) lines in Figure 2.12 (b) is carried out.

In this work, voltammetry experiments were carried out solely in three electrode cells. CVs were carried out during cleaning steps and LSVs were (largely) carried out when assessing ORR capability. Hydrodynamic conditions as outlined in the RDE / RRDE section (Section 2.2.5) were used. This method of operation induces augmented mass transport conditions and allows kinetic information to be gathered. Methods to enhance the mass transport further have been developed and have enabled researchers to assess catalyst capability more closely.[20]

2.2.3 Electrochemical impedance spectroscopy (EIS)

Electrical resistance is well understood as the ability of a circuit element to resist a current flow. This is defined by Ohm's law, where the resistance is defined by the ratio of voltage to current – however, this only applies to idealised resistors. In reality, circuit elements do not act ideally. Electrochemical impedance spectroscopy (EIS) can be described as the complex resistance encountered when current flows through any resistor, capacitor and inductor.

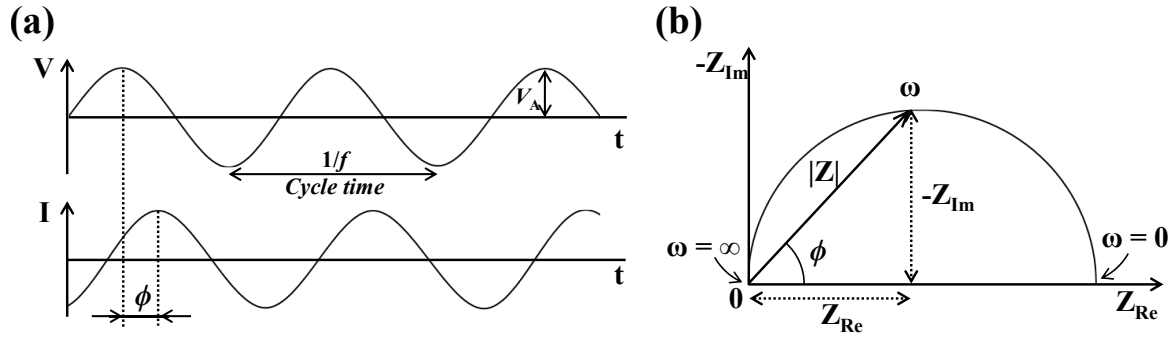


Figure 2.13: (a) Incident AC voltage and current response; and, (b) a simple Nyquist plot.[21]

EIS is usually measured by subjecting an electrochemical circuit with a low-amplitude AC voltage signal, VA, at frequency, f (s^{-1}) yielding a current response (Figure 2.13 (a)). Equation (2.24) displays voltage signal as a function of time, V(t) and the subsequent time dependant current response with a shifted phase (Equation (2.25)). This shift in phase, ϕ, is determined by the ratio of capacitive and resistive components.

$$V(t) = V_{\mathrm{A}} \sin(2\pi f t) = V_{\mathrm{A}} \sin(\omega t) \tag{2.24}$$

$$I(t) = I_{\mathrm{A}} \sin(\omega t + \phi) \tag{2.25}$$

$$R = \frac{V}{I} \tag{2.26}$$

$$Z = \frac{V(t)}{I(t)} = \frac{V_{\mathrm{A}} \sin(\omega t)}{I_{\mathrm{A}} \sin(\omega t + \phi)} = Z_{\mathrm{A}} \frac{\sin(\omega t)}{\sin(\omega t + \phi)} \tag{2.27}$$

An expression analogous to Ohm's law (Equation (2.26)) can then be derived for the impedance (Equation (2.27)). Euler's relationship can be used to express the impedance as a complex function resulting in the impedance having complex ('Imaginary', 'Im') and real ('Re') parts. Figure 2.13 (b) shows a Nyquist plot which is a commonly used graph to depict impedance data, where the magnitude of the impedance, |Z|, and its real, Z_{Re}, and imaginary, Z_{Im}, parts are depicted – these relationships are given in the following Equations (2.28) and (2.29). The phase angle, θ, which is sometimes used in other forms of impedance analysis is (such as Bode plots) is also defined (Equation (2.30)).

$$Z = Z_{\mathrm{Re}} + iZ_{\mathrm{Im}} \tag{2.28}$$

$$|Z| = \sqrt{Z_{\mathrm{Re}}^2 + Z_{\mathrm{Im}}^2} \tag{2.29}$$

$$\theta = \arctan\left(\frac{Z_{\mathrm{Im}}}{Z_{\mathrm{Re}}}\right) \tag{2.30}$$

Practically, real impedance responses are non-ideal and are collected at a variety of frequencies, f (Hz) (and therefore radial frequencies, ω) ranging from 10 mHz to 100 kHz. From an interpretation perspective, Figure 2.14 shows how, qualitatively, the resistive contributions (also referred to in Section 2.2.1) can be evaluated: the x-intercept represents the ohmic contribution to overpotential (sometimes referred to as high frequency resistance, HFR), η_{ohmic}, the smaller purple semi-circle represents the charge transfer / kinetic overpotential, η_{CT} and the larger green semi-circle is the overpotential contribution as a result of mass transport, η_{MT}.

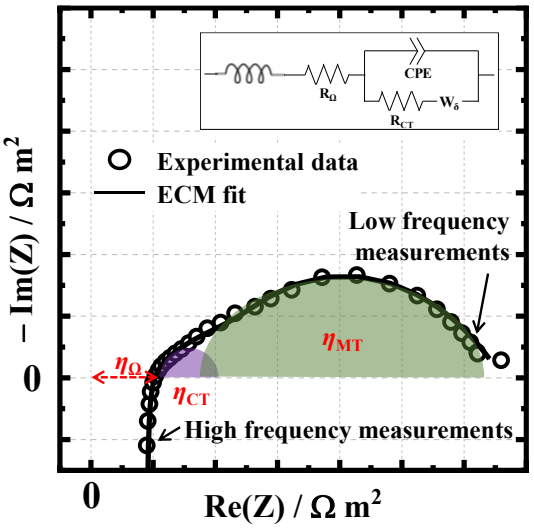


Figure 2.14: Representative Nyquist plot with regions of interest qualitatively highlighted and an inserted equivalent circuit model. This Nyquist plot was collected with a zero-gap symmetric RFB cell utilising a porous carbon cloth electrode with a quasi-reversible active species (TEMPO•/TEMPO⁺) dissolved in a MeCN-based electrolyte.

These Nyquist plots can be evaluated quantitatively using equivalent circuit models (ECMs) and fitted (insert, Figure 2.14). However, impedance data analysed using equivalent circuit elements induces ambiguity. When evaluating impedance data using ECMs, researchers should ensure that knowledge of physical processes taking place in the system is always at the forefront of model design so as to use the simplest possible ECM with the fewest equivalent circuit elements. The ECM used in this work is discussed in the relevant chapter, but in-depth comparison and evaluation of ECMs is beyond the scope of this work.

2.2.4 Assembly of electrochemical devices

2.2.4.1 Three electrode cell

Measurements, especially when measuring PGM-containing catalysts, must be carried out in extremely clean environments. The use of glass electrochemical cells is favourable for acidic and neutral systems (as during cell setup and operation the user can see what's going on in the cell). However, for alkaline systems, polytetrafluoroethylene (PTFE) (or some other non-silica containing polymer) must be used to avoid contamination by from the corrosion / leaching of silica into the alkaline electrolyte. Further, alkaline electrolytes should not come in contact with any glass material during electrolyte preparation.

Having chosen the electrochemical cell material and therefore the electrolyte, the (WE) can be prepared – in this case, three electrode cells were solely RDE measurements and therefore a glassy carbon (GC) electrode was used. The GC electrode is polished using polishing paper with incrementally smaller grains (5 μm, 1 μm) ending with a polycrystalline alumina (Al_2O_3) slurry (0.05 μm). This is followed by extensive rinsing in DI water and sonication in a DI water bath. The reference electrode (RE) is chosen according to the system in which the tests are being carried out. The REs used in this work are the RHE, the standard calomel electrode (SCE) and a mercury – mercury oxide electrode (Hg/HgO). In acidic media, the RHE is commonly used and Hg/HgO is commonly used in alkaline media. The counter electrode is also subject to change depending on the media in which the tests are carried out – in this work, Pt mesh was used in acid electrolyte and a graphitic carbon electrode was used at all other pHs.

The PTFE electrochemical cell and the various accessories (PTFE Luggin and counter holder) was machined and prepared in-house (by Lee Tooley, Imperial College London). Both the SCE and the Hg/HgO REs were purchased from Pine Instruments.

2.2.4.2 Redox flow batteries

Both RFBs and hRFBs were tested in this work. RFBs were tested in a symmetric configuration and the hRFBs tested in this work utilised hydrogen on the gas side. Liquid-side electrodes required plasma activation before inserting into the cell. The gasket materials were either Viton or Tygaflor® and the latter was cut in a laser cutter. Both AEMs (IONOMR) and PEMs (Nafion) were used and, following cutting using a ceramic knife, were subjected to activation from dry form. Preparation steps for the AEM were simply to remove backing layers, immerse in 6M KOH overnight and exchange wash-electrolyte once before inserting in the cell (depending on

the system / catalysts used, there was also a DI water wash just before inserting in the cell). Preparation of a Nafion membrane is as follows: (1) The backing layer to the membrane is then pulled away and the membrane is carefully immersed in a 5 wt% solution of hydrogen peroxide to clean the surface (2) The solution containing the membranes are then placed into an appropriate ventilated oven at 80 degrees for one hour (3) following this, the peroxide is disposed of in appropriate waste, membranes rinsed with DI water and immersed in DI water and placed in the oven for a further hour (4) this process this then repeated with H_2SO_4 and (5) DI again followed by storing the membranes DI water in a sealed jar ready of cell assembly.

Once all the preparatory steps are complete, the cell components are assembled one-by-one using Teflon guiding pins to make sure pieces to not move on final tightening. The cell framework was either provided by Scribner Associates or developed in house (by the Brushett group, MIT). First, the POCO graphite plate is secured by the inlet / outlet tubes as it is placed on top of the backing plate and gold-plated current collector. Gasket materials are fixed into position using guiding pins inserted on the edge of the face of the flow plate. A freshly activated / treated electrode is then inserted into the central gasket gap ensuring unincumbered contact with the POCO graphite end plate. The membrane is then placed on top covering the electrode fully. Then, the same process again – gaskets fixed, electrode placed in the centre and the second POCO plate ensuring there is no room for the electrode-membrane assembly to shift around. Finally, the second backing plate (along with the tightening screws) are placed atop the POCO plate ensuring secure flow of (liquid or gaseous) electrolyte, and screws incrementally and evenly tightened using a torque wrench with a final force of 4.0 N m. This process is clearly shown in a video on the Scribner website.[22]

Other than the use of a different electrode on the gas side in a hybrid system (commercially purchased GDL – 0.4 mg_{Pt} cm^{-2}, Fuel Cell Store, USA). The cell assembly is identical to 'normal' RFB assembly. The only remaining difference is the handling of external (liquid or gas) electrolyte. For liquid electrolytes, the liquid is continuously stirred using a magnetic stirrer bar. Electrolyte is pumped through chemically (and mechanically) resistant tubing (Versilon, formerly Tygon Chemical) from the external 'tank' (jar) through the system using a peristaltic pump (Masterflex L/S). A standard pumping rate of 50 mL min^{-1} was used. For gas electrolytes, a cylinder or electrolyser is used to supply the relevant gas to the system. Gas is flowed through Nylon tubing and flow rates are controlled by a mass-flow controller ('FlowView', Bronkhorst UK Ltd.). The mass-flow controller was set to supply 100 mL min^{-1}

H_2, continuously, during cell operation. The outlet of the cell was connected to a Nederman extraction arm. And, at times of idling, when no experiment was being carried out, N_2 was flowed over the Pt GDL.

2.2.5 Rotating (ring) disk electrode (RDE and RRDE)

2.2.5.1 Theory

RDE and RRDE are commonly used tools in the screening and evaluation of performance of electrocatalysts. Kinetic parameters such as rate constant and electron transfer number can be elucidated using this technique. RDE is used in a conventional three electrode setup with a central (usually) glassy carbon disk embedded in a non-conductive (e.g. PTFE) holder. The only difference for RRDE is the addition of a ring (gold or platinum) around the central WE disk that is usually held at a certain potential (therefore, RRDE is technically a four-electrode setup).

During RDE and RRDE experiments, a Luggin-Haber capillary is positioned close to the WE to minimise the uncompensated solution resistance – but not so close as to disturb the movement of active species (typically, this distance must be smaller than the diameter of the Luggin capillary). Depending on the electrochemical process, the desired gas is purged into solution for 30 minutes before the experiment takes place (i.e. when testing, for instance, ORR performance O_2 will be bubbled to return a current response). Once the catalyst is deposited onto the surface of the electrode the RDE / RRDE tip is immersed into to the solvent environment of a specific pH. In this work, during synthesis, tests were carried out in an alkaline environment (0.1 M KOH, pH 13) and later tested in a range of pH environments.

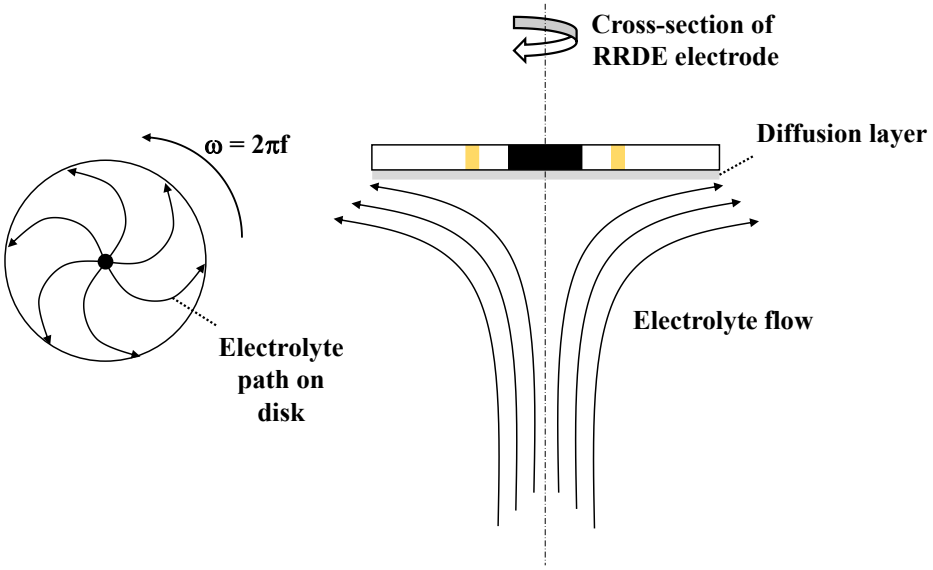


Figure 2.15: Idealised direction of flow of electrolyte when using a rotating (ring) disk electrode.

One of the drawbacks in using a stagnant electrolyte is the fact that the dominant mechanism of mass transport is diffusion, this fact prevents kinetic data being recovered. RDE is a hydrodynamic technique where, as illustrated in Figure 2.15, the RDE acts as a pump, pulling the solution vertically upwards towards the disk and then throwing it outwards. This is a way of enhancing the convective mass transport contribution (forced convection). The thickness of the diffusion layer depends on rotation speed and therefore the current is controlled by convection leading to a maximum (limiting) current (i_{lim}). Following full convective-diffusive analysis at steady state, the Levich Equation (2.31) and the Koutecký-Levich Equation (2.32) allow experimentalists to extract transport and kinetic parameters such as diffusion coefficient, viscosity and kinetic current. The difference between these equations lies simply in defining the boundary condition – the Koutecký-Levich is used when assuming a simple first order reaction or a multistep reaction in which the slow step remains the same.[19,23]

$$i_{LC} = 0.620n\text{F}AD_{\text{R}}^{2/3}\nu^{-1/6}C_{\text{R}}\omega^{1/2} \qquad (2.31)$$

Where n is the number of electrons involved in the electrochemical process, F is Faraday's constant (C mol^{-1}), A is the electrode area (m^2), D is the diffusion coefficient (m^2 s^{-1}), n is the kinematic viscosity of the solution (m^2 s^{-1}), C_R is the concentration of bulk reactant form (mol m^{-3}) and, finally, ω is the angular rotation rate (rad s^{-1}). The Levich equation applies to a totally mass-transfer-limited system.[19]

$$\frac{1}{i} = \frac{1}{i_k} + \frac{1}{i_{LC}} = \frac{1}{i_k} + \frac{1}{0.620nFAD_{\mathrm{R}}^{2/3}\nu^{-1/6}C_{\mathrm{R}}} \qquad (2.32)$$

Using the Koutecký-Levich equation additional parameters such as i_k can be deduced. i_k represents the current in the absence of an mass-transfer effects.[19]

The catalysts tested in this work were tested in a PTFE cell as glass (usually used to analyse acidic systems) is an inappropriate material that can etch / dissolve and interfere with the electrochemical processes when testing in alkaline conditions. RDE and RRDE disks used in this work had a 5 mm diameter and were purchased from PINE instruments.

2.2.5.2 Application (performance parameters)

In light of the benchmarking issues outlined by Wei et al.,[24] it is worth mentioning the performance parameters associated with the polarisation curves generated from RDE tests. Voltammetry and chrono-methods are outlined later (*vide infra*). The main performance parameters associated with the ORR are typically the halfwave potentials ($E_{1/2}$ / V), the onset potential (E_{onset} / V) and the Tafel slope (mV dec^{-1}) (Figure 2.16). The RDE technique is limited by mass transport and therefore has a limiting current density (j_{lim}). The $E_{1/2}$ is the potential at which half the limiting current density is reached. Background corrections are essential for proper extraction of kinetic parameters. For the ORR, a background correction is performed by collecting a cyclic or linear sweep voltammogram from a solution that has been purged with inert gas such as argon, Ar, or nitrogen, N_2, and subtracting its response from an identical voltammogram (same scan rate, mV s^{-1}) collected in a fully oxygenated solution. For the OER, the background is corrected by taking the average of the iR-corrected forward and backward CV. The E_{onset} should be measured following a suitable background correction. The way this is collected varies across the field – some report potentials at which a certain current density (such as 0.5 mA cm^{-2}) has been reached and others report current densities at certain overpotentials (such as, for OER, 1.55 V vs RHE). The final commonly reported parameter for the OER reaction, is the potential at which a current density of 10 mA cm^{-2} is reached, E_{10}. For bifunctional oxygen catalysts, ΔE is also reported which is the potential difference between the E_{10} and $E_{1/2}$ (Figure 2.16 (a)). The common goal for researchers working on bifunctional oxygen catalysts is to minimise ΔE.

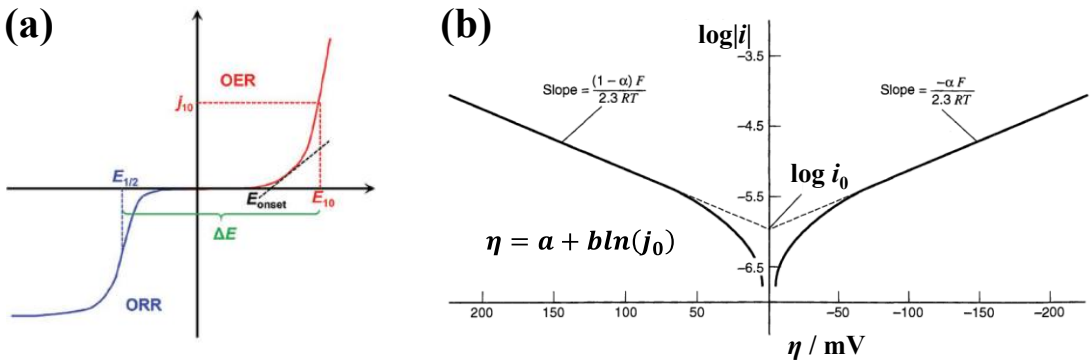


Figure 2.16: Summary of ORR / OER metrics. (a) Representative RDE polarisation curves for the ORR (blue) and OER (red); and, (b) a Tafel plot with Equation (2.21) inserted.[19,25]

It should be mentioned, however, that these metrics do not account for the catalyst loading ($mg_{cat}\ cm^{-2}$) and it is therefore possible to achieve unrepresentative / misleadingly high performances by simply increasing the amount of catalyst on the RDE tip – hence the result is only weakly or moderately dependant on the intrinsic activity of the catalyst. Alternative techniques to RDE for examining electrocatalyst performance have been developed (such as the floating electrode which tests catalysts at low loading under high mass transport conditions). Performance data should be properly scrutinised before being taken as wrote. These shortcoming are discussed in further detail in Chapter 4 and an alternative 'Bifunctionality' score is proposed for the catalysts synthesised.

Tafel plots are useful for collecting kinetic parameters – the Tafel equation (Equation (2.21)) has been inserted in Figure 2.16 (b) – both linear segments of the anodic and cathodic branches can be extrapolated to find the exchange current (i_0) (or exchange current density, j_0).[19] Finally, when using rotating rind disk electrode (RRDE) for the ORR, the electron transfer number and peroxide percentage offer insight into the extent to which the mechanism is two- or four-electron.

2.2.6 Chrono- and polarisation methods

Chrono- and polarisation methods were carried out using both RDE and an RFB systems.

2.2.6.1 Theory

Chronoamperometry and chronopotentiometry are methods that control the potential and the current, respectively. The resulting current and potential responses, respectively, are measured as a function of time. In this work, chronopotentiometry is commonly used in the hRFB cycling

studies carried out with full systems. This method demands a current from the system and measures the potential as that set current is drawn. In a RDE setup, chrono-methods are commonly used to assess the durability of an electrocatalyst, where an initial (for instance, during chronoamperometry) current is tracked over time and diminishes in magnitude. Whereas, depending on the volume of electrolyte used, chrono-methods in a RFB cell setup characterise either the durability or capacity of a system.

Polarisation is a powerful tool used by researchers to understand the relationship between cell voltage and charge / discharge currents. Polarisation curves were introduced in Section 2.2.1 and can be carried out to test the capability of a given catalyst. In this work, potentiostatic polarisation tests are carried out in two different modes. One mode is used in a three electrode cell in preparatory catalyst surface cleaning step – at high scan rate, the catalyst is polarised across the window in which it will be tested (essentially a fast CV) (ensuring surface cleaning and wetting the catalyst surface). The other mode of polarisation was used when evaluating RFB or hRFB performance. When testing the RFB, the volume of electrolyte was small (roughly 10 mL for each side of the cell) and the state of charge (SOC) needed to remain constant, therefore a positive current was held for 10 s followed by a negative current for the same time period – these currents increased in magnitude until the potential 'cut-off' was reached. When testing the hRFB, a larger volume of electrolyte (400 mL) (assumed no variation in SOC during experiment) was used and a similar method however without the intermediate negative current 'holds'.

The capacity of a RFB refers to the amount of energy available and is measured in amp hours (Ah). For RFBs, this depends on the volume and concentration of active species. The capacity passed for a galvanostatic process can be calculated using Equation (2.33) where Q(t) is the capacity passed at a given time, I(t) is the current for the given time period and t_{max} is the time period duration:

$$Q(t) = \int_0^{t_{\max}} I(t)\, dt \qquad (2.33)$$

2.2.6.2 Application (performance parameters)

In a RFB, each charge / discharge cycle is defined by its efficiencies (usually referred in percentages).[26] The coulombic efficiency (CE) can be measured in two ways either via Equation (2.34) or, if cycling is performed galvanostatically, Equation (2.35):

$$\mathrm{CE} = \frac{Q_{\mathrm{dis}}}{Q_{\mathrm{ch}}} \tag{2.34}$$

$$\mathrm{CE} = \frac{I_{\mathrm{const}} t_{\mathrm{dis}}}{I_{\mathrm{const}} t_{\mathrm{ch}}} = \frac{t_{\mathrm{dis}}}{t_{\mathrm{ch}}} \tag{2.35}$$

Where Q_{dis} and Q_{ch} is the discharge and charge capacity of the cell, respectively, I_{const} is the galvanostatic current used and t_{dis} and t_{ch} are the time it takes to fully discharge or charge the cell, respectively. The voltage efficiency (VE) is the ratio of the average discharge cell voltage (V_{dis}) to the average charge cell voltage (V_{ch}) (Equation (2.36)):

$$\mathrm{VE} = \frac{V_{\mathrm{dis}}}{V_{\mathrm{ch}}} \tag{2.36}$$

The energy efficiency (EE) is measured by the product of the CE and the VE (Equation (2.37)):

$$\mathrm{EE} = \mathrm{CE} \times \mathrm{VE} \tag{2.37}$$

2.3 References

1 MyScope, https://myscope.training/, (accessed 29 October 2021).

2 A. Mohammed and A. Abdullah, in *Proceedings of 2018 International Conference on Hydraulics and Pneumatics - HERVEX*, 2018.

3 Surface Segregation - an overview | ScienceDirect Topics, https://www.sciencedirect.com/topics/chemistry/surface-segregation, (accessed 23 November 2021).

4 S. Oswald, *Encycl. Anal. Chem.*, , DOI:10.1002/9780470027318.A2517.PUB2.

5 2020 PREM X-ray Absorption Spectroscopy and EXAFS Workshop | CHESS, https://www.chess.cornell.edu/2020-prem-x-ray-absorption-spectroscopy-and-exafs-workshop, (accessed 4 November 2021).

6 Y. Zhu, T.-R. Kuo, Y.-H. Li, M.-Y. Qi, G. Chen, J. Wang, Y.-J. Xu and H. M. Chen, *Energy Environ. Sci.*, 2021, **14**, 1928–1958.

7 Bruce Ravel XAS course 2011 part1 on Vimeo, https://vimeo.com/340202552, (accessed 19 January 2022).

8 B. Ravel and M. Newville, *urn:issn:0909-0495*, 2005, **12**, 537–541.

9 *General Electric, datos|x reconstruction: CT data optimisation and reconstruction software*, 2019.

10 L. A. Feldkamp, L. C. Davis and J. W. Kress, *J. Opt. Soc. Am. A*, 1984, **1**, 612–619.

11 G. R. Eaton, S. S. Eaton, D. P. Barr and R. T. Weber, *Quantitative EPR*, SpringerWienNewYork, 2010.
12 V. Chechik, E. Carter and D. Murphy, *Electron Paramagnetic Resonance*, OUP, 2016.
13 J. Krzystek, A. Ozarowski, J. Telser and D. C. Crans, *Coord. Chem. Rev.*, 2015, **301**–**302**, 123–133.
14 M. M. Roessler and E. Salvadori, *Chem. Soc. Rev.*, 2018, **47**, 2534–2553.
15 A. Mehmood, B. Ali, M. Gong, M. Gyu Kim, J. Y. Kim, J. H. Bae, A. Kucernak, Y. M. Kang and K. W. Nam, *J. Colloid Interface Sci.*, 2021, **596**, 148–157.
16 H. Zhang, S. Hwang, M. Wang, Z. Feng, S. Karakalos, L. Luo, Z. Qiao, X. Xie, C. Wang, D. Su, Y. Shao and G. Wu, *J. Am. Chem. Soc.*, 2017, **139**, 14143–14149.
17 Y. A. Gandomi, D. S. Aaron, J. R. Houser, M. C. Daugherty, J. T. Clement, A. M. Pezeshki, T. Y. Ertugrul, D. P. Moseley and M. M. Mench, *J. Electrochem. Soc.*, 2018, **165**, A970–A1010.
18 W. R. Browne, *Electrochemistry - Oxford Chemistry Primers*, OUP, 2018.
19 A. J. Bard and L. R. Faulkner, *ELECTROCHEMICAL METHODS: Fundamentals and applications*, 2001.
20 C. M. Zalitis, D. Kramer and A. R. Kucernak, *Phys. Chem. Chem. Phys.*, 2013, **15**, 4329–4340.
21 V. F. Lvovich, *IMPEDANCE SPECTROSCOPY: Applications to Electrochemical and Dielectric Phenomena*, Wiley, 2012.
22 Redox Flow Cell Test Fixture - Scribner Associates, https://www.scribner.com/products/redox-flow-cell-testing/redox-flow-cell-test-fixture/, (accessed 27 January 2022).
23 D. Malko, Imperial College London, 2016.
24 C. Wei, R. R. Rao, J. Peng, B. Huang, I. E. L. Stephens, M. Risch, Z. J. Xu and Y. Shao-Horn, *Adv. Mater.*, 2019, **31**, 1806296.
25 Z.-F. Huang, J. Wang, Y. Peng, C.-Y. Jung, A. Fisher and X. Wang, *Adv. Energy Mater.*, 2017, **7**, 1700544.
26 S.-H. Shin, S.-H. Yun and S.-H. Moon, *RSC Adv.*, 2013, **3**, 9095.

[CH3 insert]
MAKE SURE TO MAKE THE SECTIONS FOLLOW AFTER ONE ANOTHER PAGE NUMBERS LINE UP

Chapter 3

Investigating the effect of solvent properties and electrode microstructure on the performance of a symmetric organic redox flow battery

This chapter contains material from an article that has been published in Applied Energy, Elsevier.[1] *My work comprised all the experimental results and, as the first author, I retain the right to include the contents in this thesis.*

"If I had more time I would have written you a shorter letter." – Winston Churchill

3.1 Introduction

Improving our understanding of the relationship between microstructure and RFB cell performance is essential to progress the development of electrode architectures. The same is true of the interaction between electrodes and the electrolytes in which the active species are contained. Significant efforts have directed towards both of these improvements. Electrode design optimisation has been heavily informed by in- and ex-situ imaging techniques.[1,2] 3D imaging based on XCT has enabled researchers to gather information about porous electrodes at high resolution.[3,4] The extracted microstructural parameters such as porosity, tortuosity and volume-specific surface area (VSSA) are considered defining features of the electrodes. The porosity describes the volume fraction of void space in the material, the tortuosity is the reduction in diffusive transport caused by an obstruction of flow path in the geometry of heterogeneous media[5] and the VSSA is considered to be the active surface area where electrochemical reactions take place. Measurements of VSSA using experimental in-situ techniques has been shown to vary by two orders of magnitude,[6] indicating that a uniform, benchmark ex-situ technique, such as XCT, might be an appropriate alternative.

Experimentally, EIS and polarisation (both introduced in Chapter 2) provide informative handles on the resistive bottlenecks in the cell and the overall cell performance. EIS has been used to quantify the resistive contributions to the overall overpotential in a cell. Until recently,[1] there has been a lack of differentiation between the impedances associated with the intra- and inter-pore transport (Figure 3.1) – EIS is instrumental in isolating these unique transport effects and analysing the effect of electrode microstructures on RFBs. EIS can use ECMs to identify and quantify rate limiting processes in a cell and confirm fast reaction kinetics associated with redox couples.[7] Polarisation is another essential method for full RFB performance assessment that adjusts the current or the potential and measures the response (at a given SOC).[7] The Brushett group have developed robust symmetric cell geometries to test specific aspects of RFBs whereby, using a carefully selected electrolyte, researchers can isolate / discern between isolated properties of, for instance, electrode microstructure.[8] Used alongside one another, EIS and polarisation methods have provided the backbone of multiple experimental studies investigating the effect of viscosity on active species transport to / from the electrode surface,[9] the effect of flow rates and flow field combinations[10] and the quantification of mass-transfer coefficients.[11]

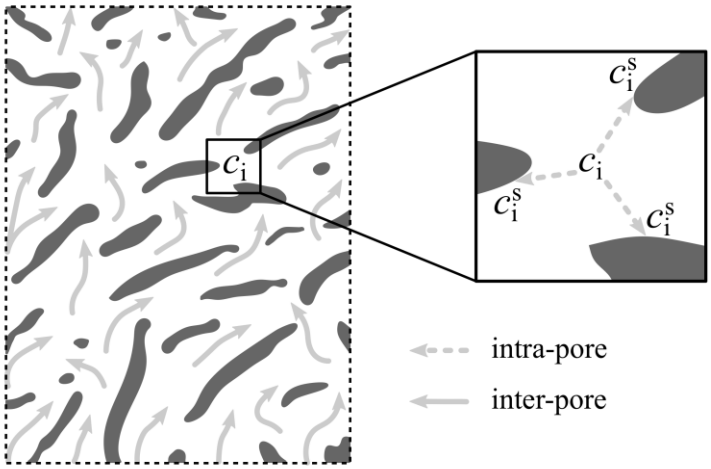


Figure 3.1: A cartoon representation of the terms intra-pore and inter-pore mass transport processes. The left hand cartoon represents a 2D cross section of a porous electrode material. The large arrows indicate inter-pore bulk flow of electrolyte through the porous matrix. The magnified region shows intra-pore transport from the bulk (with active species i, concentration, c_i) to the active electrode surface (where the concentration of the species i is, c_i^s).[1]

Mass-transfer coefficients offer helpful descriptors for the processes occurring at the intra-pore level and are often presented alongside electrolyte characteristics.[12,13] They can be calculated either experimentally, by measuring the limiting current densities in the cell (reached when the concentration of the reactants at the surface of the electrode approaches zero),[6,14] or using computational models.[9] Zero-dimensional models are generally used for monitoring or

controlling processes and, therefore, need to be fast – these models use 'lumped' physical parameters that do not provide enough information for system design. Higher dimension models (1D, 2D or 3D), while increasingly computationally expensive, reveal more distributed information about the spatial variation of field variables and are generally used for system design and optimisation. Conventional continuum models utilise a modified BV kinetics equation to account for the mass-transfer between the bulk and the electrolyte surface. In these models the mass transfer coefficient characterises the steady state movement of species across the boundary layer (Nernst diffusion layer). Milshtein et al. used a Fe^{2+}/Fe^{3+} RFB system to demonstrate the power of a simplified (BV kinetics) continuum model in the non-limiting region utilising only the electrolyte ionic potential.[11] Mass-transfer coefficients have also been determined using dimensionless group correlations including Sherwood and Reynolds or Péclet numbers with varying flow field and electrode type.[9,15] While continuum models serve an important purpose by digesting and solving for a large number of parameters and processes, this means the ability to decipher specific components and contributions to cell performance (e.g. resistance or permeability), is lost. Alternative model types, such as PNMs, can be used to isolate electrode or transport characteristics. Recently, Sadeghi et al. used a PNM to decipher improved electrode structures concluding that electrode permeability was a key performance factor.[16] This specific a conclusion would not be possible using a continuum model.

While these strides towards improved analytical techniques have been important, full understanding of the interactions between electrolytes and the electrodes through which they permeate, is still unclear. Ultimately, though, researchers that synthesise new electrodes and electrolytes are informed by these analytical studies. While not directly linked to porous carbon media, Kench et al. and Gayon Lombardo et al. have used ML to inform the development of computationally optimised SOFC electrode materials based on experimental structure-performance metrics.[17,18] This technique is likely to be extended to fibrous carbon electrodes in the near future (after overcoming the REV conundrum, introduced in Chapter 1, which questions what size or volume of a porous carbon fibre matrix is representative of a full electrode). From a more synthetic angle, following analytical reports of improved performances in RFB systems utilising electrodes with multi-modal pore size distributions,[19] Wan et al. developed an easily adjustable synthesis method for producing these types of electrodes.[20] This demonstrates the importance of collaboration leading to tangible progression in technological outputs. This chapter looks to combine electrochemical, imaging and

modelling analyses to understand the microstructure / performance relationship in order to support the next generation of porous carbon electrodes.

In line with the questions and objectives set out in Chapter 1, this chapter looks to investigate the effect of electrode microstructure and electrolyte character on overall RFB performance. In order to do this, the microstructural properties of the electrodes will be characterised in- and ex-situ and the findings pinned alongside the selected performance metrics. A holistic analysis of cell testing, imaging and modelling results will be collated, and a comprehensive recognition of the unique intra- and inter-pore transport effects on the cell performance will be presented.[1]

In order to achieve this, four commercially available carbon electrode materials were tested using a $TEMPO^{\bullet}/TEMPO^{+}$ redox couple, dissolved in two non-aqueous solvents, propylene carbonate (PC) and MeCN. With fast kinetics, this quasi-reversible redox couple engenders isolated mass transport effects associated with electrode microstructures.[19,21,22] The electrolyte was fully characterised ex-situ. The electrode materials were imaged (using an in-house machined compression rig) while compressed to mimic their form during electrochemical tests, and electrode parameters gathered accordingly using Avizo, MATLAB and TauFactor.[23] Alongside the electrode permeability, calculated using a PNM, these parameters were incorporated into a 1D continuum model to obtain the mass-transfer coefficients. The model describes the potential, concentration and overpotential distributions across the electrode thickness.[1]

3.2 Methodology

The electrochemical experiments in this work were carried out in Prof. Fikile Brushett's laboratory (Chemical Engineering department, MIT, Cambridge, USA). The XCT experiments and post-processing were carried out in the Department of Earth Sciences and Engineering (Imperial College London). Supplementary electrolyte characterisation measurements were performed by Dr Kevin Tenny. PNM and 1D model development were carried out by Dr Andrea Gayon Lombardo and Dr Catalina Pino Muñoz.

3.2.1 Electrolyte preparation

Electrolyte preparation was carried out in an argon filled glove box (MBraun, 4GB 2500, O_2 < 5 ppm, H_2O < 1 ppm). 2,2,6,6-Tetramethyl-1-piperidinyl-oxyl – TEMPO radical ($TEMPO^{\bullet}$, 98 %, Sigma-Aldrich) was used as received. Oxidised TEMPO, 2,2,6,6-Tetramethyl-1-

piperidinyloxy-oxo tetrafluoroborate – TEMPO-BF_4 ($TEMPO^+$) was prepared in-house via a chemical oxidation.[24] Tetraethyl-ammonium tetrafluoroborate ($TEABF_4$, 99.99 %, BASF) was used as received. To a clean 20 mL volumetric flask, 0.156 g of TEMPO•, 0.243 g of $TEMPO^+$ and 2.17 g $TEABF_4$ were added. The supporting solvent – either propylene carbonate (PC, 99.9 %, BASF), or acetonitrile (MeCN, 99.98 %, BASF) – was then added up to the 20 mL mark. The resulting concentrations of the active species and supporting salt were: TEMPO•, 50 mol m^{-3}; $TEMPO^+$, 50 mol m^{-3} and $TEABF_4$, 500 mol m^{-3}.

3.2.2 Electrolyte characterisation

The electrolyte characterisation methods were carried out by Dr. Kevin Tenny (MIT, Cambridge, USA). The electrolyte density (ρ_e, kg m^{-3}) was calculated by measuring the mass of 1 mL aliquots of the PC- and MeCN-based electrolytes with the concentrations previously described into tared glass scintillation vials. The conductivity (σ_e, S m^{-1}) was computed by submerging a calibrated probe (914 pH / Conductometer, Metrohm) into a glass scintillation vial containing c.a. 15 mL of the electrolytes with concentrations as previously described. Similarly, the viscosity (μ_e, Pa s) was calculated by submerging a vibrational viscometer (V-700 Viscolite, Hydramotion) into a glass scintillation vial containing c.a. 15 mL of the electrolytes with concentrations identical to the conductivity experiment.

The diffusivity (D, m^2 s^{-1}) of TEMPO• and $TEMPO^+$ were calculated with the current measured via cyclic voltammograms (CVs) of an ultramicroelectrode (UME) measurement as shown in Equation (3.1):[25]

$$D = \frac{I_{dl}}{4Fc(d/2)} \tag{3.1}$$

Where the diffusion limited current (I_{dl}, A) is measured at a plateau on the cyclic voltammogram (Figure A3.14). F is Faraday's constant (C mol^{-1}), c is the concentration of the active species (mol m^{-3}) and d is the diameter of the ultramicroelectrode (UME, m). To achieve the limiting current, the TEMPO• and $TEMPO^+$ concentrations were reduced to 5 mol m^{-3}, while retaining the 500 mol m^{-3} of $TEABF_4$. CV was performed with a 10 µm Pt UME (BASi) as the working electrode, an in-house Pt mesh as the counter electrode and a non-aqueous Ag/AgCl reference used as the reference electrode. For this study, two separate Ag/AgCl reference electrodes were used: one with the reference stored in PC and the other stored in

MeCN – each were used with the electrolyte with the respective solvent. For both the PC- and MeCN-based electrolytes, the CVs were conducted in an argon glovebox (MBraun Labmaster, O_2 < 5 ppm, H_2O < 1 ppm) using a CH 600 Series potentiostat with a scan rate of 10 mV s^{-1}. For each trial, two complete scan rates were completed spanning -0.40 – 0.10 V (vs. Ag/AgCl) and -0.05 – 0.55 V (vs. Ag/AgCl) for the PC- and MeCN-based electrolytes. The results of the electrolyte characterisation are summarised in Table 3.1. The density and viscosity of the electrolyte changed as expected on addition of the supporting salt and accompanying active species. For example, the density of MeCN-electrolyte was greater than the pure MeCN as stated by a manufacturer – 786 kg m^{-3}.[26] Similarly, the viscosity of PC-electrolyte was greater than the pure PC as stated by a data table – 2.5 × 10^3 Pa s.[27]

Table 3.1: Relevant electrolyte properties measured (N=3): ionic conductivity, σ_e; density, ρ_e; viscosity, μ_e; and species diffusivity, D (3dp).

Parameter		**PC**	**MeCN**
σ_e^* **/ S m^{-1}**		0.953 ± 0.020	4.16 ± 0.002
ρ_e^* **/ kg m^{-3}**		1210 ± 2	826 ± 3
μ_e^* **× 10^3 / Pa s**		3.92 ± 0.06	0.440 ± 0.040
D^{**} **× 10^9 / m^2 s^{-1}**	TEMPO$^{\bullet}$	0.411 ± 0.003	1.940 ± 0.005
	$TEMPO^+$	0.265 ± 0.003	1.490 ± 0.006

* $TEMPO^{\bullet}$, 50 mol m^{-3}; $TEMPO^+$ 50 mol m^{-3} and $TEABF_4$, 500 mol m^{-3}.
** $TEMPO^{\bullet}$, 5 mol m^{-3}; $TEMPO^+$, 5 mol m^{-3} and $TEABF_4$, 500 mol m^{-3}.

3.2.3 Electrode and separator preparation

Commercially available carbon materials used for testing were: AvCarb 1071, AvCarb 7497, Freudenberg H23, AvCarb MGL370. These were cut to size (1.5 cm × 1.7 cm, 2.55 cm^2) as shown in Figure 3.2 (a). The thickness of the electrode material was measured using a micrometer (Mitutoyo Caliper No. 2804S-10). Daramic 175 (Daramic LLC, Charlotte, NC) microporous separators were also cut to size (2.2 cm × 2.2 cm, 4.84 cm^2). Table 3.2 summarises the commercially stated thickness and porosity alongside the measured thickness of the carbon materials and Daramic separator. Variation between commercially stated and measured thickness is attributed to measurement error and the small force the calliper places on the material during measurement.

Table 3.2: Carbon electrode and separator specifications.[28–31]

Parameter	AvCarb 1071	AvCarb 7497	Freud. H23	AvCarb MGL370	Daramic 175
Type	Cloth	Cloth	Paper	Paper	Separator
Thickness* / µm	355	655	210	370	175
Measured thickness / µm	344 ± 16	613 ± 20	184 ± 9	419 ± 26	191
Target compressed electrode thickness / µm	267	490	147	335	--
Porosity* (%)	79	78	80	78	57

* As reported by manufacturer

3.2.4 Flow cell preparation

As stated in Chapter 2, this symmetric zero-gap flow cell design was developed by the Brushett group at MIT.[11,32,33] A separator-electrode-assembly containing two (identical) carbon electrodes separated by a Daramic separator was used. Flow-through flow fields (FTFFs, Tokai G347B graphite, MWI, Inc.), with no engrained flow pattern, double as current collectors and were used on both sides of the separator-electrode-assembly during cell tests. Figure 3.2 (b) displays images of the front and back endplates with liquid flow direction overlayed in red and an open symmetric cell with a carbon cloth inside. The nominal thickness of the carbon electrodes provided the basis for the number and thickness of poly-tetrafluoro ethane (PTFE) gaskets (W. L. Gore & Associates, Inc. Newark, DE) and gore sealing tape layers used during experiments. These leak-proof gaskets compress to 0.2 mm and helped to achieve a c.a. 20 % electrode compression on assembly and tightening (Table 3.2). The cell was subsequently dried for > 30 mins under vacuum while being cycled into the argon-filled glovebox (Inert Technologies, O_2 < 5 ppm, H_2O < 1 ppm) alongside 10 mL Savillex per-fluoroalkoxy alkane (PFA) jars and PFA tubing (1.6 mm ID, Swagelok). Figure 3.2 (c) displays a schematic representation of the symmetric cell.

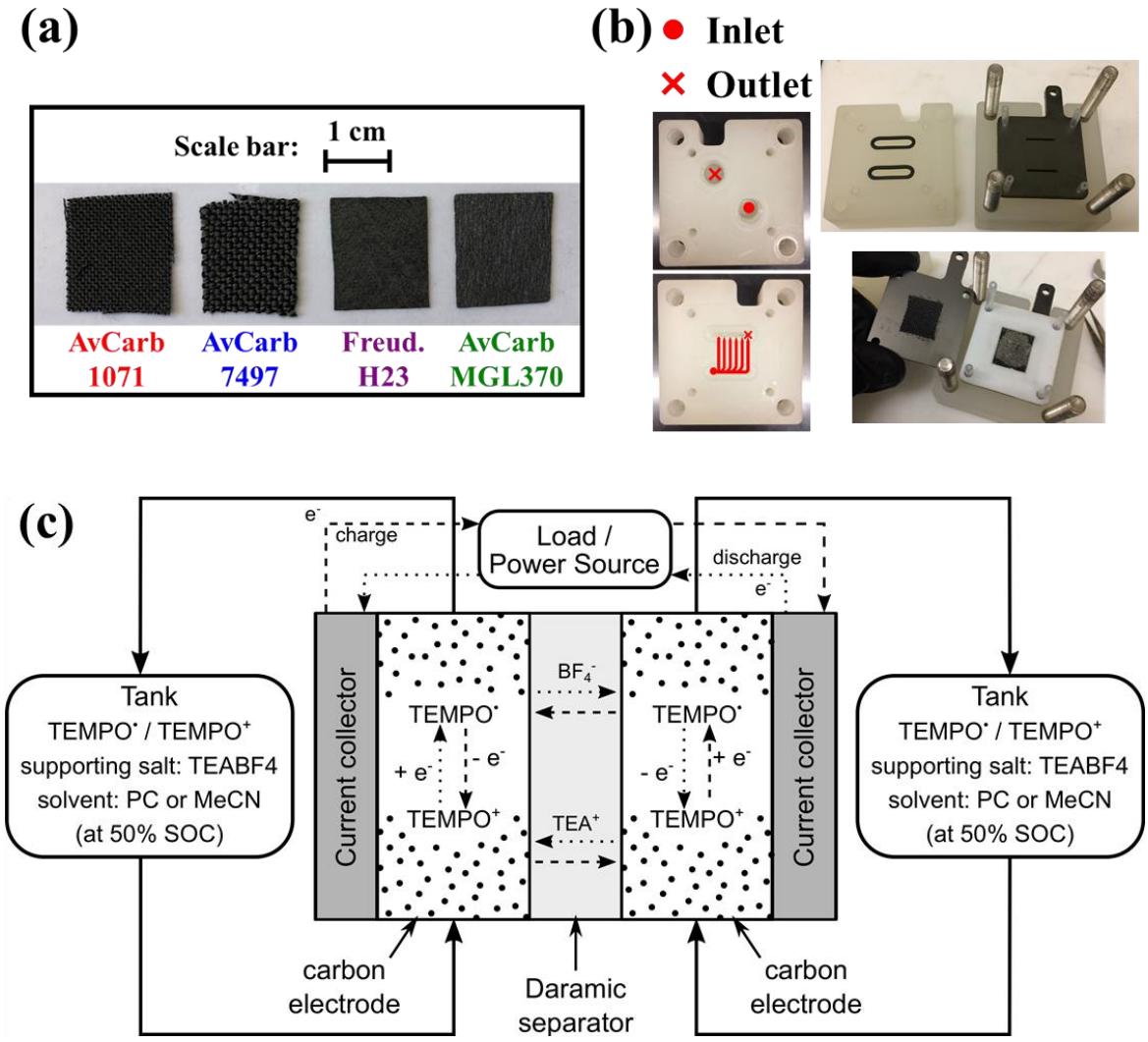


Figure 3.2: Images of (a) electrode materials; (b) symmetric cell casing showing flow-through flow plate, an end plate with overlayed flow direction inserted and some electrodes in-situ during disassembly. (c) Schematic showing the chemical composition of the symmetric cell setup during operation.[1]

3.2.5 Flow cell experiments

The electrolyte, held in two 10 mL PFA jars, was pumped through PFA tubing using a peristaltic pump (Masterflex L/S Series). Utilising the same electrolyte at 50 % SOC and the same carbon electrode type on either side of the separator allows for effective electrode scrutiny. Fresh electrolyte was made for testing each electrode in each solvent environment. A FTFF was used to ensure all the electrolyte was forced through the electrode rather than a flow-by flow field, this choice simplifies assumptions when describing transport through porous media discussed below.[10,11] Another advantage of using a FTFF is to ensure an essentially even compression of the porous electrode during cell testing.[34,35] This compression was later easily reproduced during electrode characterisation to obtain the in-operando microstructure parameters (Section 3.2.6).

The electrolyte characteristic (superficial) velocities used to normalise for electrode thickness were: 0.5, 1.0, 2.5, 5.0 cm s^{-1} (N.B., this unit is only used when referring to characteristic flow velocities in this chapter. "m s^{-1}" is used elsewhere – for instance when stating mass-transfer coefficients, k_m – and certainly in calculations). For the experiments, these velocities were converted to the relevant volumetric flow rates using the following equation:[15]

$$v = \frac{Q}{l_{ed} w_{ed}} \tag{3.2}$$

Where v is the electrolyte characteristic velocity (m s^{-1}), Q is the flow rate (m^3 s^{-1}), l_{ed} is the compressed electrode thickness (m) and w_{ed} is the width of the FTFF channel (m). Before each experiment commenced, the electrolyte was first pumped through the cell at 5.0 cm s^{-1} for 30 min to promote electrode wetting and expel bubbles trapped in the porous media. A BioLogic potentiostat (VMP3, BioLogic, Knoxville, TN, USA) was used to measure the impedance response at open circuit potential (frequency range: 200 kHz – 0.01 Hz, amplitude: 10 mV, points per decade: 6). EIS measurements were subsequently fitted with BioLogic EC-Lab® software using the Levenberg-Marquardt algorithm. Polarisation measurements were then collected by applying positive and negative galvanostatic current density holds for 30 s using 5 mA cm^{-2} increments between 0 – 100 mA cm^{-2}, with current and potential recorded every second. Polarisation measurements were halted when either the 100 mA cm^{-2} limit was reached or the working electrode potential reached a cell cut-off potential of 0.5 V, as potentials in this range indicated the limiting current had been reached and prevented unwanted side reactions / corrosion. This method is commonly used for long term polarisation tests at a fixed SOC.[7]

3.2.6 X-ray computed tomography measurements

The basics of XCT measurements have been discussed in Section 2.6. Samples were prepared using a handheld rotary punch with a 3 mm diameter. An in-house manufactured polyether ketone compression rig was designed to hold and compress the electrode sample to mimic the experimental compression (XCT section, Chapter 2). The sample window has a wall thickness of approximately 1 mm. Incompressible Kapton film (75 μm) discs 3 mm in diameter were placed above and below the sample to act as a fiducial marker. This was followed by alternating

manual tightening and radiograph recording steps, which were performed to reach the required 'Target thickness' for each electrode (Table 3.2).

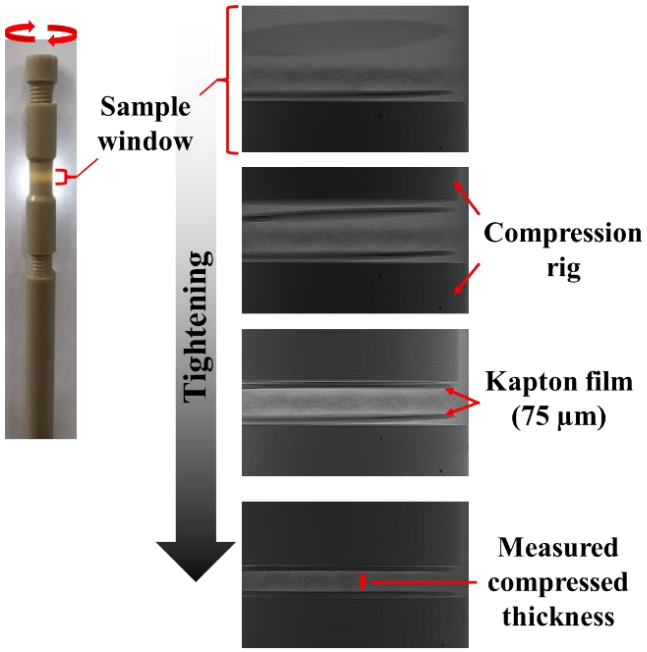


Figure 3.3: Compression rig and radiographs showing an example of a carbon electrode being iteratively compressed in a compression rig, to mimic experimental conditions, ahead of 360° XCT scanning.[1]

Tomographic data was then captured during a 360° sample rotation using the same settings for all four carbon electrodes. Tube voltage and filament current were 60 kV and 170 µA, respectively, while the number of acquired projections and voxel sizes were 2400 and 1.5^3 µm^3, respectively.

3.2.7 Segmentation technique

The super- / sub-sampling steps carried out during the segmentation of the carbon electrode XCT images ensured an accurate diameter for the carbon fibers in each of the electrode materials (step (x), Figure 3.4). This technique allows researchers to have a greater control over the fibre thickness before calculating the electrode properties (e.g. porosity, VSSA and tortuosity).

The process was performed as follows (Figure 3.4): (i) Grayscale (2284 voxel × 2284 voxel) images of carbon electrodes were captured using X-ray computed tomography system – GE Phoenix Nanotom S. The number of image slices varied according to sample thickness (AvCarb 1071 – 144 slices; AvCarb 7497 – 277 slices; Freudenberg H23 – 84 slices, and; AvCarb MGL370 – 193 slices) and was subsequently and cropped (1400 voxel × 1400 voxel) leaving a TIFF stack of purely compressed volume (though only two dimensions are stated

throughout the following methodology, the third thickness / number of slice dimension is implied when referring to 'volume'); (ii) Choose an image with representative features (void space and fibre material) from the TIFF stack; (iii) Choose a small training volume (370 voxel × 370 voxel);

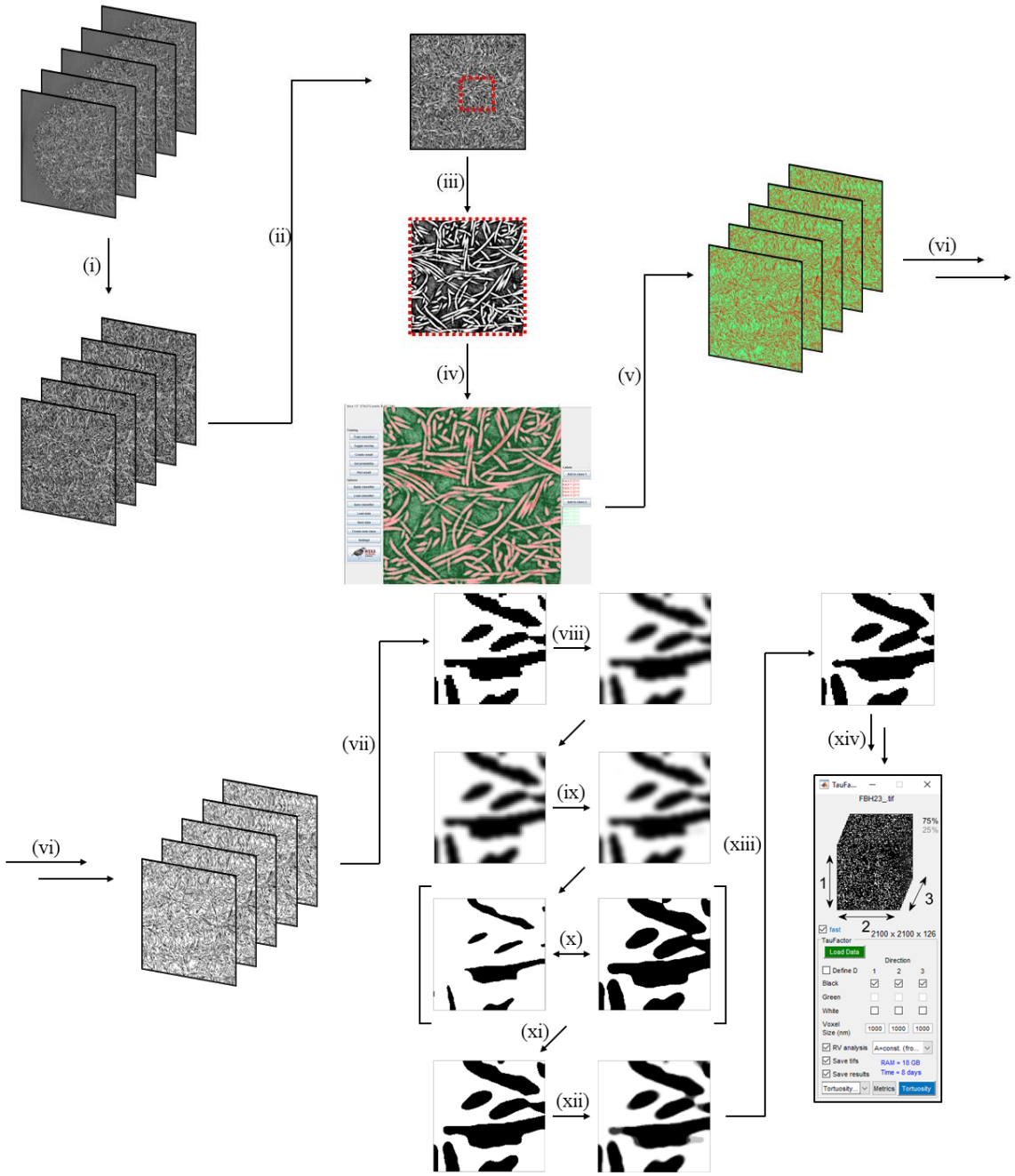


Figure 3.4: A step-by-step graphic representation of the image processing technique carried out for all carbon electrodes in Fiji / ImageJ.[36,37] The example used here shows representative steps during Freudenberg H23 image processing.[1]

(iv) Transfer the training volume into 'Trainable Weka 3D Segmentation' tool.[38] Five regions on three different images were assigned a 'class' (either carbon fibre – red, or free space – green). Here 'skeletal training' was carried out, whereby regions that were assigned carbon

fibre were undoubtedly as such, i.e., only the inner part of the fibre was highlighted and classified as fibre. Once these regions were chosen, the classifier was trained; (v) The resultant classifier was then applied to the full 1400 × 1400 voxel image stack to create a feature stack, classifying all the fibres and void space; (vi) The feature stack was then converted from an RGB colour image to a grayscale image and the contrast was adjusted accordingly to create a segmented black and white image (essentially changing green/red to white/black respectively).

Having completed the segmentation, the following steps are for accurate fibre thickness adjustment – the following steps focus on just one region but, during analysis, several regions were checked to ensure a good representation of fibre thickness. 'The image' refers to all the images in the TIFF image stack.

For step (vii) the voxel size was $(1.5\ \mu m)^3$. A representative image was chosen for this figure; (viii) The image was 'smoothed' thereby re-introducing grayscale voxels to the fibre edges; (ix) The image was then 'super-sampled' in each dimension – the number of microns $voxel^{-1}$ was reduced from $(1.5\ \mu m)^3\ voxel^{-1}$ to $(0.5\ \mu m)^3\ voxel^{-1}$. This increases the number of voxels in the image significantly. Graphically, this makes the image look 'sharper' and less 'pixelated'; (x) The contrast and min/max levels were adjusted to vary the fibre diameter size until (based on SEM, a metrological technique) the user was satisfied with the fibre thickness; (xi) Once the user was satisfied with the fibre thickness the file was saved and moved to the next step; (xii) The image was then 'sub-sampled' in each dimension – the number of microns $voxel^{-1}$ was reduced from $(0.5\ \mu m)^3\ voxel^{-1}$ to $(1.0\ \mu m)^3\ voxel^{-1}$. This re-introduces grayscale voxels; (xiii) As before in (x), the contrast and min / max levels were adjusted for fibre thickness; (xiv) Finally the image was transferred to TauFactor (a MATLAB application).

The MATLAB version used was MATLAB® R2018a. The TauFactor version used was Version: 1.208. Full RV analyses in both the y and z directions were carried out using the 'A = constant' method. This method was used as it most realistically reflects the movement of electrolyte through the electrode. The time taken for these tortuosity analyses to take place varied in accordance with electrode thickness and ranged between 10 – 69 hours on an Intel Xeon CPS E5-2660 v3, 10 Cores, 20 Logical Processors – 64-bit workstation with 256 GB RAM.

While this segmentation technique was not formally compared to alternative methods, it is believed to provide more control over fibre thickness and therefore, with the help of SEM – a metrological technique – supply accurate (and realistic) microstructural information.

3.2.8 Pore network model

Using previously reported works, the methodology for the PNM was developed and executed by Dr. Andrea Gayon Lombardo (formerly Imperial College London). While the author appreciates qualitative outcomes, understanding of model implementation is outside the scope of this thesis. Please refer to the following references to understanding for full methodologies.[1,39,40]

A PNM is a simplified topological representation of a porous volume consisting of a network of 'pores' connected by 'throats'. These pores and throats are generated by implementing a 'maximal ball' algorithm (from Avizo software) over an XCT image of a compressed carbon electrode. The PNM was used to calculate the pressure drops and, subsequently, the permeability across the electrode.

This PNM assumes a single pressure value per pore and the flow through each throat connecting two pores is calculated using the steady state Navier-Stokes equation for flow through a pipe. The pressure and velocity through the network are obtained by enforcing a mass balance at each pore (Equation (3.3)):

$$\sum_{j=1}^{N^{th}} q_{i,j} = \sum_{j=1}^{N^{th}} \frac{\pi r_{i,j}^4}{8\mu_e L_{i,j}} \left(P_i - P_j\right) \qquad (3.3)$$

Where $q_{i,j}$ is the flow rate between pores i and j ($m^3\ s^{-1}$), $r_{i,j}$ and $L_{i,j}$ represent the radius and length of the throat connecting pores i and j (m), μ_e is the viscosity of the electrolyte (Pa s), P_i is the pressure at pore i (Pa) and N^{th} is the number of pores and throats connected to pore i.

It is assumed that the flow velocity of electrolyte through the electrode is constant.[19] The experimental flow rate, Q_{exp}, as calculated in Equation (3.2), for each of the electrodes, is equivalent to the sum of the flow rates through each of the boundary throats (i.e. the throats at the edge of the XCT reconstructions, in the in-plane outlet direction). This can be expressed

in the following Equation (3.5) where q_j corresponds to the flow rate at the outlet throat j ($m^3\ s^{-1}$).

$$Q_{\text{calc}} = \sum_{j=1}^{N_{\text{out}}^{th}} q_j \tag{3.4}$$

$$Q_{\text{calc}} = \frac{KA}{\mu_e L_{\text{ed}}} \Delta P \tag{3.5}$$

Following conversion and the assumption that the flow will follow Darcy's law (Re < 1, *vide infra*),[41] the permeability of the porous electrode can be back calculated from the gradient of the estimated pressure drop as a function of the flow rate at the boundary throats (Equation (3.5)), where K is the permeability (m^2) and A is the cross sectional area of the boundary throats (m^2).

3.2.9 One-dimensional continuum model

The methodology for the 1D continuum model was developed by Dr. Catalina Pino-Muñoz (Imperial College London). While the author appreciates qualitative outcomes, understanding model implementation and fitting is outside the scope of this thesis. Please refer to the following references for full methodology understanding.[1,9,11,42,43]

The operational conditions of the experimental part of this work (Figure 3.2) allows the use of a simplified mathematical representation of the electrochemical system. Characteristic flow rates were chosen to be high allowing for the assumption of a dominant convective flow in the y-axis across the range of flow rates. At high flow rates, a very small amount of species conversion takes place, whereas at lower flow rates, higher conversion is expected. Additionally, the symmetric geometry of this system and fast charge-transfer (quasi-reversible) kinetics either side of the membrane allows for only half of the separator-electrode setup to be modelled. Figure 3.5 illustrates this model setup and includes key dimensions and boundary conditions.

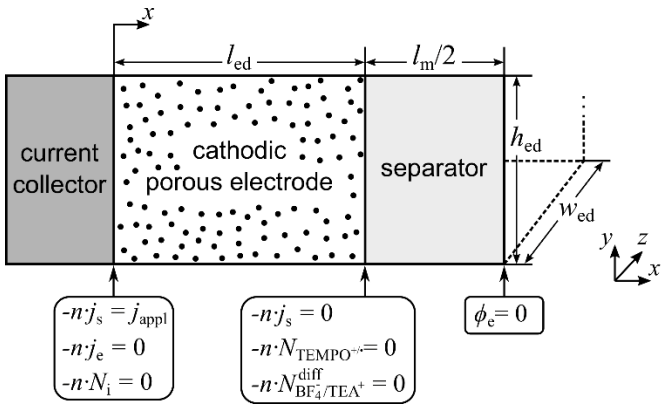


Figure 3.5: Schematic of the 1D model considering half of the separator-electrode-assembly with key dimensions and pertinent boundary conditions.

The assumptions associated with this model were as follows:

1. The system was isothermal.
2. The electrolyte was incompressible with constant density, viscosity and volume.
3. Physical properties were isotropic and homogeneous.
4. Possible self-discharge and / or side reactions were neglected, as well as any additional chemical reactions.
5. Individual electrolytes in tanks were uniformly mixed and did not deviate significantly from 50 % SOC (50 mol m^{-3} for both $TEMPO^{\bullet}$ and $TEMPO^{+}$) at any stage during the experiments.
6. A dilute solution approximation was adopted for species transport in the electrode.

Continuity equations were used to keep track of quantities such as charge and species to satisfy conservation laws. Charge was tracked using continuity equations constraining the ionic and electronic currents. Conservation of species and an electroneutrality condition were imposed in order to obtain the spatial distribution of the four species involved and to track mass movement through either the membrane or the porous electrode domains.

The charge-transfer reaction rate is controlled by an overpotential which is defined as the difference between interfacial potential and its equilibrium value. This interfacial potential is needed to deduce the area-specific Faradic current density (j^{A}_{F}, mA cm^{-2}) – the current per unit surface area of pore wall. This can be expressed using the exchange current density, j_0, which itself is calculated using Equation (3.6), where $c^{\alpha_c}_{TEMPO^{\bullet}}$ refers to the concentration of $TEMPO^{\bullet}$ with respect to the cathodic transfer coefficient, α_c, and $c^{\alpha_a}_{TEMPO^{+}}$ refers to the analogous $TEMPO^{+}$ concentration at the anodic transfer coefficient.

$$j_0 = Fkc_{\mathrm{TEMPO}^{\bullet}}^{\alpha_c} \cdot c_{\mathrm{TEMPO}^{+}}^{\alpha_a} \tag{3.6}$$

$$j_F^A = j_0 \left[\left(\frac{c_{\mathrm{TEMPO}^{\bullet}}^s}{c_{\mathrm{TEMPO}^{\bullet}}} \right) \exp\left(\frac{\alpha_a F}{RT} \eta \right) - \left(\frac{c_{\mathrm{TEMPO}^{+}}^s}{c_{\mathrm{TEMPO}^{+}}} \right) \exp\left(\frac{-\alpha_c F}{RT} \eta \right) \right] \tag{3.7}$$

In order to estimate the surface concentrations in Equation (3.7), where superscript 's' refers to the concentration of $TEMPO^+$ or $TEMPO^{\bullet}$ species at the surface, the rate at which TEMPO species is oxidized or reduced according to BV kinetics is matched to the rate at which TEMPO species arrive or leave the electrode surface.[11,44] This mass-transfer rate is considered proportional to a linear concentration gradient within a Nernst diffusion layer, subject to a mass-transfer coefficient (k_m, m s^{-1}). For simplicity, both mass-transfer coefficients were assumed to be equal for the reduced and oxidised species, as shown in Equations (3.8) and (3.9), respectively.

$$-k_m(c_{\mathrm{TEMPO}^{\bullet}}^s - c_{\mathrm{TEMPO}^{\bullet}}) = r \tag{3.8}$$

$$-k_m\left(c_{\mathrm{TEMPO}^{+}}^s - c_{\mathrm{TEMPO}^{+}}\right) = -r \tag{3.9}$$

This 1D model was selected (rather than higher order models) for its simplicity and fast implementation and evaluation time, additionally, 1D models have been shown to comprehensively describe phenomena in RFB cells using FTFFs. This model should be used for comparative analysis with respect to general cell performance trends and not for quantitative performance predictions.

3.3 Results and discussion

This section describes and discusses the main observations gathered from experimental and modelling characterisation techniques. The ex-situ characterisation of each of the electrodes' microstructural properties are evaluated using imaging analyses introduced in Chapter 2 alongside PNM simulations. In-situ electrochemical characterisation techniques are then used, taking advantage of the symmetric geometry of the system, to understand the dominant transport processes and associated resistances. Following this, correlations are made between permeability and an in-house developed performance metric. Finally, mass transfer coefficients are established using the developed 1D model.

3.3.1 Microstructural analysis

Microstructural and morphological data (Figure 3.6) was captured using SEM and XCT imaging techniques, as introduced in Chapter 2. The carbon cloths consist of a simple plain weave pattern and differ in bundle size: small (AvCarb 1071) and large (AvCarb 7497), this difference in electrode thickness is directly related to the bundle size – with larger bundle size leading to a thicker cloth.

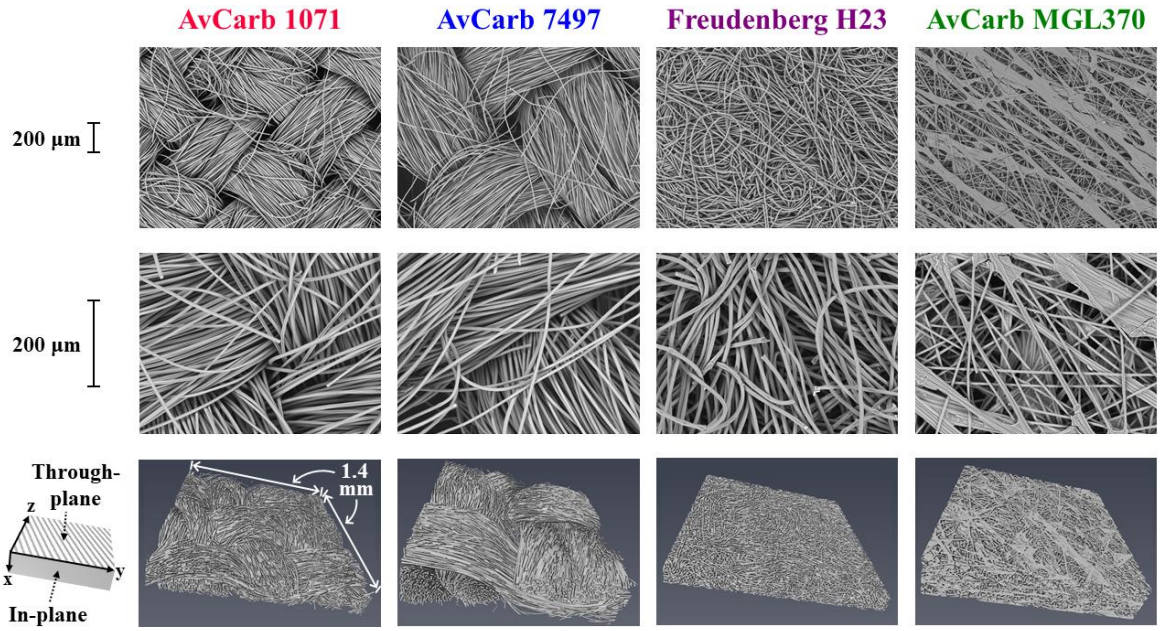


Figure 3.6: Images showing microstructural properties and morphological information over the carbon electrodes. Scanning electron microscopy images (top two rows) and representative 3D renderings (with a through plane area of 1.96 mm²) of the electrodes used in this chapter.[1]

Freudenberg H23 achieves its structure from a hydroentangling process resulting in randomly organised, mechanically bound fibres.[45] AvCarb MGL370 is a moulded graphite laminate, which is a highly graphitic material manufactured under high temperature and pressure[28] – its individual fibres, unlike Freudenberg H23, are straighter and appear taut. While it might appear that AvCarb MGL370 has binder, EDX confirmed this is not the case (see Figure A3.15), instead this material is randomly dispersed carbonaceous matrix that remains in the electrode following the lamination step and all solid species is considered equivalently able to act as an active site for electrochemical processes.

Following sample mounting, inside the in-house constructed compression rig (Section 2.1.7, Chapter 2) and appropriate tightening (Figure 3.3), XCT images were gathered. After appropriate segmentation, as outlined in the Methodology, a pore network was extracted for each of the electrodes and a pore size distribution (PSD) established (Figure 3.7).

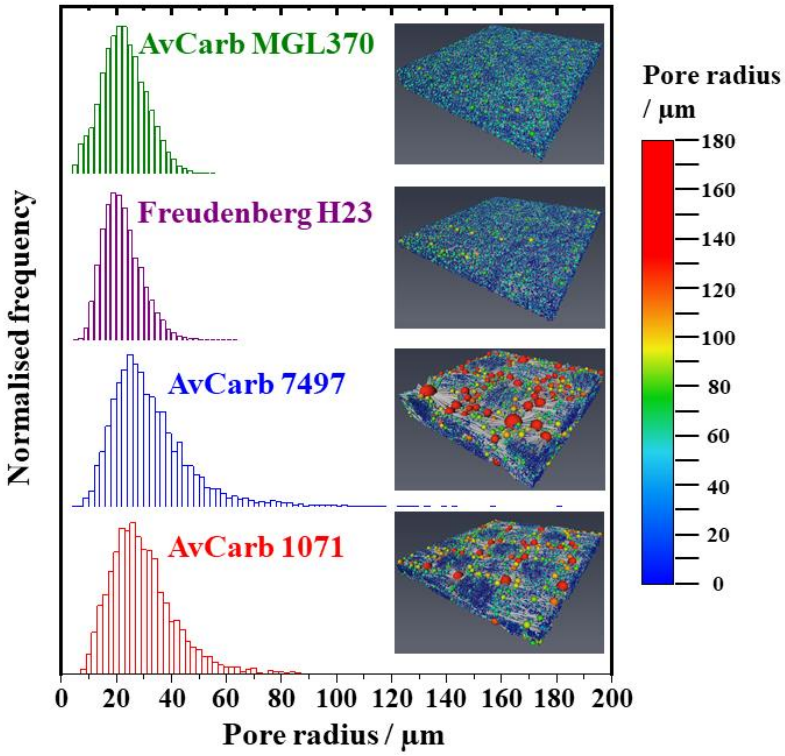


Figure 3.7: Pore size distribution alongside extracted of pore network for each of the tested electrodes. The colour bar on the right hand side pertains to the extracted spherical pores in the pore network insert.

While the maximal ball algorithm used is an imperfect method by which to detect and measure pore sizes (assuming they are perfectly spherical), it gives the user a sense of the void space available to the electrolyte travelling through the electrode. With a mean pore radius of 22.6 µm for both the Freudenberg H23 and AvCarb MGL370 carbon papers, their PSDs are similar is character. Separately, the PSDs for the two carbon cloths have a similar broader character with a longer tail – because of the woven nature of the fibre bundles, the cloths possess large interstitial weave gaps. The mean pore radius is 32.9 and 30.0 µm for AvCarb 7497 and AvCarb 1071, respectively.

The segmented images were further processed using TauFactor (version: 1.208), a MATLAB application,[23] to extract the VSSA, tortuosity and porosity of the compressed electrodes (Table 3.3). The calculated porosity was similar for each of the electrodes, save for the carbon paper values, which were slightly lower. It is widely understood that microstructural parameters change on compression, as demonstrated by Jervis et al.,[3] and this difference in porosity is attributed to increased fibre-fibre contact on compression. The calculation of VSSA using TauFactor returned marginally higher values for VSSA compared to elsewhere.[46] While this is not surprising or concerning, as values can vary drastically depending on the segmentations

method used, it should be kept in mind as misinterpretation of VSSA measurements can lead to drastically inflated or understated electrode performance. Surface area identified by XCT may not represent the exact electrochemically active surface area (as the XCT will identify surface area that is inaccessible to the electrolyte) however, this segmentation method offers a robust representation of the fibre diameter, and so, when measuring mass-transfer coefficients and dimensionless parameters, will yield more accurate values.

Table 3.3: Microstructural parameters from SEM, XCT and TauFactor.

Parameter		AvCarb 1071	AvCarb 7497	Freud. H23	AvCarb MGL370
Target compressed electrode thickness / µm		267	490	147	335
Measured compressed thickness during XCT / µm		271	489	150	336
Average fibre diameter* / µm		8.78	8.78	9.88	6.19
Integer fibre diameter (for segmentation) / µm		9	9	10	6
Porosity (%)		79.6	78.3	74.8	70.5
Volume-specific surface area / $m^2\ m^{-3}$		154000	143000	168000	143000
"Simple" Volume-specific surface area / $m^2\ m^{-3}$		363000	357000	303000	456000
Tortuosity	***x***	1.44	1.55	1.46	2.37
	y	1.20	1.28	1.25	1.39
	z	1.19	1.25	1.20	1.43

* indicates measurement carried out by SEM.

An approximate estimate for the volume specific surface area for the materials based upon a simple model considering all fibres being composed of cylinders can be estimated and compared to the values calculated. This is based on a hypothetical 1 m × 1 m × 1 m cube of the materials composted of a fibre of diameter, d; length, L; and which has a total porosity of ε (this model ignores the "ends" of fibres). Hence:

$$A = \pi d L \tag{3.10}$$

$$V = \pi \left(\frac{d}{2}\right)^2 L \tag{3.11}$$

$$\varepsilon = V/V_{\text{tot}} \tag{3.12}$$

Where V_{tot} is the volume we are performing the calculation over. Hence:

$$V_{\text{tot}} = V/\varepsilon \tag{3.13}$$

The volume specific surface area is then:

$$\text{VSSA} = \frac{A}{V_{\text{tot}}} = \frac{\pi d L \varepsilon}{\pi \left(\frac{d}{2}\right)^2 L} = \frac{4\varepsilon}{d} \tag{3.14}$$

This "simple" measure of surface area, which is commonly, used overestimates the computationally averaged surface area by a factor of 1.8 – 3.2 suggesting that such simple measures may lead to an overestimate of interfacial surface area. This overestimation likely comes from the assumption that all fibers are non-intersecting cylinders which is not the case for real fibres for which there is significant fibre-fibre intersection which leads to loss of surface area. This is especially true in the case of AvCarb MGL370 which has the highest divergence due to the extensive amalgamation of its fibres, Figure 3.6.

In all but the AvCarb MGL370 electrode, the ratio between the through-plane and in-plane (see Figure 3.6 for clarification) tortuosity is 1:0.83 (indeed the values are similar, too). Given their different morphology, the similarity in this ratio is non-trivial. The tortuosity measured at the interstitial holes (characteristic of this 'one-over one-under' plain weave pattern) will have a much lower value as diffusion more facile than the tortuosity in, for instance, the centre of the tight unidirectional fibres in a weave bundle. The geometry of the fibres throughout Freudenberg H23 is largely isotropic – it is tentatively asserted that the difficulty with which a given active species travels through this carbon paper is roughly half way between the two paths through the cloth as described above. It is asserted therefore, that this effect is averaged out across the through-plane and results in similar ratios between in-plane and through-plane paths. An interesting study to test this might involve measuring the tortuosity through a sub-sample at the interstitial hole vs. through the centre of a bundle. For the AvCarb MGL370, it is assumed that the sheet-like carbon matrix material observed in Figure 3.6 continues throughout the x-axis and so it is unsurprising there is a 68 % increase in tortuosity when

comparing the average of the *y* and *z* in-plane directions (1.41) and with the *x* through-plane direction (2.37). This ratio is unlikely to have a significant bearing on the electrochemical performance as a FTFF is used. The in-plane average is expected to provide the best indicator of RFB performance where the lower in-plane average tortuosity, the more facile the mass transport (i.e. AvCarb 1071 (1.20) > Freudenberg H23 (1.23) > AvCarb 7497 (1.27) > AvCarb MGL370 (1.41)).

3.3.2 Pressure drop and permeability

The pressure drop, ΔP, was calculated using the PNM described in the Methodology. Figure 3.8 shows a graph illustrating the pressure drop as a function of the characteristic velocity – the gradient can be used to calculate the permeability.

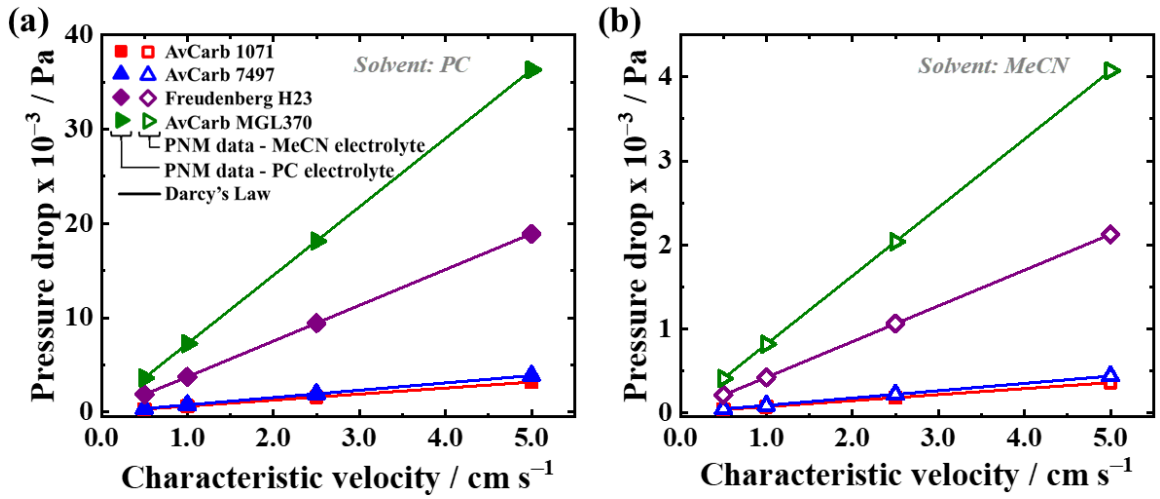


Figure 3.8: Calculated pressure drops as a function of characteristic velocity using (a) PC and (b) MeCN as solvents. The values for each electrolyte are averaged for the two directions of in-plane flow (i.e. y and z).

The fact that the Reynolds numbers calculated later in this chapter are greater than unity (1) allows the use of Darcy's Law to calculate the permeabilities (Equation (3.5)). These values are reported in Table 3.4. Contextualising these values and comparing them to equivalent experimentally sourced and computationally calculated permeabilities is essential. On the surface, these results are in line with El-kharouf et al. for uncompressed electrodes using mercury intrusion porosimetry – higher permeabilities observed in cloths relative to papers.[47] As has already been mentioned, compression can have a significant effect on the microstructural properties,[3,48] although a direct compression-permeability relationship has not been established. Table 3.4 shows that the permeabilities measured are of the same order of magnitude compared to previous literature: 1.32×10^{-11} m^2 (this work) vs. 2.0×10^{-11} m^2 for Freudenberg H23, and 8.61×10^{-11} m^2 (this work) vs. $(6.8 \pm 0.4) \times 10^{-11}$ m^2 for AvCarb 1071.[19]

The variation between these values can be attributed to the simplified approximation of the microstructure using a PNM, discrepancies in the microstructure samples and differences in compression (15 % ± 7 %[19] vs. 20 % in this work). The measured permeabilities by Tenny et al. for AvCarb 1071 and AvCarb 7497 were (1.05 ± 0.03) × 10^{-11} m^2 and (1.04 ± 0.02) × 10^{-11} m^2, respectively.[6] This value is c.a. eight to ten times smaller than the values obtained with smaller compressions (20 % in this work and 15 % elsewhere) inferring that an increased compression has an adverse effect on permeability.[1,6,19]

Table 3.4: Calculated permeabilities using pressure drop calculations from PNM simulation.

		Permeability, $K \times 10^{11}$ / m^2			
Solvent	**Plane**	**AvCarb 1071**	**AvCarb 7497**	**Freudenberg H23**	**AvCarb MGL370**
PC	*zx*	8.30	11.0	1.27	1.51
	yx	8.92	10.2	1.38	1.45
	In-plane average	8.61	10.6	1.32	1.48
MeCN	*zx*	8.29	11.0	1.26	1.65
	yx	8.93	10.2	1.38	1.48
	In-plane average	8.61	10.6	1.32	1.57

It is worth mentioning that the permeabilities reported here do not follow intuitively from the tortuosity trend stated at the end of the Section 3.3.1. It might seem reasonable to expect that the lower the tortuosity, the higher the permeability. It is proposed that this discrepancy is due to the different transport processes being measured. Tortuosity is controlled by the diffusive flow through porous media and this permeability measurements essentially characterises the resistance to convective transport – i.e. higher permeability infers lower resistance. Qualitatively, these permeability values are in line with the PSDs and extracted pore networks outlined in Figure 3.7.

3.3.3 Zero-gap RFB performance as a function of electrode and solvent

The ex-situ characterisation data reported so far is helpful. However, to contextualise the findings, electrochemical measurements are needed to establish microstructure-performance and electrolyte-performance relationships. Figure 3.9 illustrates how polarisation curves will be presented throughout this work. The iR-corrected potential is extracted by removing the ohmic potential contribution from the measured potential of the cell. This is a standard and necessary correction that leaves the potential associated with the kinetic and mass transport

contributions of the system. The choice of the TEMPO•/TEMPO$^+$ quasi-reversible organic redox couple was to minimise the kinetic resistance and so the remaining resistance pertains, in large part, to the mass transport. This is useful, as here, specific, causal resistance / performance variations are identified and can, in large part, be attributed to the mass transport as a result of the variables: electrolyte flow rate, electrolyte solvent and electrode microstructure. It should be noted, however, that the best measurement of the mass transport resistance is achieved by extracting Warburg character from impedance measurements – this is discussed later. The following data interpretation uses purely electrochemical measurements and the aforementioned assumption that quasi-reversible redox couple represents a negligible contribution to the iR-corrected potential.

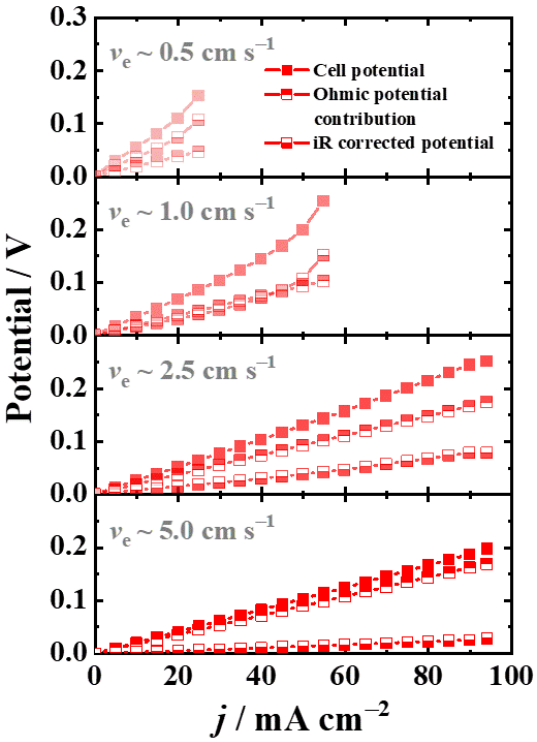


Figure 3.9: Current-potential curves as a function of flow rate. Measured potentials are displayed alongside their respective iR (ohmic / HFR) corrections and resulting 'iR-corrected' polarisation curves. These measurements were gathered using an AvCarb 1071 electrode with MeCN-type electrolyte (Figure A3.16).[1]

At low flow rates (e.g., v_e = 0.5 cm s^{-1}), the cell is dominated by the mass transport resistance contribution as a result of sluggish transport effects – this is accompanied by a relatively steep increase in potential at low current density. As the flow rate increases (to 5.0 cm s^{-1}), the mass transport resistance reduces until it becomes much less significant relative to the constant ohmic resistive contribution (associated with aspects such as solvent and separator resistances). At low flow rates, the cell cut-off potential is reached prematurely meaning, in this case, that at 30 mA cm^{-2} the cell potential reaches 0.5 V and thus no point is recorded. This low flow rate

operating regime leads to poor system performance with very unstable potentials. It is difficult to reach further conclusions about what processes are occurring and limiting the system at a microstructural level using this analysis. Previous authors have asserted that there is an uneven distribution of electrolyte across the electrode due to the existence of preferred flow paths and that this is attributed to the diverse PSD and differing inter-pore connectivity in the porous matrix.[39,49] At lower flow velocities, this flow path selectivity prevents effective electrolyte replenishment in depleted regions, leading to heightened local overpotentials and uneven electrode usage.[30]

In a similar way to corrections for HFR in polarization curves, ECMs are commonly implemented to analyse Nyquist plots since they tentatively offer quantification and separation of the resistances (as outlined in Chapter 2). Figure 3.10 presents a set of EIS and polarisation responses from a symmetric zero-gap RFB cell using AvCarb 7497 on both sides of a separator. A range of characteristic flow velocities are displayed where the RHS and LHS present measurements using PC- and MeCN-based electrolytes, respectively. The insert in Figure 3.10 (b) shows the ECM used to extract the resistances from the Nyquist curves (labelled 'Model fit' in the key) and the solid and dotted lines in the polarisation curves represent the fitting carried out by the 1D model described previously.

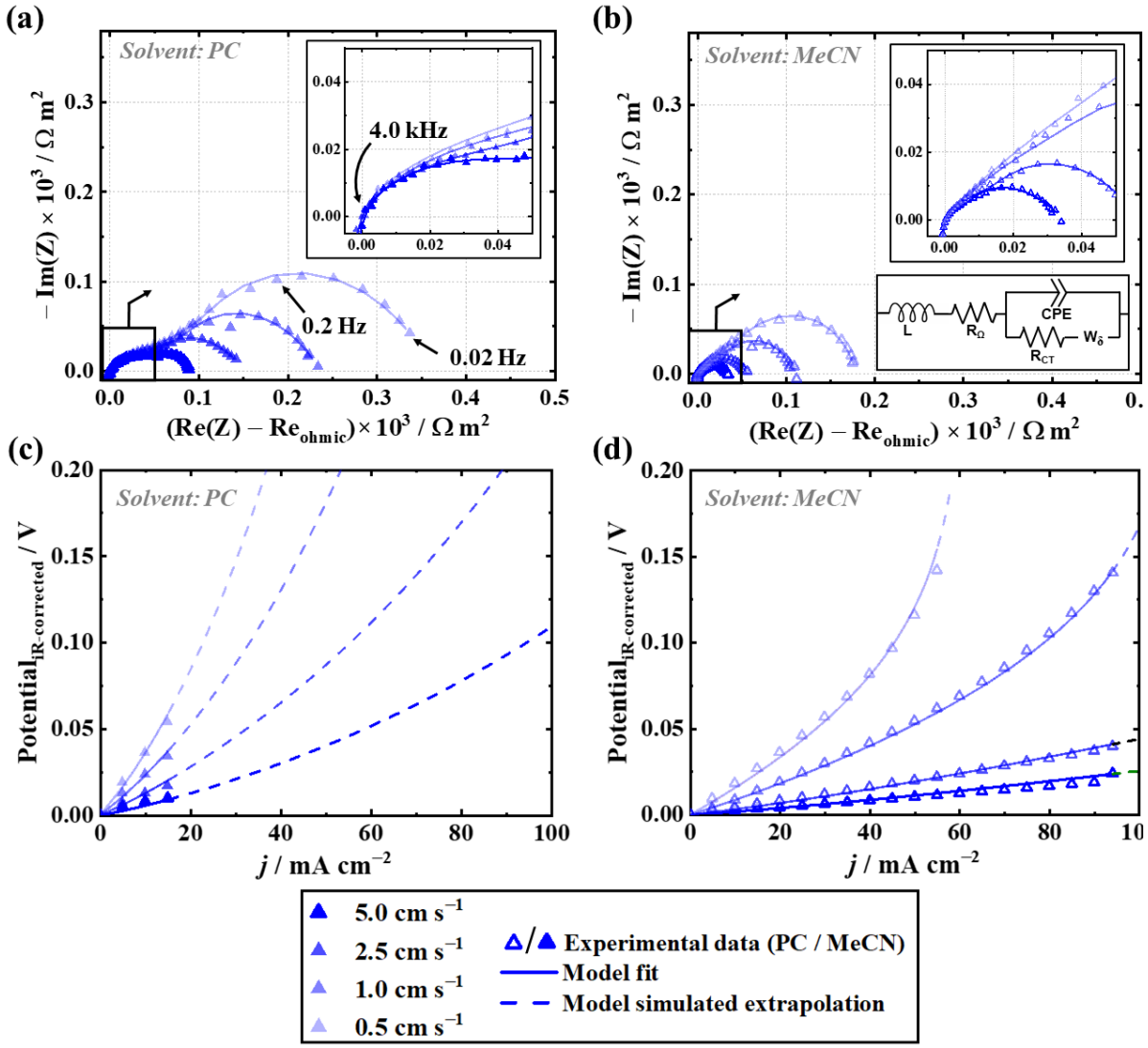


Figure 3.10: (a) - (b) Nyquist and (c) - (d) polarisation curves for electrochemical tests using AvCarb 7497 electrodes in PC-based ((a) & (c)) and MeCN-based ((b) & (d)) electrolytes. The colour shading represents chosen characteristic flow velocities.

The ECM includes standard 'resistor' elements, R_Ω and R_{CT}, to describe the classical ohmic (HFR) and charge transfer contributions to the cell resistance, respectively, with the addition of a non-classical bounded Warburg element (W_δ) representing the mass transport resistive contribution. The Warburg element, used alongside the R_{CT} resistor, helps to describe the semi-circular nature of the impedance responses at the low frequency end of the Nyquist plot.[50] This ECM has previously been used to represent the EIS response of TEMPO-based RFBs.[19,32] In either solvent, the consistent and low values for the charge-transfer resistance at multiple flow rates allow the mass-transport to vary largely independently. The iR-corrected EIS measurements show, in both solvents, that with increasing flow rate there is a decrease in the combination of mass-transport resistance to the total ASR of the system – this is explicitly illustrated in Figure 3.11. This figure also compares the solvents used to make up the

electrolytes clearly showing that there is a lower overall mass transport resistance using MeCN compared to PC. While the organic TEMPO redox couple was chosen because of its fast kinetics, the charge transfer resistance is observed to be greater in PC compared to MeCN – this is tentatively attributed to the slower rearrangement of electrolyte species in PC, following the outer sphere electron transfer, as compared to MeCN.[51] A complete set of the Nyquist plots for all the electrodes can be found in the appendix alongside the parameters extracted using a Randles circuit model and the additional ohmic (HFR) and charge transfer resistance information (Figure A3.17 and Table A3.7).

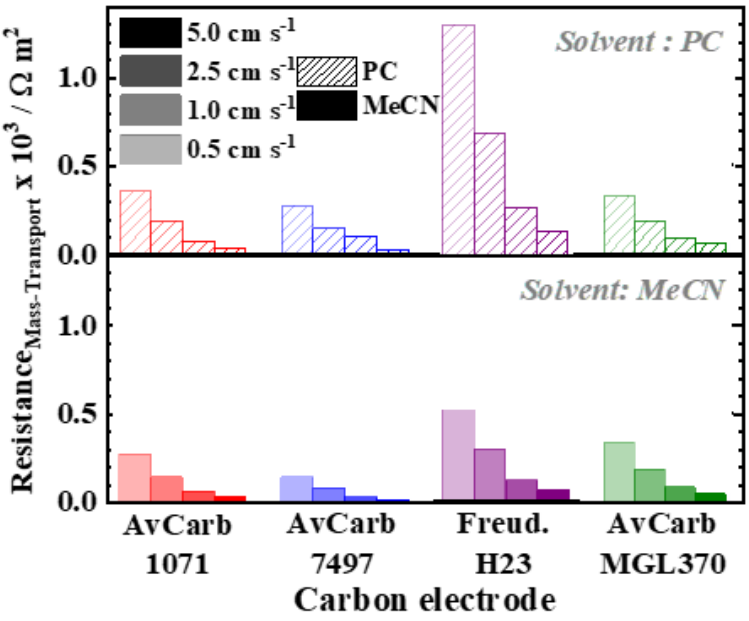


Figure 3.11: Comparison of mass-transport resistances recorded during electrochemical impedance spectroscopy experiments, calculated using an equivalent circuit model. Experiments were carried out using either PC (top) or MeCN (bottom) as the solvent during electrolyte preparation.

The general decrease in ASR, observed across all electrodes with increasing electrolyte velocity, can be attributed to both an enhanced convective transport enabling a faster replenishment of active species and, a reduced BL thickness at the active surface area, both of which result in a reduction of mass transport resistance.[52] The former corresponds to the extent of interconnectivity in the porous phase, given by the electrode microstructure, while the latter is directly related to the mass-transfer coefficient which characterises the speed with which active species can be transported from the bulk to the electrode's active surface. Figure 3.11 not only provides a comparison of the solvents (comparing the upper and lower sets of graphs) but also a comparison the overall mass transport resistance as a function of microstructure (comparing different coloured graphs on the same row). AvCarb 7497 clearly has the lowest mass transport resistance followed by AvCarb 1071, AvCarb MGL370 and Freudenberg H23.

This resistance information falls in line with our PSD observations (Figure 3.7), geometric ordered fibre alignment in the 'in-plane' direction (Figure 3.6) and intuitive deductions from permeability (Table 3.4).

As discussed in Chapter 2 and introduced in the Methodology, polarisation experiments use the relationship between overpotential and current density to evaluate the RFB performance. Figure 3.10 shows that, common to both electrolytes, at low flow rates, the system tends towards a limiting current density and the overpotentials quickly become too high to allow the experiment to continue. The apparent premature cut-off in experiments involving PC-based electrolyte is attributed to severe cell potential instability during the final step in current density (i.e., 20 mA cm^{-2} at all flow rates, for this electrode) and the especially slow reactant replenishment at active sites within the electrode. In this case, using a FTFF system, high overpotentials correspond to a mass transport limited region where the concentration overpotential dominates, and there is not enough convective flow to sustain higher applied current densities. Figure 3.10 demonstrates that the supporting solvent significantly influences the cell polarisation since even at high flow rates, while using the more viscous PC-based electrolyte, the cell is unable to reach a higher current density than 15 mA cm^{-2}. This effect is partially attributed to the limiting inter-pore diffusive transport due to the low diffusivity of TEMPO species in PC (Table 3.1). Additionally, an intra-pore diffusive process is present which limits the movement of species to and from the active surface. In PC, the active reactant species diffuse slowly, with difficulty, from the bulk of the electrolyte to the surface of the electrode; once they reach the electrode surface, they are rapidly consumed due to their fast kinetics and the high current density applied. This implies that the rate of mass-transfer towards the electrode surface is much lower than the reaction rate, resulting in an increased boundary layer thickness causing a rise in overpotential. When using MeCN-based electrolyte (Figure 3.10 (b) and (d)), high current densities can be reached as the lower viscosity (0.440×10^{-3} Pa s), and accompanying surface tension, allows the electrolyte to move more easily to empty regions in the porous matrix, preventing the presence of starved regions through the electrode. TEMPO species have higher diffusivities in MeCN than in PC electrolyte, so the resulting boundary layer is smaller, inducing a lower overpotential over the electrode during operation. The polarisation curves for the other electrodes are displayed in the appendix (Figure A3.18).

Performance metrics can be used to more easily digest the large amount of data extracted from these experiments. In this work, the iR-corrected ASR calculated using galvanostatic

polarisation data, i.e. the fitted iR-corrected potential (V) divided by the current density (mA cm^{-2}), was used at the performance metric. The iR-corrected ASR for each electrode in the highest and lowest flow regime, at a current density of 25 mA cm^{-2} ("ASR_{25}"), was calculated during polarisation and presented in Table 3.5. This metric is reasonable because it is calculated at a non-negligible current density and not simply resistance parameters.

Table 3.5: The area specific resistance calculated using the iR-corrected 1D model values at 25 mA cm^{-2} (3sf). The area specific resistance has been calculated for each electrode, in each supporting solvent at the highest (5.0 cm s^{-1}) and lowest (0.5 cm s^{-1}) characteristic flow velocities. (Parentheses indicate that 250 A m^{-2} was not reached before the cell cut-off potential was reached, the highest current density modelled is indicated next to the associated ASR.)

Electrode	Solvent	Area specific resistance, $ASR_{25\_iR\text{-}corrected} \times 10^3$ / Ω m^2	
		High flow rate	Low flow rate
AvCarb 1071	**PC**	0.101	0.577
	MeCN	0.0252	0.490
AvCarb 7497	**PC**	0.0671	0.453
	MeCN	0.0206	0.174
Freudenberg H23	**PC**	0.214	(2.49 at 7.1 mA cm^{-2})
	MeCN	0.0651	(1.15 at 15.3 mA cm^{-2})
AvCarb MGL370	**PC**	0.148	0.655
	MeCN	0.0512	0.698

The following discussion attempts to intimately tie microstructural properties and performance together. To clarify, a good 'performance' attributed to a system refers to a lower potential associated with a given current density (in this case 25 mA cm^{-2}, i.e. the lower the ASR_{25} the higher the performance). ASR_{25} demonstrates, again, that carbon cloths outperform the other tested electrodes in equivalent environments, in line with observation in previous literature.[19,46] Some authors have rationalised these findings by showing that electrodes with low inter-pore connectivity present uneven flow distributions due to the electrolyte flowing only through preferred paths.[19,39,53]

To recap, overarching observations, deduced from electrochemical polarisation data (Figure 3.10 and Table 3.5), are two-fold: firstly, overall performance of flow cells using MeCN is superior compared with PC in almost every operating condition (with the exception of AvCarb MGL370 with a characteristic flow rate of 0.5 cm s^{-1} in PC at some current densities – see Figure A3.18). This is attributed to the lower electrolyte viscosity resulting in higher species diffusivity associated with using MeCN instead of PC. Secondly, with increased flow velocity there is an increase in performance. This characteristic has been carefully separated into distinct

transport phenomena: ‘intra-pore’ transport – associated with a reduction in the size of the BL and the ease with which active species are brought to / leave the surface, and ‘inter-pore’ transport – associated with the formation of reactant starved regions in the electrode and replenishment to these regions via a convective flow. Together, these high-level observations start to account for mass-transport shortcomings in the cell.

Looking to other microstructural properties, such as VSSA, tortuosity and porosity (Table 3.3), a notable lack in correlation to performance can be found (see Figure A3.19). Firstly, in comparing the calculated VSSA with cell performance, it is reasonable to assume that a higher VSSA would lead to higher performance, since the electrode would contain more available reaction sites for the electrochemical reaction to take place. However, the results show an inverse correlation between the VSSA and cell performance (ASR_{25}) for the AvCarb 7497 and Freudenberg H23. This does not necessarily imply that a higher VSSA causes a lower performance, rather, the VSSA is either not involved in a limiting process, or that the VSSA calculated from XCT images may not provide a good indication of the actual active surface area reached by the active species.[6,39] While the VSSA obtained from XCT images provides a fair estimation of the total active surface area available, the inter-pore connectivity and the ease with which an active species can reach those reaction sites is more important. Additionally, given the precision (and magnitude) of these values, these VSSAs may be within error of one another. Secondly, when analysing the tortuosity factor, no conclusive correlation between any of the three, spatial directions and the ASR_{25} is observed. For example, AvCarb MGL370 shows a significantly higher value compared to the other electrodes, but its performance is only marginally better than Freudenberg H23, whilst Freudenberg H23 and AvCarb 7497 present a very similar tortuosity factor but differ greatly in terms of performance. This can be rationalised by first considering inter-pore mass transport processes as a joint contribution from a diffusive and a convective flow. The discrepancy between tortuosity factor and performance could be attributed to the way tortuosity is calculated, considering only steady-state diffusive flux between fixed concentration boundaries.[23] It is asserted that for RFBs, in particular those using FTFFs, the most influential factor for species transport through porous electrodes is the convective flow, which is why no correlation between tortuosity and performance is observed. Tortuosity correlations might be expected at the lower flow rates tested in this work (where diffusive flux makes up a greater share of the overall transport character); however, for all flow rates tested in this work, the ASR follows the same trend: AvCarb 7497 displays the best performance, followed by AvCarb 1071, AvCarb MGL370, and lastly Freudenberg H23. This

shows that, even at relatively low flow velocities, a convective flow is dominant over a diffusive one in the direction of the flow ('in-plane' direction). With this in mind, it is expected that repeating these experiments, using a flow-by flow field, would allow us to observe some correlations between tortuosity in the 'through-plane' direction of the electrode thickness and performance, since the predominant transport process could be diffusion especially at low flow rates and with more viscous solvents. That said, it has been shown in VRFB systems that the dominant transport process may be convection driven by the pressure difference between neighbouring channels when using a flow-by flow field.[54,55] Finally, there seems to be no strict correlation between porosities of the electrodes and their electrochemical performance (ASR_{25}). Although, in broad terms, the cloths present higher porosities than the papers, the cloth with highest porosity is not the best performing electrode. Instead, a correlation is observed between PSD and ASR_{25}: AvCarb 7497 presents the largest pores, shown as a longer tail in the PSD (Figure 3.7), followed by AvCarb 1071, AvCarb MGL370 and Freudenberg H23. These results align with analysis from previous authors, which state that a combination of larger pore size and fibre alignment, along with a high permeability, leads to a better performance in carbon electrodes.[16,19]

So far, no quantitative microstructural property has correlated with performance, only PSD has qualitatively correlated with ASR_{25}. However, taken together, the permeabilities reported in Table 3.4 and the calculated ASR_{25} values in Table 3.5 provide the clearest relationship between microstructure and performance in this work. The two carbon cloths have the lowest values for ASR_{25} and significantly higher permeabilities than the other carbon electrodes, which falls in line with the work by El-kharouf et al.[47] The trend is followed at the low performance end, too – Freudenberg H23 presents the worst performance (high ASR_{25}) and the lowest permeability, where, at low flow rate, a current density of 25 mA cm^{-2} is not reached. Figure 3.12 shows the iR-corrected ASR calculated at a current density of 25 mA cm^{-2} plotted against permeability and is used as a metric for standardising the comparison between cell performance in each environment, namely four carbon electrodes, four flow rates and two solvents.

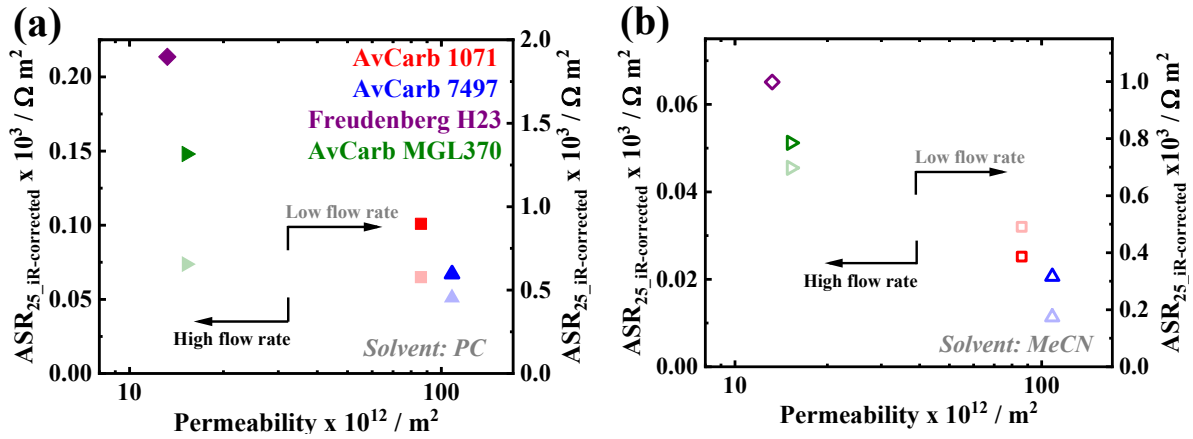


Figure 3.12: Graph showing correlation between the ability for the electrode to reach high current density and with low overpotential (ASR_{25}) as a function of the calculated permeability at the highest and lowest flow rates in: (a) PC- of (b) MeCN-based electrolyte. ASR_{25} indicated the area specific resistance calculated at a current density of 25 mA cm^{-2} using the 1D fitted model simulations. At low flow rate, Freudenberg H23 did not reach 25 mA cm^{-2} in either solvent because the cell cut-off voltage was reached first, these points are therefore omitted.

This inverse correlation between the ASR_{25} and the electrode permeability shows that the inter-pore connectivity, quantised via the permeability, directly affects this cell's performance metric. As previously stated, the higher level of connectivity and permeability in the woven cloths is given by their ordered weave structure and thus promotes a more uniform distribution of electrolyte across the whole electrode.[19,39,49,56,57] Visual detail of microstructural configuration with respect to the alignment of fibres in the electrodes is shown in Figure 3.6. Since the electrode permeability is a measure of the ease offered to a convective flow by the porous material, it is fair to conclude, as in previous literature,[16] that a material with high permeability enables an enhanced convective flow and, therefore, a better performance. This is indeed what we observe, as shown in Figure 3.12.

Finally, when considering flow battery operation, pumping rates, power assessments and efficiencies must be taken into account. This analysis is carried out in the appendix (Figure A3.20).

3.3.4 Mass-transfer coefficients

To compare the pore-level mass-transfer effects displayed by the four carbon electrodes at different operating conditions, the corresponding mass-transfer coefficients (k_m) were calculated and compared as a function of the mean linear (interstitial) velocities, ($v = Q/l_{ed}w_{ed}\varepsilon_{ed}$)), defined as the ratio of the flow rate to the cross-sectional area for flow in the in-plane direction.[14,15,58] The XCT imaging analyses of the compressed electrodes (Figure 3.6) were used to obtain the electrode porosity values (ε_{ed}) for computing the velocity of the

electrolyte in the pore-phase.[58,59] Development of the 1D model and fitting the experimental data was carried out by Dr. Catalina Pino-Muñoz using the 1D model in order to extract the mass-transfer coefficients for each cell polarisation step in each variation of experimental operating conditions—i.e., (two) supporting solvents, (four) carbon electrodes and (four) flow rates.[1]

The electrode microstructural features obtained from the XCT image analysis—porosity, tortuosity and VSSA—were used as model parameters (Table 3.3). Reaction rate constants (k) for each of the solvent environments, using the four different electrodes, were obtained by taking into account R_{CT} (see Table A3.7 in appendix for these resistance values) and the electrolyte tank concentration.[19] The range of calculated values for reaction rate constants were between 1.5×10^{-4} – 1.3×10^{-3} m s^{-1} using MeCN and between 3.8×10^{-5} – 9.4×10^{-5} m s^{-1} using PC, which were slightly larger than the ones reported by Forner-Cuenca et al.[19] The rate constants serve as coarse estimations that were based on the fitted values of charge-transfer resistances from the selected ECM and calculated using Equation (3.15).[19]

$$k = \frac{j_0}{nFC} = \frac{RT}{(nF)^2 C R_{\mathrm{CT}}} \qquad (3.15)$$

Diffusivity values for TEMPO species dissolved in PC and MeCN were measured and used as model parameters (Table 3.1). Diffusivity of BF_4^- and TEA^+ were estimated from literature as 0.464×10^{-9} and 0.261×10^{-9} m^2 s^{-1} when using PC,[60] respectively; and 11.5×10^{-9} and 6.20×10^{-9} m^2 s^{-1} when using MeCN,[61] respectively. The conductivity of the carbon electrodes is expected to be considerably higher than the conductivity of electrolytes and separator and is assumed to be high enough so that resistance to electron transport across the porous electrode is negligible.[11,39,44,56,62–64] Additionally, the HFR previously obtained was used to estimate a reference value of separator conductivity (σ_m), which was in the range of 0.73 – 0.95 S m^{-1} and 0.070 – 0.27 S m^{-1} for experiments using MeCN and PC, respectively. The measured HFR includes the resistance contribution of many components including contact resistances between the different cell components and electrolyte resistance; however, the contribution of the separator is expected to dominate, therefore providing a good approximation of the separator conductivity. All the values referred to here are used in the model and are summarised in Table A3.8 in the appendix. A reasonably good fitting of the model to the polarisation data was observed (RMSE ranging from 1.7 – 5.5 mV) and all the model fits alongside the experimental

data can be found in the appendix (Figure A3.18). To demonstrate the capability of the developed 1D model, visualisations of the concentration distribution of species, the overpotential and the ionic current density is exemplified for AvCarb 7497 in the appendix (Figure A3.21).

Following extraction of mass-transfer coefficients (Table A3.9), an electrode performance factor ($A^{V}{}_{F}k_{m}$, s^{-1}), given by the product of the electrode VSSA and the mass-transfer coefficient, as a function of the mean linear flow velocity (v, m s^{-1}) was used to compare the mass transport characteristic of each carbon electrode / solvent couple (all tabulated in Table A3.9). An empirical power law, $A^{V}{}_{F}k_{m} = b\mathrm{v}^{m}$, is commonly used to characterise the carbon electrodes where b and m are empirical (dimensionless) constants.[15,59,65] This correlation can be expressed in terms of relevant dimensionless numbers, such as the Reynolds (Re) and Sherwood (Sh), which are defined in Equations (3.16) and (3.17).

$$\mathrm{Re} = \frac{\rho_{e}\mathrm{v}d_{f}}{\mu_{e}} \qquad (3.16)$$

$$\mathrm{Sh} = \frac{k_{m}d_{f}}{D} \qquad (3.17)$$

Where d_f is the mean fibre diameter (m). These dimensionless numbers can also be related one to another by a power law, $\mathrm{Sh} = a\mathrm{Re}^{m}$, where a is another empirical (dimensionless) constant.[9,15,59,66] Sh represents the ratio of convective to diffusive mass transport, while Re represents the ratio of inertial to viscous forces within the electrolyte moving throughout the porous matrix.[41] A correlation between Re and Sh is established here to analyse the interplay between the transport processes occurring within the pores. The mean fibre diameter (d_f, Table 3.3) was selected as the characteristic length scale for the carbon electrodes to evaluate the Re numbers. The mean diffusivities for $TEMPO^{\bullet}/TEMPO^{+}$ in each solvent (Table 3.1) were calculated to be 3.38×10^{-10} in PC and 1.71×10^{-9} m^2 s^{-1} (in MeCN) and were used to evaluate the Sh numbers. Figure 3.13 (a) and (b) present the correlation between the electrode performance factor ($A^{V}{}_{F}k_{m}$) and the mean linear velocity (v) for the two solvent environments tested, and Figure 3.13 (c) shows the dimensionless mass-transfer correlations (Sh – Re). Table 3.6 summarises the relevant value ranges for parameters and dimensionless numbers. Power law values were found to be in the range of 0.90 – 1.64 and 0.69 – 1.76 when using PC and MeCN, respectively (Figure 3.13). Tenny et al. obtained power laws (Sh – Pe) using some of

the same cloths tested in this work, namely AvCarb 1071 and AvCarb 7497, and reported power law values of 0.91 and 0.66, respectively;[6] however, the authors obtained their mass-transfer coefficients experimentally and at higher electrode compressions (c.a. 30 %) – as compared to the numerical approaches in this study and lower cell compressions—while power laws were computed based on characteristic velocities and averaged effective diffusivities. This work has alternatively implemented the mean linear velocity and averaged diffusivities for obtaining the power laws (Sh – Re), since it was judged that these parameters better represent convective mass-transfer at the pore-level, aligning with works reported by other authors and the general BL theory for mass-transfer.[14,59,66,67] Importantly, using equations from previous works,[68,69] the size of the BL is calculated to be between 0.198 – 0.54 μm and between 0.621 – 1.72 μm for PC and MeCN, respectively – i.e., significantly smaller than the mean fibre diameter and pore diameter in all cases. Mass-transfer coefficients, and consequently Sh numbers, experience more sensitivity with respect to velocity for cloths at the experimental conditions tested (Figure 3.13), increasing more quickly with the flow rate as compared to the papers. The most sensitive electrode to the change in velocity is AvCarb 7497, which also displays the higher values for the performance factor ($A_{\mathrm{F}}^{\mathrm{v}} k_{\mathrm{m}}$), followed by AvCarb 1071, and then both carbon papers, Freudenberg H23 and AvCarb MGL370. Previous reported power law values for carbon papers and felts are within 0.61 – 1.18,[11,70] showing less sensitivity to velocity that the one obtained here for AvCarb 7497.

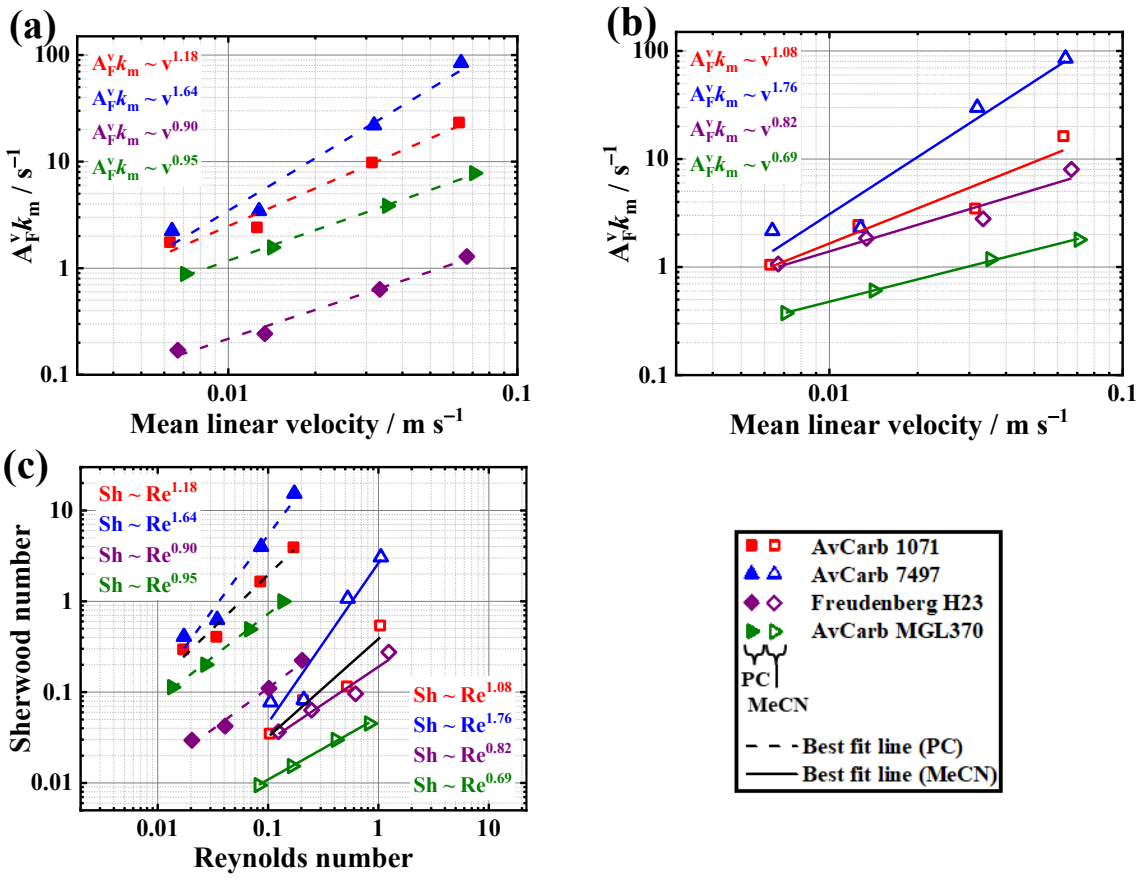


Figure 3.13: Correlation between electrode performance factor and mean linear velocity for electrodes using (a) PC-; or (b) MeCN-based electrolytes. (c) Dimensionless parameter correlations for each electrode in each electrolyte on a logarithmic graph with the Sherwood number plotted as a function of the Reynolds number. Gradients are displayed along their line respective best fit lines.

Table 3.6: Ranges of characteristic dimensionless numbers for electrodes and performance values (3sf).

Parameter	PC	MeCN
$v \times 10^3$ / m s^{-1}	6.28 – 70.9	
$A^{V}_{F}\,k_m$ / s^{-1}	0.170 – 84.5	0.374 – 85.4
Re	0.0135 – 0.204	0.0825 – 1.24
Pe	130 – 1950	25.6 – 385
Sc	9590	311
Sh	0.0295 – 15.4	0.00945 – 3.06

The convective mass-transfer coefficients are commonly considered to be an indicator of the intra-pore mass transport within the electrode pore-phase given by the diffusive transport of species from the bulk of the pores to the electrode active surface. This diffusive flow can be enhanced by an augmented flow velocity: higher flow rates reduce the BL thickness between the bulk electrolyte and surface of the electrode.[52] This concept is consistent with the results obtained for the four electrodes at different flow rates: the value of k_m increases with increasing flow rate, as shown in Figure 3.13 (a) and (b). The maximum performance factors, $A^{V}_{F}k_m$,

achieved are obtained by the carbon cloths in both solvents and the gradient of cloth fits show the higher sensitivity to the change in velocity. Dimensionless correlations between the Sh and Re numbers (Figure 11 (c)), clearly illustrate the effect of solvent viscosity on the Re number. In comparing the Sh number for the two solvents, it is observed that PC achieves comparable values of Sh number as MeCN. Given the Sh is calculated as the ratio between k_m and the electrolyte diffusivity, D – they contribute to Sh in equal part (Equation (3.17)). Barton et al. reported dimensionless correlation (Sh – Sc – Pe) for a Fe^{2+}/Fe^{3+} RFB using an SGL 29AA carbon paper and varying viscosity for different flow field configurations.[9] In that work, the authors display considerable impact on flow characteristics (Pe) due to different flow fields, however, no appreciable difference in mass-transfer features (Sh) due to viscosity were observed.

3.4 Conclusions

In this chapter, the electrolyte and electrode microstructure-performance relationship was investigated in a non-aqueous RFB using a combination matrix of different carbon electrodes and solvents to decipher and elucidate the mass transport processes that occur, and the losses associated with them. A $TEMPO^{\bullet}/TEMPO^{+}$ redox couple and $TEABF_4$ supporting salt were dissolved in two solvents (PC and MeCN) resulting in two electrolytes with unique conductivity, density and viscosity properties. The performance of four different commercially available electrodes were tested at a selection of electrolyte flow rates. High-level observations associated with the electrolyte choice include: the use of electrolyte with low viscosity and surface tension (MeCN) results in higher performance; and, within the range of flow velocities used, the expected correlation between flow rate and performance is evident.

With many parameters and variables relevant to this analysis, it is difficult to confidently assert causal relationships between electrode microstructure and performance. It is more probable that a combination of microstructural features and transport properties lead to the variations in electrochemical performance we observe in the results. Microstructural properties of porous media are closely related to the mass transport processes that take place within the cell and we observe mass transport rates to be a useful indicator for electrode performance. Under the forced convective conditions imposed on the cells in this work, it is asserted that the electrode permeability is indicative of performance. In all cases analysed, the system was predominantly dictated by convective flow and so with this assertion it is reasonable to have observed an improved performance for those electrodes with higher permeabilities. Other microstructural

parameters, such as porosity, bear no observable correlation to the performance. VSSA may well provide an accurate representation of the electrodes' volumetric surface area; however, during operation, if only a small proportion of this electrochemically active area is effectively accessed and utilised, the VSSA obtained from image analysis does not serve as a useful indicator of performance.

A 1D model of the separator-electrode-assembly accounting for the properties of the electrode and electrolyte was implemented and fitted to experimental results yielding mass-transfer coefficients, k_m, for each distinct operating condition. These mass-transfer coefficients serve as a useful measure with which to analyse the intra-pore mass-transport limitations associated with active species moving from the bulk to the electrode active surface. It is established that the best performing electrodes also displayed the highest k_m and are therefore believed to have the thinnest boundary layers.

Having analysed many different parameters in the electrode, this chapter identifies key properties in a flow-through configuration that may inform specific electrode design/ choice for a given system. Notwithstanding the alternative route taken, we arrive at a similar conclusion as previous authors investigating electrode morphologies: the best system performances are those observed utilising the cloths demonstrated both by their higher permeability and mass-transfer coefficients. In this particular case, we conclude that AvCarb 7497 shows the most favourable microstructural properties leading to its superior performance, both at higher and lower flow rates due to high inter-pore connectivity and permeability. These properties are a result of the relatively large pore size and the periodic fibre alignment unique to woven materials which promote a more uniform distribution of electrolyte across the electrode. However, we also acknowledge the changes in electrode compression and accessible surface area can influence electrochemical and fluid dynamic outcomes in unknown ways.

With respect to the questions presented in Chapter 1, this chapter investigated how the microstructure of the electrodes tested affects the performance of a zero-gap symmetric RFB. Further, this work confirms and discusses intuitive deductions about advantageous electrolyte properties associated with convective flow through porous media. Permeability is found to be the most strongly correlating parameter with the RFB performance metric chosen. Some questions arise from this work such as:

- How robust is this correlation and could the performance of porous electrode materials be deduced just from imaging and pressure drop calculations?
    - With what accuracy?
    - Can these be simulated by stitching together REVs of a given electrode?
- How far reaching are these findings – will they hold for different compressions / geometry / solvents / microstructures / temperatures?
- What does an 'ideal' electrode look like?
- At what point does permeability improvement have diminishing returns from a performance perspective?
- Can we assume that compression is bad for permeability and therefore performance?

3.5 Appendix

3.5.1 Species diffusivity calculation

Figure A3.14 shows the current responses with varied voltage on a UME. These experiments were completed to measure the diffusivity of the electrolyte using each supporting solvent, where positive currents represent reduction. The diffusivity of each TEMPO species was calculated using Equation (3.1).

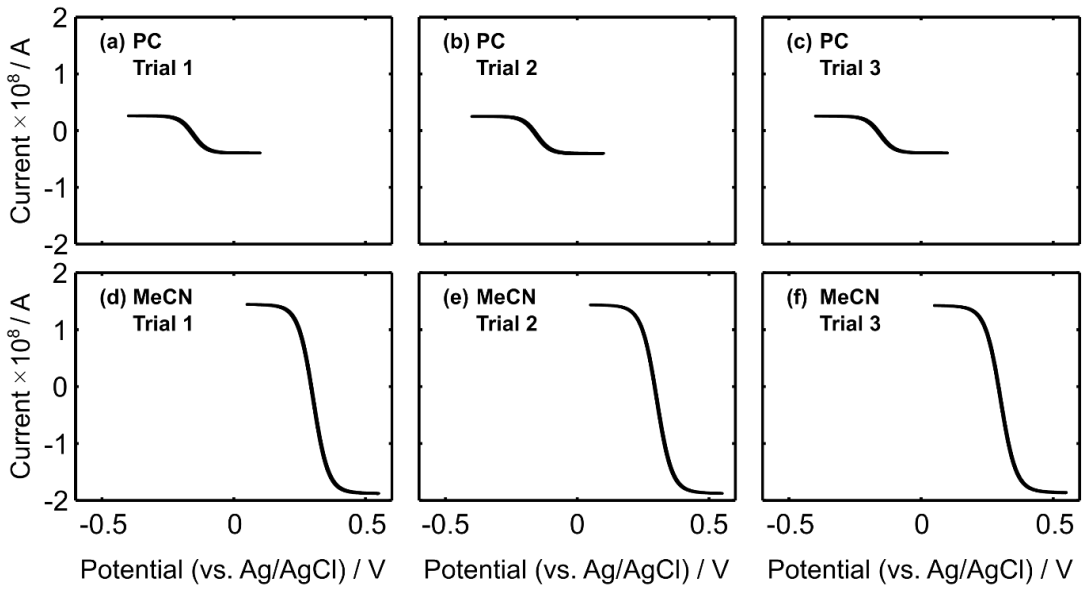


Figure A3.14: The UME CVs for trials 1-3 for the (a-c) PC- and (d-f) MeCN-based electrolytes. For all CVs, a 10 mV s^{-1} was used under quiescent conditions with a 10 µm diameter Pt UME, a Pt mesh counter electrode, and a Ag/AgCl reference electrode.

3.5.2 SEM-EDX fluorine absence confirmation

This figure shows there is no perfluorinated binder in AvCarb MGL370. This is important because, during image capture using XCT, perflourinated binders, such as PTFE, are indistinguishable from the 'active' carbon fibres. There is not any perfluorinated binder in AvCarb MGL370, and, therefore, all the surface captured by the XCT image is active and available for electrochemical reaction.

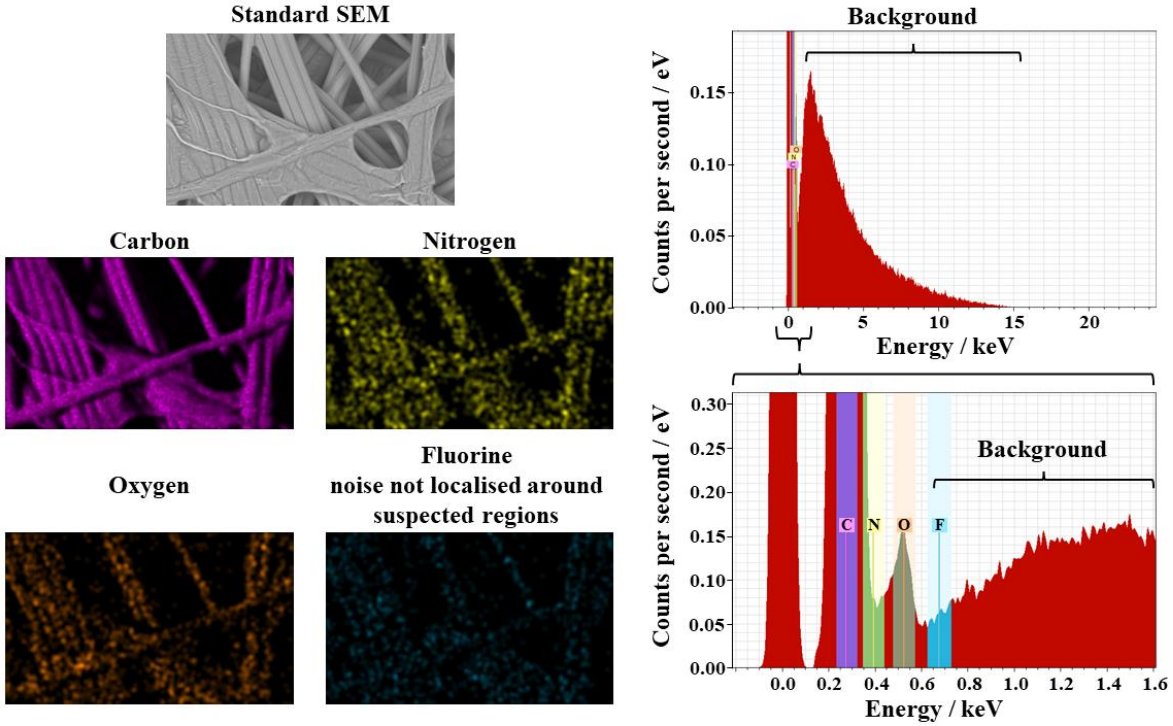


Figure A3.15: Scanning electron microscopy coupled with energy dispersive X-Ray spectroscopy, showing no fluorinated croups in AvCarb MGL370 matrix.

3.5.3 Resistance contributions to polarisation measurements

This figure shows how the individual iR-corrected and ohmic potentials contribute to the overall cell potential at various flow rates when using acetonitrile (MeCN) as the solvent.

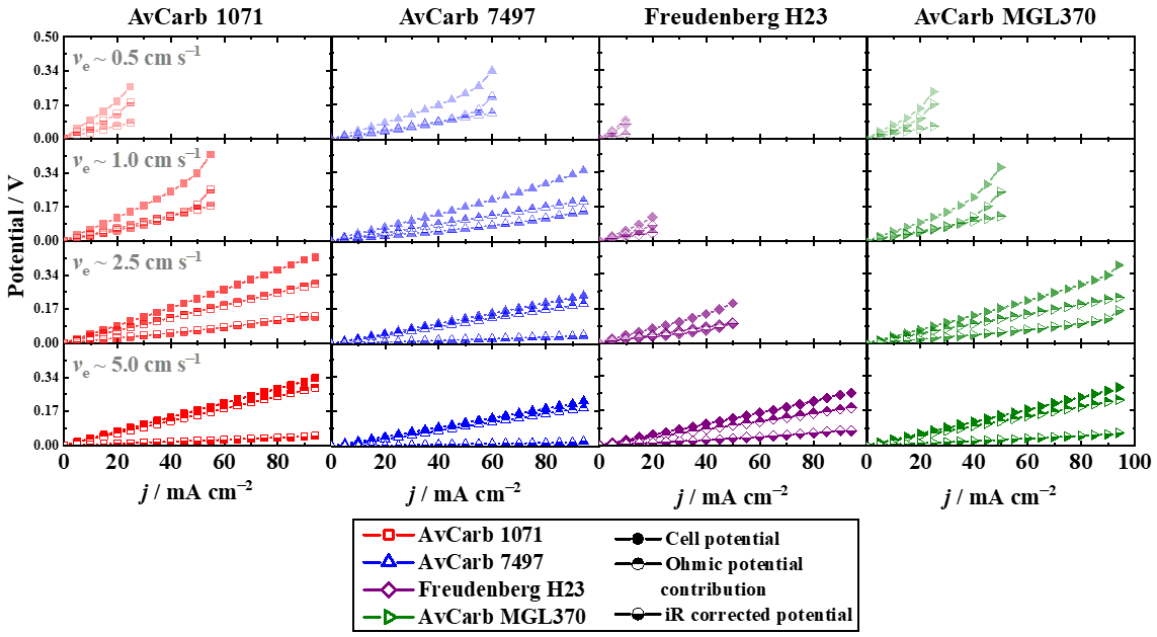


Figure A3.16: Separation of ohmic potential contribution from the cell potential leaving the iR-corrected potential illustrating the effect of flow rate on relative ohmic / HFR vs. charge / mass-transfer resistances in MeCN for each electrode (a-d).

3.5.4 Complete EIS data and ECM fitting

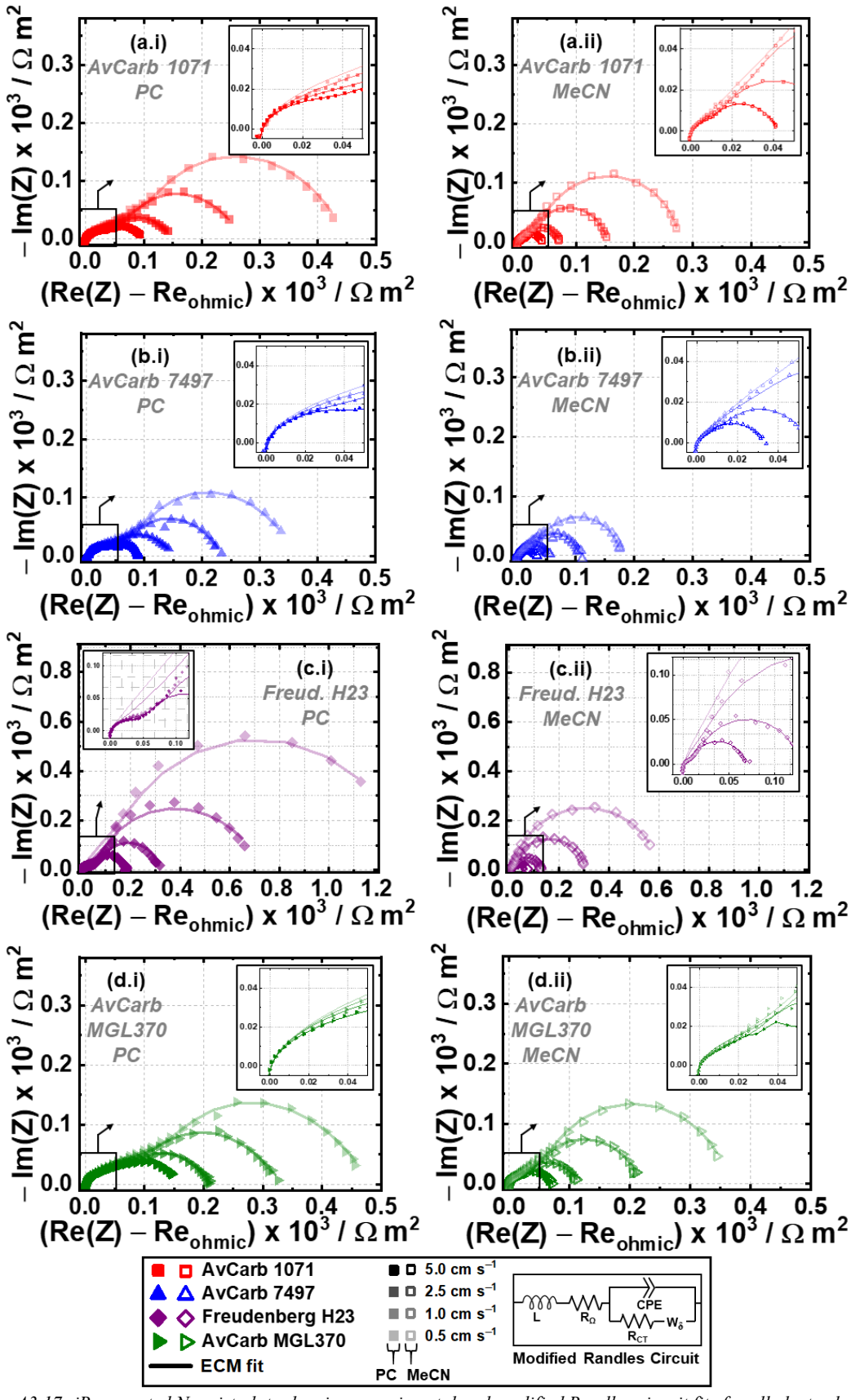


Figure A3.17: iR corrected Nyquist plots showing experimental and modified Randles circuit fits for all electrodes (a-d) tested at each velocity in (i) PC- or (ii) MeCN-based electrolyte.

3.5.5 ECM fittings and EIS results

Table A3.7: Experimental high frequency resistances and all electrochemical impedance spectroscopy equivalent circuit model parameters for four electrodes, at four flow rates in two different electrolytes (= dimensionless).*

Electrode	Solvent	Characteristic velocity / cm s^{-1}	L × 10^{-6} / H	Ohmic resistance × 10^3 / Ω m^2		Q / F $s^{(a-1)}$	a / *	CT resistance × 10^3 / Ω m^2	MT resistance × 10^3 / Ω m^2	T / s	χ^2 × 10^{-3} / *
				Exp.	Model						
AvCarb 1071	PC	5.0	1.928	1.75	1.75	0.500	0.418	0.0957	0.0213	0.185	0.853
		2.5	1.937	1.76	1.76	0.344	0.481	0.0846	0.0749	0.399	1.44
		1.0	1.919	1.78	1.77	0.375	0.461	0.931	0.207	0.850	5.71
		0.5	1.925	1.78	1.78	0.228	0.562	0.912	0.360	2.54	6.16
	MeCN	5.0	1.662	0.180	0.177	0.552	0.567	0.0148	0.0308	0.187	0.170
		2.5	1.649	0.185	0.182	0.465	0.614	0.0152	0.0599	0.388	0.140
		1.0	1.665	0.186	0.184	0.277	0.692	0.0128	0.142	1.27	0.823
		0.5	1.666	0.187	0.185	0.167	0.713	0.00576	0.274	3.12	2.00
AvCarb 7497	PC	5.0	1.77	2.51	2.50	0.274	0.472	0.0821	0.0215	0.160	0.664
		2.5	1.77	2.48	2.48	0.226	0.514	0.0297	0.0594	0.346	0.541
		1.0	1.78	2.50	2.49	0.262	0.499	0.0989	0.147	0.783	6.67
		0.5	1.799	2.50	2.49	0.241	0.524	0.0993	0.274	1.78	8.03
	MeCN	5.0	1.858	0.209	0.207	1.15	0.522	0.0223	0.0150	0.0436	0.176
		2.5	1.870	0.208	0.205	0.854	0.526	0.0146	0.0450	0.124	0.444
		1.0	1.852	0.209	0.207	0.646	0.636	0.0298	0.0830	0.454	1.15
		0.5	1.861	0.210	0.209	0.507	0.714	0.0376	0.145	1.43	1.72
Freud. H23	PC	5.0	1.815	1.79	1.79	0.138	0.580	0.0515	0.137	0.834	3.34
		2.5	1.808	1.79	1.79	0.0471	0.714	0.0388	0.277	2.10	15.3
		1.0	1.839	1.79	1.79	0.0652	0.657	0.0313	0.650	5.75	59.2
		0.5	1.819	1.80	1.80	0.242	0.759	0.0181	1.30	10.4	289
	MeCN	5.0	2.095	0.196	0.193	0.261	0.594	0.00605	0.0647	0.399	0.504
		2.5	2.086	0.198	0.196	0.253	0.670	0.00371	0.125	0.879	2.46
		1.0	2.072	0.200	0.201	0.500	0.817	0.00324	0.303	1.80	11.6
		0.5	2.079	0.201	0.203	0.672	0.853	0.00457	0.597	3.00	17.7
AvCarb MGL370	PC	5.0	1.961	0.650	0.642	0.195	0.507	0.113	0.0560	0.103	0.538
		2.5	1.962	0.651	0.642	0.207	0.503	0.136	0.0899	0.221	1.16
		1.0	1.916	0.665	0.658	0.198	0.522	0.156	0.184	0.659	7.13
		0.5	1.940	0.661	0.654	0.197	0.531	0.169	0.323	1.54	7.09
	MeCN	5.0	1.717	0.237	0.234	0.443	0.560	0.0305	0.0455	0.200	0.361
		2.5	1.736	0.237	0.233	0.467	0.564	0.0379	0.0828	0.582	0.951
		1.0	1.726	0.240	0.237	0.389	0.621	0.0408	0.181	1.93	4.44
		0.5	1.707	0.242	0.239	0.326	0.641	0.0351	0.334	4.63	4.37

3.5.6 1D model parameters

The following tables outlines ("include other tables omitted from main text?" and) the numerical values used for the 1D model.

Table A3.8: 1D continuum model parameters.

Parameter	Solvent	AvCarb 1071	AvCarb 7497	Freudenberg H23	AvCarb MGL370
$k \times 10^4$ / m s^{-1}	PC	0.632 ± 0.090	0.613 ± 0.100	0.940 ± 0.030	0.379 ± 0.050
	MeCN	5.19 ± 2.00	2.71 ± 1.00	13.0 ± 3.0	1.51 ± 0.20
σ_m / S m^{-1}	PC	0.0989 ± 0.0008	0.0701 ± 0.0003	0.0975 ± 0.0001	0.266 ± 0.003
	MeCN	0.949 ± 0.020	0.837 ± 0.003	0.881 ± 0.010	0.732 ± 0.007
$D_{TEMPO^{\cdot}}$ × 10^{-9} / m^2 s^{-1}	PC	0.411 ± 0.003			
	MeCN	1.940 ± 0.005			
D_{TEMPO^+} × 10^{-9} / m^2 s^{-1}	PC	0.265 ± 0.003			
	MeCN	1.490 ±0.006			
Electrode thickness / µm	--	267	490	147	335
VSSA / m^2 m^{-3}	--	154000	143000	168000	143000
Porosity	--	79.6	78.3	74.8	70.5
Tortuosity	--	1.195	1.265	1.225	1.410

3.5.7 Polarisation results – experimental and model fit

This figure shows a complete set of all the expeimental polarisation and corresponding 1D model fits tested at each flow velocity in each solvent – 'colour sorted' by electrode.

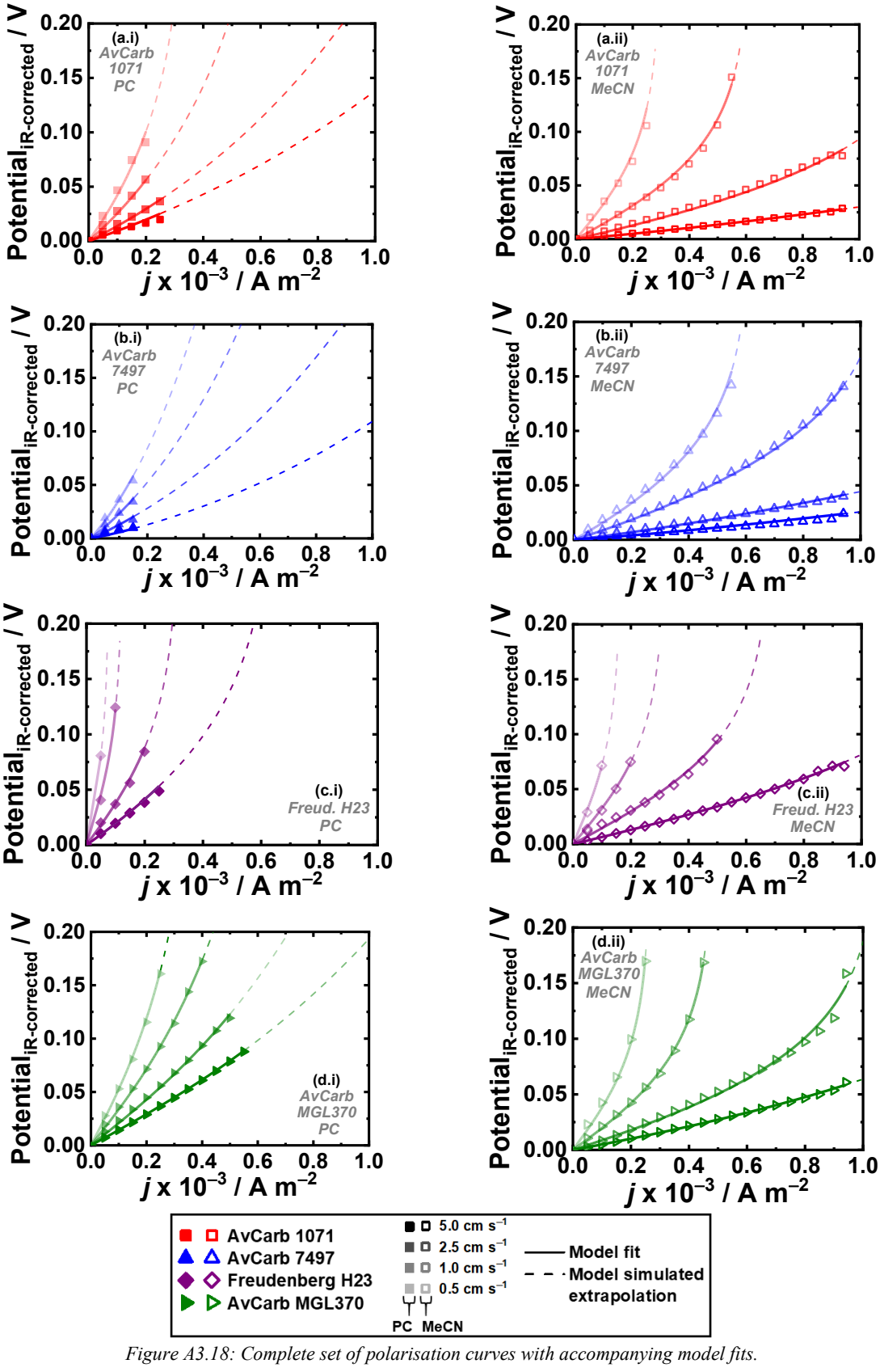


Figure A3.18: Complete set of polarisation curves with accompanying model fits.

3.5.8 Polarisation results and 1D model fitting

The following table displays some of the calculated parameters used to fit the 1D model to the experimental polarisation curves.

Table A3.9: Summary of results of 1D continuum model after fitting to galvanostatic polarisation data (3sf).

Electrode	Characteristic velocity / cm s^{-1}	Mean linear flow velocity / cm s^{-1}	PC				MeCN			
			σ_m / S m^{-1}	$k_m \times 10^6$ / m s^{-1}	N_{pol}	RMSE / mV	σ_m / S m^{-1}	$k_m \times 10^6$ / m s^{-1}	N_{pol}	RMSE / mV
1071	0.5	0.628	0.102	11.4	4	3.67	1.00	6.81	5	3.34
	1.0	1.26		15.7	4			15.9	11	
	2.5	3.14		63.7	5			22.6	19	
	5.0	6.28		151	5			106	19	
7497	0.5	0.639	0.0718	15.7	3	2.25	0.827	15.2	11	5.49
	1.0	1.28		24.1	3			16.1	19	
	2.5	3.19		154	3			210	19	
	5.0	6.39		591	3			597	19	
H23	0.5	0.668	0.101	1.01	1	2.70	0.885	6.35	2	1.80
	1.0	1.34		1.44	2			11.0	4	
	2.5	3.34		3.77	4			16.6	10	
	5.0	6.68		7.66	5			47.7	19	
MGL370	0.5	0.709	0.291	6.19	6	1.68	0.770	2.62	5	2.95
	1.0	1.42		10.9	8			4.24	9	
	2.5	3.55		26.9	10			8.26	19	
	5.0	7.09		54.5	11			12.5	19	

3.5.9 Correlating microstructural properties with performance metrics

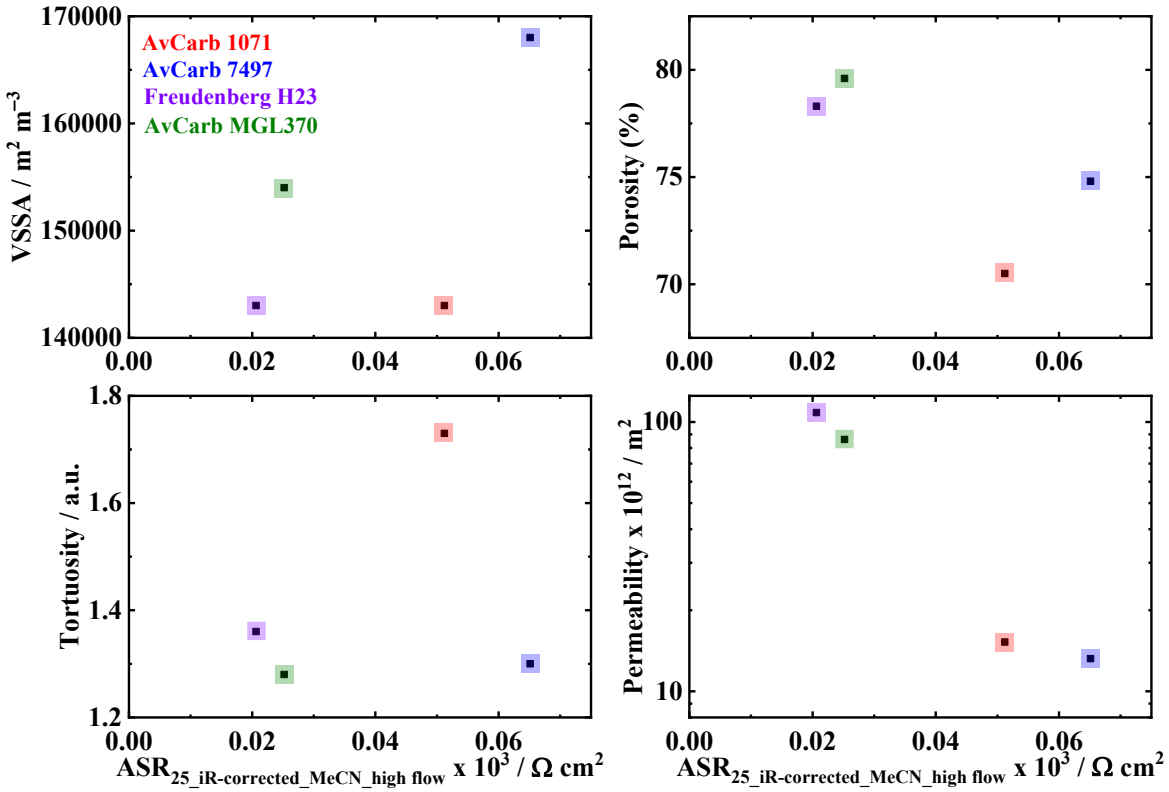


Figure A3.19: Plots showing a lack of correlation between several commonly used microstructural properties: (a) volume-specific surface area, (b) porosity and, (c) tortuosity. (d) shows the positive correlation between permeability and ASR_{25} relealing its importance relative to the other microstructural properties. The performance metric used here was recorded in a high-flow (5.0 cm s^{-1}) zero-gap flow-through RFB using MeCN as the supportiong solvent.

Figure A3.19 is shown here for completeness. It demonstrates that no other, standard, microstructural parameter correlates well with the performance metric chosen in this work. Clearly, the ASR_{25} was measured under a specific operational environment (using MeCN as the supporting solvent and flowing electrolyte though the cell at the highest flow rate tested – 5.0 cm s^{-1}). The scale bars for each of the sub-plots in this figure also highlight that, the absolute values do not change very much for the non-permeability microstructural properties. Permeability is shown to correlate best with the chosen metric.

3.5.10 Electrical and pumping power assessment

On inspection of the ratio between pumping power (input) and electrical power (output) at a potential of 25 mV, as a function of characteristic velocity, it is observed that as the flow rate increases there are diminishing returns in performance. Figure A3.20 illustrates the proportion of power spent on moving the electrolyte through the electrodes in each solvent as a function of the characteristic flow velocity. These data were gathered using the fitted polarisation dataset

and ΔP was taken from the PNM calculations. The electrical power was calculated at 25 mV and the pumping power calculated via the following Equation (A3.18):

$$P_{\text{pump}} = \Delta P \times \frac{Q}{\epsilon_{\text{pump}}} \qquad (A3.18)$$

Where P_{pump} is the pumping power (W), ΔP is the pressure drop (Pa), Q is the volumetric flow rate (m^3 s^{-1}) and ϵ_{pump} is the pump efficiency (dimensionless). The pump efficiency varies widely in literature, for the purposes of this analysis, ϵ_{pump} is assumed to be 75 %.[71–73]

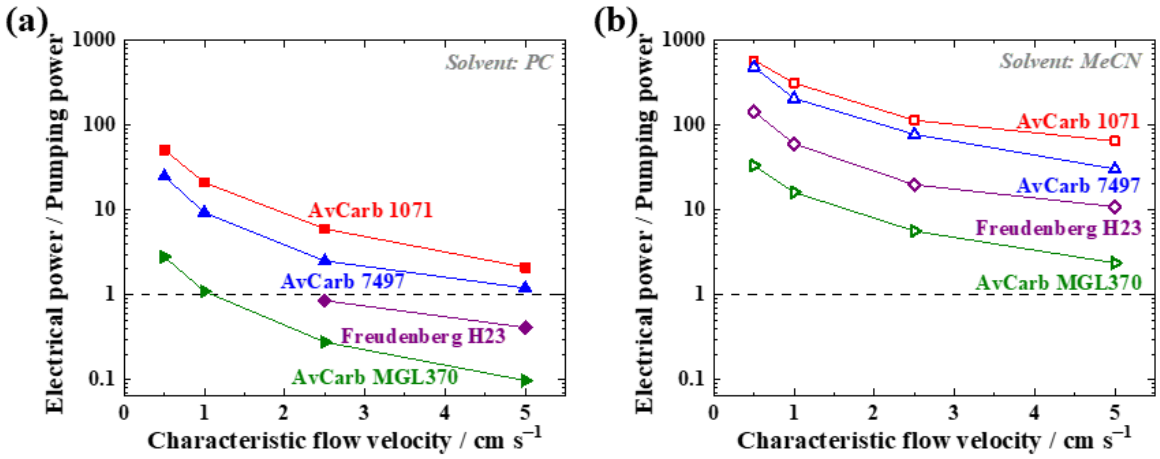


Figure A3.20: The ratio of input pumping power to output electrical power at a calculated 0.025 V iR-corrected potential (during polarisation), as a function of characteristic flow rate in (a) PC and (b) MeCN (assumes a pump efficiency of 75%). The parity (dotted) line indicates the ratio below which there is no net generated power.[1]

As expected, the position on the vertical axis is strongly influenced by electrolyte viscosity; it is more difficult to move the electrolyte through the electrode and therefore a more significant proportion of power is spent on this demanding process. The relative positions of the electrodes are in line with the trends in other forms of analysis throughout the paper (generally, cloths performing better than the papers). The parity (dotted) line indicates the point at which the input pumping power is equal to the output electrical power. Operation below a ratio of 1 leads to no net generated power and must be avoided. This is the case for Freudenberg H23 and AvCarb MGL 370 (at the higher two flow rates) using ϵ_{pump} = 75 % (Figure A3.20 (a)). The curve's gradient indicates how changing the flow velocity influences the proportion of input power converted to the 'useful' output power. For instance, in MeCN (Figure A3.20 (b)), comparing AvCarb 1071 and AvCarb 7497, increasing the flow velocity from 2.5 to 5.0 cm s^{-1} improves the electrical output to a greater degree in AvCarb 7497 than for AvCarb 1071. This indicates that there may be meaningful improvements in performance with an increased flow for AvCarb 7497 compared to AvCarb 1071. This proportional power / velocity relationship

helpfully compares these systems and would be relevant and scalable to larger systems. This power analysis interestingly highlights both how the electrolyte viscosity affects this power ratio (electrical power / pumping power) with flow rate progression, and how the cloths' advantageous microstructural orientation caters for a greater system efficiency, compared to the carbon papers examined in this work. Forner Cuenca et al. observed a similar trend using a single electrolyte in a previous contribution.[19]

3.5.11 Distribution of concentration, overpotential, and ionic current density

Figure A3.21 presents the calculated concentrations of active species, overpotentials and ionic current densities along the cathode thickness (through-plane, x-coordinate) corresponding to an applied discharge current density of 25 mA cm^{-2}, for the four characteristic velocities tested on AvCarb 7497 cloth using PC and MeCN. During discharge, the reduction reaction occurs at the positive electrode while the oxidation takes place at the negative electrode, and, therefore, a higher concentration for TEMPO$^{\bullet}$ is expected with respect to the concentration of TEMPO^{+}, as shown in Figure A3.21 (a) and (b), respectively. In both plots, the consumption / production of species is localised mostly close to the separator (particularly when PC is used), and, as the flow rate of electrolyte increases, both concentrations tend towards the concentration of TEMPO species in the tank (50 mol m^{-3}) due to the faster replenishment of active species. The concentration profiles are also affected by the diffusive and electrophoretic transport, which are expected to be slower when using PC as supporting solvent due to the lower diffusivity values (Table 3.1) and, therefore, steeper concentration gradients are expected in this case. When comparing the effect of supporting solvent on overpotential profiles, we observe higher values of overpotential with increasingly steep gradients towards the cathode / separator interface ($x = l_{ed}$) when using PC, as opposed to the lower (essentially constant) values of overpotential across the electrode when using MeCN (Figure A3.21 (c)). This demonstrates that when the cell is operating with MeCN, a more even distribution of the reaction rate for the charge-transfer process between TEMPO$^{\bullet}$ and TEMPO^{+} is expected to appear across the carbon electrode. This even reaction rate is also exemplified by the rate of change of the ionic current density, which changes from zero at the current collector / electrode interface ($x = 0$) to 25 mA cm^{-2} at the cathode / separator interface ($x = l_{ed}$), as shown in Figure A3.21 (d). Similar figures have been obtained by previous authors,[42,64] and equivalent profiles for the other carbon electrodes examined in this work are shown in Figure A3.21.

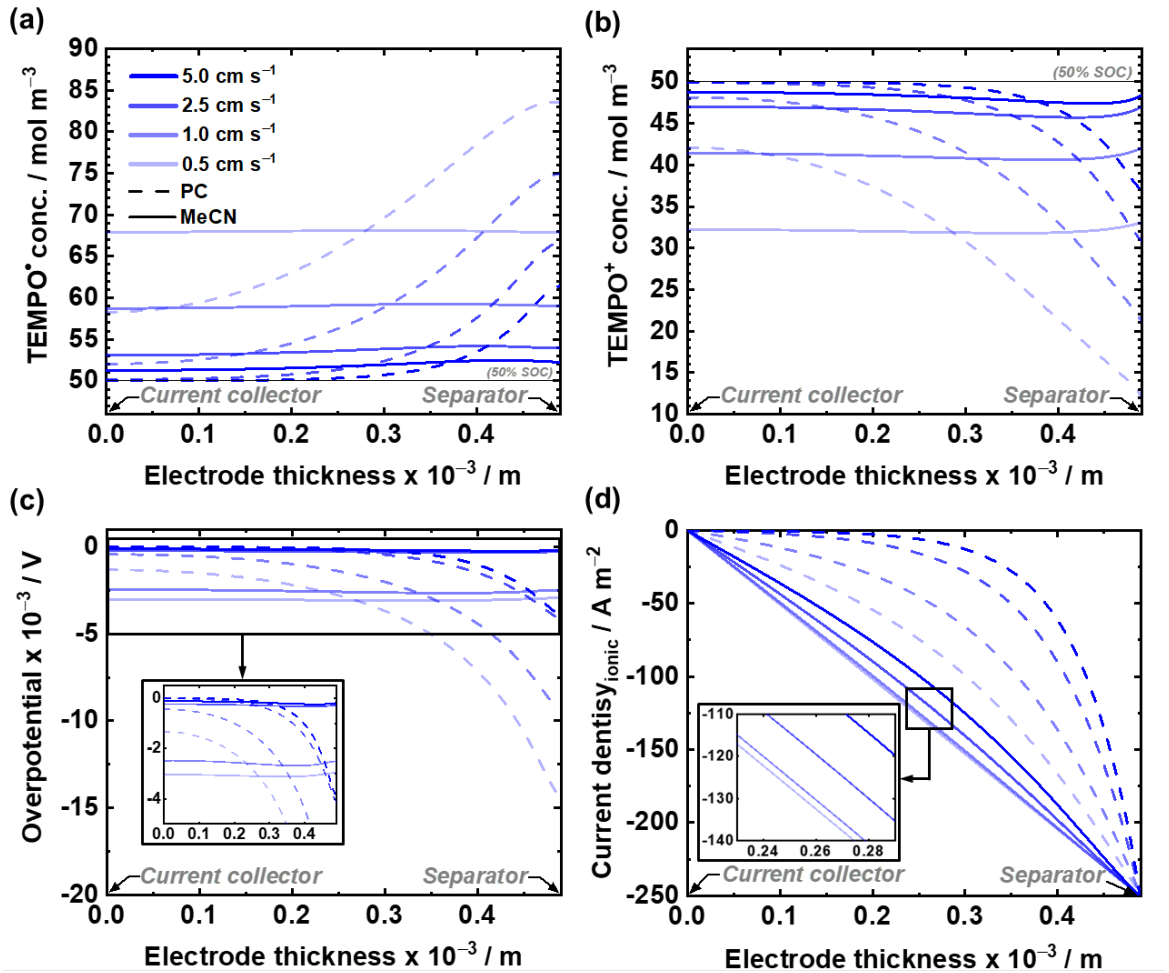


Figure A3.21: Distribution of concentration of (a) TEMPO•, and (b) TEMPO⁺, (c) overpotential, and (d) ionic current density, along the cathode thickness when a discharge current density of 25 mA m^{-2} is applied to AvCarb 7497 carbon cloth in PC- (dashed line) and MeCN-based (solid line) electrolytes and under the four flow velocities tested.

3.6 References

1 B. A. Simon, A. Gayon-Lombardo, C. A. Pino-Muñoz, C. E. Wood, K. M. Tenny, K. V. Greco, S. J. Cooper, A. Forner-Cuenca, F. R. Brushett, A. R. Kucernak and N. P. Brandon, *Appl. Energy*, 2022, **306**, 117678.

2 R. H. Jervis, L. D. Brown, T. P. Neville, J. Millichamp, D. P. Finegan, T. M. M. Heenan, D. J. L. Brett and P. R. Shearing, *J. Phys. D. Appl. Phys.*, 2016, **49**, 434002–434010.

3 R. Jervis, M. D. R. Kok, T. P. Neville, Q. Meyer, L. D. Brown, F. Iacoviello, J. T. Gostick, D. J. L. Brett and P. R. Shearing, *J. Energy Chem.*, 2018, **27**, 1353–1361.

4 M. D. R. Kok, R. Jervis, T. G. Tranter, M. A. Sadeghi, D. J. L. Brett, P. R. Shearing and J. T. Gostick, *Chem. Eng. Sci.*, 2019, **196**, 104–115.

5 B. Tjaden, S. J. Cooper, D. J. L. Brett, D. Kramer and P. R. Shearing, *Curr. Opin. Chem. Eng.*, 2016, 12, 44–51.

6 K. M. Tenny, A. Forner-Cuenca, Y.-M. Chiang and F. R. Brushett, *J. Electrochem. En. Conv. Stor.*, 2020, **17**, 041108-1–13.

7 Y. A. Gandomi, D. S. Aaron, J. R. Houser, M. C. Daugherty, J. T. Clement, A. M. Pezeshki, T. Y. Ertugrul, D. P. Moseley and M. M. Mench, *J. Electrochem. Soc.*, 2018, **165**, A970–A1010.

8 A. Forner-Cuenca and F. R. Brushett, *Curr. Opin. Electrochem.*, 2019, **18**, 113–122.
9 J. L. Barton, J. D. Milshtein, J. J. Hinricher and F. R. Brushett, *J. Power Sources*, 2018, **399**, 133–143.
10 X. L. Zhou, T. S. Zhao, L. An, Y. K. Zeng and L. Wei, *J. Power Sources*, 2017, **339**, 1–12.
11 J. D. Milshtein, K. M. Tenny, J. L. Barton, J. Drake, R. M. Darling and F. R. Brushett, *J. Electrochem. Soc.*, 2017, **164**, E3265–E3275.
12 S. Middleman, *An Introduction to Mass and Heat Transfer: Principles of Analysis and Design*, Wiley, 1997.
13 Q. Xu and T. S. Zhao, *Phys. Chem. Chem. Phys.*, 2013, **15**, 10841–10848.
14 L. F. Arenas, C. Ponce de León and F. C. Walsh, *Electrochim. Acta*, 2016, **221**, 154–166.
15 L. F. Arenas, C. Ponce de León and F. C. Walsh, *J. Energy Storage*, 2017, **11**, 119–153.
16 M. A. Sadeghi, M. Aganou, M. D. R. Kok, M. Aghighi, G. Merle, J. Barralet and J. T. Gostick, *J. Electrochem. Soc.*, 2019, **166**, A2121–A2130.
17 S. Kench and S. J. Cooper, *Nat. Mach. Intell. 2021 34*, 2021, **3**, 299–305.
18 A. Gayon-Lombardo, L. Mosser, N. P. Brandon and S. J. Cooper, *npj Comput. Mater.*, 2020, **6**, 1–11.
19 A. Forner-Cuenca, E. E. Penn, A. M. Oliveira and F. R. Brushett, *J. Electrochem. Soc.*, 2019, **166**, 2230–2241.
20 C. T.-C. Wan, R. R. Jacquemond, Y.-M. Chiang, K. Nijmeijer, F. R. Brushett and A. Forner-Cuenca, *Adv. Mater.*, 2021, **33**, 2006716.
21 T. Suga, Y.-J. Pu, K. Oyaizu and H. Nishide, *Bull. Chem. Soc. Jpn.*, 2004, **77**, 2203–2204.
22 L. Marx and B. Schoïlhorn, *New J. Chem.*, 2006, **30**, 430–434.
23 S. J. Cooper, A. Bertei, P. R. Shearing, J. A. Kilner and N. P. Brandon, *SoftwareX*, 2016, **5**, 203–210.
24 N. G. Connelly and W. E. Geiger, *Chem. Rev.*, 1996, **96**, 877–910.
25 M. B. Moressi and H. Fernández, *J. Electroanal. Chem.*, 1994, **369**, 153–159.
26 Sigma-Aldrich - MSDS - 271004, https://www.sigmaaldrich.com/MSDS/MSDS/DisplayMSDSPage.do?country=GB&language=en&productNumber=271004&brand=SIAL&PageToGoToURL=https%3A%2F%2Fwww.sigmaaldrich.com%2Fcatalog%2Fproduct%2Fsial%2F271004%3Flang%3Den, (accessed 15 August 2020).
27 Viscosity, Surface Tension, Specific Density and Molecular Weight of Selected Liquids, https://www.accudynetest.com/visc_table.html#006, (accessed 15 August 2020).
28 Product Page (MGL) - AvCarb, https://www.avcarb.com/product-page-mgl/, (accessed 28 February 2020).
29 Product Page (Fabric) - AvCarb, https://www.avcarb.com/product-page-fabric/, (accessed 28 February 2020).
30 X. Wei, W. Duan, J. Huang, L. Zhang, B. Li, D. Reed, W. Xu, V. Sprenkle and W. Wang, *ACS Energy Lett.*, 2016, **1**, 705–711.
31 X. Wei, L. Li, Q. Luo, Z. Nie, W. Wang, B. Li, G. G. Xia, E. Miller, J. Chambers and Z. Yang, *J. Power Sources*, 2012, **218**, 39–45.
32 J. D. Milshtein, J. L. Barton, R. M. Darling and F. R. Brushett, *J. Power Sources*, 2016, **327**, 151–159.
33 J. D. Milshtein, A. P. Kaur, M. D. Casselman, J. A. Kowalski, S. Modekrutti, P. L. Zhang, N. H. Attanayake, C. F. Elliott, S. R. Parkin, C. Risko, F. R. Brushett and S. A. Odom, *Energy Environ. Sci*, 2016, **9**, 3531.
34 Q. Wang, Z. G. Qu, Z. Y. Jiang and W. W. Yang, *Appl. Energy*, 2018, **220**, 106–116.

35 J. Millichamp, T. J. Mason, T. P. Neville, N. Rajalakshmi, R. Jervis, P. R. Shearing and D. J. L. Brett, *J. Power Sources*, 2015, 284, 305–320.
36 J. Schindelin, I. Arganda-Carreras, E. Frise, V. Kaynig, M. Longair, T. Pietzsch, S. Preibisch, C. Rueden, S. Saalfeld, B. Schmid, J. Y. Tinevez, D. J. White, V. Hartenstein, K. Eliceiri, P. Tomancak and A. Cardona, *Nat. Methods*, 2012, 9, 676–682.
37 J. Schindelin, C. T. Rueden, M. C. Hiner and K. W. Eliceiri, *Mol. Reprod. Dev.*, 2015, **82**, 518–529.
38 I. Arganda-Carreras, V. Kaynig, C. Rueden, K. W. Eliceiri, J. Schindelin, A. Cardona, H. S. Seung and H. J. A. Paulson, *Bioinformatics*, 2017, **33**, 2424–2426.
39 A. Gayon Lombardo, B. A. Simon, O. O. Taiwo, S. J. Neethling and N. P. Brandon, *J. Energy Storage*, 2019, **24**, 100736.
40 J. T. Gostick, M. A. Ioannidis, M. W. Fowler and M. D. Pritzker, *J. Power Sources*, 2007, **173**, 277–290.
41 M. Kaviany, *Principles of Heat Transfer in Porous Media*, Springer-Verlag New York, Inc., 1995, vol. 53.
42 C. L. Chen, H. K. Yeoh and M. H. Chakrabarti, *Electrochim. Acta*, 2014, **120**, 167–179.
43 M. Vynnycky, *Energy*, 2011, **36**, 2242–2256.
44 A. A. Shah, M. J. Watt-Smith and F. C. Walsh, *Electrochim. Acta*, 2008, **53**, 8087–8100.
45 R. W. Atkinson, Y. Garsany, B. D. Gould, K. E. Swider-Lyons and I. V. Zenyuk, *ACS Appl. Energy Mater.*, 2018, **1**, 191–201.
46 D. Zhang, A. Forner-Cuenca, O. O. Taiwo, V. Yufit, F. R. Brushett, N. P. Brandon, S. Gu and Q. Cai, *J. Power Sources*, 2020, **447**, 227249.
47 A. El-kharouf, T. J. Mason, D. J. L. Brett and B. G. Pollet, *J. Power Sources*, 2012, **218**, 393–404.
48 L. D. Brown, T. P. Neville, R. Jervis, T. J. Mason, P. R. Shearing and D. J. L. Brett, *J. Energy Storage*, 2016, **8**, 91–98.
49 G. Qiu, C. R. Dennison, K. W. Knehr, E. C. Kumbur and Y. Sun, *J. Power Sources*, 2012, **219**, 223–234.
50 A. J. Bard and L. R. Faulkner, *ELECTROCHEMICAL METHODS: Fundamentals and applications*, 2001.
51 D. F. Shriver, M. Weller, T. Overton, J. Rourke and F. Armstrong, *Inorganic Chemistry*, OUP, Oxford, 6th edn., 2014.
52 R. B. Bird, W. E. Stewart and E. N. Lightfoot, *Transport Phenomena*, Wiley, Rev.2nd E., 2002.
53 F. Tariq, J. Rubio-Garcia, V. Yufit, A. Bertei, B. K. Chakrabarti, A. R. Kucernak and N. P. Brandon, *Sustain. Energy Fuels*, 2018, **2**, 2068–2080.
54 H. R. Jiang, B. W. Zhang, J. Sun, X. Z. Fan, W. Shyy and T. S. Zhao, *J. Power Sources*, 2019, **440**, 227159.
55 H. R. Jiang, J. Sun, L. Wei, M. C. Wu, W. Shyy and T. S. Zhao, *Energy Storage Mater.*, 2020, **24**, 529–540.
56 G. Qiu, A. S. Joshi, C. R. Dennison, K. W. Knehr, E. C. Kumbur and Y. Sun, *Electrochim. Acta*, 2012, **64**, 46–64.
57 D. Zhang, Q. Cai, O. O. Taiwo, V. Yufit, N. P. Brandon and S. Gu, *Electrochim. Acta*, 2018, **283**, 1806–1819.
58 F. C. Walsh, *A first course in electrochemical engineering*, Electrochemical Consultancy, Romsey, 1993.
59 X. You, Q. Ye and P. Cheng, *J. Electrochem. Soc.*, 2017, **164**, E3386–E3394.
60 M. Saito, S. Kawaharasaki, K. Ito, S. Yamada, K. Hayamizu and S. Seki, *RSC Adv.*, 2017, **7**, 14528–14535.
61 P.-Y. Yang, S.-P. Ju, H.-S. Hsieh and J.-S. Lin, *RSC Adv.*, 2017, **7**, 55044–55050.

62 D. You, H. Zhang and J. Chen, *Electrochim. Acta*, 2009, **54**, 6827–6836.
63 S. Won, K. Oh and H. Ju, *Electrochim. Acta*, 2015, **177**, 310–320.
64 Y. A. Gandomi, D. S. Aaron, T. A. Zawodzinski and M. M. Mench, *J. Electrochem. Soc.*, 2016, **163**, A5188–A5201.
65 D. Schmal, J. Van Erkel and P. J. Van Duin, *J. Appl. Electrochem.*, 1986, **16**, 422–430.
66 D. Schmal, J. Van Erkel and P. J. Van Duin, *J. Appl. Electrochem.*, 1986, **16**, 422–430.
67 F. J. Recio, P. Herrasti, L. Vazquez, C. Ponce de León and F. C. Walsh, *Electrochim. Acta*, 2013, **90**, 507–513.
68 K. Vafai and C. L. Tien, *Int. J. Heat Mass Tran.*, 1981, **24**, 195–203.
69 V. S. Bagotsky, *Fundamentals of Electrochemistry*, Wiley, 2nd Ed., 2005.
70 K. Kinoshita and S. C. Leach, *J. Electrochem. Soc.*, 1982, **129**, 1993–1997.
71 S. König, M. R. Suriyah and T. Leibfried, *J. Power Sources*, 2015, **281**, 272–284.
72 A. Tang, J. Bao and M. Skyllas-Kazacos, *J. Power Sources*, 2014, **248**, 154–162.
73 M. Messaggi, P. Canzi, R. Mereu, A. Baricci, F. Inzoli, A. Casalegno and M. Zago, *Appl. Energy*, 2018, **228**, 1057–1070.

Chapter 4

Synthesis and characterisation of a low iridium, ZIF-67-based multifunctional electrocatalyst

"The more you know, the more you know you don't know." – Aristotle (paraphrased)

4.1 Introduction

Energy storage and energy conversion devices such as fuel cells, electrolysers, sensors and redox flow batteries (RFBs) regularly use electrocatalysts to facilitate fundamental small molecule reactions and will help to change the way electricity is used. In fuel cell research, substantial effort has been channelled towards simultaneously reducing the cost of electrocatalyst materials (i.e. reducing the proportion of PGMs in electrocatalysts) and achieving impressive performance targets (e.g. 600 mA cm^{-2} at 0.7 V with less than 30 % degradation over 1000 h).[1,2] Projects are funded by governmental and international funding bodies such as the US Department of Energy (DoE) and the Fuel Cells and Hydrogen Joint Undertaking (FCH-JU) and these projects are carried out with the ultimate goal of encouraging the adoption of electrochemical technologies broadly.[3,4] The ORR is most efficiently catalysed using platinum-based catalysts, accelerating the kinetics of an otherwise slow reaction.[5] As discussed in Chapter 1, advances in the development of non-precious metal catalysts with new synthesis techniques enabling the introduction of metal or heteroatom centres enhancing carbon surfaces towards the ORR (and other fundamental small molecule processes) is continuing to inform community understanding of these electrochemical process. While there is no agreed definitive mechanism, the higher concentration of electrons on the nitrogen atom (occasionally simplified to 'lone pair') in nitrogen doped carbon (NC) materials is thought to play an important, stabilising role in oxygen-carbon centres' interaction involved in the transition state during ORR.[6,7] Further understanding of this stabilisation is critical and may eventually lead to the production of electrocatalysts precluding the use of precious metal catalysts completely.[8] On the other hand, the oxygen evolution reaction (OER) poses a serious threat to carbon-based catalysts as sluggish kinetics, and thus requirement for high overpotentials, lead to high positive

potentials on carbon-based materials. This high potential causes oxidation on surface of the catalyst and the formation of undesirable, non-conductive, oxygen functional groups, ultimately causing degradation.[9]

The pH environments must also be considered when performing these reactions. Entirely different fundamental reaction mechanisms can occur depending on the pH of the system.[7,10] For instance, in acidic conditions NC materials are much less effective, compared to metal centres – again, the reasons for this are not widely agreed but it is thought to be as a result of the protic environment oxidising the NC surface (potentially protonating the all-important N centres) – whereas, in this acidic environment, metal centres have extensive d-orbital (/ d-band) vacancy enabling the incorporation of nucleophilic oxygen adsorption.[11] Once oxygen is bound for the ORR reaction, two reaction pathways can occur – the two- or four-electron pathways – again, discussed in Chapter 1. The nature of active site across the catalyst induces different mechanisms which leads to various degrees of peroxide formation during the ORR reaction. Generally, the two-electron process dominates when active centres are predominantly carbon-based – this mechanistic pathway leads to the production peroxide and this is important because prolonged exposure of carbon to peroxide damages the carbon surface.[12,13] While these chemical phenomena must be considered for the ORR, a similar set of considerations exist for the OER that are not always compatible with high performing ORR activity.[8] ZIF-based materials were introduced in Chapter 1. These carbon, nitrogen and metal-containing materials serve as a good substrate (or starting point) on which to produce an electrocatalyst given their relative cost (compared to PGM materials) and advantageous chemical make-up. Zinc-containing ZIF-8, as stated before, has been shown to provide the basis for an extremely highly performing single atom catalyst.[14] This chapter focuses on its cobalt-based analogue – ZIF-67. ZIF-67 was chosen, in part, because of the high performance of cobalt containing catalysts towards OER in alkaline conditions.[15]

Most catalysts are used to perform a single function, however, for devices whose proper functioning relies on a forward and backward (redox) reaction to occur at one electrode, bifunctional electrocatalysts are potentially very useful. Devices utilising bifunctional oxygen electrocatalysts (performing both the ORR and OER), such as metal-air secondary batteries,[16] have higher gravimetric energy densities compared to other conventional electrochemical devices, as oxygen can be drawn from the air and does not need to be stored within the device. Compared with the theoretical specific energy density of zinc bromine device technologies

(572 W h kg^{-1}),[17] the theoretical specific energy densities for zinc-air batteries is 1350 W h kg^{-1} which is around three times higher than Li-ion batteries (410 W h kg^{-1}).[18,19] Development of bifunctional oxygen catalysts must carefully balance the strengths and weaknesses of alternative electrocatalytic materials for OER and ORR. For example, while mixed transition metal alloys may perform extremely well in certain environments for either ORR or OER, very rarely are both processes equally impressive for a given alloy in a given environment.[8] Similarly, underexplored carbon-based catalysts are increasingly being shown to have remarkable ORR capability, especially those with integrated metallic single atom centres,[2] however, only very few carbon-based catalysts show stable catalysts that are as durable for the OER.[8] Some single-atom iridium and cobalt containing catalysts have been shown to display fantastically high multifunctional performances towards the ORR and OER achieving overpotentials of under 420 and 350 mV, respectively, in both acid and alkaline.[20,21]

Having discussed the danger of high oxidising potentials for NC catalysts, it is worth briefly discussing the PGMs that are commonly used (indeed, used in this work) to develop fundamental oxygen catalysts in acid or alkaline conditions. Platinum, ruthenium and iridium are commonly considered when producing catalysts with a view to performing either the OER and ORR in acid or alkaline conditions. In acid, platinum is known to be the best metal catalyst available for catalysing the ORR reaction, however it is a poor OER catalyst due to oxidation at its surface at high oxidising potentials.[22] Ruthenium and iridium are also effecting ORR catalysts in acid but, it has been shown that iridium is more stable in acid and is also more effective at catalysing the OER reaction.[23] Under basic conditions, again, these three PGMs are among the most active but ruthenium is shown to be more active than iridium in catalysing the OER reaction.[23,24] Given the goal in this work is to develop a multifunctional catalyst across a range of pHs, iridium was chosen to catalyse the OER this multifunctional catalyst at different pHs as it, holistically had the greater capability.

The HOR reaction is the subject of significant interest as a result of its central use in PEMFCs. While it is six orders of magnitude faster than the ORR reaction due to the absence of the varied adsorption / desorption and strong bond cleavage involving O-containing intermediates,[7] it still requires effective platinum catalysts.[25,26] The challenge for researchers now is to either an electrode engineering one (by reducing the platinum loading of HOR catalysts to vanishingly small quantities) or developing new non-PGM catalysts that can work as effectively. In terms of extending this bi-functionality to the hydrogen fundamental processes, hRFBs have recently

employed a hydrogen gas electrode that undergoes the HOR and HER reaction.[27–29] Catalysts that are active towards catalysing the HOR are, as mentioned to in Chapter 1, able to catalyse the HER and therefore are considered bifunctional towards these fundamental hydrogen reactions.

In line with the question set out in Chapter 1: 'Is it possible to develop an inexpensive, carbon-based, high-performing bifunctional oxygen electrocatalyst?' this chapter looks to explore a low-cost, versatile and high-performing bifunctional electrocatalyst with starting materials free of precious metals. As this work is carried out, further questions will be confronted and addressed, such as:

- What are the optimum pyrolysis temperatures?
- How can metal content be minimised?
- What are the active sites' characteristics – does the iridium in the catalyst have single atom character or an alternative morphology?
- Is the catalyst active across a range of pHs?
- Does the catalyst catalyse hydrogen reactions?
- Can we reliably measure the metal content to return meaningful mass activities?

In-house synthesised ZIF-67 is used as a starting material, providing a cobalt-containing NC soft-templating scaffold where small amounts of iridium (1 – 8 wt%) are introduced after pyrolysis steps. Initially the catalyst capability will be investigated in alkaline conditions as NC materials are known to be stable towards the ORR in this environment, but, ultimately, will be tested across the pH range. Several state of the art physical and electrochemical characterisation techniques are used to inspect the active site(s) of the catalyst. The catalyst will then be tested for its activity towards ORR / OER and HOR / HER processes and the mass activities will be critically discussed. The best performing OER and ORR catalyst is shown to degrade slowest in basic medium. At the end of this study, chronoamperometry is tested over the catalyst on a RDE and the mass activities are examined. It is found that mass-activities, especially of iridium-containing species, have the potential to be misleading if not stated with sufficient qualification.

4.2 Methodology

4.2.1 Catalyst preparation

4.2.1.1 Carbon catalysts

A modified version of a previously reported facile hydrothermal synthesis of ZIF-67 nanocrystals was performed using $CoNO_3 \cdot 6H_2O$ and 2-methylimidazole.[30] 2-methylimidazole was dissolved in a minimum amount of water and vigorously stirred until almost all the solid was dissolved. An aqueous solution of the cobalt salt was then added (immediately producing a deep purple colour). The details for this synthesis procedure are discussed at the beginning of the Results section as additional modifications to the literature synthesis technique were carried out. The resulting purple powder was then pyrolysed at T_1 (800 / 900 / 1000 °C) to produce NC_T_1 – a black powder. This powder was then immersed in 2 M H_2SO_4 (acid in large excess) and left to stir overnight to remove any unbound cobalt in the pyrolysed structure. The powder was then filtered and washed in triplicate (3 × 300 mL DI) and dried in a vacuum oven overnight at 70 °C. Following this, a methanol solution of NC_T_1 was made (c.a. 0.75 mg mL^{-1}), to which 150 wt% (with respect to mass of NC_T_1) $IrCl_3 \cdot 6H_2O$ was added and, while stirring, was set to reflux for 24 hours. After cooling, the solution was filtered to remove excess iridium in solution and washed with water before being immersed in 0.5 M H_2SO_4 to remove the physisorbed Ir-ions, followed by a further three thorough water washes to remove any sulfate residue. The powder was, again, dried overnight in the vacuum oven at 70 °C. The resulting material, Ir_NC_T_1, was pyrolysed again at T_2 (850 / 900 / 950 °C) to produce Ir_NC_T_1_T_2. Pyrolysis conditions during catalyst synthesis were universally under a flow of argon and at a ramp rate of 3 °C min^{-1}.

Synthesis of an equivalent catalyst without any iridium, Blank_NC_T_1_T_2 was carried out in an identical fashion to Ir_NC_T_1_T_2 except without adding the $IrCl_3 \cdot 6H_2O$ during the reflux step.

It is important to clarify here, and this will become clear later too, that the term NC is actually a misnomer. NC in this particular catalyst contains a certain amount of cobalt (determined later). Iridium is included in the way this catalyst is named because it was subsequently added to a carbon-based material that had just been through an acid leaching step (but that still contained some cobalt). Therefore, in this chapter, NC implies the use of cobalt.

4.2.1.2 Commercial iridium-based catalysts

20 wt% Ir on carbon was bought from Premetek. To ensure minimal presence of IrO_2 on the surface (after possible oxidation following exposure to air) the material was pyrolysed for one hour under a flow of argon at 900 °C (following a ramp rate of 5 °C min^{-1}). IrO_2 was purchased (Alfa Aesar) and used as received.

4.2.2 Ink preparation

Catalyst inks were prepared for electrochemical characterisation techniques. All Ir_NC_T_1_T_2 type inks were made up in ethanol, set as 1 wt% and consisted of a catalyst to Nafion ionomer ratio of 2:1. The following procedure was used: to a clean glass vial containing 5 mg of catalyst powder, 564 µL of ethanol was added and sonicated (Ultrasonic 8800, Branson®) for 30 minutes. To this ethanol / catalyst suspension, 54.1 µL of Nafion (5 wt%) was added and the mixture was sonicated for a further 1.5 hours.

The Blank_NC_T_1_T_2 catalyst ink was made in an identical way as above. Ir_Premetek and IrO_2 inks were also made using ethanol and the same catalyst to Nafion ratio.

Loadings for the Ir_NC_T_1_T_2 catalyst inks were either 0.2 or 0.4 mg_{cat} cm^{-2} and this is outlined where catalyst performance results are displayed. Loading for the Ir_Premetek and the IrO_2 inks were 0.1 mg_{cat} cm^{-2}. Whenever inks were made on previous days they were always stored at 4.0 °C and sonicated for at least 30 minutes before subsequent use.

4.2.3 Physical characterisation

Information set out here is specific to the samples and analytical techniques carried out in this chapter. A large portion of the theory is set out in Chapter 2 and provides the basis for this section.

4.2.3.1 Nitrogen physisorption (Brunauer–Emmett–Teller – BET)

As outlined in Chapter 2, catalysts were transferred to BET tubes and dried under a stream of nitrogen at 130 °C overnight before nitrogen physisorption analysis. This analysis was carried out to determine the porosities and specific surface areas (SSAs) of the catalysts synthesised. Pore volumes are calculated using the (Barrett-Joyner-Halenda) BJH method and micropores are calculated using the t-plot method.

4.2.3.2 Electron microscopy

When preparing samples for SEM in this chapter, around 2 mg of catalyst powder were ground thoroughly in a pestle and mortar and subsequently deposited onto carbon tape that was affixed to an SEM sample holder. A thin 5 μm layer of chromium was sputter coated on the carbon-based samples' surface to ensure sufficient conductivity and the ability to collect high quality images.

TEM samples were prepared by, again, grinding the catalyst powder in a pestle and mortar and suspending 1 mg into 1 mL of ethanol. For the same reason ethanol was used to prepare the catalyst inks, ethanol was the chosen as the solution in which the best suspension could be formed, following 30 minutes of sonication. TEM microgrids (carbon-coated copper) were then placed on a petri dish and a few drops of the suspension were cast on it.

Once the TEM samples were loaded into the electron microscope (JEOL 2100Plus), STEM mode was engaged (after tilting the sample 15°) in order to identify the chemical composition of the particles.

4.2.3.3 X-ray diffraction (XRD)

After grinding the catalyst powder in a pestle and mortar around 10 mg was deposited and flattened in the circular, flat-based XRD holder using a clean glass slide. The analysis was carried out to identify the crystalline features on the surface of the catalyst.

4.2.3.4 X-ray photoelectron spectroscopy (XPS)

Around 1 mg of the ground catalyst powder was dropped and flattened on c.a. 2 mm × 2 mm pieces of carbon tape and mounted on the XPS plate. This analysis was carried out to explore the nature of elemental sites at the catalyst surface (~ 2 nm penetration). The coverage and thickness of the sample in question is considered to be sufficient to shield any contamination that might come with the carbon-based sample tape. Post-processing was carried out using the Avantage Data System with the help of Dr Gwilherm Kerherve.

4.2.3.5 X-ray absorption spectroscopy (XAS)

The XAS measurements were used to probe the Ir L_{III}–edge (11215 eV) X-ray absorption near edge structure (XANES) and the Fourier transform of the extended X-ray absorption fine structure (EXAFS). Samples were prepared by Mr B. Ali from Dongukk University and the technicians at South Korea's Pohang Light Source-II (PLS-II) (1D KIST-PAL and BL7D). The

datasets for these XAS measurements were collected in two batches. The measurements for these batches were gathered using different beamlines and modes (transmission mode for the first set in 2019 and fluorescence mode for the second set in 2020). Ir foil, commercial Ir nanoparticles (20 %) supported on carbon (Premetek) and IrO_2 standards were used as the reference materials. This analysis was carried out to determine the local environment surrounding the Ir in sample.

4.2.3.6 Inductively coupled plasma – mass spectrometry (ICP-MS)

Sample solutions with a density of 1 mg mL^{-1} were prepared in small glass vials and left to sonicate for 30 minutes. Small portions of these solutions (1 – 4 µL) were transferred to polypropylene centrifuge tubes and a 155 µL of Aqua Regia (strongly acidic and corrosive) was added to digest the sample and extract the metal content from the catalyst solid into solution. The centrifuge tubes containing the samples were subjected to one of three heating regimes (Table 4.1).

Table 4.1: ICP-MS sample preparation heating regimes.

Sample prep. method	Description
1	No heat: Simply immersed in Aqua Regia
2	Heated: Immersed in Aqua Regia at 80 °C in an oil bath overnight
3	Heated: Immersed in Aqua Regia at 80 °C in an oil bath for one week

Once these regimes were carried out, the samples were diluted in a less concentrated acid matrix (1 % HCl and 2 % H_2SO_4) suitable for the machine and subsequently filtered to ensure no undissolved solid carbon entered the machine. This ICP-MS analysis was used to determine the metal content of the catalyst. The dissolution of iridium has been carried out more successfully using concentration hydrochloric acid and sodium chlorate at elevated temperatures (between 125 and 150 °C).[31]

4.2.4 Electrochemical characterisation

Inks were dropcast onto thoroughly cleaned glassy carbon (GC) electrodes which, before each use, were polished to a mirror using 0.3 and 0.1 µm (fabrication paper) and 0.05 µm Al_2O_3 polish. Following this, during drying, the RRDE was rotated at a rate of 300 rpm to give a thin, even coverage of the GC.

Sulfuric acid (0.5 M H_2SO_4, VWR), a buffered acetic acid solution (0.5 M MeCOOH, VWR) and potassium hydroxide (0.1 M KOH Alfa Aesar) were used as electrolytes in acid, neutral and basic environments, respectively. They were made to their respective concentrations using deionised water (DI) (18.2 MΩ cm, Milli Q IQ 7005, Merck Millipore). For reference electrodes: a standard calomel electrode (SCE, Pine Research) was used in acid and neutral media and a mercury / mercury oxide (Hg/HgO, Pine Research) electrode was used in basic media. The standard potentials for the SCE and mercury electrodes used in this work were 0.240 and 0.162 V vs. NHE, respectively. All potentials using reference electrode readings have been converted and are reported in this chapter versus RHE, for consistency. A graphite rod was used as the counter electrode in the three-electrode systems and the container in which these RDE experiments took place was made from PTFE as glass is not compatible with basic media due to aggressive hydroxide ions etching the glass and effectively leaching silicates.[32]

Before RRDE experiments commenced, the solution was purged with oxygen for 30 minutes. The sparger used for these experiments could not be the typical glass sparger fitted with a frit as these materials are incompatible with the alkaline environments necessary when testing these catalysts. An in-house designed sparger (made from PTFE) was used instead for these purging steps. The RRDE tip was immersed ~0.5 cm into the oxygen-saturated electrolyte and rotated at 1,600 rpm for the duration of the catalyst testing. The following 'break-in' procedure was carried out to clean the catalyst surface and wet the carbon layer sufficiently: cyclic voltammograms (CVs) were recorded by cycling between 0.1 – 1.1 V at 100 mV s^{-1} (×25), 10 mV s^{-1} (×5) and 5 mV s^{-1} (×1).

ORR performance measurements then commenced with five cathodic linear sweep voltammograms (LSVs) recorded at a scan rate of either 5 mV s^{-1} or 2 mV s^{-1}. Interestingly, in acid, the anodic LSV returned a more positive $E_{1/2}$ and therefore five anodic LSVs were taken when measuring in acid. Following initial ORR measurements, the solution was purged with nitrogen or argon 30 minutes respectively and, at 5 mV s^{-1}, CVs (×2) and LSVs (×3) in the ORR region (0 – 1.1 V) were recorded to correct for background capacitance. Initial OER performance was then measured by recording CVs with a scan rate of 5 mV s^{-1}, between 1 – 1.7 V. After measuring OER performance, the solution was purged with oxygen and ORR performance was measured again in an identical way as described above. Re-measurement of ORR background and OER performance was then performed under the inert gas. Following this, both the ORR and OER performance measurements were repeated once more.

Equivalent experiments for the fundamental hydrogen reactions were carried out too. These experiments were carried out with the lower of the two loadings (0.2 mg_{cat} cm^{-2}) and scan rate (2 mV s^{-1}). Finally, chronoamperometry was carried out for each of these configurations in each both acidic and basic pH for two hours in order to explore the catalyst durability in RDE.

Impedance measurements, used to make an iR correction, were recorded before and after each ORR / OER / HER and HOR requisition (1 V, 100,000 – 0.1 Hz with 10 points per decade).

4.3 Results and discussion

4.3.1 Synthesis and initial characterisation

Initially, commercially available ZIF-67 was used to synthesise the desired catalyst. The morphology of this ZIF-67 was inspected by SEM and was shown to be amorphous with aggregated particles of irregular shape – varying in size but agglomerates are c.a. 500 nm in diameter (Figure 4.1, left-hand side – LHS). Homemade ZIF-67 starting material was then used as the standard carbon starting material. On synthesis of the catalyst, using a method set out by Qian et al.,[30] particle size is shown to be controllable by varying the concentration of the reaction mixture during the first step. Improved morphologies of homemade starting materials are shown below – initially by large particle ZIF-67 (mostly individual particles with usually only one fused face) and extended to small particle ZIF-67 which employs a more concentrated reaction mixture during the self-assembly mechanistic step. Approximate sizes of in-house synthesised large and small ZIF-67 particles were 300 – 400 nm and 100 – 150 nm, respectively. Internal discussions with commercial catalyst manufacturers indicate that optimum particle and aggregate size is in the range 100 – 600 nm. Catalyst particles smaller than this result in the catalyst layers produced in devices being too dense and preventing the easy distribution of gaseous electrolyte (oxygen) into the layer; whereas particles larger than this, result in the layer being non uniform and diffusion into the catalyst layer becomes slow.

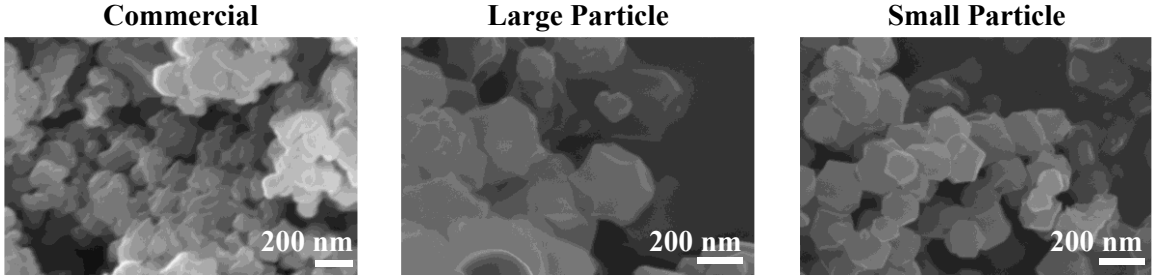


Figure 4.1: Scanning electron microscopy images of ZIF-67 with varied morphology demonstrating controlled MOF synthesis.

Having carried out the procedure outlined in the methodology, the synthesised catalysts' performance was tested by drop-casting the formulated inks onto a rotating ring disk electrode (RRDE). Given this study aims to develop NC-based catalysts (containing the coordinated cobalt in ZIF-67), alkaline conditions were used to routinely test their electrochemical capability towards catalysing the ORR and OER reactions in 0.1 M KOH (Figure 4.2). The catalyst synthesised using large particle (LP) ZIF-67 (Ir_NC_900_900_LP) was compared to the catalyst synthesised using commercially available ZIF-67 as a starting material (Ir_NC_900_900_Com), the improved morphology is shown to induce a significant improvement in ORR performance (62 mV improvement in $E_{1/2}$, Figure 4.2 (a)). Interestingly, there was no significant increase in OER activity comparing their E_{10}, however, an improved onset potential was observed for the homemade LP ZIF. Reducing the ZIF-67 starting material particle size further (by c.a. 200 nm) achieved by increasing the concentration of the reaction mixture (as outlined by Qian et al.,[30] SP) and subsequent catalyst preparation (forming, Ir_NC_900_900_SP) led to improved OER performance (40 mV improvement in E_{10}) with no further boost in ORR performance in comparison to Ir_NC_900_900_LP. This iterative improvement implies firstly, that a defined, consistent starting material morphology improves the half-wave potential for ORR in basic media, and secondly, that OER performance is improved by smaller ZIF-67 starting materials. These findings are consistent with those of Wu et al., who observed that the best ORR activity of similar ZIF-based catalysts (ZIF-8) were those with a starting material particle diameter of 50 nm.[33] One puzzling aspect of the ORR responses was the variation of limiting current. All limiting currents should be the same unless, either there are differing amounts of H_2O vs. H_2O_2 produce (the number of electrons transferred varies between two and four electrons), or there is incomplete catalyst coverage over the glassy carbon electrode. In this case it is assumed, given their similar characteristics and therefore mechanism, that there is some difference in the catalyst coverage between LSV scans with these catalysts. An additional complicating factor may be that in some of these ORR tests, the amount of oxygen present in the background was much higher than what is usually acceptable (see Figure A4.15 in the appendix).

In order to inspect the effect of iridium on the ORR and OER reactions, the synthesis procedure was carried out omitting the iridium salt from the reflux step (Blank_NC_900_900). As expected, the OER performance suffered significantly without the presence of iridium on the catalyst, indeed it is well known that iridium plays an important role in OER catalysis.[34] The

ORR performance was not significantly affected, inferring the ORR reaction unlikely to involve iridium atoms. Figure 4.2 shows the RRDE iR-corrected polarisation responses for these catalysts, set against standard Pt (Pt/C, JM) and Ir (Ir/C, Premetek) benchmarks for the ORR and OER reactions, respectively.

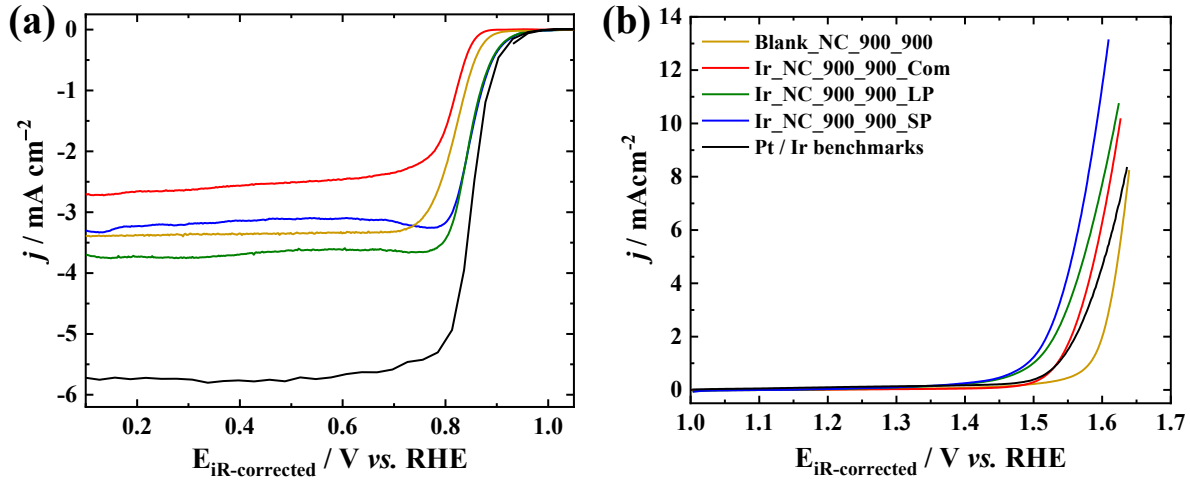


Figure 4.2: Progressive ORR and OER perforamcne improvement of catalyst synthesis on a RRDE in 0.1M KOH at a rotation speed of 1600 rpm, scan rate of 5 mV s^{-1} and a catalyst loading of 0.4 mg_{cat} cm^{-2}.

Having established that using small particle ZIF-67 and iridium deposition produced the highest performing bifunctional catalyst, these conditions were used to produce the starting material for all further synthesis optimisation. The temperatures, $T_1 = T_2 = 900°C$ were the (arbitrary) starting point for each of the pyrolysis steps. In order to optimise the synthesis procedure, T_1 and T_2, were varied to show how temperature has an effect on the catalyst performance. Three temperatures for each pyrolysis step were tested resulting in a set of five catalysts: {Ir_NC_900_900, Ir_NC_800_900, Ir_NC_1000_900, Ir_NC_900_850, Ir_NC_900_950}. The reason T_1 was varied by 900 ± 100°C and T_2 only by 900 ± 50°C was because the function of the first pyrolysis was to vary the nitrogen content – changing pyrolysis temperature by 100 °C was considered to have an appreciable effect on this nitrogen concentrations. Variation in T_2 was carried out to inspect how, if at all, this iridium 'activation pyrolysis' temperature might affect the catalysts' performance.

Performance benchmarking and their associated experiments were discussed in the Chapter 1 and, in agreement with Wei et al., it was concluded that they are essential for setting a 'level playing field' and for electrocatalyst progression and development.[32] It is widely known that for the ORR and the OER the commonly used metrics are $E_{1/2}$ and E_{10}, respectively. Bifunctional oxygen catalysts perform both the ORR and OER and use the metric, 'delta E',

ΔE – the difference between E_{10} and $E_{1/2}$ ($E_{10} - E_{1/2}$). This definition can misrepresent the relative importance of ORR and OER reactions in electrocatalysts used in a bifunctional way (more often in 'air-breathing' devices). These commonly used metrics can vary to a high degree as a function of catalyst loading thereby substantially changing ΔE for a given bifunctional catalyst. In this work, we provide an alternative metric to rank the electrocatalyst performance in a less-biased way. A figure of merit 'score', dubbed 'Bifunctionality', is presented where overpotentials associated with the usual metrics of the fundamental oxygen reactions are input into the following equation (Equation (4.1)) and subsequently normalised:

$$\text{Bifunctionality}_{\text{oxygen}} = \frac{1}{\left(\frac{20}{j_{\text{lim}}}\right)\eta_{\text{ORR}} + \eta_{\text{OER}}} \qquad (4.1)$$

The coefficient preceding η_{ORR} is to correct for the discrepancy in current density reached during ORR and OER on the RRDE. This value is then normalised according to the dataset of catalysts that are being compared (the details of this normalisation are outlined in the appendix, Table A4.4). The overpotentials are measured from the equilibrium potential (1.229 V) to $E_{1/2}$ (for ORR) and to E_{10} (for OER). The limiting current, j_{lim}, observed when using rotating disk techniques, is a mass-transport feature associated with the relative rates of reactant arrival / product departure to / from the active surface during the electrochemical experiment. The bifunctionality score normalises for this mass-transport effect as the relative speed of diffusion of OH^- ions away from the catalyst layer, produced during ORR, compared to gaseous O_2 molecules, produced during OER must be accounted for. While the catalyst loading has some impact on this bifunctionality score, its effect on this metric is supressed.

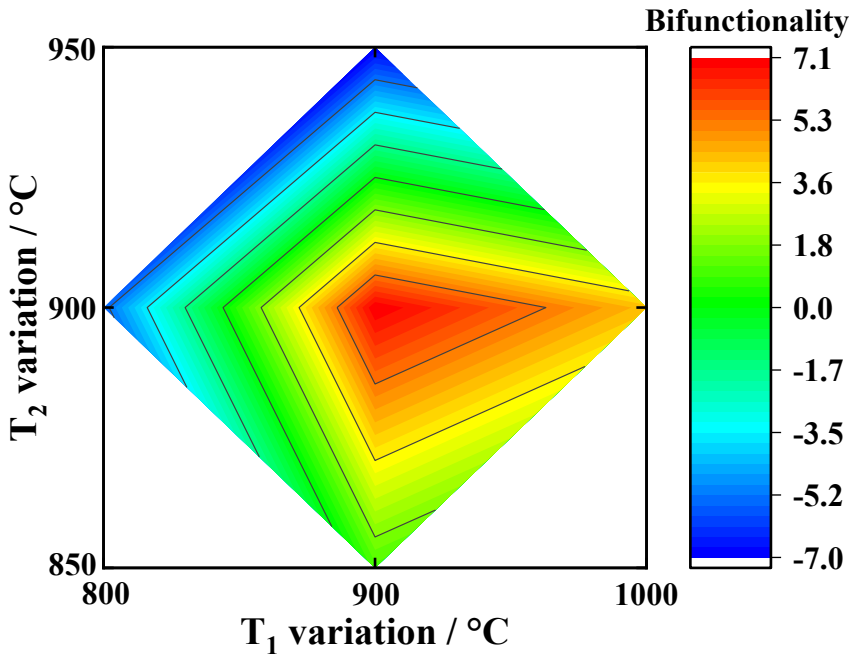


Figure 4.3: Heat map representing overall performance of catalyst according to the 'Bifunctionality' score towards fundamental oxygen reactivity, as a function of T_1 and T_2.

Figure 4.3 shows that, by this bifunctionality metric, the best performing catalyst is synthesised using a max heating temperature of 900 °C in both pyrolysis steps i.e. Ir_NC_900_900. For this dataset, comparison of Ir_NC_1000_900 and Ir_NC_900_900 highlights the utility of the bifunctionality score. ΔE for Ir_NC_1000_900 and Ir_NC_900_900 is 720 mV and 725 mV respectively, implying that Ir_NC_1000_900 is the better catalyst. The bifunctionality score normalises by placing more 'weight' on the 5 mV performance improvement in the ORR compared with the 10 mV performance loss in the OER. While we believe that this metric helps to rank the similar electrocatalysts synthesised in this work and confirm the optimised pyrolysis temperatures used herein, it is not necessarily advised that it should be used to compare across a wide range of catalysts. This is because j_{lim} will vary according to the mechanism (i.e. differing amounts of hydrogen peroxide production) and pH environment (solubility and diffusivity of oxygen) – it is asserted, rather, that this metric should be used for catalyst studies looking to optimise a synthesis, or to compare catalyst performances in similar environments. Full polarisation curves (LSVs and CVs) and calculations of the bifunctionality score are displayed in the appendix (Figure A4.16 and Table A4.4) and summarised in the heat map displayed in Figure 4.3.

The primary role of the initial pyrolysis step is to make the carbon conductive by carbonising the starting material. A simultaneous effect of this initial (T_1) step is to alter the form and

number of N sites in nitrogen containing carbon materials. Pyrolysis has been shown to diminish the number of N sites with an increased pyrolysis temperature.[35] Given this synthesis involves two pyrolysis steps, and no XPS measurements were carried out on the catalysts after a single heat treatment, it is difficult to observe such causal relationships between N content and pyrolysis temperature. The second pyrolysis (T_2) is included in order to activate the catalyst after the iridium component was added – this is commonly carried out to ensure good conductivity between active sites and the supporting carbon.[36] In developing a new catalyst, it is extremely important to understand the form of the active site. The next section explores the physical characterisation techniques used in this work to examine the active site of this catalyst.

4.3.2 Physical characterisation

On pyrolysis of carbon materials, under a stream of argon, high-level macroscopic structural intricacies are lost and amorphous carbon with some graphitic component is formed. Other, harder, ZIF template materials are able to retain their structure, such as ZIF-8.[37] The characteristics of the resulting amorphous carbon material (surface area, porosity, metal content) is strongly dependant on the starting structure and the additives (if any) in the furnace with the carbon material.[35,38]

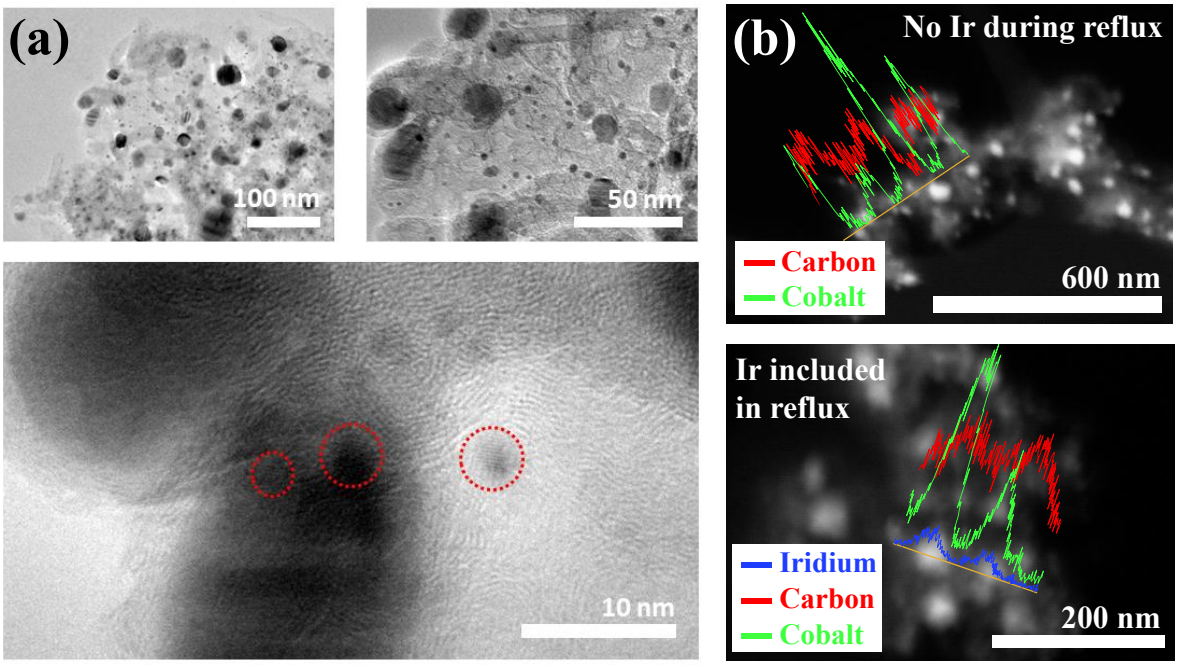


Figure 4.4: (a) Transmission electron microscope images showing agglomerated cobalt particles and (circled in red) iridium nanoparticles and, (b) line-scan energy dispersive X-ray spectroscopy images over a catalyst with and without iridium included in the reflux step.

Figure 4.4 (a) shows images from TEM and HAADF STEM analysis and is accompanied, in (b), by EDS responses of the electrocatalyst. The top rows of TEM images show metallic

agglomerates (dark spots) that range dramatically in size (5 – 50 nm in diameter). These metallic cobalt agglomerates are formed after the first pyrolysis step and the second pyrolysis has little effect on their size or character. The function of the leaching step in the synthesis protocol was, originally, to remove all the cobalt (making way for the iridium ions in the following step) however, while the melting temperature of cobalt (the characteristic metal in ZIF-67) is well above the maximum temperatures used in this work, at high temperatures it is shown to form agglomerates – this has recently been observed by Hammud et al.[39] On closer inspection (lower TEM image at higher magnification) it is clear that these cobalt agglomerates are wrapped and / or lodged amongst layers of graphitic carbon. This cobalt agglomerate was observed to be very insoluble (very resistant to strong acid leaching) and this is tentatively attributed to the stable, acid resistant graphitic-shell-like feature that is formed around the metallic cobalt, protecting it – this has been observed for smaller cobalt nanoparticles previously.[40] The red dotted circles indicate smaller particles by their different (more closely spaced and differently orientated) diffractive line-spacing patterns amongst the graphitic carbon. This provides the first indication of a different crystal structure that is considered to be as a result of iridium nanoparticle formation on / in the cobalt agglomerate. EDS line scans were carried out while the electron microscope was in STEM mode and are displayed in Figure 4.4 (b). These confirm that iridium is co-located with the cobalt. While this was not the intended morphology expected of the catalysts – iridium was thought to be dispersed evenly over the catalyst in the place of leached cobalt (iridium single atom catalysts have shown extremely high activities)[20] – this was shown to have interesting activities (Figure 4.2). XRD was carried out (Figure A4.17) and further demonstrates the interaction of iridium with cobalt whereby the catalyst synthesised without any iridium in its the reflux step (Blank_NC_900_900) displays highly crystalline features (shown by the long-range signals at c.a. 76 and 92 degrees). In the Ir_NC_900_900 sample the long-range features are lost and the characteristic features at lower angled reflections are observed broader indicating some interference in the cobalt crystal structures visible to the XRD pattern. This XRD signals were not deemed high enough quality for the main text in this chapter and so are displayed in the appendix – Figure A4.17. These pieces of data suggest that the large cobalt particles act as anchoring sites for iridium nanoparticle growth whereby the iridium nanoparticles are either inserted into or cover the cobalt agglomerates.

The physiochemical properties of the catalysts were inspected by nitrogen physisorption analysis including the pore size distribution and the volume specific surface area. The BET

surface areas extracted from physisorption analysis show the catalysts have a similar surface area to oligomerised diaminonaphthalene (ODAN)[41] – i.e. not particularly high compared to some other NC or aerogel materials.[35,42] Table 4.2 shows a collection of surface area measurements collected during nitrogen absorption measurements.

Table 4.2: Collection of nitrogen physisorption surface area and BJH desorption cumulative volume measurements.

Catalyst	BET surface area / $m^2\ g^{-1}$	BJH desorption cumulative surface area / $m^2\ g^{-1}$	BJH desorption cumulative volume / $cm^3\ g^{-1}$
Ir_NC_800_900	408.9	337.9	1.212
Ir_NC_900_900	560.3	473.9	1.868
Ir_NC_1000_900	414.5	352.7	1.305
Ir_NC_900_850	574.3	508.3	1.758
Ir_NC_900_950	488.1	432.2	1.757
Ir_NC_900_900 commercial	668.8	688.5	1.675
ODAN Fe–N–C[2]	463	-	-
Pyrolised ZIF-8 based catalyst[14]	~1000	-	-

The catalysts show hysteresis in their respective nitrogen absorption-desorption isotherms – as expected for mesoporous materials (Figure 4.5 (a)). The isotherms display a higher gas uptake with increased T_1 pyrolysis temperature – this shows the pyrolysis temperature has a significant effect on gas uptake – this is tentatively attributed to a reduction in coordinating N centres leading to a greater loss in cobalt during acid leaching, leaving larger holes in which N_2 is absorbed during absorption measurements. While this trend is contrary to similar recently reported materials,[35] the tentatively suggested mechanism holds and is supported, in Figure 4.5 (b), where more successful leaching after high (T_1) temperature synthesis steps can be seen by the presence of greater numbers of mesopores with pore widths in the 2.5 – 7 nm range.

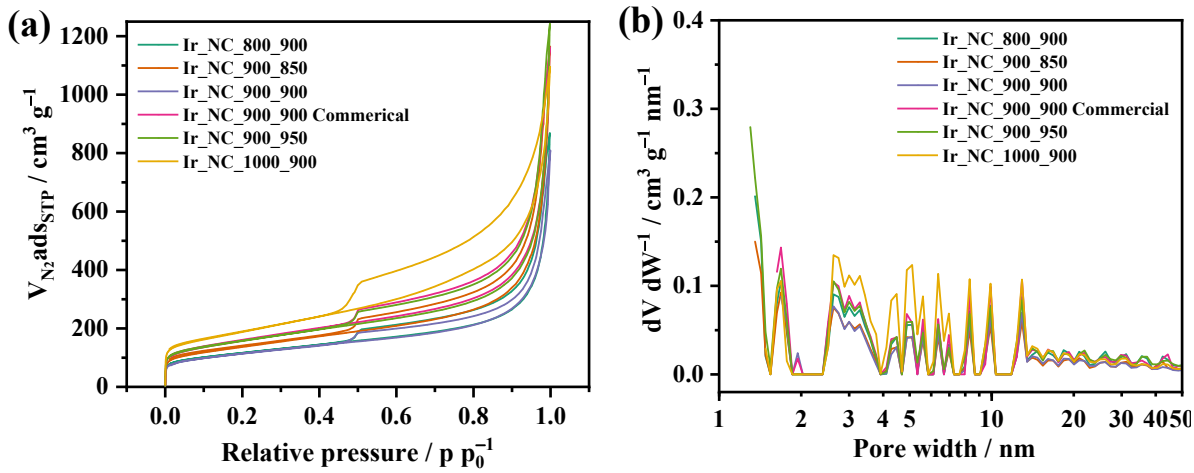


Figure 4.5: For each of the catalysts: (a) N_2 absorption–desorption isotherms; and, (b) pore size distribution measurements.

As stated previously, SEM images show that these catalysts, post pyrolysis steps appear (at a macroscopic level) as amorphous carbon materials, however, these BET images demonstrate that, at a microporous level, there is a structure with a reliable synthesis technique. Nitrogen sorption methods cannot provide information about ultra small pores – carbon dioxide sorption methods should be used for determination of pores smaller than 1 nm. However, it appears that, with a greater initial pyrolysis temperature, the volume of micropores decreases. Cumulative pore volumes are displayed in the appendix (Figure A4.18). It should be noted that while this measurement technique is helpful in identifying catalyst surface areas, it uses the adsorption and desorption of gas to take measurements. Therefore, this technique is most informative for catalysts that catalyse gaseous species.

XPS analysis was carried out to reveal information about the surface properties of the catalyst. An exemplary, 'peak search' XPS spectrum is presented in the appendix highlighting each of the features of interest (Figure A4.19 (a)). Firstly, given the severe heating regime the catalyst has been subjected to, the carbon is assumed to be almost completely sp^2 in character and therefore the binding energy of the 1s orbital is set to 284.5 eV – this is the reference that was considered to be a sufficient assumption and was used when processing XPS responses.[43] It is understood that Raman spectroscopy would be needed to confirm the extent of the hybrid nature of the carbon material. Starting from the lowest significant binding energy, the iridium $4f_{7/2}$ and $4f_{5/2}$ orbitals are found to fall at the same position as the cobalt 3p which leads to a complex doublet peak shape (Figure 4.6 (a)).

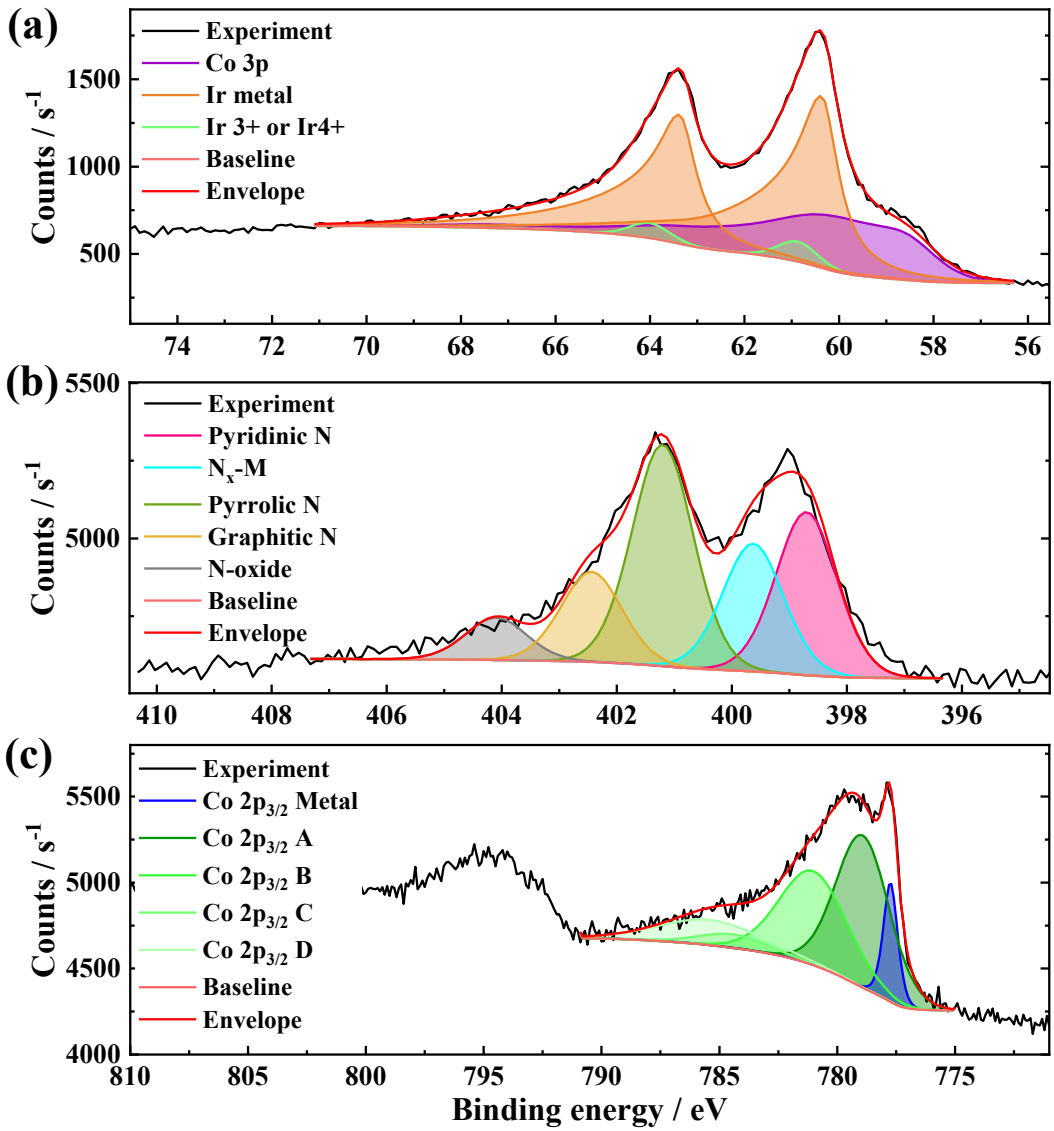


Figure 4.6: Comparison of an XPS response for an Ir_NC_900_900 electrocatalyst sample with simulated signal components and resulting fitting envelope for the (a) Ir 4f; (b) N 1s; and, (c) Co 2p characteristic binding energies.

The sum of the counts as a result of the Co 3p orbitals are indicated by the pink envelope that appears at the same binding energy as the Ir 4f signals. These were established from the XPS spectra of the Blank_NC_900_900 and are shown, separated, in the appendix Figure A4.19 (b)). Co 3p signals at identical shifts, FWHM and proportional concentrations were applied when processing XPS spectra of subsequent iridium-containing samples. It is important to mention here that, given our findings from XRD analysis that iridium interferes with the cobalt surface or is inserted into the cobalt particle structure, this superimposition is not entirely accurate as the Co 3p shape would change slightly on iridium interference. Similar co-location of titanium 3s XPS signals with iridium characteristic 4f signals has been observed recently and the same parameters are used in this analysis.[44] Two doublets have been assigned to the Ir

4f orbital. The first, at lower binding energy (orange), is asymmetric and indicates metallic iridium, likely in nanoparticle form. The second (green) is symmetric and assigned to ionic iridium species in either 3+ or 4+ oxidation state. Relative concentrations of these iridium species indicate the presence of significantly more Ir^0 compared to Ir^{3+} / Ir^{4+}. The heating regimes for the catalysts appear not to affect the total iridium concentrations. Omitting the Ir_NC_800_900 sample (with a 4.8 atomic weight percent, at%) their concentrations are 0.60 ± 0.07 at% (Table 4.3).

Table 4.3: Overview of XPS measurements across each of the elements of interest and a breakdown of how the nitrogen components are split into their respective environments. Surf. comp. denotes 'Surface composition' and 'Quat.' denotes 'Quaternary'.

Method		Blank_NC _900_900	Ir_NC _900_900	Ir_NC _1000_900	Ir_NC _800_900	Ir_NC _900_850	Ir_NC _900_950
Surf. Comp. (at%)	C 1s	93.1	92.5	94.6	78.6	91.9	92.3
	O 1s	2.8	3.1	2.5	9.5	2.5	2.0
	N 1s	2.8	2.6	1.8	2.3	4.0	3.8
	Ir 4f	--	0.7	0.5	4.8	0.6	0.6
	Co2p	1.3	1.1	0.6	4.8	1.0	1.3
Co/Ir ratio		--	1.6	1.2	1.0	1.7	2.2
Fraction of nitrogen (%)	Pyridinic	23.8	25.3	21.8	21.4	24.4	24.1
	N_x-M	19.6	19.8	16.7	24.0	20.3	19.1
	Pyrrolic	34.9	34.3	39.0	31.7	33.3	36.5
	Graphitic	14.6	14.0	15.3	15.1	15.0	13.4
	N-oxide	7.1	6.6	7.2	7.8	7.1	6.9

Moving to higher binding energy, DFT analysis by Kabir et al. on similar catalysts has shown the existence of several nitrogen states,[45] similar constraints including FWHM are kept for analysis of the catalyst samples synthesised in this work and are shown in Figure 4.6 (b). The Ir_NC_800_900 sample clearly displays large atomic percentages of iridium, cobalt and oxygen with respect to the measurements of the other catalysts. This may be due to the greater proportion of N sites as a result of the lower initial pyrolysis temperatures (though, surprisingly, this is not shown in the measurements). Unfortunately, as mentioned previously, XPS measurements were not collected after the first pyrolysis iteration. However, this greater proportion of metal may be due to the sample having an especially large cobalt agglomerate on the surface of the sample, however, this sample may also have been collected in error. With this in mind, the atomic weight of nitrogen content is decreased with increased initial pyrolysis temperature – this is observed elsewhere.[35] The second pyrolysis temperature, interestingly

does not show any clear trend. Figure 4.7 shows the relative concentrations of nitrogen sites across electrocatalysts varying (a) T_1 and (b) T_2. In both cases, the pyrrolic N-sites are highest in concentration. Variation in T_1 (and T_2) temperature appears to correlate positively with pyrrolic N-site concentration and negatively with N_x-M site concentration.

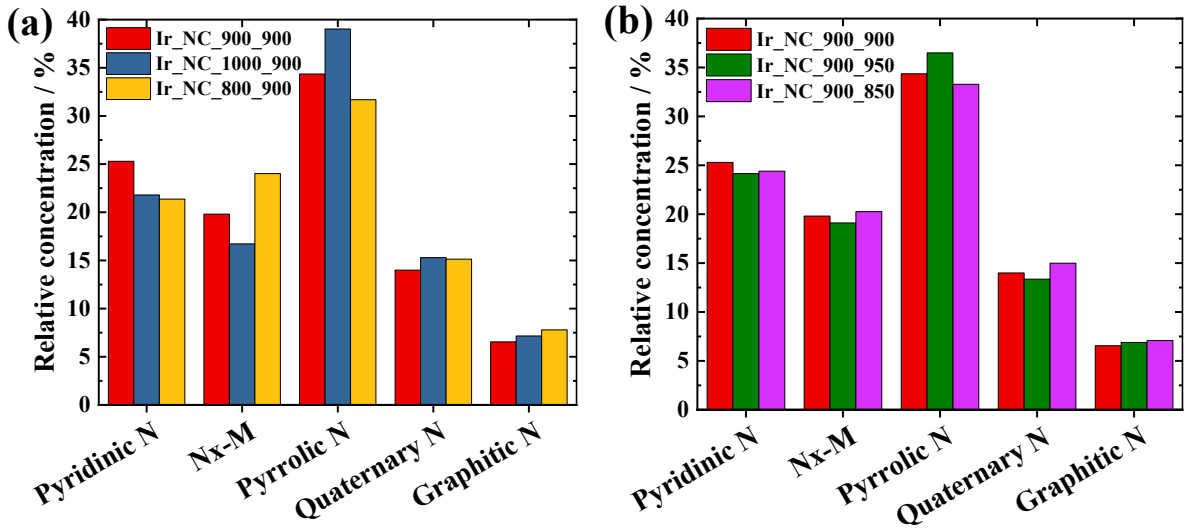


Figure 4.7: Calculated relative concentrations of N-sites in catalyst samples varying (a) T_1; and, (b) T_2.

A summary of the relative N site (pyridinic, N_x-M, pyrrolic, quaternary and graphitic) concentrations over the N 1s region are shown for each of the catalysts synthesised at different pyrolysis temperatures in Table 4.3.

The Co $2p_{3/2}$ peak (at 775 – 790 eV) is typically used as the characteristic peak when assessing cobalt-containing species in XPS.[46] At the lower end, the asymmetric metallic cobalt feature is observed (in blue in Figure 4.6 (c)) and the characteristic Co^{2+} peaks appear at higher binding energies. These Co^{2+} peaks are usually associated with CoO species and while this may be present in some concentration, these peaks are expected to be mostly attributed to Co-N_x species. Relative to the total concentration of cobalt in the catalyst (including cobalt in higher oxidation states), across the catalysts tested in this work, metallic cobalt is calculated to have a relative concentration of 17.2 ± 9.8 %.[47] The final ratio of interest in these catalyst materials is the ratio of cobalt to iridium. This relationship has been studied in this group and elsewhere but it considered to be an important ratio that affects the performance of the catalyst.[48] The average Co:Ir ratio amongst these catalysts is 1.5:1. This, qualitatively, seems like a much greater proportion of iridium than that which can be deduced from the STEM measurements in Figure 4.4 (a).

Having alluded to the abundant presence of graphitic-like carbon sheets surrounding the cobalt / iridium features in the TEM images, XPS provides important insight from a surface perspective as to what lies near the surface. However this technique is likely to significantly underestimate the 'atomic concentration' of the catalyst as a whole. Indeed, with only a 2 nm penetration during XPS this is likely to disproportionately feature carbon 'wrapped around' cobalt and iridium species as observed in TEM. On converting atomic % to weight %, we observe a low weight % of cobalt metal, which supports this assertion.

XAS can be used to establish the local coordination surrounding metal ions in a carbon-based metal-NC ORR catalysts.[35] In the present chapter XAS measurements were carried out over the Ir L_{III}–edge (11215 eV) for catalysts with T_1 variation (and using the same T_2 temperature of 900 °C). This is because it was judged that the majority of the changes to the carbon framework occurs during the first pyrolysis – the XANES and EXAFS responses are shown in Figure 4.8 (a) and (b), respectively.

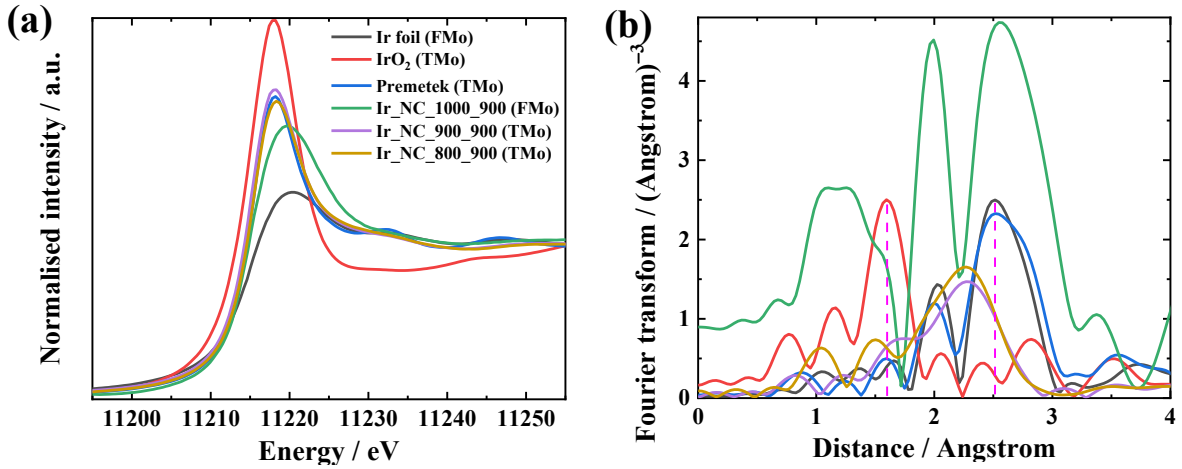


Figure 4.8: XAS measurements for the catalyst samples and standards. (a) Normalised responses following X-ray absorption near edge spectroscopy at the Ir L_{III} edge; and, (b) extended X-ray absorption fine spectra. Pink dashed lines indicate the inter-atomic distance between Ir-atoms in the provided standards and FMo and TMo indicate measurements recorded in fluorescence or transmission mode, respectively.

While these data are gathered in transmission mode (TMo) and fluorescence mode (FMo) and therefore the datasets are not exactly comparable, some important takeaways can be gleaned from these XAS responses. First, within those responses gathered in TMo, Ir_NC_T_1_900 (where T_1 = 900 and 800 °C) has a similar character to Premetek indicating that the iridium in these samples has an oxidation state of zero and is presumably in metallic (nanoparticulate) form. Measured in FMo, Ir_NC_1000_900 and Premetek is shown to be similar in character, notwithstanding peak intensity indicating similar characteristics to the samples synthesised using lower pyrolysis temperatures (Figure 4.9 (a), the same Premetek sample was measured

in TMo and FMo). The EXAFS spectra in Figure 4.8 (b) display results that confirm the above assertion – the distances between iridium atoms in samples with T_1 and T_2 variation is between 1.6 – 2.5 Å (i.e. the Ir-Ir distance in 'single-atom' and nanoparticulate catalysts, respectively). These are in line with literature findings.[49] The value for Ir_NC_1000_900 appears to have a large nanoparticulate / metallic component as well as a component at the same atomic radii as the other T_1 variant catalysts. This could be indicative of the presence of an especially large Ir particle in the sample chamber – unfortunately this cannot be verified. More likely, however, this spectrum could be misshapen due to the mode in which the measurement was collected. The EXAFS region is much more difficult to fit correctly when measurements are collected in fluorescence mode – this is because, fluorescence cannot be collected quantitatively by fluorescence detectors as comprehensively as transmission detectors detect transmitted radiation.

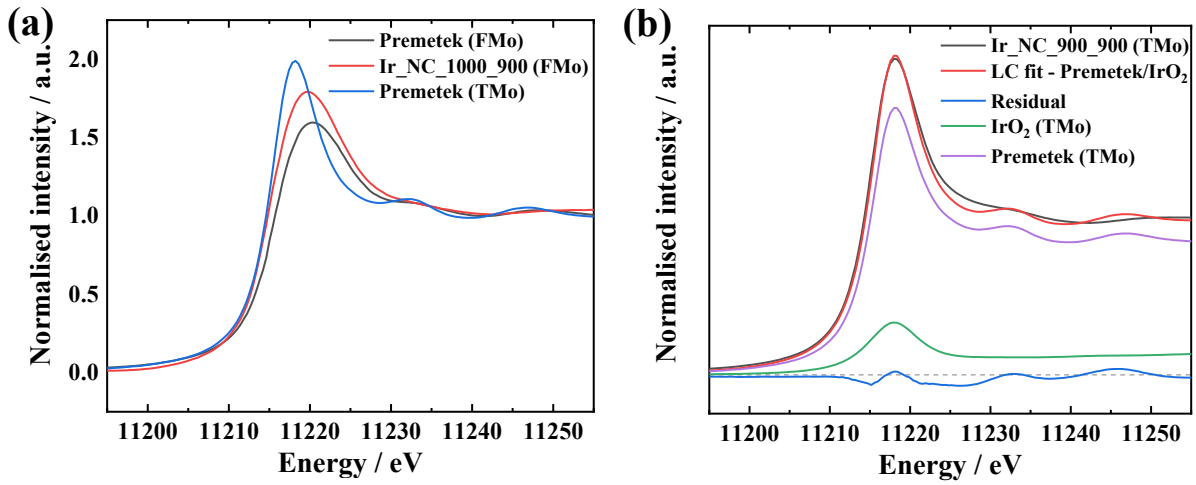


Figure 4.9: XAS analysis outlining in (a) the similarity in Premetek character with Ir_NC_1000_900 as well as the differences in Premetek sample measurements as a function of analysis mode; and, (b) a linear combination (LC) fitting Ir_NC_900_900 with IrO_2 and Premetek character – purple and green lines show their relative contributions to the overall fit (86.5 and 13.5 %, respectively).

Linear combinations of standard samples can be used to establish what proportion of a sample has certain characteristics. Lengke et al. investigated gold precipitation by the interaction of cyanobacteria and gold chloride aqueous solution during real-time radiation absorption measurements, revealing the formation of previously unknown intermediate Au^+ species using gold 'standards'.[50] In this case, our hypothesis is that Ir_NC_T_1_T_2 samples are partly metallic iridium (Ir^0) and partly Ir^{4+} in character. Unfortunately, the discrepancy in TMo and FMo analysis modes prevent reasonable, reliable analysis of this form over each of the samples. However, two standards and Ir_NC_900_900 were measured under the same conditions and

with the same analysis mode and therefore rough estimates of proportionality can be resolved (Figure 4.9 (b)).

This (imperfect) linear combination method establishes that the iridium contained within Ir_NC_900_900 is 86.5 % nanoparticle and 13.5 % single atom (using the naive assumption that Premetek and IrO_2 samples are purely nanoparticle and 'single atom dispersed' samples, respectively). This proportionality would fall in line with the findings from TEM and STEM where the majority of the iridium was found collocated with the cobalt agglomerates and with the XPS findings (considering the nature of the samples in each of these physical characterisation techniques).

The final form of physical characterisation carried out in this work is ICP-MS. ICP-MS measurements are central to establishing the mass of metals in catalyst powders. Aqua regia is an aggressive, highly oxidative and corrosive acid that is used to dissolve metals into solution. This method works well for metals or metal compounds that are easily dissolved, however, there are some compounds that are notoriously difficult to dissolve such as iridium dioxide, IrO_2.[51] Its high Gibbs free energy of formation makes it an attractive OER catalyst (especially in acid) however, assessing the mass of iridium in a certain catalyst is therefore extremely difficult.[52] As a result iridium is therefore found in very small concentrations in catalysts and this often leads to catalysts being presented as having misleadingly high mass activities and dissolution discrepancy measured across different devices.[53] In this chapter, samples of the best performing catalyst were subjected to one of three heating regimes (outlined in the methodology) demonstrating the importance of comprehensive acid leaching when preparing samples for ICP-MS (Table 4.1).

The amount of metal recovered from the catalyst during acid leaching (in aqua regia) varies widely depending on the heating regime used. Figure 4.10 shows the measured weight percentages of iridium (in (a)) and cobalt (in (b)) in the catalysts after each of the three types of heating regimes. The measured proportional mass of iridium changes between 4× – 7.5× on heating the catalyst during the digestion step for a week compared with no heating overnight (as is standard practice). Comparing this to proportional cobalt weights – these data show that the proportional mass of cobalt does not vary by any appreciable amount on heating regime, indicating that stronger acid leaching conditions are not required on account of catalysts containing cobalt (varying less than 35 % on average). Alternative methods have been

considered to leach the metal from iridium containing samples – microwave-assisted acid digestion and electrochemical dissolution.[51,54]

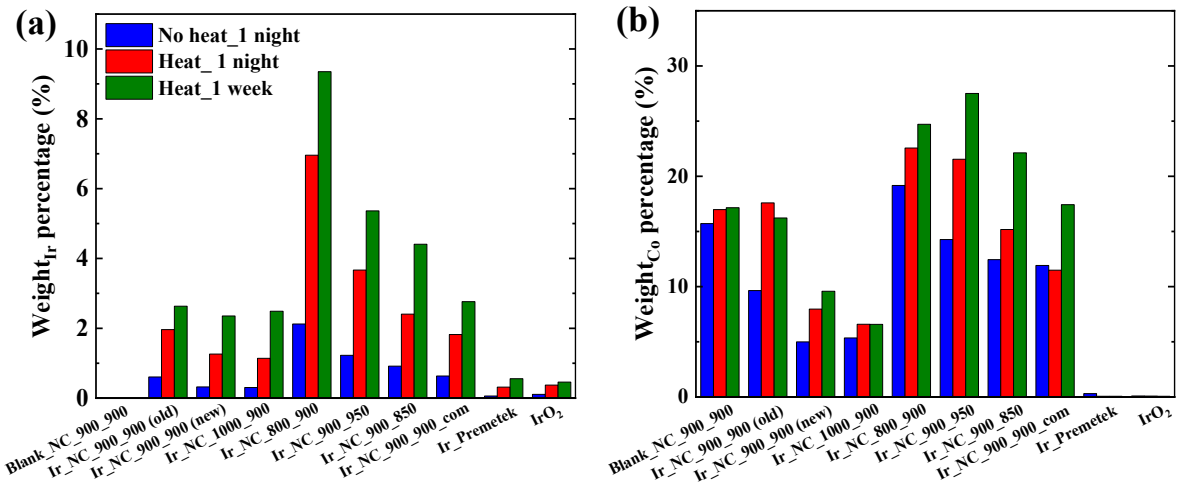


Figure 4.10: Weight percentages of (a) iridium and (b) cobalt in Ir_NC_T1_T2 catalysts and standards. Each weight percentage measurement was gathered from individual samples of catalyst and underwent just one of the three heating regimes set out in Table 4.1.

Briefly, in terms of the concentrations of iridium and cobalt within each of the catalysts: comparing the catalysts with T_1 variation shows that, compared to the higher temperatures, T_1 = 800 °C produced catalysts with much higher concentrations of iridium and cobalt – this could be as a result of the higher concentration of nitrogen owing to a lower initial pyrolysis temperature (contrary to N 1s XPS measurements). The elevated metal content seen here is in line with the measurements gathered by XPS. The reason for significant difference in relative metal concentration following T_2 variation is unknown but highlights how, especially iridium containing catalysts, ICP-MS is an imperfect method by which to establish / state metal concentrations – multiple repeats of multiple samples are needed in future and alternative methods of measurements are advised, such as X-ray fluorescence (XRF). Alternative methods have been explored and established, as mentioned in Section 4.2.3.6.

4.3.3 Catalyst performance

Having established a protocol for the reliable synthesis of a durable (after 500 OER scans, Figure A4.20) bifunctional oxygen catalyst under basic conditions, and begun to unpick its physical characteristics, the catalyst was additionally tested in acidic and neutral environments to investigate its performance. The ORR and OER responses in these pH environments are shown in Figure 4.11 (a) and (b), respectively. The acid and base concentrations (0.5 M H_2SO_4 and 0.1 M KOH) should be noted – KOH concentration (1.0 M vs. 0.1 M) has been shown to have a significant effect on the overall catalyst performance,[55] and these concentrations were

chosen because they were deemed the most relatable to literature and suitable for the catalyst (sulfate was not considered to detrimentally affect this catalyst significantly).

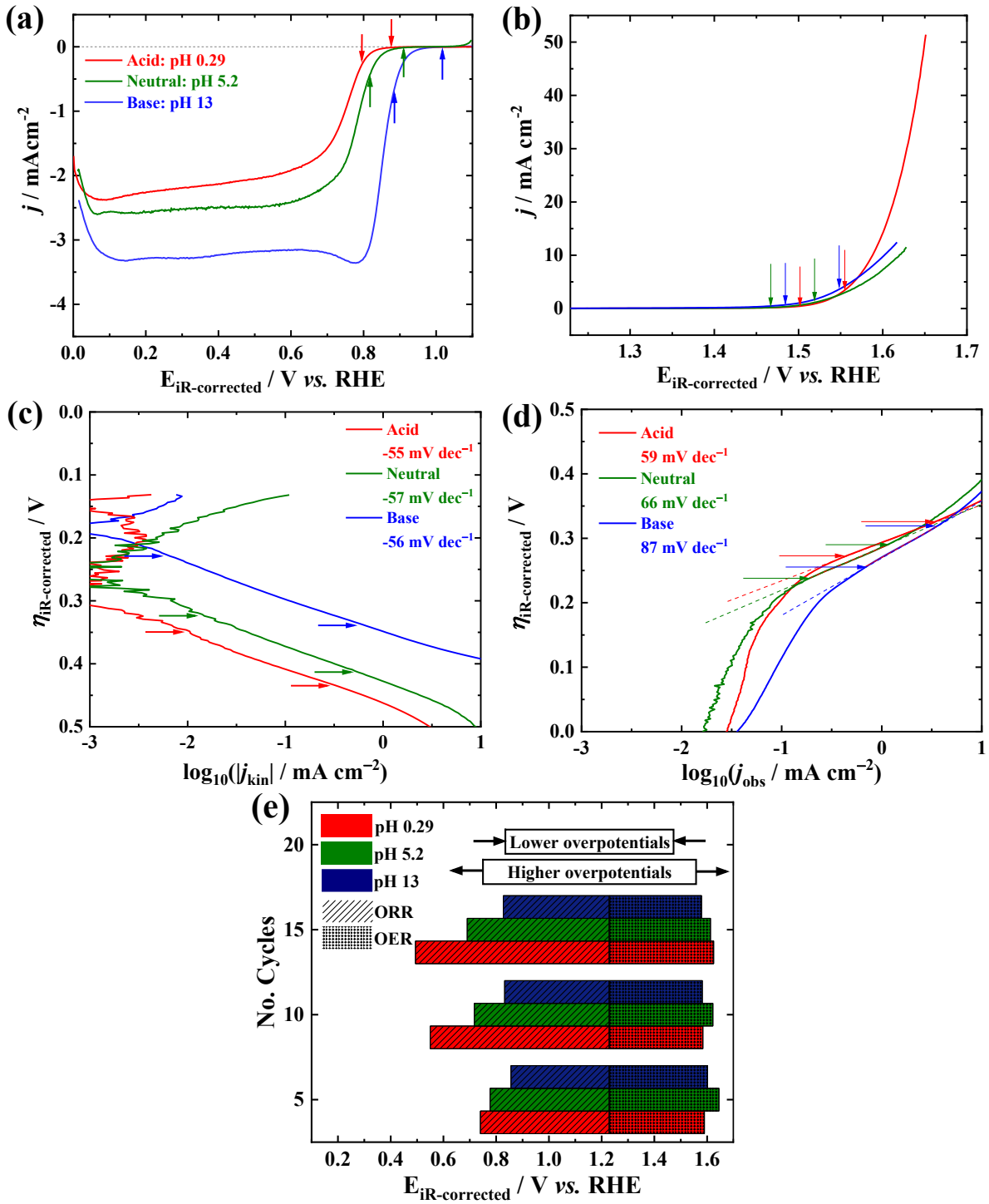


Figure 4.11: (a) ORR and (b) OER responses from Ir_NC_900_900 in a variety of pHs. (c) Tafel slopes pertaining to kinetic region in ORR curves indicated by arrows in each specific pH. The kinetic current is plotted due to the availability of a limiting current in ORR on RDE (d) Tafel slopes pertaining to kinetic region in OER curves indicated by arrows in each specific pH. The log of the observed current density is plotted as there is no limiting current. (e) Progressive overpotentials (as a function of cycle number) accocaited with $E_{1/2}$ in ORR region and E_{10} in the OER region. RDE conditions: catalyst loading: 0.4 mg_{cat} cm^{-2}; rotation rate: 1600 rpm; scan rate: 5 $mV\ s^{-1}$.

With half wave potentials between 0.7 – 0.8 V, the catalyst ORR performance in non-basic media is poor compared to Pt-containing catalysts in equivalent environments (Figure 4.2). Whereas the OER performance in acid is high reaching 50 mA cm^{-2} at an overpotential of 420 mV. This high OER performance in acid is tentatively attributed to the electrochemical oxidation at the metal surface producing IrO_2 and / or cobalt oxides which are both known, effective OER catalysts[56] – the subsequent poor performance in ORR would then be attributed by the well known poor performance of IrO_2 towards ORR.[57] The performances in neutral pH are not particularly impressive and this is attributed to the partial protonation of N sites (to a lesser extent compared to the acidic environments) as well as the occupation of d-band orbitals with acetate ions from the buffered solution. Adsorption of acetate at catalytic metal centres has been observed elsewhere.[58] In acidic media, the SO_4^{2-} ions are known to adsorb on the active sites hindering the approach of dissolved oxygen and thereby reducing ORR performance.[59] In base, with an $E_{1/2}$ of 0.856 V, this catalysts compares favourably similar catalysts – Zhang et al. reported a (ZIF-67 derived) cobalt-containing carbon nanotube catalyst with an $E_{1/2}$ of 0.828 V in the same environment.[60] The kinetic regions of the ORR responses (indicated by the arrows in (a) and (b) for each respective pH) were investigated further in order to calculate the Tafel slopes for each pH. These Tafel plots are displayed, using the logarithmic kinetic current in Figure 4.11 (c) and show similar gradients in their kinetic regions. This is an unexpected finding – it is expected that the Tafel plots would have different gradients as a result of the (expected) different mechanisms with which ORR proceeds in their respective pH environments. In alkaline, it is expected that the ORR occurs at an N-site whereas, due to nitrogen protonation, ORR is expected to occur at the metal site in acid. These two mechanisms are expected to have different RDSs and therefore different Tafel slopes.[61] Such low values of the Tafel slope may be an indication that the catalyst is undergoing reduction and it is the reduced surface that is oxidised. As the applied potential is decreased more active sites become available for the reaction. Figure 4.11 (d) shows a Tafel plot using, simply, the logarithm of the observed current density and the overpotential. The gradients for these processes at different pHs have, as expected, different values inferring different mechanistic processes. Lower gradients (observed using acid) indicates that for a given increase in overpotential, the current will increase most in acid compared to higher pH where, as expected, higher increasing gradients are observed.[62]

Finally, while the performance of the catalyst (towards OER) is high in acid, it is observed to degrade the fastest. Figure 4.11 (e) shows how the overpotentials of the ORR (indicated by the

$E_{1/2}$) and the OER (indicated by E_{10}) change with numbers of cycles. These data were collected by carrying out an LSV in the ORR region five times, followed by five CVs in the OER region and measuring the overpotentials associated with these voltammograms in each case. This figure clearly shows the swift performance degradation of the catalyst in non-basic environments, especially in the ORR region. It is suggested that, in reality, the catalyst is oxidised and corroded at high potentials (i.e. during the OER CVs) and the carbon surface is etched resulting in non-conductive moieties developing on the carbon surface (reducing the active area available on the carbon surface for ORR). This trend supports the assertion that, at high potential, the iridium nanoparticles (active site location for ORR in acid) are oxidised too resulting in the formation of IrO_2. In turn, when ORR activity is then tested poor performance is observed with the oxidised iridium site. This also might partially explain why there is a constant or even reducing overpotential shown in the OER (in alkaline conditions) – during this corrosion the ORR active area is etched away resulting in more available metal centre sites at which the OER can occur.[63] This damage to the catalyst in neutral and acid conditions is unsustainable if this catalyst were to be used in a bifunctional fashion.

For the subsequent RDE experiments, it was found that, when carrying out background measurements for capacitance in the ORR region, background oxygen levels were not reduced to a suitably low value to enable measurements under oxygen free conditions. It was decided that argon would be used when gathering background voltammograms as it is better able to expel oxygen from the system (Figure A4.15). So, for the subsequent ORR tests in the main body of this chapter, the limiting current is lower than has been shown previously. Additionally, catalyst loadings in the rest of this section were 0.2 mg_{cat} cm^{-2} rather than 0.4 mg_{cat} cm^{-2} as in previously displayed data – this was decided after revisiting the ink formulation method. This catalyst was subsequently tested for its activity towards catalysing fundamental hydrogen reactions. These proof-of-concept tests were carried out as, if the catalyst were found to be active towards these processes too, it could find potential application in a number of additional devices (such as FCs, and hRFBs involving hydrogen reactions) (Figure 4.12).

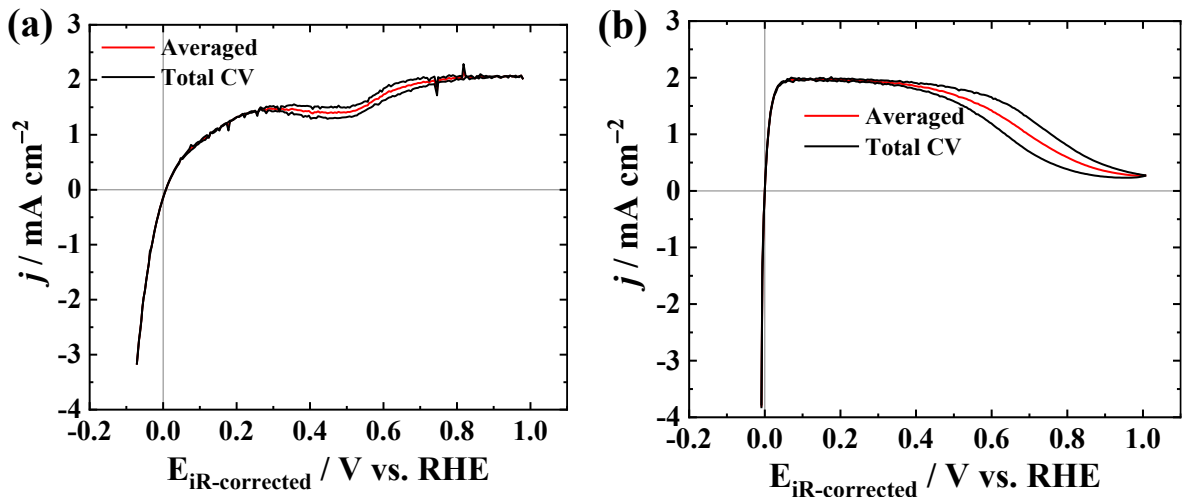


Figure 4.12: RDE experiments showing Ir_NC_900_900 catalysing fundamental hydrogen reactions in (a) basic (0.1 M KOH) or (b) acidic (0.5 M H_2SO_4) conditions. These experiments were carried out using an RDE at a scan rate of 2 mV s^{-1}, with a rotation rate of 1600rpm and a catalyst loading of 0.2 mg_{cat} cm^{-2}.

Iridium catalysts are rarely studied as a catalyst for the HER, however Pi et al. demonstrated monodispersed IrM (M = Ni, Co or Fe) in perchloric and sulfuric acid and have high performances reaching 20 mA cm^{-2} at 30 mV overpotential for the IrCo analogue in acid.[64] Polarisations were only measured to 3 mA cm^{-2} in this work (making HER results difficult to compare to literature) but this was achieved with a very low overpotential (4.3 mV). A good comparison table of catalysts for hydrogen fundamental reactions (and ORR) can be found in the supplementary material of the following reference.[65] As expected, the hydrogen reactions in basic media proceed with a larger overpotential compared to those in acid.

A summary of these multifunctional data catalysing both oxygen and hydrogen processes (with a loading of 0.2 mg_{cat} cm^{-2} and using argon as the gas expelling other gases from the electrolyte) is shown here (Figure 4.13). One commonly used metric to quantify electrocatalyst capability is to calculate their mass activity. Mass activities are a common metric by which researchers compare electrocatalysts. While there has been discussion of misrepresentation of iridium concentration in catalysts, in order for this work to be comparable to literature, the mass activities with respect to the iridium content (assuming a 2.49 wt% iridium loading) have been calculated for these catalysts and are displayed in Figure 4.13 (to demonstrate the range of mass activities that could be reported as a function of heating regime, Figure A4.21 shows the mass activity in the OER for E_{10}). The mass activity of OER in acid for instance was comparable to IrO_2 nanoparticles reported elsewhere.[57,66] In alkaline (left hand graphs (a) and (c) in Figure 4.13), the ORR is seen to occur after a much smaller overpotential and the kinetic currents appear to have a higher gradient than in acid (this is unlike the findings in Figure 4.11 which

showed similar gradients) and a much greater magnitude. This difference in kinetic current highlights the fact that the processes occurring in these environments are different and it is not as a result of a difference in solubility or diffusion coefficient. On the other hand, the hydrogen reactions are shown to be multiple orders of magnitude more sluggish in alkaline conditions compared to acid – this is in line with what is commonly observed.[65]

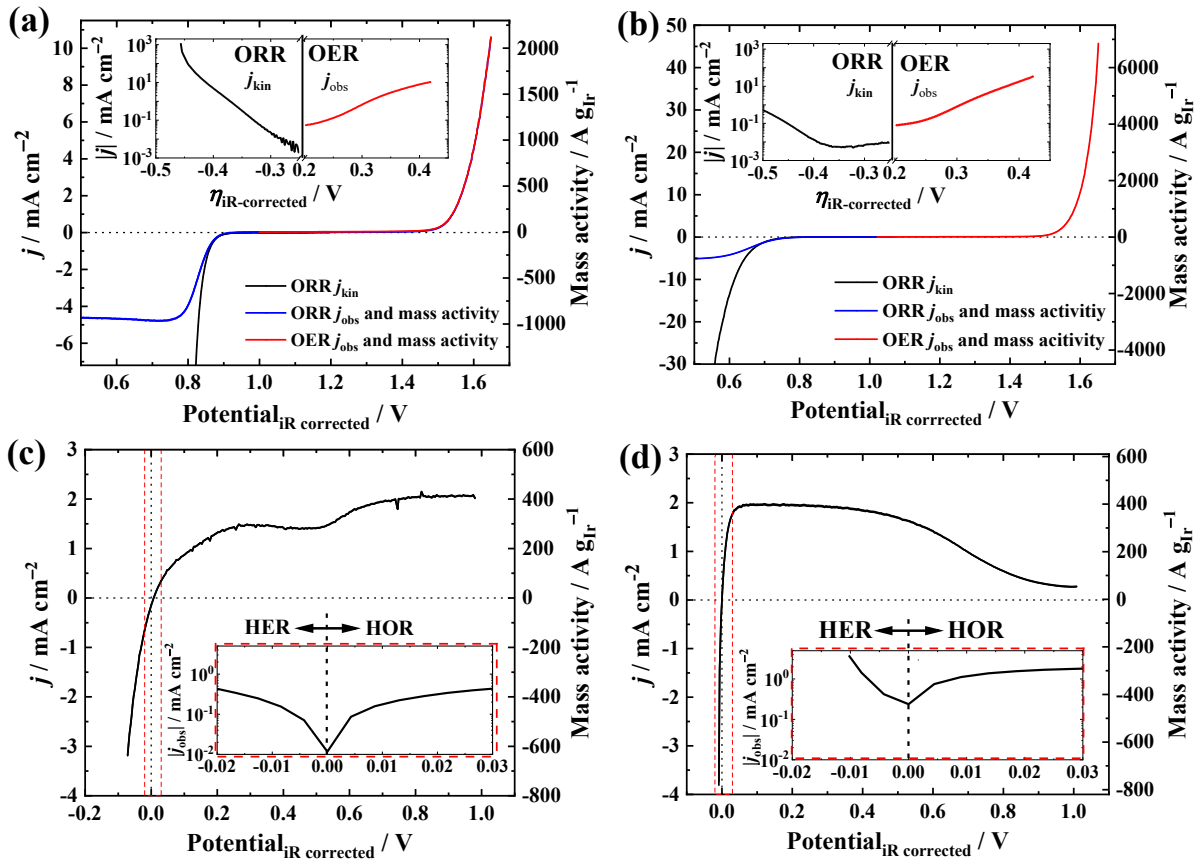


Figure 4.13: Rotating disk electrode measurements displaying the potential (vs. RHE) and mass activities as a function of iridium concentration in base ((a) and (c)) and acid ((b) and (d)). The iridium concentration assumed for this dataset is 2.49 wt% (i.e. the measurement after one week of catalyst leaching). The catalyst loading for these experiments was 0.2 mg_{cat} cm^{-2} and the rotation rate was 1600 rpm.

Figure 4.14 shows chronoamperometric holds at specific potentials for two hours in both alkaline ((a) and (c)) and acid environments ((b) and (d)). Before these are commented on, it should be noted that electrochemical measurements, alone, are insufficient measures of intrinsic stability. Frydendal et al. note that knowledge of specific activity, and therefore the electrochemical active surface area is important when assessing stability.[67] These critical metrics should be assessed before catalyst ranking is asserted.[68] In alkaline environments, CV measurements over Ir_NC_900_900 in the OER region show stability over a number of cycles (as in Figure 4.11 (e)) – this translates well to the chronoamperometry experiments which display relatively good stability during chronoamperometric holds. Spikes in current responses

correspond to sudden availability in catalyst active site as a result of product gaseous oxygen (bubbles) build up and sudden dislodgement. In contrast, the OER performance in acid appears to be poor as continued potentiostatic holds at high oxidative potentials significantly damages the catalyst resulting in severe degradation. After all measurements, the GC electrode was fully polished so that no corrosion could affect subsequent chronoamperometric holds. For the HOR, the current density achieved in acid was c.a. twice that of HOR in base and at roughly one third of the overpotential. The HER was also, as expected, more promising in acidic conditions. A steady current density was achieved with an overpotential of 10 mV for HER in acid. In basic conditions, there is a c.a. 10 % degradation in current density over a two hour period. Overall the chronoamperometry experiments for the HOR and HER in both acid and alkaline were encouragingly stable (for the following chapter where their stability would be required at device level).

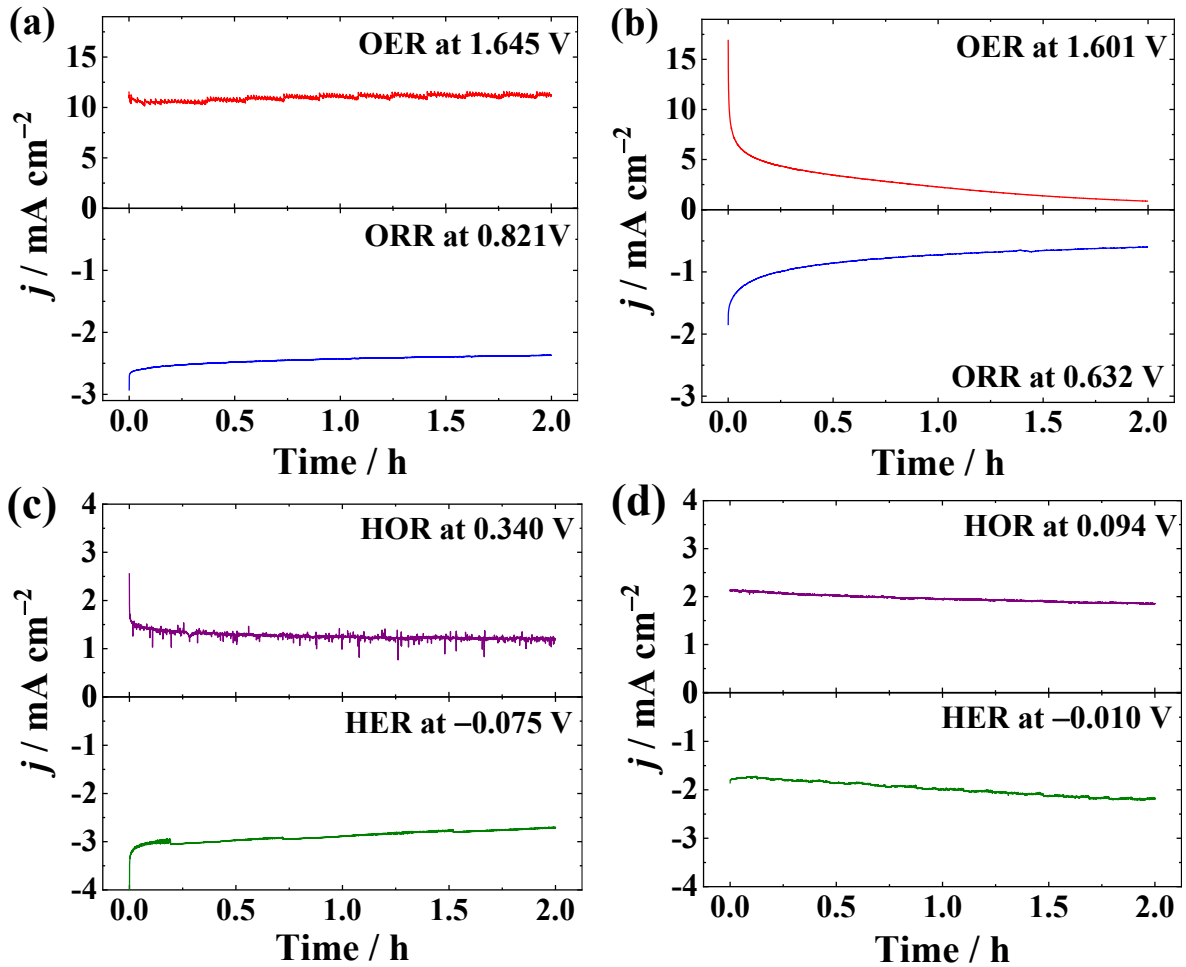


Figure 4.14: Summary of chronoamperometric holds on RDE using the Ir_NC_900_900 electrocatalyst. Basic experiments ((a) and (c)) were carried out using 0.1 M KOH; acid experiments ((b) and (d)) were carried out using 0.5 M H_2SO_4. Rotation rate: 1600 rpm; catalyst loading of 0.2 mg_{cat} cm^{-2}.

4.4 Conclusions

A synthesis protocol utilising inexpensive, carbon-based starting materials, small amounts of metal and involving two pyrolysis steps has been reported reliably producing a multifunctional catalyst. Catalysts produced using small-particle, homemade ZIF-67 starting material outperform equivalent larger particle size or commercially purchased ZIF-67 based catalysts in ORR and OER. Synthesis optimisation confirmed that the ideal tested maximum temperatures for the pyrolysis steps was 900 °C and that OER largely takes place at the metal surface and the state of the carbon has little effect on its OER performance.

From a physical characterisation perspective, the catalyst does not have a particularly high surface area according to BET and, via SEM, appears as an amorphous carbon material. That said, BET measurements do show a consistent pore size distribution for these catalysts – inferring some micro-level order. Further electron microscopy (TEM and STEM) demonstrates the catalyst has an interesting structure whereby the cobalt agglomerates (that form during the first pyrolysis step) either act as an anchoring site for the growth of iridium nanoparticles, or, iridium is inserted into the cobalt structure providing the active site for the OER reaction. In line with literature, the high concentrations of graphitic and pyrrolic N-sites at the catalyst surface (examined by XPS) help explain the high ORR performance in basic conditions. XAS measurements further clarified that the iridium in Ir_NC_T_1_T_2 samples have a similar structure to those in Premetek (nanoparticles). This was further confirmed by linear combination fittings estimating total iridium character was c.a. 84 % nanoparticle (a large majority). These measurements were consistent with the findings from STEM and XPS. ICP-MS measurements of these materials demonstrate the large discrepancy that might be seen in the mass activities of iridium-containing electrocatalysts. It is concluded that it is essential to heat catalysts during ICP sample preparation – especially those containing iridium.

This electrocatalyst operates in different pH environments and its activity towards catalysing both hydrogen and oxygen reactions is interesting from a catalyst functionality perspective. The ORR performance of Ir_NC_900_900 in basic conditions is good when compared to similar catalysts previously reported in literature and durability tests reveal that this catalysts is much more stable in base then any other pH environments. The relative ORR performance of the catalyst in acid and neutral pH is shown to be moderate with $E_{1/2}$ below 0.8 V (but above 0.7 V) and this is tentatively attributed to a combination of anions (such as HSO_4^-) effectively

blocking ORR active sites (likely electropositive metal centres) and protonation of N-sites in acidic oxidative conditions. OER performance in acid is high – it is tentatively asserted that this is as a result of the electrochemical oxidation at the metal centre producing IrO_2 and / or cobalt oxides. This performance is soon overshadowed by the damage to the carbon surface in acid at these high potentials and oxidative (acidic) environments rendering it a poor bifunctional catalysts in this environment.

4.4.1 Future work

4.4.1.1 Synthesis improvements using sustainable materials

One major area of improvement that must be considered is the number of pyrolysis steps in the synthesis. While the viability of a catalyst is dependant on its resulting performance, with the performance of the present 'best performing' catalyst reported here the relative gains are unlikely to justify the energy spent on producing it. While no formal analysis was set out in the present work, syntheses need to be made more facile and less energy intensive and, as such, significant efforts are being directed at reducing the energy intensity associated with producing materials for renewable energy.[35] Quantifying the cost of incorporating pyrolysis steps into syntheses may be useful when considering the scale up of catalyst materials.

While this work attempts to minimise its use, clearly, this catalyst incorporates iridium which is a precious metal. Iridium is an unsustainable resource – under ten tonnes are mined each year.[69] Additionally, the majority of global cobalt deposits are located in regions of the Congo. Mineral extraction in this country is carried out to some degree by children in dangerous conditions and is the subject of international moral disagreement.[70]

4.4.1.2 Active site understanding

XAS analysis is an extremely powerful form of analysis that is effective at identifying local geometries and information about specific nuclei. Establishing the form of the active site with all the standards and samples measured in the same session / mode would be extremely helpful in understanding how this catalyst operates.

Given previous discussion regarding BET measurements establishing surface areas using gaseous nitrogen adsorption, it is considered an important step to establish the surface area of these electrodes with nitrite stripping revealing the electrochemical surface area (ECSA). These measurements will reveal more informative values for these catalysts given their potential use

in RFBs as ‘air-breathing’ electrodes. These measurements can be carried out using the FE setup mentioned in the next sub-section.

4.4.1.3 Catalyst capability

Following on from improvements in surface area analysis and given ECSA measurements are gathered using the FE setup, it would be interesting to observe the full capability of the electrocatalyst without the bounds afforded by the mass transport in an RDE setup. Other than for OER, the FE has been shown to be effective in demonstrating full propensity of electrocatalysts (as they would perform in a scaled up system). Equivalent measurements for OER using different materials that are less susceptible to corroding at high oxidative potentials are currently being explored in this group. Further durability tests in alkaline conditions would be important to understand the true stability of this catalyst and its potential suitability in AEMFCs.

Improvements in screening catalysts for activity towards the processes such as CO_2 reduction, have also been made in the development of the GAME (and, soon, iGAME) establishing catalyst capability in an extremely efficient way, so exploring how this multifunctional catalysts, or some derivative thereof, would also be interesting.

4.5 Appendix

4.5.1 Supplementary information for synthesis optimisation

Figure A4.15 shows the supposed background capacitance measurements for the catalyst when using nitrogen or argon as the purge gas with the in-house designed sparger. Clearly, for the RDE measurements where nitrogen was used as the purge gas, the limiting currents should be c.a. 0.5 mA cm^{-2} more negative (greater in magnitude). Of course, halfwave potentials will have also been affected in these measurements resulting more negative (lower performing) values for $E_{1/2}$. Unfortunately, the not insignificant presence of oxygen when recording the background LSV in the ORR was only realised after the catalyst synthesis had been optimised.

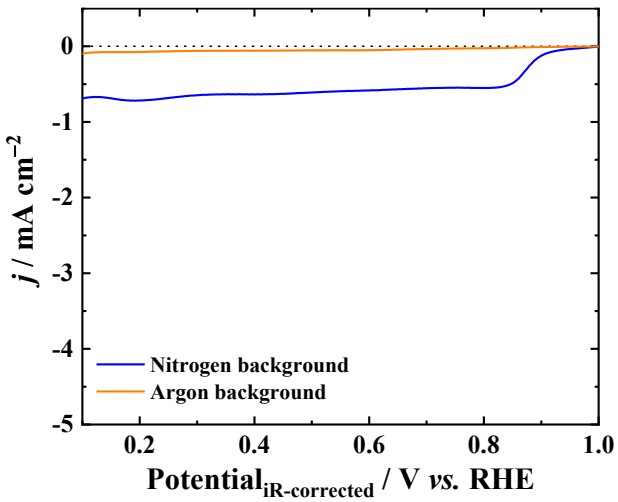


Figure A4.15: Linear sweep voltammograms of backgrounds highlighting the presence of oxygen dissolved in solution after purging nitogen gas for 30 minutes using the in-house desinged sparger versus the background when purging with argon.

The following table (Table A4.4) shows the overpotentials and calculations used to reveal the bifunctionality scores. Figure A4.16 (a) and (b) shows the LSVs for the ORR and the average potential for the CVs in the OER region ((c) and (d)) all in an alkaline environment.

Table A4.4: Bifunctionality calculations varying T_1 and T_2. The average bifunctionality score is taken across the dataset and then subtracted from the individual scores in order to normalise around a zero value. Bifunctionality scores were then multiplied by 100 to return 'sensible' values. This metric places more value on ORR (highighted by the weighing of the $ORR_{coeff.}$

Catalyst	η_{ORR} / V	η_{OER} / V	ΔE / V	j @ E_{10} | j @ $E_{1/2}$ | $ORR_{coeff.}$ | OER_{coeff}	Average score	Bifunc. score
Ir_NC_900_900	0.373	0.352	0.725	10 | 1.5 | 6.67 | 1	0.3451	0.0714
Ir_NC_1000_900	0.378	0.342	0.720			0.0427
Ir_NC_800_900	0.387	0.364	0.751			-0.0546
Ir_NC_900_950	0.386	0.381	0.767			-0.0665
Ir_NC_900_850	0.378	0.368	0.746			0.0112

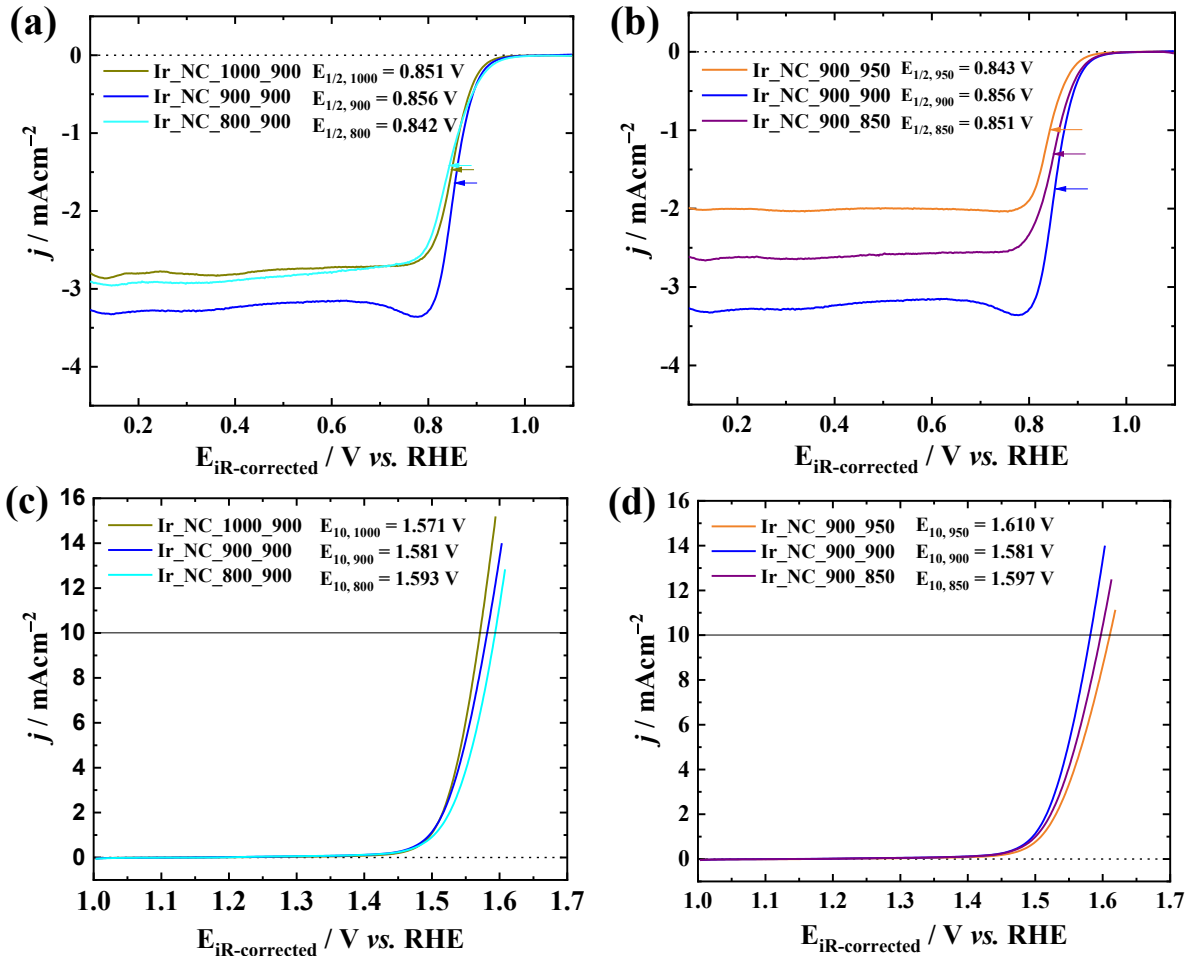


Figure A4.16: Rotating disk electrode ORR (a) and (b) and OER (c) and (d) measurements for Ir_NC_T_1_T_2 catalysts. Variation in T_1 pyrolysis temperature for the ORR and OER reactions are shown on the left hand side – (a) and (c); and T_2 pyrolysis temperature variation is on the right hand side – (b) and (d). Catalyst loading of 0.4 mg_{cat} cm^{-2}, scan rate of 5 $mV\ s^{-1}$ and a rotation rate of 1600 rpm.

4.5.2 Supplementary physical characterisation

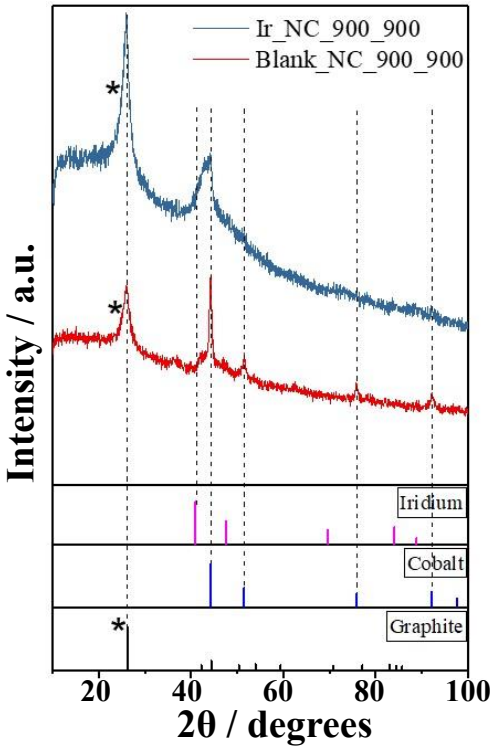


Figure A4.17: X-ray diffraction patterns of the catalysts with (blue) and without (red) iridium included in the reflux step compared with database XRD patterns of graphite, iridium and cobalt for comparison.

The XRD patterns shown in Figure A4.17 demonstrate the interaction of iridium with cobalt whereby the catalyst synthesised without any iridium in its the reflux step (Blank_NC_900_900) displays more crystalline features (shown by the long-range signals at c.a. 76 and 92 degrees). In the Ir_NC_900_900 sample the long-range features are lost and the characteristic features at lower angled reflections are observed broader indicating some interference in the cobalt crystal structures visible to the XRD pattern. These pieces of data suggest that the large cobalt particles act as anchoring sites for iridium nanoparticle growth whereby the iridium nanoparticles are either inserted into or cover the cobalt agglomerates.

Figure A4.18 shows a pore volume histogram for each of the catalysts measured during nitrogen absorption analysis. A general trend shows that higher cumulative pore volumes are associated with catalysts that have higher pyrolysis steps. Unfortunately, however, BET measurements were only recorded after the second pyrolysis meaning that no clear trend can be observed.

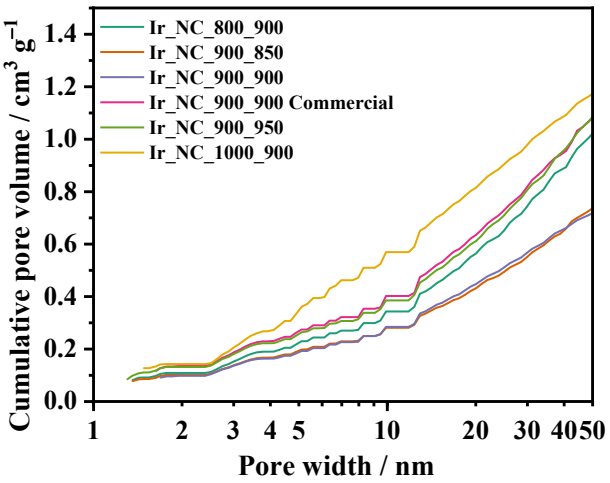


Figure A4.18: Histograms outlining the cumulative pore volume for each of the catalysts.

The following Figure A4.19 (a) shows a full binding energy 'peak search' over the samples measured in XPS. These measurements are taken to check that all expected peaks are present before deconvolution individual signals. Figure A4.19 (b) shows four characteristic peaks associated with the Co 3p orbital. These measurements were taken in order to collect peak ratio and FWHM data so that overlapping Ir 4f signals could be deconvoluted.

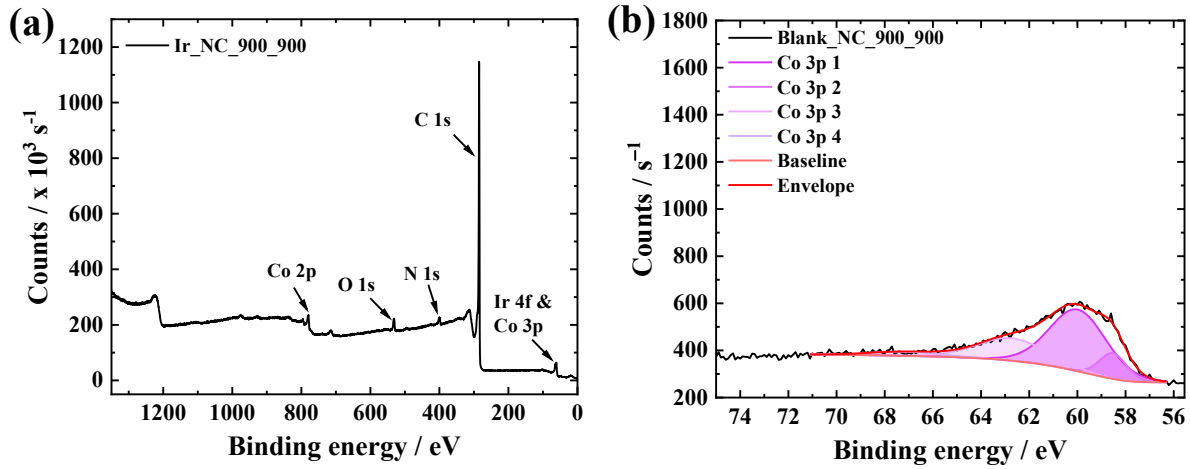


Figure A4.19: (a) full energy range 'peak search' over a sample of Ir_NC_900_900 highlighting characteristic elemental orbital signals. (b) Measurement of the Ir 4f region in Blank_NC_900_900 to find 'background' Co 3p signal ratios underneath other samples' Ir 4f signals.

4.5.3 Supplementary electrochemical measurements

The following RDE measurements show how the Ir_NC_900_900 catalyst catalyses the (a) ORR and (b) OER over the course of 500 OER CVs at a scan rate of 50 mV s^{-1} in alkaline conditions. The onset potential in the OER region becomes more positive relatively quickly but takes longer to degrade from a current perspective. The ORR performance initially

degrades in alkaline but the halfwave potential does not continue to degrade during the latter 400 OER cycles.

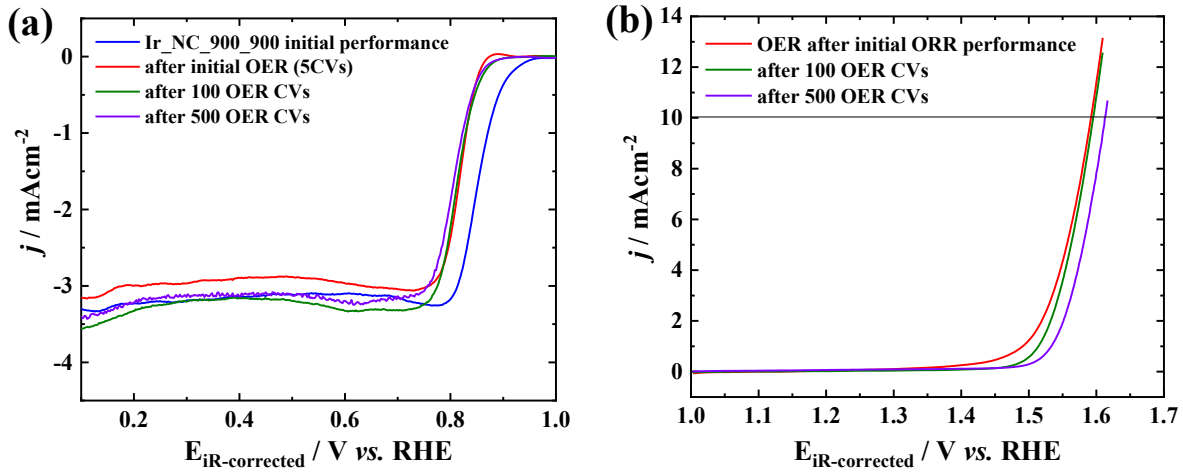


Figure A4.20: RDE durability tests in 0.1 M KOH using Ir_NC_900_900 with a catalyst loading of 0.4 mg_{cat} cm^{-2}, scan rate of 50 mV s^{-1} and a rotation speed of 1600 rpm.

Figure A4.21 shows how, in the specific case of the OER in alkaline conditions, incorrect measurement of iridium content using ICP-MS without heating regimes can lead to significant errors in mass activity – e.g. Ir_NC_900_900 with and without a basic heating regime leads to a c.a. 8-fold difference in activity.

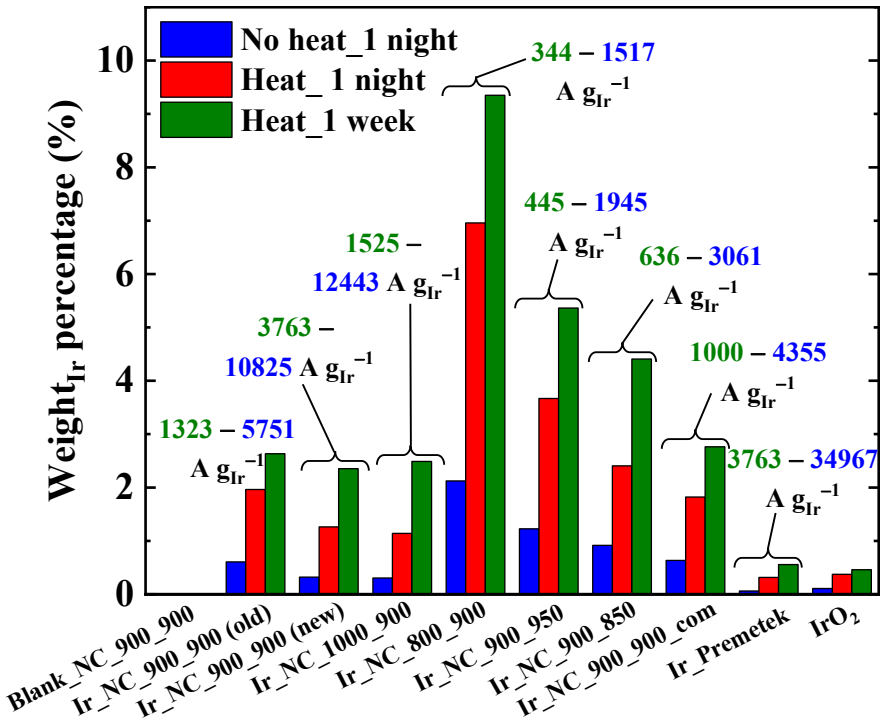


Figure A4.21: Iridium weight percentages measured by ICP-MS following different heating regimes with accompanying mass activities at E_{10} for the oxygen evolution reaction with a catalyst loading of 0.4 mg_{cat} cm^{-2}. It should be noted that the iridium content in Ir_Premetek was stated to be 20 wt %, amounting to 100 A g_{Ir}^{-1}.

4.6 References

1 Home, https://www.crescendo-fuelcell.eu/index.php, (accessed 30 January 2022).

2 M. Primbs, Y. Sun, A. Roy, D. Malko, A. Mehmood, M. T. Sougrati, P. Y. Blanchard, G. Granozzi, T. Kosmala, G. Daniel, P. Atanassov, J. Sharman, C. Durante, A. Kucernak, D. Jones, F. Jaouen and P. Strasser, *Energy Environ. Sci.*, 2020, **13**, 2480–2500.

3 'Joint EASE/EERA recommendations for a European Energy Storage Technology Development Roadmap towards 2030, The European Association for Storage of Energy (EASE)', https://www.eera-set.eu/wp-content/uploads/148885-EASE-recommendations-Roadmap-04.pdf.

4 Hydrogen and Fuel Cell Technologies Office | Department of Energy, https://www.energy.gov/eere/fuelcells/hydrogen-and-fuel-cell-technologies-office, (accessed 30 January 2022).

5 K. Shinozaki, J. W. Zack, R. M. Richards, B. S. Pivovar and S. S. Kocha, *J. Electrochem. Soc.*, 2015, **162**, 1144–1158.

6 A. Zhao, J. Masa, W. Schuhmann and W. Xia, *J. Phys. Chem. C*, 2013, **117**, 24283–24291.

7 R. Ma, G. Lin, Y. Zhou, Q. Liu, T. Zhang, G. Shan, M. Yang and J. Wang, *npj Comput. Mater.*, 2019, **5**, 1–15.

8 C. Hu, Q. Dai and L. Dai, *Cell Reports Phys. Sci.*, 2021, **2**, 100328.

9 C. L. Bentley, M. Kang and P. R. Unwin, *J. Am. Chem. Soc.*, 2016, **138**, 12755–12758.

10 M. Plevová, J. Hnát and K. Bouzek, *J. Power Sources*, 2021, **507**, 230072.

11 F. Ando, T. Gunji, T. Tanabe, I. Fukano, H. D. Abruña, J. Wu, T. Ohsaka and F. Matsumoto, *ACS Catal.*, 2021, **11**, 9317–9332.

12 Y. Bu, Y. Wang, G. F. Han, Y. Zhao, X. Ge, F. Li, Z. Zhang, Q. Zhong and J. B. Baek, *Adv. Mater.*, 2021, **33**, 2103266.

13 K. H. Wu, D. Wang, X. Lu, X. Zhang, Z. Xie, Y. Liu, B. J. Su, J. M. Chen, D. S. Su, W. Qi and S. Guo, *Chem*, 2020, **6**, 1443–1458.

14 A. Mehmood, M. Gong, F. Jaouen, A. Roy, A. Zitolo, A. Khan, M.-T. Sougrati, M. Primbs, A. M. Bonastre, D. Fongalland, G. Drazic, P. Strasser and A. Kucernak, *Nat. Catal.*, 2022, **5**, 311–323.

15 J. Chi, H. Yu, G. Li, L. Fu, J. Jia, X. Gao, B. Yi and Z. Shao, *RSC Adv.*, 2016, **6**, 90397–90400.

16 H. Miao, B. Chen, S. Li, X. Wu, Q. Wang, C. Zhang, Z. Sun and H. Li, *J. Power Sources*, 2020, **450**, 227653.

17 A. Khor, P. Leung, M. R. Mohamed, C. Flox, Q. Xu, L. An, R. G. A. Wills, J. R. Morante and A. A. Shah, *Mater. Today Energy*, 2018, **8**, 80–108.

18 H.-F. Wang, C. Tang and Q. Zhang, *Adv. Funct. Mater.*, 2018, **28**, 1803329.

19 T. B. Reddy, Ed., *Linden's Handbook of Batteries*, McGraw-Hill, 4th Editio., 2011.

20 Q. Zhang, Z. Duan, Y. Wang, L. Li, B. Nan and J. Guan, *J. Mater. Chem. A*, 2020, **8**, 19665–19673.

21 W. Xie, Y. Song, S. Li, J. Li, Y. Yang, W. Liu, M. Shao, M. Wei, W. Xie, Y. Song, S. Li, J. Li, Y. Yang, W. Liu, M. Shao and M. Wei, *Adv. Funct. Mater.*, 2019, **29**, 1906477.

22 M. Favaro, C. Valero-Vidal, J. Eichhorn, F. M. Toma, P. N. Ross, J. Yano, Z. Liu and E. J. Crumlin, *J. Mater. Chem. A*, 2017, **5**, 11634–11643.

23 E. Antolini, *ACS Catal.*, 2014, **4**, 1426–1440.

24 J. Gao, C.-Q. Xu, S.-F. Hung, W. Liu, W. Cai, Z. Zeng, C. Jia, H. Ming Chen, H. Xiao, J. Li, Y. Huang and B. Liu, *J. Am. Chem. Soc.*, 2019, **141**, 3014–3023.

25 C. M. Zalitis, A. R. Kucernak, J. Sharman and E. Wright, *J. Mater. Chem. A*, 2017, **5**,

23328–23338.
26 C. Jackson, X. Lin, P. B. J. Levecque and A. R. J. Kucernak, *ACS Catal.*, 2022, **12**, 200–211.
27 B. K. Chakrabarti, J. Feng, E. Kalamaras, J. Rubio-Garcia, C. George, H. Luo, Y. Xia, V. Yufit, M. M. Titirici, C. T. J. Low, A. Kucernak and N. P. Brandon, *ACS Appl. Mater. Interfaces*, 2020, **12**, 53869–53878.
28 J. Rubio-Garcia, A. Kucernak, D. Zhao, D. Li, K. Fahy, V. Yufit, N. Brandon and M. Gomez-Gonzalez, *J. Phys. Energy*, 2018, **1**, 015006.
29 V. Yufit, B. Hale, M. Matian, P. Mazur and N. P. Brandon, *J. Electrochem. Soc.*, 2013, **160**, A856–A861.
30 J. Qian, F. Sun and L. Qin, *Mater. Lett.*, 2012, **82**, 220–223.
31 F. A. Cotton, G. Wilkinson, C. A. Murillo and M. Bochmann, *Advanced Inorganic Chemistry, 6th Ed.*, Wiley-Interscience, 1998.
32 C. Wei, R. R. Rao, J. Peng, B. Huang, I. E. L. Stephens, M. Risch, Z. J. Xu and Y. Shao-Horn, *Adv. Mater.*, 2019, **31**, 1806296.
33 H. Zhang, S. Hwang, M. Wang, Z. Feng, S. Karakalos, L. Luo, Z. Qiao, X. Xie, C. Wang, D. Su, Y. Shao and G. Wu, *J. Am. Chem. Soc.*, 2017, **139**, 14143–14149.
34 Y. Lee, J. Suntivich, K. J. May, E. E. Perry and Y. Shao-Horn, *J. Phys. Chem.Lett*, 2012, **3**, 54.
35 A. Mehmood, B. Ali, M. Gong, M. Gyu Kim, J. Y. Kim, J. H. Bae, A. Kucernak, Y. M. Kang and K. W. Nam, *J. Colloid Interface Sci.*, 2021, **596**, 148–157.
36 Z. Y. Wu, M. X. Chen, S. Q. Chu, Y. Lin, H. W. Liang, J. Zhang and S. H. Yu, *iScience*, 2019, **15**, 282–290.
37 Y. Guo, L. Feng, C. Wu, X. Wang and X. Zhang, *J. Catal.*, 2020, **390**, 213–223.
38 W. Zhang, R. R. Cheng, H. H. Bi, Y. H. Lu, L. B. Ma and X. J. He, *New Carbon Mater.*, 2021, **36**, 69–81.
39 H. H. Hammud, H. Traboulsi, R. K. Karnati, S. G. Hussain and E. M. Bakir, *Catal. 2022, Vol. 12, Page 39*, 2021, **12**, 39.
40 A. H. Lu, W. C. Li, N. Matoussevitch, B. Spliethoff, H. Bönnemann and F. Schüth, *Chem. Commun.*, 2005, 98–100.
41 D. Malko, T. Lopes, E. Symianakis and A. R. Kucernak, *J. Mater. Chem. A*, 2016, **4**, 142–152.
42 H. Qian, A. R. Kucernak, E. S. Greenhalgh, A. Bismarck and M. S. P. Shaffer, *ACS Appl. Mater. Interfaces*, 2013, **5**, 6113–6122.
43 T. Susi, T. Pichler and P. Ayala, *Beilstein J. Nanotechnol.*, 2015, **6**, 177.
44 E. Calì, G. Kerherve, F. Naufal, K. Kousi, D. Neagu, E. I. Papaioannou, M. P. Thomas, B. S. Guiton, I. S. Metcalfe, J. T. S. Irvine and D. J. Payne, *ACS Appl. Mater. Interfaces*, 2020, **12**, 37444–37453.
45 S. Kabir, K. Artyushkova, A. Serov, B. Kiefer and P. Atanassov, *Surf. Interface Anal.*, 2016, **48**, 293–300.
46 M. C. Biesinger, B. P. Payne, A. P. Grosvenor, L. W. M. Lau, A. R. Gerson and R. S. C. Smart, *Appl. Surf. Sci.*, 2011, **257**, 2717–2730.
47 J.-M. Lee, J.-W. Kim, J.-S. Lim, T.-J. Kim, S.-D. Kim, S.-J. Park and Y.-S. Lee, *Carbon Lett.*, 2007, **8**, 120–126.
48 A. Yu, C. Lee, M. H. Kim and Y. Lee, *ACS Appl. Mater. Interfaces*, 2017, **9**, 35057–35066.
49 Y. Lu, T. Liu, C.-L. Dong, Y.-C. Huang, Y. Li, J. Chen, Y. Zou, S. Y. Wang Lu, Y. Zou, S. Wang, T. Liu, Y. Li, C. Dong, Y. Huang and J. Chen, *Adv. Mater.*, 2021, **33**, 2007056.
50 M. F. Lengke, B. Ravel, M. E. Fleet, G. Wanger, R. A. Gordon, G. Southam, M. Lengke, M. Fleet, G. Wanger, G. Southam, B. Ravel and R. Gordon, *Can. J. Chem.*, 2011, **85**,

651–659.
51 P. Jovanovič, N. Hodnik, F. Ruiz-Zepeda, I. Arčon, B. Jozinović, M. Zorko, M. Bele, M. Šala, V. S. Šelih, S. Hočevar and M. Gaberšček, *J. Am. Chem. Soc.*, 2017, **139**, 12837–12846.
52 Y. Ping, R. J. Nielsen and W. A. Goddard, *J. Am. Chem. Soc.*, 2017, **139**, 149–155.
53 J. Knöppel, M. Möckl, D. Escalera-López, K. Stojanovski, M. Bierling, T. Böhm, S. Thiele, M. Rzepka and S. Cherevko, *Nat. Commun.*, 2021, **12**, 1–9.
54 P. Grinberg, R. E. Sturgeon, L. D. O. Diehl, C. A. Bizzi and E. M. M. Flores, *Spectrochim. Acta Part B At. Spectrosc.*, 2015, **105**, 89–94.
55 S. A. Shah, Z. Ji, X. Shen, X. Yue, G. Zhu, K. Xu, A. Yuan, N. Ullah, J. Zhu, P. Song and X. Li, *ACS Appl. Energy Mater.*, 2019, **2**, 4075–4083.
56 N.-I. Kim, Y. J. Sa, S.-H. Cho, I. So, K. Kwon, S. H. Joo and J.-Y. Park, *J. Electrochem. Soc.*, 2016, **163**, F3020–F3028.
57 G. C. Da Silva, M. R. Fernandes and E. A. Ticianelli, *ACS Catal.*, 2018, **8**, 2081–2092.
58 A. Boualouache, A. Boucenna and G. Otmanine, *SAGE*, 2019, **44**, 74–91.
59 H. A. Gasteiger, S. S. Kocha, B. Sompalli and F. T. Wagner, *Appl. Catal. B Environ.*, 2005, **56**, 9–35.
60 E. Zhang, Y. Xie, S. Ci, J. Jia, P. Cai, L. Yi and Z. Wen, *J. Mater. Chem. A*, 2016, **4**, 17288–17298.
61 T. Shinagawa, A. T. Garcia-Esparza and K. Takanabe, *Sci. Rep.*, 2015, **5**, 1–21.
62 T. Nishimoto, T. Shinagawa, T. Naito and K. Takanabe, *ChemSusChem*, 2021, **14**, 1554–1564.
63 X. Liu, M. Gong, S. Deng, T. Zhao, T. Shen, J. Zhang and D. Wang, *Adv. Funct. Mater.*, 2021, **31**, 2009032.
64 Y. Pi, Q. Shao, P. Wang, J. Guo, X. Huang, Y. Pi, Q. Shao, P. Wang, X. Huang and J. Guo, *Adv. Funct. Mater.*, 2017, **27**, 1700886.
65 Z. Pu, R. Cheng, J. Zhao, Z. Hu, C. Li, W. Li, P. Wang, I. S. Amiinu, Z. Wang, Min Wang, D. Chen and S. Mu, *iScience*, 2020, **23**, 101793.
66 L. Moriau, G. Koderman Podboršek, A. K. Surca, S. Semsari Parpari, M. Šala, U. Petek, M. Bele, P. Jovanovič, B. Genorio and N. Hodnik, *Adv. Mater. Interfaces*, 2021, **8**, 2100900.
67 R. Frydendal, E. A. Paoli, B. P. Knudsen, B. Wickman, P. Malacrida, I. E. L. Stephens and I. Chorkendorff, *ChemElectroChem*, 2014, **1**, 2075–2081.
68 H. A. El-Sayed, A. Weiß, L. F. Olbrich, G. P. Putro and H. A. Gasteiger, *J. Electrochem. Soc.*, 2019, **166**, F458–F464.
69 Johnson Matthey, *PGM Market Report*, 2021.
70 The Bureau of International Labor Affairs, *List of Goods Produced by Child Labor or Forced Labor | U.S. Department of Labor*, 2020.

Chapter 5

Application of ZIF-based electrocatalysts and various electrodes in multiple electrochemical devices

"Only stupid people don't change their minds." – Boutros Boutros-Ghali

5.1 Introduction

A great deal of effort is directed towards developing new catalysts at the half-cell level.[1–4] These catalysts are tested using RDEs and new, more informative testing methods currently being further developed in this group.[5–7] Increasingly though, it is becoming necessary for researchers to include device-level tests in their publications.[3,8] This transfer from half-cell catalyst testing – presented in Chapter 4 (alongside physical characterisation) – to device-level testing is essential for new technologies and materials to be scaled up.[9]

As discussed in previous chapters, one of the main aims for researchers is to reduce the amount of (or obviate the need for) PGMs in electrocatalysts due to their high cost and limited availability.[10,11] The catalyst synthesised in Chapter 4 attempts to achieve this by using a carbon-based ZIF material (containing cobalt) and, on it, deposit very small amounts of iridium. This chapter looks to use this catalyst in various FC devices and in a hRFB. Iridium was initially chosen as the PGM catalyst of choice as compared to ruthenium and platinum, as it presents high activity towards both fundamental oxygen reactions (ORR and OER) in acid.[12] Under alkaline conditions, iridium is second only to ruthenium in catalysing the oxygen reactions,[13] but in acid, iridium is more stable.[14] In terms of the fundamental hydrogen reactions, it is understood that platinum is the best performing electrocatalyst across all pHs,[15,16] but iridium (under alkaline conditions) is a close second and is also able to achieve the other functions with sufficient performance – hence, iridium was judged to be a better metal for use in this multifunctional catalyst.[17] At device level, iridium is of further interest because of its relative poison tolerance compared to the other PGM catalysts in PEMFCs.[18] AEMFCs have been recently reviewed – one of the outstanding points made by these reviews is the urgent

need for low-cost catalyst materials.[19,20] Significant steps have been made towards developing new highly performing AEM materials that are much more resistant to nucleophilic species often found at high pHs.[21,22] These high performances were only achieved using PGM catalysts which are, to date largely Pt-based (HOR) or Pt/Ru-based (ORR).[19] Iridium alloys, however, were shown to perform well as HOR catalysts compared to their platinum couterparts.[23]

Devices with a symmetrical geometry are attractive to manufacturers as only one type of catalyst or electrode material needs to be produced. In this case, 'symmetrical' refers to symmetry in the electrode materials used only – not symmetric processes occurring either side of the membrane, as in Chapter 3 where quasi-reversible organic redox couples mirror each other either side of the membrane. This has not been achieved in PEFCs with functionalised (non Pt) materials meaning the same catalyst has not been used either side of a FC to any reasonable degree of performance. Developing a multifunctional catalyst that is able to perform both the HOR and ORR (in a FC) or both the OER and HER (in a water electrolyser) would be useful, from a manufacturing perspective. Indeed, if a multifunctional catalyst is able to perform opposite functions (e.g. ORR and OER), it would also find significant use in devices where reversibility is required – such as in secondary batteries.

Chapter 3 surveyed four commercially available carbon electrodes and tested them in two different electrolytes in an attempt to establish the most important characteristics associated with electrode microstructure for maximal device performance. In Chapter 4, the synthesis and optimisation of a multifunctional electrocatalyst was outlined and its versatility was demonstrated with a RDE in a variety of pH environments. This chapter aims to bring these two outputs together. In line with the two-pronged question set out in Chapter 1: 'Can this catalyst be used in devices at different pHs and can we validate the 'microstructure / performance' findings?' this chapter looks to both explore a range of devices and to test the permeability-performance relationship observed in Chapter 3 in a device with very different operating conditions (acidic, aqueous vs. organic, non-aqueous). As this work is carried out, further questions will be confronted, such as:

- Is the polymer developed by IONOMR (ion exchange membrane / polymer distributor) an effective polymer for use in devices operating an alkaline environment?

- Given the encouraging RDE responses, is it possible for the multifunctional catalyst to be simultaneously effective in both electrodes of a FC?
- Will different catalyst coating methods have an effect on the performance of the device?
- Will the performance of the carbon cloths (with higher) permeability be the best performing irrespective of alternative electrolyte environments?

Proof of concept devices at each end of the pH spectrum are assembled in order to both test the multifunctional catalyst and explore if the findings in Chapter 3 regarding electrode microstructural characteristics 'hold' in acidic aqueous environments (in addition to the non-aqueous environments tested previously). First, the electrocatalyst is tested in an AEMFC (basic environment). The catalyst is appended to electrode substrates and is systematically tested on either side of the membrane with the ultimate goal of testing the AEMFC using a symmetric geometry as discussed earlier. A variety of problems presented themselves with this device – primarily associated with the catalyst layer. Catalyst testing at the anode in a PEMFC demonstrated promising performance however, unfortunately, reference data, repeats or comparative commercial / synthesised catalysts could not be measured for these fuel cell devices. Lastly, the previously mentioned Mn/H_2 hRFB system was tested using a subset of the electrodes surveyed in Chapter 3. Once the optimised electrode configuration was established in the liquid side, the catalyst synthesised in Chapter 4 was used to replace platinum in the gas side – acting as a bifunctional HOR / HER catalyst in acidic conditions.

Disappointingly, due to significant restrictions on time in the laboratory (due to Covid-19), improvements on several aspects of these devices could not be carried out and extra reference data could not be collected.

5.2 Methodology

Information set out here is specific to the samples and analytical techniques carried out in this chapter. A large portion of the theory is set out in Chapter 2 and provides the basis for this section.

5.2.1 Alkaline anion exchange membrane fuel cell

5.2.1.1 Electrode preparation

Inks were prepared using an anion exchange polymer (AEMION$^+$, Ionomr Innovations Inc.). Ink formulation following guidance from the manufacturer.[24] Light yellow, fibrous solid

ionomer is dissolved in an 80:20 (volume) ethanol:acetone mixture yielding a 1 wt% stock solution. Since the ionomer did not fully dissolve, even after prolonged stirring, it was passed through a glass wool filter inside a pipette to remove the remaining solid impurities. Testing the ionomer stability in solution by leaving it to stir for multiple days showed that, after 48 hours, the yellow colour had disappeared – it was judged that the inks could not be left in solution for any significant length of time (even in the fridge) and therefore that, as soon as the ink was made, it should be appended to the carbon substrate (SGL 29 BC, Fuel Cell Store). This carbon substrate is a structured, fibrous support material with a microporous layer (MPL) on one face, on which electrocatalysts are – its thickness is [235 μm]. This carefully engineered material goes some way to handle water management within the electrode during cell operation.

Enough stock solution was then added to platinum supported on carbon, Pt/C (nominally 40 wt%, HiSPEC 4000), platinum-ruthenium supported on carbon, PtRu/C (nominally 20 wt% PtRu, Premetek) or Ir_NC_900_900 (in-house synthesised) catalysts suspended in either a mixture of water / ethanol or pure ethanol (ethanol forms the best suspensions with Ir_NC_900_900) to produce an ink with a catalyst to ionomer ratio of 15 % (recommended by the manufacturer, IONOMR). The target catalyst loading for the Pt/C and PtRu/C electrodes was 0.4 mg_{metal} cm^{-2}. Whereas, the target loading for the Ir_NC_900_900 catalyst was 3 mg_{cat} cm^{-2} (stated in 'cat' indicating amount of 'carbon catalyst' as the exact mass of iridium is unknown). Using the ICP-MS results from Chapter 4, the iridium loading was taken to be 2.49 wt% inferring a target metal loading of c.a. 0.075 mg_{Ir} cm^{-2}.

Once the ink was produced, pre-weighed carbon electrode substrates with an MPL (SGL 29BC) were placed on a hot plate (set to 65 °C) and ink deposition could commence. A drop-casting method was carried out for the electrodes tested in this device as not enough is understood about the anion exchange polymer to carry out spray-coating. Once drop-casting was complete, the electrodes were cut to size – 5 cm^2 – and stored until required for cell testing. All 5 cm^2 electrodes used in this work were cut into squares i.e. 2.24 cm × 2.24 cm.

The membrane, AEMION$^+$, was activated by removing its backing layers and immersing it in 1 M KOH for at least 24 hours with at least one solution exchange, as suggested by the manufacturers. Immediately before inserting it in the cell, it was removed from the alkaline

solution and briefly rinsed using DI water to remove excess KOH, specifically, unwanted K^+ cations.

5.2.1.2 Fuel cell assembly

The 5 cm^2 Fuel Cell Fixture was provided by Scribner Associates. The blue anodised end-plates lay adjacent to gold plated current collectors and serpentine POCO graphite flow fields (POCO stands for Petrolium Oil Company and is a specific type of graphite). The two electrodes were separated by AEMION$^+$, a relatively new offering to the range of commercially available AEMs. The compression of the two electrodes was c.a. 20 % and was controlled by a number of layers of incompressible, PTFE gaskets (Tygaflor). The thickness of each of the electrodes and membrane was taken into account when calculating the number of gaskets needed. The cell was gently closed and tightened using guiding pins and a torque wrench with a final force of 4.0 N m. Unlike in PEMFCs (where MEAs are produced by hot-pressing before cell assembly), in-situ hot-pressing is commonly carried out in AEMFCs.[22]

Hydrogen was supplied by either an electrolyser (Parker | Dominick Hunter Ltd.) or, like the ultrapure oxygen (99.9998 %), from a compressed cylinder (BIP Plus, Air Products). The Test System is then connected to the cell via temperature controlled gas inlets. The cell was placed in a well ventilated compartment during operation and outlets were connected to an extraction arm (Nedermann). Conditioning procedures and gas management are outlined in the following section.

5.2.1.3 Fuel cell experiments

Figure 5.1 shows a schematic of the AEMFC system as has been described previously. Experiments carried out with this system were operated within an 850 Fuel Cell Test System (Scribner Associates). This system is of significant interest from both a research and commercial perspective for finding alternative energy conversion devices that utilise less expensive components. The experiments carried out in this chapter were standardised such that the electrodes and electrocatalysts were the only variable (as is the case with the other devices tested here).

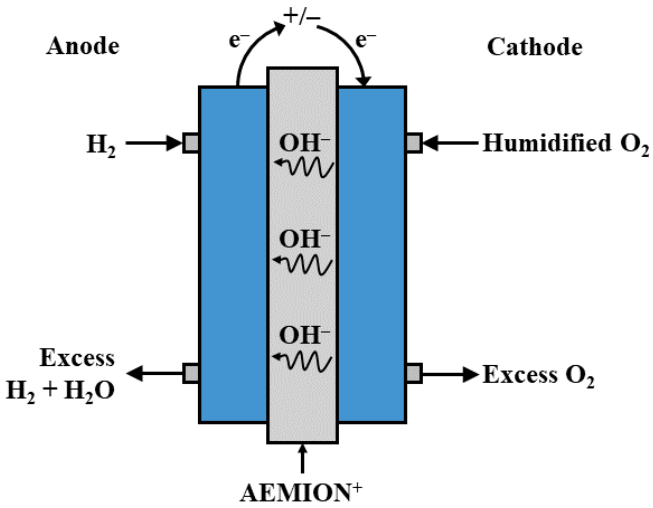


Figure 5.1: Alkaline anion exchange membrane fuel cell schematic. The 850 Fuel Cell Test Station controls the flow, humidity and temperature of the gas into the cell. Heating rods are inserted into the end plates controlling the cell temperature.

Equations (5.1) and (5.2) (introduced in Chapter 1) represent the processes occurring in the AEMFC. The theoretical OCP for this cell is 1.229 V as a result of reduction potentials of -0.828 and 0.401 V vs. SHE, respectively.

$$H_2 + 2OH^- \longrightarrow 2H_2O + 2e^- \quad (5.1)$$

$$\frac{1}{2}O_2 + H_2O + 2e^- \longrightarrow 2OH^- \quad (5.2)$$

Table 5.1: AEMFC membrane electrode assemblies. 'AEI' denotes 'anion exchange ionomer'. The number in parentheses indicates the catalyst loading in mg_{PGM} cm^{-2}.

MEA No.	Anode	Membrane	Cathode
1	PtRu/C + AEI	Aemion$^+$	Pt (0.4) + AEI
2	PtRu/C + AEI	Aemion$^+$	Ir_NC_900_900 (c.a. 0.1)
3	Ir_NC_900_900 (c.a. 0.1)	Aemion$^+$	Pt (0.4) + AEI
4	Ir_NC_900_900 (c.a. 0.1)	Aemion$^+$	Ir_NC_900_900 (c.a. 0.1)

A conditioning procedure was followed to activate the MEA before starting polarisation experiments. First, the MEA was raised to the set temperature (50 °C) by gradually increasing the temperature of the endplates (using the heating rods) in tandem with a flow of hydrogen and oxygen (using the temperature controlled gas inlets) over the anode and cathode – anode:cell:cathode (50:50:50), respectively. A backpressure of 200 kPa was then imposed over the cathode side – this has been shown to enhance performance elsewhere.[25] Once a stable temperature and potential was reached, nitrogen was flowed over the electrodes for a humidification step where the relative humidity is set. Having established a stable relative

humidity (RH), hydrogen and oxygen were then flowed over their respective electrodes inlets and a potential was held at 0.5 V (break-in) until a stable current was realised.[22] The RH in each of the electrodes for this device were informed by Adabi et al. and resulted in the following temperatures being used 44:47:50 (i.e. 88 and 94 % RH in the anode and cathode, respectively).[25]

After this break-in procedure, polarisation experiments were carried out. Usually tests are carried out comparing pure oxygen and air flowing over the cathode, while hydrogen was supplied to the anode. When oxygen flows over the cathode, the performance is much greater compared to when air flows (as manufacturers would want to operate it in a practical device. Manufacturers would also use a CO_2 scrubber at the 'air' inlet to minimise, or ideally totally prevent, the formation of carbonate). However, on initial testing under a flow of oxygen, it was judged that the performance would be too low if this was carried out with the cathode under a flow of air, so only pure oxygen was tested. Polarisation holds were carried out at across a range of irregularly spaced current densities (more at the start to capture kinetic character of a device and more widely spaced at the end at higher current densities), each held for 30 s before moving to the next. Polarisation experiments were not carried out at higher temperatures because the melting point of the AEMION ionomer (65 °C) was not high enough to reach a cell potential of 70 °C.[24]

5.2.2 Proton exchange membrane fuel cell

5.2.2.1 Electrode preparation

Initially, catalyst inks were formulated in a similar way to those prepared for the RDE experiments. The main difference between RDE level and device level formulations is the ratio of catalyst to ionomer (Nafion) ratio – 2:1 catalyst:ionomer (at device level). This higher ionomer ratio is commonly used in the group for similar carbon electrocatalyst materials when producing electrodes for device-level testing.

Following this, inks were thoroughly sonicated producing a stable suspension that was subsequently transferred to a spray-coater 'cup' (Kustom Eclipse CS, Iwata) fitted to an air compressor (CS 25, CIF). The ink was then sprayed onto an electrode that itself was appended to a hot plate set to 65 °C (see Figure A5.9 in the appendix for an image illustrating this). Once the electrode had dried, it was weighed and compared to its original weight revealing the loading of catalyst. The loadings of these 'Nafion ionomer-containing' electrodes was between

3 – 4 mg_{cat} cm^{-2} (the same assumptions were made about the iridium loading as in the AEMFC – c.a. 0.075 mg_{Ir} cm^{-2}). After this step, the electrodes were cut to size – 5 cm^2 before producing the MEA. The MEA was fabricated by hot-pressing the Ir_NC_900_900 anode and commercial cathode on each side of a pre-activated Nafion 211 membrane at 130 °C for three minutes under an applied pressure of 400 kg cm^{-2}.[26]

5.2.2.2 Fuel cell assembly

This assembly was very similar to that of the AEMFC but is presented in full here for completion.

The 5 cm^2 Fuel Cell Fixture was provided by Scribner Associates. The blue anodised end-plates lay adjacent to gold plated current collectors and serpentine POCO graphite flow fields. The two electrodes were separated by a proton exchange membrane (usually Nafion 212 – a commonly used proton exchange membrane). The compression of the two electrodes was c.a. 20 % and was controlled by a number of layers of incompressible, PTFE gaskets (Tygaflor). The thickness of the electrodes and membrane was taken into account when calculating the number of gaskets needed. The cell was gently closed and tightened using a guiding pins and a torque wrench with a final force of 4.0 N m.

Ultrapure hydrogen and oxygen (99.9998 %) were supplied to the 850 Fuel Cell Test System by a compressed cylinder (BIP Plus, Air Products). Occasionally, hydrogen was supplied by an electrolyser (Parker | Dominick Hunter Ltd.). The Test System is then connected to the cell via temperature controlled gas inlets. The cell was placed in a well ventilated compartment during operation and outlets were connected to an extraction arm.

5.2.2.3 Fuel cell experiments

Figure 5.2 shows a schematic of the PEMFC system as has been described above. Experiments carried out with this system were operated by a 850 Fuel Cell Test System (Scribner associates). With many variables, this system is of significant interest from both a research and commercial perspective for direct energy conversion and transport applications. The experiments carried out in this chapter were standardised such that the electrodes and electrocatalysts were the only variable (as is the case with the other devices tested here).

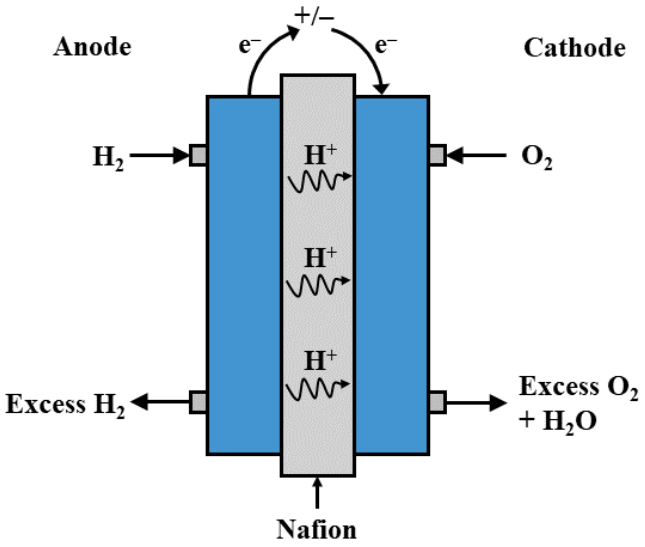


Figure 5.2: Proton exchange membrane fuel cell schematic. The 850 Fuel Cell Test Station controls the flow, humidity and temperature of the gas into the cell. Heating rods are inserted into the end plates controlling the cell temperature.

Equations (5.3) and (5.4) (introduced in Chapter 1) represent the processes occurring in the PEMFC. The theoretical OCP for this cell is 1.229 V as a result of reduction potentials of 0 and 1.229 V vs. SHE, respectively.

$$H_2 \longrightarrow 2H^+ + 2e^- \qquad (5.3)$$

$$\tfrac{1}{2}O_2 + 2H^+ + 2e^- \longrightarrow H_2O \qquad (5.4)$$

Polarisation experiments with this device were carried out in two ways – with either oxygen or air flowing over the cathode. When oxygen flows over the cathode, the performance is much greater compared to when air flows. This is due to the much lower proportion of oxygen (20 %) getting to the active sites. This, in turn, enables the cell to reach much higher current and power densities but, at the same time, may lead to accelerated corrosion. Therefore, just one oxygen polarisation curve is collected and the others are collected with air flowing over the cathode. During oxygen runs, hydrogen and oxygen were supplied at 200 standard cubic centimetres per minute (sccm). During 'air runs', hydrogen flowed at 300 sccm and air was flowed at 1000 sccm. The gases in these tests were set to 100 % RH and the cell temperature was set to 80 °C. Polarisation curves were recorded by holding the cell voltage for one minute at each point.

5.2.3 Manganese / hydrogen hybrid redox flow battery

5.2.3.1 Electrode preparation

On the liquid side, Freudenberg H23, AvCarb 1071 and graphite felt (Sigracell®GFD 4.6, SGL) were used. These materials were cut to size (5 cm^2) and, immediately before insertion into the cell for testing, were placed in a plasma chamber and were subjected to an oxygen plasma treatment (as outlined in Chapter 2).

On the gas side, a platinum electrode (0.4 mg_{cat} cm^{-2}, ELE027-10321015978, Johnson Matthey) was used for the majority of the experiments (ensuring the gas side of this reaction was never a limiting factor). These were cut to size but did not undergo any pre-treatment ahead of being utilised in a cell. For the final experiment however, after incrementally testing the liquid side of the system with a number of commercially available electrodes, the commercial Pt electrode was replaced with an Ir_NC_900_900 electrode produced using the spray coating technique outlined in the PEMFC devices (i.e. using the Nafion ionomer binder and an SGL 29 BC substrate). This final experiment was carried out to tie together the learnings from Chapters 3 and 4.

5.2.3.2 Electrolyte preparation

Titanium oxysulfate ($TiOSO_4$, Sigma Aldrich) was added in three batches to DI water (half the total final volume) and vigorously stirred until the solution was faintly cloudy. The concentration of TiO^{2+} in solution at this point was roughly 2 M and therefore was considered to be strongly acidic with a pH close to 0.5.[27] Sulfuric acid (H_2SO_4, VWR International) was then added slowly and the solution was left to cool until the solution reached room temperature. The solution was then transferred to a suitably sized volumetric flask and made up to the mark with DI water. The masses and volumes of $TiOSO_4$ and H_2SO_4, respectively, ensured the final concentrations of this 'stock' acidic TiO^{2+} solution were 5 M H_2SO_4 and 1 M $TiOSO_4$. The final step to complete the preparation of the standard electrolyte was carried out only immediately before the experiment was to be carried out. It involved adding a mass of $MnCO_3$ (Alfa Aesar) to the stirring stock solution, ensuring the end Mn^{2+} concentration was 1 M. On adding the manganese salt, the highly acidic solution protonates one of the oxygen atoms on the carbonate to produce 1 M water – ultimately leading to the production of CO_2 (g) (assumed to be fully lost to the atmosphere). The solution was left to stir gently for at least 30 minutes once all the solid is dissolved. The end Mn^{2+}, Ti^{4+} and 'sulfur' concentrations were 1 M, 1 M and 6 M, respectively. This electrolyte is discussed in much greater detail in the next chapter.

Both cycling and polarisation procedures were carried out when testing the electrodes and electrocatalysts in this device. Cycling tests demanded a small volume of 20 mL and for the polarisation tests outlined in this chapter, 400 mL of electrolyte was prepared and charged to the maximum SOC.

5.2.3.3 Hybrid redox flow battery assembly

The hybrid-flow / fuel-cell fixture was provided by Scribner Associates. The liquid side (red anodised end-plate side) and gas side (blue anodised end-plate side) lay adjacent to gold plated current collectors and serpentine POCO graphite flow fields. The two electrodes were separated by a proton exchange membrane (usually Nafion 212). The compression of the two electrodes was c.a. 20 % and was controlled by a number of layers of incompressible, glass-reinforced PTFE gaskets (Tygaflor). The thickness of the electrodes and membrane was taken into account when calculating the number of gaskets needed (see Figure A5.10, in the appendix, for gasket calculations). The cell was gently closed and tightened using a guiding pins and a torque wrench with a final force of 4.0 N m.

Masterflex tubing (Versilon™) and appropriately sized connectors were attached to the liquid outlet and a peristaltic pump (Cole-Parmer) was used to pump the liquid electrolyte through the liquid side of the cell at a standard rate of 50 mL min^{-1}. Hydrogen was supplied through Nylon tubing by an electrolyser (Parker | Dominick Hunter Ltd.) and connected to the inlet of the gas side of the cell via a mass-flow controller (Bronkhorst). The mass-flow controller was set to supply 100 mL min^{-1} hydrogen, continuously, during the charge and discharge of the cell. The outlet of the cell was connected to a Nederman extraction arm. In the intermediate time, between cycles when the cell was not being used but the electrolyte still flowing through the liquid side, nitrogen was passed over the platinum electrode to ensure no electrochemically parasitic discharge reaction occurred (hydrogen did flow, however, during the transient measurements perhaps contributing partially to reduction of the active species in the electrolyte).

5.2.3.4 Hybrid redox flow battery experiments

Experiments carried out with this system were operated by a range of potentiostats. Cycling was carried out using a Gamry Reference 3000, charging large volumes of electrolyte ahead of polarisation steps was carried out on an 857 Redox Flow Cell Test System (Scribner

Associates) and polarisation tests were carried out using an 850 Fuel Cell Test System (Scribner Associates). These setups can be shown in Figure A5.11. Figure 5.3 shows a schematic of the Mn/H_2 hRFB system as has been described above. With many variables, this system is of significant interest from both a research and commercial perspective for grid-scale energy storage. The experiments carried out in this chapter were standardised such that the electrodes and electrocatalysts were the only variable (as is the case with the other devices tested here).

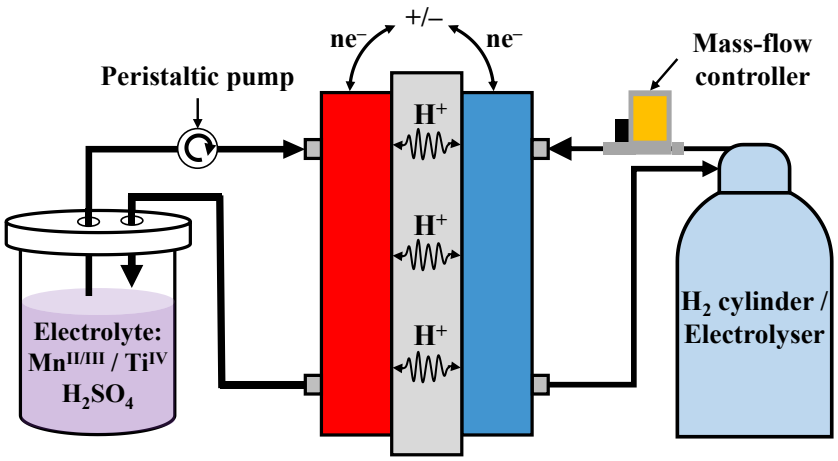


Figure 5.3: Mn/H_2 hydrogen redox flow battery experimental schematic. The system as a whole is controlled by an exterally connected potentiostat. Electrolyte flow on the liquid side is controlled by a peristaltic pump. Hydrogen flow on the gas side is controlled by a mass-flow controller positioned between an electrolyser and the cell.

The forward reactions in Equations (5.5) and (5.6) show the processes occurring in the hRFB cell during charging steps (these reversible reactions occur in the backward direction during the discharge). The overall OCP of this cell is 1.509 V.[28]

$$2H^+ + 2e^- \rightleftharpoons H_2 \qquad (5.5)$$

$$Mn^{2+} \rightleftharpoons Mn^{3+} + e^- \qquad (5.6)$$

The membrane electrode assemblies (MEAs) are described in Table 5.2.

Table 5.2: Flow-through configuration of electrode and membrane materials for testing in a manganese-hydrogen hybrid redox flow battery. MEA = Membrane electrode assembly. (Parentheses alongside liquid and gas side electrodes indicates number of electrode layers used and the catalyst loading in mg_{PGM} cm^{-2}, respectively.)

MEA No.	Liquid side	Membrane	Gas side
1	Felt (1)	Nafion 212	Pt (0.4)
2	Felt (1)	Pemion	Pt (0.4)
3	Freud. H23 (1)	Nafion 212	Pt (0.4)
4	AvCarb 1071 (2)	Nafion 212	Pt (0.4)
5	AvCarb 1071 (3)	Nafion 212	Pt (0.4)
6	AvCarb 1071 (3)	Nafion 212	Ir_NC_900_900 (c.a. 0.1)

Graphite felt (SGL carbon, Sigracell®GFD 4.6), Nafion proton exchange membranes and platinum on carbon (JM) was used initially in an attempt to reproduce the results reported by Rubio Garcia et al.[29] Pemion proton exchange membrane was tested to see if this, much thinner, membrane could withstand the hydraulic pressure placed on it without significant crossover or leaking. Potential benefits could include much lower HFRs resulting in higher VEs. Freudenberg H23 and AvCarb 1071 were tested in this device as they represent two ends of permeability spectrum established in Chapter 3 (AvCarb 7497 was not available for testing in this work package, unfortunately). AvCarb 1071 is considered to have a high permeability and Freudenberg H23 has a much lower permeability. In the electrochemical environment and configuration tested in Chapter 3 this translated to AvCarb 1071 having a much higher performance. The number of AvCarb 1071 layers, latterly, was varied to ascertain an optimal electrode thickness. And, finally, the platinum electrode was replaced by an electrode with Ir_NC_900_900 (developed in Chapter 4) spray-coated onto a carbon substrate (SGL29 BC, Fuel Cell Store). This in-house synthesised electrode was made from the same batch as those tested in the PEMFC system.

Cycling experiments were carried out using chronoamperometry whereby a current was demanded of the cell until the cell cut-off potential is reached (1.8 V or 0.5 V during charging or discharging steps, respectively). Efficiencies of these cycles were then evaluated. Current densities of between 50 – 225 mA cm^{-2} were tested (current densities as low as 25 mA cm^{-2} are tested in the next chapter).

A large volume of electrolyte (400 mL) was charged at 75 mA cm^{-2} using a 25 cm^2 cell alongside a 857 Redox Flow Cell Test Station. This electrolyte was then disconnected and (quickly) transferred to the smaller cell undergoing the polarisation tests (controlled by a 850

Fuel Cell Test Station). The large volume of electrolyte is used to ensure that polarisation tests are carried out at a more or less consistent SOC over the course of the polarisation test. Cell performance is heavily dependant on SOC in RFB systems.[30] Polarisation was carried out by sequentially holding current densities for 20 seconds at semi-regular intervals between 0 – 1300 mA cm^{-2} (only semi-regular because more data points are desired at the beginning of the polarisation where the system is kinetically limited).

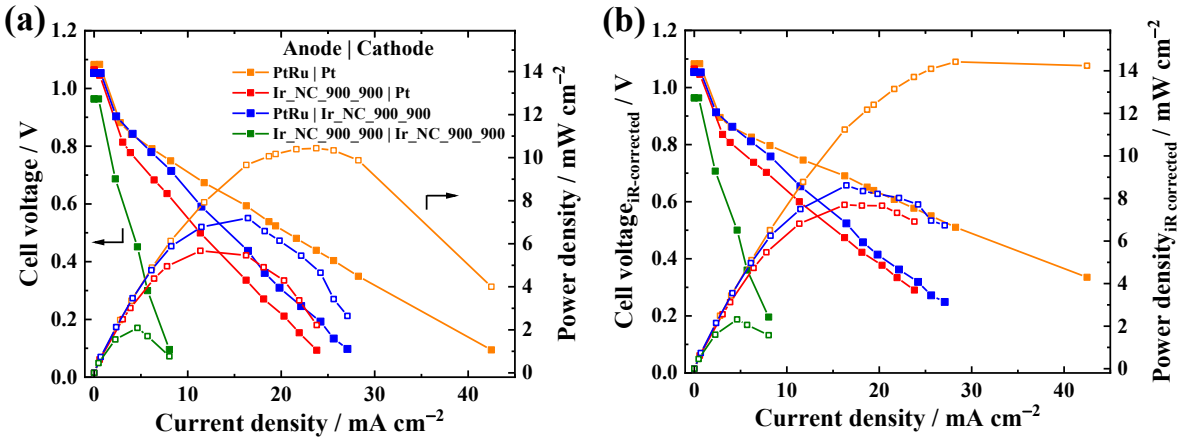
5.3 Results and discussion

5.3.1 Alkaline anion exchange membrane fuel cell

AEMION – a relatively new addition to the commercial anion-exchange polymer market – was first reported by Thomas et al.[31] and is used in the AEMFCs tested in this work. These ion exchange polymers crowd the C2 position (by attaching multiple methyl groups to N-positions) in benzimidazolium hydroxide moieties affording these molecules with high resistance to aggressively nucleophilic OH^- ions.[31] One of the challenges for alkaline fuel cell technology, moving away from liquid electrolytes, is to develop thin membranes (<10 μm) with high conductivities (> 100 mS cm^{-1}) to allow the delivery of sufficient current density (0.5 A cm^{-2}) while simultaneously achieving the 5000 hour target operation duration at 80 °C.[19,32] The layers for the commercial Pt/C and PtRu/C catalyst were cracked and it was expected that resistance issues would be prevalent in the tests. The layer prepared using Ir_NC_900_900 catalyst needed to be high in thickness to achieve the target catalyst loading (3 mg_{cat} cm^{-2}) (the average electrode thickness after drop-casting was c.a. 400 μm). Given the large volume of ink used to drop-cast the catalyst layer onto the carbon electrode substrate, the catalyst layers were thick, very cracked and, to varying degrees, peeling away from the substrate – see appendix for photographs (Figure A5.8 (a) and (b)).

Before polarisation experiments were carried out, it was suspected that in addition to the poor mass transport in the catalyst layer, the electrodes may have been flooded during the conditioning step. It was observed that during the break-in period – 0.5 V potential hold for one hour – that the Pt/PtRu system was stable then, indicated by a large increase in ohmic drop, becomes very unstable after c.a. 45 minutes – presumably when flooding occurs. The cell was then dried using nitrogen and flooding subsided indicated by the increase in potential. Polarisation curves at 60 °C were then measured.

The polarisation data displayed in Figure 5.4 (a) and (b) shows extremely poor performance. Current state of the art devices using PtRu and Pt catalysts in the anode and cathode respectively are able to reach peak power densities of 2 W cm^{-2} and current densities of 100 mA cm^{-2} at 0.9 V (low overpotential).[25,33] Electrodes incorporating this anion exchange polymer have been shown to work effectively at device level in an AEMFC – supporting current densities of >1000 mA cm^{-2} and power densities of 370 mW cm^{-2}.[21] MEA 1, using PtRu and Pt at the anode and cathode respectively, was used as the reference MEA. These electrodes were shown to yield the best performance in the AEMFC compared to the other MEAs, with a peak power density of c.a. 10 mW cm^{-2}. Subsequent peak power densities using electrodes containing the anion exchange polymers alongside in-house synthesised catalyst (Ir_NC_900_900) and the anion exchange membrane (AEMION^{+}) yielded extremely low power densities. The reason for these low performances is tentatively attributed to a combination of the Ir_NC_900_900-containing electrodes not being as effective catalysts towards their respective purposes (compared to Pt-based catalysts), but also perhaps due to the lower catalyst loading which led to a thinner electrode layer allowing the active species access catalyst active sites. Particularly poor performances were observed (in MEA 2 and 4) where the Ir_NC_900_900 catalyst was used in the anode – i.e. performing HOR in base. This, at least, is in line with the results from Chapter 4 (which showed particularly high overpotentials required to reach peak HOR activity). However, it is surprising that, in the kinetic region (low current densities), the iridium containing electrodes appear to have a similar character to MEA 1.



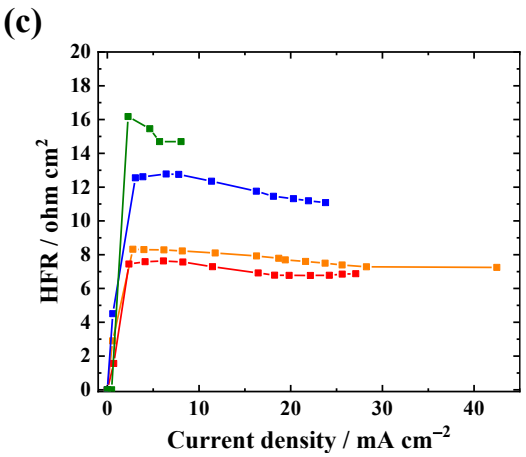


Figure 5.4: Alkaline anion exchange membrane fuel cell polarisation data using in-house synthesised electrodes flowing oxygen and hydrogen over the cathode and anode, respectively. (a) and (b) show the voltage and power density curves without and with an iR-correction, respectively. (c) shows the area specific resistances encountered during each of these polarisation experiments.

The HFRs (ohmic losses) in these cells are extremely high and there was therefore no reasonable expectation for these cells to reach high (or even low) current densities or return reasonable power densities. As alluded to previously, the reason for this high area resistance is largely considered to result of the high membrane resistance. Bicarbonate in the membrane which may have formed following aggressive nucleophilic hydroxide attack on trace dissolved atmospheric CO_2 (this may have occurred to an extent during membrane activation), will also raise the membrane resistance (bicarbonate is not conductive). While the fuels used in this section are ultrapure hydrogen and oxygen (therefore with negligible CO_2), this bicarbonate will persist in the membrane without any way being removed. Additional resistances are expected in the mass transport region as a result of the poor catalyst layer deposited on the carbon substrate, alongside a fundamental lack of understanding of the physical properties of the anion exchange polymer. Improvements are discussed in the 'Future work' section below and could not be carried out for this project because of limited time in the laboratory due to Covid.

5.3.2 Proton exchange membrane fuel cell

Only a small amount of cracking was observed on the electrode before it was hot-pressed (Figure A5.8 (c)). This hot-pressing step induces extremely good contact between the catalyst and membrane while preserving an effective GDL enabling active gaseous species to reach the catalyst active sites.

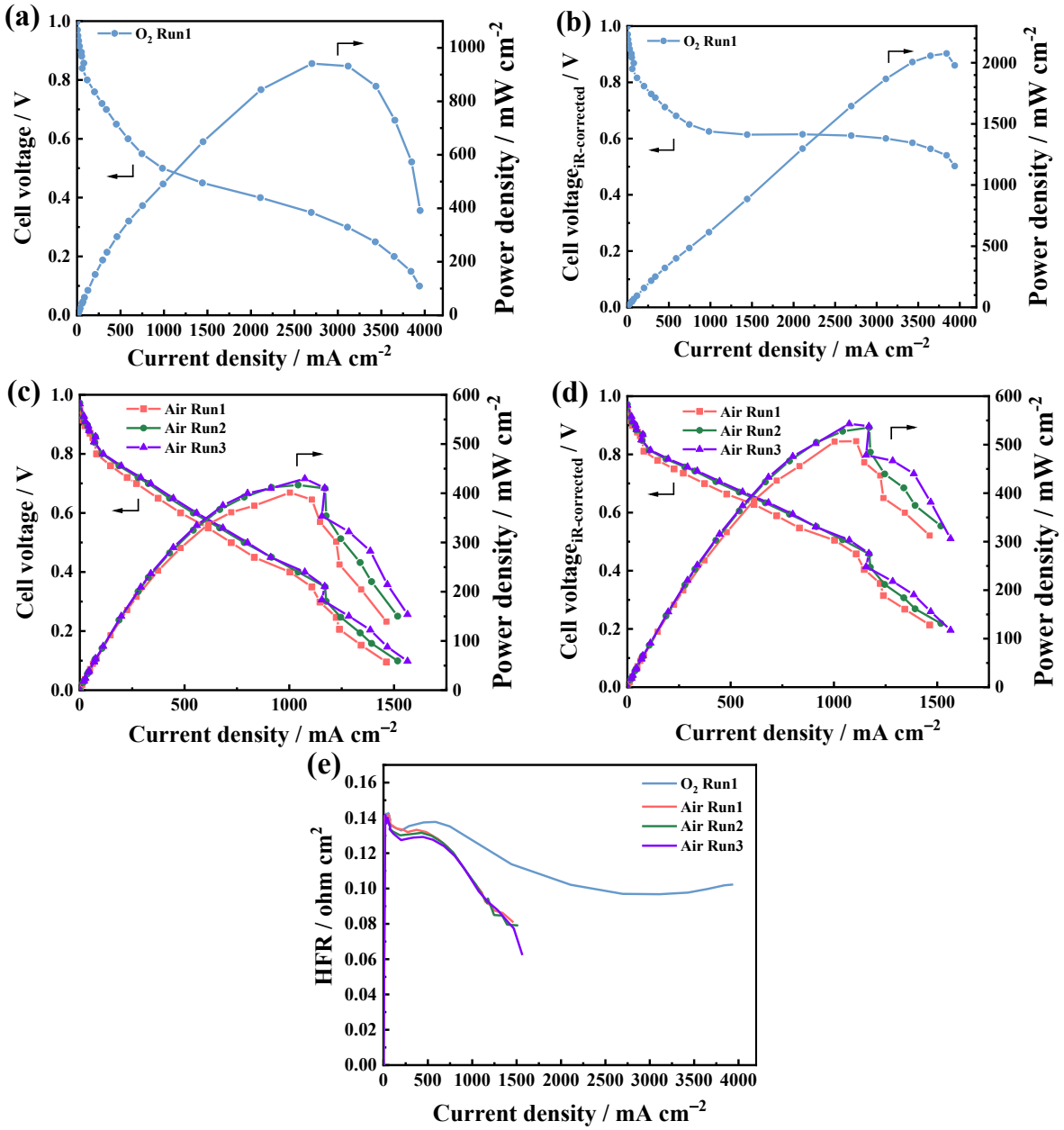


Figure 5.5: Proton exchange membrane fuel cell tests using Ir_NC_900_900 as the catalyst at the anode and a commercial platinum electrode (JM, 0.4 mg_{Pt} cm^{-2}) at the cathode with an active are of 5 cm^2. (a) and (c) show the polarisation curves free of iR correction with oxygen and air flowing over the anode resectively; (b) and (d) show their iR-corrected counterparts. The HFR during these potential holds is displayed in (e). Oxygen tests are carried out with a flow rate of 200 sccm on both sides of the cell. Air tests are carried out with flow rates of: hydrogen at 300 sccm and air at 1000 sccm. The cell temperature was 80 °C and gases have an RH of 100 %.

The Ir_NC_900_900 catalyst is shown to perform fairly well in this electrochemical device. Peak iR-corrected power densities of over 2 W cm^{-2} and 500 mW cm^{-2} in oxygen and air, respectively, are comparable with other precious metal-containing catalysts.[10,18] This infers, in line with promising RDE tests, that the catalyst is able to effectively perform the HOR in a PEMFC even at very large operating current densities. The single cell performance level

obtained with Ir_NC_900_900 as the anode catalyst are matching or even better than some of the reported iridium or cobalt catalysts.[10,18,34–36]

5.3.3 Manganese – hydrogen hybrid redox flow battery

Using the work set out by Rubio Garcia et al. as a convenient 'starting point' for these tests,[29] carbon electrodes were first tested in the liquid side. Nafion 212, graphite felt and a platinum cathode were used in the first cell as the standard components for the membrane, anode and cathode materials in the first instance. This sub-section focusses on the variation of anode carbon material with minor alterations in the membrane and the cathode (only briefly mentioned). Cycling experiments were carried out to investigate the VEs of cell cycling as a function of current density. Figure 5.6 (a) shows an example of charge and discharge cycles using two layers of AvCarb 1071 as the cathode. Increasing the current density leads to a smaller portion of the electrolyte being converted to the 'charged state' – this is due to the requirement of greater overpotentials for higher current densities resulting in less active species being able to reach the electrode surface for conversion.

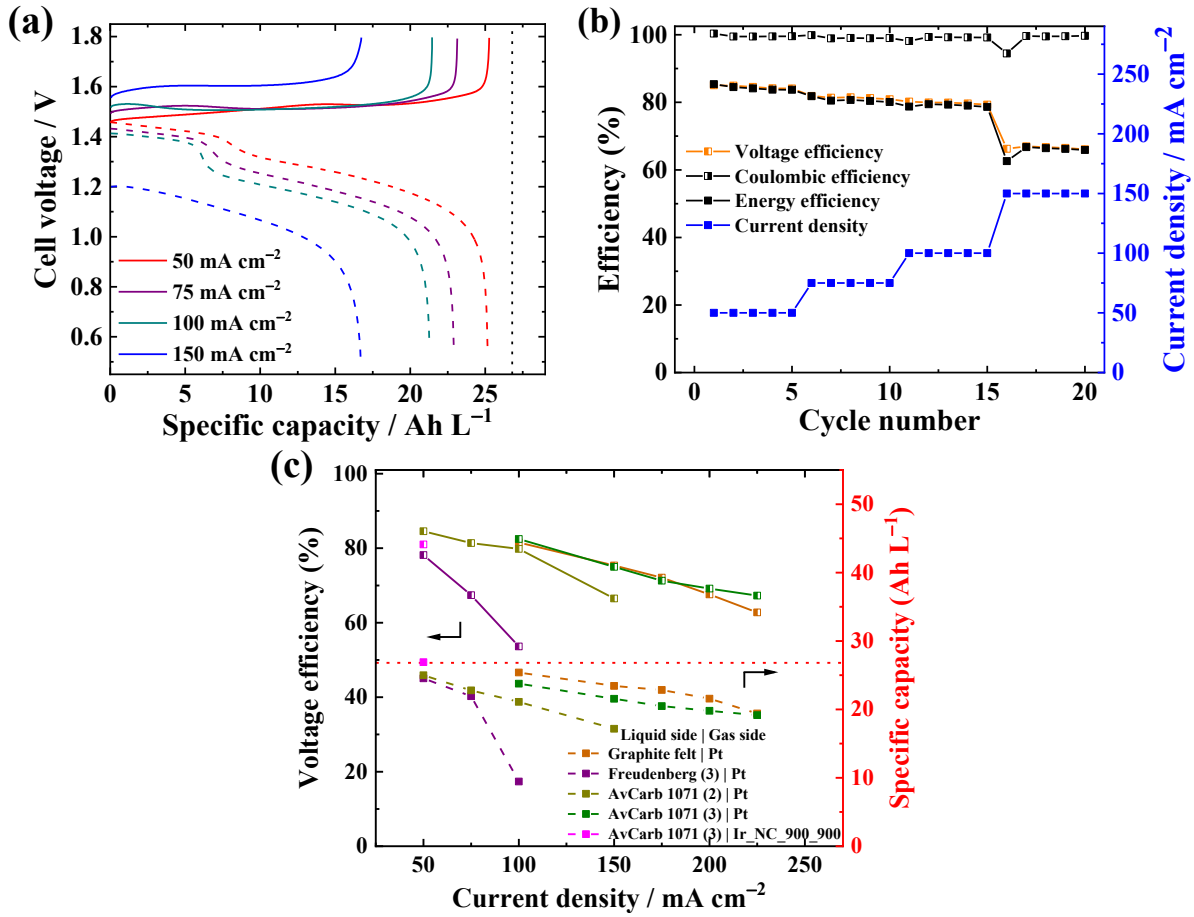


Figure 5.6: (a) and (b) utilise a manganese hydrogen hRFB system employing two layers of AvCarb 1071, Nafion 212 and a commercial platinum electrode where; (a) potential is plotted as a function of the specific capacity for a series of charge (solid line) and discharge (dashed line) cycles at different current densities. The dotted line at 26.8 Ah L^{-1} which corresponds to the theoretical maximum specific capacity for 20 mL of this electrolyte; (b) summarises the voltage (left half

filled square), coulombic (right half filled square) and their product, the energy efficiency (full square) of a number of cycles with this specific assembly. (c) A summary of the average voltage efficiencies and achieved specific capacities of the cycles measured at a specific current density. Different colours represent different configurations. Nafion 212 was used in each of these configurations.

If the active species in a redox couple are stable, the coulombic efficiency (CE) is usually very high as there are no unwanted side reactions. It is well known that Mn^{3+} disproportionates in solution (this is subject of intense discussion in the next chapter), however, the Ti^{4+} additive added to the electrolyte is shown to have a stabilising effect on the Mn^{3+} (or some pseudo-species) meaning that the great majority of the coulombs passed into the electrolyte are recovered. The VE of a cycle is usually a good indicator of the overall energy efficiency therefore. The efficiencies, including the VE (introduced in Chapter 2) of each cycle using one electrode configuration is shown in Figure 5.6 (b) alongside the current densities. This was repeated at a range of different current densities for the other configurations outlined in Table 5.2 and summarised in Figure 5.6 (c). 75 % efficiency represents the lower bound of acceptable VEs in RFBs otherwise they are considered to be too inefficient for consideration for scale-up. These data show that, in terms of VE, three layers of AvCarb 1071 outperform graphite felt at the highest current densities measured. This is significant since felts have, historically, dominated standardised testing in RFB systems. After cycling at 50 mA cm^{-2} with promising energy efficiency (magenta data in Figure 5.6 (c)), the highest performing electrode configuration in the liquid side (3 layers × AvCarb 1071) alongside the in-house synthesised Ir_NC_900_900 gas electrode failed immediately when exposed to a current of 75 mA cm^{-2}. It was decided to immediately carry out the polarisation experiments with this configuration (rather than attempting to capture more cycling data potentially damaging the gas electrode). The motivation to test the Ir-containing catalyst in this system was out of curiosity rather than in order to technologically improve the system. Commercially available Pt/C, clearly, works very well and replacing it with another precious metal catalyst would be technologically futile.

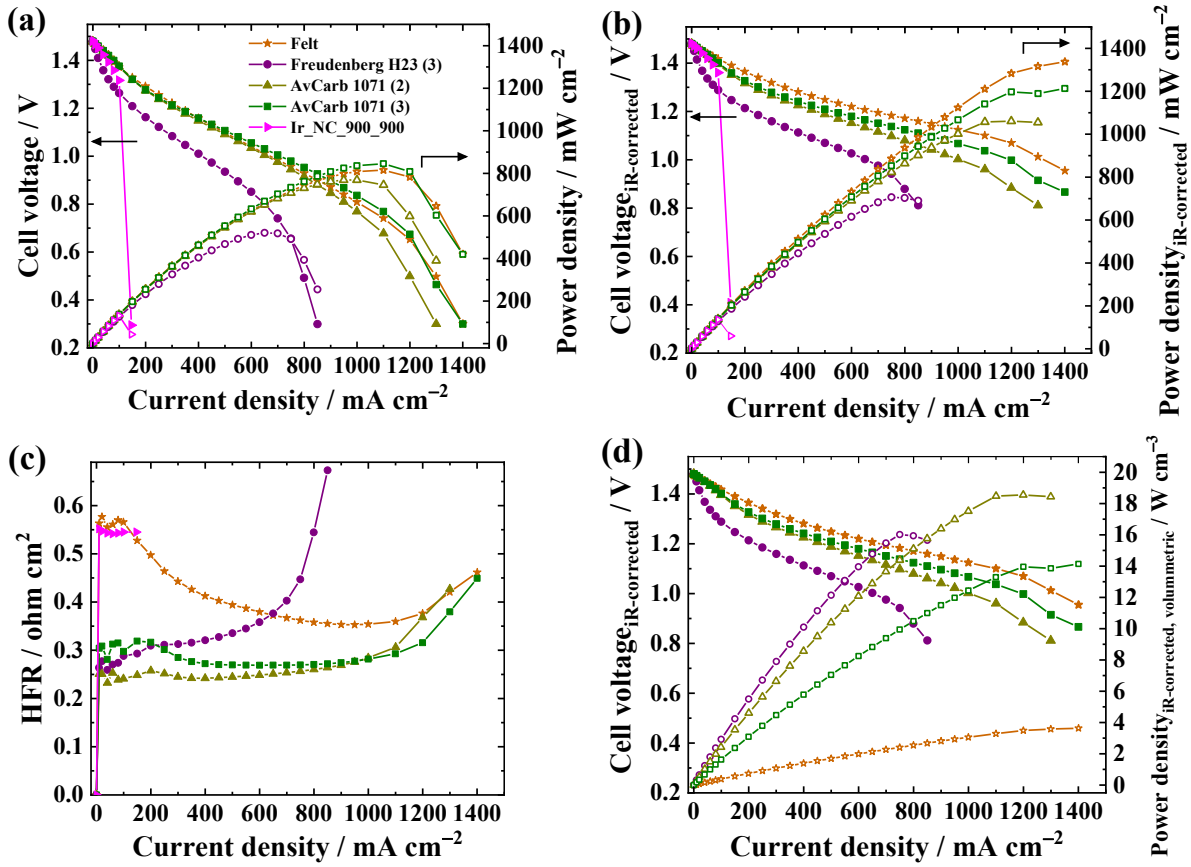


Figure 5.7: Polarisation curves examining the capability of electrode materials in a manganese hydrogen redox flow battery. (a) and (b) display polarisation (left hand axes) and power curves (right hand axes) without and with iR-corrections (respectively) for each of variations in liquid side electrode configuration and the gas side variation using Ir_NC_900_900 alongside 3 layers of AvCarb 1071 (magenta). (c) HFR responses during polarisation experiments. (d) Alternative representation of (b) using compressed thickness of electrodes in liquid side to display volumetric power densities.

The polarisation curves shown in Figure 5.7 (a) and (b) show that the woven carbon cloth materials perform almost as well as the graphite felts, reaching peak power densities of 1.21 W cm^{-2} (vs. 1.34 W cm^{-2} for graphite felt) using three layers of AvCarb 1071. The ASR of the systems utilising woven carbon cloths is much lower than either of the other carbon materials. This is tentatively attributed to, as it was in Chapter 3, an enhanced ability of carbon cloths to be able to distribute the electrolyte around the available active area on the electrode. Three layers of Freudenberg were used in order to compare comparatively thick liquid-side electrode configurations. High frequency resistances with this electrode array, interestingly, remain lower than those of felt for the initial part of the polarisation (purple circles), but quickly rise as a result of increasing overpotential with current density.

While these findings appear unremarkable, these measurements only illustrate area-specific capability. Using these carbon cloths, however, a significantly larger volumetric power density is achieved (Figure 5.7 (d)). This may be extremely valuable to manufacturers producing RFBs

in all geometries as utilising these periodic, woven carbon materials allow much greater volumetric power densities to be achieved – thereby reducing stack size and, ultimately, capital costs.

When carrying out these polarisation measurements, reproducibility was difficult because, while the trends hold for each of the electrode configurations across the board, the variation in starting potential was much greater than expected for a stable electrolyte. This is discussed and examined in much more detail in Chapter 6 but could be partly as a result of the changing solution equilibria at high concentrations of Mn^{3+} (due to disproportionation). This is not expected to have a meaningful effect on the polarisation curves displayed here (as the volume of electrolyte is large), but is to be considered if these experiments are to be repeated – after carrying out a polarisation experiment at maximum SOC, the operator must discharge to below c.a. SOC 25 % before then charging up again if they are to expect replicable results – noting that this is extremely time consuming.

Finally, drawing on previous findings from Chapter 3 pertaining to the correlation of electrode permeability with performance, AvCarb 1071 outperforms Freudenberg H23 in this electrochemical environment by far. While there are always exceptions, this strongly suggests that the microstructural-performance metrics established in Chapter 3 hold across a range of electrochemical environments.

5.4 Conclusions

This chapter ties together the findings in Chapter 3 and Chapter 4 by testing some of the electrodes in Chapter 3 (AvCarb 1071 and Freudenberg H23) with the best performing electrocatalyst synthesised in Chapter 4 (Ir_NC_900_900) in a Mn/H_2 hRFB. Additionally, the catalyst was tested in FCs at two different pHs meaning the overall goal of testing the catalyst at device level have been achieved, with varying degrees of success.

Having established, in Chapter 4, that the catalyst was effective towards catalysing the ORR and, to a limited degree, the HOR in alkaline conditions, the goal in the AEMFC experiments was to get the same catalyst to catalyse these processes on each side of the membrane (in a symmetrical fashion) at device level. Clearly, this was not achieved with any reasonable performance, but it is asserted that this was because of contact and mass transport issued associated with the layer, high membrane resistances and a fundamental lack of understanding

about the physical properties of the anion exchange polymer, rather than any significant catalyst shortcoming.

Moving to a different pH environment, there were different expectations of the catalyst. No parallel can be made between these devices in terms of layer quality because of the number of different factors changing at device level (pH, catalyst deposition method, temperature, ionomer). The electrodes were spray-coated with a manual spray gun – while this was an extremely laborious task, it provided a layer that was only marginally cracked and, after hot-pressing, produced an MEA that worked effectively. This iridium catalyst acting as an HOR catalyst in the anode of this PEMFC showed surprisingly good performance (in line with the results from Chapter 4) using air as the electrolyte, showing current densities of 480 mA cm^{-2} at 0.7 V (iR corrected) and peak power densities of 543 mW cm^{-2}. (It should be noted that an iridium containing electrode, prepared in the same spray coating fashion as for these PEMFCs, was used in the manganese hydrogen hRFB (acid) system but was not hot-pressed. The results from this hRFB polarisation experiment were poor indicating that hot-pressing is likely to have a significant effect on the performance of the device.)

The manganese hydrogen hRFB system tested a subset of the electrodes surveyed in Chapter 3. From a performance perspective, the findings in this chapter were consistent – showing that the woven material, with much greater permeability, performs better in a system where (a dominant) convective flow pushes the liquid electrolyte through the electrode. While this correlation between permeability and performance holds for AvCarb 1071 and Freudenberg H23, the relationship becomes more complicated when considering felts. The carbon cloth marginally outperforms the felt tested in this work – this is considered to be as a result of the periodic arrangement of carbon fibre bundles being better able to distribute electrolyte over the whole active area in the cell. Representing electrode ability in terms of volumetric power density shows that, for instance, in the case of designing stack level manganese hydrogen hRFBs (out of the liquid-side electrode variations tested in this work) two layers of AvCarb 1071 enables the most power dense cell output. This is important if manufacturers are to continue improving their cell power densities and lowering the ultimate stack cost.

While these conclusions describe tentative agreement with the findings of previous chapters, with more time, catalyst layers would have been optimised and a greater breadth of tests would have either confirmed or contradicted the assertion that, combined, the principles outlined in

Chapter 3 and the catalyst synthesised in Chapter 4 would have led to promising device-level performance. Some thoughts for future work are described in the next sub-section.

5.4.1 Future work

Ideally, the lab-scale spray-coater (ExactaCoat, Sono-Tek) would have been operational at some point during the course of this PhD. Availability of this spray-coater would have provided the capability to make extremely uniform catalyst layers (of the same quality as those commercially distributed) which would have removed the issues surrounding the layer and potentially improved FC and hRFB performances involving in-house synthesised electrocatalysts.

Testing the catalyst in additional devices where 'air-breathing' materials are required would have been interesting for inspection of the breadth of devices the catalyst could be used in. A zinc-air device and electrolyser would have provided interesting frameworks from which to investigation. Additionally, given the findings in Chapter 4, demonstrating the multifunctional catalyst operates in a device at neutral pH in addition to the ones attempted in this chapter would have also been interesting. The following subsections refer to specific aspects of each of the tested devices in this chapter.

5.4.1.1 AEMFC

- Optimise the ink layer
    - Test different solvents that might be more compatible.
    - Change compositions varying the exchange polymer and catalyst concentrations.
    - Try using Nafion ionomer (given this was shown to perform at RDE level in alkaline conditions).
- Understand the relationship between catalyst layer and humidity.
- Use the literature available as a starting point.
- Repeat the experiments.

5.4.1.2 PEMFC

As mentioned at the beginning of this chapter, laboratory time was limited for this aspect of the work due to Covid restrictions and it was not possible to carry out equivalent experiments with reference materials. The results may well have motivated optimisation of the catalyst layer

and the RH in the anode and cathode. Future work with this electrochemical device would also include durability tests whereby chronoamperometry would be carried out over the cell.

5.4.1.3 Mn/H_2

It is suggested that different formulations of electrolyte (e.g. with higher or lower SO_4^{2-} concentration) would give different cycling efficiencies. Preparing alternative concentrations of stock solution (as described in the methodology) may provide interesting revelations about the effect of sulfate or Mn^{3+} concentration on the voltage efficiency or the location of the step in the discharge (during cycling). Carrying out polarisation curves alongside these changes in SO_4^{2-} concentration, at different SOCs on the charging arm would provide interesting information about what peak power densities are achievable and how they relate to sulfate concentration.

These electrochemical devices, ultimately, will be used for grid scale long duration energy storage and so carrying out durability tests comparing these electrodes would be interesting. Given it was found that different electrode assemblies with different microstructures and number of carbon layers significantly affect the performance, it would also be interesting to explore the limitations in terms of power density with different electrodes. Usually, during operation, charging / discharging steps would be initiated without any form of ramping, so gradual increases in current densities would enable higher current densities to be reached. The high HFR peaks at the beginning of charging steps indicated large resistances at the electrolyte-solid interface. The working hypothesis for this is that deposition of solid material occurs at the surface and then behaves as a catalyst the rest of the charging cycle. Identifying what may be deposited on the surface of the electrode during charging would be interesting – its exact composition is unknown but is the subject of continued investigation. A good place to start for this would be to deposit a thin layer of gold or another metal onto the surface of the electrode in the liquid side to see if this affects the HFR and ultimately the maximum current. Operando methods by which to measure how the electrolyte evolves over the course of the charge / discharge cycle would also be interesting. The next chapter investigates some of these aspects.

5.5 Appendix

5.5.1 Supplementary catalyst layer preparation

Figure A5.8 (a) and (b) show catalyst layers that were produced using the drop-casting method with AEMION (IONOMR) used as anion exchange ionomer. These layers were first attempts

and would require extensive optimisations and further understanding of the ionomer before being confident the layer is not a limiting factor in the device. (c) and (d) are equivalent spray-coated catalysts using Nafion as the ionomer. Clearly their layers are much better – Figure A5.8 (c), however, has significant cracking at the edges. Following hot-pressing, this poor layer feature did not appear to have a significant effect on the PEMFC performance.

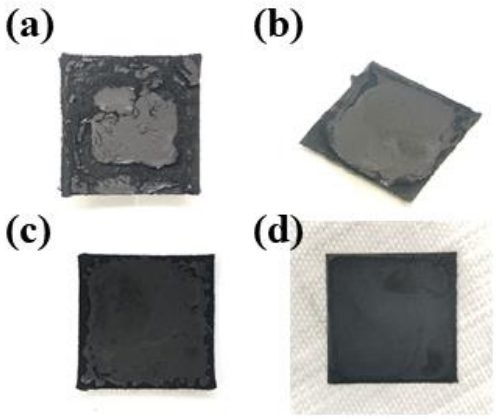


Figure A5.8: Images of electrodes (5 cm^2) with (a) the words and (b) the best catalyst layers achieved using a drop casting method with inks containing anion exchange polymer. Catalyst layers deposited by (c) spray coating and (d) drop casting (this electrode not used in this work) nafion-containing inks for using in PEMFC and Mn/H_2 electrochemical devices.

Figure A5.9 is an image showing the setup used to spray-coat a 20 cm^2 substrate (before cutting it into four 5 cm^2 pieces) using the spray gun in the bottom right corner of the photograph.

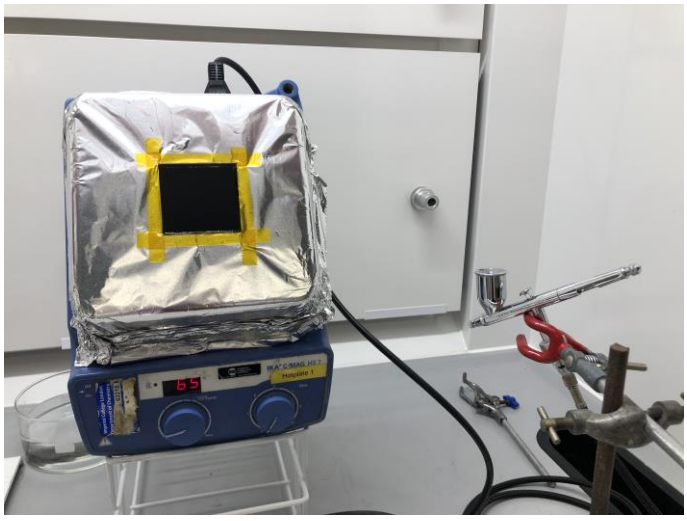


Figure A5.9: Image displaying how electrodes were spray-coated with electrocatalyst while fixed to a hotplate.

5.5.2 Manganese hydrogen hybrid redox flow battery setup

Figure A5.10 is a screenshot of the spreadsheet used to calculate the theoretical compression of the electrodes using the incompressible Tygaflor gaskets.

Assembly Date:	03/03/2021					
Screw torque (Nm)	4	**Electrode Area / cm^2**	5			
Anode	**Notes**	**Thickness /µm**	223	**Electrode Material**	**Gas / Flow (mL/min)**	
Pt/C + H2		**Loading / mg cm^{-2}**	0.4	JM(?)	100	
Separator	**Notes**	**Thickness /µm**	50.8			
Nafion 212						
Cathode	**Notes**	**Thickness /µm**	*4600*	**Electrode Material**	**Gas / Flow (mL/min)**	
SGL felt		**Loading / mg cm^{-2}**	-	SGL	50	
Electrolyte	**Notes**	**Cycling Volume / mL**				
Ti(II) + Mn (II/III) + H2SO4	1M:1M:3M	20				
				Active species/mol	**Coulombs expected / C**	
Active species concentration / molar	1			**0.02**	**1929.7**	
Gaskets thickness / µm	**80**	**117**	**133**	**220**	**Total (mm)**	**(Compression)**
Anode	1	1			**197**	**12%**
Cathode	1	1		15	**3497**	**24%**
					3694	
					↓	
		Uncomp thickness	**4873.8**	**Tot. compression:**	**24.2%**	
NOTES:						
Anode Electrolyte: 1M Ti(II) + 1M Mn (2+ <--> 3+) + 3M H2SO4						
Method:						
Cathode electrolyte: H2 from electrolyser						
200 rpm = 50mL/min (peristaltic pump)						
Membrane activation						

Figure A5.10: Screengrab of spreadsheet used to calculate number of gaskets needed.

Figure A5.11 shows images of several different test stations and potentiostats used to operate the Mn/H_2 hRFB device used in this work. The working electrode and working sense electrode connections were place on the liquid (red) side and the counter and reference connections were placed on the gas (blue) side.

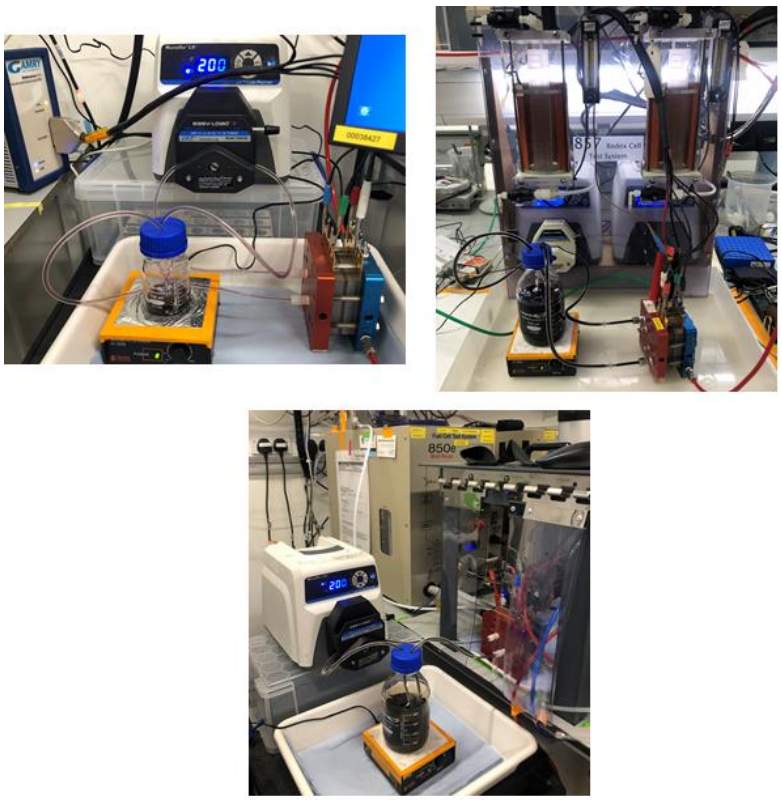


Figure A5.11: Photographs of manganese-hydrogen hRFBs operated by different potentiostats and testing systems: top left – Gamry 600; top right – 857 Redox Flow Cell Test System; and, bottom – 850 Fuel Cell Test System.

5.6 References

1 Y. Zheng, Y. Jiao, Y. Zhu, L. H. Li, Y. Han, Y. Chen, A. Du, M. Jaroniec, & Shi and Z. Qiao, *Nat. Commun.*, 2014, **5**, 3783.

2 G. Wu, A. Santandreu, W. Kellogg, S. Gupta, O. Ogoke, H. Zhang, H.-L. Wang and L. Dai, *Nano Energy*, 2016, **29**, 83–110.

3 H. Osgood, S. V Devaguptapu, H. Xu, J. Cho and G. Wu, *Nano Today*, 2016, **11**, 601–625.

4 Y. Chen, S. Ji, C. Chen, Q. Peng, D. Wang and Y. Li, *Joule*, 2018, **2**, 1242–1264.

5 G. Zhang and A. Kucernak, *ACS Catal.*, 2020, **10**, 9684–9693.

6 X. Lin, C. M. Zalitis, J. Sharman and A. Kucernak, *ACS Appl. Mater. Interfaces*, 2020, **12**, 47467–47481.

7 C. Jackson, L. F. J. M. Raymakers, M. J. J. Mulder and A. R. J. Kucernak, *Appl. Catal. B Environ.*, 2020, **268**, 118734.

8 Q. Cheng, S. Han, K. Mao, C. Chen, L. Yang, Z. Zou, M. Gu, Z. Hu and H. Yang, *Nano Energy*, 2018, **52**, 485–493.

9 H. A. Gasteiger and N. M. Marković, *Science (80-.).*, 2009, **324**, 48–49.

10 Z. Chen, M. Xiao, J. Zhu, G. Li, N. Li, S. Li, Z. P. Cano, L. Ma, P. X. Cui, P. Xu, G. Jiang, H. Jin, S. Wang, T. Wu, J. Lu, A. Yu and D. Su, *Angew. Chemie*, 2019, **131**, 9742–9747.

11 Q. Zhang, Z. Duan, Y. Wang, L. Li, B. Nan and J. Guan, *J. Mater. Chem. A*, 2020, **8**, 19665–19673.

12 E. Antolini, *ACS Catal.*, 2014, **4**, 1426–1440.

13 J. Gao, C.-Q. Xu, S.-F. Hung, W. Liu, W. Cai, Z. Zeng, C. Jia, H. Ming Chen, H. Xiao, J. Li, Y. Huang and B. Liu, *J. Am. Chem. Soc.*, 2019, **141**, 3014–3023.

14 N. Mamaca, E. Mayousse, S. Arrii-Clacens, T. W. Napporn, K. Servat, N. Guillet and K. B. Kokoh, *Appl. Catal. B Environ.*, 2012, **111**–**112**, 376–380.

15 C. M. Zalitis, A. R. Kucernak, J. Sharman and E. Wright, *J. Mater. Chem. A*, 2017, **5**, 23328–23338.

16 R. Zhao, X. Yue, Q. Li, G. Fu, J.-M. Lee and S. Huang, *Small*, 2021, 2100391.

17 J. Durst, C. Simon, A. Siebel, P. J. Rheinländer, T. Schuler, M. Hanzlik, J. Herranz, F. Hasché and H. A. Gasteiger, *ECS Trans.*, 2014, **64**, 1069–1080.

18 X. Yang, Y. Wang, X. Wang, B. Mei, E. Luo, Y. Li, Q. Meng, Z. Jin, Z. Jiang, C. Liu, J. Ge and W. Xing, *Angew. Chem. Int. Ed.*, 2021, **60**, 26177–26183.

19 T. B. Ferriday and P. H. Middleton, *Int. J. Hydrogen Energy*, 2021, **46**, 18489–18510.

20 H. A. Firouzjaie and W. E. Mustain, *ACS Catal.*, 2020, **10**, 225–234.

21 A. G. Wright, J. Fan, B. Britton, T. Weissbach, H.-F. Lee, E. A. Kitching, T. J. Peckham and S. Holdcroft, *Energy Environ. Sci.*, 2016, **9**, 2130–2142.

22 L. Wang, E. Magliocca, E. L. Cunningham, W. E. Mustain, S. D. Poynton, R. Escudero-Cid, M. M. Nasef, J. Ponce-González, R. Bance-Souahli, R. C. T. Slade, D. K. Whelligan and J. R. Varcoe, *Green Chem.*, 2017, **19**, 831–843.

23 H. Wang and H. D. Abruña, *J. Am. Chem. Soc.*, 2017, **139**, 6807–6810.

24 The Solutions Center - Resources - Ionomr Innovations Inc., https://ionomr.com/resources/#handling, (accessed 20 January 2022).

25 H. Adabi, A. Shakouri, N. Ul Hassan, J. R. Varcoe, B. Zulevi, A. Serov, J. R. Regalbuto and W. E. Mustain, *Nat. Energy*, 2021, **6**, 834–843.

26 A. Mehmood, B. Ali, M. Gong, M. Gyu Kim, J. Y. Kim, J. H. Bae, A. Kucernak, Y. M. Kang and K. W. Nam, *J. Colloid Interface Sci.*, 2021, **596**, 148–157.

27 K. Kozma, M. Wang, P. I. Molina, N. P. Martin, Z. Feng and M. Nyman, *Dalt. Trans.*, 2019, **48**, 11086–11093.
28 A. J. Bard, R. Parsons and J. Jordan, *Standard potentials in aqueous solution*, New York : Marcel Dekker, 1985.
29 J. Rubio-Garcia, A. Kucernak, D. Zhao, D. Li, K. Fahy, V. Yufit, N. Brandon and M. Gomez-Gonzalez, *J. Phys. Energy*, 2018, **1**, 015006.
30 J. Rubio-Garcia, A. Kucernak, A. Parra-Puerto, R. Liu and B. Chakrabarti, *J. Mater. Chem. A*, 2020, **8**, 3933–3941.
31 O. D. Thomas, K. J. W. Y. Soo, T. J. Peckham, M. P. Kulkarni and S. Holdcroft, *J. Am. Chem. Soc.*, 2012, **134**, 10753–10756.
32 S. Gottesfeld, D. R. Dekel, M. Page, C. Bae, Y. Yan, P. Zelenay and Y. S. Kim, *J. Power Sources*, 2018, **375**, 170–184.
33 N. U. Hassan, M. Mandal, G. Huang, H. A. Firouzjaie, P. A. Kohl and W. E. Mustain, *Adv. Energy Mater.*, 2020, **10**, 2001986.
34 X. Xie, C. He, B. Li, Y. He, D. A. Cullen, E. C. Wegener, A. J. Kropf, U. Martinez, Y. Cheng, M. H. Engelhard, M. E. Bowden, M. Song, T. Lemmon, X. S. Li, Z. Nie, J. Liu, D. J. Myers, P. Zelenay, G. Wang, G. Wu, V. Ramani and Y. Shao, *Nat. Catal.*, 2020, **3**, 1044–1054.
35 X. X. Wang, D. A. Cullen, Y.-T. Pan, S. Hwang, M. Wang, Z. Feng, J. Wang, M. H. Engelhard, H. Zhang, Y. He, Y. Shao, D. Su, K. L. More, J. S. Spendelow and G. Wu, *Adv. Mater.*, 2018, **30**, 1706758.
36 Y. Deng, B. Chi, J. Li, G. Wang, L. Zheng, X. Shi, Z. Cui, L. Du, S. Liao, K. Zang, J. Luo, Y. Hu, X. Sun, Y. J. Deng, B. Chi, J. Li, G. H. Wang, L. Zheng, X. D. Shi, Z. M. Cui, L. Du, S. J. Liao, K. Zang, J. Luo, Y. F. Hu and X. L. Sun, *Adv. Energy Mater.*, 2019, **9**, 1802856.

Chapter 6

In-operando techniques examining manganese speciation during manganese / hydrogen hybrid redox flow battery operation

"There is nothing new under the sun, but there are a lot of old things we do not know." – Ambrose Bierce

6.1 Introduction

One of the central strategies for reducing the capital cost associated with RFBs is to reduce the cost of their constituent components. Depending on the system, aside from the membrane, one of the most expensive components is the electrolyte, making up roughly 53 % of the total capital cost in a 15 hour VRFB.[1] However, as previously mentioned, VRFBs suffer from price volatility largely due to the change in fluctuating demand for stainless steel (ferrovanadium is a hardening agent used in steel production). Widespread unpredictability and rarity of metal ores such as vanadium and rare earth metals such as cerium make broad commercial rollout using these materials difficult.[2,3] Reducing the price of the electrolyte can be achieved by using inexpensive active materials. One method for this, discussed in Chapter 1, is with the use of organic materials – several groups are focussed on making this route a viable option by producing stable organic species with high cyclability.[4] Another is to use inexpensive inorganic materials. Manganese is the 12th most abundant element in the Earth's crust. It is the second most abundant transition metal (behind iron) and can be found in large deposits in South Africa, Australia and China – this ample supply and extraction capability (c.a. 12 million tonnes extracted per year)[3] makes it inexpensive and, if its rich and diverse redox chemistry can be harnessed and fully understood, may prove to be an ideal candidate for research and industrial use in flow battery systems at large scale.

As discussed in Chapter 1, alternative technologies need to be developed to make up the patchwork of devices that will support the scaled roll out of renewable energy-capturing

resources. Among these, coupling the insights gained from FCs with RFBs, hRFBs are a technology of significant interest given the advantages associated with separating out any potential liquid crossover species in the gaseous side. Recently, hydrogen has been used as a fuel for these systems and possesses the additional advantage of being a compressible gas, resulting, potentially, in high energy density systems. The process outlined below has been discussed in previous chapters (Equation (6.1)).

$$2H^+ + 2e^- \rightleftharpoons H_2 \qquad (6.1)$$

Manganese has encountered problems in electrochemical devices (RFBs and FCs) before associated with the formation of very thermodynamically stable, usually insoluble MnO_2 (the production of which is the subject for discussion later).[5–7] However researchers found that, with the introduction of Ti^{4+} additives, a certain level of reversibility in this process can be achieved.[8,9] Bringing these two initiatives together (utilising manganese-titanium electrolytes in RFBs and taking learnings from FCs) Rubio Garcia et al. reported a technology with promising characteristics – a manganese hydrogen hRFB (herein referred to as Mn/H_2 hRFB) – the chemistry involved in the operation of this device is the basis of this chapter.[7]

Following on from the final overarching question set out in Chapter 1: "Is there a way of developing an enhanced understanding of manganese speciation occurring within a manganese electrolyte during cell cycling?" many more questions demand consideration alongside, and some even beforehand. These include the following:

- What are the possible processes that can occur in a manganese-containing solution?
- What are the possible processes that can occur in a titanium-containing solution?
- What (manganese or titanium) species are formed?
- How do they interact?
- How does the surrounding environment (pH, viscosity, temperature) affect the formation of these potentially formed species?
- What analytical or operational handles do we have over this system?

The reason the overarching question has been expanded before the end of this introduction is because the rest of the introduction looks to inform some of these sub-questions stated above. The majority of the remainder of this introduction is devoted to reviewing the extensive

established and hypothesised manganese and titanium chemistry. With this context, the Methodology then sets out the methods used to assess the overarching question stated earlier and the Results systematically introduces and highlights the unique features associated with this manganese-titanium based electrolyte. A discussion of the results in light of the introductory context follows, providing the most up-to-date understanding of this electrolyte. Unlike Chapters 3 – 5, this chapter contains separate results and discussion sections. The reason for this is to aid the reader in understanding the system and approach, and then to digest and discuss the findings in the results with all the presented information hand.

Finally, before launching into two of the main components in the electrolyte, it should be stated that only aqueous or sulfate-containing complexes are considered in these mini-reviews. This is because (currently) this device utilises concentrated sulfuric acid media of c.a. 5 M (it will become clear why this is the case). The equilibrium constants for each proton dissociation of sulfuric acid are stated below in Equations (6.2) and (6.3).[10]

$$H_2SO_4 \rightleftharpoons H^+ + HSO_4^- \quad K_a = 10^2 \tag{6.2}$$

$$HSO_4^- \rightleftharpoons H^+ + SO_4^{2-} \quad K_a = 0.012 \tag{6.3}$$

These equilibrium constants assume species are in dilute solutions, unity activity coefficients and no ion pairing. As will become clear, this assumption cannot be made for the electrolyte examined here. For the concentrations of sulfuric acid used in this work, the overwhelmingly dominant species is HSO_4^- – this is discussed later. The thermodynamic values for these sulfate species and water are required later so they are included here for completeness (Table 6.1). These thermodynamic data can also be linked to the Gibbs energy of reaction, Δ_rG^0, by the equation: $\Delta_rG^0 = -RT\ln(K)$ – which (using Table 6.1) can be used to calculate a more exact acid dissociation constants, $K_{a,H2SO4} = 98.81$ and $K_{a,HSO4-} = 0.010$.

Table 6.1: A summary of Gibbs free energies of formation for relevant sulfur species.

Species	Δ_fG^0 / kJ mol^{-1}	Reference
SO_4^{2-}	-744.63	Bard[11]
HSO_4^-	-756.01	Bard[11]
H_2SO_4	-744.63	Bard[11]
H_2O	-237.18	Bard[11]

6.1.1 Manganese chemistry review

Manganese is an extremely important element in nature. Tetranuclear manganese-based clusters play a central role in photosystem II which is a protein complex crucial to photosynthesis. Its function is to biologically split water and provide the electrons for photosynthesis to occur. As such, tetranuclear manganese clusters and their chemistries have been studied in depth.[12–15]

The first thing that must be said about manganese chemistry is that, with over 30 phases, it is extensive and its speciation is very complex.[16] Manganese displays extensive redox chemistry with a multitude of oxidation states (2+, 3+, 4+ and 7+ being the most prevalent). This mini-review of manganese chemistry focusses on the oxidation states 2+ to 4+, inclusive. It should also be noted that equilibrium constants are stated for only selected processes outlined below – this is because of occasional subtleties in reaction products and due to uncertainty surrounding reaction conditions. Gibbs free energies are offered in the summary at the end of this section. Logically, a good starting point when discussing element-specific aqueous chemistries is the Pourbaix diagram – also sometimes referred to as E_H-pH (herein referred to as E-pH) diagrams.[17] The Pourbaix diagram for manganese is shown here.

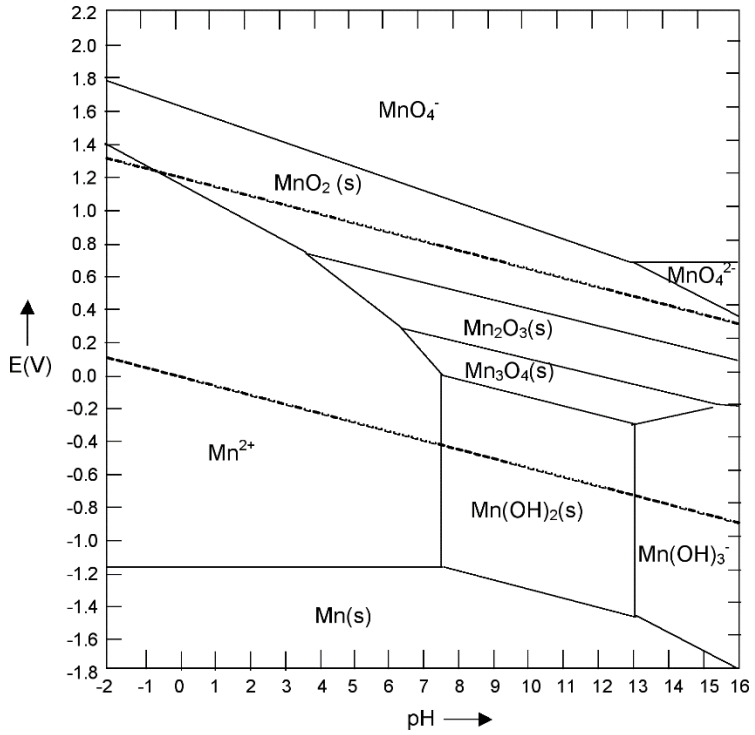


Figure 6.1: Pourbaix diagram for manganese. This diagram includes the region corresponding to the redox stability of water (dashed lines with gradient -0.059 V pH^{-1}).

Pourbaix diagrams are constructed using thermodynamics and the Nernst equation to describe the relationship between possible phases for elements. These diagrams do not account for any kinetics and, crucially, they do not account for the localised nature of corrosion and provide general prediction of the bulk species formed in solution.[18] This will be discussed in due course, especially with respect to the solid species formed.

6.1.1.1 Chemical speciation and transformations of manganese species

Starting, logically, with Mn^{2+} – this is manganese's most stable oxidation state. In simple neutral or acidic solutions, it exists in an octahedral environment (hexaaqua) with six ligands and appears very pale pink as a result of its spin- and parity-forbidden orbital transitions (when in a tetrahedral environment, parity transitions are not forbidden and solutions have a much more intense yellow-green colour).[19] In basic media, the hydroxide $Mn(OH)_2$ is formed which appears as a gel-like white solid that darkens on exposure to air (it is easily oxidised).[19] Depending on the concentration of acid used, $Mn(OH)_2$ dissolves in more protic environments briefly forming $Mn(OH)^+$ returning to its most stable state in neutral or acidic environments.[20] Among the most pertinent chemical processes associated with the Mn^{2+} species occurring in the electrolyte examined in this work are the hydrolysis processes – Equations (6.4) and (6.5).[21] The high pK_a constant mean the equilibrium lies to the left hand side in all but the most alkaline solutions. The second hydrolysis could not be found but is also expected to be high. This suggests that in acid solutions (as in this chapter), ionic Mn^{2+} is most common Mn^{2+} species present.

$$Mn^{2+} + H_2O \rightleftharpoons Mn(OH)^+ + H^+ \quad pK_a = 10.5 \tag{6.4}$$

$$Mn(OH)^+ + H_2O \rightleftharpoons Mn(OH)_2 + H^+ \tag{6.5}$$

Conversely, even in highly acidic aqueous solutions, Mn^{3+} species are significantly hydrolysed.[19,22] Equations (6.6) and (6.7) show Mn^{3+} acts as an acid – the K_a for this acid is 1.02 ± 0.14.[21] The second hydration has been reported to have a K_a of 0.5.[23] Taken together, these two hydrolysis steps can be combined and the $Mn(OH)_2^+$ species could precipitate – this leads to the formation of a thermodynamically stable oxyhydroxide species that is mentioned in more detail later when solid species are discussed (formed via rearrangement in Equation (6.8) (pK_a not found) and the overall reaction is shown in Equation (6.9)).

$$Mn^{3+} + H_2O \rightleftharpoons Mn(OH)^{2+} + H^+ \quad pK_a = 0.009 \tag{6.6}$$

$$Mn(OH)^{2+} + H_2O \rightleftharpoons Mn(OH)_2{}^{+} + H^+ \quad pK_a = -0.301 \tag{6.7}$$

$$Mn(OH)_2{}^{+} \rightleftharpoons MnOOH + H^+ \tag{6.8}$$

$$Mn^{3+} + 2H_2O \rightleftharpoons MnOOH + 3H^+ \quad pK_a = -4.1^{a} \tag{6.9}$$

[a] dependent on solid phase formed (see below)

Manganese oxides with Mn^{3+} centres such as Mn_2O_3 (bixbyite), and Mn_3O_4 (hausmannite) are known to form, usually in more alkaline solutions.[24] Disproportionation is a commonly reported process characteristic of Mn^{3+} ions in solution (Equation (6.10)). The mechanism by which this process proceeds is unclear but will depend on the specific chemical environment. Marcus theory might suggest that both Mn^{2+} and Mn^{4+} ions are formed, the latter of which rapidly reacts to form MnO_2 as a result of its instability in acid.

$$2Mn^{3+} + 2H_2O \rightleftharpoons Mn^{2+} + MnO_2 + 4H^+ \tag{6.10}$$

$$2Mn(OH)^{2+} \rightleftharpoons (MnOMn)^{4+} + H_2O \tag{6.11}$$

$$(MnOMn)^{4+} \rightleftharpoons MnO^{2+} + Mn^{2+} \tag{6.12}$$

Another suggestion has been as a result of a cascade of condensation / polymerisation reactions (Equations (6.11) and (6.12) – these are speculative).[22] This may proceed through a process whereby MnO_2 with a terminating (-OH) will react with another $Mn(OH)_2{}^{+}$ to add another layer of MnO_2 terminated by an (-OH) from the newly arrived monomer unit (releasing a Mn^{2+} ion in the process). The MnO^{2+} species formed in Equation (6.12) is speculative but would rapidly react in solution as a result of its electrophilic nature.

A hypothetical schematic representing techniques by which Mn^{3+} can be stabilised is shown in Figure A6.34. On standing, solutions of Mn^{3+} have been observed to become cloudy as a result of this solid formation following disproportionation.[22] Mn^{3+} has been shown to be stabilised by (a) increasing of solution acidity; (b) increasing the Mn^{2+} concentration; or, (c) complex formation (these stabilisation techniques are expected on inspection of Equation (6.10)).[22] The first of these two techniques is well understood by Le Chatelier's Principle, but the complexation is of extra interest in this chapter primarily because of its effect on Mn^{3+}. Complexation / co-ordination of Mn^{3+} leads to a decreased driving force towards the formation of MnO_2 (as a result of the more negative formation energy of complexed Mn^{3+}). The following set of equations show that Mn^{3+} forms strong complexes in acidic media (Equations (6.13) – (6.15)).[22]

$$Mn^{3+} + HF \rightleftharpoons MnF^{2+} + H^{+} \quad K_{eq} = 1.6 \times 10^{3} \tag{6.13}$$

$$Mn^{3+} + Cl^{-} \rightleftharpoons MnCl^{2+} \quad K_{eq} = 13.5\ M^{-1} \tag{6.14}$$

$$Mn^{3+} + H_2C_2O_4 \rightleftharpoons MnC_2O_4{}^{+} + 2H^{+} \quad K_{eq} = 1.64 \times 10^{5}\ M \tag{6.15}$$

$$Mn^{2+} + SO_4{}^{2-} \rightleftharpoons MnSO_4 \quad K_{eq} = 10^{2.3} \tag{6.16}$$

It is suggested that in the strongly acidic electrolyte used in this work, bisulfate (HSO_4^-, the main sulfurous species in the electrolyte, see methodology) will also form strong complexes with Mn^{3+}. While it has already been clarified that HSO_4^- is the dominant sulfate species present in solution, it should also be mentioned that $MnSO_4$ complexes readily form in dilute sulfuric acid solution (Equation (6.16)).[25] Bisulfate (HSO_4^-) is less commonly discussed in solution as high concentrations of acid are rarely used, however a series of manganese hydrogen sulfate crystal structures ($Mn(HSO_4)_2$, $Mn(HSO_4)_2 \cdot H_2O$ and $Mn(HSO_4)(H_2SO_4)$ have been reported.[26] The complexation of Mn^{2+} with SO_4^{2-} is included here for completeness and,[25] while SO_4^{2-} does not form to any particularly high concentration at the (high) concentrations of acid used in this electrolyte, Mn^{2+} stabilisation contributes to point (b), above. However, using these alternative ligands / salts may induce a lower overall cell potential and / or unwanted side reactions (e.g. evolution of HF or poisoning of Pt catalyst in the cathode as a result of electrolyte crossover). Introducing a kinetic barrier involves blocking the formation of some physically favourable oligomer. These techniques are summarised in a rough energy level diagram in Figure A6.34. Aside from these species, the only other notable Mn^{2+} solid species are MnO which is a dark green powder that is insoluble in water (this mainly forms in alkaline solutions).[19]

Disproportionation of Mn^{3+} leads to the formation of Mn^{2+} in solution and solid species containing Mn^{4+} centres. The exact polymorph of solid species and the mechanism by which it is formed is dependant on the surrounding chemical environment.[11] Polymorphs are species that have the same chemical formula but different crystal structures – there are several polymorphs in aqueous manganese chemistry that will be discussed now. Manganese forms a large number of oxides that are diverse in structure and function.[27] Manganese dioxide, MnO_2, represents a 'family' of polymorphs that finds utility across a number of chemistries. The main polymorphs reported are α-, β-, δ-, λ- and R-MnO_2 (with hollandite, pyrolusite, birnessite, spinel and ramsdellite crystal structures, respectively). They each have different crystal structures that are displayed in Figure 6.2. β-MnO_2 is the most thermodynamically stable

polymorph of manganese dioxide but it has been shown that the introduction of intercalating metal centres can preferentially form specific crystal structures.[28]

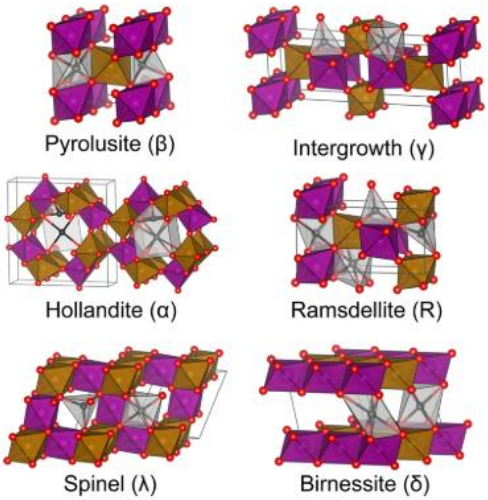


Figure 6.2: Manganese oxide crystal structures.[28]

A summary of these species is provided at the end of this section. Another pertinent family for this work are the manganese oxyhydroxides, MnOOH, the central species being α-, β-, λ-MnOOH. Polymorphs with similar chemical constituent parts, such as MnO_2 and MnOOH, can have similar structural properties and are known to be isostructural pairs – among the manganese oxides examples include γ-MnOOH / β-MnO_2, and α-MnOOH / R-MnO_2. While γ-MnOOH is thermodynamically the most stable polymorph of these oxyhydroxides, β-MnOOH has been shown to form preferentially at temperatures close to 0 °C,[29] however this polymorph, is known only in fine-grained mixtures and the crystal structure has not yet been determined.[16]

Before summarising the electrochemical processes and possible degradation mechanisms associated with these species, the existence of metastable species with regards to their influence on driving solutions down non-equilibrium pathways towards their most thermodynamically stable states, must be addressed. If a system or species is defined as metastable, it is thought to have reached a local energy minima but is capable of reaching a lower energy state. The Pourbaix (E-pH) diagram describes the thermodynamic stability of bulk species in aqueous solution and does not account for the thermodynamic stability of nanoparticles with low surface energies. Sun et al. outlines the fact that manganese oxides form according to Ostwald's Rules of Stages,[30] where a variety of metastable manganese oxides and oxyhydroxides nucleate and grow prior to the formation of the equilibrium (bulk) phase – metastable phase formation is

possible from a supersaturated solution if the barrier to nucleation is lower than the stable phase.[31] Chen et al. helpfully illustrates this progression in the schematic shown in the top half of Figure 6.3.[32] As nanoparticles of metal oxides nucleate and grow, it has been found that there can be dramatic crossovers in polymorph stability as a function of nanoparticle size and bulk solution composition.[32–34]

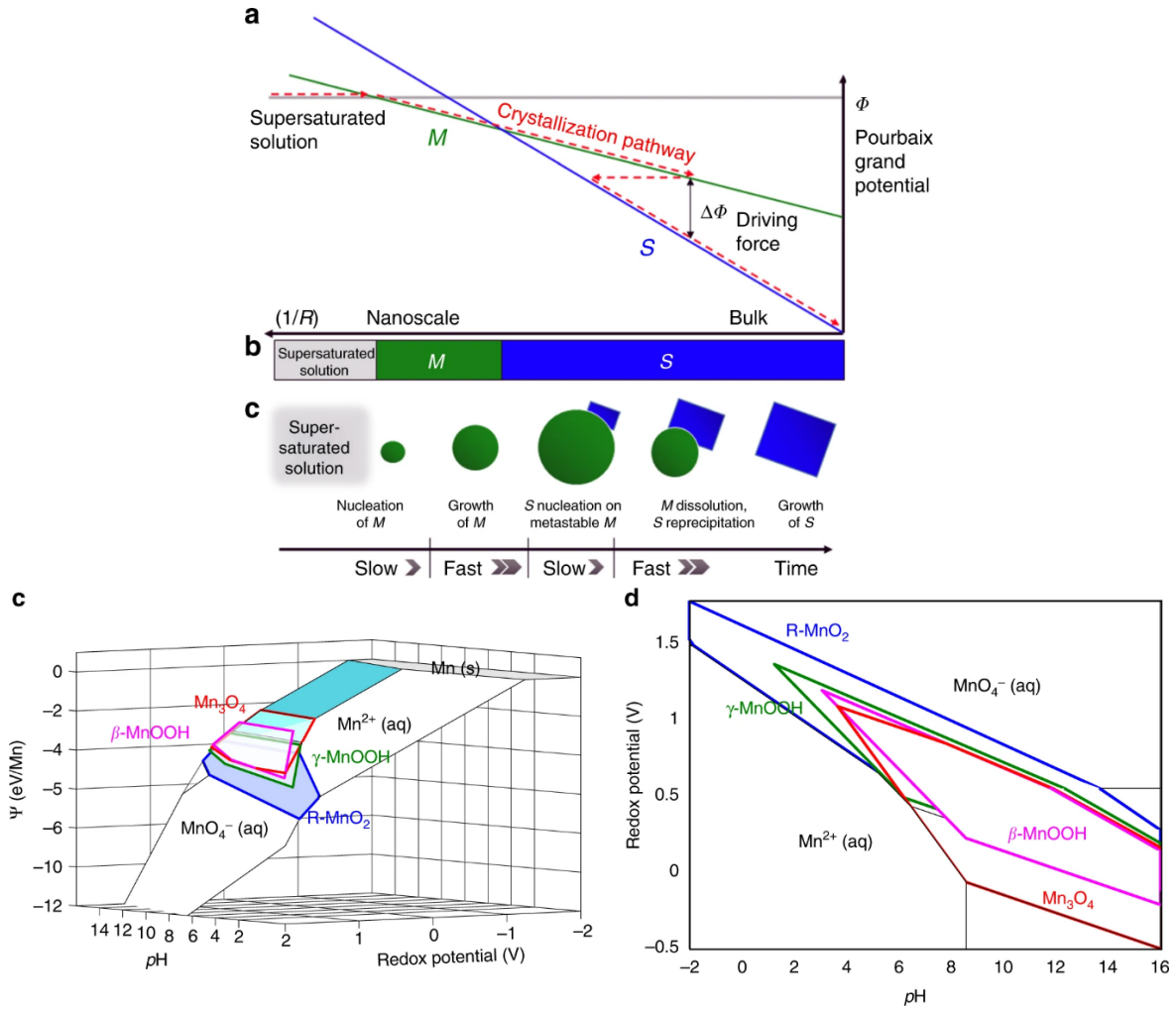


Figure 6.3: Above: (c) Pourbaix free-energy planes of metastable β-MnOOH, γ-MnOOH, R-MnO2, and full aqueous stability region of Mn3O4. (d) Projection of aqueous metastability regions onto E-pH axis.[31] Below: Schematic representation of remnant metastability in a crystallization pathway (a) Free-energy of three phases (supersaturated solution (gray), M (green), S (blue)) as a function of the surface-area-to-volume ratio, 1/R (R is a particle radius). The gray line corresponds to the free-energy of a supersaturated solution, green is a metastable phase M that is size-stabilized by a low surface energy (given by the slope), and blue is the bulk equilibrium phase S, with high surface energy. (b) Phase diagram in the 1/R axis created from the projection of lowest free-energy phases. (c) A multistage crystallization pathway (red arrow in a) proceeds downhill in energy, but phase transformations are limited by nucleation. Crystal growth of M prior to the induction of S means M can grow into a size-regime where phase M is metastable. S will then nucleate, and quickly grow by consuming M via dissolution-reprecipitation. The characteristic length scale of size-driven phase transitions lies in the 2 nm–50 nm range.[32]

The free energy axis uses a thermodynamic grand potential (Pourbaix potential – which encompasses the sum of the proton and oxygen activity and the electrochemical potential) which corresponds to an aqueous ion precursor or metal oxide precipitate in open exchange

with a water reservoir at a given pH, redox potential, and dissolved metal ion concentration.[31] These Pourbaix potentials can be used to obtain a free energy surface for a metastable species – as shown in on the left hand side of the bottom half of Figure 6.3. Projecting these metastable species onto the E-pH part of this plot returns the figure on the right hand side, revealing the phase boundaries for metastable β-MnOOH, γ-MnOOH and R-MnO_2. Nanoparticles can become stabilised due to the low surface energies they exhibit as a result of their large surface area to volume ratios.[32] This surface energy, which accounts for the size-dependant thermodynamics of nucleation and growth towards a stable phase, is inversely related to the bulk stability.[31] DFT measurements carried out by Sun et al. further suggest that surface energies for the oxyhydroxide are lower when comparing isostructural MnOOH and MnO_2 frameworks (i.e. γ-MnOOH / β-MnO_2, and α-MnOOH / R-MnO_2) – implying a greater bulk stability.[31] While clearly these DFT measurements are theoretical, they do fall in line with the experimentally established values reported by Birkner and Navrotsky for Mn_3O_4, Mn_2O_3 and β-MnO_2.[35] So while researchers have reported pathways stating sound synthesis routes towards formation of solid species,[36] there are elusive metastable, subtleties during the formation of these bulk species that currently elude full understanding. With further kinetic variability, these metastable species are, understandably, difficult to isolate, observe or quantify.

6.1.1.2 Electrochemical transformations of manganese species

Having briefly discussed some of the subtleties of manganese oxides reaching their most stable states, electrochemical processes should be outlined and suggested degradation pathways briefly discussed. Mn^{3+} is thermodynamically unstable (hence its absence from the Pourbaix diagram in Figure 6.1). Mn^{2+} can be electrochemically oxidised in a single electron transfer to form Mn^{3+} in solution (Equation (6.17)). This electrochemical process is the central electrochemical process this chapter, and device, is focussed on.[17] Some of following reduction potentials are based on the free energies of the species involved, using the relationship: $\Delta_r G^0 = -nFE^0$ (Equations (6.18) – (6.26)).[11,17]

$$Mn^{3+} + e^- \rightleftharpoons Mn^{2+} \qquad E^0 = 1.509\ V \qquad (6.17)$$

$$Mn(OH)^+ + H^+ + e^- \rightleftharpoons Mn^{2+} + H_2O \qquad E^0 = 0.624\ V^\star \qquad (6.18)$$

$$Mn^{4+} + e^- \rightleftharpoons Mn^{3+} \qquad E^0 = 1.633\ V \qquad (6.19)$$

$$Mn(OH)_2{}^{2+} + e^- \rightleftharpoons Mn(OH)_2{}^{+} \qquad E^0 = 1.301\ V \qquad (6.20)$$

$$Mn_2O_3 + H_2O \rightleftharpoons 2MnO_2 + 2H^+ + 2e^- \qquad E^0 = 1.014\ V \qquad (6.21)$$

$$MnO_2 + 4H^+ + 2e^- \rightleftharpoons Mn^{2+} + 2H_2O \qquad E^0 = 1.23\ V \qquad (6.22)$$

$$\beta\text{–}MnO_2 + H^+ + e^- \rightleftharpoons \gamma\text{–}MnOOH \qquad E^0 = 1.016\,V \qquad (6.23)$$

$$R\text{–}MnO_2 + H^+ + e^- \rightleftharpoons \alpha\text{–}MnOOH \qquad E^0 = 1.013\,V^\star \qquad (6.24)$$

$$\gamma\text{–}MnO_2 + H^+ + e^- \rightleftharpoons \alpha\text{–}MnOOH \qquad E^0 = 1.132\,V \qquad (6.25)$$

$$\alpha\text{–}MnO_2 + H^+ + e^- \rightleftharpoons \gamma\text{–}MnOOH \qquad E^0 = 1.141\,V^\star \qquad (6.26)$$

Please note: the potentials with the ★ adjacent to 'SHE', indicate these reduction potentials were calculated using Gibbs energies from different sources. Electrochemical oxide / hydroxide interconversion is interesting from a potential perspective as, if solid species were to dominate in solution (possibly depositing on the electrode surface), these potentials would play an important role in the overall cell potential. The reduction potentials set out here are by no means a complete set – in fact, Equation (6.23) represents the conversion between the two oxides' most thermodynamically stable states (which are also isostructural) and Equation (6.24) represents another conversion between the isostructural ramsdellite and the groutite. As briefly mentioned earlier, during a reaction process, less (thermodynamically) stable polymorphs may, on nucleation, form preferentially. The reason these polymorphs might be the dominant species formed could be because of accompanying ions or water molecules interrupting crystal structure formation and leading to the formation of off-stoichiometric species. This has been investigated by a number of research groups focussing largely on alkali metal incorporation – of interest because of battery research.[28,37,38] Portehault et al. used Mn^{2+} and MnO_4^- in aqueous solution to show in detail how polymorphs of manganese oxides (MnO_2 and MnOOH) evolve with time and temperature highlighting the importance of surface charges – in particular the relationship between $(-110)_{\gamma\text{-}MnO_2}$ and $(-101)_{\alpha\text{-}MnOOH}$ faces.[38] The group later produced a helpful reaction scheme / flow chart highlighting that, at very low pHs, the formation of either the α- or γ-MnO_2 polymorph is favoured.[37] With time and / or the presence of small cations these polymorphs would eventually dissolve and recrystalise forming the most stable β-MnO_2. They subsequently pointed to other research that had confirmed the favourable production of α-MnO_2 in strongly acidic conditions (and who also conveniently illustrate the intercalation of ions and hydrating species).[39]

Finally, attention must directed towards chemical degradation pathways. It has been suggested that different polymorphs may be produced according to their formation method e.g. either electrochemically or via a chemical degradation pathway. It is difficult to observe degradation pathways for manganese species in solution due to the growth and subsequent dissolution of metastable species. Equations (6.25) and (6.26) are included here as Bahdad et al. suggest these

conversions are favoured (over the β-MnO_2 to γ-MnOOH interconversion) citing Bard.[11,23] However Bard (only) states that the γ- to α- conversion is favourable in alkaline environments – and therefore the assumption that this is true in acidic conditions may well be a poor one (for the reasons mentioned earlier regarding the high dependence on pH environment).[11] Therefore, from a bulk thermodynamic perspective, the following chemical degradation may occur following the double hydrolysis of the Mn3+ ion (Equations (6.6) and (6.7)), and assuming the most thermodynamically stable γ-MnOOH polymorph forms during the subsequent acid-base process (Equation (6.27)), then the electrochemical process might ultimately follow Equation (6.23) (across isostructures), suggesting an overall degradation mechanism shown below (Equation (6.28) – essentially equivalent to Equation (6.10)). This is alternatively represented using a different (hydrolysed) form of Mn^{3+} (Equation (6.29)). Clearly, this does not fall in line with the polymorph-evolution suggested by Portehault et al.[37] but it should be mentioned nonetheless. Examples of additional non-classical crystal growth mechanisms have been reported and discussed,[40] but further discussion of manganese oxide evolution is beyond the scope of this thesis.

$$Mn(OH)_2{}^{+} \rightleftharpoons \gamma\text{–}MnOOH + H^{+} \quad (6.27)$$

$$\gamma\text{–}MnOOH + Mn^{3+} \rightleftharpoons Mn^{2+} + H^{+} + \beta\text{–}MnO_2 \quad (6.28)$$

$$\gamma\text{–}MnOOH + Mn(OH)^{2+} \rightleftharpoons Mn^{2+} + H_2O + \beta\text{–}MnO_2 \quad (6.29)$$

Table 6.2 and Figure 6.4 attempt to summarise most of the pertinent information.

Table 6.2: A summary of Gibbs free energies of formation for relevant manganese species. "★" indicates that this free energy was collected from computationally calculated values.

Species	OS	$\Delta_f G^0$ / kJ mol^{-1}	Reference
Mn^{2+}	2	-228.01	Bard[11]
$Mn(OH)^{+}$	2	-405.01	Wagman[41]
$Mn(OH)_2$	2	-615.00	Bard[11]
$MnSO_4$	2	-957.36	Bard[11]
Mn_3O_4	2/3	-1283.2	Bard[11]
Mn^{3+}	3	-83.00	Bard[11]
$Mn(OH)^{2+}$	3	-324.4	Bahdad[23]
$Mn(OH)_2^{+}$	3	-557.93	Bahdad[23]
α-MnOOH	3	-557.70	Bard[11]
β-MnOOH	3	-547.07★	Sun[31]
γ-MnOOH	3	-563.20	Bard[11]
Mn_2O_3	3	-881.10	Bard[11]
Mn^{4+}	4	+74.85	Gramm-Osipov[42]
α-MnO_2	4	-453.13	Bahdad[23]
β-MnO_2	4	-465.14	Bard[11]
γ-MnO_2	4	-448.50	Bard[11]
δ-MnO_2	4	-438.24★	Kitchaev[28]
R-MnO_2	4	-459.95★	Kitchaev[28]

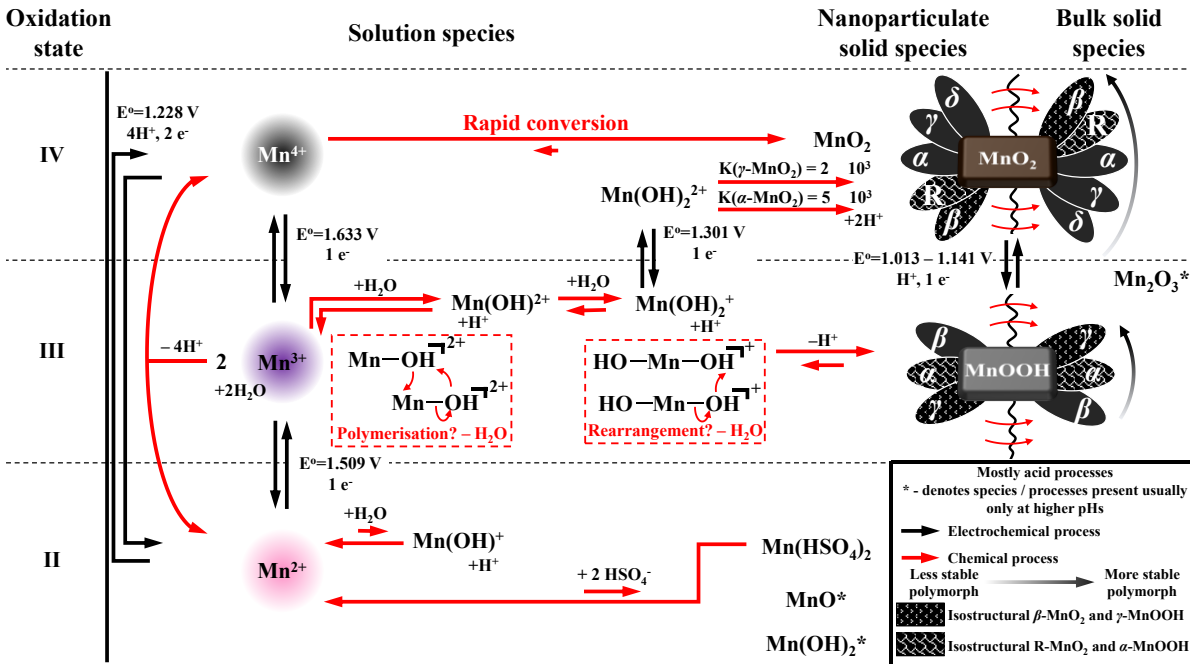


Figure 6.4: Manganese speciation map in an acid environment.

6.1.2 Titanium chemistry review

As before, this titanium review should be started with its respective Pourbaix diagram (Figure 6.5).[17,43] The domain of thermodynamic stability for titanium does not overlap with that of

water.[17] When exposed to air, titanium forms oxide films at its surface rendering its metallic form passive – it follows that titanium in aqueous media is not in a true state of equilibrium and its standard potentials cannot be measured accurately.[11,17] No aquated Ti^{4+} salts can be isolated, but Ti^{4+} possibly exists in solution though the main species are hydrolysed.[19]

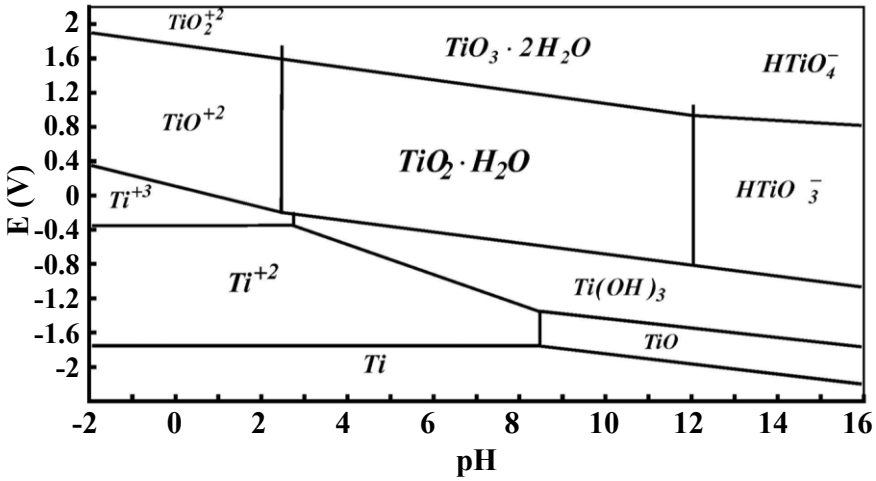


Figure 6.5: Pourbaix diagram for Titanium using hydrated titanium species.[43]

Like manganese, titanium has a rich, versatile chemistry making use of most of its four available electrons, forming compounds in its 2+, 3+ and 4+ oxidation states. There are only few inorganic compounds with Ti^{2+} metal centres – the vast majority of research with this oxidations state is devoted to developing Ziegler-Natta catalysts for ethylene or propylene polymerisation at room temperature and pressure.[44,45] Ti^{3+} is used extensively as a reducing agent – the fully hydrated form of Ti^{3+} ($[Ti(H_2O)_6]^{3+}$) can be formed on reduction of Ti^{4+} in acidic conditions ($[H^+]$ = 0.3 M – 12 M) but this violet solution reduces oxygen and so should be handled under nitrogen.[19] The reduction reactions for this process in this pH region are as follows:

$$Ti^{4+} + e^- \rightleftharpoons Ti^{3+} \quad E^0 = 0.2\ V\ vs.\ SHE \tag{6.30}$$

$$Ti(OH)_2^{2+} + 2H^+ + e^- \rightleftharpoons Ti^{3+} + 2H_2O \quad E^0 = 0.0077\ V\ vs.\ SHE \tag{6.31}$$

For the purposes of this work, Ti^{4+} is of the most interest. Briefly, regarding solid species: the naturally occurring, TiO_2 has three crystal modifications – rutile, anatase and brookite. Rutile (where Ti centres are in a regular octahedral coordination site) is the most abundant but anatase where Ti centres are slightly distorted from octahedral) is more thermodynamically stable.[19] Another family of solid crystal structures – Titanates – as the name suggests, involve titanium in mixed metal oxide structures (perovskite and spinel being the most prominent titanates).[19]

TiO_2 is used as a white pigment and is generally made by the hydrolysis of $Ti(SO_4)_2$ and under hydrothermal conditions, have been known to produce zeolites.[46]

Fujishima and Honda demonstrated the photooxidation capability of simple earth abundant TiO_2.[47] However detailed understanding of its production (even at lab scale) continues to be poorly understood. This is evidenced by continued hydrolysis speciation and sulfate complexation studies and wide ranging disagreement among researchers surrounding hydrolysis equilibrium constants in acidic environments.[48–50] These successive four hydrolysis reactions can be generalised into the following Equation (6.32) (where x = 0 – 3, inclusive). The latter hydrolysis steps are more likely in higher pHs resulting in complex species such as $Ti_3O_4^{4+}$ leading, eventually to colloidal or precipitated $TiO_2{\cdot}nH_2O$.[19] In strongly acidic conditions, the dominant Ti^{4+} species in solution is TiO^{2+} which is considered to be in equilibrium with the doubly hydrolysed $Ti(OH)_2^{2+}$ and Ti^{4+} though,[19] the equilibrium constant for this is expected to be very low. It has been suggested that, at particularly low concentrations of titanium in acidic media, there is a window in which the $TiOOH^+$ species exists between TiO^{2+}, TiO_2 and $TiO(OH)_2$ – however this should be treated with caution because of changes in activity coefficients (Equation (6.33)).[24]

$$\mathrm{Ti(OH)_x^{(4-x)+} + H_2O \rightleftharpoons Ti(OH)_{x+1}^{(3-x)+} + H^+} \qquad (6.32)$$

$$\mathrm{TiO^{2+} + H_2O \rightleftharpoons TiOOH^+ + H^+} \qquad (6.33)$$

$$\mathrm{Ti(OH)_2^{2+} + xSO_4^{2-} \rightleftharpoons [Ti(OH)_2(SO_4)_x]^{(2-2x)}} \quad K = 3.4 \text{ or } 12.02 \qquad (6.34)$$

Investigation and understanding of oxysulfate dissolution and or the interaction of sulfate ions with TiO^{2+} centres has developed over time, even since it was investigated by researchers in the Royal School of Mines, Imperial College London.[51] Since then it has been asserted that in the presence of sulfate ions, the dominant complex pair is $[Ti(OH)_2(SO_4)_x]^{(2-2x)}$ (where x = 1 or 2, Equation (6.34)).[48,50] More recently, on inspection of speciation of $TiOSO_4$, Kozma et al. found that $TiOSO_4$ concentrations below 0.2 M will not dissolve in water as a result of hydrolysis overcoming the dissolution process due to the self-buffering behaviour of Ti^{4+} centres (bound water deprotonates) yielding acidic solutions.[52] 1 M $TiOSO_4$ self-buffers to a solution pH of 0.77.[52] Using EXAFS and small-angle X-ray scattering, $\{Ti_{18}\}$ titanium-oxo clusters were found to form in higher concentration solutions after vigorous stirring for four to six hours although, a crystal structure has not been fully elucidated due to the size of this species. Metal-oxo clusters are often used to further understand crystallisation and self-

assembly mechanisms and reaction pathways,[53] however titanium-oxo clusters have not yet clearly informed the formation of TiO_2.[52] It should be repeated, however, that in the sulfuric acid environment discussed in this work, the sulfate species is almost universally in it's bisulfate (HSO_4^-) form (see later).

Table 6.3: A summary of Gibbs free energies of formation for relevant titanium species.

Species	OS	$\Delta_f G^0$ / kJ mol^{-1}	Reference
Ti^{2+}	2	-314.00	Bard[11]
Ti^{3+}	3	-350.00	Bard[11]
$Ti(OH)^{2+}$	3	-577.7	Brown[24]
$Ti(OH)_3$	3	-1049.80	Bard[11]
TiO^{2+}	4	-577.40	Bard[11]
TiO^{2+}	4	-631.3	Brown[24]
$TiOOH^+$	4	-805.55	Bard[11]
$TiO(OH)^+$	4	-854.3	Brown[24]
$HTiO_3^-$	4	-955.90	Bard[11]
$TiO(OH)_2$	4	-1074.3	Brown[24]
$TiO_2{\cdot}H_2O$	4	-821.30	Bard[11]
TiO_2	4	-888.8	Brown[24]

6.1.3 Manganese-titanium electrolyte

Before looking to combine manganese and titanium in an electrolyte, some similarities in their chemistries should first be noted. Clearly, titanium does not have as many redox states as manganese but, at least in their 4+ oxidation state, both elements demonstrate low stability in aqueous solution. Their species both undergo acid-base reactions in similar pHs, interact strongly with sulfates and precipitate / polymerise easily in aqueous solution. These facts make understanding their combined interaction in solution at these low pHs all the more challenging. One of the main takeaways from these mini-reviews should be that the formation of solids in flow batteries is a critical issue for the operation of RFBs utilising solution based electrolytes (as flow pathways can get blocked leading to bottlenecks, increased pressure drop, leakage and irreversible capacity loss). This demands significant understanding about how the species interact and, specifically, how Mn^{3+} can be stabilised.

The electrolyte used in the present work combines manganese, titanium and sulfuric acid. Titanium additives (such as titanium oxysulfate, $TiOSO_4$ and titanium disulfate, $Ti(SO_4)_2$) have been shown to enable Mn-Ti electrolyte containing systems to charge and discharge,[8,9] though the role of titanium in manganese speciation is still not fully understood.[7,23] This is subject of active scrutiny in the Kucernak research group alongside commercial partners using a number

of different analytical techniques. A company, Sumitomo Electric Industries Inc. (SEI),[54] found that on testing a titanium manganese flow battery in which there had been mixing of the two electrolytes (likely serendipitous following crossover) the resulting electrolyte was 'more stable'.[8] Under normal conditions oxidation of Mn^{2+} in acid quickly results in growth of significant amounts of MnO_2 which coagulates, crystallises and forms a "sludge" whereas, on addition of a Ti^{4+} additive, the deep purple colour characteristic of Mn^{3+} in aqueous solution (see later), remains visible indefinitely (or for at least one year – this was not explicitly measured, however – Figure 6.6).



Without Ti^{4+} additive **With Ti^{4+} additive**

Figure 6.6: Photographs of partially oxidised Mn^{2+} solution with and without a Ti^{4+} additive.

Initially, it was suggested that Ti^{4+} directly supresses the Mn^{3+} disproportionation, but since then alternative hypotheses for this stabilisation have been asserted, such as, modifications to the chemical equilibria on Ti salt addition.[8,9,23] The current working principle is that the Ti^{4+} additive significantly reduces the size of the colloid particles and prevents agglomeration so that no intractable "sludge" forms even at high Mn^{3+} concentration. Kaku et al. identified the formation of the polymorphs α- and γ-MnO_2 in a titanium manganese electrolyte. Using XRD, they found that on addition of one equivalent of Ti^{4+} (to Mn^{2+} starting concentration), compared to electrolyte containing no Ti^{4+} additive, the size of the MnO_2 structures were much smaller and no α-MnO_2 was present in the precipitates.[9] This might suggest that Ti^{4+} additives do, in fact, block the formation of α-MnO_2. The mechanism for these transitions is of interest especially with respect to the three previously mentioned methods towards preventing or slowing the disproportionation reaction. The Ti^{4+} additive may contribute to all three methods in some way – the effect of the large (18-centre) titanium-oxo cluster may disrupt the formation of specific aspects of MnO_2 polymorphs. The buffering ability of the titanium containing solution may increase the concentration of protons (stabilising Mn^{3+}).

To summarise, manganese speciation in strong sulfuric acid is not fully understood and Ti^{4+} additives further complicate the chemical and physical transitions that occur in the electrolyte.

Research groups have utilised Ti^{4+} additives' stabilising effect on the electrolyte but few have attempted to identify the cause.[9,23] This work uses a combination of thermodynamic, kinetic, electrochemical and real-time manganese species concentration data to better understand the electrolyte and the hRFB system as a whole – including assessing the exact origins of the measured cell potential. Gathering real-time concentrations of species and the requirement of in-operando techniques is the subject of the next part of the introduction.

For the purposes of the rest of this work, we will consider only the following (high-level) features of the chemistries of manganese and titanium to be at play until the discussion section is reached:

- The oxidation of Mn^{2+} to Mn^{3+} is the only electrochemical process taking place during galvanostatic charging / discharging steps.
- Mn^{3+} hydrolyses in the prepared electrolyte.
- Mn^{3+} disproportionates at sufficient concentrations, precipitating solid species.
- These solid species redissolve quickly, initially, but more slowly as the Mn^{2+} concentration is electrochemically diminished (with increasing SOC) eventually agglomerating into suspended nanoparticles.
- Titanium interacts with the manganese centres allowing for a full recovery of manganese in its 2+ oxidation state (fully discharged – SOC 0).

6.1.4 In-operando techniques for electrochemical systems

Typically, in RFB systems, during charging and discharging, the information provided by the devices operating the cell (in this chapter, a Scribner Redox Cell Test Station) is limited to current and potential applied / measured, HFR, cell temperature and volumetric flow rate. From these data, further information can be gathered but is limited to power, coulombic and capacity calculations. Alongside these calculations, a whole range of ex-situ measurements, such as SEM or XCT electrode imagine can also be made – these non-destructive analytical methods can reveal important information about what occurs at the location of interest in any RFB system. In-operando methods (shortened occasionally to 'operando') for data collection are interesting to researchers as they provide real-time information, sometimes providing important enhanced understanding of aspect in a system.

A recent study carried out by Zhao et al,[55] presented a multi-modal characterisation study examining the intermediate steps in the electrochemical reaction mechanism involving an organic anthraquinone redox couple involved in an organic-inorganic RFB.[55] NMR and EPR were simultaneously carried out revealing the elusive radical anion intermediate ($DHAQ^{3-\bullet}$) and enabling the researchers to calculate rate constants associated with conversion of species. Several interesting imaging studies have been carried out to understand the flow through serpentine flow fields and to establish improved operation techniques for certain electrode-electrolyte combinations.[56,57] Neyhouse et al. devised an experimental setup employing an electrochemical sensor to measure the concentration and (therefore the) real-time SOC of an organic RFB.[58] While this organic (symmetric) RFB is uncomplicated and was only developed for as a proof of concept for analytical means, it demonstrates the potential versatile ability for this geometry of microelectrodes to be used to keep track of a RFBs state of health.[58]

In this chapter, the two operando analytical techniques employed are UV-vis and EPR and these were introduced in Chapter 2. UV-vis takes advantage of transitions of electrons from lower to higher energy molecular orbitals and associated absorption coefficients of solution-based complexes. In transition metals, as is the case in manganese solution chemistry, the energy associated with these transitions are dependent on the geometry surrounding the central metal ion. Neutral or aqueous Mn^{2+} solutions have a low absorption coefficient (0.701×10^{-3} M^{-1} cm^{-1})[59] and appears pale pink in solution. Aqueous Mn^{3+} possesses a much greater absorption coefficient (c.a. 250 M^{-1} cm^{-1} – varies according to literature)[9,60,61] and appears dark purple / black and optically dense. One way to combat samples with a high absorption coefficient is to ensure the pathlength through the optically dense solution is short as then the absorbance is not too high and the measurement avoids becoming 'saturated' (usually, sample chambers allow for a cuvette with a pathlength of 1 cm – assuming a sample concentration of 1.0 mol dm^{-3} – the absorption should be ideally be below 2 M^{-1} cm^{-1}). This technique is described in much greater detail later. Commonly reported characteristic Mn^{3+} peaks appear at wavelengths just above 522 nm indicating the $^5B_{1g}$ to $^5B_{2g}$ MO transition.[62] A much broader peak with a relatively high wavelength peaking at around 840 nm (low energy) is far less reported but is considered to indicate the $^5B_{1g}$ to $^5A_{1g}$ transition.[62] Operando UV-vis measurements have been carried out employing a VRFB alongside a fibre optic probe attached to a UV-vis spectrophotometer to allowing for continuous measurement during charge and discharge (this is not exactly the same setup as that reported in this chapter but, crucially, it demonstrates a zero dilution, truly operando method).[63] The growing interest in materials

utilising TiO_2 photocatalysts in solar cells for the conversion of light into energy has dominated solid state UV-vis measurements surrounding Ti species. The previously discussed difficulty of getting Ti^{4+} species in solution makes literature in this field sparse. However it has been shown that Ti-based compounds have very high absorbances (low transmittance) at low wavelengths (high energy) up to 350 nm.[64]

With this context and this stated set of assumptions, the following section outlines the methods used to capture important information about the hRFB. New, detailed analysis methods designed to measure the Mn^{2+} and Mn^{3+} concentrations in real-time are developed. Analysis of concentration and potential transients is carried out with a view to revealing bulk kinetic information. Following this, a discussion is outlined with the help of ongoing thermodynamic analysis developed by Professor Anthony Kucernak and is used to illustrate and explain, the results presented.

6.2 Methodology

6.2.1 Electrolyte preparation

Titanium oxysulfate ($TiOSO_4$, Sigma Aldrich) was added in three batches to DI water (half the total final volume) and vigorously stirred until the solution was faintly cloudy. The concentration of TiO^{2+} in solution at this point was roughly 2 M and therefore was strongly acidic with a pH close to 0.5 M.[52] Sulfuric acid (H_2SO_4, VWR International) was then added slowly and the solution was left to cool until the solution reached room temperature. The solution was then transferred to a suitably sized volumetric flask and made up to the mark with DI water. The masses and volumes of $TiOSO_4$ and H_2SO_4, respectively, ensured the final concentrations of this 'stock' acidic TiO^{2+} solution were 5 M H_2SO_4 and 1 M $TiOSO_4$. The final step to complete the preparation of the standard electrolyte was carried out only immediately before the experiment was to be carried out. It involved adding a mass of $MnCO_3$ (Alfa Aesar) to the stirring stock solution, ensuring the end Mn^{2+} concentration was 1 M. On adding the manganese salt, the highly acidic solution protonates one of the oxygen atoms on the carbonate to produce 1 M water – ultimately leading to the production of CO_2 (g) (assumed to be fully lost to the atmosphere). Once all the $MnCO_3$ was dissolved, the solution was left to stir gently for 30 minutes before beginning the experiment. The end Mn^{2+}, Ti^{4+} and sulfur-containing species (in all their potential forms: SO_4^{2-}, HSO_4^-, H_2SO_4, or in complexes with appropriate ratios) concentrations were 1 M, 1 M and 6 M, respectively. In the present chapter,

$MnCO_3$ is used as a more inexpensive source of Mn^{2+}. Addition of $MnCO_3$ to the $TiOSO_4 \cdot H_2SO_4$ 'stock' solution, leads to the thermodynamically favourable production of CO_2 (g). Two equivalents of H^+ are assumed to be consumed here but the next sub-section outlines the working understanding of the speciation of titanium / sulfate in this system.

Table 6.4: Aqueous electrolyte composition used in this work.

Species	Main atom OS	Concentration / mol dm^{-3}
$MnCO_3$	2	1.0
$TiOSO_4$	4	1.0
H_2SO_4	6	5.0

6.2.1.1 Speciation in a titanium / sulfate system

Given the findings of Kozma et al., the 'stock' (acid-titanium) solution is thought to contain $\{Ti_{18}\}$ clusters and does not show any signs of precipitation (to forming TiO_2) even after 60 days under ambient conditions.[52] Additionally, as was repeatedly referred to in the introduction, following ongoing discussions in the Kucernak group, assuming only the three main forms of sulfate exist in solution, sulfate was calculated to almost exclusively exist in its bisulfate (HSO_4^-) form across the pH range used in this chapter (and device as a whole) – Figure 6.7 shows the calculated average anion charge as a function of the H_2SO_4 concentration (using standard equilibrium constants for each proton dissociation).

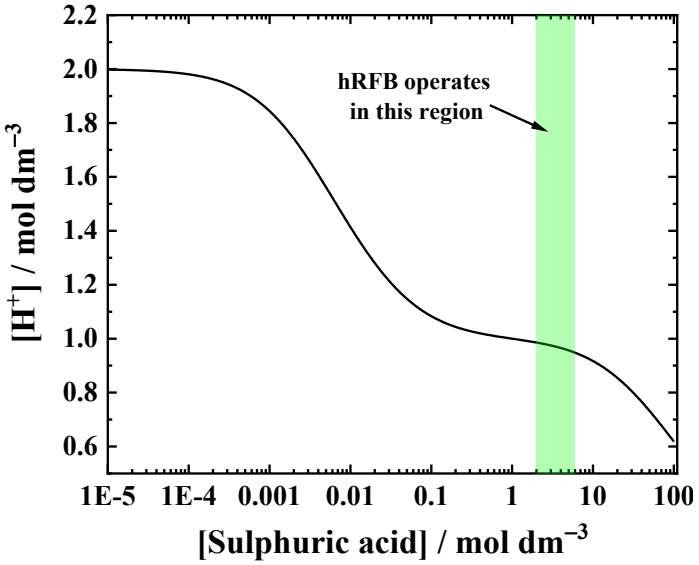


Figure 6.7: Average sulfate anion charge.

These concentrations do not take into account the buffering ability of titanium or manganese species or the potential interaction of Ti-clusters with any protons or bisulfate ions which, as inferred in the introduction, is unlikely to be the case. However, the following set of equations,

developed by Prof. Kucernak, account for the speciation in the system – the concentration of sulfur-containing species governs the projected proton concentration. Expressions representing the deprotonations of sulfuric acid are shown in Equations (6.2) and (6.3) and a simplified one for the titanium system (based on the hydrolysis of TiO^{2+} – Equation (6.33)) are shown below.

$$K_{A,H_2SO_4} = \frac{a_{H^+} a_{HSO_4^-}}{a_{H_2SO_4}}, \; K_{A,HSO_4^-} = \frac{a_{H^+} a_{SO_4^{-2}}}{a_{HSO_4^-}} \tag{6.35}$$

$$K_{A,TiO^{+2}} = \frac{a_{H^+} a_{TiOOH^+}}{a_{TiO^{+2}}} \tag{6.36}$$

$$a_{H^+} + 2a_{TiO^{+2}} + a_{TiOOH^+} = 2a_{SO_4^{-2}} + a_{HSO_4^-} \tag{6.37}$$

$$\text{Total sulfate} = a_{SO_4^{-2}} + a_{HSO_4^-} + a_{H_2SO_4} \tag{6.38}$$

$$\text{Total titanium} = a_{TiO^{+2}} + a_{TiOOH^+} \tag{6.39}$$

Equation (6.37) accounts for electroneutrality in the solution (total anion charge = total cation charge), whereas Equations (6.38) and (6.39) equate the total amount of titanium- and sulfur-containing species present in its different forms, respectively. We know $K_{a,H2SO4}$ (~100) and $K_{a,HSO4-}$ (~0.01) from literature.[10] Assuming simple acid-base behaviour in the TiO^{2+} from the known variation of pH with different concentrations of $TiOSO_4$ solution, an estimate of $K_{a,TiO^{2+}}$ was taken using literature.[52] One can also be calculated using the data in Table 6.3 alongside Equation (6.33) (0.026131). Six equations and six unknowns ($a_{H^+}, a_{TiO^{+2}}, a_{TiOOH^+}, a_{SO_4^{-2}}, a_{HSO_4^-}, a_{H_2SO_4}$) can therefore be solved.

6.2.2 Hybrid-redox flow battery setup

The hybrid-flow / fuel-cell fixtures was provided by Scribner Associates. The liquid side (red anodised end-plate side – taken from the RFB Test Fixture, Scribner Associates) and gas side (blue anodised end-plate side – taken from the Fuel Cell Fixture, Scribner Associates) lay adjacent to a gold plated current collectors and serpentine POCO graphite flow fields. On the gas side, a platinum electrode (0.4 mg_{cat} cm^{-2}, ELE027-10321015978, Johnson Matthey) was used and plasma-treated (30 seconds under a stream of oxygen, "low pressure plasma systems" – NANO, Diener Electronic GmbH)carbon felt (SGL carbon, Sigracell®GFD 4.6) on the liquid side. Depending on the size of the cell, the electrodes were cut into 5 cm^2 or 25 cm^2 squares. The two electrodes were separated by Nafion 212 (593363, Fuel Cell Store), a commonly used proton exchange membrane (thickness: 50.8 μm). The compression of the two electrodes and the membrane was c.a. 20 % and was controlled by a number of layers of incompressible, glass-reinforced PTFE gaskets (PTFE coated glass cloth, Tygaflor, PAR Group Ltd.). The thickness

of the electrodes and membrane was taken into account when calculating the number of gaskets needed. The cell was gently closed and tightened using guiding pins and a torque wrench with a force of 4.0 N m applied to standard threaded (5 mm diameter) rods in the Scribner hybrid flow / fuel-cell fixture.

Masterflex tubing (Versilon™) and appropriately sized connectors were attached to the liquid outlet and a peristaltic pump (Cole-Parmer) was used to pump the liquid electrolyte through the liquid side of the cell at a standard rate of 50 mL min^{-1}. Hydrogen was supplied through Nylon tubing by an electrolyser (max flow: 500 mL min^{-1}, hydrogen purity: > 99.99995 %, , Deliver pressure 5 bar, 60H-MD, Parker | Dominick Hunter Ltd.) and connected to the inlet of the gas side of the cell via a mass-flow controller (flow range: 0 – 1 L min^{-1}, accuracy: ± 0.5 %, max pressure: 5 bar, EL-FLOW® Select Bronkhorst). The mass-flow controller was set to supply 100 mL min^{-1} hydrogen, continuously, during the charge and discharge of the cell. The outlet of the cell was connected to a Nederman extraction arm. In the intermediate time, between cycles when the cell was not being used but the electrolyte still flowed through the liquid side, nitrogen was passed over the platinum electrode to ensure no electrochemically parasitic discharge reaction occurred (hydrogen did flow, however, during the transient measurements perhaps contributing partially to reduction of the active species in the electrolyte).

6.2.3 Hybrid redox flow battery experiments

A Scribner Redox Cell Test System (Scribner Associates 857) was used to charge and discharge the cell galvanostatically (constant current) using a wide range of current densities 25 – 125 mA cm^{-2}, with cut off potentials for the charge and discharge at 1.8 V and 0.5 V, respectively. This testing system enables users to monitor the high frequency resistance (HFR) continuously during galvanostatic holds – providing a real-time measurement of the combined membrane and solution resistance. Potentiostatic electrochemical impedance spectroscopy (EIS) was carried out (where possible) at the pre-equilibrated OCP of the cell using a V_{p-p} sinusoidal modulation with a 10 mV amplitude with a frequency range of 10 kHz – 0.1 Hz (10 points per decade).

Given the nature of the electrolyte and the uncertainty associated with the SOC, after a given cycle, an extra discharge step at 10 mA cm^{-2} was carried out in order to ensure all cycles ‘start’ from the same ‘effectively zero’ SOC and are comparable. The electrolyte presenting with a

light pink colour and no suspended material was usually a good indicator of zero SOC. It was clear, especially after high current density cycles that the electrolyte was not sufficiently discharged (the electrolyte still appeared dark purple / black).

6.2.4 Electrolyte characterisation

Given this chapter is, essentially, all about characterising the electrolyte, this section is poorly named as there are many more techniques used other than those specified here. However, given the composition of the electrolyte changes during the course of a cycle, some electrolyte physical characteristics were measured at specific points during cell operation. Conductivity, pH and viscosity measurements were judged to be the most essential. For the former two measurements (conductivity and pH), a Orion™ Versa Star Pro™ pH/ISE Benchtop Multiparameter Meter (VSTAR40B) was used in tandem with measurement-specific modules and probes (explained in more detail below).

For conductivity, an Orion™ Versa Star Conductivity Measurement Module (VSTAR-CND) alongside a Orion™ 2 Cell High Range Conductivity Probe (10 μS cm^{-1} to 2000 mS cm^{-1}, Mini-DIN, Glass, Platinum, platinized, 018020MD) was used as the electrolyte has a high concentration of conductive ions and therefore is highly conductive. Flow conductivity meters are available, but it was judged that single measurements should be used so that a cleaning step (three step process: following measurement immerse the meter in excess $Ti(SO_4)_2$, followed by 3 M H_2SO_4 and finally excess DI water) could be incorporated between measurements (avoiding the possibility of any unwanted deposition on the conductivity meter sensor electrodes).

An Orion™ Thermo Scientific pH probe (8157BNUMD, ROSS Ultra pH / ATC Triode) was used in this work. Unfortunately, while the meter is able to show negative pHs, no successful pH measurements were achieved as the pH of the electrolyte was outside the operable range (pH 0 – 14) of the respective probe. This is particularly unfortunate as accurate measurements of pH (and thus H^+ concentration) would be extremely helpful for this work. There are a few industrial pH units which can measure such low pHs, but are large and difficult to source. Most lab based glass pH sensors take longer and longer to equilibrate as pH becomes lower (this is, indeed what was observed when this was attempted). Other approaches to measure pH such as electrochemical methods (e.g. using a hydrogen electrode, where the RHE potential is dependent on proton activity – noting that this approach is prohibited by the presence of a

strong – manganese – redox couple which overwhelms the hydrogen reaction) are complicated because of the high concentration of redox species which perturb the hydrogen reaction. Chemical methods were disregarded as titrations would totally change the chemistry of the buffered solution returning inaccurate results.

Viscosity measurements were measured using an m-VROC Viscosimeter. A syringe (Hamilton) was used to extract a small amount of electrolyte (c.a. 500 µL), placed in the viscosimeter sample holder and then passed through the chip at a specific shear rate. It was discovered, however, that there was a fault in the chip used to measure the viscosity and so the viscosity measurements were off by an unknown factor. Regrettably, these experiments could not be repeated due to the reduced lab time and long lead times on the arrival of replacement parts as a result of the pandemic. These experiments must be carried out very carefully so as not to block the flow path within the viscosimeter chip. Viscosity data would help to reveal information about the global diffusivity of species within an electrolyte.

6.2.5 In-operando techniques

In-operando techniques provide unique perspective to processes in all sectors in science – they enable real-time inspection of processes occurring during system operation. The primary reason in-operando techniques were needed in this work is because isolation of the electrolyte at certain SOCs and subsequent manipulation (e.g. sample dilution in preparation for RDE) leads to a presumed deviation in the nature of the chemistry of the species within the electrolyte.

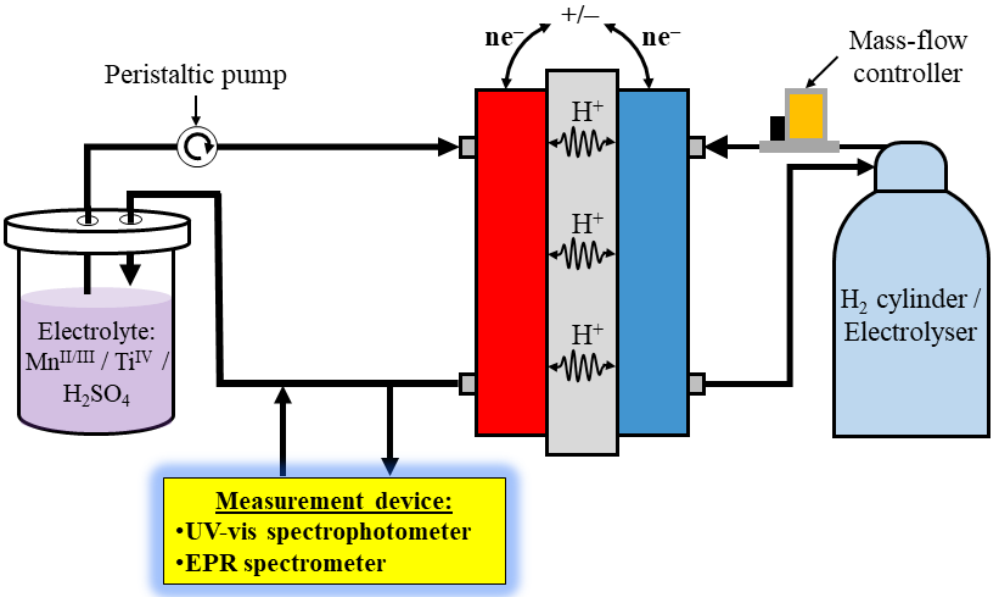


Figure 6.8: Schematic outlining the in-operando experimental techniques used alongside the hRFB setup.

Every in-operando technique is unique. The data collected from this setup, shown in Figure 6.8, must be handled carefully. In this case, the time delay between the electrolyte leaving the cell and arriving at the measurement device should be kept in mind. The species in the electrolyte may change, physically and chemically, in this intermediate time. For instance, in this system, if solid species form inside the cell but, after a time suspended in the bulk electrolyte, will dissolve back into solution. Additionally, the importance of the positioning of the measurement device is essential – in this work, the device is placed between the outlet and the tank rather than between the inlet and the tank meaning these electrolyte measurements are following one 'pass' through the cell, rather than bulk inlet electrolyte properties.

Building on the experimental setup outlined in Chapter 5, Figure 6.8 shows a measurement device placed between the outlet of the hRFB cell and the tank containing the bulk electrolyte. This work employs two types of in-operando technique: UV-vis and EPR. These analysis techniques are outlined and discussed in detail in Chapter 2 but are briefly revisited in the next two sub-sections.

6.2.5.1 In-operando UV-vis spectroscopy

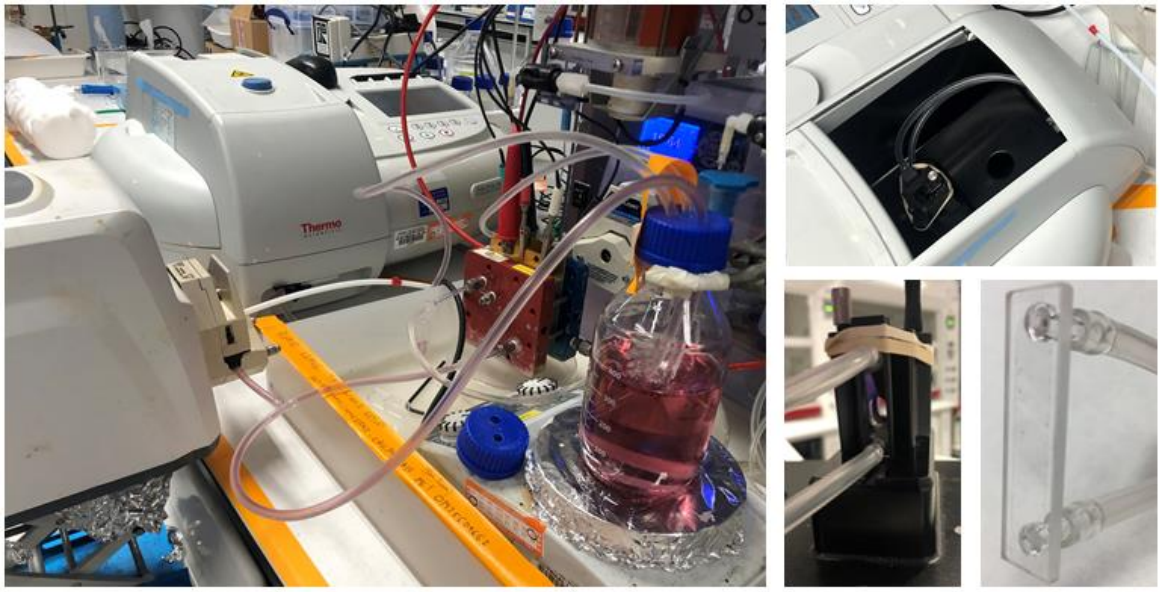


Figure 6.9: Images displaying a full UV-vis hRFB cell operando setup and with specific component features. The images in the lower right part of the figure display the flow cell used with a small path length.

In-operando UV-vis measurements were carried out by installing a T-piece (T0-2PP, Cole-Parmer Instrument Co.) and peristaltic pump (Masterflex) into the outlet tube of the hRFB cell to divert a portion of the electrolyte through the thin flow cell (48/Q/0.1 and CH/2049 holder, Starna) inside a spectrophotometer (Evolution™ 220, ThermoFisher Scientific) at a flow rate of 10 mL min^{-1}. A 3 M H_2SO_4 solution was used for the baseline for these measurements (see

later sections for this) and the device settings were as follows: wavelength window: 950 – 330 nm; bandwidth: 1 nm; integration time: 0.50 seconds; interval: 1.00 nm; and scan speed: 120 nm min^{-1}. This resulted in a total scan time of just over five minutes. It must be recognised that there are two time differentials to consider – one representing the time it takes for electrolyte to leave the cell and reach the detector (c.a. 30 s) and the other representing the change in electrolyte composition between the beginning and the end of the measurement (five minutes). The first of these differentials represents a systematic error which, in this particular case, does not make a substantive difference to the absorbance measurements as they will all be 'off' by the same amount. The extent to which the parameters of the experiment matter a great deal in this setup. In the worst case, the smallest volume of electrolyte tested (200 mL) would be cycled at the highest current density tested (100 mA cm^{-2}) over the course of the cycle the SOC of the electrolyte would change by 3.9 % (750 C / 19297 C). This is not considered to be a concerning change in SOC and, in any case, specific UV-vis transitions would not take a full five minutes to measure (five minutes indicates the full spectrum). This time differential was taken into account when measuring the absorptions at different SOCs and usually volumes of greater than 200 mL and current densities of 75 mA cm^{-2} were used for UV-vis measurements.

6.2.5.2 In-operando electron paramagnetic resonance spectroscopy

A Bruker EMX equipped with an ER4122SHQE resonator was used to collect these data (Figure 6.10 (a)). The EPR techniques carried out in this work take advantage of the paramagnetic state of Mn^{2+} in the electrolyte during hRFB cell operation.

Much like the setup outlined for the in-operando UV-vis, a T-junction was used to divert a small portion of the electrolyte through the EPR resonator. The main differences between the setups lie in the flow cell positioned inside the resonator and the flow rate through the measurement devices. The electrolyte was passed through the resonator at roughly half the volumetric flow rate – 6 mL min^{-1} – compared to the UV-Vis spectrometer due to the much smaller cross sectional area through which the liquid electrolyte passed. This augmented pressure increased with SOC due to the coating of solid material on the inner tubing walls and the capillary (which reduces the inner diameter through which the liquid flows raising the pressure drop marginally), peaking at the tubing-capillary joint and potentially leading to leakage. Figure 6.10 (b) shows the in-house designed flow cell used to safely flow electrolyte through the resonator. Appropriately sized tubing (Masterflex) and a safeguarding shrink wrap

(RS Components) that covered the whole setup ensured that if a leak formed, it would not corrode the inside of the resonator. Straight-forward CW measurements were repeatedly and continuously taken (one after another) as the hRFB cell experiments took place (experiments were sometimes carried out for over 24 hours). Each measurement took three minutes to complete scanning across a magnetic field between 950 – 6500 G.

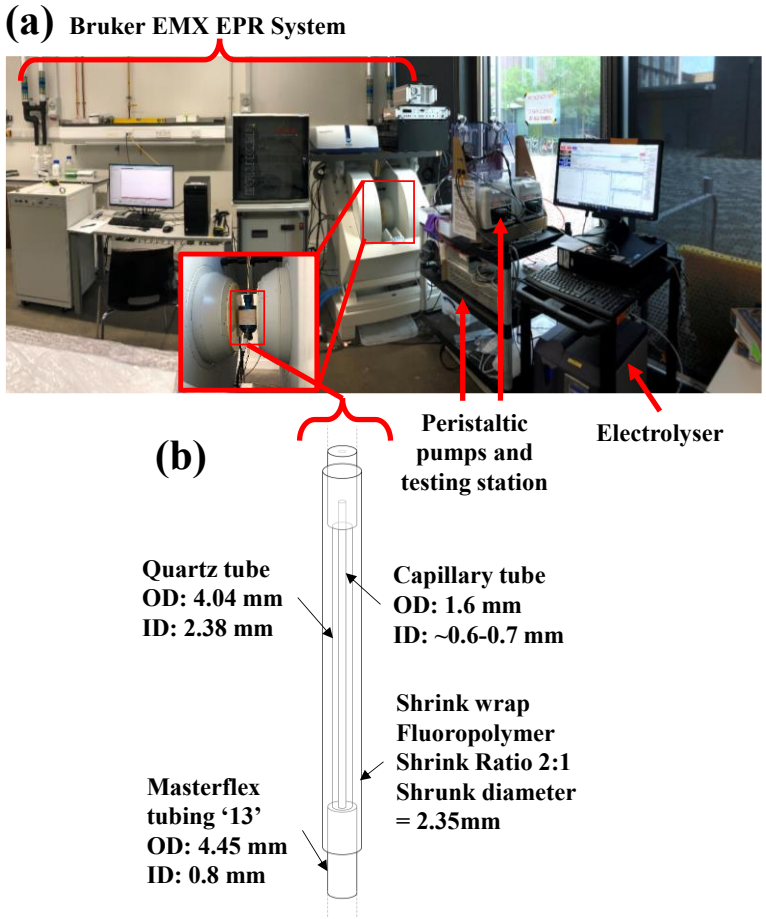


Figure 6.10: (a) Image showing in-operando EPR arrangement. (b) Diagram of flow cell in within the resonator with relevant safeguards.

The relevant theoretical background for the EPR carried out in this work was presented in Chapter 2 and, as mentioned, resonator operation and raw data collection was carried out by Dr. Collauto.

6.2.6 Thermodynamic analysis of manganese speciation as a function of state of charge

Thermodynamic equations and calculations were derived and carried out by Prof. Anthony Kucernak. Equations (6.35) – (6.39) were used alongside extra equations (shown below) representing possible manganese speciation and an updated charge balance equation to calculate the SOC.

$$K_{a,Mn^{3+}} = \frac{a_{H^+} a_{MeOH^{2+}}}{a_{Mn^{3+}}}, \; Mn^{3+} + H_2O \rightleftharpoons H^+ + Mn(OH)^{2+} \quad (6.40)$$

Constants calculated from the possible formation of solid MnOOH or MnO_2 (Equations (6.41) – (6.42)).

$$K_{D,Mn^{3+}} = \frac{(a_{H^+})^4 a_{Mn^{2+}}}{(a_{Mn^{3+}})^2}, \; 2Mn^{3+} + 2H_2O \rightleftharpoons Mn^{2+} + 4H^+ + MnO_2 \quad (6.41)$$

$$K_{D,Mn^{3+},MnOOH} = \frac{(a_{H^+})^3}{a_{Mn^{3+}}}, \; Mn^{3+} + 2H_2O \rightleftharpoons MnOOH + 4H^+ \quad (6.42)$$

And, finally, the equations for the total manganese (in all its forms), charge balance and SOC are presented here (Equations (6.43) – (6.45)).

Total manganese:

$$a_{Mn^{2+}} + a_{Mn^{3+}} + a_{Mn(OH)^{2+}} + a_{Mn(OH)_2{}^+} + a_{MnOOH} + a_{MnO_2} \quad (6.43)$$

Charge balance:

$$a_{H^+} + 2a_{TiO^{2+}} + a_{TiOOH^+} + 3a_{Mn^{3+}} + 2a_{Mn(OH)^{2+}} + 2a_{Mn^{2+}} + a_{Mn(OH)_2{}^+} = 2a_{SO_4{}^{2-}} + a_{HSO_4{}^-} \quad (6.44)$$

SOC (varies between 0 – 2):

$$(a_{Mn^{3+}} + a_{Mn(OH)^{2+}} + a_{Mn(OH)_2{}^+} + a_{MnOOH} + 2a_{MnO_2})/\text{total manganese} \quad (6.45)$$

6.3 Results

6.3.1 Standard charging, discharging and conductivity analysis

It is important to bear in mind systems that have similar (or comparable) operating conditions to the Mn/H_2 hRFB. The VRFB and hydrogen-bromine (H_2-Br) systems are among the most widely reported,[65–68] and recently a vanadium-hydrogen system was reported which has a clear resemblance too.[69] Initially, simple galvanostatic charge and discharge cycles were carried out to inspect the nature and durability of the Mn/H_2 hRFB system. Figure 6.11 (a) shows the potential responses to these charge and discharge cycles at different current densities. As expected, the length of time it takes to charge the battery decreases with increased current density.[70] An important feature in these potential profiles which is not seen in other typical redox flow batteries is the step in the discharge curves (dashed lines). Initially, the potential

during the discharging cycle is high, however, after around 40 % of the discharge, there is a step in the potential profile (leading to a reduction in VE, vide infra).

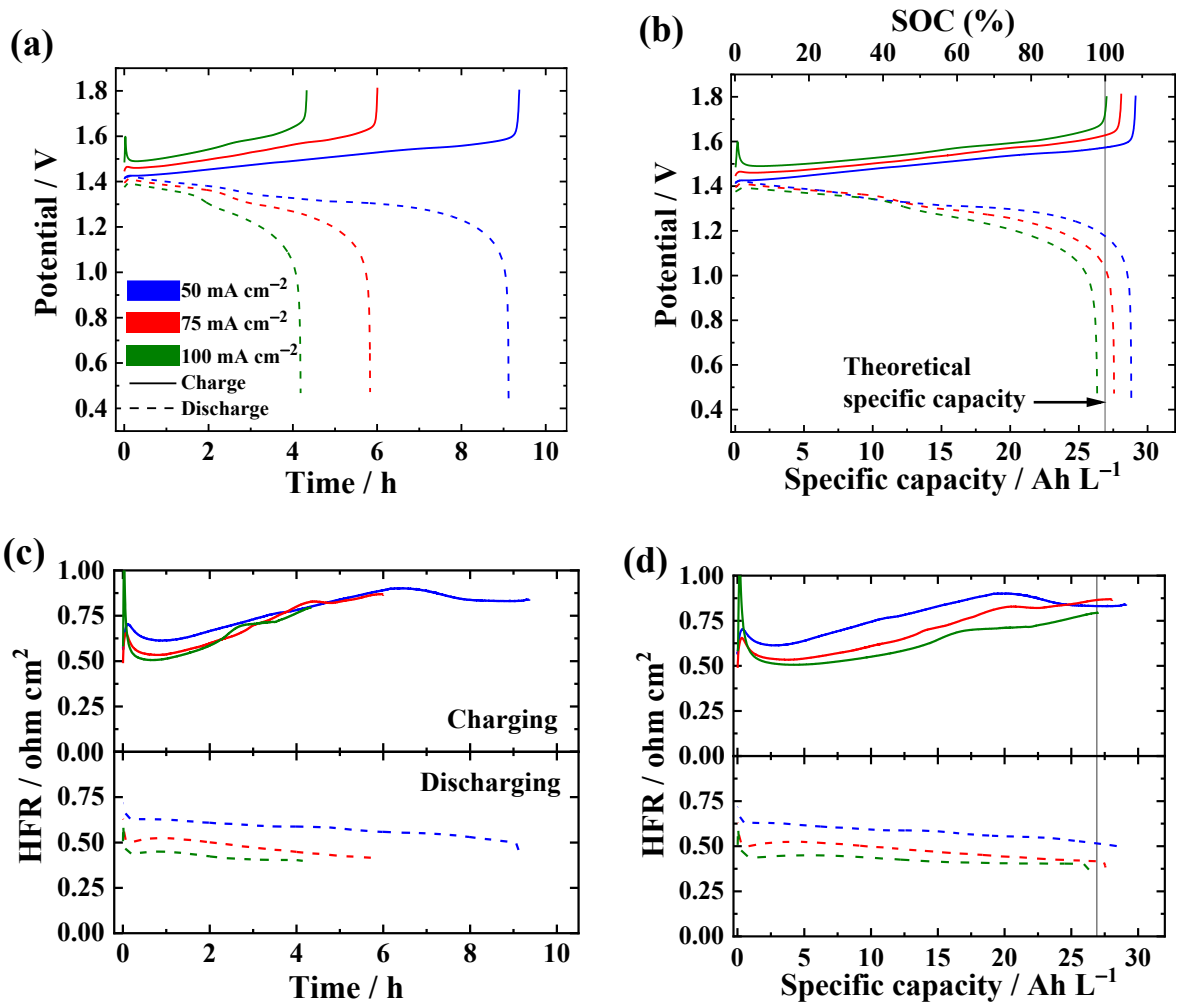


Figure 6.11: (a) General form of potential-time profiles for a Mn/H_2 hRFB during charging and discharging cycles at current densites of 50, 75 and 100 mA cm^{-2}. (b) Equivalent potential profiles using specific capacity and SOC as x-axes – this plot includes the theoretical specific capacity of the electrolyte. (c) and (d) show the HFR responses during these charges and discharges using respective x-axes. These experiments were carried out using an electrolyte volume of 400 mL (leading to the theoretical specific capacity of 26.9 Ah L^{-1} assuming a straight-forward single electron process).

As discussed earlier Mn^{3+}, in high enough concentration, disproportionates producing additional Mn^{2+} not initially considered in calculations. Importantly, this is a chemical process which occurs simultaneously during the implemented electrochemical processes in the system. Therefore, it is implied that Mn^{2+} is continually chemically produced at higher rates with increasing SOCs and never reaches a zero concentration explaining why a greater than expected specific capacity is observed (Figure 6.11 (b)). In fact, this suggests that, in theory, for every mole of Mn^{2+}, two moles of electrons can be used for oxidation (assuming Mn^{3+} fully disproportionates). This disproportionation and variation in solution equilibria will be considered in more detail later.

The high frequency resistance (HFR) of the system during these galvanostatic charges and discharges is displayed in Figure 6.11 (c) and (d). The HFR incorporates the resistances associated with the solution and membrane. These results show a generally higher rate of increase in HFR during charging cycles compared with the rate of decline in HFR during the discharge. At these current densities, the nature of the HFR during the charge is similar, whereas during the discharge the HFR decreases with increasing current density. One reason that may cause this lower HFR during the discharge is reduction in membrane resistance – during discharge, the gas side of the hRFB produces protons (following HOR at the Pt electrode) that travel across the membrane replacing any other cations (e.g. Mn or Ti ions) that may have become stuck / co-ordinated to the negatively charged head-groups in the Nafion during the charging step. Large cation dislodging may result in this enhanced membrane conductivity (and thus lower HFR). This phenomenon was systematically investigated by Wang et al. when they investigated how the membrane conductivity changed as a function of Fe and Cr ion concentration.[71]

In order to investigate this, the electrolyte conductivity was measured in the tank at various points during a cycle and the redox flow system was continually measuring the conductivity in the cell. With these two measurements, the membrane resistance can start to be deconvoluted. Figure 6.12 (a) displays the electrolyte conductivity (top half) and corresponding solution ASR (bottom half) which was calculated via the resistivity (ohm cm) and assuming a perpendicular distance of 0.184 cm as the average distance of ion transport through the electrode (this is an approximation and was used because it represents half the thickness of the compressed felt electrode). Alongside, Figure 6.12 (b) shows the HFR and the resulting membrane resistance as a function of SOC. It is important to emphasise here that measurements were taken from the tank (i.e. the inlet and not the outlet, as in the case of the in-operando measurements) – this has led to a the existence non-negligible hysteresis. (For instance, the trough feature HFR observed early in the discharge is more broadly observed in the conductivity measurements on a delay.)

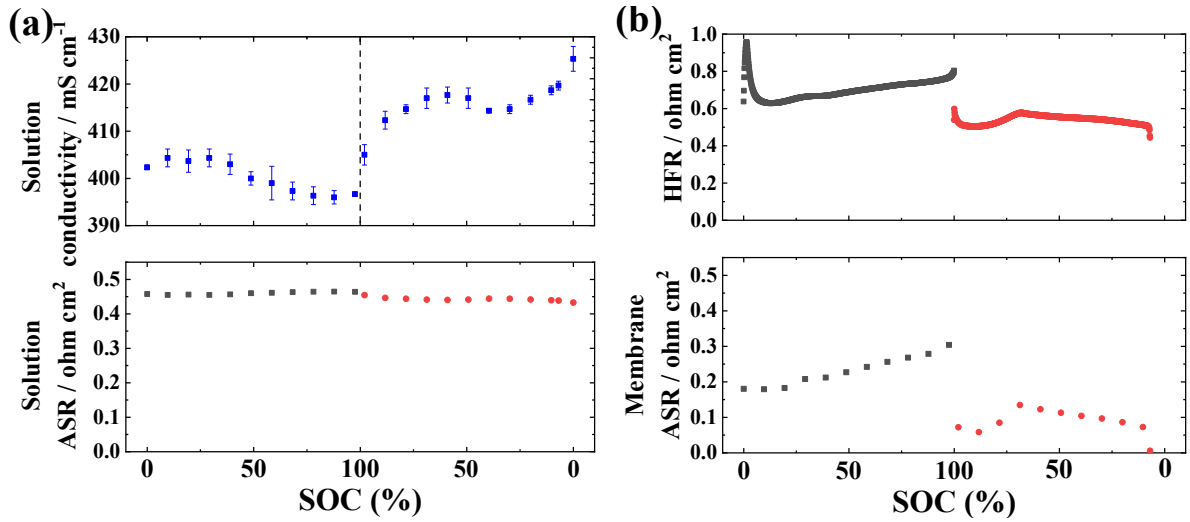


Figure 6.12: (a) Conductivity readings and corresponding solution resistances. Conductivity measurements were taken in triplicate during a 75 mA cm^{-2} simple charge / discharge cycle of 100 mL electrolyte. (b) The top set of curves display the HFR measurement during this standard cycle and below is the calculated membrane resistance.

First, it is important to notice that over the course of these measurements the solution resistance varies by approximately 7 % whereas the HFR varies by around 40 %. This suggests that most of the change in HFR is as a result of changes in membrane conductivity. Rough, back-calculations of membrane conductivity can be made from the calculation of membrane ASR assuming a membrane thickness of 40.6 µm (50.8 µm compressed by 20 %). Area resistances ranging between 0.1 – 0.3 ohm cm^2 correspond to membrane conductivities of 40.6 – 135 mS cm^{-1}. This corresponds to similar systems that measure the conductivity in alternative ways (including EIS).[72–74] Frustratingly, as mentioned in the Methodology, the pH could not be measured because there are no lab-scale pH sensors that can measure such high proton concentrations. However, during charge, it is known that HER occurs on the gas side of the hRFB meaning that H^+ ions travel across the membrane to the gas side leaving the liquid side, in theory, at a higher pH and lower conductivity – in the pH ranges used in this system (where $[H_2SO_4] < 4$ M) a lower concentration of protons does induce a lower conductivity.[75] Figure 6.12 (a) does display this trend with a diminishing conductivity as the system is charged and vice versa during discharge, however, the change (in both cases) is very small with a maximum variation of only c.a. 15 mS cm^{-1} (the difference in conductivity between a solution of 3 M and 2 M H_2SO_4 solution is c.a. 130 mS cm^{-1}).[75] In the introduction, it was highlighted that Ti^{4+} solutions self-buffer,[52] and it is also known that Mn^{3+} is an acid (Equation (6.6)). The large peak in the HFR at the very beginning of the charge could be explained by an initial step where a catalytic coating develops on the surface of the fibres resulting in an augmented 'active site'-'solution' contact. The other clear feature is the drop in resistivity at the beginning of the

discharge (clearly connected to the previously seen step potential measurement (i.e. higher overpotential required). Ultimately, these data show that, either, there is combination of solid-phase and solution-phase factors leading to the initially higher VEs during the discharge, or, given we do not have proof of solid deposition on the electrode fibres, that these effects are purely as a result of solution-phase phenomena.

Finally, the discontinuity in the conductivity is interesting as it would be expected that once the discharge ends and the SOC returns to zero (as it is at the beginning of the charge), the conductivity would be the same as the solution competition should be the same. These measurements were repeated and the same trends were observed and it is unknown why this general increase in conductivity occurs but could indicate some level of electrolyte aging.

6.3.2 Voltage efficiency as a function of state of charge

Greater overpotentials are required to satisfy a more demanding (larger) current densities – as expected, this is observed in the cycles shown in Figure 6.11 (a) and (b). As mentioned previously, this greater overpotential induces lower voltage efficiencies (VEs) in each cycle. Figure 6.13 (a) shows the charge (solid black line) and discharge (dashed black line) potential profiles for a 75 mA cm^{-2} cycle. The voltage efficiency can be deduced by dividing the discharge potential by the charging potential at corresponding SOCs. The SOC is calculated based on the amount of charge passed into (or out of) the solution during charge or discharge. The red solid line in between the curves in Figure 6.13 (a) indicates the VE for the cycle (black lines) as a function of SOC. In this system, the instantaneous VE increases with SOC – this is unlike other systems, such as VRFBs and H_2/Br devices,[76,77] where the VE remains flat (or with a consistent shallow gradient) throughout the cycle. An unstable VE during a simple cycle could be indicative of a number of things including: unaccounted for processes occurring in the cell resulting in progressively greater overpotentials needed to carry out the galvanostatic process, or; a change in solution equilibria, or; a change in environment at the electrode. The sudden decrease in VE at either end of the charge or discharge is normal and is explained by the mass-transport effects that ultimately lead to the cell 'cut-off' being reached at the end of a charge or discharge cycle (due to low concentration of active species being able to get to the electrode surface).

To clarify, the cycling data presented so far have only shown cycles where, once the cut-off potential is reached, the discharge step (almost) immediately begins (this will become

important imminently). The VEs for each of the simple charge / discharge cycles shown in Figure 6.11 are presented (solid lines) in Figure 6.13 (b). For completeness, referring back to the opening statement in this sub-section, the VE is lower for successively greater current densities because the overpotential required to fulfil these current densities is greater – this feature is commonly observed in RFBs.[76] It is surprising, however, that we see a large (c.a. 2.5 %), quite consistent reduction or 'step' in VE for these cycles at around 50 – 80 % SOC and it is interesting that these steps begin at lower SOCs as the current density increases.

To investigate this step in the VE, and bearing in mind that it is known that Mn^{3+} chemically disproportionates, the cells were cycled to 100 % SOC at their various current densities and, with the electrolyte still circulating through the cell, the cell was left to rest while potential transients were measured (Figure 6.13 (c)) and are briefly evaluated now. Over 'short time' an initial c.a. 20 mV drop over the first minute is followed by a plateau. The width of the plateau was dependent on the current density with which the cell was cycled. This was followed by a further 20 – 40 mV drop over the three hours the transient was measured. The length of time the potential plateaus for and speed at which the OCV drops appears to be dependent on the charging rate – with a faster charging rate the potential plateau lasts longer and the decay in potential is slower. The point at which the system begins to plateau during this potential transient (after initial drop) could be related to the relative concentrations of Mn^{2+} and Mn^{3+} in solution.

Following these transients, galvanostatic discharge was carried out and the VEs were, again, calculated. These are shown as the dashed lined in Figure 6.13 (b). Clearly, the step in the VE (observed with 'No pause' at maximum SOC) essentially disappears after this three hour pause (during transient measurement) at maximum SOC. This indicates that something has changed during this transient perhaps related to one (or more) of the three features mentioned earlier: (1) unaccounted for processes occurring in the cell, or; (2) a change in solution equilibria, or; (3) a change in environment at the electrode.

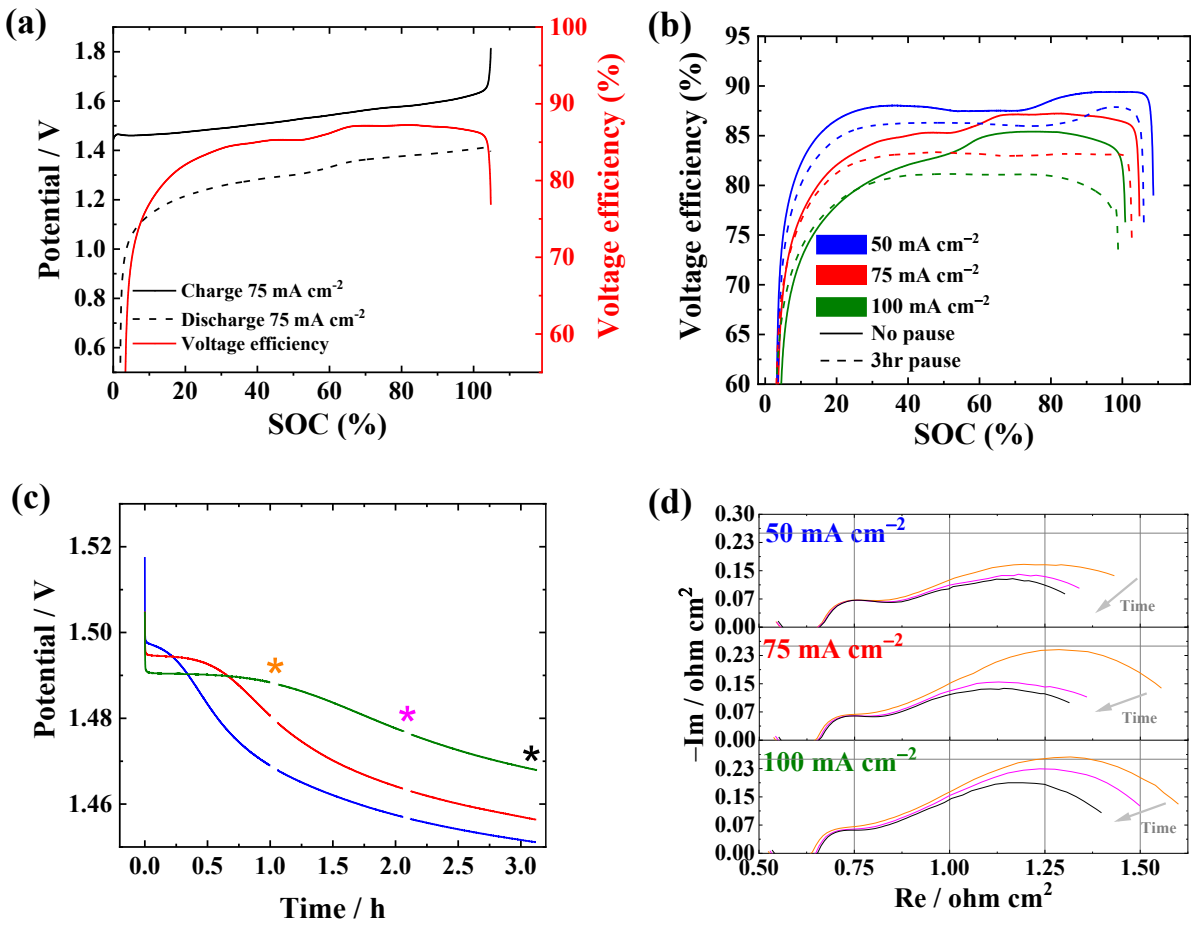


Figure 6.13: (a) Potential responses as a function of SOC alongside voltage efficiency. (b) Voltage efficiencies as a function of SOC for each current denisity without (solid lines) or with (dashed lines) three hour transient between charge and discharge arms. (c) Potential transients after charges to cut off at different current denisties. (d) Nyquist plots measured during potential transient after each charge at different current densities. Colours of Nyquist plots are associated with corresponding coloured asterisks in (c).

The Nyquist plots presented in Figure 6.13 (d) indicate the progressive resistive contributions in the cell during the previously mentioned potential transients (indicated by the three asterisks in Figure 6.13 (c)). They show that, generally, the resistive mass transport component for the process happening in the cell during the transient decreases with time. Additionally, comparing the potential change across all the transients with the overall low frequency readings across all the EIS measurements, the largest single decrease in potential (shown between the first and second EIS measurements after the charge at 75 mA cm^{-2}) is accompanied by the largest difference in low frequency measurements – this indicates that the potential may be linked to certain aspects that contribute to the mass transport resistances.

To further inspect the step in the VE, iterative charging, at c.a. 5 % SOC at a time, was carried out to inspect if the max SOC reached made a difference to the VE. The potential profiles as a function of SOC are outlined in Figure 6.14 (a).

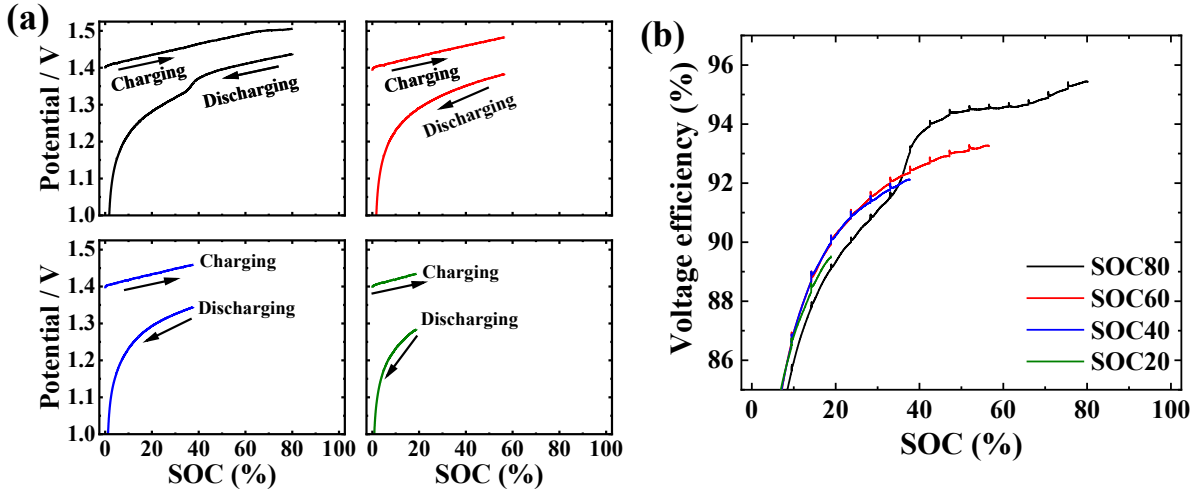


Figure 6.14: (a) Potential profiles as a function of state of charge illustrating iterative charging to 20, 40, 60 and 80 % state of charge. (b) summary of the voltage efficiencies (as a function of state of charge) for each of the iterative cycles outlined in (a). These cycles were carried out at 75 mA cm^{-2} using a Mn/H$_2$ hRFB using 200 mL of room temperature electrolyte at a rate of 50 mL min^{-1}.

The VEs for each of these partial charges are displayed in Figure 6.14 (b). They show that, as the cell passes between SOC 60 and SOC 80, something occurs in the bulk electrolyte or at the electrolyte-electrode interface that aids the reduction process (reducing the reduction overpotential) occurring in the liquid-electrolyte side (making the VEs appreciably more positive). This infers, almost, that there are two 'modes' through which the reduction occurs. Further experiments may consist of inspecting this region (SOC 60 – 80) with more granular iterations in SOC (e.g. 5 or 10 % at a time).

Following these last two sub-sections, some unanswered questions remain about how the cell operates, such as: what causes the step in the discharge resulting in a step in the VE? What is the reason for the different shapes in potential transient profile depending on the rate of the previous charge? What happens in the system, after charging past 60 % SOC, that makes the VE increase? These questions are addressed in more detail in the discussion section. The following sub-section explores the fact that SOCs of over 100 % can be reached.

6.3.3 Overcharge of the hybrid redox flow battery

This sub-section addresses the ability with this system to overcharge the hRFB. It has been established that more Mn^{2+} (i.e. oxidisable species) is produced during cell operation, as Mn^{3+}

chemically disproportionates. And, additionally, we have observed that even at relatively high current densities (e.g. 100 mA cm^{-2}), a SOC of greater than 100 % is reached regularly (Figure 6.11 (b)). Usually for RFBs, overcharging causes problems for the overall health of the device. For instance in VRFBs issues such as, oxidised surface groups,[78] faradic imbalance,[79] gas evolution[80] and solid formation,[65,81] that arise during cell operation are suspected to cause long-term VRFB ill-health. The ability for this Mn/H_2 system to achieve overcharge and still be able to function in subsequent cycles (following a full discharge) is quite unusual. In this section, especially high SOCs can be achieved by charging very slowly – at 25 mA cm^{-2}. Finally, in a single electron scenario (as is the case for $Mn^{2+} \leftrightarrow Mn^{3+}$), reaching a SOC exceeding 100 % corresponds to the formation of higher oxidation state of Mn. Given we know this is not likely to have happened electrochemically (because of the overpotentials likely to be needed to drive the electrochemical reaction), it must have happened chemically due to conservation of charge laws.

Figure 6.15 displays the equivalent standard experiments displayed in the last few sub-section for a slow cycling (using a current density of 25 mA cm^{-2}) hRFB cell (where equivalent responses at 100 mA cm^{-2} are shown as a reference). Using this lower current density, a SOC of over 130 % could be reached (Figure 6.15 (a)). One important feature, only observed in this work when cycling at this slow rate, is the peak at c.a. 90 % SOC on the charging 'arm' – this is not commonly observed in RFB devices. A peak in a V/t profile infers a chemical change in the solution or at the surface of the electrode. An increase in potential might suggest either a decrease in the rate at which active species reach the surface which, in turn, may be as a result of solution characteristic change (increased viscosity) or a reduction in active surface area at which electrochemical processes can occur which may be as a result of less conductive solids coating the fibres within the carbon electrode. Assuming no change in current density, a potential decrease may be as a result of the opposite of these effects occurring (i.e. new / different electroactive material is able to get to the surface of the electrode or, the non-conductive coating solid is removed or dissolved back into solution). (It should also be noted that the cell and electrolyte were not elevated to higher temperatures – it is expected that overcharge would be more readily achieved at higher current densities in this case.)

There are a few curious features that appear in the HFR responses for these lower current density cycles (Figure 6.15 (b)). Firstly, during the 'charging arm', the HFR is much greater at lower SOCs than it is while charging with a greater current density. This is not in line with

previous results which usually display similar HFR at a given SOC, regardless of current density (Figure 6.11 (c)). Secondly, there is a drop in HFR at c.a. 60 % SOC implying some (nearly step) change in membrane resistance (this assumes there is no significant change in solution conductivity when cycling at 25 mA cm^{-2} – probably a fair assumption given earlier solution conductivity measurements). The HFR, during the discharge follows the usual trend seen before and its higher value, again, is tentatively attributed to a slower rate of metal ion 'flushing' while the protons travel through the membrane leading to a lower membrane conductivity (and therefore higher resistivity).

It should be noted that, in terms of the general features of these potential and HFR profiles, these experiments are broadly repeatable. However, the height, the position of peaks and the final maximum SOC reached do change slightly for each experiment – it is considered that these changes largely fall within the extremities of experimental error. Variation in lab temperature and ageing of electrode and electrolyte components may also contribute to these differences perhaps affecting the kinetics. The cause of these features are tentatively discussed later.

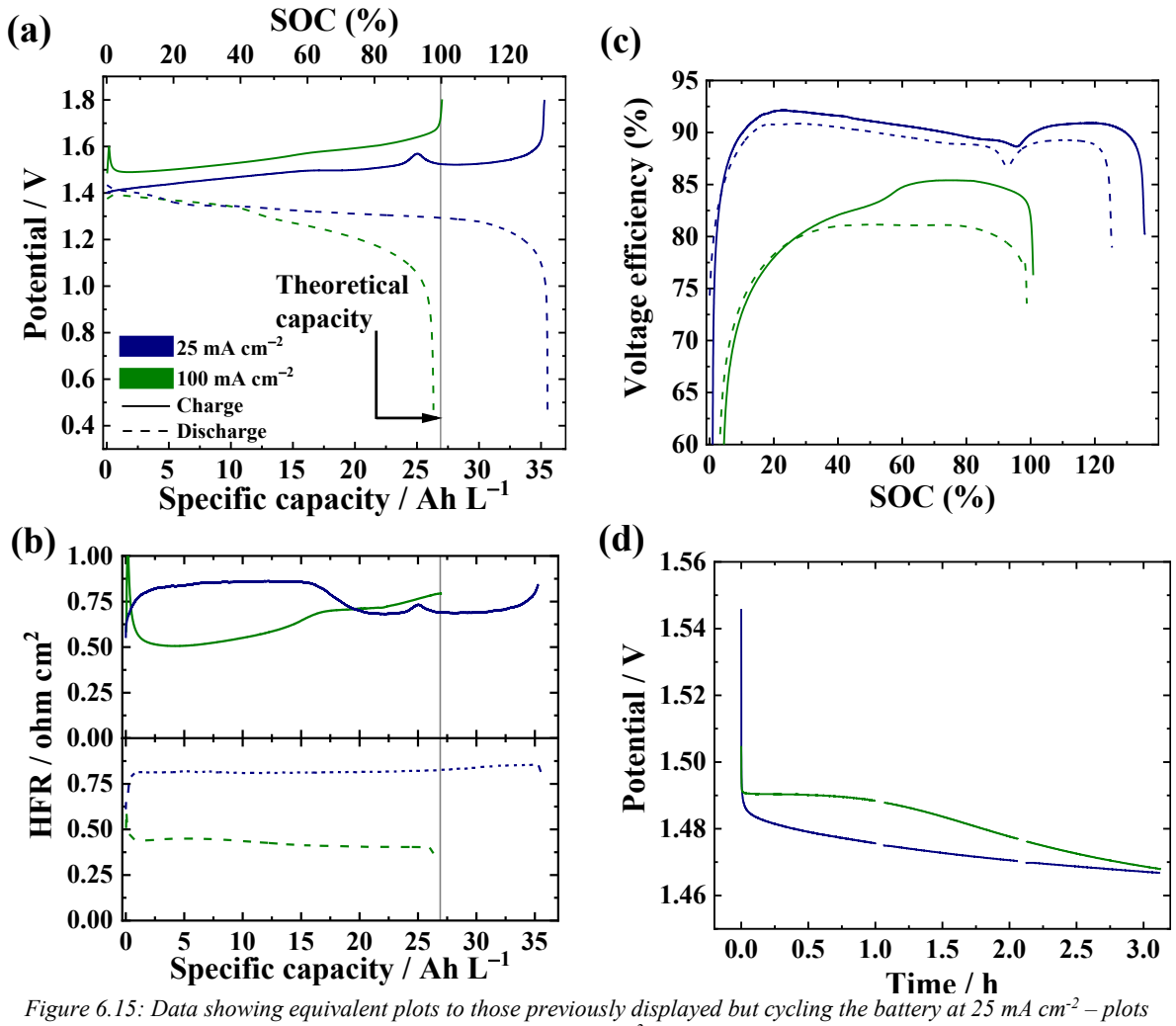


Figure 6.15: Data showing equivalent plots to those previously displayed but cycling the battery at 25 mA cm^{-2} – plots showing equivalent profiles using a current density of 100 mA cm^{-2} are shown for comparison. (a) Potential profiles using specific capacity and SOC as x-axes – including the theoretical specific capacity of the electrolyte. (b) shows the HFR responses during these charges and discharges using the same x-axes. (c) The voltage efficiencies for these cycles with (dashed line) and without (solid line) a resting period at the maximum SOC. (d) The potential transients for the cycles that incorporated a resting period at maximum SOC. These experiments were carried out using an electrolyte volume of 400 mL.

The elevated VEs for the cycles with and without the pause at maximum SOC were as expected – a lower overpotential is required to force a current of 25 mA cm^{-2} meaning that the potentials for the charge and discharge were more similar (Figure 6.15 (c)). However, one very interesting feature was that, compared to the cycles using higher current density, there was no step in the VE. This infers that whatever had happened in solution, or at the electrode that aided the beginning of the discharge (reduction) for the cycles at higher current density (with no pause at max SOC), did not occur at the beginning of the slower discharge step (with no pause at max SOC). Additionally, the potential transient after slowly charging the cell to the maximum SOC does not follow the previous trend (where a slower SOC leads to a plateau with a higher potential, Figure 6.13 (b)). Instead, this potential transient appears to immediately start decaying – the reason for this is unknown but will be considered later (Figure 6.15 (d)).

Usually, the potential of a cell is indicative of the SOC.[82] Given the potential at maximum SOC has been shown to be unstable in this device, the potential stability was explored as a function of SOC. Iterative charging was carried out at 25 mA cm^{-2} in order to inspect this. After each galvanostatic charging step, a short OCP was measured, followed by an impedance measurement, followed by another short OCP measurement (the potential readings during the impedance are not shown in the V/t profile) (Figure 6.16 (a)). Towards the beginning of the charging cycle, an equilibrium is reached quickly (indicated by a stable potential being reached soon after the charging step has finished – lower left inset in Figure 6.16 (a)) – this behaviour is usually how RFBs operate as the potential is simply determined by the relative concentrations of active species in solution. However, at around 90 % SOC, the equilibrium potential is not reached, and the potential transient shows it slowly moving to achieve its equilibrium value (upper left inset in Figure 6.16 (a)). The potential change during the course of these transients at higher SOCs show the system is no longer able to reach an equilibrium quickly after each step. The potentials measured over the course of each of these mini-transients clearly show that at a certain stage in the charging process, the time required to reach the equilibrium potential becomes significantly longer than what has been measured at lowed SOCs. A summary of the final potential measured and the (small) changes in potential over the course of the mini-transient is shown in Figure 6.16 (b) on the left and right hand axes, respectively. This qualitatively shows that, when charging at 25 mA cm^{-2}, after 90 % SOC, significant changes in the potential occur (even over the course of the mini-transient) and, after full charge, rapid arrival at the equilibrium potential does not occur until the end of the following discharge cycle.

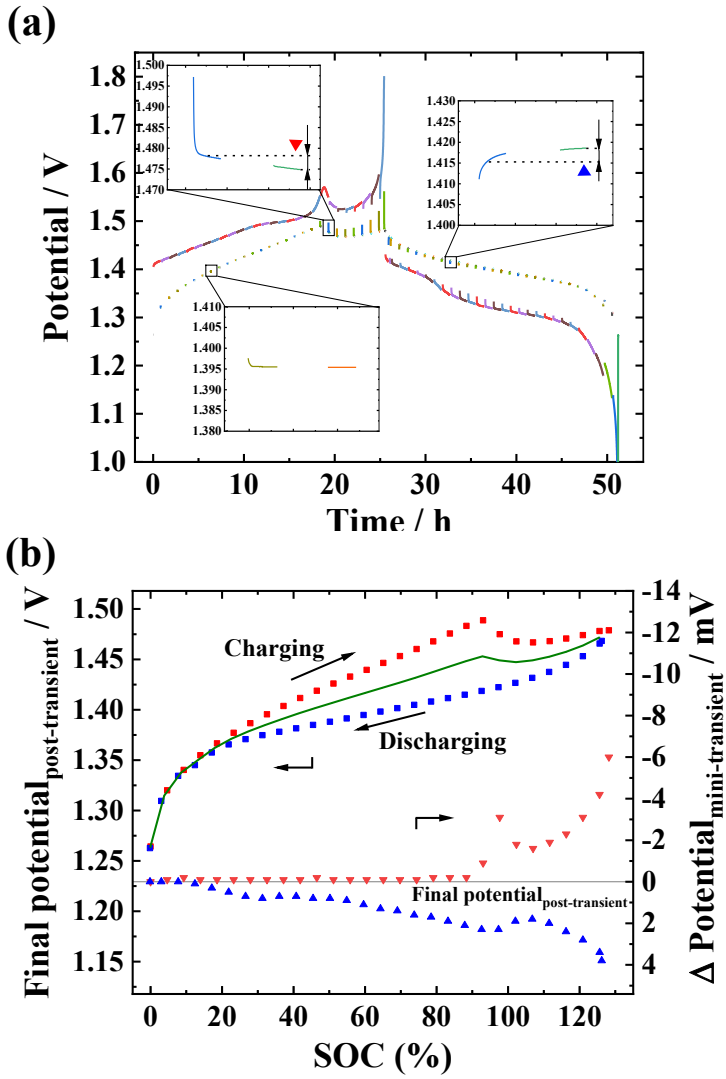


Figure 6.16: (a) V/t profile displaying iterative charging of a Mn/H_2 hRFB in approximately 5 % SOC steps. In between each step, OCP mini-transients are recorded in which the OCP is tracked over 120 seconds and an impedance is run over c.a. three minutes between each 'mini-transient'. Some selected transients are inset in the spare regions in the graph visually outlining how information is gathered from these transients for (b); (b) Final potentials after the mini transients (charging arm – red, discharging arm – blue) are recorded on the left hand axis (squares) while the change in potential in the latter part of the mini-transient is recorded on the right hand axis (triangles).

As was previously mentioned, the impedance was measured in between each of the mini-transients shown in Figure 6.16 (a). Nyquist plots of these impedance data during the charge and discharge are displayed in Figure 6.17 (a) and (b), respectively. While Nyquist plots are, qualitatively, helpful to understand the rough contributions to the cell resistance, ECMs are important tools commonly used to fit to these data in order to extract quantitative information about resistive components (indeed, an ECM was used to process the EIS data in Chapter 3). This analysis was not carried out here because of uncertainty surrounding a suitable ECM for this system, and time constraints associated with the pandemic. Therefore, this quantitative analysis is allocated to the Future work library and the following Nyquist analysis is qualitative.

It is clear from these data that the mass transport resistance is large when the cell is fully discharged – indicated by the large semi-circular components on the low-frequency side of the Nyquist plots. This mass transport component is rapidly reduced at the beginning of the charge inferring a large improvement in mass transport around the electrode. At the same time, as the cell is charged, the reduction in contribution to the charge transfer resistance (seen in the enlarged section below) infers that the electrode becomes more catalytically active towards the reaction. Overall, these reductions in resistive contributions indicate that, at the beginning of the charge, the cell is controlled by slow electrokinetics. At higher SOC, the electrokinetics speed up and the system tends towards being dominated by mass transport ultimately, in the overcharge region leading to the formation of a Warburg tail indicating the system has become more catalytically active towards the reaction occurring in the cell.[83]

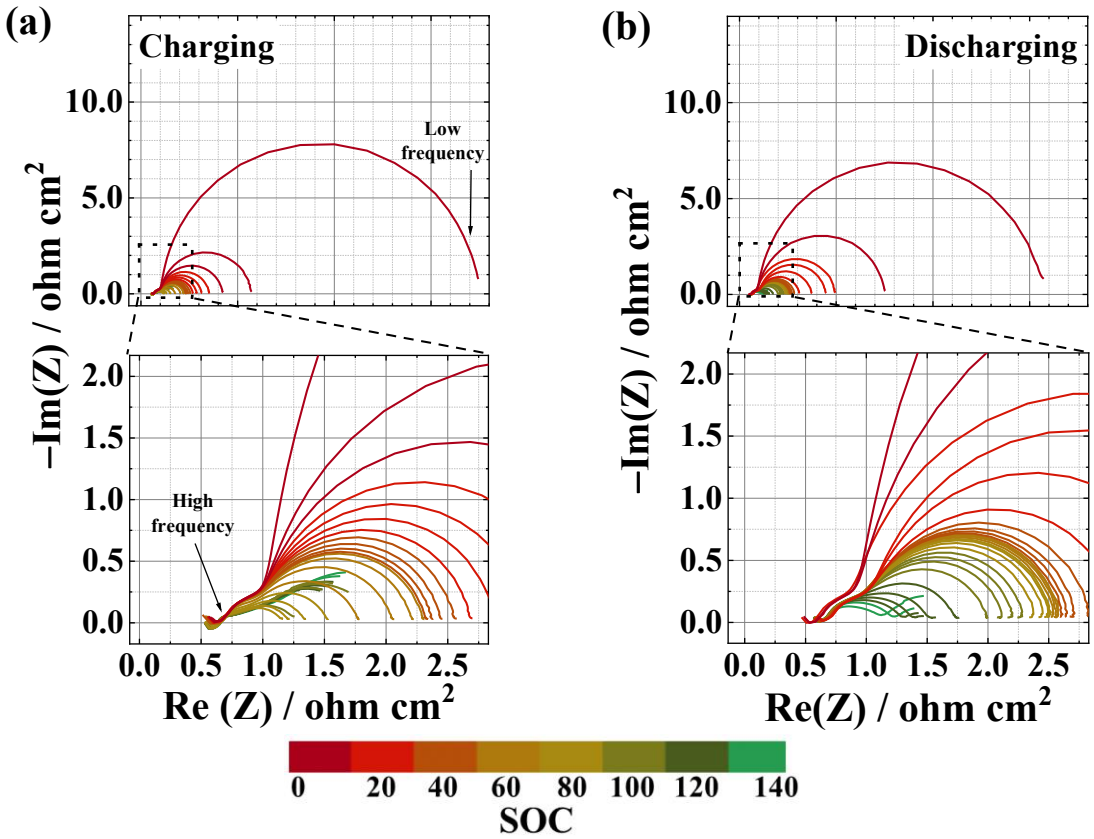


Figure 6.17: Impedance measurements in Nyquist plot form during (a) charge and (b) discharge of a cell at 25 mA cm^{-2}. Colour bar roughly indicates the SOCs.

Once the system is switched to discharge, the kinetic contribution to the resistance increases. The mass-transport contribution to the cell resistance increases too, until slowing significantly at around SOC 70 %. After this slowing, the cell appears to returns to being controlled by slow electrokinetics. Given we know that, at these high SOCs, the Mn^{3+} concentration is expected to be high whereas the main chemical process occurring is disproportionation, this falls in line

with the earlier inference that the solids produced may act as an electrocatalyst (that is, assuming there is no kinetic barrier gaseous processes that may be occurring on the other side of the cell – this is a good assumption in this environment as the hydrogen reaction is much faster).

6.3.4 Deconvolution of speciation chemistry as a function of state of charge

The experiments outlined so far have demonstrated that the potential goes some way to describing how the solution evolves as the hRFB cell is cycled. However, while global observations of the system can be made (using the cell potential), there are clearly still significant gaps in the understanding of what happens from a speciation perspective. The following section further introduces and develops two methods aiming to deconvolute this complicated speciation. Starting, logically, with the lower oxidation state species, Mn^{2+} – harnessing the fact that Mn^{2+} centres are paramagnetic with five unpaired electrons – in-operando EPR is used here to track the this species' concentration. On charging, Mn^{3+} is produced – this work uses the strong adsorption coefficient associated with Mn^{3+} alongside UV-vis spectroscopy to track this species' concentration in the subsequent sub-section. The next sub-sections walk through these analytical techniques that attempt to measure concentrations of active species in this electrolyte in real time and the results they show.

6.3.4.1 In-operando EPR measurements

EPR is used in this work to selectively measure the concentration of Mn^{2+} – this is possible as a result of this species' paramagnetic nature. No other species are considered to interfere with these signals and therefore this is considered to be a good measurement by which to track the concentration of Mn^{2+}. There are two main methods by which EPR signals are processed to assert quantitative values (i.e. numbers of spins and, following this, concentration). The first method, and more common, is via double integral – as the name suggests, this is achieved by integrating the EPR response twice. The other method is via line width which is determined by electron spin relaxation. Line broadening is associated with interference from neighbouring spin-active centres and is often observed in viscous and / or highly concentrated samples.[84] The reason line width is used throughout this work is because the concentrations used are high, and with the in-operando setup used it is considered to return more accurate measurements of the concentration of Mn^{2+}.

Figure 6.18 (a) shows a simple Mn^{2+} EPR signal at relatively low concentration (c.a. 0.25 mol dm^{-3}). As discussed in Chapter 2, this TM centre has a spin nucleus of I = 5/2; and so, according to the general rule for hyperfine splitting (as a result of loss in degeneracy due to interactions with neighbouring nuclei) the number of hyperfine lines observed is six (2nI + 1, where n is the symmetry number (½)). Figure 6.18 (b) shows the EPR signals of the detectable manganese centres as the cell is charged and discharged. While the experimental setup ensured a low volume of electrolyte in the resonator at any given point, clearly this does not affect the concentration and at zero SOC, the concentration of Mn^{2+} is as high as 1.0 mol dm^{-3} – this results in line broadening due to unwanted interaction between neighbouring Mn^{2+} centres.[84] As the concentration of Mn^{2+} decreases, during charging, the lines become less intense and much more sharp and defined. The linewidth was then calculated by Dr Collauto and from each of these signals the concentration of Mn^{2+} was calculated using the calibration curve shown in Figure 6.18 (c).

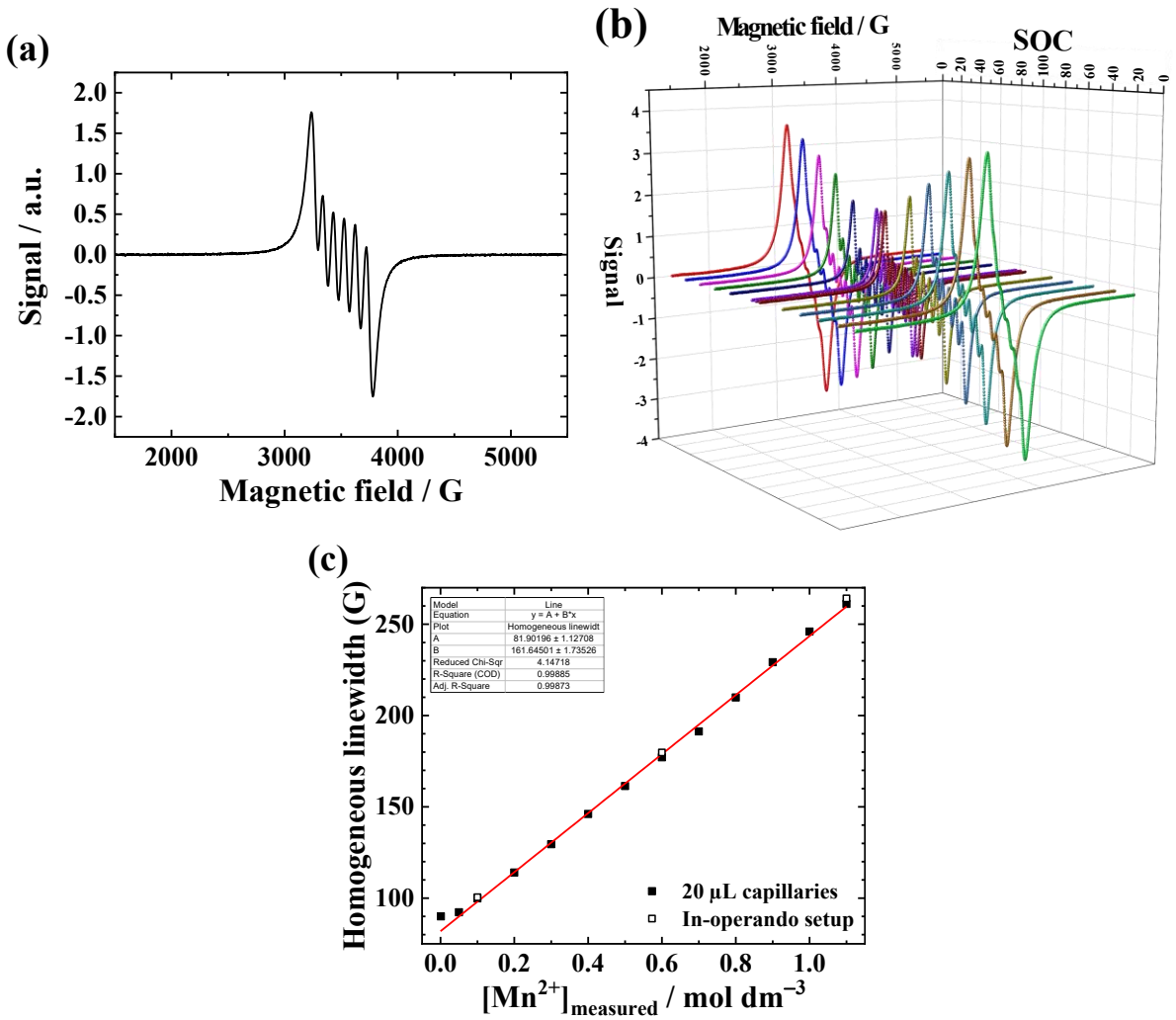


Figure 6.18: (a) An example of a first derivative EPR response to a sample containing Mn^{2+} with a concentration of c.a. 0.25 mol dm^{-3} measured in a capilliary tube. (b) A 3D stack of first derivative responses from the EPR resonator displaying how the signal changes as an hRFB cell is charged and discharged. (c) Calibration curve showing [Mn^{2+}] measured

individually and in the in-operando fashion – this was carried out to ensure [Mn^{2+}] can be deduced in further in-operando experiments.

Figure 6.18 (c) shows EPR responses measured using the line width from volumetrically prepared (individual) samples 'ex-situ' (filled black squares, Figure 6.18 (c)) and with the in-operando setup as described in the methodology across the measurement range (and beyond – up to 1.1 M Mn^{2+}). This confirms the in-operando step returns reliable results.

Figure 6.19 (a) shows a simple charge / discharge cycle at 75 mA cm^{-2} with its accompanying Mn^{2+} concentration profile (black dashed line). The SOC on the right-hand axis (red line) indicates the SOC according to the coulomb count (red solid line). The Mn^{2+} concentration never reaches zero because, as asserted earlier, it is expected from the chemistry that Mn^{3+} disproportionates to form additional Mn^{2+} (and "MnO_2" – in quotation marks as the exact form / phase of the solid species is unknown), simultaneously during electrochemical oxidation of Mn^{2+} (charging).[22] The overlayed solid luminescent green line extrapolated from the early part of the charging cycle indicates hypothetically how the concentration of Mn^{2+} would change assuming the production of no additional Mn^{2+} (i.e. no disproportionation – in an ideal case). Taken to the extreme, assuming theoretically, full disproportionation of Mn^{3+}, two moles of electrons are required for every mole of Mn^{2+}. While these two SOC measurements individually, are poor representations of the SOC, together, the Mn^{2+} concentration and the number of coulombs spent on charging / discharging the cell provide enough information to reveal interesting assertions about the hypothetical concentrations of Mn^{3+} and Mn^{4+} species using the average oxidation state – as discussed elsewhere.[79]

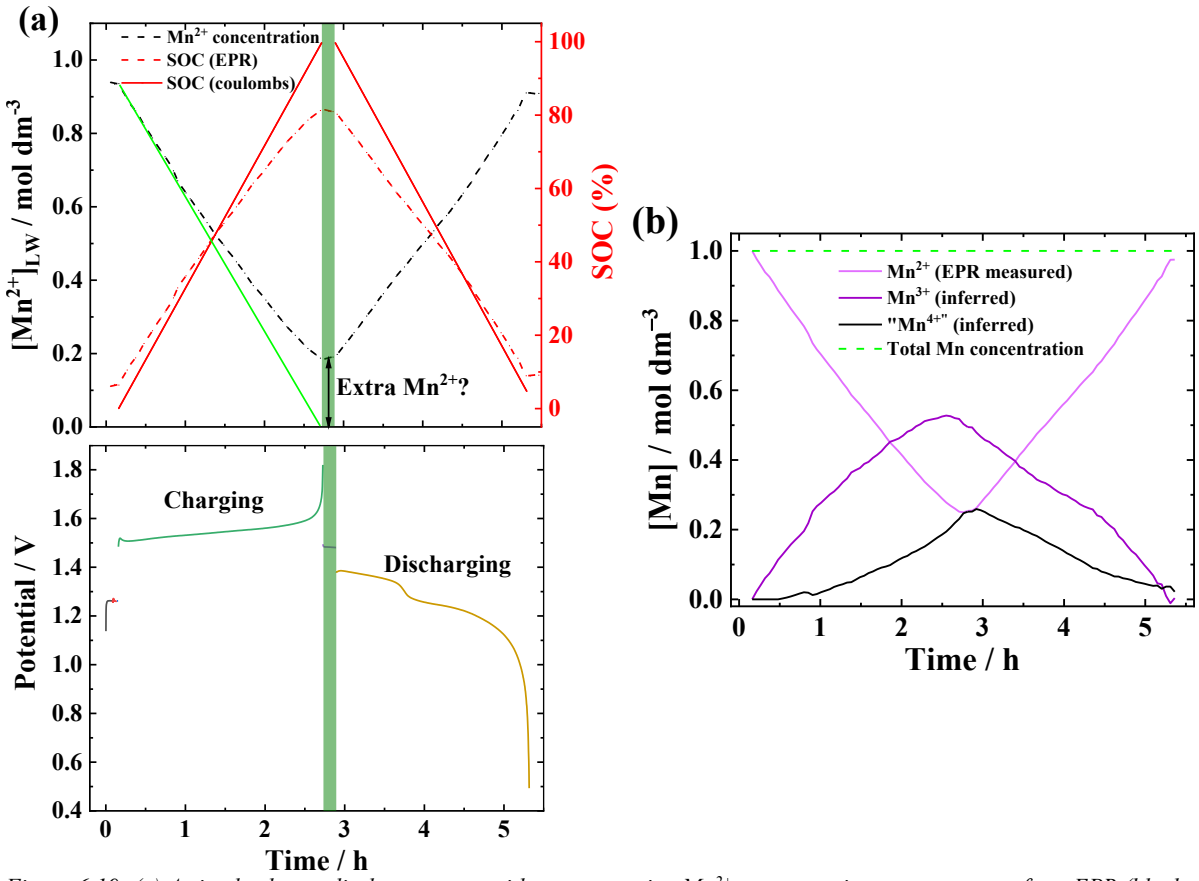


Figure 6.19: (a) A simple charge discharge curve with accompanying Mn^{2+} concentration measurements from EPR (black dashed line) with SOC values calculated using coulomb counting (red solid line). The green bar indicates a short OCP tracking pause at max SOC. The solid fluorescent green line overlay is an extrapolation of the Mn^{2+} concentration from the beginning of the cycle. (b) The measured Mn^{2+} concentration and the resulting calculated concentrations of Mn^{3+} and Mn^{4+} species using the methods outlined in the main text. These measurements were taken using a hRFB Mn/H_2 cell cycled at 75 mA cm^{-2} with 180 mL electrolyte.

Figure 6.19 (b) uses the measured concentration of Mn^{2+} combined with the number of coulombs passed into the electrolyte to calculate the theoretical concentration of Mn^{3+} and Mn^{4+} species. This technique is used when assessing the faradic imbalance in other RFB systems.[79] Only two assumptions are used to carry out these calculations:

- First, the concentration of manganese in any form is 1.0 mol dm^{-3} and there is no additional Mn species (an initial correction to the Mn^{2+} concentration was made to ensure this at the beginning of the cycle – SOC zero); and,
- Second, all electrons are used in single electron processes to convert Mn^{2+} species to Mn^{3+} during charging, or vice versa during discharge – i.e. there are no parasitic reactions which consume change such as oxygen evolution or carbon corrosion.

The latter constraint is reasonable as the cell has been shown to have very good coulombic efficiency over charge / discharge cycles suggesting that there are no parasitic processes occurring. The Mn^{2+} concentration is known throughout the charge and discharge from the EPR measurement. At each measurement of $[Mn^{2+}]$, the total charge, Q, passed into the electrolyte is known simply by integrating the current (I, A) with respect to the time elapsed since the start of the galvanostatic hold.

$$Q = \int_0^t I \, dt \tag{6.46}$$

We define the SOC as the total number of coulombs of electrons removed from the electrolyte compared to the total charge necessary to oxidise all the Mn^{2+} to Mn^{3+} – i.e. a one electron reaction, where F is Faraday's constant (C / mol) and V is the volume of electrolyte (dm^3) and c is the concentration of manganese in the electrolyte.

$$SOC = \frac{Q}{FcV} \tag{6.47}$$

This charge can then be used to calculate the average manganese oxidation state – $Ox_{Avg.\ Mn}$ – of the electrolyte based on the number of electrons used to oxidise Mn^{2+} to Mn^{3+} (Equation (6.48)). The average oxidation state of the manganese is then a function of the SOC, being 2 when the system is fully discharged and 3 when it is fully charged.

$$Ox_{Avg.Mn} = Ox_{Mn^{2+}} + SOC \tag{6.48}$$

We can determine the average oxidation state of the oxidised manganese (i.e. non-Mn^{2+}) using the known SOC of the system (calculated from the number of coulombs consumed) and the measured Mn^{2+} concentration from the EPR measurements

$$Ox_{non-Mn^{2+}} = \frac{SOC}{c - [Mn^{2+}]} + Ox_{Mn^{2+}} \tag{6.49}$$

Where $[Mn^{2+}]$ is the detected amount of Mn^{2+} in solution and $Ox_{non\text{-}Mn^{2+}}$ is expected to be range between 3 and 4 if we assume the only available oxidation states for the oxidised Mn are (3+) and (4+). Hence, we can calculate the relative amount of Mn^{3+} and Mn^{4+} via a linear combination of the concentrations of each of those species (Equations (6.50) and (6.51)):

$$[Mn^{4+}] = (Ox_{non-Mn^{2+}} - 3)(c - [Mn^{2+}]) \quad (6.50)$$

$$[Mn^{3+}] = (4 - Ox_{non-Mn^{2+}})(c - [Mn^{2+}]) \quad (6.51)$$

Figure 6.19 (b) shows the result of these calculations for the cycle shown in (a). In-operando EPR experiments were carried out during cycling at three different current densities (25, 75 and 150 mA cm^{-2}). The above calculations were carried out for these cycles and yielded the Mn concentration profiles displayed in Figure 6.20.

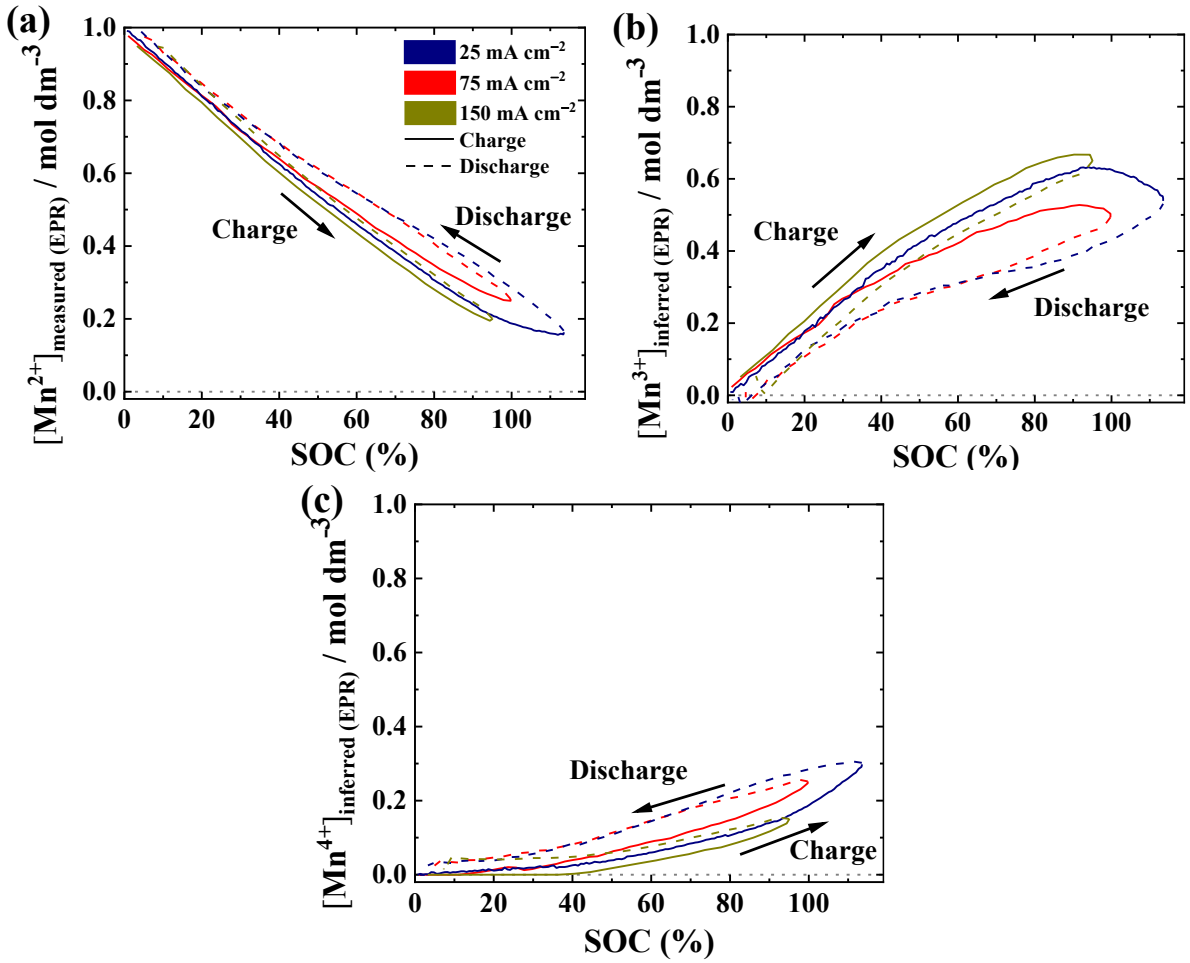


Figure 6.20: (a) Mn^{2+} (measured)-, (b) Mn^{3+}- and, (c) Mn^{4+}-concentration profiles as a function of state of charge while cycling at different current densities. The volume of the electrolyte used in these systems was 180 mL and the state of charge was calculated according to the number of coulombs passed into solution.

This figure highlights a number of interesting features that appear to occur during the cycle. All of these profiles (the measured Mn^{2+} and the estimated Mn^{3+}/Mn^{4+}) display a certain degree of hysteresis. Some hysteresis might be expected because of the length of time it takes the electrolyte to fully mix and the fact that the manganese concentrations at the outlet of the cell will be different to those in the tank. The magnitude of hysteresis in the Mn^{3+} profiles is equal to the sum of the hysteresis magnitudes for Mn^{2+} and Mn^{4+}. This is what we expect if we assume disproportionation to occur in solution (indeed, this is how the calculations were carried out) – and, clearly, the Mn^{2+} and Mn^{4+} concentrations are greater during the discharge as a result of this disproportionation. Interestingly, the (measured) Mn^{2+} concentration profiles using different current densities are quite similar. The level of hysteresis varies with current density where the lower current density (25 mA cm^{-2}) displays the greatest hysteresis – this is as expected as if the current density is lower, the charging is slower, allowing more time for the Mn^{3+} species to disproportionate (thereby producing more Mn^{2+}). The calculated Mn^{4+} profiles provide interesting operational insight. If we assume Mn^{4+} to immediately oxidise to MnO_2, Figure 6.20 (c) infers that with a higher current density MnO_2 does not form until an SOC of c.a. 40 %. This may be interesting to commercial operators as, while disproportionation might be a chemical problem, if using higher current densities leads to reduced formation of solids then operators may choose to maximise the current density at which they operate their devices and not charge to high SOCs. An additional profile of the manganese concentrations during a slow cycle (at 25 mA cm^{-2}) to the maximum SOC is displayed in the appendix (Figure A6.36).

Clearly, these measurements are theoretical but are in line with the assertion that solid species are formed as the charge is carried out. It is important, now to experimentally validate these calculations by measuring the concentration of Mn^{3+} via UV-vis.

6.3.4.2 In-operando UV-vis measurements

The theory outlining how UV-vis spectroscopy is carried out is largely outlined in Chapter 2, however the essential theory is re-stated here with some additional comments for the readers convenience. The measurement of absorbance is achieved by directing electromagnetic radiation of a known wavelength through a sample, with a known concentration and path length, and measuring the intensity of the transmitted radiation. Sometimes, the intensity of the radiation is too low for there to be any significant transmitted radiation intensity – this is known as saturation and is accompanied by immeasurably high absorbances. The Beer Lambert law

states that multiplying the concentration, c (mol dm^{-3} or 'M'), path length, l (cm^{-1}) and (species-, electrolyte- and wavelength / transition-specific) absorption coefficient, ε (M^{-1} cm^{-1}), returns an absorption (a.u.) at a given wavelength. Manganese ions have several oxidation states each of which have specific absorption coefficients. Literature values for the absorption coefficient for Mn^{3+} at its commonly considered characteristic absorption (corresponding to a wavelength of 522 nm) vary but are reported to be around 250 M^{-1} cm^{-1} (they vary because of differing experimental measurement conditions and therefore transition energies and also there are multiple species with close absorbances).[9,60,61] This is very high compared to its reduced counterpart, Mn^{2+}, which has an absorption coefficient of 0.701×10^{-3} M^{-1} cm^{-1}.[59] Given this characteristic wavelength of c.a. 522 nm lies firmly in the visible region (c.a. 380 – 700 nm) this means that, optically, a 1 M vial of Mn^{2+} and Mn^{3+} would be pale pink (see Figure 6.9 as a rough example) and black (/ very dark purple), respectively. Clearly, this means that characteristic absorbances measuring a sample of Mn^{3+} would be too high for the spectrophotometer to reliably detect, which presents a problem when measuring UV-vis responses. This difference in absorption coefficient is useful, but if it is to be harnessed, the absorbance needs to be reduced. Given the absorption coefficient is fixed and, as previously discussed, the solution concentration cannot be changed, the path length needs to be reduced. As mentioned in this chapter's methodology, a thin flow cell was used to reduce the sample path length (100 μm pathlength) allowing the measurement of reasonable absorbances at higher concentrations of Mn^{3+}. This in-operando arrangement allows the user either to continuously measure the absorbance of Mn^{3+} (and therefore concentration) at one characteristic wavelength, or to take a full spectrum while electrolyte flows through it during cell operation. The full spectrum measurement settings for the experiments reported in this chapter, were stated in the methodology. It is worth mentioning, though, that it took just over five minutes to record each of the spectra. At the flow rate used (to divert the outlet electrolyte to the flow cell in the UV-vis, 10 mL min^{-1}), c.a. 50 mL of electrolyte passed through the flow cell and – this systematic error was discussed in the methodology and does not need to be considered further as, with the volumes of electrolyte used, over the course of a five minute period, the SOC was not expected to change significantly.

The first thing to briefly mention is the baseline measurements shown in Figure 6.21 – these scans were measured to a lower wavelength (250 nm) to ensure no further features could be deciphered. While 3 M H_2SO_4 is certainly considered to be the correct baseline, manganese-

free electrolyte, (i.e. the 'stock' solution) containing just the acid (5 M) and dissolved titanium oxysulfate (1 M), was also measured and showed a large signal at the low wavelength periphery (herein referred to as the 'low wavelength band') – this corresponds to a high energy orbital transition. This low wavelength band must therefore be as a result of a transition involving a titanium energy level – potentially from an oxygen 2p orbital to a titanium 3d (t_{2g}).[85] Literature discussing the Ti^{4+} species in solution is sparse as a result of the difficulty dissolving Ti^{4+} species without polymer formation.[86–88]

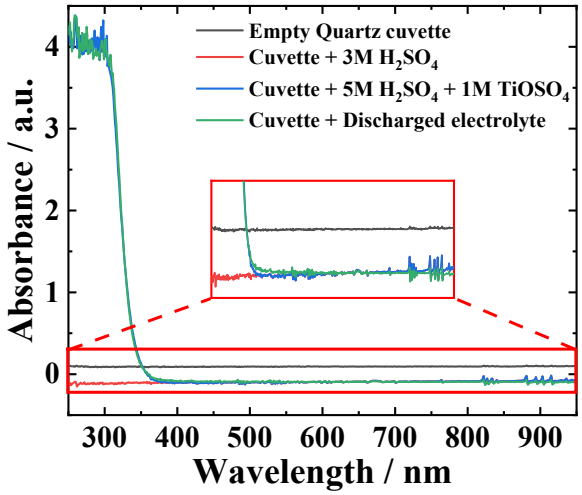


Figure 6.21: UV-vis baseline testing. H2SO4, stock acidified titanium oxysulfate solution and discharged electrolyte (containing Mn species).

On addition of the manganese carbonate (resulting in a Mn^{2+}-containing solution – 1 M), this discharged electrolyte was measured and was shown to have a nearly identical UV-vis response. A small deviation in the low wavelength band is observed – while this may be an experimental artefact it is worth mentioning a Mn^{3+} absorption (likely associated with the $^1t_{1u} \rightarrow {}^2e_g$ transition) between 210 – 220 nm with a very high absorption coefficient of c.a. 4000 M^{-1} cm^{-1}.[22,89] Clearly, in this fully discharged electrolyte the vast majority of manganese species are largely expected to be found in the 2+ oxidation state, however there may be trace oxidised Mn^{3+} species resulting in a large low wavelength (very high energy) absorption. This low wavelength band is the subject of discussion later.

Figure 6.22 shows a potential profile with its accompanying UV-vis spectra. The grey area indicates the first charging phase (at 75 mA cm^{-2}) to 73 % SOC (it will become clear later why the cell is not cycled to higher SOCs). During the charging period, a peak starts to form at around 522 nm and the low wavelength band starts to grow and / or shift (to the right) in the high wavelength direction. While the exact cause of the band is unknown and was discussed

earlier (combination of, (a) a low wavelength Mn^{3+} transition with very high absorption coefficient and, (b) Ti^{4+} species transitions), it is asserted that an element of Raleigh scattering is present as a result of the formation of small particles, observable in the stream of electrolyte at the outlet of the cell (on attempting to extract this Rayleigh-type, λ^{-4}, scattering effect however, it was shown to provide an imperfect representation).[90] Later time-dependant transient experiments show that this assertion – that solid (colloid) precipitation results in this low wavelength band at higher SOCs overwhelming the spectrum – has solid grounding.

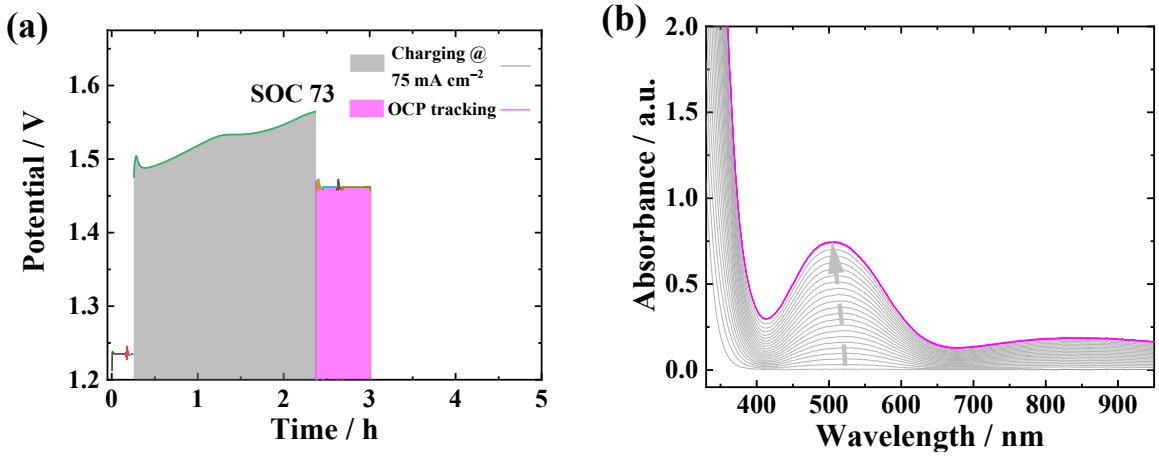


Figure 6.22: (a) Simple potential profile during charging step with OCP transient. (b) UV-vis absorption spectra during charging regime and OCP transient.

Additionally, another, much broader peak develops at high wavelength (low energy) – c.a. 840 nm – this peak is not commonly reported in literature (as usually UV-vis spectra are not measured at such high wavelengths) but is considered to be as a result of $^5B_{1g} \rightarrow {}^5A_{1g}$ transition.[22,62] There follows a c.a. 45 minute OCP tracking / transient time where spectra continue to be taken which the Mn^{3+} concentration is stationary, demonstrated by the effectively identical absorbance spectra (eight almost identical pink spectra, Figure 6.22 (b)).

Figure 6.23 (a) shows the absorbances during the steady charging step outlined in the previous figure. Red and green lines are overlayed over these spectra indicating the absorbances at the low and high wavelength signals, respectively. The dotted lines on each signal indicate the peak absorbances and the solid lines indicate the wavelengths deemed 'central' to the energy transition. The major peak (starting at 522 nm) is shown to appear to drift to lower wavelength with charging. It is asserted that this is due to the interference of the low wavelength band shifting / growing to higher wavelengths. The broader, higher wavelength signal at 840 nm appears to have a more linear trajectory as the electrolyte is charged. As the dotted green line shows, there are occasional fluctuations in peak position and, despite smoothing the data (using

Fast Fourier Transform and Savitzky-Golay smoothing corrections) this could not be corrected for. This is likely due to the insufficient sensitivity of the graphing tools used in this work, despite, the true peak in this broad UV-vis response cannot be identified but lies closer to 845 nm in the 827 – 845 nm window highlighted by the green line overlaying the spectra.

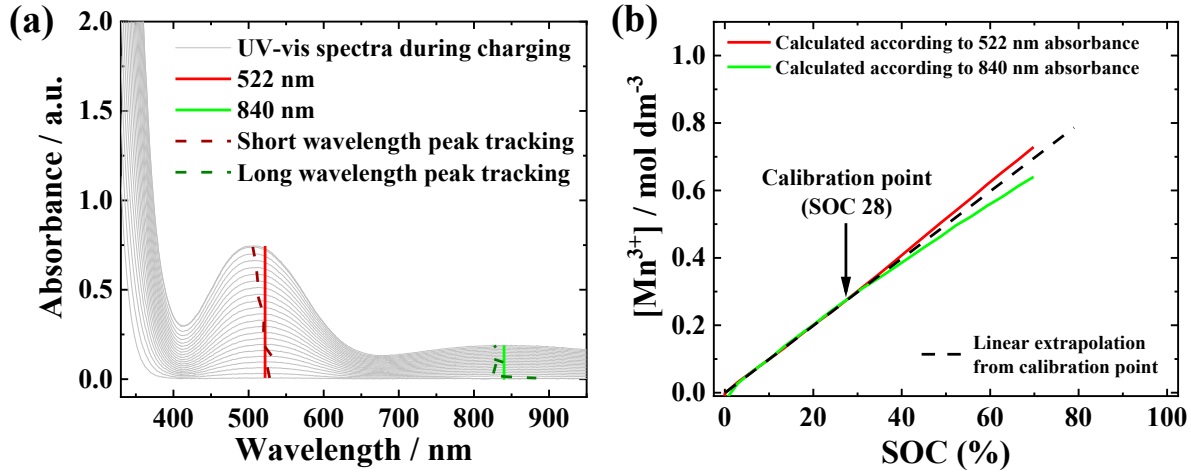


Figure 6.23: (a) UV-vis spectra with overlayed peak tracking (solid lines) compared with single wavelengths (dotted lines) and (b) back-calculated calibration curves for Mn^{3+} concentration as a function of state of charge. A calibration point was used as this is the highest state of charge where neither signal is significantly affected by the low wavelength band.

The absorbances correspond to a concentration which, in turn, is plotted as a function of SOC. Given the absorbance increases fairly linearly until c.a. 30 % SOC, this is taken to be the 'calibration point', up to which absorbances correspond linearly with SOC (it was judged that there was no considerable interference from the low wavelength band until this point). After this point, the calculated Mn^{3+} concentrations as a function of absorbance according to the low wavelength band (red solid line) diverges from the Mn^{3+} concentration calculated from the higher wavelength peak (green solid line). The (essentially, calibration) curve associated with the peak at lower wavelength curves upwards gently after c.a. SOC 30. Whereas the higher wavelength peak curves downwards to SOC 72 %. This is in line with the EPR calculations outlined in Figure 6.20 (b) – inferring the production of solids and potentially. This broad peak at higher wavelength is considered to be a superior measurement of Mn^{3+} in this electrolyte composition as it is relatively unaffected by the encroaching low wavelength band compared to the sharper, more prominent, peak at c.a. 522 nm.

With these data, finally, UV-vis and EPR experiments can be directly compared. This is the subject of the following sub-section.

6.3.4.3 Combining in-operando techniques

The previous two sub-sections have outlined the development of two in-operando techniques tracking the concentrations of Mn^{2+} and Mn^{3+} in real-time. This section presents these concentrations side-by-side (Figure 6.24).

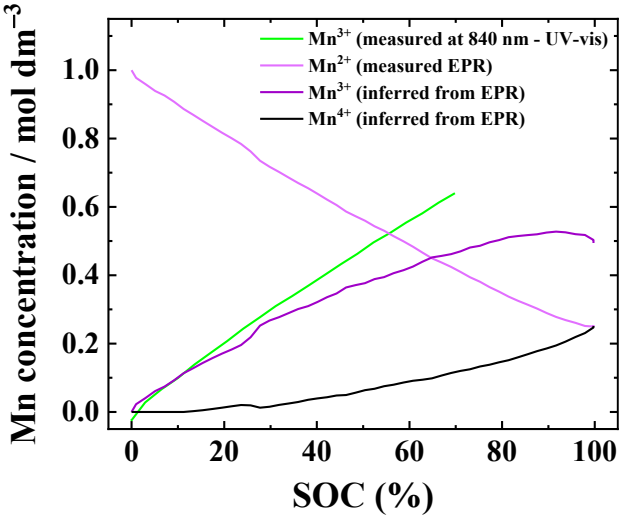


Figure 6.24: Combined UV-vis and EPR analysis. Concentrations from UV-vis measurements are calculated using the higher wavelength peak (at 840 nm). Mn^{2+} concentrations are measured by EPR and the inferred concentrations of the oxidised states from these measurements is shown here.

Figure 6.24 shows the charging arm of the cycle displayed in Figure 6.19 overlayed with the calculated Mn^{3+} concentrations from absorbance measurements using just the high wavelength absorbance from Figure 6.23. The measurements of Mn^{3+} from the UV-vis start to diverge from the EPR measurements at c.a. SOC 30 %. In-operando UV-vis gives us a fairly good handle on the overall nature of the electrolyte during the initial part of charging (up to c.a. 30 % SOC if EPR measurements are considered more reliable). It is expected, however, that the absorbance measurements overestimate the concentration of Mn^{3+} for two reasons. Firstly, the low wavelength band encroaches on the major peak at c.a. 522 nm (and the broader peak at c.a. 840 shortly afterwards) resulting in greater absorbances (and misshapen peaks). And secondly, during charging, nanoparticles of MnO_2 / MnOOH are expected to form and be suspended in solution.[23,91,92] These complexes would be expected to absorb at similar wavelengths to aqueous Mn^{3+} species. Additionally, the interaction of titanium oxo-clusters with manganese species is unknown but is expected to alter the absorption coefficients. Deciphering this complicated interaction further was beyond the scope of this chapter. Given diluting this electrolyte to inspect specific components of this electrolyte (e.g. via RDE) is not an option (as dilution modifies the chemistry), it is considered that EPR is likely to be a superior analytical technique to reliably track at least one specific species (Mn^{2+}) throughout a cycle. First though,

these techniques are compared in their ability to potentially capture kinetic information from time-dependent transient data.

6.3.4.4 Transient analysis using UV-vis and EPR

It is important to recognise and remember, firstly, that the results displayed so far do not reveal anything about the form of the species or how long they last in solution and, secondly, that these chemical processes continuously and simultaneously occur. Solution evolution was tentatively investigated in the potential transients in Figure 6.13 (b) and was implied from the observed hysteresis in Figure 6.20. Given these findings, understanding how this electrolyte evolves over time could be helped by measuring concentration and potential transients. A system is said to be transient when it is in the process of trying to reach a steady state. From a potential perspective, a steady state is reached when all the reactions in the system are occurring in the forward and the backward direction at the same rate (as was the case during the mini-transients shown at low SOCs during the charging arm in Figure 6.16 (a)). Kinetic information can be recovered from transient data that can be useful for modelling a given system and, ultimately, deeper understanding.[93]

Continuing the experiment carried out in Figure 6.22, Figure 6.25 (a) shows the next steps outlining the slower charging (at 25 mA cm^{-2} indicated in blue) raising the SOC to 92 % (calculated via coulomb counting) to find the point at which uncontrolled chemical conversion occurs. Once this SOC is reached, the OCP is measured over 4.7 hours. During this period, as in Figure 6.13 (b), the potential continuously decays, indicating a steady state equilibrium is not achieved. The UV-vis demonstrates initial steadiness (as does the potential, shown by the initial plateau) in the low wavelength band. Soon, though, the low wavelength band grows to higher wavelengths overwhelming the characteristic peak at 522 nm and ultimately the longer wavelength peak at 840 nm too. While the absorbance responses are accentuated by the characteristic Mn^{3+} peak at c.a. 522 nm, the rate at which the band shifts to higher wavelengths is similar to the potential response, perhaps indicating that solid (Rayleigh scattering) species affect the potential in some way. It should be reiterated, however, that the measurement of potential and solution absorbance takes place at different locations in the setup meaning that the solid particles observed in the UV-vis measurements may be in a different physical (and electrochemical) state in the UV-vis spectrophotometer compared to the hRFB cell.

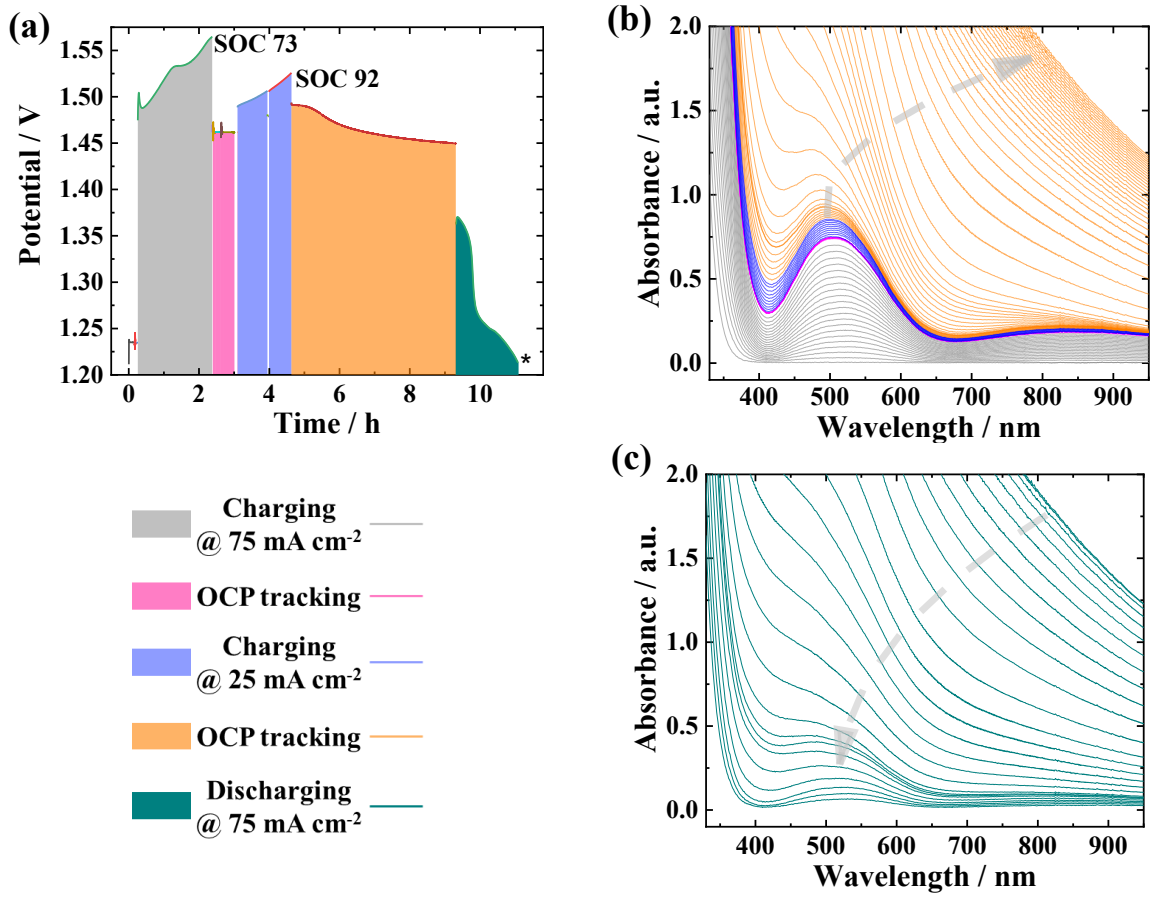


*Figure 6.25: UV-vis transient information (a) Simple potential profile during stepwise charging with intermittent resting times. (b) The additional spectra now included show a slow charge to SOC 92 (blue lines) followed by a chemical process (orange lines) leading to the formation of solids that scatter the incident light (likely due to disproportionation). (c) In-operando UV-vis spectra of the electrolyte during the electrochemical discharge. It is important to point out that the very defined shape are not recovered at equivalent states of charge during the discharge arm. The grey arrow in this figure represents time. In both (b) and (c) the grey arrow represents time. *Unfortunately, the UV-vis spectrophotometer malfunctioned c.a. 5 % before the end of the discharge – meaning there was still some un-reduced Mn^{3+} still present in solution – hence the signal at c.a. 522 nm in (c).*

Ideally, the spectra (from where the galvanostatic step ends) would now be corrected, removing the contribution from the low wavelength band, revealing lone peaks with absorbances that vary over time. However, the low wavelength band is likely to be as a result of multiple factors including unknown species (with very high absorption coefficients) and solid nanoparticles that are able to scatter the incident light in the UV-vis spectrophotometer. This task was beyond the scope of this thesis and therefore kinetics information was not extracted using this technique. Further experiments charging the cell to lower SOCs (such as 85 %, for example) and waiting for longer to see if the low wavelength band eventually overwhelms the system, were not carried out. An SOC of 92 % was considered to be only just above the threshold beyond which disproportionation overwhelms the electrolyte solution.

Finally, at the end of the five-hour OCP tracking step, in line with the measurements displayed in Figure 6.16 (b), Figure 6.25 (c), discharge was carried out. UV-vis measurements during discharge do not match respective SOCs during the charge until very low SOCs are reached. This could be due to continued scattering as a result of the presence of solid nanoparticles suspended in solution. The idea that electroactive solids persist in solution is in line with the findings in Figure 6.16 (b), where the mini-transient does not reach an equilibrium potential until very low SOCs on the discharging arm.

In order to understand the rate at which these processes are occurring, EPR was used to measure the Mn^{2+} concentration during a series of transient measurements after the cut off potential was reached after charging with a current density of 75 mA cm^{-2}. The concentration measurements of Mn^{2+} are considered to be reliable as no other species can interfere with these readings. Figure 6.26 (a) and (b) are exaggerated schematic representations of the concentration gradient across the operational (tank and cell) and analytical components (EPR) in the liquid side of this hRFB system (a) during charging and (b) after five hours of electrolyte continuously flowing through the cell. Of course, the concentration of the measured species will be different to the concentration within the tank during charge because the cell will have passed charge into the electrolyte changing the solution equilibrium. Once the cell stops charging / discharging, this concentration gradient across the components will, gradually, subside and a uniform concentration will be formed over the whole system (Figure 6.26 (b)). Clearly, this gradual transition to a 'uniform state' will be unique and characterised by the current density (extent to which there is a concentration gradient), the lengths of tubing between components and the flow rate exerted on the system. This is considered the 'mixing time'. Additionally, it should be noted that just because the cell has reached a uniform state, this does not necessarily mean that the reaction in solution has ended – this could be a completely different process.

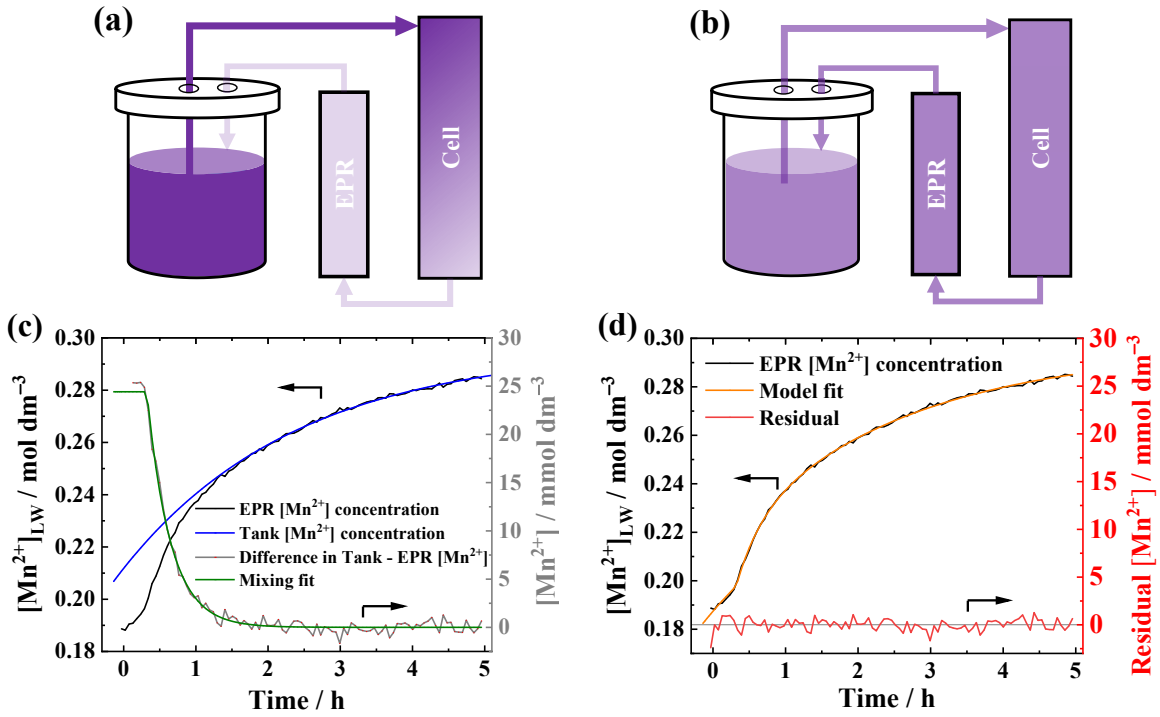


Figure 6.26: EPR transient information (a) a schematic of liquid-side of hRFB with exaggerated species concentration gradient across the Tank, Cell and EPR during operation and (b) after the system has reached a uniform state. (c) Mn^{2+} concentrations separated into 'reaction' (blue) and 'instrumental' (grey) components with their respective model fits. (d) Original Mn^{2+} concentration measurements with the model fit.

Figure 6.26 (c) shows (in black) the measured concentration of Mn^{2+} in solution. For the purposed of this analysis, two processes are considered to be occurring simultaneously over the course of this transient: (a) mixing (discussed previously) and (b) a homogeneous reaction in solution. These components are expressed in Equation (6.52), below, where time, $t = 0$ is the point at which galvanostatic charging ends.

$$[Mn^{2+}] = [Mn^{2+}]_{t=0} + \Delta[Mn^{2+}]_{reaction}\left(1 - e^{-t/\tau_{reaction}}\right) - \Delta[Mn^{2+}]_{instrumental}\left(e^{-\left(\frac{t_{delay}-\tau_{instrumental}}{\tau_{instrumental}}\right)}\right) \quad (6.52)$$

Where $\Delta[Mn^{2+}]_{reaction}$ is the amount of Mn^{2+} produced by the homogeneous reaction in the solution, $\Delta[Mn^{2+}]_{instrumental}$ is the amount of Mn^{2+} change seen as during operation the cell is not seeing the true tank concentration but the outlet of the cell – it is thus an instrumental artefact in the way the manganese is measured which must be removed to recover the true homogeneous reaction time constant. This value can be confirmed separately, as it depends on the inlet concentration of Mn^{2+} to the cell and the flow rate and current density (as described previously). $\tau_{instrumental}$ is the measurement time of the system (and also includes the time it takes

for the electrolyte to flow into the cell). There is an extra tau instrumental offset for the time because it takes a delay of $\tau_{instrumental}$ before any changes can be registered (t_{delay} - $\tau_{instrumental}$).

Using this equation, the components described can be separated and deconvoluted. Figure 6.26 (c) shows this deconvolution of the separated components which, taken together, produce an excellent fit to original data shown by the very small residuals on the right axis in Figure 6.26 (d). It should be noted that the calculated tank concentration follows a first order process rather than a second order process that might be expected from the overall chemical reaction. This suggests that the formation of Mn^{2+} occurs in a slow (potentially, rate-determining) step which is first order. Table 6.5 collects the parameters gathered from the five hour-long concentration transient displayed in Figure 6.26 alongside four additional transients prepared in an identical way but only lasting three hours (Figure A6.37). For reference the SOC, calculated using the amount of charge passed into the solution over the course of the charging cycle, is included alongside the initial, calculated Mn^{2+} concentration ($[Mn^{2+}]_{t=0}$) indicating significant disproportionation had already been occurring during the course of the cycle (as has been observed / suggested in previous experiments).

Table 6.5: Parameters extracted from Mn^{2+} concentration transient tracking. mM = milli-molar = mmol dm^{-3}. "Exp. dur." denotes "Experiment duration". "inst."denotes "instrumental". "reac." denotes "reaction".

Exp. #	Exp. dur. / h	$SOC_{coulombic}$ (%)	$[Mn^{2+}]_{t=0}$ / M	$\Delta[Mn^{2+}]_{reac.}$ / mM	$\tau_{reac.}$ / s	$\Delta[Mn^{2+}]_{inst.}$ / mM	$\tau_{inst.}$ / s
1	5	101	0.212	84.0	8680	24.4	1160
2	3	104	0.210	88.1	9070	27.3	1080
3	3	105	0.216	91.5	11300	31.2	1310
4	3	106	0.220	91.0	12000	31.1	1270
5	3	106	0.209	87.9	7480	19.0	1070

These transients were measured after galvanostatic charging at 75 mA cm^{-2} and the number of coulombs used to charge the system varied between charges resulting in slightly different SOC and initial Mn^{2+} concentrations. Further transients at different SOCs were collected (Figure A6.38 (a)). While it is assumed these transients would have a similar mixing feature at the beginning of the transient (as the flow rate and current density used to reach the SOCs was the same), the homogenous reaction in solution was not observed to have first order kinetics and appeared to reach a steady state concentration very quickly compared with those cycles displayed in Figure 6.26 and Figure A6.37.

Finally, when considering the accompanying potential transients (Figure A6.38 (b)), we are faced with the question of what affects the potential within the cell. The tank concentration can be considered to be the inlet Mn^{2+} concentration but, at least for the first hour, the measured (outlet) Mn^{2+} concentration changes. This indicates that, in addition to the homogeneous process occurring in the bulk solution, Mn^{2+} undergoes a reaction resulting in its consumption as it is passed through the cell as the measured Mn^{2+} concentration is lower. The reasons for this are unclear but are discussed in the next section.

To conclude, while no kinetic information was gathered in this chapter, there is ongoing work looking to ascertain the kinetic parameters associated with the disproportionation of Mn^{3+} to Mn^{2+} and MnO_2 (as outlined in Equation (6.10)). It was shown that multiple unknowns would have to be solved before being able to extract out the low wavelength band to reveal reasonable kinetic parameters with any certainty. It was established, using EPR measurements, that the tank concentration appears to follow a first order rate law.

6.4 Discussion

Investigation into this device and how its electrolyte evolves is ongoing. The results mentioned here represent the most recent efforts to decipher how the electrolyte develops during a cycle and how it evolves over time. While these experiments are helpful, it is also worth considering how speciation might occur from a purely thermodynamic perspective. Prof. Anthony Kucernak has developed analytical models for thermodynamically 'ideal' electrolytes where the activity of its constituent species is unity – clearly, at the high concentrations used in this chapter, the activities of these species is lower than unity. The following section introduces new components to the electrolyte systematically accounting for interactions as a result of the effect of Mn^{3+} hydrolysis, Ti^{4+} addition and solid formation, from a thermodynamic perspective. Following this section some discussion is provided with respect to some features from the results section that are yet to be fully understood.

6.4.1 Systematic thermodynamic modelling of speciation

This section systematically models the hRFB cell from a purely thermodynamic point of view – that is assuming all the components have unity activity, there is no kinetic drive required for species to form and the system is in equilibrium. The following situations are modelled – Table 6.6.

Table 6.6: Modelled scenarios with incremental changes. Atomic concentrations are stated here to avoid confusion as a result of speciation. 'Form. const.' denotes 'Formation constant'.

Case	[Mn] / mol dm^{-3}	[Ti] / mol dm^{-3}	[S] / mol dm^{-3}	Mn^{3+} hydrolysis?	Solids?	Form. const. *K*	Eqn. considered
Case 1	1.0	0	5.0	No	No	N/A	*(6.2), (6.3), (6.17)*
Case 2	1.0	0	5.0	Yes	No	N/A	*(6.2), (6.3), (6.6), (6.17)*
Case 3	1.0	1.0	6.0	Yes	No	N/A	*(6.2), (6.3), (6.6), (6.17), (6.33)*
Case 4	1.0	1.0	6.0	Yes	MnOOH	10.6	*(6.2), (6.3), (6.6), (6.9), (6.17), (6.33)*
Case 5	1.0	0	5.0	No	*-MnO_2	50	*(6.2), (6.3), (6.10), (6.17)*
Case 6	1.0	0	5.0	No	γ-MnO_2	2.24×10^6	*(6.2), (6.3), (6.10), (6.17)*

Cases 1 – 3 are shown in Figure 6.27. It should first be noted that the potential in these plots are governed (only) by the relative concentrations of Mn^{2+} and Mn^{3+}. This explains the small change in potential at either end of the cycle (calculated potential is shown in the top pane of these thermodynamic plots, Figure 6.27). The next pane down is displayed using a '$\log_{10}$(concentration)' axis to illustrate the overwhelming dominance of the bisulfate (HSO_4^-) ion from sulfuric acid. These concentrations, essentially, do not change to any significant degree across the SOC range. The calculated concentration of H^+ ions diminishes more slowly and to a lesser extent when considering the hydrolysis of Mn^{3+}. As shown in Equation (6.6), on hydrolysis, Mn^{3+} acts as an acid, resulting in an overall greater acid concentration across the SOC range. Accounting for this hydrolysis leads to the formation of a new Mn^{3+} species, $Mn(OH)^{2+}$ – hence the Mn^{3+} ion concentration is not only related to the Mn^{2+} concentration it is additionally influenced by the equilibrium constant that exists between its singly hydrolysed form.

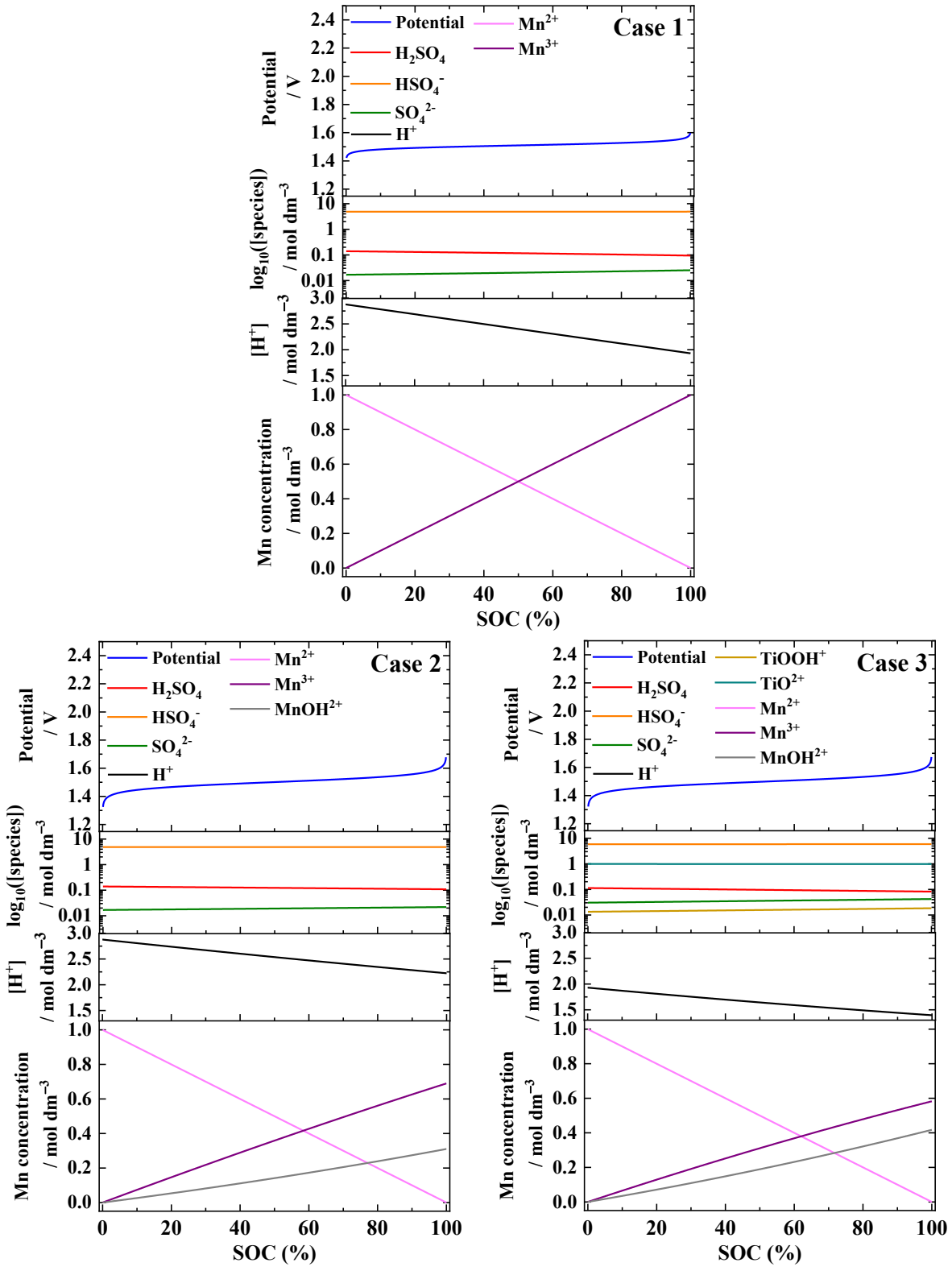


Figure 6.27: Thermodynamic calculations of species' concentration accounting for speciation assuming all activity coefficients are unity. Case 1 represents the ideal case where Mn^{2+} and Mn^{3+} exist as isolated, well-behaved ions. Case 2 introduces a single hydrolysis of the Mn^{3+} ion forming $Mn(OH)^{2+}$. Case 3 introduces titanium species.

Case 3 shows the case for when Ti^{4+} species are added. As a reminder, Ti^{4+} additive addition is essential for cell operation and electrolyte 'stability' and, with the addition of 1 M, comes

another 1 M 'sulfur' contribution. This change in 'sulfur' (referred to as sulfur because 'sulfate' infers a specific ion) results in an overall reduction in proton concentration by 1 M. For clarity, as outlined in the introduction, TiO^{2+} is expected to be the dominant titanium (Ti^{4+}) species in solution shown by its essentially having a concentration of 1 M over the SOC range. The equilibrium constant for the hydrolysis of this ion is low (discussed in Section 6.2.1.1) (Equation (6.33)). The gradient associated with the reduction of proton concentration during the charge is lower in Case 3 compared with the previous cases. The overall effect of the reduction of proton concentration has an effect on the hydrolysis of the Mn^{3+} ion. The difference in concentration distribution between Mn^{3+} and $Mn(OH)^{2+}$ is reduced. So far, there has been no consideration of solids. This is rectified in Figure 6.28.

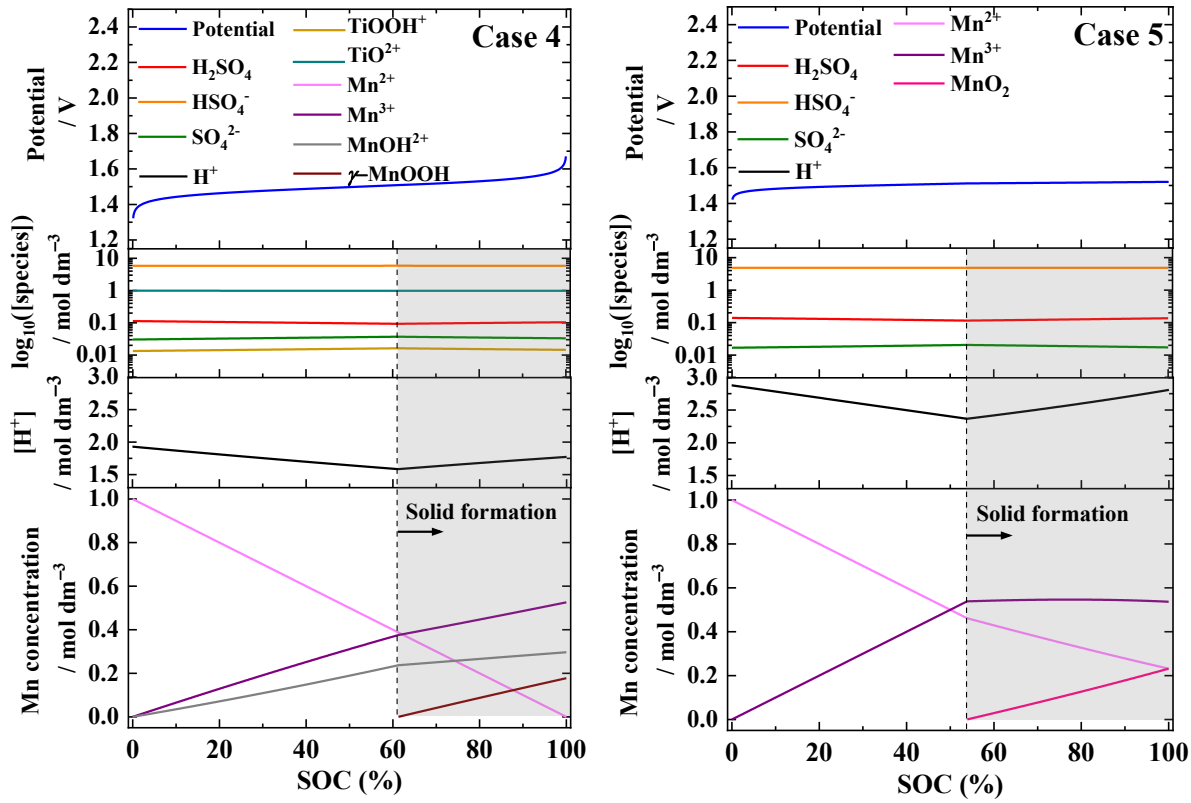


Figure 6.28: Thermodynamic calculations of species' concentration accounting for speciation assuming all activity coefficients are unity. Case 4 introduces the effect of γ-MnOOH precipitation. Case 5 shows a more simplified case where Mn^{3+} hydrolysis and titanium species are not considered. In addition, an equilibrium constant of 50 ($K_{Mn(2+)/MnO2} = 50$) is used here – note: this is far too low and is 'unphysical' but is used to illustrate the effect (thermodynamically) of including MnO_2 in the speciation of the system. Reasonable values of the equilibrium constant for the formation of MnO_2 is shown in the appendix and presents a number of additional problems to the other manganese species' concentrations.

Using the Gibbs formation energies for the species involved in Equation (6.6) – (6.8) a formation constant, *K*, can be calculated following the double hydrolysis of Mn^{3+} and the subsequent formation of γ-MnOOH. This suggests, thermodynamically, that γ-MnOOH will start to be formed from c.a. SOC 61 % (Figure 6.28 (a)).

This was extended to considering the formation of MnO_2. The calculations associated with simultaneously considering the Mn^{3+} hydrolysis, the titanium speciation and the production of MnO_2 were too complex to confidently report at this stage and therefore this case (Case 5) should only be compared with Case 1 (as there is only one newly introduced factor between them). Case 5 shows how the production of MnO_2 affects the thermodynamically predicted concentration of Mn^{2+}. It must be noted however that the formation constant, *K* was set to 50. This is a hypothetical formation constant and corresponds to a polymorph of MnO_2 with a Gibbs formation energy of 402.56 kJ mol^{-1} – this is 62 kJ mol^{-1} lower than that of β-MnO_2. The hypothetical *K* is used here to illustrate how the formation of MnO_2 affects the Mn^{2+}, Mn^{3+} and H^+ concentration. As expected, MnO_2 production infers Mn^{2+} is also being produced (due to disproportionation Equation (6.10)) resulting in the Mn^{2+} concentration not reaching zero. Importantly, the proton concentration is also shown to change its course dramatically. In a purely homogeneous reaction, the proton concentration is shown to decrease linearly with SOC as you are using protons to form hydrogen in the gas side (Case 1 – 3, Figure 6.27), however, with the formation of solid oxides (following disproportionation), more protons are generated than are being consumed at the gas side (Case 4 and 5, Figure 6.27). To link this to the results – changes and inflections in conductivity are observed over the course of a cycle (Figure 6.12) – however, two changes in gradient are observed inferring a more complicated, chemical process occurring in the real system not (yet) considered in these thermodynamic calculations.

As has been eluded to, the formation constant (*K*) for these solid species' polymorphs varies, as the free energy of formation for each of their crystal structures is different. Figure 6.29 shows notional values of *K* at which, thermodynamically, precipitation of (a) MnOOH and (b) MnO_2 can be expected to begin. The formation constants can be calculated using the relationship $\Delta_r G^0 = -RTln(K)$. These will vary according to the polymorph – so, for instance, the formation constants for γ-, α-, and β-MnOOH are 10.6, 1.15 and 0.0158, respectively. These are plotted in Figure 6.29 (a) and show that, under the conditions in the system, only the γ-MnOOH polymorph is able to be formed – this is, of course, what is projected in Case 4 (Figure 6.28) where γ-MnOOH is shown to start being precipitated at SOC 61.

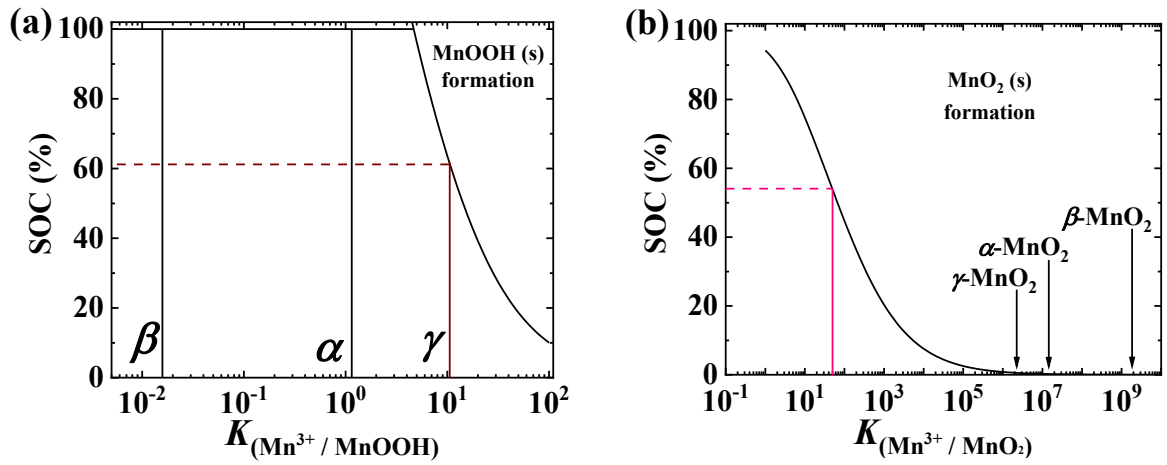


Figure 6.29: Notional values of K illustrating the thermodynamic boundary at which it is expected for solids to be precipitated. Vertical lines indicate the calculated formation constants associated with different solid polymorphs. (a) shows the notional values of K at which solids (a) MnOOH and (b) MnO_2 will start precipitating.

Figure 6.29 (b) shows the equivalent plot for MnO_2. Clearly, this looks very different and infers that, essentially, MnO_2 is immediately produced (in all forms). In Case 5, as stated earlier (in Figure 6.28), a hypothetical *K* of 50 was used to illustrate what would happen at a speciation level if a hypothetical MnO_2 polymorph were formed (this is shown in pink). This does not represent a formation constant of a known MnO_2 polymorph, though – Figure 6.30 shows what speciation would occur if the real *K* values indicated in Figure 6.29 (b) for γ-MnO_2 were used. MnO_2 is shown to form immediately as the cell starts to charge and the concentration of Mn^{3+} would remain very low, and essentially constant, across the range of SOCs calculated. This very low concentration of Mn^{3+} implies the cell would be under severe mass transport limitation during a discharge (as the Mn^{3+} would be consumed very quickly).

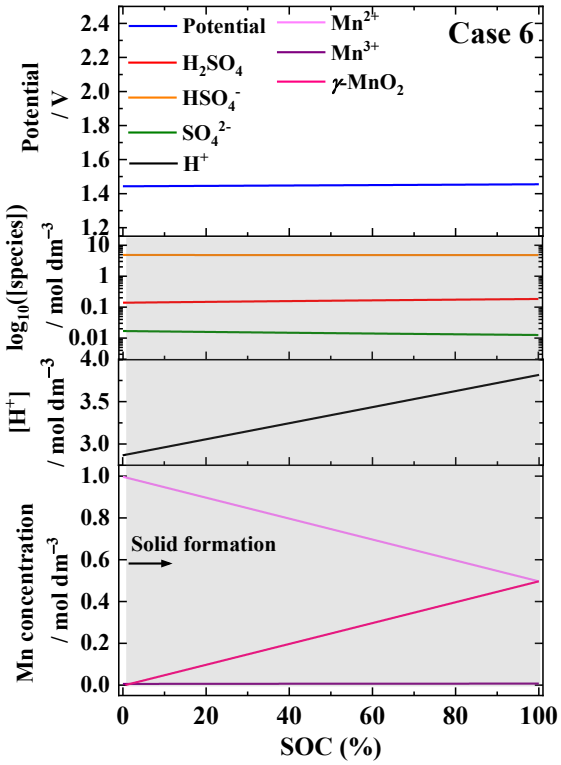


Figure 6.30: Thermodynamic calculation of species' concentration accounting for speciation assuming all activity coefficients are unity and with a reasonable formation constant for γ-MnO_2. Solid formation starts immediately as Mn^{3+} formation energy is much more positive than MnO_2.

One interesting feature to consider too, is to mention how these notional values of *K* change with a change in sulfur concentration. Experimentally, this is achieved by increasing the concentration of H_2SO_4 and partly explains why such low pHs are used in these systems. Figure 6.31 (a) and (b) show how thermodynamically expected values of *K* (at which precipitation starts occurring) changes with pH. The concentrations accompanying these boundaries represent the concentration of sulfur in the system and the speciation does not include the role of titanium.

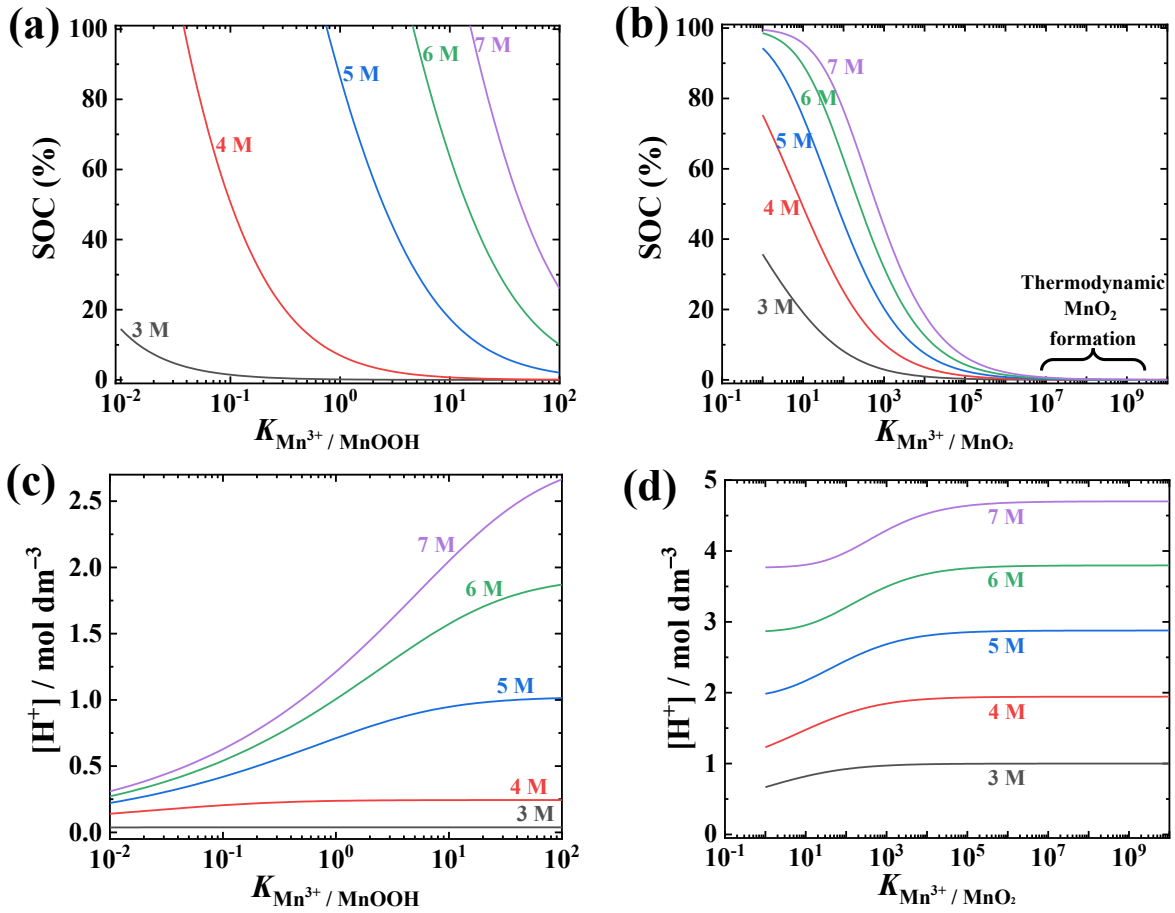


Figure 6.31: (a) and (b) Variation of notional values of K at which point solids (a) MnOOH and (b) MnO_2 are expected to start to precipitating, as a funtion of sulfur concentration. (c) and (d) show the proton concentrations for the point at which precipitiation is expected to occur for a given K.

This can be extended to (in Figure 6.31 (c) and (d)) calculating, at a given *K* the thermodynamically predicted concentration of protons in solution at the point of precipitation. These calculations show the effect of pH on precipitation. Again, the $K_{Mn(3+)/MnO2}$ values are all so large because of the strong thermodynamic driving force towards the formation of MnO_2 and so the change in concentration of protons does not have as great an effect, thermodynamically, on the point at which these species are expected to precipitate

As mentioned at the beginning of this section, these data assume that all species have an activity coefficient of one. While this is helpful as it gives an idea of what is thermodynamically possible, the activity coefficient is not one in these concentrated solutions and so these data should be used with caution. Additionally, as discussed in the introduction, these values only take into account the 'bulk' thermodynamics, so these data also do not account for the formation of metastable nanoparticulate species. These two cautionary points infer that solids form later or earlier, respectively – i.e. only considering bulk thermodynamics infers that a

kinetic driving force is required for the formation of these solids (hence, precipitation may start later for a given *K*); whereas consideration of metastable species formation infers that nanoparticles may start to form earlier than what might be thermodynamically expected.

6.4.2 Interpretation of results

Using these thermodynamic expectations as context, some of the findings and outstanding questions mentioned in the results can be discussed in more detail now. The general themes of these questions surround solid formation, the synergetic interaction they have with soluble species dissolved in the electrolyte and the overall effects these have on the operation of the hRFB cell.

Previous experiments in the Kucernak group showed that, without the addition of titanium additives, solids are formed very early in the charging cycle, presumably as a result of rapid disproportionation of Mn^{3+} in solution (Figure 6.6). Thermodynamic calculations are in agreement with this, as shown in Case 7 considering the high Gibbs free energies associated with MnO_2 polymorphs (Figure 6.30). The electrolyte has since been modified by the addition of a Ti^{4+} additive that has been shown to affect aspects of electrolyte speciation (Case 2 vs 4 vs 4, Figure 6.27 and Figure 6.28) and is presumed to influence the solid manganese oxides formed in solution in some unknown way. It is tentatively suggested that the titanium cations (e.g. TiO^{2+}) present in solution interfere by destabilising these manganese oxides or inducing the formation of a different, unstable polymorphs that immediately dissolve in solution under the conditions early in the SOC. The presence of large cations has been shown to favourably induce the formation of less stable polymorphs of MnO_2 in acidic environments elsewhere.[37] That said, the existence and potential interference of large multi-centre titanium-oxo clusters has not been properly considered.[52]

In this work, the overcharge observed in the very first experiments may be partially explained by the disproportionation of Mn^{3+} which would result in the formation of Mn^{4+} and likely therefore, solid species. However (other than by eye, on monitoring the outlet tube of the hRFB cell), the first place solids are explicitly shown to be present in solution is during in-operando UV-vis transient measurements at high SOC (Figure 6.25 (b)). The solids appear to form in an uncontrolled, initially accelerating way presumably due to chemical disproportionation and subsequently the UV-vis spectra is overwhelmed (saturation), as a result of scattering and / or high absorbance. It is important to note here, that this uncontrolled disproportionation occurred

at a SOC of 92 %. This solid, scattering material is then shown to stay in solution during the discharge (Figure 6.25 (c)). The subsequent paragraphs discuss and hypothesise what effects these solids could have on the solution and device as a whole.

Given we know that solids form, the next question should be: what effect does this have on the cell? The first experiments the effect of solid precipitation is potentially observed is on inspection of the VE as a function of current density. The solid lines in Figure 6.13 (b) show steps in the VE (as a result of steps in the discharge potential profiles) that are present only when the cell is immediately switched to discharge having charged to the cells maximum SOC for the given current density. This step in the discharge is not observed when the cell is left to rest of three hours at the maximum SOC before starting the discharge, instead following the trajectory of the lower VE from the start. This difference in VE could be as a result of precipitated solids acting as a catalyst for the electrochemical reduction of Mn^{3+} to Mn^{2+} during the discharge. While solid deposition (on the fibres) is not observed or characterised in this chapter (and so this is speculative), solid deposition and catalytic solid deposition on electrodes reducing required activation energy has been observed by other research groups.[8,9,23,94,95] This concept is not a foreign one – the addition of catalysts to substrates is a technique used extensively by those looking to test catalysts in RDE, indeed even in Chapter 4 of this thesis. This augmented VE is inspected in Figure 6.14 which shows that the greater VE is only achieved after cycling to a SOC between 60 – 80 %. If solids are in fact deposited on the electrodes, this infers deposition occurs in that SOC window. It is important to point out that this window lies before the solution-phase precipitation highlighted earlier (at SOC 92 %) inferring, potentially, that precipitation in solution and deposition on the electrode fibres (if it occurs) happen at different points. This hypothesis may also influence how long the plateaus in the potential transients after the charging arms using different current densities (Figure 6.13 (c)). The plateau lasts longer after higher charging at higher current densities. This could be for two different reasons: either the concentration of Mn^{3+} at the point cut-off is not high enough when charging with high current densities to significantly disproportionate and change the potential quickly (as is observed for lower current densities); or, the deposited solids that nucleate and subsequently grow when charging at a higher current density are more difficult to dislodge mechanically as a result of their morphology. Changes in morphology as a result of different current density are established for other metals such as tin.[96]

In the special case where the cell is charged slowly (at 25 mA cm^{-2}), using the assumption above, where solids nucleate and grow on the electrode fibres, Figure 6.16 shows the interesting effect this could have on the potential. While this chapter is sceptical of some aspects in the work carried out by Bahdad et al.,[23] they raise the interesting possibility that multiple potentials may contribute in part to the overall measured potential. They assert that, above a certain SOC, the measured potential is characterised by a mixed potential of two redox systems whereby the potential associated with the solution phase Mn^{2+} / Mn^{3+} redox couple (Equation (6.17)) is mixed with a solid phase redox process involving MnOOH and MnO_2 (expressed in Equations (6.23) – (6.26)). This is a compelling hypothesis and, if true, may be expanded by this chapter, suggesting that once the solid material is deposited onto the fibres, it remains (only slowly being removed by convective flow through the electrode) and continues to interfere with the measured potential reading (this is shown by the continued change in potential over the course of the mini-transients in Figure 6.16 (b)) until after the step in the discharge inferring the solid species is removed from the fibres. UV-vis measurements during the discharge show the presence of solid species in solution until low SOCs (Figure 6.25 (c)).

Section 6.3.4.3 briefly compared the concentrations of manganese species measured by the in-operando UV-vis and in-operando EPR techniques developed in this chapter. While the UV-vis measurements are interesting and provide a handle on the Mn^{3+} concentrations (at two different wavelengths) at low SOCs, the EPR measurements and subsequent calculations (Equations (6.46) – (6.51)) are considered to provide more reliable concentrations for the Mn species in the electrolyte. With the help of the in-operando EPR measurements, a new approach to understanding / calculating the share of oxidation states in the electrolyte (given the measured Mn^{2+} concentration) for the oxidised species is useful and can be compared to the thermodynamic calculations carried out in the previous sub-section in this discussion.

The following figures compare the manganese concentrations as a result of the thermodynamic speciation calculations (Case 4 and Case 5 in which solids are formed) compared to the measured (Mn^{2+}) and calculated (Mn^{3+} and Mn^{4+}) values from the EPR experiments. The 'charging arm' of the 150 mA cm^{-2} cycle (only) is compared here to minimise the extra chemical and kinetic effects it is now clear occur continuously and simultaneously with the electrochemical action. Figure 6.32 is meant to simply compare the EPR calculations to the thermodynamically predicted Mn species concentrations. It is understood that, other than for the Mn^{2+} concentrations (Figure 6.32 (a), 'like for like' species are not, in fact being compared.

Overall, a fairly good agreement is found between the completely theoretical results (Case 4 and Case 5) and the EPR-based calculations. It is important to remember, though, that the *-MnO_2 species is completely hypothetical (with a much more positive Gibbs free energy of formation) and was only used to show what would happen if it were predicted, thermodynamically, that MnO_2 were precipitated. Clearly this shows that as soon as MnO_2 is produced the Mn^{3+} concentration does not increase any more at all. In the real system, though, it has been shown that the cell obtains nearly 100 % coulombic efficiency (Figure 6.11 (b)) over multiple cycles and so, if MnO_2 is formed, either it itself must be electrochemically reduced back to Mn^{2+} or it must convert (chemically or electrochemically) to a Mn^{3+} species before then being reduced to Mn^{2+}. If this were to occur, the titanium species would be considered, somehow, to be essential in this process.

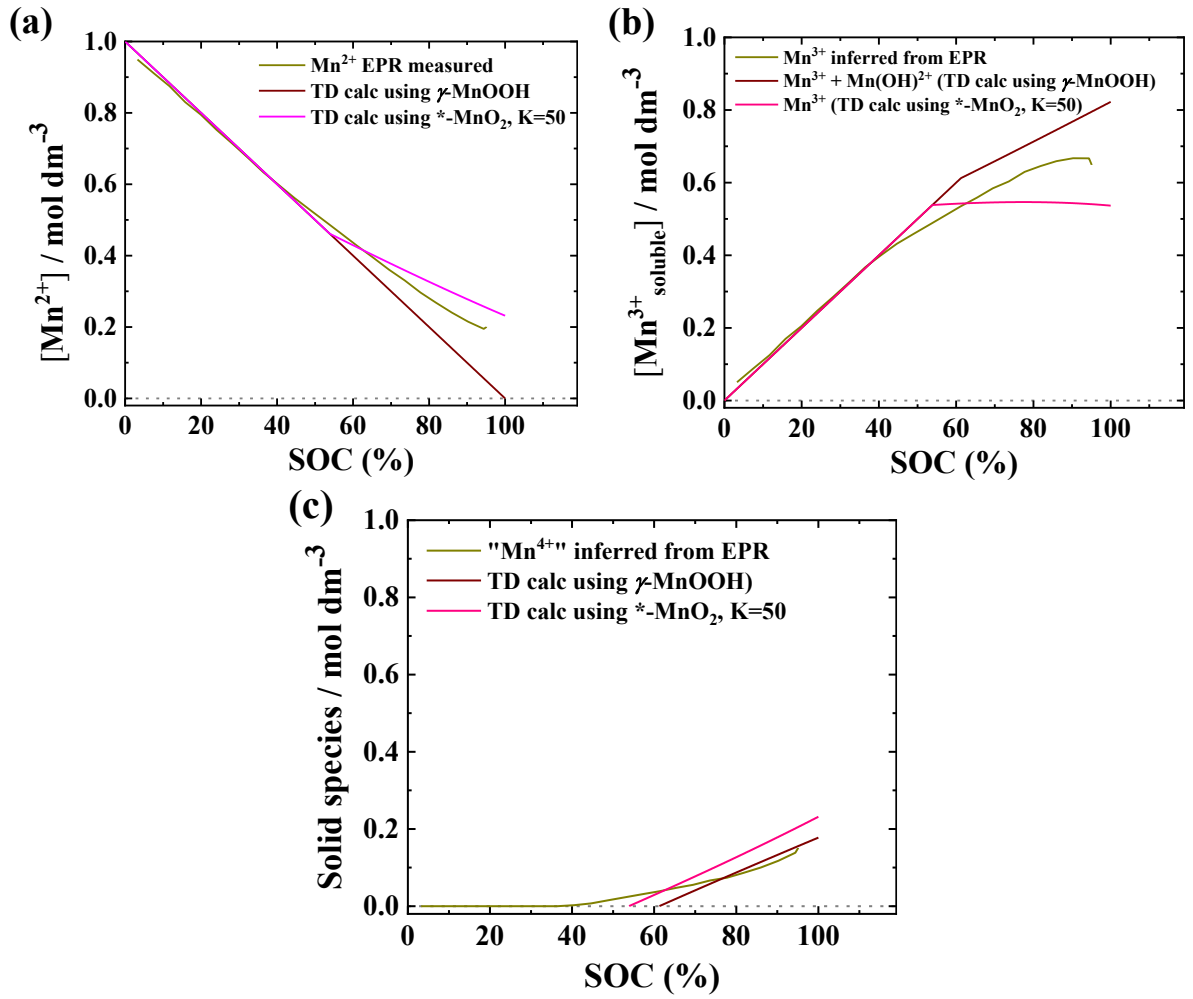


*Figure 6.32: EPR measurements (Mn^{2+}) and calculations (Mn^{3+} and Mn^{4+}) compared with thermodynamic calculations outlined in Case 4 and Case 5 in which solids (γ-MnOOH and hypothetical *-MnO_2) are formed. The hRFB cell used was charged at 150 mA cm^{-2} using the in-operando EPR setup and the measured Mn^{2+} concentration is shown in (a), alongside the thermodynamically calculated Mn^{2+} concentrations in Case 4 and Case 5. (b) The caluclated Mn^{3+} concentration from EPR measurements alongside the solution-phase Mn^{3+} species accounted for alongside the formation of solids. (c) The calculated Mn^{4+} species (from Mn^{2+} EPR measurements) and thermodynamically calculated concentrations of solid species.*

Including the formation of γ-MnOOH does not make any difference to the Mn^{2+} concentration of course as it just involves hydrolysis steps and an acid-base conversion (Equations (6.6) – (6.8)). Figure 6.32 (b) includes just the soluble Mn^{3+} species while (c) includes the concentration of Mn^{3+} solid species (γ-MnOOH) to compare to the Mn^{4+} species from the EPR measurements.

With these observations a schematic has been derived, shown in Figure 6.33, qualitatively describing some of the processes that may occur in the hRFB system.

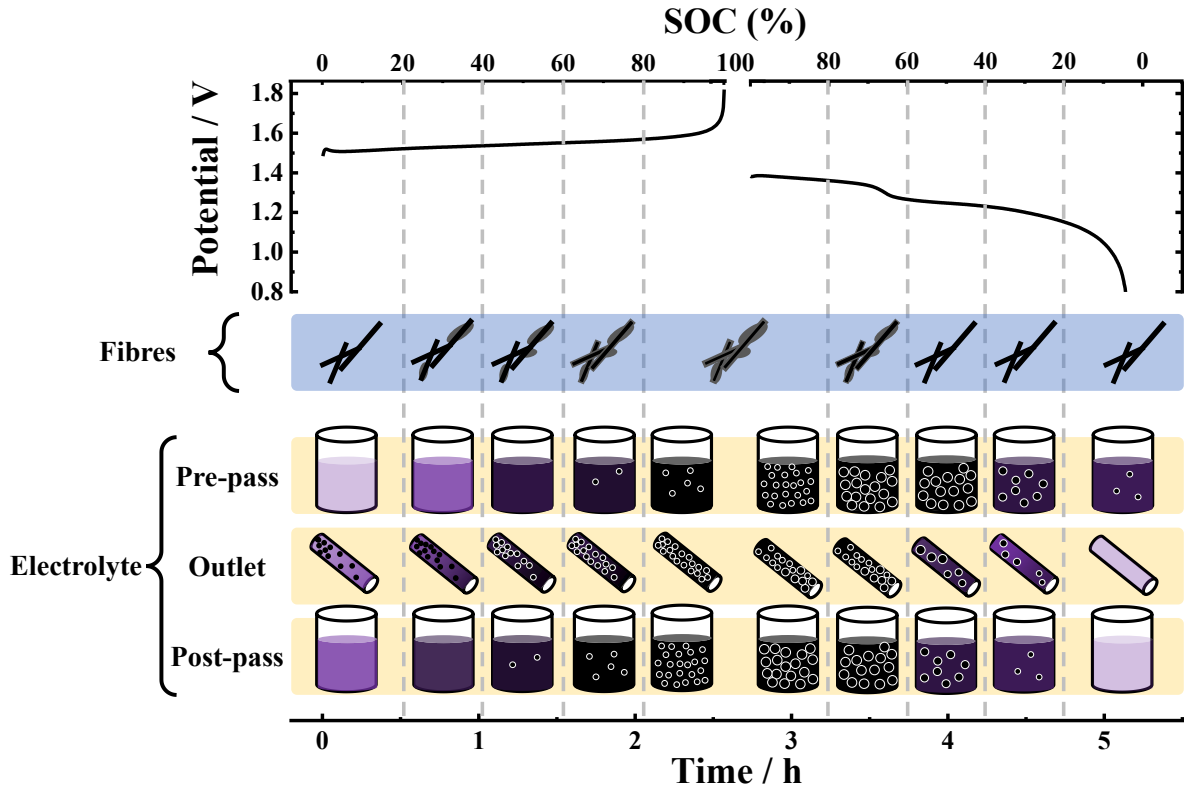


Figure 6.33: Schematic illustration of the processes occuring in the electrolyte and at the fibres in a standard cycle (> 25 mA cm^{-2}) with no relaxation period at maximum SOC. Solid species from c.a. SOC 40 are shown with a white outline here – this is just to show their existance and suggested growth trajectory (not because the acutal particles are in any way white).

Figure 6.33 roughly outlines the working understanding of how the electrolyte and electrode fibres evolve over the course of a standard (fast, > 25 mA cm^{-2}) cycle. It must be stressed that this understanding is constantly changing and will likely evolve again before seeking publication.

Firstly, considering the fibres, at the start of the charge these are thought to be bare but quickly form some catalytic species at the surface giving rise to the small peak at the beginning of the charge (observed as a resistive peak in the HFR, Figure 6.11 (c)). These species catalyse the

oxidation of Mn^{2+} during the first part of the charge until 60 – 80 % SOC where, in line with the experiments carried out in Figure 6.14, it is tentatively asserted that the local conditions enable the formation of a firm layer of catalytic solid material across the fibre surface area. It is presumed that consolidation of the solid species occurs in the final part of the charge. In the electrolyte, at the beginning of the charge, it is observed at the outlet of the tube, by eye, that solids form in the cell. They soon dissolve back into solution resulting in significant darkening of the electrolyte early on (see Figure 6.9 which shows the UV-vis operando setup immediately after a charging step starts) – this darkening is observed and harnessed by the UV-vis. It is presumed that gradually, with increasing Mn^{3+} concentration, solid species are less able to dissolve back into solution. This proposed evolution is depicted in the outlet section of Figure 6.33 and is based on the fact that 'clean' UV-vis measurements are reliably returned until at least SOC 72 % (Figure 6.22). Following this, on further charging, likely at some point after 85 – 90 % SOC (based on the UV-vis transient measurements, Figure 6.25 (b)) precipitation in solution is considered to occur. However, it is believed that this broad Mn^{3+} instability is more associated with time in solution. One interesting observation is that, even though after 40 minutes during the UV-vis transient, it is clear there is widespread precipitation. Comparing this to the charging arm SOC 90 % Mn^{2+} transient in EPR (Figure A6.38 (a)), there is no such significant increase in Mn^{2+} concentration – this may infer that this solid formation is not associated with Mn^{3+} disproportionation. Some other solid species may 'suddenly' be formed that does not demand the regeneration of Mn^{2+}, such as some MnOOH polymorph.

In the early part of the discharge, the solid material on the fibres begins to be removed until c.a. 60 % SOC, at which point they are considered to be bare, hence the lower VE in the second half of the discharge. In the electrolyte, solid species are considered to have grown (shown by the larger particle sizes in Figure 6.33) only slowly dissolving after each pass through the cell. They remain in solution until the very end of the cycle and the colour of the electrolyte remains dark until the very end of the discharge.

Finally, the kinetic features gathered from the EPR transients must be addressed. The main surprising outcome from these data is that the trajectory of the modelled homogeneous reaction producing Mn^{2+} follows a kinetically 1st order process. From the main disproportionation equation, it might expected that Mn^{2+} formation would be 2nd order (two Mn^{3+} centres are needed for disproportionation, Equation (6.10)). This suggests that the chemical reformation of Mn^{2+} does not follow a typical disproportionation path, instead these results suggest Mn^{2+}

is formed in a slow, 1st order step. This process is unknown. Lastly, in an attempt to understand the potential transients shown in Figure A6.38 (b), a Nernstian model simply using the measured Mn^{2+} concentrations and the inferred Mn^{3+} concentration (from the EPR measurements) was compared to project the potential – these concentrations poorly reflect the measured potential implying other electrochemical steps were taking place during the homogenous reaction. Further discussion how this potential can be modelled is not included here but is the subject of continued work in the group. In the introduction, the formation of bulk species is discussed outlining the possible formation of metastable species that are kinetically stabilised by their very low surface energies as a result of their high surface area to volume ratio (Figure 6.3). The formation of these species precedes the subsequent formation of solid manganese bulk species (as outlined by Pourbaix). The formation of these metastable species and the influence of Ti^{4+} species in solution is unknown but they are considered to have an effect on the kinetics of the disproportionation in the electrolyte and on the potential of the cell. Ongoing cross-departmental work is devoted to modelling how these potentials might change on, for instance, solution phase precipitation or dissolution of solids from the surface of the electrode.

6.5 Conclusions

This chapter is a work in progress. As such, specific conclusions are still being morphed and constructed. The hRFB system was initially introduced highlighting a step in the VE (under certain conditions) as well as the ability for the electrolyte to be overcharged when charging sufficiently slowly. Following this, two in-operando methods examining the liquid electrolyte used in this system were developed. With its promising ability to measure absorbances at different wavelengths and inform the user about the solid species in the cell, UV-vis measurements were shown to overestimate Mn^{3+} concentrations across the full range of SOCs. EPR measurements, on the other hand, enabled the ability to keep track of the Mn^{2+} concentrations over the course of the cycle with the additional ability to back-calculate hypothetical concentrations of Mn^{3+} and Mn^{4+} species. Specifically, these EPR measurements confirm that Mn^{2+} is being produced during the cycle – indicated by its concentration never reaching zero. Lastly, transient measurements began to uncover information around the chemical processes occurring in the system and the kinetics that define the rates at which they proceed. These found that, while it might be expected the homogenous reaction occurring in solution continuously produces Mn^{2+} is a 2nd order process, Mn^{2+} production appears to follow a 1st order process – inferring Mn^{2+} is formed during a slow step.

Returning to the high-level question set out in the introduction: “Is there a way of developing an enhanced understanding of manganese speciation occurring within a manganese electrolyte during cell cycling?” It is fair to say that with the developed in-operando techniques presented in this chapter, a greater understanding of the electrolyte and how species evolve over the course of the cycle, has been gained. The sub-questions stated in the introduction were largely addressed other than the question of how manganese and titanium interact – this was beyond the scope of this work.

This chapter has developed our hypotheses surrounding the electrolyte. While the speciation is still not fully understood, more experiments and analyses are underway to further understand the processes occurring in this system.

6.5.1 Future work

Future work will be directed at firstly, further understanding the nature of the electrolyte; secondly, developing techniques with a view to identifying the solid species that form in solution; and, thirdly trying to operate the cell at a greater power density and efficiency. Below are a few examples of the experiments that are being / will be worked on in this research group (and in some cases in tandem with the operando techniques reported here).

Overall electrolyte characterisation and cell operation:

- Test to see if increasing the acidity of the electrolyte changes the point at which solids begin to be formed. Hypothesis, based on thermodynamic calculations: greater acidity, greater stability of Mn^{3+} for longer – solids start to form at higher SOC.
- Develop an ECM suitable for the system and extract qualitative information from Nyquist plots.
- Viscosity measurements needed – will help carry out diffusivity calculations of specific species in this electrolyte.
- Conductivity (and viscosity) measurements at a low current density (to try and understand the change in HFR / membrane conductivity a bit better).
- RDE experiments using manganese oxides and their polymorphs as potential catalysts towards the oxidation or reduction of Mn^{2+} and Mn^{3+}, respectively.
- Sputter coating the electrode materials with other metals (such as gold) to see if this has an effect on the VE.

- Build kinetics into a model including time-dependant precipitations kinetics to keep track of SOC.

UV-vis specific measurements:

- Measure solutions with systematic 'sulfur' concentration variation.
- Systematic measurement in order to understand the effect of titanium in UV-vis measurements – go to lower concentrations of Mn^{3+} to identify any peaks in the low wavelength band with extremely high absorption coefficients.

EPR specific measurements:

- Alter the acid concentration to inspect the local environment around the Mn^{2+} centre – any change in the EPR signal?

There are many types of experiment that need to be carried out both using the in-operando techniques developed in this work but also new ones. One particularly useful experiment would be some type of in-operando dynamic light scattering (DLS) directed at the species very near the cell tubing outlet. Varying species' relative concentrations is expected to have an effect on the particle size and the point at which precipitation is expected to occur.

6.6 Appendix

6.6.1 Manganese (III) stabilisation techniques

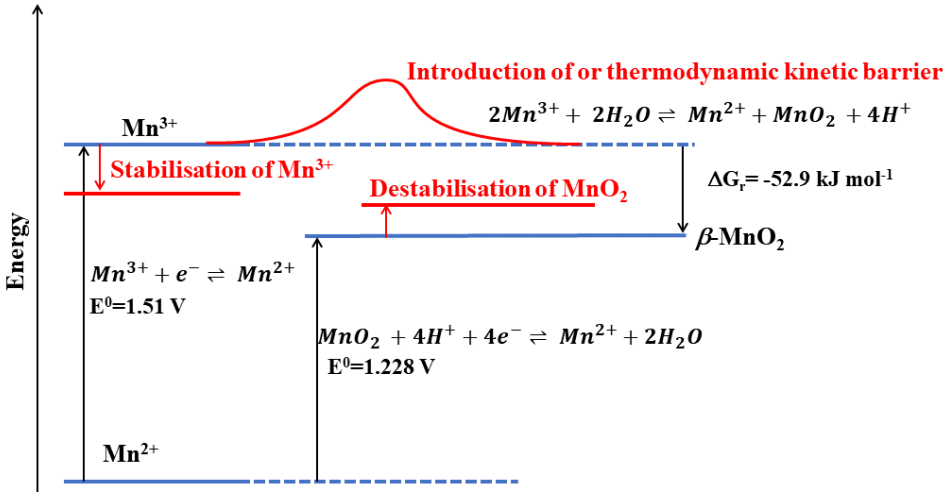


Figure A6.34: Schematic demonstrating techniques potentially used to stabilise Mn^{3+} in solution. Energy axis is not to scale.

6.6.2 UV-vis peak comparison

The ratio of the absorbances associated with the wavelengths outlined in Figure A6.35 are shown to generally increase with SOC, especially after 30 % SOC. This is attributed to continued (and increasing) overlap of the low wavelength band with the signal at 522 nm. When using the absorbance captured by the single wavelength, the ratio is shown to be largely flat until 30 % SOC. This is roughly the calibration point used to calculate the concentrations of Mn^{3+} in the main text.

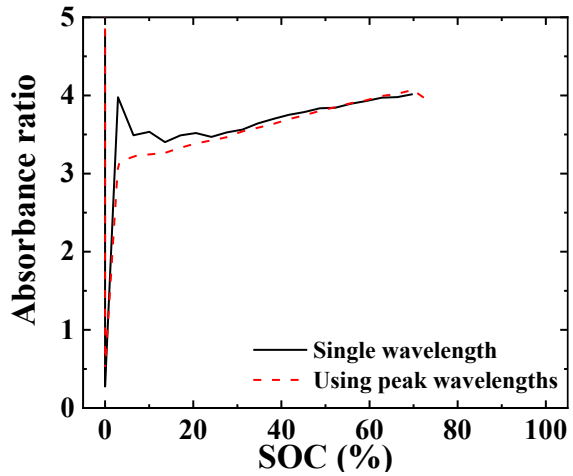


Figure A6.35: Ratio in absorbances for UV-vis signals at high (840 nm) vs low (522 nm) wavelenths.

6.6.3 EPR based manganese concentration calculations for a slow cycle

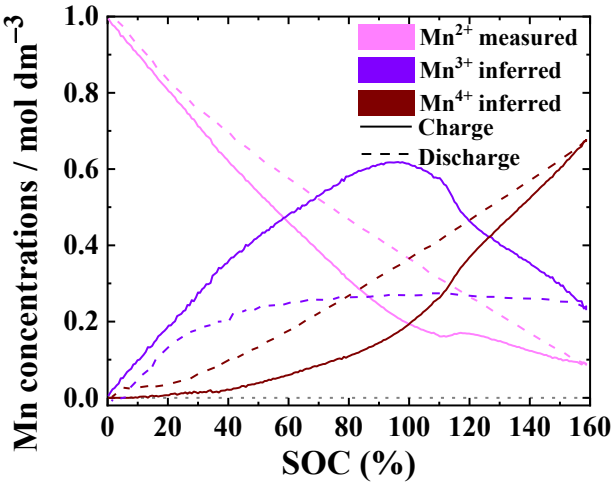


Figure A6.36: Measured concentration of Mn^{2+} alongside theoretical calculations for a slow cycle using a current density of 25 mA cm^{-2} with an electrolyte volume of 180 mL.

6.6.4 Extra EPR transients

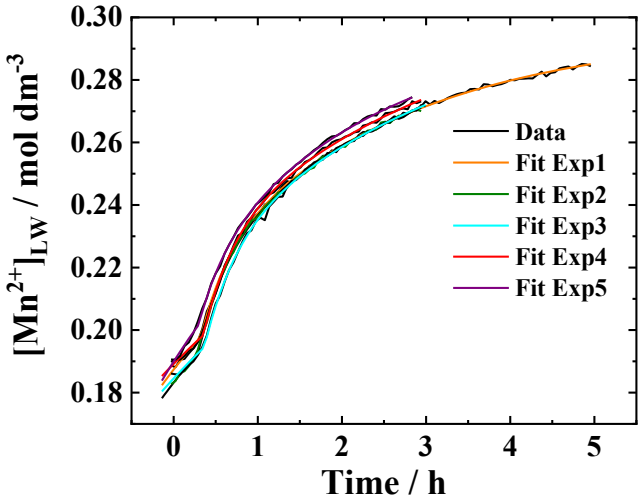


Figure A6.37: Repeated concentration transient fittings after charging 180 mL electrolyte at 75 mA cm^{-2} to the maximum SOC (until cut-off).

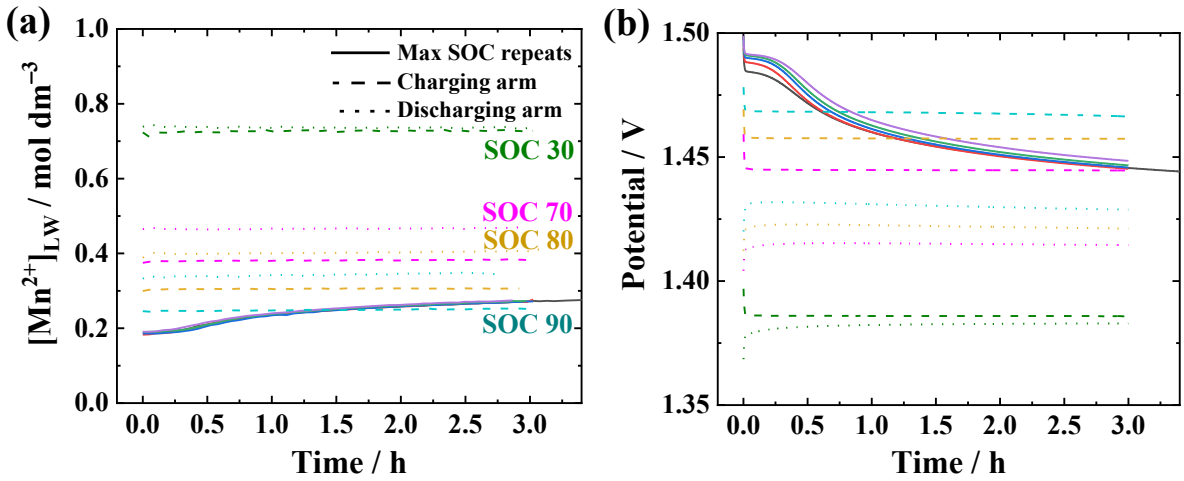


Figure A6.38: All (a) Mn^{2+} concentration and (b) cell potential transients at different SOCs.

6.7 References

1 L. Joerissen, J. Garche, C. Fabjan and G. Tomazic, *J. Power Sources*, 2004, **127**, 98–104.

2 C. Wadia, P. Albertus and V. Srinivasan, *J. Power Sources*, 2011, **196**, 1593–1598.

3 S. Renner and F. W. Wellmer, *Miner. Econ.*, 2019, **33**, 311–340.

4 D. G. Kwabi, Y. Ji and M. J. Aziz, *Chem. Rev.*, 2020, **120**, 6467–6489.

5 Y. Dong, H. Kaku, H. Miyawaki, R. Tatsumi, K. Moriuchi and T. Shigematsu, *SEI Tech. Rev.*, 2017, **84**, 35–40.

6 D. A. Finkelstein and H. D. Abruna, *ACS Energy Lett.*, 2017, **2**, 1439–1443.

7 J. Rubio-Garcia, A. Kucernak, D. Zhao, D. Li, K. Fahy, V. Yufit, N. Brandon and M. Gomez-Gonzalez, *J. Phys. Energy*, 2018, **1**, 015006.

8 Y.-R. Dong, H. Kaku, K. Hanafusa, K. Moriuchi and T. Shigematsu, *ECS Trans.*, 2015, **69**, 59.

9 H. Kaku, Y.-R. Dong, K. Hanafusa, K. Moriuchi and T. Shigematsu, *ECS Trans.*, 2016, **72**, 1–9.
10 J. R. Rumble, T. J. Bruno and M. J. Doa, *CRC handbook of chemistry and physics : a ready-reference book of chemical and physical data*, 2021.
11 A. J. Bard, R. Parsons and J. Jordan, *Standard potentials in aqueous solution*, New York : Marcel Dekker, 1985.
12 V. J. DeRose, I. Mukerji, M. J. Latimer, K. Sauer, V. K. Yachandra and M. P. Klein, *J. Am. Chem. Soc.*, 2002, **116**, 5239–5249.
13 K. Wieghardt, *Angew. Chem. Int. Ed.*, 1994, **33**, 725–728.
14 F. A. Armstrong, *Philos. Trans. R. Soc. B Biol. Sci.*, 2007, **363**, 1263–1270.
15 S. Mukhopadhyay, S. K. Mandal, S. Bhaduri and W. H. Armstrong, *Chem. Rev.*, 2004, **104**, 3981–4026.
16 J. E. Post, *Proc. Natl. Acad. Sci.*, 1999, **96**, 3447–3454.
17 M. Pourbaix, *Atlas of electrochemical equilibria in aqueous solutions*, National Association of Corrosion Engineers, Houston, Texas, 1974.
18 D. Surovtseva and K. Kannoorpatti, in *Abstract from Annual Conference of the Australasian Corrosion Association (ACA 2014)*, Darwin, Australia, 2014.
19 F. A. Cotton, G. Wilkinson, C. A. Murillo and M. Bochmann, *Advanced Inorganic Chemistry, 6th Ed.*, Wiley-Interscience, 1998.
20 R. K. Fox, D. F. Swinehart and A. B. Garrett, *J. Am. Chem. Soc.*, 2002, **63**, 1779–1782.
21 D. H. Macartney and N. Sutin, *Inorg. Chem.*, 1985, **24**, 3403–3409.
22 G. Davies, *Coord. Chem. Rev.*, 1969, **4**, 199–224.
23 A. O. O. Bahdad, Y. Li and T. Van Nguyen, *J. Electrochem. Soc.*, 2021, **168**, 070524.
24 P. L. Brown and C. Ekberg, *Hydrolysis of Metal Ions*, Wiley-VCH Verlag GmbH & Co. KGaA, 2016.
25 J. J. Morgan, *Geochim. Cosmochim. Acta*, 2005, **69**, 35–48.
26 A. Stiewe, E. Kemnitz and S. Troyanov, *Zeitschrift fur Krist. - New Cryst. Struct.*, 1998, **213**, 654–658.
27 S. K. Ghosh, *ACS Omega*, 2020, **5**, 25493–25504.
28 D. A. Kitchaev, S. T. Dacek, W. Sun and G. Ceder, *J. Am. Chem. Soc.*, 2017, **139**, 2672–2681.
29 J. D. Hem, C. E. Roberson and R. B. Fournier, *Water Resour. Res.*, 1982, **18**, 563–570.
30 J. Nývlt, *Cryst. Res. Technol.*, 1995, **30**, 443–449.
31 W. Sun, D. A. Kitchaev, D. Kramer and G. Ceder, *Nat. Commun.*, 2019, **10**, 1–9.
32 B. R. Chen, W. Sun, D. A. Kitchaev, J. S. Mangum, V. Thampy, L. M. Garten, D. S. Ginley, B. P. Gorman, K. H. Stone, G. Ceder, M. F. Toney and L. T. Schelhas, *Nat. Commun.*, 2018, **9**, 1–9.
33 A. Navrotsky, *ChemPhysChem*, 2011, **12**, 2207–2215.
34 A. Navrotsky, C. Ma, K. Lilova and N. Birkner, *Science (80-.).*, 2010, **330**, 199–201.
35 N. Birkner and A. Navrotsky, *Am. Mineral.*, 2012, **97**, 1291–1298.
36 R. M. McKenzie, *Miner. Mag.*, 1971, **38**, 493–502.
37 D. Portehault, S. Cassaignon, E. Baudrin and J. P. Jolivet, *J. Mater. Chem.*, 2009, **19**, 2407–2416.
38 D. Portehault, S. Cassaignon, E. Baudrin and J. P. Jolivet, *J. Mater. Chem.*, 2009, **19**, 7947–7954.
39 Q. Feng, H. Kanoh and K. Ooi, *J. Mater. Chem.*, 1999, **9**, 319–333.
40 X. Liang, J. E. Post, B. Lanson, X. Wang, M. Zhu, F. Liu, W. Tan, X. Feng, G. Zhu, X. Zhang and J. J. De Yoreo, *Environ. Sci. Nano*, 2020, **7**, 238–249.
41 D. D. Wagman, W. H. Evans, V. B. Parker, I. Halow, S. M. Bailey and R. H. Schumm, *Selected values of chemical thermodynamic properties*, National Bureau of Standards,

1969.
42 L. M. Gramm-Osipov, *Manganese Miner. Geochemistry Mineral. Terr. Mar. Depos.*, 1997, 301–308.
43 C. C. Chen, J. H. Chen, C. G. Chao and W. C. Say, *J. Mater. Sci. 2005 4015*, 2005, **40**, 4053–4059.
44 G. Wilkinson, *Science (80-.).*, 1974, **185**, 109–112.
45 T. Cuenca, E. Y.-X. Chen, A. Rodriguez-Delgado, M. Bochmann, D. M. P. Mingos and R. H. Crabtree, *Comprehensive Organometallic Chemistry : Volume 3*, Elsevier Ltd., 3rd Ed., 2007.
46 X. Liu and J. K. Thomas, *Chem. Commun.*, 1996, 1435–1436.
47 A. Fujishima and K. Honda, *Nature*, 1972, **238**, 37–38.
48 A. Pichavant, E. Provost, W. Fürst and J. F. Hochepied, *J. Chem. Thermodyn.*, 2019, **131**, 184–191.
49 I. Szilágyi, E. Königsberger and P. M. May, *Inorg. Chem.*, 2009, **48**, 2200–2204.
50 F. Baillon, E. Provost and W. Fürst, *J. Mol. Liq.*, 2008, **143**, 8–12.
51 I. Cservenyák, G. H. Kelsall and W. Wang, *Electrochim. Acta*, 1996, **41**, 563–572.
52 K. Kozma, M. Wang, P. I. Molina, N. P. Martin, Z. Feng and M. Nyman, *Dalt. Trans.*, 2019, **48**, 11086–11093.
53 O. Sadeghi, L. N. Zakharov and M. Nyman, *Science (80-.).*, 2015, **347**, 1359–1362.
54 Redox Flow Battery | Sumitomo Electric Industries, https://sumitomoelectric.com/products/redox, (accessed 14 February 2022).
55 E. W. Zhao, E. Jónsson, R. B. Jethwa, D. Hey, D. Lyu, A. Brookfield, P. A. A. Klusener, D. Collison and C. P. Grey, *J. Am. Chem. Soc.*, 2021, **143**, 1885–1895.
56 F. Tariq, J. Rubio-Garcia, V. Yufit, A. Bertei, B. K. Chakrabarti, A. R. Kucernak and N. P. Brandon, *Sustain. Energy Fuels*, 2018, **2**, 2068–2080.
57 R. H. Jervis, L. D. Brown, T. P. Neville, J. Millichamp, D. P. Finegan, T. M. M. Heenan, D. J. L. Brett and P. R. Shearing, *J. Phys. D. Appl. Phys.*, 2016, **49**, 434002–434010.
58 B. J. Neyhouse, K. M. Tenny, Y.-M. Chiang and F. R. Brushett, *ACS Appl. Energy Mater.*, 2021, acsaem.1c02580.
59 M. Malik, K. H. Chan and G. Azimi, *RSC Adv.*, 2021, **11**, 28014–28028.
60 J. E. Jee, O. Pestovsky and A. Bakac, *Dalt. Trans.*, 2010, **39**, 11636–11642.
61 W. Partenheimer, *Adv. Synth. Catal.*, 2004, **346**, 297–306.
62 T. S. Davis, J. P. Fackler and M. J. Weeks, *Inorg. Chem.*, 2002, **7**, 1994–2002.
63 T. C. Gokoglan, S. K. Pahari, A. Hamel, R. Howland, P. J. Cappillino and E. Agar, *J. Electrochem. Soc.*, 2019, **166**, A1745–A1751.
64 Y. Kaneko, *J. Nanosci. Nanotechnol.*, 2011, **11**, 2458–2464.
65 W. M. Carvalho, L. Cassayre, D. Quaranta, F. Chauvet, R. El-Hage, T. Tzedakis and B. Biscans, *J. Energy Chem.*, 2021, **61**, 436–445.
66 E. Sánchez-Díez, E. Ventosa, M. Guarnieri, A. Trovò, C. Flox, R. Marcilla, F. Soavi, P. Mazur, E. Aranzabe and R. Ferret, *J. Power Sources*, 2021, **481**, 228804.
67 K. Lourenssen, J. Williams, F. Ahmadpour, R. Clemmer and S. Tasnim, *J. Energy Storage*, 2019, 25, 100844.
68 M. Küttinger, R. Brunetaud, J. K. Włodarczyk, P. Fischer and J. Tübke, *J. Power Sources*, 2021, **495**, 229820.
69 J. Rubio-Garcia, J. Cui, A. Parra-Puerto and A. Kucernak, *Energy Storage Mater.*, 2020, **31**, 1–10.
70 Y. A. Gandomi, D. S. Aaron, J. R. Houser, M. C. Daugherty, J. T. Clement, A. M. Pezeshki, T. Y. Ertugrul, D. P. Moseley and M. M. Mench, *J. Electrochem. Soc.*, 2018, **165**, A970–A1010.
71 H. Wang and J. A. Turner, *J. Power Sources*, 2008, **183**, 576–580.

72 Z. Tang, R. Svoboda, J. S. Lawton, D. S. Aaron, A. B. Papandrew and T. A. Zawodzinski, *J. Electrochem. Soc.*, 2013, **160**, F1040–F1047.
73 A. Khataee, D. Pan, J. S. Olsson, P. Jannasch and R. W. Lindström, *J. Power Sources*, 2021, **483**, 229202.
74 R. M. Darling, J. D. Saraidaridis, C. Shovlin, M. Fortin, L. A. Murdock and B. C. Benicewicz, *J. Electrochem. Soc.*, 2021, **168**, 040516.
75 H. E. Darling, *J. Chem. Eng. Data*, 2002, **9**, 421–426.
76 H. R. Jiang, J. Sun, L. Wei, M. C. Wu, W. Shyy and T. S. Zhao, *Energy Storage Mater.*, 2020, **24**, 529–540.
77 M. Skyllas-Kazacos, *J. Electrochem. Soc.*, 1987, **134**, 2950.
78 F. Mohammadi, P. Timbrell, S. Zhong, C. Padeste and M. Skyllas-Kazacos, *J. Power Sources*, 1994, **52**, 61–68.
79 M. Nourani, C. R. Dennison, X. Jin, F. Liu and E. Agar, *J. Electrochem. Soc.*, 2019, **166**, A3844–A3851.
80 L. Wei, T. S. Zhao, Q. Xu, X. L. Zhou and Z. H. Zhang, *Appl. Energy*, 2017, **190**, 1112–1118.
81 N. Roznyatovskaya, J. Noack, H. Mild, M. Fühl, P. Fischer, K. Pinkwart, J. Tübke and M. Skyllas-Kazacos, *Batter. 2019, Vol. 5, Page 13*, 2019, **5**, 13.
82 S. Ressel, F. Bill, L. Holtz, N. Janshen, A. Chica, T. Flower, C. Weidlich and T. Struckmann, *J. Power Sources*, 2018, **378**, 776–783.
83 A. J. Bard and L. R. Faulkner, *ELECTROCHEMICAL METHODS: Fundamentals and applications*, 2001.
84 G. R. Eaton, S. S. Eaton, D. P. Barr and R. T. Weber, *Quantitative EPR*, SpringerWienNewYork, 2010.
85 T. Krämer, F. Tuna and S. D. Pike, *Chem. Sci.*, 2019, **10**, 6886–6898.
86 M. Pacia, P. Warszyński and W. Macyk, *Dalt. Trans.*, 2014, **43**, 12480–12485.
87 Lucas Mangold, Hubert Halleux, Sébastien Leclerc, Aurélien Moncomble, Gérard Cote and Alexandre Chagnes, *RSC Adv.*, 2021, **11**, 27059–27073.
88 N. Bityurin, L. Znaidi, P. Marteau and A. Kanaev, *Chem. Phys. Lett.*, 2003, **367**, 690–696.
89 C. E. O. Andrade, A. F. Oliveira, A. A. Neves and M. E. L. R. Queiroz, *Spectrochim. Acta Part A Mol. Biomol. Spectrosc.*, 2016, **168**, 253–257.
90 A. J. Cox, A. J. DeWeerd and J. Linden, *Am. J. Phys.*, 2002, **70**, 620.
91 D. K. Bhui, H. Bar, P. Sarkar, G. P. Sahoo, S. P. De and A. Misra, *J. Mol. Liq.*, 2009, **145**, 33–37.
92 A. R. Studart, E. Amstad and L. J. Gauckler, *Langmuir*, 2007, **23**, 1081–1090.
93 K. Tsaur and R. Pollard, *J. Electrochem. Soc.*, 1986, **133**, 2296–2308.
94 F. Q. Xue, Y. L. Wang, W. H. Wang and X. D. Wang, *Electrochim. Acta*, 2008, **53**, 6636–6642.
95 E. R. Stobbe, B. A. De Boer and J. W. Geus, *Catal. Today*, 1999, **47**, 161–167.
96 M. Mallik, A. Mitra, S. Sengupta, K. Das, R. N. Ghosh and S. Das, *Cryst. Growth Des.*, 2014, **14**, 6542–6549.

Chapter 7

Conclusions

"Begin at the beginning and go on till you come to the end: then stop." – Lewis Carroll

7.1 Final conclusions

The overall objective of this work was to develop an improved understanding of some of the components in hRFBs. Part III in Chapter 1 set out the main four research questions this thesis looked to address and which are the basis of the four results chapters in this thesis. Within each of the chapters, these questions were broken down into sub-questions, the objectives were clarified and the studies carried out. Those original four questions are repeated here:

- How is the microstructure of porous carbon paper and cloth electrodes related to the performance of the RFB system in which they operate?
- Is it possible to develop an inexpensive, carbon-based, high-performing bifunctional oxygen electrocatalyst?
- Can this catalyst be used in devices at different pHs and can we validate the 'microstructure / performance' findings?
- Is there a way of developing an enhanced understanding of manganese speciation occurring within a manganese electrolyte during hybrid redox flow battery cell cycling?

While the following sub-sections summarise the conclusions gained from each of the individual chapters in bullet-point form, it is important to discuss the broad findings from the thesis as a whole and what they tell future researchers when they are faced with similar scenarios or questions. As the title of this thesis infers, the aspects of hRFBs discussed are separate but adjacent and bound to one another – there are three overarching themes of conclusion. They concern the electrode, the electrocatalyst and the electrolyte. Firstly, with regard to the electrode, Chapters 3 and 5 demonstrate that understanding the mass transport resistances in the cell is important in order to extract the greatest performance from electrodes. In Chapter 3,

electrode permeability is shown to be the most important characteristic for high performance in the convective liquid flow environment employed in this work. In a different (opposite) way, Chapter 5 bolsters this message, by demonstrating (albeit in a gaseous system) that mass transport through the catalyst layers is essential for proper electrochemical device functionality. Secondly, Chapters 4 and 5 focus on the synthesis of a versatile catalyst and how it can be transferred to real electrochemical devices with varying degrees of success. These chapters also emphasise the importance of transparently reporting catalyst capability at both the three electrode cell- and device-level. Finally, the electrolyte is essential across all the chapters – in Chapter 3 an organic quasi-reversible electrolyte was used for largely analytical reasons that allowed for the isolation of specific mass transport features in the electrode. In Chapter 4, different electrolytes are used to investigate how an electrocatalyst behaves in different pH environments revealing interesting mechanistic intricacies. And, finally, Chapter 6 nicely wraps together all three of these themes. While the chapter clearly focusses on the acidic manganese-titanium electrolyte, its intimate relationship with the electrode is evidenced by the assertion that nucleation and growth of electrocatalytic material occurs to some degree on the electrode fibres. While the details remain an open question, this deposited species then catalyse the oxidative and reductive processes that occur during the charge / discharge cycle. The overarching conclusion from Chapter 6 is that a complete understanding of a given devices' electrolyte is essential to understand the full extent of how an electrolyte can be used.

7.1.1 Chapter 3

This chapter looked to address the first question to understand the relationship between the electrode microstructure and the overall performance. This was achieved by establishing microstructural information using X-ray computed tomography and electron microscopy and, following this, testing their performance in a (symmetric) RFB cell alongside a quasi-reversible redox couple (TEMPO) dissolved in two supporting solvents. In summary, the following conclusions were gained from this work:

- Electrolytes with lower viscosity and surface tension, and those that are passed through the electrolyte at greater flow rates, demonstrate greater performance, presumably as a result of thinner boundary layers.
- While a combination of microstructural features collectively contribute to the overall performance, the mass transport rates through the electrode are a useful indicator of

electrode performance; as such, under the convective conditions imposed on the electrodes in this work, the permeability is the best indicator of performance.

- Other individual microstructural parameters such as volume specific surface area, porosity and tortuosity, have poor correlation with the performance.
- With an extracted pore network from ex-situ imaging techniques, a pore network model can be used to predict, relatively, how well an electrode is likely to perform.
- A 1D model was used, alongside the electrochemical polarisation measurements, to establish mass-transfer coefficients – these values further characterise / focus these conclusions by deciphering inter- and intra-pore contributions to the mass transport resistance. The best performing electrodes display the highest mass transfer coefficients.
- Practically, AvCarb 7497 is deemed the best performer because of its high permeability and inter-pore connectivity, fibre alignment and its ability to distribute electrolyte effectively throughout the electrode volume.

It is asserted that the question has been answered but, equally, it is acknowledged that the findings are specific to the environment, geometry, experimental parameters and redox chemistry employed in this work.

7.1.2 Chapter 4

The second question, outlined earlier, regarding the possibility of synthesising a high performing carbon-based bifunctional oxygen catalyst was a challenging one. A ZIF-based material was used to develop a catalyst that had more functionality than expected. Synthesis optimisation was carried out in an alkaline environment as it is widely known that NC catalysts perform more effectively towards ORR in non-acidic, non-oxidising environments.

- Synthesis optimisation showed, using a bifunctionality metric which places more importance on the performance in the ORR, that the optimal pyrolysis conditions are to heat at 900 °C for both the heating steps.
- Physical characterisation, via techniques such as electron microscopy and XRD, show the resulting electrocatalyst morphology contains large cobalt agglomerates that act as docking particles for smaller iridium nanoparticles.
- XPS shows high relative concentrations of pyrrolic and graphitic N-sites that contribute to explaining the high ORR activity in base.

- XAS is used to estimate the relative Ir-site character. Tentatively, this is shown to have a c.a. five to one – nanoparticle to single atom – iridium distribution which, given the available information, seems reasonable.
- Activity information available on RDE is limited (due to the innate limitations of the technique) however Ir_NC_900_900 shows the most reliable oxygen activity in basic conditions (additionally shown by chronoamperometry). In acidic conditions, very high but fleeting performance is observed towards the OER.
- Proof of concept HOR / HER RDE tests were carried out and considered to have sufficient activity to be tested at device level (Chapter 5).
- ICP-MS measurements can misrepresent mass activity data, especially those involving iridium-containing catalysts. Improved methods of iridium extraction should be developed or at least a week-long heating step must be included during sample preparation.

The original question asked if it were possible to develop an inexpensive, high-performing carbon based bifunctional oxygen catalyst. This work has not produced such a catalyst, however the chapter explored interesting tangential avenues down which (a) interesting metallic geometries are discovered; (b) moderate levels of activity across the pH range are achieved; and, (c) the catalysts is active and fairly durable towards both hydrogen and oxygen fundamental reactions. Clearly, iridium – a PGM – is used and deposited on the catalysts in a 'non-single-atom' manner therefore the electrocatalyst cost is likely to be relatively high.

7.1.3 Chapter 5

The aims of Chapter 5 were two-fold. Firstly, to demonstrate use of the electrocatalyst (developed in Chapter 4) in electrochemical devices at different pHs and, secondly, to explore the new electrolyte environment and operating regime with respect to the microstructure-performance findings (from Chapter 3). There has been mixed success in answering this two-pronged question or achieving the objectives set out in the chapter.

- It is essential to optimise the layer in a FC system in order to ensure good catalyst contact, membrane, ionomer composition enabling proper transport of electrolyte through the electrode. Only once these catalyst / layer engineering features are optimised should the catalyst ability be assessed.

- Compared to Nafion, the anion exchange polymer used in the AEMFC is not understood.
- PEMFC results display broadly good performance with an urgent need to modify the catalyst layer and test the catalyst durability.
- While the performance parameters measured for the Mn-H_2 system were not the same, it is clear that the carbon cloth electrodes were the best performing electrode materials – exceeding the performance of the (more commonly used) felts.
- Considering the volumetric energy density (i.e. including the through-plane dimension in the electrode materials) carbon cloth electrodes have extremely promising performance abilities (as shown in Chapter 3) as a result of their periodic, woven structure.

With respect to the question, the electrocatalyst developed showed moderate to good performance in a PEMFC but poor performance in an AEMFC. So, no, this work has not demonstrated a catalyst with high performance. In terms of making the catalyst perform bifunctionally in a device, the Mn-H_2 cycling data shown using the catalyst implies that, yes, this catalyst was used bifunctionally in an hRFB – but only in acidic conditions for the hydrogen reaction.

7.1.4 Chapter 6

The final question asked if there was a way of understanding the manganese speciation more thoroughly. As outlined in the chapter itself, analysis of the electrolyte is difficult because any manipulation of concentration is expected to change the equilibria and therefore the form of the species. However, two in-operando analytical techniques have allowed measurement of chemical speciation and to evaluate how the electrolyte evolves chemically and electrochemically with time without dilution or altering the solution equilibria in any way. Again, this chapter is a work in progress, but the following are the conclusions reached so far.

- This Mn/H_2 hRFB is able to reach overcharge without damaging its long term durability as a result of its unique solution phase speciation behaviour involving the formation of solids and the unknown role of Ti^{4+} additive.
- A step in voltage efficiency after reaching a high state of charge is observed and this is tentatively attributed to some form of solid electrocatalytic coating on the carbon

electrode fibres (on initial inspection, solids have been observed on the fibres of the electrodes, but this is yet to be comprehensively assessed).

- UV-vis measurements utilise the absorption coefficients associated with Mn^{3+} to provide an estimate of the concentration of oxidised species during the charge and, additionally, confirm solution phase bulk precipitation at a certain SOC (or after a certain length of time).
- A flow-EPR in-operando design enabled the real-time measurement of Mn^{2+} in solution as a result of its paramagnetism.
- Accurate Mn^{2+} concentration measurements demonstrate that Mn^{2+} never reaches zero concentration (with the current densities tested), inferring that Mn^{2+} is regenerated during charging, which, during can only be as a result of chemical disproportionation processes leading to a Mn^{4+} species, as expected from the thermodynamics of Mn^{3+} in these acidic environments.
- Mn^{2+} concentrations alongside coulomb tracking allows for the concentrations of manganese species with higher oxidation states (Mn^{3+} and Mn^{4+}) to be inferred.
- Mn^{2+} concentration transients at high SOCs demonstrate the ability to extract the mixing time of the in-operando setup revealing the production of Mn^{2+} in an, unexpected, 1st order process.
- No conclusions about potential transients have been reached though they are briefly discussed in the chapter, inferring the probable interference of other redox processes (involving solid species).

These in-operando techniques, alongside thermodynamic speciation calculations, have provided a deeper understanding of the processes occurring in the solution. The next section discusses how these learnings can inform future steps towards a more complete understanding of the components of these electrochemical devices.

7.2 Future work

Given all the specific future work items are mentioned in their respective chapters, this section will summarise the main future work directions with respect to the three overarching themes inferred in the title of this thesis.

7.2.1 Electrode development

Given it was concluded that permeability was the best indicator of electrode performance in a RFB dominated by convective transport, this correlation should be tested for its robustness. These carbon cloth electrode materials should be tested varying their weave pattern, compression and accompanying electrolyte.

More regular use of cloth electrodes is to be tested with the Mn/H_2 hRFB to see if these electrodes can with stand long term durability tests and perform as well as the graphite felt electrodes. Additionally, sputter coating an electrode with a potentially electrocatalytic metal may reveal information about the active site of the asserted electrocatalyst that nucleates and then grows on the electrodes' fibres.

7.2.2 Electrocatalyst development

Future direction with this electrocatalyst is two-fold – firstly, at a synthetic level, improvements in understanding the catalyst active site (N centres or the Ir-Co complex) are important as well as further reducing the iridium concentration involved in the synthesis step; and, secondly: further device level testing.

The active site can be further inspected using floating electrode techniques developed within this group – it is considered an important step to establish the surface area of these electrodes with nitrite stripping revealing the electrochemical surface area (ECSA). These measurements will reveal more information about the catalyst capability.

Device-level capability needs to be more thoroughly tested too. Catalyst interaction with anion exchange polymers is of interest in developing electrodes that perform better in FC devices. Further than this, though, testing this catalyst in a water electrolyser and towards CO_2 reduction would be interesting.

Deep investigation of the catalytic behaviour of the solid material that hypothetically forms in the Mn/H_2 hRFB is to be investigated using different MnO_2 polymorphs as a starting point – this is the subject of ongoing work in the Kucernak research group in collaboration with RFC Power.

7.2.3 Electrolyte development

The central electrolyte discussed in this work is that of the titanium-containing manganese electrolyte in the Mn/H_2 hRFB. Significant efforts to understand this chemical equilibria are currently being carried out in the Kucernak group alongside RFC Power. The specific avenues that need to be explored are numerous. The identity of the solids species that form in electrolyte during charging and how they age over time is of significant interest. Isolating these solids is challenging but may eventually be achieved by some kind of filtration technique or in-operando DLS experiment. Some way of understanding the interaction between manganese and the titanium species in solution should also be tackled, this is difficult though without changing the equilibria

At a solution level, relative concentrations of Ti:Mn:S should be altered to see how the bulk electrolyte behaves differently. Of course, thermodynamic calculations outline what is thermodynamically possible and this is extremely useful, but there is no substitute for actual testing.

There is still a large amount of uncertainty about potential and how what species affect it – this is particularly evident in the transient measurements. One of the plights associated with the capture of kinetic parameters at an RDE is due to the deposition / nucleation of solid species on the RDE tip prohibiting the observation of purely solution-phase species. However, this may be a good place to start in terms of understanding how the solid species evolve over time in convective conditions.

| END |